Springer Series in Materials Science 224

Lynnette D. Madsen
Erik B. Svedberg *Editors*

Materials Research for Manufacturing

An Industrial Perspective of Turning Materials into New Products

Springer

Springer Series in Materials Science

Volume 224

The Springer Series in Materials Science covers the complete spectrum of materials physics, including fundamental principles, physical properties, materials theory and design. Recognizing the increasing importance of materials science in future device technologies, the book titles in this series reflect the state-of-the-art in understanding and controlling the structure and properties of all important classes of materials.

More information about this series at http://www.springer.com/series/856

Lynnette D. Madsen · Erik B. Svedberg
Editors

Materials Research for Manufacturing

An Industrial Perspective of Turning Materials into New Products

Springer

Editors
Lynnette D. Madsen
Svedberg Science, Inc.
Falls Church, VA
USA

Erik B. Svedberg
Svedberg Science, Inc.
Falls Church, VA
USA

ISSN 0933-033X ISSN 2196-2812 (electronic)
Springer Series in Materials Science
ISBN 978-3-319-23418-2 ISBN 978-3-319-23419-9 (eBook)
DOI 10.1007/978-3-319-23419-9

Library of Congress Control Number: 2015951368

Springer Cham Heidelberg New York Dordrecht London

Printed on acid-free paper

Springer International Publishing AG Switzerland is part of Springer Science+Business Media (www.springer.com)

This book is dedicated to our parents: Dawn and David Madsen, and Kerstin and Karl-Erik Svedberg.

Foreword

Economic forces and technological evolution have changed the way we conceive, design, make, distribute, and support products and services. Manufacturing today is regarded as only a part, albeit a critically important one, of the entire value chain from R&D to delivered products and services. Businesses, therefore, focus on this entire system to ensure the value they create cannot be easily replaced. Global competition from low labor cost countries has challenged corporations in the developed world, to reimagine how manufacturing is done so they can compete effectively. I commend the editors of this book for the timely views on manufacturing from different companies, both large and small, that they succeeded in putting together. In this tough economic climate, the tenacity of the editors in persuading companies to get their leaders to contribute valuable chapters with key learnings is a significant achievement.

The companies in this volume, all leaders in their field, range from small companies (with fewer than 500 employees) to international conglomerates:

American Process, Inc.
American Superconductor (AMSC)
Catalytic Materials, LLC
Corning, Inc.
Dow Chemical Company
General Electric Corp.
Kemet Corp.
IRradiance Glass, Inc.
Procter & Gamble Company
Trans-Tech, Inc.
The book covers a wide range of topics including:

- low cost processing of nanocellulose that is incorporated into plastics,
- modeling plastics at the molecular level for consumer products,
- light-weight polymer matrix composite (PMC) fan blades for aircraft engines,
- capacitors that work in extreme environments with military reliability,

- production of second generation high temperature superconducting wire,
- high purity graphene nanofibers for advanced energy storage devices and chemical processes,
- reverse osmosis and the manufacturing of ultrafiltration membranes for water purification,
- ceramic matrix composites (CMCs) for aircraft engines and industrial gas turbines,
- production of batteries that operate efficiently,
- microwave dielectrics for commercial and military applications,
- advanced chalcogenide glasses for infrared optics, and
- glass and ceramic component-level technical products.

More importantly, insight into the thought processes underlying the development and advanced manufacturing of new products is revealed, and an explanation of anticipated future needs is provided.

After more than three decades of working at DuPont in various roles, including as Vice President of Central Research and Development and subsequently as Senior Vice President and Chief Science and Technology Officer, I can heartily recommend this book. Naturally, students and professors in science, engineering, and manufacturing will find benefit in the book as it provides real case studies extending well beyond the fundamentals often taught in academia. Deans of engineering, technology and science will find the concluding sections of the chapters that focus on outstanding challenges and future needs, to be particularly worthwhile. The excerpt below highlights a challenge (beyond the technical realm) that curricula need to address:

> *"For years, the main players in microwave magnetics were in the United States, Japan, and France and in microwave dielectrics in the United States, United Kingdom, Japan, and somewhat in South Korea. However, in the last few years several companies have appeared in China producing both microwave magnetic and dielectric materials. These companies are a serious threat to the established players."*
>
> *—Trans-Tech*

Most graduates will find employment in industry; but do students envision their future there? This excerpt highlights the needs for skills and talent:

> *"We will continue to need people with backgrounds in physics (particularly optical physics), chemistry, materials science (especially glass science, ceramics, and polymer science), biological sciences, math, and computer science. We also need people who can take inventions and make them into practical embodiments that can actually be manufactured, so people from the same industrial sectors but with engineering backgrounds are especially important."*
>
> *—Corning*

> *"A strong background in chemistry and physics of materials and processes, keen analytical abilities and an aptitude for problem solving are highly desirable."*
>
> *—KEMET*

"Professionals with chemical engineering and materials science expertise will be at the top of the list along with personnel who have experience in the marketing and sales area."
—Catalytic Materials

"New and experienced practitioners in this field must be able to integrate computational approaches with experimental design and results to drive the development of truly predictive materials models."
—Proctor and Gamble

I also believe that many researchers, manufacturing experts, and executives in industry will enjoy and learn from the book because of its real manufacturing examples and hold it as a valuable resource. Perhaps they will want to be included in any future volumes to further demystify manufacturing today, tell their stories and attract new hires.

Overall, this book, with its contributions from industry, is a gem. Clearly, the two co-editors, Drs. Lynnette Madsen and Erik Svedberg, were well-suited to take this on—Lynnette has more than a dozen years of experience as a Program Director at the National Science Foundation in the Division of Materials Research plus early in her career, she worked at a large company for a decade. Erik on the other hand, has six years of experience at a large company and two years at a small company; he has served as a Senior Program Officer at The National Academies for the National Materials and Manufacturing Board for the past seven years.

We are fortunate to have such a collection to read—I hope you enjoy it! Additionally, this book comes at an excellent time in the United States—at a point when we are seeing signs of a revival in manufacturing.

Uma Chowdhry Ph.D.
Member, National Academy of Engineering
Senior Vice President and Chief Science and
Technology Officer Emeritus
E. I. du Pont de Nemours and Company

Preface

The genesis of this volume came about when Lynnette was approached by the publisher to edit a book. The ensuing discussion between us led away from the publisher's original suggestion to an idea that is a truly exciting one, to provide the reader with real-world examples on how new materials can play a key difference in our future and how those materials actually become part of a product. To many people it is unclear what is actually involved in this process. It might appear that a material expert gets an idea and moments later, there is a new product taking advantage of this improved material. This scenario is very far from the truth so much so that it forms part of the motivation for this book. In reality, the effort and the large number of iterations before an idea becomes a new product is not only significant but also very exciting, in essence, a story worth telling. This book is not printed as a collection of material that was already partially presented or described elsewhere that was simply in search for a home. Rather, each chapter was specifically tailored and written in the past year for this book "Materials Research for Manufacturing: An Industrial Perspective of Turning Materials into New Products" by materials scientists and engineers actively working in industry. To our knowledge there are very few comprehensive examples (or indeed collections of examples) published about working industrial processes where one can learn about the latest developments.

First and foremost, this book with its collection of edited chapters is written with the reader in mind; a reader that has asked her-/him-self exactly what has to happen in order to turn materials into new products in today's industrial setting. This concept we felt should not be conveyed by academics, university researchers at the leading edge of materials research; rather, it should be written by the very materials experts working everyday at the industrial forefront. That said, universities are where the future materials scientists are created and as such, these universities and the materials research carried out there play a key role.

It is our hope that this book will be read by new and soon-to-be university and college graduates who will next turn their focus to industry and who are ready to address today's challenges. As well, we believe that the book will interest industry

researchers in related fields and professors who are teaching advanced courses in manufacturing. Materials science and engineering is a very interdisciplinary field—it draws on knowledge from many disciplines (including physics, chemistry, and other branches of engineering). Through studying these current examples of today's production processes, we expect that the readers will gain insights that help them to address other problems.

During the development of new materials to solve manufacturing problems, unexpected results emerge that have the potential to make further improvements in a product or enable completely new products. We believe that discoveries during the process of introducing new materials during manufacturing serve as key pillars of innovation that drives progress. As Lynnette and I talked about our image of the ideal book, it was clear that both large well-established companies with a long history of new materials and products should be sharing their examples alongside smaller more recently established companies. The thought processes of these two groups are identical in some respects, but differ in other ways, mainly due to the research capabilities in-house and the subsequent motivation to reach out to universities. We also wanted the book to deal with new and emerging areas such as graphene and the usage of nanocellulose. We wanted to explore recent materials progress made in well-known areas such as glass, superconductivity, and composites, and examine how modeling of materials were incorporated into such processes. The book also introduces the chapter authors that worked on these materials (with both their photographs and biographies) with the hope that it might inspire more to join the ranks in any future volumes.

In closing, I would like to specially thank:

- Dr. Lynnette Madsen, without her dedicated partnership, this book would have never been written.
- Dr. Jan-Eric Sundgren at Volvo Group, the one that truly introduced me to materials science and spent years guiding and encouraging me in my research and for the book's Afterword.
- Prof. Clive Randall at Penn State University for putting us in touch with people at KEMET Electronics.
- Prof. Bridget Rogers at Vanderbilt University, School of Engineering, for her encouragement with the book and for the many exciting discussions on materials science that brought me closer to manufacturing.
- Dr. Uma Chowdhry for the book's Foreword.
- All the chapter authors for their contributions.

Happy reading—enjoy!

Falls Church, Virginia Erik B. Svedberg

Contents

Introduction

In total, there are ten company chapters in this book. Each is distinct; however, they have some common features—in turn, they explain the relevant background in some detail, each describes their recent developments at their company in terms of manufacturing, and finally they give some insight into future challenges.

Chapter 1 titled "Designing a New Future with Glass and Optics" by *Corning, Inc.*, a large company, presents three distinct products: (i) Gorilla® Glass for touch-enabled glass displays, (ii) Epic® Sensors used for label-free optical sensing of drug-target interactions, and (iii) Clearcurve® and a discussion of bend-insensitive and bend-resistant multimode optical fibers. As well, Corning clearly describes the educational background, skills, and talents needed at their company.

Chapter 2 titled "Technology Transfer from University to Industry" by *IRradiance Glass*, Inc., contrasts to the first chapter. Although they also work with glass, specifically they deal with the design and production of infrared-transparent chalcogenide glasses, but their approach is quite different because they are a small company. They describe their technology for the selective formation of nanocrystals in glass that allows the creation of chalcogenide glass lenses with advanced optical functionality. As well, they provide an overview of the current legal and institutional status of technology transfer processes and tell the reader how these issues impact commercial development process.

Chapter 3 titled "Selected Applications of Ceramics and Composite Materials" is written by *General Electric (GE)*. This chapter describes three manufacturing innovations: (1) the oldest, the development of ceramic matrix composites, a materials technology now used in aircraft engines and industrial gas turbines, (2) the industrial development at GE of a polymer matrix composite that is light-weight fan blades for aircraft engines, (3) sodium-metal (NaMx) Durathon™ batteries that are based on a nickel-sodium chloride chemistry that rely heavily on ceramics for their efficient operation, which began production most recently (around 2012). The chapter authors also delve into future needs, and the tools needed for producibility and design.

Chapter 4 titled "Breakthroughs in Capacitor Technology" was written by *KEMET Electronics*, a relatively new company (formed in 1990) and another small company. The production volume of capacitors today exceeds two trillion pieces per year and as such accounts for the majority of the parts mounted on almost any printed circuit board in any application. In this chapter the high temperature need for future capacitors are discussed together with modeling and accelerated life testing. The chapter also looks at the paradigm shift in high reliability capacitors and discusses military and space applications as well as testing and other challenges for the research community. This chapter and the next two have a common aspect: rare earth elements. KEMET's goal is to reduce rare earth elements and to eliminate all Pb.

Chapter 5 titled "Second Generation Superconductor Wire—From Research to Power Grid Applications" is written by *American Superconductor (AMSC)*. Superconductors have a long history; they were discovered in 1911 (by Dutch physicist Heike Kamerlingh Onnes, who subsequently won the Nobel Prize in 1913). In 1972, the Nobel Prize in Physics was awarded jointly to John Bardeen, Leon N. Cooper, and John R. Schrieffer "for their jointly developed theory of superconductivity, usually called the BCS-theory."[1] A year later, the Nobel Prize in Physics was split between Leo Esaki and Ivar Giaever "for their experimental discoveries regarding tunneling phenomena in semiconductors and superconductors, respectively" and Brian D. Josephson "for his theoretical predictions of the properties of a supercurrent through a tunnel barrier, in particular those phenomena which are generally known as the Josephson effects."[2] More than a decade later (in 1986), J. Georg Bednorz and K. Alexander Müller discovered the so-called high temperature superconductors and in 1987 shared the Nobel Prize in Physics[3]; concurrently, the company, AMSC was founded. These cuprate-perovskite ceramic materials have a critical temperature above 90 K, a temperature 12 °C higher than previously known, and as a result an explosive amount of work was undertaken across hundreds of laboratories around the world. First generation materials were based on the subsequently newly discovered bismuth-based ceramics. Second generation materials are rare earth-based $Ba_2Cu_3O_{7-\delta}$ materials. They operate at higher temperatures with higher background magnetic fields (today efforts are focused at reducing the effective wire cost). This chapter examines how the material is designed to be effective in fault current limiters and cable projects around the world.

Chapter 6 titled "Perspectives on the Development Process for New Microwave Dielectric and Magnetic Ceramics" is presented by *Trans-Tech*. This chapter describes three different drivers for the development of materials and the procedure followed with examples in the wireless infrastructure domain. It also describes the technology trends necessitating further development, and the critical materials

[1] http://www.nobelprize.org/nobel_prizes/physics/laureates/1972/, accessed April 7, 2015.
[2] http://www.nobelprize.org/nobel_prizes/physics/laureates/1973/, accessed April 7, 2015.
[3] http://www.nobelprize.org/nobel_prizes/physics/laureates/1987/, accessed April 7, 2015.

issues that arise with respect to tantalum replacements. It includes a description of their efforts in magnetic materials. This chapter includes a section on critical materials (incl. rare earth elements) specifically describing the availability and cost fluctuations in raw materials and how that affects materials design.

Chapter 7 titled "Graphene Nanofibers—from Research to Manufacture" comes from *Catalytic Materials*, another small company formed in 1995. There has been a flurry of C-related work in recent years—carbon nanotubes, fullerenes or bucky balls, single-crystal silicon carbide, and now graphene. Although graphite oxide has been known for more than century, the recognition of graphene, a single layer from graphite packed in hexagonal pattern, is rather new. Looking back, there was a 2002 patent application[4] and in 2004 Andre Geim and Konstantin Novoselov were credited with demonstrating that a single layer could be produced.[5] Subsequently, the 2010 Nobel Prize in Physics was awarded to them "for groundbreaking experiments regarding the 2D material graphene."[6] This chapter looks at the cost of producing graphene fibers on a commercial scale and its use as a catalyst, a battery, and as a fuel cell material. Traditional production starting with graphite is too expensive based on the required processing steps. The key breakthrough in the process has been the design of a catalyst system that is capable of generating high purity graphene nanofibers from a different source material.

Chapter 8 titled "Materials Science Contributions to Membrane Production" deals with *Dow Chemical's* work. Over the years membrane developers have looked for ways to manufacture higher flux and higher rejection membranes, and there has been significant effort focused on novel membrane materials. In this chapter reverse osmosis membranes and ultrafiltration membranes are described as well as modules, challenges, recent developments, impact areas, and the unmet needs that help to define research opportunities.

Chapter 9 titled "Production of Low Cost Nanocellulose for Renewable, Advanced Materials Applications" by *American Process*, picks up nicely from Dow's chapter. Nanocellulose has a strong sustainability profile (because it is abundant in nature, renewable and green), the development of this material is rather new (since ca. 1980), and it is being hailed as the *new plastic*. Derived from a biomass, it is not only renewable, but also biodegradable and can be incorporated into many different products. For example, the novel hydrophobic lignin-coated variety of nanocellulose can be incorporated into plastics, which overcomes a well-known barrier to commercial utilization of nanocellulose. However, as mentioned in this chapter, several challenges for large-scale production remain such as

[4]United States Patent: 7071258, "Nano-scaled graphene plates", Filed: October 21, 2002, http://patft.uspto.gov/netacgi/nph-Parser?Sect2=PTO1&Sect2=HITOFF&p=1&u=%2Fnetahtml%2FPTO%2Fsearch-bool.html&r=1&f=G&l=50&d=PALL&RefSrch=yes&Query=PN%2F7071258.

[5]K. S. Novoselov, A. K. Geim, S. V. Morozov, D. Jiang, Y. Zhang, S. V. Dubonos, I. V. Grigorieva, A. A. Firsov, "Electric Field Effect in Atomically Thin Carbon Films", Science 306, 666–669 (2004).

[6]http://www.nobelprize.org/nobel_prizes/physics/laureates/2010/press.html, accessed April 7, 2015.

drying nanocellulose suspensions in an economical fashion, establishing standards for entire supply chain, and determining or developing high-throughput, low-cost process and product quality control characterization techniques. Nanocellulose has global interest: Russia, Brazil, Canada, United States, China, Democratic Republic of the Congo, and Australia all have more than one million km^2 of forested areas.[7] Although reports show that development of this material is high in several of these countries, large-scale activities are also underway in Norway, Sweden, Finland, United Kingdom, Switzerland, Germany, France, and Israel.[8]

Finally, the last chapter a product of *Procter & Gamble Company* employees deals with "Current State and Future Needs in Materials Modeling." Although the chapter is focused on plastics, the modeling methods can be widely applied across all materials groups. Often years of R&D development effort are spent trying to make improvement or solve problems. This chapter provides an introduction to some of the current challenges in computational material science, design, and modeling and puts it in a context associated with packaged consumer goods. In doing so, they review the tools and methodologies used in modeling and provide insight into how these tools guide development of new materials. They also address general application challenges and describe the critical gaps for moving forward.

[7] http://en.wikipedia.org/wiki/List_of_countries_by_forest_area, accessed May 30, 2015.

[8] E.g., D. Nguyen, Life Cycle Energy Assessment of Wood-Based Nano Fibrillated Cellulose, ESA report no. 2014:5 (2014).

Editors and Contributors

About the Editors

Dr. Lynnette D. Madsen has worked at the National Science Foundation (NSF) as a Program Director since 2000. She has been directly responsible for more than 500 awards totaling $\$155M^{+}$ and co-funding has increased her effective budget by more than 20%. During her tenure, she has grown the Ceramics Program budget from ~ \$6M to ~\$11M annually. She has completed three detail assignments at NSF: one focused on increasing the advancement of women in academic careers, another focused on international efforts with Africa, and third addressed strategic human capital analysis and planning at NSF. She has led new cooperative activities with European researchers; she has been instrumental in forwarding NSF programs and initiatives on manufacturing, nanotechnology, sustainability, education, and diversity; and has an active independent research program. Her research includes epitaxial and pseudomorphic film growth and characterization, combinatorial nanomaterials science applied to perpendicular magnetic recording media, contact formation to silicon carbide, and the characterization of nanoscale graphite intercalation compounds. She held a visiting/adjunct faculty position at Carnegie Mellon University and a faculty position at Linköping University in Sweden where she was promoted to Docent (Associate Professor). Previously she held postdoctoral positions at both Linköping University and the University of Illinois in Urbana-Champaign. Earlier, she spent a decade working in industry at Nortel Networks in Canada. She has enjoyed support from industry (ABB, Siemens and Nortel Networks) for her research and consulting. Her qualifications include a B.A.Sc. and B.A. (University of Waterloo), M.Eng. (Carleton University) and Ph.D. (McMaster University). To date she has published 90 journal, conference and magazine articles; been awarded two patents; and delivered more than 85 invited talks. NSF has recognized her with two Director Awards, nine Performance Awards and an Incentive Award for Timely Program Management. As well, she has received an AVS Excellence in Leadership recognition, Society of Hispanic Professional Engineers Junipero Serra Award, University of Waterloo Professional Achievement

Alumni Medal in Engineering, and Materials Research Society Presentation Award. She is a Fellow of the American Ceramic Society, has served as a panelist for the National Research Council and currently serves as an Advisory Board Member for the Rosalind Franklin Society.

Dr. Erik B. Svedberg is currently the Senior Program Officer of the National Materials and Manufacturing Board at the U.S. National Academies. In this role, he works with experts from across the nation to develop, negotiate, and oversee scientific and technical advisory studies for federal agencies related to questions of materials science, manufacturing and engineering design. His previous and current activities at the National Academies include work as a Study Director for: Materials Needs and R&D Strategy for Future Aerospace Propulsion Systems; Corrosion Research Grand Challenges; Opportunities in Protection Materials; Optics and Photonics, Essential Technologies for Our Nation; Review of the National Nanotechnology Initiative; and Airport Passenger Screening, Backscatter X-Ray Machines. Additionally he engages the community in workshops such as: Big Data in Materials Research and Development; Limited Affordable Low-Volume Manufacturing; Materials and Manufacturing Capabilities for Sustaining Defense Systems; and New and Novel Processes that are on the Verge of Industrial Modernization. Since 2007 he has also run his own company (Svedberg Science, Inc.) dealing with forecasting and analysis in the materials science area. He was awarded both a Masters' degree and Doctorate in Physics from Linköping University in Sweden. He went to Seagate Research as the year 2000 holder of the Welch Scholarship from the International Union for Vacuum Science, Technique and Applications (IUVSTA). He continued working as a Research Staff Member at Seagate and in 2002 he also became a Guest Researcher at NIST. From 2006 to 2008, he worked as a Research Scientist at a small company, DVTI. His performance has been recognized with awards at both Seagate and the National Academies. He has been awarded five federal or industrial research grants, been granted two patents, published over 80 scientific articles, and his work is cited over 800 times.

Contributors to Foreword and Afterword

Dr. Uma Chowdhry is Senior Vice President and Chief Science and Technology Officer, Emeritus, at DuPont; she retired from full duties late in 2010. Her initial education was in physics at Mumbai University (B.S. 1968), followed by a degree in engineering science from California Institute of Technology (M.S. 1970), and a doctorate in materials science from MIT (1976). Her career started at DuPont shortly thereafter where she held positions of increasing responsibility. She was elected as a member of the National Academy of Engineering in 1996 and was appointed to Governing Council in 2012. She was also elected as a member of the American Academy of Arts and Science (2003), elevated to Fellow of the American Ceramic Society (1989), and recipient of several recognitions: Caltech's Distinguished Alumnus Award (2013), Industrial Research Institute (IRI) Medal for DuPont Leadership (2011) and American Chemical Society Award for Leadership in Chemical Research Management (2011). She has been appointed to the Board of Directors, Baxter International (2012), MIT Corporate visiting committee for sponsored Research (2011), Board of LORD Corporation (2010) and the Visiting Committee for Advanced Technologies at NIST (2010).

Dr. Jan-Eric Sundgren is a Senior Adviser to the Chief Executive Officer at Volvo Group Headquarters in Göteborg, Sweden. In 2006, he joined Volvo Group as Executive Vice President; he was promoted to his present position in 2013. His current responsibilities include Volvo Group's research policy and long term university cooperation. Prior to joining the Volvo Group, he was President of Chalmers University of Technology (1998–2006) and before that he served as Secretary General of the Swedish Research Council for engineering science while he was also a Professor in Thin Film Physics at Linköping University. Sundgren holds a Ph.D. in Materials Physics. As a researcher he authored more than 300 scientific papers and ranked as one of the most cited researchers in materials science (in an analysis covering papers from 1981 to 2008). He is a member of the Swedish Royal Academy of Engineering Sciences, a Fellow of the American Vacuum Society and received the AVS John Thornton Memorial Award. He is currently chairman of the board for the Swedish Technical Research Institute, a board member of the software company Hogia AB and a board member of the European Research and Innovation area board (ERIAB) at the EU commission. He is chairing the Business Europe Working group for Research and Innovation strategies, and chairing the associate group of the European Round Table of Industrialists.

Other Contributors

Dr. R. Terry K. Baker is currently Vice President for Research and Development at Catalytic Materials LLC, a company he co-founded in 1995. His role has been the generation and development of novel technologies in the area of catalysis and carbon nanomaterials and their applications. For over four decades Dr. Baker has been involved in research. He joined the Atomic Energy Research Establishment, Harwell, Oxford, U.K. as Senior Scientific Officer/Group Leader in 1968. In 1975 he moved to the Corporate Research Laboratories, Exxon Research and Engineering Co., Clinton, New Jersey reaching the position of Senior Research Associate. He became Professor, at the Department of Chemical Engineering, Auburn University, in 1986, later moved to the Materials Research Laboratory, The Pennsylvania State University in 1992 and subsequently joined the Department of Chemistry, Northeastern University, Boston, MA 1996. In 2001, he decided to devote all his efforts to his own company, Catalytic Materials LLC.

His innovative mind has led to numerous breakthroughs including the marriage of catalysis and carbon research that resulted in the development of the landmark mechanism for the formation of carbon nanomaterials. He pioneered the use of controlled atmosphere transmission electron microscopy and was the first researcher to directly observe a catalyst particle in action. With over 45 patents, 250 papers, 6 books edited, over 66 plenary lectures as well as over 200 invited scientific presentations, and he has demonstrated his invaluable worth as leader of research. He has been engaged in the design and development of systems for the large-scale manufacture of the most advanced carbon nanomaterials. He has led Catalytic Materials LLC along the pathway to acquire the most comprehensive portfolio of patents for a wide set of applications. His work has been recognized by the following awards. American Carbon Society George D. Graffin Lecturer (1985), American Carbon Society Charles E. Pettinos Award (1987), Hougen Visiting Professor, University of Wisconsin, Madison (1988). Light Metal Award Winner of the Minerals, Metals and Materials Society (TMS) 1993, Distinguished Visiting Professor, Institute of Advanced Material Study, Kyushu University, Fukuoka, Japan, 1993. Winner of the 1995 Pittsburgh–Cleveland Catalysis Award, Winner of the 1998 Catalysis Society of Metropolitan New York Award for Excellence in Catalysis and Fellow of the American Carbon Society, July, 1999.

Dr. Stephan Biller is the Chief Manufacturing Scientist at General Electric. He is responsible for GE's global advanced manufacturing strategy and the development of GE's Brilliant Factory initiative across GE businesses to increase speed and productivity. Prior to being named to this position in April 2012, he was a Technical Fellow and Global Group Manager for Manufacturing Systems at General Motors' R&D. Stephan received a degree in Electrical Engineering from RWTH Aachen, Germany, a Ph.D. in Industrial Engineering and Management Science from Northwestern University, and an MBA from the University of Michigan. He has been serving on the executive advisory boards of the Digital Manufacturing and Design Innovation Institute, America Makes, Northwestern

University, Cambridge University, Georgia Tech Manufacturing Institute, and Rensselaer Polytechnic Institute. He has been granted 10 patents, has developed 22 trade secrets, and co-authored more than 60 peer-reviewed publications.

Dr. Dana C. Bookbinder joined Corning in 1991 after a nine-year career with General Electric, where he co-invented the modification of Lexan® polycarbonate that resulted in the resin used for compact discs. During his career at Corning, Dr. Bookbinder's most significant inventions have been in the areas of Optical Waveguide inorganic compositions, process technology, and surface coatings, Specialty Materials fused silica compositions and processes, Life Sciences polymer surface chemistry and products, and processing technology for the technical ceramics used to produce catalytic convertors and diesel filter substrates. He was a co-inventor of Corning® ClearCurve™ optical fiber, which received the R&D 100 Award and was featured as one of Time magazine's "Best Inventions of the Year." Dr. Bookbinder's success has come from working across research, development and manufacturing groups and implementing technology into commercialization. These efforts have resulted in the generation of a significant number of new products and revenue.

Dr. Bookbinder was the 1999 recipient of the Corning's Stookey Award for Exploratory Research and was appointed to the position of Corporate Fellow in 2007. He has been granted more than 100 patents and has over 40 additional patents pending.

Dr. Bookbinder received a Bachelor of Science in Chemistry from Northern Illinois University in 1978, and was a Dreyfus summer scholar at the University of Chicago in 1977. He received a Ph.D. in Chemistry from the Massachusetts Institute of Technology in 1982 under the direction of Mark Wrighton.

Dr. Gregory S. Corman is a Principal Scientist at GE Global Research. Since joining the organization in 1986, he has worked on various aspects of ceramic matrix composite materials and process development. For the past 24 years his focus has been on the development of melt infiltrated CMCs for gas turbine engine applications. He is a co-inventor of the prepreg melt infiltrated composite system. His efforts have included the development of the prepreg MI CMC process, CMC material characterization and testing, and the design and testing of gas turbine hardware made from this material. He has also conducted research on the development and testing of high temperature fibers for CMC reinforcements. From 1984 to 1986, Dr. Corman was a Staff Scientist at the Westinghouse Electric Corporation Research and Development Center in Pittsburgh, PA. While there Dr. Corman conducted research on the sintering and microstructural control of oxide-based nuclear fuels and on the processing and electrical properties of zinc oxide varistors. He was awarded B.S and Ph.D. degrees in Ceramic Science and Engineering from the Pennsylvania State University in 1979 and 1984, respectively. Dr. Corman is the author of over 20 publications and over 45 technical society presentations, and holds 19 patents related to ceramic composite processing and turbine component fabrication. He is a member of the American Ceramic Society and Keramos.

Dr. Matthew Dejneka joined Corning as a ceramic engineer in the Glass Research group in 1995, after completing his Ph.D. in Ceramic Science and Engineering from Rutgers University. He worked on transparent glass ceramics, display glasses, fiber amplifiers, and new fiberization methods in his early career, eventually co-inventing the tapered fiber laser and fabricating high NA rectangular core Yb3+ doped fibers that broke the 1W barrier of 980 nm single mode output. He is well-known for his work in rare-earth-doped glasses, including brightly fluorescing glasses and microbarcodes. Dr. Dejneka also contributed many new low and negative expansion ceramics for Corning Environmental Technologies. More recently, Dr. Dejneka has been a lead inventor and developer of the Gorilla® family of glasses, inventing both compositions and significant manufacturing innovations. He was a key inventor of Gorilla® Glasses with Native Damage Resistance®, and more recently demonstrated the first fusion formable glass ceramics. Matt received Corning Incorporated' prestigious Stookey Award in 2004 and was elevated to Fellow of the American Ceramic Society in 2012. He holds 34 granted patents and has authored 38 publications.

Dr. Yulin Deng is a full Professor in the School of Chemical and Biomolecular Engineering at Georgia Institute of Technology. He has extensive knowledge and research experience in nanoscience and nanotechnology, biomass conversion, bioenergy, and electric cell technology (solar cell, fuel, supercapacitor). Dr. Deng is a fellow of International Academy of Wood Science. He has published more than 180 peer-reviewed papers and managed many government-sponsored projects, including NSF, DOE, and USDA projects. He has been a co-PI in more than 10 other government-sponsored projects and more than 20 industrial projects. Dr. Deng currently advises six Ph.D. students and six visiting scholars and students. His group recently reported in *Nature Communications* the creation of direct biomass fuel cells that have great potential to directly convert almost all nature biomasses to electricity at low temperature. His research interests include biomass and bioenergy, nanomaterial synthesis, colloid and surface science and engineering, polymer synthesis, and papermaking and paper recycling. Yulin received a B.S. from Northeast Normal University, China and a Ph.D. from Manchester University, United Kingdom.

Dr. Russell DeVane is currently a Scientist in the Corporate R&D Modeling and Simulation (M&S) group at Procter & Gamble. In this role, he works to develop M&S capabilities, applies M&S techniques to address materials needs across business units and provides training in various M&S techniques. His qualifications include a B.S. in Chemistry from Florida Southern College and a Ph.D. in Computational Chemistry from the University of South Florida. Following his graduate work, he was a National Science Foundation Postdoctoral Fellow at the University of Pennsylvania in Michael Klein's group. After postdoctoral work, he joined the Chemistry Department at Temple University as an Assistant Research Professor. In 2011, he joined P&G. To date, he has published over 30 scientific articles and his work is cited over 1000 times.

Dr. Adam J. Ellison is a Corporate Research Fellow. In this role, he maintains and expands Corning's leadership in specialty glasses for a variety of applications, especially high performance display substrate glasses, ion-exchangeable glasses and glass ceramics for a variety of applications. In addition, he is a champion for early-stage research and for identification and management of technical talent. Ellison joined Corning as a senior research scientist in April 1996. Ellison either invented or developed all of Corning-drawn glasses since 1996, including 1737G, EAGLE XG™ glass substrates; Corning Lotus™ Glass for Display Technologies and High Performance Display; and Corning® Gorilla® Glass. As an innovator in materials beyond glass, Ellison has made technical contributions to all Corning businesses, including composition innovations for Corning® DuraTrap® AT; improved batch materials for ultrathin-wall catalytic converter substrates; diffusion-doping systematics for SMF-28 ULL; novel glasses for optics, photonics, and solid-state lasers; and novel growth media for liver hepatocytes. Ellison received a B.A. from Occidental College in 1983, and a Ph.D. in Geological Sciences from Brown University in 1988. He worked as a Postdoctoral Fellow at Princeton University until 1991, and from 1991–1996 worked at Argonne National Laboratory on a variety of materials science topics. He has 40 issued U.S. patents, has roughly that many applications pending, and has had 75 publications in peer-reviewed journals. Corning awarded him the Stookey Award for Exploratory Research in 2007.

Dr. Ye Fang is the Research Director and Research Fellow of the Biochemical Technologies in the Science and Technology Division at Corning Incorporated in New York (NY, USA). He received his B.Sc. in Chemistry from the Hubei University, M.Sc. in Physical Chemistry from the Wuhan University, and Ph.D. in Physical Chemistry from the Institute of Chemistry, Chinese Academy of Sciences, China. Following postdoctoral research at the University of Vermont from 1995 to 1996, and at the Johns Hopkins University School of Medicine from 1996 to 2000, he joined Corning Incorporated as a Senior Research Scientist. He is an editorial board member of *Sensors*, *Current Drug Discovery Technologies*, *Chemical Sensors*, *World Journal of Biological Chemistry*, *Journal of Biochips and Tissue Chips*, and *Journal of Integrated Omics*. He has published one book, one market report, 18 book chapters, and more than 110 journal articles. He holds 24 US granted patents and 66 patent applications. His current research interests are biosensors, biophysics, chemical biology, systems pharmacology, and bioprocessing.

Dr. Luke Franklin is currently an Associate Engineering Manager for Dow Water and Process Solutions. His present work is focused on next generation product development, as well as near term process development for ultrafiltration, reverse osmosis, and nanofiltration technologies. The role affords him the opportunity to leverage his expertise to variety of projects spanning element/module component design, materials selection, process optimization, and mechanical test development. He began his career at Dow Chemical as a Senior Research Engineer in 2011 and

was immediately involved with the design of the newest generation of Dow's UF module, brought to market in 2013 under the IntegraPac™ and IntegraFlo™ trade names. Luke received Ph.D., MS, and BS degrees in Mechanical Engineering from the University of Minnesota, Minneapolis, MN. He has authored or co-authored 10 peer-reviewed papers in diverse fields ranging from filtration to renewable fuels utilization.

Dr. Yuri Freeman received M.S. and Ph. D. in solid-state physics from Kharkov Polytechnic Institute in Ukraine. He worked as Principal Scientist in Russian capacitor industry and later at Vishay Sprague, focusing on high efficiency and high reliability Tantalum and Niobium-based capacitors. Yuri is now Technical Fellow / Vice President at the Tantalum Division of Kemet Electronics. As a visiting Professor he is also teaching *Material Science in Electronic Components* at the Clemson University. Yuri was awarded 39 patents and published more than 40 peer-reviewed papers in the field of science, technology and applications of Tantalum and Niobium-based capacitors.

Dr. Caleb V. Funk is currently a Process Research Scientist for Dow Water & Process Solutions. In this role, he has led a variety of membrane development efforts involving reverse osmosis membrane support and selective layer chemistries, as well as ultrafiltration fiber formulation and spinning. Additionally, he has developed multiple manufacturing process models, supporting both the RO and UF businesses within Dow. In his spare time, he serves the synthetic membrane community on the board of directors of the North American Membrane Society. Before joining Dow in 2008, he obtained his Ph.D. in Chemical Engineering from The University of Texas at Austin, studying microporous polymer membrane formation.

Dr. Sinue Gomez is currently a Development Associate at Corning Incorporated. Previous to her current role, Gomez spent nine years as a scientist in the Glass Research group, after she joined Corning in 2006, where she made significant technical contributions in the area of strengthened glass, glass ceramics, and processes in support of the Corning® Gorilla® Glass business. In 2008, Gomez was recognized as a technical rising start in the Women of Color Technology awards, which recognizes the contributions of women with a diverse ethnic background to the fields of science, technology, engineering and math. She is also an active member and advocate of several diversity groups that concentrate on supporting the growth and value of minorities in the technology community. Gomez received a B. A. from the "Universidad Simon Bolivar" in Caracas-Venezuela in 1998, and a Ph. D. in Materials Science from the University of Connecticut in 2006. She has 17 issued U.S. patents, 24 patent applications, and is the author and co-author of 45 invention disclosures. She has also authored and co-authored 10 internal and 14 external reports.

Dr. Timothy M. Gross has been a Senior Research Associate (Science and Technology) since 2014. Tim joined Corning after earning a Ph.D. in Materials Engineering from Rensselaer Polytechnic Institute in 2008. He is recognized as an expert in fracture mechanics and glass formulation. Tim has authored 12 peer-reviewed technical publications, has filed 34 patent applications, and has been granted six U.S. patents. Tim is the inventor or co-inventor of several iterations of Corning® Gorilla® Glass. Tim received the Stookey Award in 2012, the highest award for exploratory research in the Corning Science and Technology division.

Dr. Abhijit Gurav is the Vice President of Ceramic Technology at KEMET Electronics Corporation, Greenville, SC. He received B.S. and M.S. degrees in Metallurgical Engineering and Materials Science from the Indian Institute of Technology, Mumbai, India, and a Ph.D. degree in Chemical Engineering from the University of New Mexico, Albuquerque, NM. Prior to joining KEMET, he was a Postdoctoral Fellow with the NSF Center for Micro-Engineered Materials at UNM. He has 18 refereed publications and over 75 conference proceeding contributions. His areas of expertise include internal electrode and dielectric materials, processing and reliability of MLCCs, production and characterization of metal and ceramic powders, aerosols, nanomaterials, and electron microscopy.

Dr. Adriaan van Heiningen holds the J. Larcom Ober Chair in the Department of Chemical and Biological Engineering at the University of Maine, Orono, USA. He obtained a B.Sc. in Chemistry, and an Ir. degree in Chemical Engineering at the State University of Groningen in the Netherlands. He has a Ph.D. degree in Chemical Engineering from McGill University, Montreal, Canada. His research interests are in fundamental chemical engineering aspects of wood pulping, pulp bleaching, and recovery of waste pulping chemicals. He is also much involved in the "Integrated Forest Products Refinery" which produces bioenergy and biomaterials besides pulp, paper and wood products.

Dr. Michael D. Hill received his Bachelor of Science (B.S.) degree in Materials Engineering from Virginia Tech in 1986. He received a Master's Degree in Materials Science and Engineering from Virginia Tech in 1988. From 1989 until 1996 he worked at the National Institute of Standards and Technology (NIST), where his work focused on the crystal chemistry of high Tc superconductors and the synthesis of lead-based perovskites. In 1996 he received a Ph.D. in Materials Science and Engineering from the University of Maryland. In 1996, he joined the R&D department of Trans-Tech where his work is focused on new formulations for microwave dielectric and magnetic materials, as well as specialty advanced materials including thermal barrier coatings and solid-oxide fuel cells. In 2007, he was promoted to Technical Director of the R&D group at Trans-Tech and is responsible for developing or overseeing the development of all new formulations at Trans-Tech.

Dr. Mikhail Iakovlev is an R&D Group Leader at American Process Inc. He obtained his D.Sc. (Tech.) degree in Aalto University in 2011. He specializes in chemistry and technology of lignocellulosics conversion into cellulose-based products, biofuels and commodity chemicals. For the past seven years, his research has focused on the AVAP® fractionation process utilizing SO_2-organic solvent-water mixtures. This work has resulted in over 20 peer-reviewed articles.

Jon E. Johnson is a Senior Research Specialist at Dow Water and Process Solutions, where he is the research team leader for Module Design and Materials. His work relates to spiral wound modules for reverse osmosis, and includes the development of new spiral-wound element configurations, the design and testing of structural components, and the modeling and optimization of spacer materials. Areas of special interest include the design of feed spacers for reduced pressure drop, improved mass transfer, and less fouling. He has authored several case studies which describe best practices for pilot testing and side-by-side comparison of commercial reverse osmosis membranes. He is a Mechanical Engineer with degrees from the Colorado School of Mines and the University of Minnesota. Prior to employment with Dow, he worked as a Researcher at the U.S. Bureau of Mines, studying the mass transfer performance of catalytic devices used for particulate oxidation, and as a Process Engineer for Chevron Chemical Company. He has authored more than 20 scientific articles and holds eight patents.

Steven Jons has been involved in membranes research at Dow Chemical for more than 20 years. For 17 of those years, he has been located at the FilmTec site, where Dow's reverse osmosis and nanofiltration membranes and modules are fabricated. In his current position, he is a Technical Advisor to several R&D platforms within Dow Water & Process Solutions and is the focal point for IP issues related to membranes and new technologies. He was the principal chemist responsible for several Dow commercial reverse osmosis and nanofiltration membrane launches. However, his research activities have been varied, focusing at various times on ultrafiltration and reverse osmosis membrane formation, membrane and element test methods, element fabrication, and system performance prediction. He is listed as an inventor on 27 patent applications.

Dr. Ming-Jun Li joined Corning in 1991 and is currently a Corning Fellow. He has been a key inventor and contributor to many telecom and specialty fibers including bend-insensitive ClearCurve® optical fiber for FTTH, which received the R&D 100 Award and was featured as one of Time magazine's "Best Inventions of the Year", LEAF® fiber, which won four industrial awards and was deployed with more than 30 million of kilometers of fiber in long haul networks, ultra-low PMD fiber and low loss fiber for high data rate transmission, low SBS fiber for analog signal transmission, high bandwidth multimode fiber for data centers, various specialty fibers for use in connectors, fiber lasers, sensors and endoscopes, and recently new multicore fibers and few mode fibers for future space division multiplexing. His research efforts have resulted in the generation of a significant number of new products and revenue. Dr. Li received the 1988 French National

Prize on Guidedwave Optics for his work on Cerenkov second harmonic generation, the 2005 Stookey Award for exploratory research at Corning Incorporated, and the 2008 Northeast Regional Industrial Innovation Award from American Chemical Society. He is a Fellow of Optical Society of America and a Senior Member of the IEEE Photonics Society. He is currently serving as Deputy Editor (2012-present), and has served as Coordinating Committee Member (2008−2012), and Associate Editor (1999−2005) of the Journal of Lightwave Technology. He has also served as a Guest Editor for the special issue on Optical Fiber Nanotechnology of Nanophotonics (2013), Technical Committee Member for OECC (2013), Steering Committee Chair for ACP (2011-present), IEEE Photonics Conference Technical Committee Member (2012-present), Guest Editor for the special issue on Microstructured Fibers of Journal of Lightwave Technology (2007), OFC Technical Committee Member (2004−2007), CLEO Technical Committee Member (2007−2011), LEOS Winter Topic Meeting Technical Committee Member (2007), APOS Technical Committee Member (2010-present), Program Chair for OECC (2009), General Chair for ACP (2010), Program Chair for ACP (2009), APOC Subcommittee one Chair (2007−2008), APOC Technical Committee Member (2004−2006), ITCom Technical Committee Member (2002−2006). Dr. Li holds 104 U.S. patents and has published three book chapters and authored and co-authored over 200 technical papers in journals and conferences. Dr. Li received a B.Sc. degree in Applied Physics from the Beijing Institute of Technology, Beijing, China, in 1983, a M.Sc. degree in Optics and Signal Processing from University of Franche-Comté, Besancon, France, in 1985, and a Ph.D. degree in Physics from University of Nice, Nice, France, in 1988.

Dr. Krishan L. Luthra is currently the Chief Scientist for the Manufacturing, Chemical and Materials Technologies at GE Global Research in Niskayuna, NY. He got his Ph.D. in Metallurgy and Materials Science from the University of Pennsylvania in 1976. Since then he has been at GE Global Research, head quartered in Niskayuna, NY, USA, where he has had a variety of technical and management roles over the years. He is well recognized for his work on high temperature thermochemistry, oxidation of high temperature materials, and ceramic matrix composites. He has been involved in the development of SiC/SiC composites at Global Research from its inception over 25 years ago. He is co-inventor of GE's melt infiltrated SiC/SiC composites to be commercialized for GE Aircraft Engines starting in 2016. He has presented over 100 talks at conferences, has authored over 100 technical papers, and has 36 patents based on his research activities. He is a Fellow of the American Ceramic Society. He is also the recipient of the Coolidge Fellow award at GE Global Research, the highest honor accorded to a scientist and engineer at GE Global Research.

Jennifer McKinley is the Chief Financial Officer of IRradiance Glass, Inc. She holds a B.S. degree in Chemistry and an M.S. in Materials Science and Engineering from the University of Central Florida. Her professional work includes three years of academic research experience studying oxide and chalcogenide glasses at the

University's Center for Research and Education in Optics and Lasers (CREOL) and five years of industrial experience in materials characterization at Lucent Technologies/Agere Systems, supporting semiconductor manufacturing and research. She was co-founder and CFO of NanoSpective, Inc., a materials analysis company that specializes in providing scientific evidence for patent infringement cases, for nine years. She is a co-author on several publications, is named on two patents and has presented at numerous national and international conferences.

Dr. Arie Mulyadi is a doctoral student in Dr. Yulin Deng's research group in the School of Chemical and Biomolecular Engineering at Georgia Institute of Technology. His current research interest is in the area of cellulose nanofibrils surface modification utilizing chemical treatment. He is expected to graduate in 2016 and currently lives in Atlanta. Arie received a B.S. in Chemical Engineering from University of Wisconsin-Madison in 2011.

Dr. Bruce Murch has been leading the Computational Chemistry section in Corporate Modeling and Simulation Global Capability Organization at Procter and Gamble since 2004. We lead the development of capabilities to drive the design and development of materials and formulations for formulated and assembled products. We focus on developing methods for the assessment of product performance and stability properties based on molecular-level assessment of complex compositions and materials. Dr. Murch received his Ph.D. in Inorganic Chemistry from Cornell University in 1987, and has received over 30 patents during his career at P&G.

Dr. J. David Musgraves is the President and CEO of IRradiance Glass, Inc. He was formerly a Research Assistant Professor at Clemson University studying infrared-transparent glasses. The group's research focused on the development and characterization of glasses for bulk, thin-film, and fiber applications. His individual research was focused on the integration of quantum computational modeling, optical spectroscopy, and thermal analysis as a means to evaluate the evolution of amorphous structure across multiple length scales and to correlate this emergent structure with material properties.

Dr. Kim Nelson is the Vice President of Nanocellulose Technology Development at American Process Inc. Ms. Nelson holds a Ph.D. in Chemical Engineering from the Georgia Institute of Technology, an M.S. in Pulp and Paper Engineering from the Institute of Paper Science and Technology, and a BA in Mathematics and Chemistry from Agnes Scott College. As part of Dr. Yulin Deng's research group at Georgia Tech, her Ph.D. thesis focused on the synthesis and morphological control of organic and inorganic nanoparticles including nanocellulose. She has published six articles in this field and regularly presents the AVAP® nanocellulose technology at industrial and scientific conferences and workshops. Dr. Nelson is an inventor of one granted patent and 23 pending patent applications in the biorefinery and nanocellulose field. She has experience in mill operations, project management, environmental permitting and regulatory compliance, grant writing, R&D management, innovative technology development, and new product development . Prior

to joining American Process, Dr. Nelson a Pulp Mill Process Engineer with MeadWestvaco. Her interests include, nanocellulose manufacturing, new product development, commercialization, sustainability, biomaterials, biofuels, biomass conversion, process development, and nanotechnology. Dr. Nelson is an active member of the Agenda 2020 Technology Alliance's Cellulosic Nanomaterials Team whose mission is to advance the commercial production and end use of nanocellulose.

Dr. Michael S. Pambianchi is currently Research Director, Glass Research at Corning Incorporated. He has responsibility for Corning's research in glass chemistry and composition. Since starting with Corning in 2000, Mike has held a number of product line and business development roles in telecommunications and advanced optics. Most recently he was Portfolio Manager, Exploratory Markets and Technologies, where he managed a portfolio of new business development efforts, including solid oxide fuel cells, semiconductor lasers, and organic semiconductors. Before joining Corning, Mike was a member of technical staff at Hypres, Inc., where he designed superconducting high speed digital circuits. Mike received his BA in Physics in 1989 from Cornell University, Ph.D. in Physics in 1995 from the University of Maryland, College Park, and MBA in 2000 from Harvard Business School.

Martin Peery is currently the associate R&D Director in the Water and Process Solution group of The Dow Chemical Company. In this role since 2006, he has responsibility for the global Reverse Osmosis (RO) and NanoFiltration (NF) membranes research organization, with groups Edina, MN, USA; Shanghai, China; and Tarragona, Spain. He is accountable for the development and implementation of strategic technology plans which deliver membrane technology solutions to critical industrial and societal water treatment problems. Under his leadership, the RO/NF research organization in Dow has developed several new membrane modules which have greatly reduced the cost of water treatment. This includes the DOW FILMTEC™ ECO membrane module which delivers 40% higher water purity with 30% less energy when compared to standard elements, has received as Dow's second Breakthrough to World Challenges, and has been nominated for the 2014 Edison Award. Martin's career spans 25 years, all of which has been focused on RO/NF membrane and module research with Dow. Martin has a Bachelor's degree in Mechanical Engineering from South Dakota School of Mines and Technology.

Dr. Erik Reed first joined KEMET in 1976 as a Technician in the QA Environmental Test Lab after receiving a BS in Broadcast Engineering from Bob Jones University. While at KEMET he studied Electrical Engineering at Clemson University, receiving a B.S. in 1985, M.S. in 1988, and Ph. D. in 1990. He has also been employed by the Lawrence Livermore National Lab, Clemson University, and NASA's Jet Propulsion Lab. He most recently rejoined KEMET in 2007 to work in

their Advanced Technology Group. Dr. Reed has authored numerous technical papers concerning electromagnetic theory, capacitor performance, and capacitor reliability. He is named inventor or co-inventor in nine patents.

Dr. Theodora Retsina is the CEO of American Process Inc. She received a B.Sc. and Ph.D. in Chemical engineering from Imperial College, University of London and is a licensed professional engineer in the United States. Her career began at Parsons & Whittemore, where she held positions as Project Engineer, Project Manager and Process Manager in various international construction projects. In 1995, she founded American Process—a company that focuses on value enhancement of the forest products industries through process integration and biorefinery technology applications. American Process also provides engineering EPCM and process integration consulting services. This unique blend of experience enables the company to develop technically and financially viable biorefineries. American Process has built one of the first commercial cellulosic biorefineries the Alpena Biorefinery, in Alpena, Michigan, which is currently producing and selling commercial quantities of cellulosic ethanol. Dr. Retsina is an inventor of 12 granted patents and 70 pending patent applications in the biorefinery and nanocellulose field.

Dr. Nelly M. Rodriguez is currently the President of Catalytic Materials LLC. For over three decades Nelly M. Rodriguez has been involved in research in Industrial and Academic Institutions and in recent years been involved in the management of Catalytic Materials LLC. Her interest in carbon nanomaterials has led to several breakthroughs including the determination of the interplay of the crystallographic features of catalyst particle and the physical nature of the resulting material. Using in situ transmission electron microscopy combined with in situ electron diffraction techniques, she was the first researcher to directly characterize the chemical state of the catalyst particle under reaction conditions. Using this approach she also established that graphite forms a bond with phosphorus leading to the formation of a phosphorous structure located at the arm-chair regions of the carbon material. These findings led to the development of a protective treatment for graphite towards attack by various gaseous species. She designed a system for the direct observation of graphite undergoing attack in an atomic oxygen environment. This provided a unique method of simulating the events that occurred when materials were exposed to low earth orbit (LEO) conditions. One of her most valuable contributions has been the development of 3D models of graphene nanofibers, which provided insights into the potential use of these materials for a variety of applications, including Li ion batteries, energy storage media and PEM fuel cells. She has been co-inventor of 28 patents and authored 110 papers as well as giving numerous scientific presentations. She assembled an outstanding team of scientists and has been intimately involved in the design and development of systems that have led to commercial production of both multi-walled carbon nanotubes and graphene nanofibers. She obtained a B.S. Chemistry from Universidad Nacional de Colombia, Bogota, Colombia, 1978 and a Ph.D. Chemistry from the University Of

Newcastle Upon Tyne, United Kingdom, 1986. She worked at Universidad Industrial de Santander, Bucaramanga, Colombia, 1979–1986, Airco Carbon, Niagara Falls, New York (Internal Researcher) 1985 and at the Corporate Research Laboratories, Exxon Research & Engineering Co., Clinton, New Jersey (Researcher) 1985. In 1986, she was an Invited Researcher at Hokkaido University, Sapporo, Japan. In 1986 she joined the Department of Chemical Engineering, Auburn University, Auburn, Alabama as Postdoctoral Research Associate and moved to The Pennsylvania State University, Materials Research Laboratory in 1992 to reach the Associate Professor of Materials. In 1996, she became Associate Professor of Chemistry at the Northeastern University. In 2001, she became engaged full time as President of Catalytic Materials LLC, the company she Co-Founded in 1995.

Dr. Abhishek Roy is currently the technical platform leader for RO membrane chemistry platform in Dow Water and Process Solution. Abhishek did his Ph.D. from Virginia Tech under the guidance of Prof. James E. McGrath on Macromolecular Science and Engineering program. His research was focused on understanding the transport properties of ion containing polymers and to develop novel structure–property relationships to guide next gen research PEM research. Abhishek joined Dow in the RAP program in Core R&D in the year 2008 and conducted research on fouling, 2D HT LC-GPC and on understanding the structure–property relationships of polyolefins and elastomers. He joined DW&PS in 2009 and since then has been involved in fundamental product research for next generation membrane chemistry for reverse osmosis applications. He led the innovation and development of four generations of membrane chemistries which has been translated into several commercial products focusing on reducing energy consumption by 35% and at the same time improving water quality by 40%.

Abhishek has coauthored more than 30 peer-reviewed journal publications (with 700 plus citations), over 25 patent applications filed and received awards from ACS divisions of Fuel chemistry and polymer chemistry. He has been recently selected as the outstanding recent graduate alumnus from College of Science. Credited as the primary inventor for ECO elements, Dr. Abhishek Roy has been declared as the winner of Dow's prestigious Sustainability Innovator Award.

Dr. Martin W. Rupich is currently the Senior Technical Manager of Materials R&D at AMSC in Devens, Massachusetts where he leads the advanced R&D and manufacturing improvements of second generation (2G) high temperature (HTS) superconducting wire. In this role, he has worked closely with experts from national laboratories, universities and government agencies addressing questions related to the material science, manufacturing and engineering aspects of the superconducting wire. He has been a leader in the development of the large-area, solution-based processes for the deposition of epitaxial oxide films in roll-to-roll systems. His work at AMSC also includes the synthesis and characterization of Bi-2223 superconducting powders and the development and manufacture of the first generation Bi-2223/Ag composite superconducting wire. Prior to joining AMSC in

1990, he spent 12 years at EIC Laboratories in Norwood Massachusetts carrying out research and development on alkali metal batteries, methanol fuel cells, Raman spectroscopy, electrochemical sensors, metal oxide film growth, and conductive polymer films. At EIC Laboratories, he was responsible for the development of novel electrochemical and catalytic sensors that formed the foundation for the gas sensor technology developed and marketed as the Gas Sentry by Bascom-Turner Instruments of Norwood, MA. He also worked at New England Nuclear (now Dupont) on the development of commercial generators for the production of ^{99m}Tc isotopes resulting from the decay of a ^{99}Mo isotope and the synthesis of Tc-based compounds utilized for radioactive isotope imaging in medical diagnostic studies. He received his B.S. degree in Chemistry form John Carroll University in 1974 and his Ph.D. degree in Inorganic Chemistry from Northeastern University in 1980. He has authored or co-authored over 100 journal, book and conference articles and holds 39 U.S. Patents. Rupich can be reached at AMSC, 64 Jackson Road, Devens, MA 01434, USA.

Dr. Srivatsan Sathyamurthy is a Senior Scientist at AMSC in Devens, MA, focusing on the research, development and manufacturing of the second generation (2G) high temperature superconducting (HTS) wire. His primary role is developing new and improved processes in the R&D laboratory and transitioning them to the HTS wire manufacturing factory. Prior to joining AMSC in 2008, he was a Research Assistant Professor at the University of Tennessee, and an Adjunct Scientist at Oak Ridge National Laboratory. His particular area of expertise is the solution-based processing of epitaxial oxide films on metal substrates. With over 15 years of experience in materials, and R&D, his research focus includes epitaxial thin films, and functional nanomaterials. He received his B. Tech. in 1993 from Indian Institute of Technology, Chennai, India in Metallurgical Engineering, his MS in 1995, and his Ph.D. in Materials Science and Engineering from the University of Houston in 2000. He has authored/co-authored over a 100 publications, and delivered numerous contributed and invited talks in various conferences. Sathyamurthy can be reached at AMSC, 64 Jackson Road, Devens, MA 01434.

Dr. Jo Anne Shatkin is President of Vireo Advisors, LLC, in Boston, Massachusetts focused on sustainability strategies for new and nanotechnology development and innovation. She has extensive experience in working with entrepreneurs to guide responsible product development and commercialization. She develops state of the art analyses on behalf of public and private organizations to inform safe and sustainable new product development. Dr. Shatkin is an environmental health scientist and recognized expert in environmental science and policy, health risk assessment, emerging substance policy, and environmental aspects of nanotechnology.

Since 2005, Jo Anne has provided leadership on the responsible development of nanotechnology, and on approaches for decision-making under uncertainty. She served as an expert to several international committees on nanotechnology safety, including the joint WHO/FAO Expert Panel on Nanotechnology in Food, the

Canadian Council of Academies, and the US/Russia Bilateral Commission for Science and Technology Nanotechnology Environmental Health and Safety Panel. She pioneered the use of life cycle thinking in risk analysis for nanomaterials, collaborating with the U.S. Environmental Protection Agency to develop several case studies that informed EPA's risk analysis, research agenda and policies for nanomaterials.

Jo Anne developed and uses NANO Life Cycle Risk Analysis to inform safe development strategies for nanomaterials, described in her book, *Nanotechnology Health and Environmental Risks Second Edition* (CRC Press 2012). She is leading efforts to develop methods and standards for environmental health and safety for TAPPI and participates in the US Technical Advisory Group to ANSI on EHS Standards Development for nanocellulose. Jo Anne received an Individually Designed Ph.D. in Environmental Health Science and Policy and her MA in Risk Management and Technology Assessment from Clark University, Worcester, Massachusetts and possesses a Bachelor of Science degree from Worcester Polytechnic University in Molecular Biology and Biotechnology.

Dr. Abhishek Shrivastava is a Research Scientist in Dow Water and Process Solutions. In his current role he is responsible for research and development and commercialization of novel water purification technologies including reverse osmosis, nanofiltration and particle filtration. Shrivastava joined the Dow Water & Process Solutions' R&D organization in 2007 in Edina, Minnesota. Here, he led R&D, application development, cost savings and commercialization projects for FILMTECTM RO membranes and modules for brackish water desalination, seawater desalination and nanofiltration applications. He also served as the focal point for the development of ROSA (Reverse Osmosis Systems Analysis) software. In addition, Shrivastava led multiple technology platforms aimed at accelerating product and process development through fundamental research on transport phenomena and thermodynamic analysis of membrane systems.

Shrivastava holds a Ph.D. in Chemical Engineering from the University of Minnesota and a Bachelor of Technology in Chemical Engineering from the Indian Institute of Technology, Kharagpur. He has more than 15 peer-reviewed publications and technical presentations and holds a Dow-issued patent.

Shatil Sinha is a Lab Manager for Composites Processing Lab under Composites Technology in the Manufacturing and Materials Directorate at GE Global Research. He has more than 20 years of manufacturing experience including last 8 years of experience managing PMC and CMC development research for GE Aviation and GE Power & Water. He has led external collaborative effort on various PMC material and process related activities. He has been active in guiding the research and innovation for speed and business impact. He is passionate about new material introduction, bears a strong thermal and fluid background. Shatil has a B.S. and a M.S. in Mechanical Engineering from Ohio University.

Dr. Sean M. Sweeney received his B.S. in Ceramic Engineering Science from Alfred University and M.S. and Ph.D. in Materials Science and Engineering with a Ceramic Emphasis from the Pennsylvania State University. Prior to joining GE Global Research in July 2005, he held a postdoctoral position at the INPG in Grenoble, France. Dr. Sweeney specializes in ceramic processing including wet and dry processing and sintering of conventional powders and nanopowders to high density/transparency as well as to high porosity. He has seven peer-reviewed articles and three issued patents.

Dr. Pushkar Tandon joined Corning in 1998 and is currently a Development Fellow in Corning Optical Communications Applied Research and Development group at Sullivan Park. He received his B. Tech in Chemical Engineering from Indian Institute of Technology, Delhi (India) in 1990 and earned his Ph.D. also in Chemical Engineering from Yale University in 1995. His postdoctoral research was at the Institute of Medicine and Engineering at the University of Pennsylvania. His work at Corning has resulted in significant new process and product development which has been commercialized in the manufacturing of optical fibers, diesel particulate filters, and specialty glasses. He has authored 49 archival journal publications and 35 conference presentations, holds 50 issued U.S. patents, with 41 other patent applications pending. Dr. Tandon work has resulted in products that have received a number of industry awards, including voted as Time magazine's "Best Inventions of the Year" (2007), R&D 100 Award and IEEE Corporate Innovation Award. He also has been the recipient of the *American Chemical Society Regional (Northeast) Industrial Innovation Award*, Corning's *Outstanding Publication Award* and Corning's *Development Excellence Award*. He serves as a reviewer for more than a dozen of leading journals in the area of chemical and glass/ceramic sciences.

Dr. Cornelis L.H. Thieme is a Senior Technical Manager and metallurgist at AMSC in Devens, Massachusetts. He leads alloy development and scaling, as well as the development of novel methods for texture development in alloys with reduced stacking fault energy. His particular interests have scaling NiW alloy production, from small lab quantities to multiton versions of the same alloy without loss of desirable properties, and its integration in the manufacture of second generation (2G) high temperature (HTS) superconducting wire. His extensive knowledge of alloy manufacturing and texturing techniques has provided the foundation for the RABiTS (Rolling Assisted Bi-axially Textured Substrates) substrates used in the 2G HTS wire manufacturing. He has served as Program Manager for various low AC loss conductor projects for both US Navy and US Air Force programs. Before joining AMSC in 1995, he worked at MIT as a scientist on low temperature superconductors for the ITER project. In 1988, he received his Ph.D. from Twente University in the Netherlands for his work on high magnetic field properties of powder metallurgy Nb_3Al superconducting wire. In 1975, he obtained his M.Sc. degree from Twente University in Materials science, with a thesis on novel electro-mechanical properties of PLZT ferroelectrics. Cornelis Thieme can be reached at AMSC, 64 Jackson Road, Devens, MA 01434, USA.

Dr. Ian A. Tomlinson is a Research Fellow working with Dow Water and Process Solutions and Dow Microbial Control. In this role he is responsible for driving key growth projects in the areas of reverse osmosis and nanofiltration including breakthrough synthesis and antifouling. He is also active in the development of novel microbial control solutions for food safety, hygiene applications and the oil and gas industry. He is also involved in many external projects with academic and industrial partners accessing novel technologies to address opportunities within Dow's development pipeline. During his early career at Dow, Ian was involved in the development of Starburst Dendrimer technology before holding various roles in pharmaceutical process research, development of technologies for drug delivery and with the ANGUS Specialty Amines business.

Ian joined The Dow Chemical Company in 1985 after receiving his Ph.D. in Organic Chemistry from The University of Wales, Cardiff in 1985 and a B.Sc. with First Class Honours in Chemistry from The University of Wales, Aberystwyth in 1982. Ian holds twenty one U.S. patents and eight scientific publications and invited technical presentations. Ian is a member of the Royal Society of Chemistry and the American Chemical Society.

Dr. Ram Upadhyay is a Senior Principal Engineer for Composites Technology in the Manufacturing and Materials Directorate at GE Global Research. He has more than 30 years of experience working with numerous GE businesses—Aviation, Power & Water, Health Care, Lighting, Plastics, and Transportation. His expertise includes Polymer and Ceramic Matrix Composites processing, process modeling, automation, and pro-active manufacturing process control. Ram has a B.Tech. in Aerospace Engineering—Indian Institute of Technology at Kanpur, and MS and Ph.D. Cornell University. His main thrust has been to support introduction of light-weight composite parts in GE aircraft engines notably F404, F414, GE90, GEnX. For the last five years he has been focusing on introducing Information Technology tools and Automation in manufacturing environment to reduce cost and increase productivity. Dr. Upadhyay is the author of over 40 publications and technical society presentations, and holds over 10 patents related to various composite processing and manufacturing technologies.

Peter Wachtel is the Chief Operating Officer of IRradiance Glass, Inc. Mr. Wachtel was previously a Glass Scientist at Kopp Glass Inc. in Pittsburgh, PA. There he was the lead for the Night Vision Compatible Glass (NVC) production line, and custom glass developments. In this capacity, he helped to increase the NVC line yields by 16% through implementation of technical seminars, an easy to use melt parameter database, and a statistical glass component to property model. His experience in custom glass development ranged from designing filter glasses meeting physical, thermal, and optical customer needs to the modification of the current glass types in production to be RoHS compliant and still meet customer specifications. These glass developments required the melting of glasses on a small lab scale and up scaling the glass melt to full production. Mr. Wachtel received his B.S. in Glass Science and Engineering and his M.S. in Glass Science at Alfred

University. His thesis work consisted of defining the mechanism behind the Near-IR light-enhanced gas diffusion of transition metal doped hollow glass microspheres that are to be used as the fuel source in hydrogen fuel cells.

Dr. Matthew Wagner is currently a Section Head at the Procter & Gamble Company, the largest consumer packaged goods company in the world. Matt received his Ph.D. in Chemical Engineering from the University of Washington in 2002 and his B.E. in Chemical Engineering and Biomedical Engineering from Vanderbilt University in 1998. After completing his Ph.D., Matt joined the National Institute of Standards and Technology as a National Research Council Postdoctoral Research Fellow. In both his graduate and postgraduate work, Matt developed surface and data analysis methods for the characterization of biological and polymeric surfaces. In 2004, Matt joined the Procter & Gamble Company in Cincinnati, OH, to lead the development of surface analysis methods applied in the consumer packaged goods industry. His current research focuses on the cleaning of surfaces and deposition of actives.

Dr. Shanshan Wang is an Operations Researcher in the Management Science Lab at GE Global Research. She received her Ph.D. in Industrial Engineering from Arizona State University in 2010. She specializes in real-time simulation and scheduling, agent-based simulation.

Dr. Xilin Xu is a Technical Manager at KEMET Electronics. He received his B.S. and M.S. degrees in Materials Science and Engineering from the Nanjing University of Technology, Nanjing, China in 1993 and 1996, respectively. After working in the industry in China for four years, he went to the Missouri University of Science and Technology (formerly University of Missouri-Rolla) and received a Ph.D. degree in Ceramic Engineering in 2004. His experience and expertise include piezoelectric and dielectric ceramic material processing and characterization, electronic ceramic product development, and project management. His current interests mainly focus on developing high performance multilayer ceramic capacitors, including new dielectric materials, electrode pastes, thin dielectric layer processing methods, and reliability improvement, as well as their applications.

Contributors

R. Terry K. Baker Catalytic Materials, Pittsboro, NC, USA

Stephan Biller General Electric Global Research, Niskayuna, NY, USA

Dana Bookbinder Corning Incorporated, Corning, NY, USA

Uma Chowdhry DuPont Experimental Station, Wilmington, DE, USA

Gregory Corman General Electric Global Research, Niskayuna, NY, USA

Russell H. DeVane The Procter & Gamble Company, West Chester, OH, USA

Matthew Dejneka Corning Incorporated, Corning, NY, USA

Yulin Deng American Process Inc., Atlanta, GA, USA

Adam Ellison Corning Incorporated, Corning, NY, USA

Ye Fang Corning Incorporated, Corning, NY, USA

Luke Franklin Dow Energy and Water Solutions, The Dow Chemical Company, Minneapolis, MN, USA

Yuri Freeman KEMET Electronics Corporation, Simpsonville, SC, USA

Caleb V. Funk Dow Energy and Water Solutions, The Dow Chemical Company, Minneapolis, MN, USA

Sinue Gomez Corning Incorporated, Corning, NY, USA

Timothy Gross Corning Incorporated, Corning, NY, USA

Abhijit Gurav KEMET Electronics Corporation, Simpsonville, SC, USA

Michael D. Hill Research and Development, Trans-Tech Inc. (Division of Skyworks Solutions Inc.), Adamstown, MD, USA

Mikhail Iakovlev American Process Inc., Atlanta, GA, USA

Jon E. Johnson Dow Energy and Water Solutions, The Dow Chemical Company, Minneapolis, MN, USA

Steven Jons Dow Energy and Water Solutions, The Dow Chemical Company, Minneapolis, MN, USA

Ming-Jun Li Corning Incorporated, Corning, NY, USA

Krishan Luthra General Electric Global Research, Niskayuna, NY, USA

Lynnette D. Madsen Svedberg Science, Inc., Falls Church, VA, USA

Jennifer McKinley IRradiance Glass Inc, Orlando, FL, USA

Arie Mulyadi American Process Inc., Atlanta, GA, USA

Bruce P. Murch The Procter & Gamble Company, West Chester, OH, USA

J. David Musgraves IRradiance Glass Inc, Orlando, FL, USA

Kim Nelson American Process Inc., Atlanta, GA, USA

Michael S. Pambianchi Corning Incorporated, Corning, NY, USA

Martin Peery Dow Energy and Water Solutions, The Dow Chemical Company, Minneapolis, MN, USA

James Price Corning Incorporated, Corning, NY, USA

Erik Reed KEMET Electronics Corporation, Simpsonville, SC, USA

Theodora Retsina American Process Inc., Atlanta, GA, USA

Nelly M. Rodriguez Catalytic Materials, Pittsboro, NC, USA

Abhishek Roy Dow Energy and Water Solutions, The Dow Chemical Company, Minneapolis, MN, USA

Martin W. Rupich Materials R&D, AMSC, Devens, MA, USA

Srivatsan Sathyamurthy Materials R&D, AMSC, Devens, MA, USA

Jo Anne Shatkin American Process Inc., Atlanta, GA, USA

Abhishek Shrivastava Dow Energy and Water Solutions, The Dow Chemical Company, Menlo Park, CA, USA

Shatil Sinha General Electric Global Research, Niskayuna, NY, USA

Jan-Eric Sundgren Volvo Group, Gothenburg, Sweden

Erik B. Svedberg Svedberg Science, Inc., Falls Church, VA, USA

Sean Sweeney General Electric Global Research, Niskayuna, NY, USA

Pushkar Tandon Corning Incorporated, Corning, NY, USA

Cees Thieme Materials R&D, AMSC, Devens, MA, USA

Ian A. Tomlinson Dow Energy and Water Solutions, The Dow Chemical Company, Midland, MI, USA

Ram Upadhyay General Electric Global Research, Niskayuna, NY, USA

Adriaan van Heiningen American Process Inc., Atlanta, GA, USA

Peter Wachtel IRradiance Glass Inc, Orlando, FL, USA

Matthew S. Wagner The Procter & Gamble Company, West Chester, OH, USA

Shanshan Wang General Electric Global Research, Niskayuna, NY, USA

Xilin Xu KEMET Electronics Corporation, Simpsonville, SC, USA

Chapter 1
Corning Incorporated: Designing a New Future with Glass and Optics

Michael S. Pambianchi, Matthew Dejneka, Timothy Gross, Adam Ellison, Sinue Gomez, James Price, Ye Fang, Pushkar Tandon, Dana Bookbinder and Ming-Jun Li

Abstract Corning Incorporated is a world leader in glass and ceramic products, and has been innovating in these materials since 1851. The company sells component-level technical products that are integrated into systems made by its customers. In most cases, those systems are significantly more efficient or in some instances fundamentally enabled by the performance of the Corning product. Corning calls its products "keystone components" for this reason. Keystone components often result from a combination of both material and process innovations, which tend to be difficult for other companies to duplicate. Developing keystone components requires patient investment in R&D (both materials and process) over long periods of time, and depends upon a culture of innovation and dedication to fundamental understanding. We highlight in this chapter three different keystone components developed by Corning in the past two decades—Corning® Gorilla® Glass for touch-enabled displays, Epic® sensors for drug discovery, and ClearCurve® optical fiber. In each case we provide an overview of Corning's contributions to each field, describe the areas of technical challenge that still need to be addressed by the research community, and link those to the skills and capabilities that are needed to ensure further success in each.

1.1 Introduction

Corning Incorporated is a world leader in specialty glass and ceramics. It has been producing significant, life-changing innovations since 1851. Major innovations produced by Corning include glass envelopes for light bulbs (1870s), shatter-proof

Gorilla®, Epic®, ClearCurve®, and nanoStructures® are trademarks of Corning Incorporated.

M.S. Pambianchi (✉) · M. Dejneka · T. Gross · A. Ellison · S. Gomez · J. Price · Y. Fang · P. Tandon · D. Bookbinder · M.-J. Li
Corning Incorporated, One Riverfront Plaza, Corning, NY 14831, USA
e-mail: PambiancMS@Corning.com

L.D. Madsen and E.B. Svedberg (eds.), *Materials Research for Manufacturing*, Springer Series in Materials Science 224,
DOI 10.1007/978-3-319-23419-9_1

railroad signals (1880s), heat-resistant glass (1910s), the ribbon machine for mass production of light bulbs (1920s), silicones (1930s), television picture tubes (1940s), glass-ceramics (1950s), optical fiber (1970s), ceramic substrates for catalytic converters (1970s), precision glass for liquid crystal display (LCD) substrates (1980s), and cover glass for touch-enabled displays (2000s). Through these innovations, Corning has helped to light the world, bring TV into our culture and fashion into our kitchens, clean up the smog in our cities, wire the internet across the oceans, and enable the touchscreens on smartphones and tablets. This legacy of life-changing innovations, and the chance to continue it for another 164 years, is what drives Corning today.

In 2015 Corning Incorporated has five business segments: Display Technologies, Optical Communications, Life Sciences, Environmental Technologies, and Specialty Materials. All of these segments manufacture products based on glass, ceramics, and polymers. All of Corning's products, sold on the basis of their technical performance, fulfill special roles in the systems into which they are integrated. In most cases, the system relies heavily on the performance of the Corning product, and would have to be completely redesigned to function without Corning's product. This type of specialized technical product is sometimes referred to as a "keystone component".

Optical fiber is a good example of a keystone component. Telecommunication networks were originally built with copper wiring and coaxial cable, so the amount of data they could carry was limited, and the amount of power required per bit of data was very high. There was no way that global telecommunications on the scale of what we have today would have been possible with copper wire. Optical fiber has become the core of a completely new type of data network, which is capable of carrying billions of times more data, routing it further and at higher speeds, and doing so with much less power per bit. Today the entire long distance transport network has been redesigned around the use of optical fiber. Lasers, fiber amplifiers, wavelength add-drop multiplexers, and dispersion compensation have all been added in order to take advantage of the benefits of optical fiber.

Keystone components take a long time to develop. Optical fiber with transmission loss below 20 dB/km was first demonstrated in 1970, but it was not until the late 1990s that a large market for optical fiber emerged with the growth of the internet. So Corning's net payback on optical fiber was negative for the first 25 years. Because of this slow payback, Corning is often the only company working on these types of keystone components, and has to develop all of its own supply chain, manufacturing technology, and technical understanding. But if things go well, Corning can find itself in the advantageous position of being one of only a handful of suppliers of a very valuable component. Corning has found that by focusing on keystone components, it can deliver life-changing innovations to the world, good return on investment to its shareholders, excellent growth opportunities for its customers, and a means for its own continuous renewal, all at the same time. But to keep delivering keystone components, Corning needs to maintain a high level of materials research, focused product development, and advanced manufacturing.

1.1.1 Research

Corning needs to stay at the cutting edge of materials research in the areas where it focuses—glass, ceramics, and polymers. Corning carries out extensive research in glass, including glass composition, chemistry, properties, structure, and melting and forming behaviors. The company needs to be ready to develop keystone components in potentially any industry or application, so it must maintain deep understanding in a range of areas, even if they are not directly applicable to today's products. In glass, this includes non-silicate glass systems, non-oxide glass systems, plasma and submerged combustion melting, and many different techniques for forming glass, some of which are proprietary. It also includes research on techniques for modifying glass properties, such as relaxation, annealing, and ion-exchange strengthening. Also, it includes research on glass frits (powdered glass used in hermetic sealing) and glass-ceramics (glass that is internally crystallized through heat treatment).

In the area of ceramics, Corning's research includes rheology, pastes, binders, various forming processes, firing processes, and the link between composition, microstructure, and final physical properties of ceramics. Much of the ceramics research is carried out in support of Corning's business in catalytic converter substrates and diesel particulate filters. Other areas of research include next generation refractory materials for glass manufacturing, tape cast electrolytes for batteries and fuel cells, and transparent ceramics. The ceramics research is focused mainly on oxide compositions, but covers some non-oxide ceramics as well.

Organic materials play a big role in many Corning products, so the company maintains a specialized capability in polymer science, emphasizing Corning's areas of application. These include UV-curable coatings for optical fiber, organic binder vehicles for ceramic extrusion, and a few others. Corning also supports its life science business with research in biochemical technologies, in particular, how living cells interact with chemicals, surfaces, environments, and other cells.

Many of Corning's product attributes are surface attributes, not bulk attributes. For example, in display glass, Corning sells an extremely smooth, flat as-made glass surface that is suitable for deposition of thin-film transistors. In Gorilla®Glass, Corning sells a glass whose surface has been strengthened by ion-exchange. Likewise many of Corning's life science products get their performance advantages from the surface properties (e.g., adhesion, functionalization) of the material. Given this, Corning carries out a broad portfolio of research on thin films and surfaces. It investigates subjects such as surfaces for film deposition, adhesives for glass–glass bonding, and glass etching properties.

Corning also performs research in optical physics, network integration and connectivity, and optical semiconductors, all in support of its telecommunications businesses. These all require inorganic and organic materials, with a focus on the optical properties. The optical physics group pioneers new ways to manipulate light with materials, and new approaches to use the interaction between light and materials.

This covers a lot of ground, from precision optics to lighting and illumination, to optical fiber research, to data storage and quantum computing.

All of the above areas of materials research rely on a very strong competency in materials characterization. Corning maintains a cutting edge capability in characterization science, and pioneers many of its own methods and instruments for measuring the properties of its materials. Because of its central importance to materials research, characterization science is the largest research department in the company. This group supports research in materials, but also the wide range of measurements needed in development and manufacturing groups. And finally, modeling and simulation are a crucial part of Corning research. Corning scientists build models that predict glass properties, show how to optimize manufacturing processes, and provide data for developing new ones, all for much less money and time than the real experiments would take. Corning builds the models at the same time it is developing the materials and processes, so that one does not go forward without the other.

These competencies (see Fig. 1.1) form the basis of Corning's research capability. Projects are structured by drawing upon these competencies. The strength of Corning's innovation comes from the diversity of expertise that can be found among these groups, and from the extremely valuable areas at the intersection between them. It could be said that Corning's true core competency is its technical diversity and ways of leveraging it.

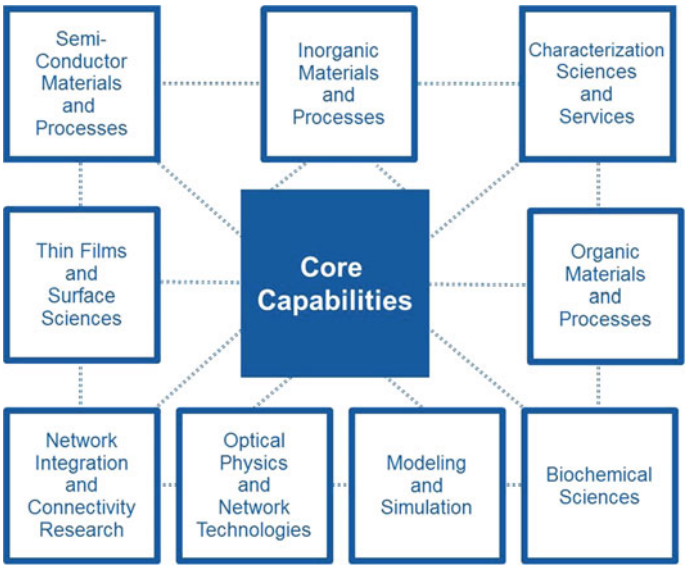

Fig. 1.1 Core research areas at Corning incorporated

1.1.2 Development and Engineering

Development is the functional organization in which proprietary knowledge obtained through research is used to create actual Corning products (keystone components). This function balances the possibilities of materials and manufacturing processes with the requirements of customers and the market. Because neither the technology nor the markets are perfectly understood, the work of Development is extremely challenging. It is certainly more focused on the use of Corning's manufacturing assets. In Glass Development, this means working on things like cooling curves, refractory compatibility, and ways of avoiding devitrification [1]. The required skills are a combination of glass science (chemistry, properties) and glass technology (melting, forming, finishing, the assets used in each, and the measurements that accompany each). In Ceramics Development it means familiarity with Corning's extrusion and firing facilities, and how the material needs to be designed for them. And in optical fiber it means knowing about soot deposition, blank consolidation, draw tower operations, and the measurements used in each to control the product performance attributes.

Since many of Corning's products are unique and are sometimes being developed for an entirely new industry, new measurements are usually needed in order to characterize the product and the manufacturing process. These measurements and characterization tools are often developed in research, but are refined for industrial use in the development and engineering organizations. Sometimes these measurements are part of the set of standards that are developed for a new industry (for example, telecommunications standards like ITU-T rec. G.652.D—see below in the section on ClearCurve® optical fiber), so Corning also has a standards organization designed to participate in, and often lead, the definition of the relevant measurement standards for its products.

Finally, the Engineering function brings it all together to produce Corning products. Since keystone components are often combinations of new materials and new processes, the manufacturing assets for making the product may not exist at all, or may need to be substantially modified in order to manufacture Corning's products. Corning maintains a large Engineering organization that develops machines and manufacturing processes for production of Corning's unique keystone components. The skills and capabilities required for this organization include machine systems, robotics, mechanical and electrical engineering, as well as specialized skills such as glass melting, forming, and extrusion.

These capabilities in Research, Development, and Engineering work together to identify, develop, and manufacture Corning's keystone components. The way these groups work together in a coordinated fashion has been the key to Corning's success for the past 164 years. We describe below three different keystone components (Gorilla® Glass, Epic® sensors, and ClearCurve® optical fiber) that were developed by Corning over the past two decades. In each case, we describe the state of the art of the technology, highlight Corning's contributions to the field, and

describe some of the remaining challenges that require further research. We conclude by describing the skills and capabilities needed to address the technical and manufacturing challenges of products like these.

1.2 Corning® Gorilla® Glass for Touch-Enabled Displays

Gorilla® Glass is Corning's most recent large business: the initial concept was considered in 2007; with focused effort it has developed to where today it is the product of choice for many portable electronic devices. It was born out of the revolutions in wireless communications, miniaturization of computing power, and touch screen technology. These three trends combined in the late 2000s to produce the smartphone, a powerful computer small enough to fit in a shirt pocket or clutch and equipped with radio technology that allowed users to access the internet anywhere, at any time. At the time of this writing just 8 years later, nearly every person in the developed world has a smartphone, and people are linked with information and with each other in ways that could only be imagined just 10 years ago. Smartphone technology has begun to penetrate into larger devices (tablets) and redefine personal computers.

Touch screen technology has been a crucial part of the smartphone and tablet revolution. While personal computers have a pointing device (mouse) to access links on the internet, this is not practical on a mobile device carried in a pocket. Device buttons can be used to move a cursor around on a screen, but there is no good substitute for being able to point the cursor freely at anything on the page. Touch screens enable this by detecting the location of the user's finger while remaining transparent to the display underneath.

Touch screens have created an entirely new role for glass—being the functional interface between humans and machines. The cover material of a touch screen has to serve three functions: enable user input, protect the display beneath it, and transmit the information on the display to the user even after years of use. Thus the material has to be mechanically durable, scratch resistant, thin, stiff, dimensionally stable, flat, smooth, impermeable to water, and transparent to both visible light and radio waves. While polymers can supply some of these attributes, glass is much better for scratch resistance, stiffness, dimensional stability, and water impermeability. However, ordinary glass is too fragile for a touch screen cover material, so cover glass needs to be strengthened.

1.2.1 Strengthening of Glass

Glass is much harder and more scratch resistant than plastic, so it is ideal for applications such as touch screens and windshields where scratches would negatively impact the visual performance. Silicate glasses have a theoretical strength

estimated to be between 14 and 32 GPa, but handling and use creates microscopic surface flaws that act as stress concentrators and limit the practical strength of glass to less than 1% of its theoretical strength [2]. Thus, practical glass tends to be very strong in compression, weak in tension, and breaks originate from flaws predominantly from the surface [3]. Glass can be strengthened or tempered by putting the surface of the glass under compression. This compressive stress not only makes the glass harder, making it more resistant to scratches in the first place, but also puts any existing surface flaws under compression. When loading such a glass, this surface compression must first be overcome before the flaw can experience tension, thereby increasing the useful strength of the glass as well as the retained strength after use and abrasion.

There are three main methods of tempering: thermal, lamination, and ion exchange. Thermal tempering is achieved by rapidly quenching a glass from a viscosity of $\sim 10^8$ Pa-s to below the strain point (viscosity of $10^{13.5}$ Pa-s) where the glass becomes a rigid solid. The rapid quench is critical so that the surface cools quickly and hardens, while the interior cools slowly and continues to contract after the exterior has become rigid. The interior contraction pulls on the exterior surface, putting it into compression. The total volume integrated surface compression must exactly match the total volume integrated tension [3, 4]. Lamination relies on differences in thermal expansion rather than differential cooling. The lamination process fuses lower expansion cladding or skin glass to higher thermal expansion core or body glass so that on cooling the interior thermally contracts more than the skin, putting the skin under compression [5, 6]. Ion exchange (chemical tempering) can be used to create a compressive stress on the surface, by swapping out mobile cations in the glass with larger ones from a molten salt bath. Compression can also be achieved by ion exchanging the glass above the glass transition temperature (T_g) with an ion that lowers the coefficient of thermal expansion (CTE), resulting in compressive stress due to CTE mismatch, similar to lamination. As with any tempering method, the surface compression is force balanced by central tension in the interior [7].

Thermal tempering is the most economical method of tempering, but is typically limited to glasses thicker than 3 mm to achieve differential cooling and results in a parabolic stress profile through the thickness of the glass article. Cover glasses on touch screens are typically 1 mm thick or less to reduce device thickness and weight, so thermal tempering is not an option. Laminates are a possibility, but require an additional protective layer or modifications to the device design in order to address the exposed central tension on the edges of the parts after they have been cut out from a large sheet. Thus ion exchange is the most suitable strengthening process for touch screens and consumer electronic devices as it can be done after the cover glass is cut and finished, provides higher surface compression than thermal tempering, strengthens all exposed surfaces and edges, can be done on curved or complex shapes, and the compressive depth of layer can be controlled with bath temperature and time. Since it is currently more expensive than tempering or lamination, ion exchange is used when parts are thin or performance is essential

such as airplane and bullet train windshields, magnetic memory disk substrates, touch screens, and eyeglasses.

1.2.2 Chemical Tempering of Glass

Glass was first ion exchanged by Schulze who immersed a soda-lime glass in molten silver nitrate and demonstrated that Ag^+ ions from the molten salt replaced Na^+ ions in the glass, but the ion exchange temperatures were above T_g so all the stress from the size mismatch was annealed away [8]. Stookey was the first to use ion exchange for strengthening. He ion-exchanged a sodium aluminosilicate glass in a lithium salt bath above T_g. As the Li^+ replaced the Na^+ ions, β-eucryptite nano-crystallites precipitated producing a low expansion surface that went into compression as the material cooled, producing strengths of up to 830 MPa. He made both transparent and opaque glass ceramics using this ion exchange ceram process [9, 10]. The following year, Sam Kistler, better known for the invention of aerogels [11] and then Dean of Engineering at the University of Utah (and independently Acloque and Tochon [12]) used ion exchange below the glass transition temperature to create surface compression via stuffing and improved the strength of glass rods (Corning 0088) three-fold using a K^+ for Na^+ exchange [13].

Shortly thereafter, researchers at Corning found that Al_2O_3 and ZrO_2 in the glass both increased the strength after ion exchange in KNO_3 by a factor of 1.8 and more importantly increased the abraded strength of the ion exchanged glass by a factor of 8 over soda-lime glass [14]. Strength after abrasion is governed by the depth of the compressive layer (DOL). A shallow compressive layer is easily penetrated by abrasion or mechanical insult, while a deeper DOL provides a thicker layer of armor that retains more strength even after abrasion or damage. The DOL is governed by diffusion and increases with the square root of diffusivity and time. Thus the DOL can be increased by ion exchanging for longer time, by optimizing the glass composition to increase the mutual diffusivity of the mobile ions, or by increasing the bath temperature to increase the diffusivity. Increasing temperature also increases the rate of stress relaxation and at T_g all stresses relax within minutes, so the ion exchange is typically done $\sim$200 °C below the glass transition. Soda-lime glasses are easy to melt and have a very low T_g around 540 °C. The diffusivity of K^+ ions in soda lime glass is relatively low and attempts to increase the DOL with increased time or temperature are countered by increased stress relaxation, limiting soda lime type glass to less than a 15 micron DOL and 700 MPa compressive stress. Aluminosilicates have high K^+ diffusivities and higher T_g enabling one to obtain over 50 microns DOL and compressive stresses from 750 to 1050 MPa. However, they are also harder to melt, requiring higher melting and refining temperatures, so more expensive equipment and fining agents are required.

A team of scientists in Corning optimized the aluminosilicate compositions for ion exchange performance, strength, manufacturability, and quality. As a result, Corning announced Chemcor in 1962, an ion exchanged glass that could be made

into large sheets that could be bent, or formed into cups that bounced after a nine story drop onto a steel plate. Corning invented the fusion process in 1959 to make flat sheet with two pristine surfaces. After many improvements and subsequent inventions, the fusion process was married with Chemcor to make large flat pristine sheets for automotive safety windshields in 1969. When broken, the ion exchange glass fragmented into granular pieces rather than dagger like shards as annealed glass tended to do, and the fragmented glass provided enough visibility to enable the driver to safely stop the car. Unfortunately the product did not last long. Float glass was also improving its optical quality, dicing pattern, and reducing cost and by 1970 laminated safety glass with two layers of thermally tempered float soda lime glass bonded to a polyvinyl butyral (PVB) polymer dominated the automotive safety windshield market (and still does today). Chemcor could not compete in automotive, and found new applications in aircraft windshields and magnetic tape reels, so its revenue was limited to a few million dollars [15]. Corning then introduced fusion drawn photochromic sunglasses in 1976. While Chemcor was a Na-based glass that was ion exchanged in a KNO_3 bath, the photochromic lenses contained Li_2O and were ion exchanged in a mixed $NaNO_3$–KNO_3 salt bath. The Na^+ for Li^+ exchange was very fast and produced a very deep DOL with low compressive stress, while the K^+ provided a shallow layer of very high compressive stress providing good scratch, safety, and drop performance for the ophthalmic market. After nearly a decade of success, Corning exited the Chemcor ophthalmic business in 1984 and all of its manufacturing assets were converted to running alkali-free glasses for what would become the LCD substrate business. As the LCD glass market evolved from small applications like watches and gasoline pump displays to computer monitors and eventually LCD TV, the fusion draw machines grew from a modest 0.5 m wide (Gen2) to enormous Gen 10 sheets 3 m square (Fig. 1.2) to satisfy the demand for manufacturers to make multiple large screen TV panels on one mother sheet. Since transistor performance increased with deposition temperature, customers sought higher temperature glasses which required new isopipe materials capable of handling the harder glasses [16]. The flat, smooth pristine surface obtained by fusion is ideal for display makers to deposit their thin film transistors (TFTs) and build displays. Float glass is not flat enough and required grinding and polishing to compete with the as drawn fusion surface and posed challenges for making thin sheet where fusion is ideally suited.

1.2.3 Gorilla® Glass

Mobile phone use accelerated in the late 1990s as costs came down and cellular coverage increased. One of the biggest problems was that the plastic screen protectors scratched and obscured the screen. So after 35 years, Corning revived its work on chemically tempered glasses and began testing them for touch screen cover glass applications. Corning's first potential customer was interested because chemically tempered glass could be much thinner than thermally tempered glass,

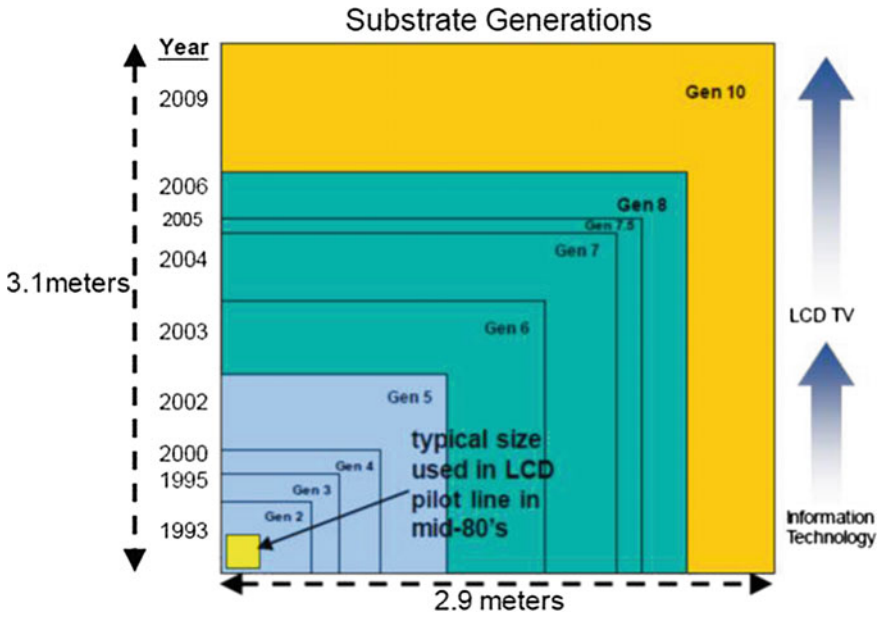

Fig. 1.2 Generations of LCD substrate glass

had higher compressive stress and was also transparent to radio and microwave frequencies, which would turn out to be important later when smartphones emerged. Corning was then approached by a second potential customer interested in high strength scratch resistant glass. This new customer was delighted with the performance and wanted production quantities in only a few months. It represented the first significant business opportunity for chemically tempered alkali aluminosilicate glasses that had strong customer pull.

There were only a few problems. First, there was not enough time to build a factory or new manufacturing capacity, which meant that the glass had to be made on existing manufacturing assets. Second, all of Corning's glass tanks had by then migrated to larger, higher temperature platforms with which the old Chemcor composition was now incompatible. Third, while aluminosilicates had superior ion exchange performance to soda lime glass, they were much more difficult to melt; fining was also an issue in that the old Chemcor glass was fined with arsenic to remove the bubbles, an environmentally undesirable component. While a 100 micron bubble or inclusion is not perceptible in a windshield, it could block an entire pixel in a display, so the specifications on maximum number of inclusions for cover glass were much tighter than those for windshields. Fourth, Chemcor had a slight amber tint that could reduce the brightness and shift the color of the display behind it, so the visible transmission of the glass needed to be improved. Finally, it would be ideal if the mechanical performance could be improved to survive accidental drops. Below we discuss how Corning overcame these challenges with

technology, creativity, and sweat, and developed an entirely new chemically tempered glass composition for the smartphone revolution.

Historically new glass composition developments took years since the process was iterative, going from concepts to small crucible melts which were fabricated into test samples used for key property measurements, which, in turn, supplied data for new composition ideas. After a few iterations, the promising candidates were then scaled up for a full battery of characterization and the best ones evaluated on a pilot line. After tuning the process on a pilot line, the best composition was taken to a development trial in the plant with a few backup compositions in hand in case they were needed. If the development trial went well and customer feedback was positive the glass then went into production.

The first challenge was to come up with a new alkali aluminosilicate glass that was compatible with existing manufacturing lines, and to do this very quickly, since production was needed in just a few months. There was no time for the usual set of melt iterations, nor a pilot, nor development trial, so it had to work the first time. While Chemcor had been fusion drawn in the 1960s, it was on smaller manufacturing lines, and with looser dimensional tolerances. A fraction of a millimeter of warp is not noticeable on a windshield, but it could cause interference in a display stack.

In a downdraw process, warp can occur when the glass falls faster than it is being pulled. The pull rate is set by the desired sheet thickness and glass flow, so the glass viscosity must be high enough so that the glass must be pulled off of the bottom of the isopipe rather than sag under its own weight. In other words, the pulling force needs to be greater than the gravitational force on the molten glass [17]. Thus a glass composition with a 4x higher liquidus viscosity was required such that the glass could be drawn at higher viscosities to provide flatter sheet at larger sizes without devitrification [1]. The viscosity of a glass melt decreases exponentially with increasing temperature, as shown in Fig. 1.3. If the liquidus viscosity is only $\sim 10^3$ Pa-s, the glass must be formed at a viscosity below 10^3 Pa-s where the only option for forming glass sheet is rolling. Rolling leaves a mottled surface which must be

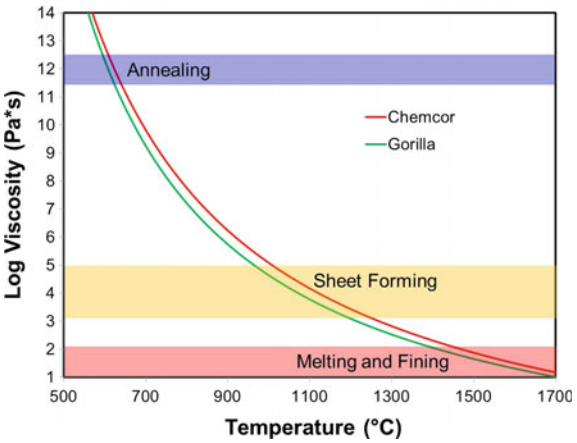

Fig. 1.3 Viscosity curves of Chemcor and Gorilla® Glass

subsequently ground and polished to achieve optical quality, and it is difficult to do at the required thickness (1 mm or thinner). Grinding and polishing wastes time, money, and glass, and can also introduce subsurface damage that can compromise strength. So for touch screen cover glass it is highly desirable to form flat sheet directly with a process which produces a pristine surface. And while the float process is capable of making optical quality surfaces, one side has surface imperfections from contact with the molten bath and the other particles of glass and partially oxidized tin, all of which reduce the strength of the glass [1]. The float process also introduces Sn^{2+} ions to the bath side of the glass that slows ion exchange, resulting in asymmetric ion exchange and warp. The fusion draw process is the best choice for product attributes since it produces two pristine untouched surfaces, but requires very high liquidus viscosity. The viscosity curve can be modified by changing composition, but large composition moves would be required to increase the viscosity by the needed factor of four, such that most other properties (including ion exchange rate and compressive stress) would also be radically affected. Since it only takes a 50 °C change in temperature to change the viscosity by a factor of four, the biggest lever for increasing the liquidus viscosity, in order to permit fusion forming, was to decrease the liquidus temperature of the glass.

The liquidus temperature can be decreased by lowering the chemical activities of the crystalline phase components. In the case of Chemcor, the crystalline phase was forsterite ($2MgO*SiO_2$) so the activities of MgO and or SiO_2 needed to be decreased. While chemical activity is approximately proportional to the concentration of the species, it is also governed by the complex interplay of all other components in the glass—some of which can have a much larger impact than the offending component itself! Simply decreasing the MgO content seems to be the obvious move for lowering the liquidus temperature, but it turns out that by the time enough MgO was removed to get an acceptable liquidus viscosity, the properties of the glass were significantly degraded. Thus the solution turned out to be a composition with greater solubility for MgO achieved by optimizing the amounts of the other oxides in the glass. Ironically this new alkali aluminosilicate glass contained even more MgO and improved the liquidus viscosity by more than an order of magnitude without sacrificing ion exchange performance. This move also made the new alkali aluminosilicate glass easier to melt, increasing the chances of success in the plant. Removing TiO_2 from the composition increased the visible transmission of the glass especially in the blue portion of the spectrum. Even though TiO_2 made Chemcor easier to melt and form, the new composition more than compensated for its loss [18].

A display glass tank was quickly converted to this new glass composition. The melting process was tuned, the As_2O_5 fining package did its job eliminating bubbles from the glass, and the first version of Corning® Gorilla® Glass was born in May 2007 when the first fusion sheets came down the draw. The higher liquidus viscosity of the new composition enabled the experienced engineers to quickly get the 1.3 mm thick sheets flat, uniform, and in specification, going straight from development to production in a record 2 weeks and bypassing the usual pilot and development qualification runs to meet the customer deadline.

1.2.4 Thermal History

The impact of thermal history turned out to be significant. It is well known that unlike crystals, most properties of glasses, such as density and refractive index will change slightly with the thermal history of the glass [19, 20]. Rapidly cooled glasses have a lower density than well-annealed glasses by 0.1–0.5% depending on composition and quench rate. Since all of the experimental work was done on crucible melts that were poured into patties more than 100 mm wide and 10 mm thick, the glass had to be annealed to relieve stress and prevent it from shattering. Sheet drawn in Corning's fusion process, however, is ~1 mm thick and of uniform thickness so it is cooled evenly and thus does not have to be annealed. To investigate the impact of cooling rate before going to production, thin plates of glass were cut and polished from the crucible melts and fan quenched from high temperature, to simulate the thermal history of as-drawn fusion glass. The thin plates survived the thermal down shock very well and were 0.3% less dense than their annealed counterparts. While this difference seems insignificant, Corning discovered that it improved the ion exchange DOL 100 times more than the density-between 20 and 40% depending on glass composition [21]. Figure 1.4 compares the K_2O chemical profile of a fast quenched sample and an annealed sample of the same glass composition, ion-exchanged together at 430 °C for 8 h. The quenched piece has a 20% deeper penetration, which means the K^+ for Na^+ diffusivity is 1.44 times faster. So an 8-h ion exchange on typical annealed glass would only take 5.6 h on as-drawn fusion sheet, increasing ion exchange throughput by 1.44 x. The downside to the fast quenched glass is a ~10% penalty in compressive stress due to the lower modulus and higher rates of stress relaxation of the lower density structure.

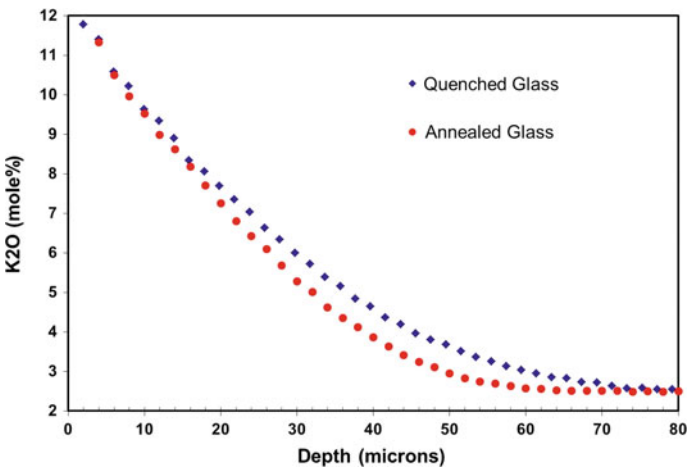

Fig. 1.4 K^+ penetration profile after ion-exchange at 430 °C for 8 h, for annealed and quenched Gorilla® Glass

So Corning now understood the impact of thermal history on properties and had an innovative new alkali aluminosilicate glass composition that ion exchanged quickly, melted well, had improved visible transmission, and had a high enough liquidus viscosity for fusion forming large sheets.

1.2.5 Fining

Corning's first iteration of Gorilla® Glass in terms of its properties and its range of product applications spelled success that surpassed all expectations. However, both Corning and its customers wanted to remove the As_2O_5 to make a more environmentally friendly product. So Corning began investigating alternate fining packages before Gorilla® Glass even hit the market. Glass melts always contain lots of bubbles or "seeds" in the early stages of melting. Since the glass batch is a mixture of granular materials such as sand and aluminum oxide, there is air in between all the particles, some of which becomes trapped in pockets as the batch melts, forming bubbles. Additionally some batch materials such as sodium carbonate decompose as they heat up, releasing CO_2 and further contributing to the gas load in the melt. Since bubbles are lighter than molten glass, they float to the top, but the rate at which they rise is determine by the viscosity of the surrounding glass melt. The upward terminal velocity v of a bubble of radius r in a glass melt of viscosity η, and density ρ is given by

$$v = 2gr^2\rho/(9\eta) \tag{1.1}$$

where g is the acceleration due to gravity [22]. While larger bubbles rise fast enough to be eliminated quickly, the smaller bubbles are the most troublesome. To easily observe this at room temperature just vigorously shake a half empty bottle of a viscous liquid like liquid soap and watch the large bubbles race past the tiny ones on their ascent. A 0.1 mm diameter bubble will only rise about 10 cm/day in a glass melt of 10 Pa-s viscosity, which is far too slow for effective removal. However a 1 mm bubble will rise 100 times faster. Thus the key is make small bubbles larger so they can be removed quickly. As_2O_5 is a very effective fining agent and has been used for centuries, since it tends to reduce at high temperatures (liberating oxygen) and oxidize at low temperatures according to [17]:

$$As_2O_5 \leftrightarrow As_2O_3 + O_2 \tag{1.2}$$

Because there is a nucleation barrier to generating new bubbles, the O_2 generated by the As_2O_5 reduction will preferentially go into existing bubbles during fining, making them larger and more easily removed. As the glass is conditioned and cooled for forming, any residual small O_2 bubbles will be resorbed as the As_2O_3 is oxidized back to As_2O_5. As_2O_5 is ideal for chemical fining because there is a large shift in the redox ratio at typical glass melting temperatures and it has a large

solubility in most glasses. However, As_2O_5 is toxic and thus highly regulated. SnO_2 is a safe non-toxic multivalent oxide also capable of chemical fining via the reaction

$$SnO_2 \leftrightarrow SnO + {}^1/_2O_2 \tag{1.3}$$

Unfortunately, SnO_2 has a much lower solubility than As_2O_5 in most glasses of interest, so its concentration is limited to a few tenths of a weight%, thus limiting the amount of chemical fining. At high SnO_2 concentrations the liquidus temperature increases and crystalline SnO_2 (cassiterite) will precipitate, negating all the hard work done to increase the liquidus viscosity of the glass. Furthermore, only several percent of the SnO_2 actually reduces to SnO at typical fining temperatures, further limiting its fining capacity, unlike As_2O_5 which exhibits almost an order of magnitude greater redox change. In fact, when the 1 wt% As_2O_3 in the glass was replaced with 0.45 wt% SnO_2 (the solubility limit) in lab melts, the bubble concentration increased by orders of magnitude, so it became clear that environmentally friendly bubble-free glass was going to be a big challenge.

Figure 1.5 shows the bubbles in a cross section of glass cored from a glass melted in a crucible at 1450 °C for 1 h followed by 1 h at 1550 °C. This mimics fining in a tank, but with lower times and temperatures to increase the bubble signal and enhance differences between conditions. The first glass without any fining agent shows thousands of bubbles and while the SnO_2 fining agent added to the second helps, there are still hundreds of bubbles remaining. By tuning the base composition and increasing the excess alkalis Corning was able to improve fining and increase SnO_2 solubility as shown in the middle photograph in Fig. 1.5, although it was still not good enough. Then by tuning the process temperatures and

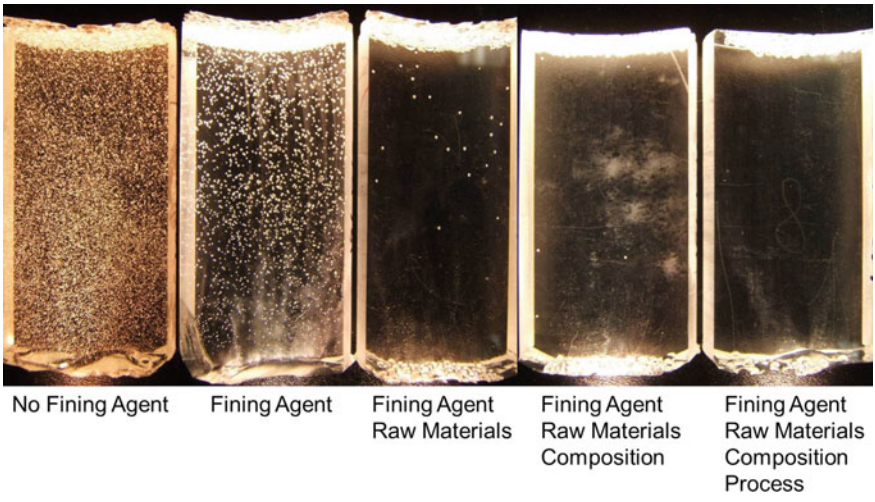

Fig. 1.5 Crucible melts of Gorilla® Glass, showing the effects of fining agents, and adjustments to raw materials, overall glass composition, and the melting process to remove bubbles from the glass

raw materials for the new composition whose viscosity curve is plotted in Fig. 1.3, Corning was able to obtain low bubble count as seen in the right two photographs in Fig. 1.5 [23, 24].

Corning finally tested this new composition out in the pilot line. By midnight the first night, Corning's team was able to tune the controllers, stabilize the tank, and get glass flowing. The team was pleasantly surprised by the lack of bubbles in the glass with the new composition and setup, even when pushed to higher rates of flow. The team then ran four backup compositions and fining packages while they had time on the pilot line. This was important since once the glass went to the production unit, there was no time for failure. Two of the backup compositions resulted in hundreds of solid defects per pound due to solubility problems with a raw material (even though they had performed well in crucible melts). Three different sources of the troublesome component were tried and none worked. So Corning's team went to the plant with their main candidate glass and only one backup composition in hand.

In the production tank, Corning started decreasing the As_2O_5 and increasing the SnO_2 as the tank transitioned towards the next generation alkali aluminosilicate Gorilla Glass composition. The production team obtained the desired composition the following week with neither As_2O_5 nor bubbles. The fusion sheet was ion-exchanged and performed just as the quench tests predicted and the product was a success!

1.2.6 Resistance to Damage

While searching for a glass composition to enable As_2O_5-free fining, Corning discovered a new family of glasses with remarkable resistance to damage. Experimental compositions are melted in crucibles and poured out onto a metal plate to quench the glass into a large freeform plate called a "patty," before loading into an annealer. The annealed patty must be cut into various pieces, each for measuring different properties. To quickly cut the patty, it is scored and then broken along that score mark. Glass is strong until a flaw is introduced, so to quickly cut glasses, a score wheel is used to create a sharp flaw running the entire length of the "cut" to be made. The score is then put under tension by a mechanical stress (bending by hand or gently tapping the back surface of the glass with a hammer to break it along the score line). In one particular set of glasses, the first scored normally with the usual feel and light screech and shear sound of the score wheel as it made its mark. However, each successive composition became noticeably harder to score and by the last composition, the wheel almost silently rolled across the surface and barely left a mark even though the author was putting his full weight on the score wheel. Something was clearly different.

To quantify the scribe effect, the hardness and indentation cracking threshold of the glass were measured both before and after ion exchange. Polished plates of glass 1 mm thick were indented with 0.5 kg of force on a Vickers diamond. Figure 1.6 shows the resulting indents in conventional soda lime glass which exhibits median

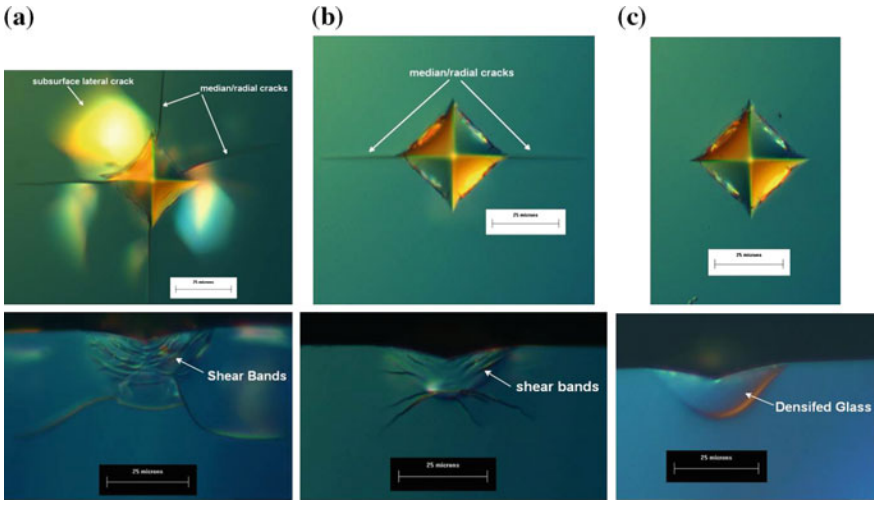

Fig. 1.6 Indentation threshold in **a** soda lime glass, **b** Gorilla® Glass, and **c** Gorilla® Glass with increased resistance to damage. The *bottom row* shows the cross section of the indent while the *top row* shows the *top down view*

and subsurface lateral cracking, in comparison with original Gorilla® Glass which shows only median cracks, as well as the newly discovered glass that showed only densification. Sharp flaws are what degrade the strength of the glass and studies of touch screen failures from the field indicate that most fail from damage introduction followed by stress far below that of the pristine glass strength. Thus it is critical to resist this type of damage for better retained strength in use.

After ion exchange the glasses are able to withstand even higher loads and the threshold load for crack initiation is shown in Fig. 1.7. Note that before ion exchange only a 100 g load is required to introduce cracking in soda lime silicate glass, but after ion exchange it takes 750 g of force. This is compared to ion-exchanged Gorilla® glass, which can take up to 7000 g of force before cracking. The new damage resistant glass does not show any signs of cracking at 7000 g of force and can withstand up to 35,000 g of force before cracking [25, 26], which is 45 times greater load than ion exchanged soda lime! This new damage resistant glass composition results in better scratch resistance and higher retained strength after indenting or scratching, which has enabled Gorilla® Glass to continue its success in the market.

1.2.7 Higher Compressive Stress

The magnitude of the compressive stress (CS) on the surface of the glass determines the load to failure. Corning optimized the glass composition to increase the CS and

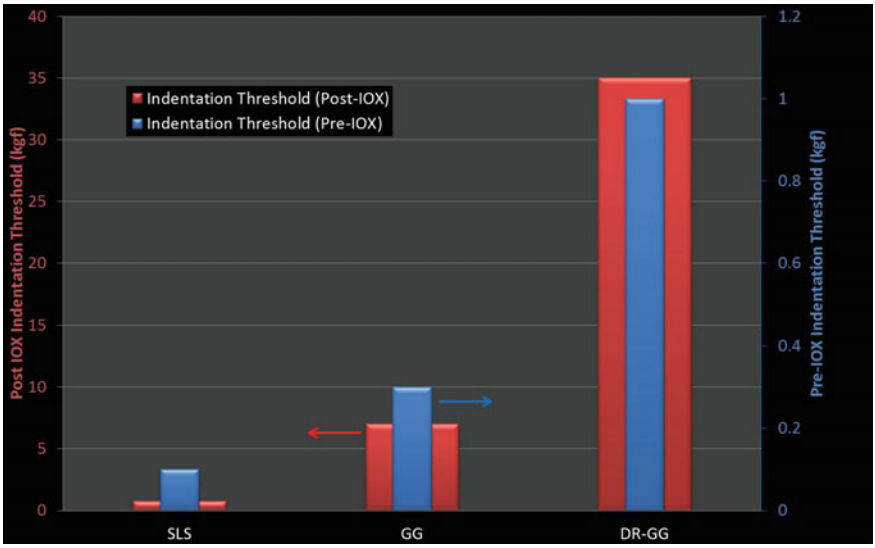

Fig. 1.7 Effects of ion-exchange on indentation threshold for soda lime glass (SLS), Gorilla® Glass (GG), and Gorilla® Glass with increased resistance to damage (DR-GG)

minimize stress relaxation during ion exchange, resulting in glasses that could achieve a CS of more than 900 MPa while still maintaining a deep DOL [27]. The enhanced compressive stress coupled with the greater damage resistance of the new base glass enabled thinner glass with greater retained strength and damage tolerance.

Figure 1.8 compares the load to failure for different thicknesses of the new aluminosilicate composition with improved CS and damage resistance with soda lime glass, both after ion exchange and abrasion according to ASTM C158. Pristine glass is very strong, but loses that strength as soon as flaws are introduced, so abrasion is used to estimate the "in use" or retained strength. Note that 1 mm thick soda lime fails at a load of 25 kgf, while the new Gorilla® Glass with high CS does not fail until 125 kgf which is five times the load. In fact, Gorilla® Glass with 0.55 mm thickness bears three times the load of 1 mm thick soda lime glass, enabling thinner glass with greater strength. Thus even at half the thickness, the new damage resistant glass with high CS still has three times the retained strength of ion exchanged soda lime.

Figure 1.9 compares the ring-on-ring load to failure of the soda lime, Gorilla® Glass and damage resistant Gorilla® Glass after scratching with a Vickers diamond at various loads. Note that while ion exchanged soda lime losses nearly all of its strength when scratched with a 0.5 N load, it takes 2 N to deplete the strength of Gorilla® Glass and more than 3 N to deplete damage-resistant high CS Gorilla® Glass. By understanding the fundamental damage mechanisms that degrade strength and then addressing them by changing the glass composition and atomic

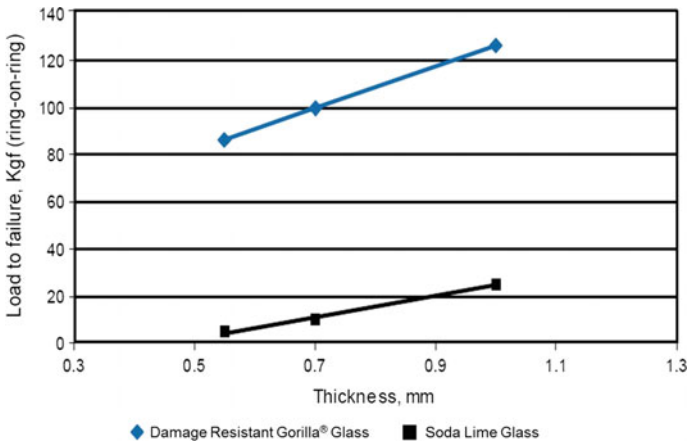

Fig. 1.8 Abraded load to failure of soda lime and damage resistant Gorilla® Glass as a function of glass thickness

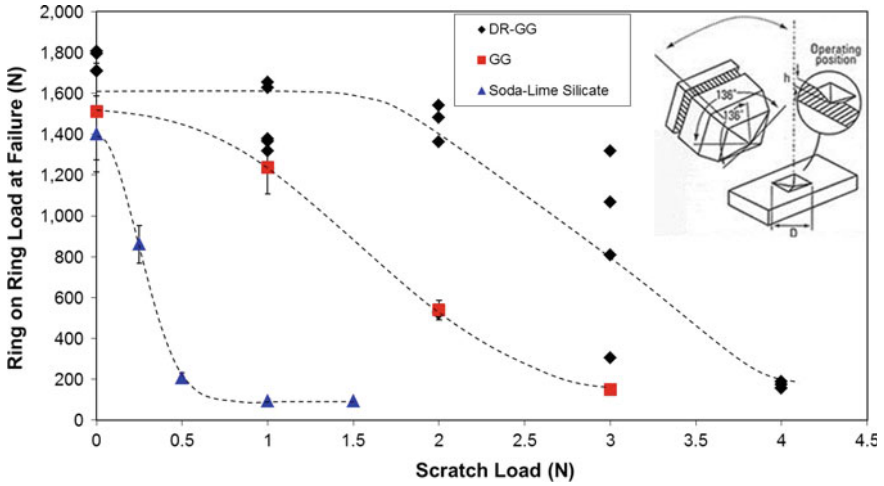

Fig. 1.9 Ring-on-ring load to failure as a function of Vickers diamond scratch load for 0.7 mm thick samples. Inset shows geometry of Vickers indenter

structure to increase CS, DOL, and damage tolerance, Corning created a version of the product whose mechanical performance surpasses that of soda lime, Chemcor, and the original versions of Gorilla® Glass itself. Thus Gorilla® Glass now protects more than three billion devices because the mechanical performance of the glass composition coupled with the pristine surfaces that the fusion process delivers, providing an ideal solution for thin, rugged touch screens and covers.

1.2.8 Future

Great progress has been made in the science and technology of glass composition and forming enabling vast improvements in the strength, transmission, damage tolerance, cost, performance, and quality of cover glass while reducing the environmental impact. As a result, Corning® Gorilla® Glass is used on devices from watches and cell phones to tablets and automobiles, on product lines from more than 40 major brands. But even with all these improvements, glass still breaks and requires significant energy and capital to manufacture. Thus there is a large opportunity for scientists, engineers, and technologists to explore and discover new strong scratch resistant materials, solve material interaction problems, and further reduce the environmental impact of making such materials.

Glass-ceramics offer enhanced toughness and strength over glass, but none have been made with both transparency and high toughness, so this is an area ripe for study. Glass-ceramics are dependent not only on composition, but also on heat treatment schedules so the space to explore is vast and less studied than glass. In addition, unstable crystalline phases can be precipitated from glass-ceramics that are impossible or impractical to make by other means, providing the opportunity to make novel materials with unique properties [28].

Glass, transparent ceramics, and single crystal materials like spinel, diamond, and sapphire all require high temperatures and large amounts of energy and capital to produce. Can such materials be made at lower temperatures with chemical processes like sol-gel, co-precipitation, or nanotechnology? Can these processes be used to enhance mechanical properties or make 3-D shapes? Currently, precision forming of transparent 3-D parts with optical quality requires either long cycle times or mechanical post finishing to achieve tight tolerances. Are their clever ways to make precision parts quickly?

There are many opportunities in the area of mechanical properties of glass and ceramic materials. Transparent materials must have band gaps greater than 3 eV to prevent visible absorption, but do strong bonds preclude ductile materials and must strongly bound materials always be brittle? Some recent work has shown that even glasses can be made to densify rather than crack, so the limits of this phenomenon need to be found. Device manufacturers are constantly pushing for thinner and thinner cover glass. Force balance limits the DOL of tempered glass to less than $\sim$ 20% of thickness for chemically or thermally tempered glass, so are there tricks to make flexible 0.1 mm thick glass sheets strong and damage resistant with only a 20 μm thick compressive layer?

Finally there is a need for good models of glass properties and behavior. Glass is a complex material whose properties primarily depend on composition, but as we have shown, also upon thermal history (unlike crystalline materials). While some properties like density are easy to predict with linear regression, others like liquidus temperature exhibit cusps and discontinuities as a function of composition and the most valuable compositions lie at those discontinuous minima. Consequently, clever modelers are needed to predict target glass compositions hitting multiple

desired attributes simultaneously to speed glass innovation and limit the amount of empirical "cook and look" work required.

1.3 Epic® Sensors: Label-Free Optical Sensing of Drug-Target Interactions

Corning's business in life sciences has traditionally been based on general labware and equipment. In the early 2000s, Corning was emerging from the crash of the telecom industry, and had strong capabilities in optical physics because of its participation in that industry. Application of these capabilities to the field of drug discovery led to the development of Epic® technologies.

1.3.1 Fluorescent Labels in Drug Discovery

The early stages of drug discovery process are dominated by label-dependent, high throughput screening (HTS)-compatible and target-based approaches [29]. These approaches screen drugs in the context of a predefined and target-based hypothesis in vitro to identify maximally selective drugs for single target-based therapies ("magic bullets") [30]. The dominance of target-based screen in early drug discovery has been coincident with the continuous decline in productivity of pharmaceutical research and development in the past quarter of century [31]. Single target-based approaches are postulated to be de facto ineffective, in particular, for unmet therapeutic needs and unexploited biological mechanisms [32]. This is because the target chosen in a screen may be non-druggable [29]; the molecular mechanism of action (MMOA) under investigation may not be efficacious [32]; and the drug identified may display unknown but clinically relevant polypharmacology [33]. Furthermore, fluorescent and luminescent molecular probes are essential to both in vitro screening assays and in vivo imaging techniques because these labels can markedly increase assay sensitivity and robustness, a prerequisite for HTS campaigns. However, these labels may alter performance or functions of proteins and cells, thus introducing bias or artifacts in results [34, 35]. The early finding that resveratrol is an activator of sirtuin-1 was lately shown to be an artifact of the label technique used in the screen [34]. Our recent study showed that D-luciferin is a partial agonist of GPR35, a poorly characterized orphan G protein-coupled receptor [35]. D-luciferin (firefly luciferin) is a yellow-green light-emitting molecule utilized by luciferase of fireflies, and is one of the most widely used probes for in vitro assays and in vivo imaging because of the high quantum yield of the luciferin-luciferase reaction and the change in bioluminescence color caused by subtle structural differences in luciferase [36].

1.3.2 State of the Art in Sensing of Drug-Target Binding

Drug binding is the prerequisite step to all drug-target interactions. The binding affinity of a drug to its primary target is traditionally used as an acceptable surrogate for its in vivo efficacy assessment. Thus, quantifying ligand binding to target receptors is critical to both fundamental research and drug discovery and development. Historically, the use of radioactive or fluorescent labeled probe molecules was common practice to perform competitive binding assays. Since 1990s, label-free technologies have been emerging as alternatives to directly characterize drug binding. Label-free detection has advantages associated with its inherent simplicity, ease of use, and ability to manifest the complex biology of drug action. Surface plasmon resonance (SPR) became the first commercially available label-free optical biosensor in early 1990s, and nowadays has become a standard technique to determine the binding kinetics of drug-target interactions in vitro [37], a parameter important to the in vivo efficacy and safety profiles of drugs [38]. However, SPR has clear limitations in throughput and application, because its angular sensitivity only permits the use of chips with small footprint for sensing and its microfluidic design only allows for direct binding analysis.

Drugs have to initiate desired biological responses after binding to their target(s) in order to cause therapeutic benefits. Functional testing of drug action is also critical to drug discovery. Historically, the biological functions of a drug were primarily examined using live tissues. In the past quarter of century, cell-based assays have become dominating in HTS campaigns. These assays often use labeled techniques to examine the effect of drugs in genetically engineered cell lines. Although label-free techniques such as patch clamping for ion channel drug profiling had been used, there were no HTS-compatible label-free platforms available for cell-based screens in early 2000s. Therefore, there was a strong need to develop HTS-compatible label-free platforms for examining drug-target interactions both in vitro and in living cells without the bias that could be introduced by fluorescent labels.

1.3.3 Corning's Contributions to Label-Free Detection

Since early 2000s Corning has been developing Epic® technologies for drug discovery and diagnostics (Fig. 1.10a). Although resonant waveguide grating (RWG) biosensor was invented long ago, it was limited to single sample analysis. To overcome its limitation in throughput as most label-free techniques have, we first invented a series of Epic biosensor microtiter plates. Microplates of 96-well, 384-well, or 1536-well are the de facto formats used in drug screening and profiling. Common to these Epic® microplates is that there is a RWG biosensor located in the bottom of each well. The biosensor typically consists of a three layer structure, a glass bottom substrate, a polymeric diffractive nanograting structure, and a top waveguide thin film (Fig. 1.10b). The waveguide surface is further coated

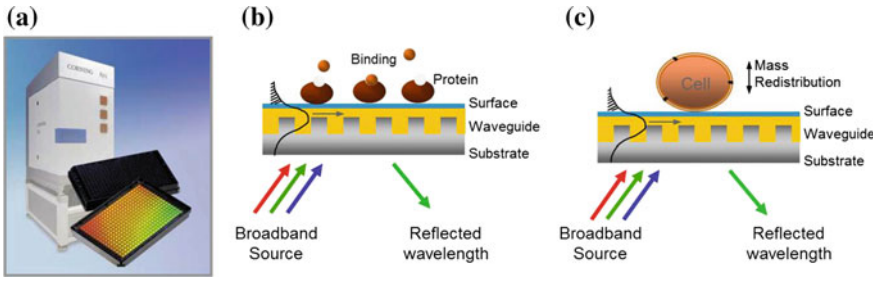

Fig. 1.10 Epic® technologies. **a** The Gen I HTS-compatible Epic® system and 384-well biosensor microplate. The color image of the microplate was obtained by illuminating with *white light* source under a specific angle. (b) Epic® enables biochemical assays by measuring the wavelength shift in the reflected light arising from the binding of small molecules to the proteins immobilized on the surface of the biosensor. (c) Epic® enables cell-based assays by measuring the wavelength shift in the reflected light arising from the drug-induced dynamic mass redistribution within the cells

with different chemistries for different applications. For in vitro biochemical assays the biosensor microplates are coated with polymer hydrogels to facilitate the robust immobilization of protein targets with minimal non-specific background binding. For cell based assays the biosensor microplates are cell culture treated or coated with an extracellular matrix protein to enable reliable cell culture and assays. Leveraging Corning manufacturing excellence in labware, together with inventive biosensor design and expertise in material sciences, has made it possible to produce high quality biosensor plates with extremely low intrinsic variability so it is amenable to HTS applications.

To address specific needs of different market segments, Corning has developed three generations of Epic® systems that enable quantitative biology studies using the RWG biosensors. This is made possible by inventive system designs and rigorous optical engineering. The first generation instrument was introduced in 2006 as the first standalone label-free system tailored to HTS applications. This system is a wavelength interrogation reader system consisting of a temperature-control unit, an optical detection unit, and an on-board liquid handling unit operated by internal robotics [39]. The detection unit uses a stationary array of fiber optics to repetitively scan a microtiter plate with a temporal resolution of 15 s. The second generation instrument, the EnSpire™ system, was co-developed with PerkinElmer and introduced in 2011 for basic research laboratories. This system is a multi-modular system containing a label-free Epic® module, plus fluorescence and chemiluminescence detection units. The Epic® module uses a single optical head to scan the plate with a temporal resolution of ~88 s. The third generation, Epic® BT system, was introduced in 2013 as a standalone bench top for both general and HTS laboratorial applications [40]. This system uses a swept wavelength interrogation scheme, in conjunction with a high speed complementary metal-oxide semiconductor digital camera, to simultaneously record the resonant wavelength images of all biosensors within the entire microplate with a temporal resolution of 3 s and a spatial resolution of 90 µm. This system is applicable to different microplate

formats and has a small footprint and simple operational procedure so it can be used in different settings including assays under physiological conditions.

To overcome the limitation in applications that conventional label-free techniques have, Corning also invented label-free cell-based receptor assays. Conventional optical biosensors including SPR and RWG were almost exclusively used to study the direct binding of small molecules to immobilized protein targets (Fig. 1.10b) [37]. For cell-based assays, label-free biosensors such as optical waveguide light mode biosensors and electric impedance biosensors were previously only used to investigate cell proliferation and death. Our theoretical and numerical modeling suggests that the surface-bound evanescent wave of the RWG biosensor generated under resonant light illumination condition is sensitive to minute changes in local refractive index arising from the drug-induced dynamic mass redistribution (DMR) within the cells, and the resultant DMR signal is a holistic and global representation of the functional consequences of the drug acting on living cells [41]. Follow-up experimental data have confirmed for the first time that Epic® sensors, and label-free optical biosensors in general, have great potential in cell-based drug discovery, including multi-target screening, target identification, MMOA determination, lead selection, and cardiotoxicity assessment [42–44]. The biosensor-enabled cell phenotypic assays offer clear advantages in rich information content, real-time kinetics, high sensitivity, highly flexible assay formats, and high throughput, besides their wide pathway coverage and ability in multi-target profiling and screening that are common to all phenotypic assays [42, 43]. These assays have made it possible to investigate endogenous receptors in native cells including stem and primary cells, and provide novel insights in drug pharmacology [45] and receptor biology [46, 47].

The development of Epic® technologies has taken advantages of multiple core competencies within the company. Modeling is essential to sensor design, manufacturing process optimization, and fundamental understanding of biosensor output signals particularly for cell based applications [41]. Deep understanding of materials science and manufacturing processes is critical to ensure the fabrication of biosensor microplates with high precision, given that label-free is often sensitive to environmental fluctuation and small molecule screening requires a limit of detection of adsorbed mass down to 0.1 ng/cm^2 [48]. Optical physics and engineering are indispensable to develop reliable and robust systems, in particular for HTS applications. Deep knowledge in cell biology, biophysics and drug discovery has contributed to the dramatic expansion in applications.

1.3.4 Future Needs in Label-Free Detection of Target Binding

Single cell analysis including genomics, proteomics and biological functions is the new frontiers in cell biology and is critical to both fundamental research and clinical diagnostics. Next generation biosensors shall have high spatial and temporal

resolution enabling single cell studies [49, 50]. This requires high precision optics, as well as the development of new bioinformatics tools that are capable of sorting signal heterogeneity and identifying factors controlling cell systems robustness. Given the increasingly recognized importance of drug residence time in the clinical features of drugs [38], next generation biosensor systems shall have ability to perform high throughput kinetics measurement [51]. This requires integration of microfluidics with high density microplates, which poses significant challenges for system design and engineering. Furthermore, given the prerequisite of current bioaffinity screening for the robust immobilization of functional proteins which is labor intensive and may be difficult for some target classes, new generation biosensors shall enable homogeneous binding assays [52]. This requires the discovery and utilization of new biophotonics phenomena. Furthermore, low cost manufacturing of biosensor devices such as microplates is essential to the wide adoption of label-free techniques in early drug screening. This requires the development of new and reliable manufacturing processes. The potential of label-free biosensors in basic research, drug discovery and healthcare is still far from full realization. New sensor design and instrumentation, together with innovative applications, will continue driving the development of these biosensors in the future.

1.4 Clearcurve® Optical Fiber

The need for a bend-resistant optical fiber was identified early on in the history of fiber optics. When fibers are bent too much, light leaks out of them and causes the signal to noise ratio to drop, which can lead to high error rates and broken communication links. However, the method of making bend resistant fibers was actually discovered by accident. A fiber blank was left in a consolidation furnace for too long and ended up being filled full of nanoscopic gas bubbles. When the blank was drawn into fiber, the holes elongated into “airlines”, lowering the effective refractive index of the glass in the region where the airlines were present, while remaining small enough to not scatter light. It was realized that if one could lower the index in this way in an annular region around the core, it would result in tighter mode confinement and greater tolerance to tight bends. So what was at first a defect turned out to be an important innovation that led to the development of bend-resistant optical fibers.

1.4.1 Basic Idea of Light Confinement in Optical Fibers

Light is confined in an optical fiber by means of total internal reflection, a phenomenon discovered by John Tyndall in 1870. When a light beam traveling from a higher refractive index medium strikes a boundary of another medium with lower

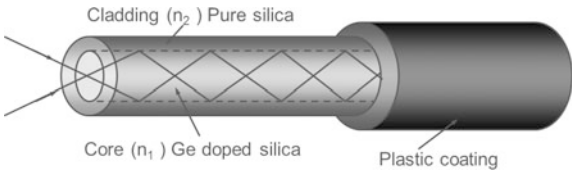

Fig. 1.11 Optical fiber comprising glass core and cladding, along with the outside polymer coating layer

refractive index, the beam will be partially refracted at the boundary surface, and partially reflected. However, if the angle of incidence is larger than a particular critical angle with respect to the normal to the surface, the beam will not cross the boundary and instead be totally reflected back internally. This total internal reflection is the fundamental principle behind fiber optics.

An optical fiber consists of a glass core, a glass cladding and a protective plastic coating as shown in Fig. 1.11. The refractive index of the core n_1 is greater than the refractive index n_2 of the cladding. Light is guided inside the core by the total internal reflection at the boundary between the core and the cladding.

In principle, when total internal reflection happens, light will propagate in the core without loss if the materials forming the fiber have no light absorption and scattering. However, in practice, a material will always have absorption and scattering and it is essential to minimize them to achieve low loss optical fiber. In 1970, the team of Maurer, Keck, and Schultz at Corning demonstrated the first low loss glass optical fiber with an attenuation of 20 dB/km, which made optical fiber viable for practical communications systems. Today's optical fibers have attenuation below 0.2 dB/km, which is much lower than copper wires. In addition, the bandwidth of optical fibers is much higher than that of copper wires, making it ideal transmission medium for telecommunications.

However, there is one basic aspect where fiber lags behind copper cable: so-called "bending loss". When a fiber is bent, the total internal reflection condition is disturbed, causing light tunneling out from the core to the cladding. Although fiber optic cables are much more flexible and easy to handle than copper, when standard single mode fiber (i.e. compliant to ITU-T rec. G.652.D) is bent around a corner with 5 mm radius, the optical power is essentially lost. To solve this problem, new fiber designs have been developed to improve the fiber bend performance and meet the network requirements and, at the same time, be compatible with large scale manufacturing and field installation procedures.

1.4.2 Corning's Contribution to Bend Resistant Optical Fibers

Designing bend insensitive fibers for fiber to the home (FTTH) poses significant technical challenges. The first challenge is to reduce the bending loss to meet the

requirements of harsh, copper cable-like handling conditions in multiple dwelling units (MDU) applications. This requires a bend-insensitive fiber to have very low (almost zero) bend loss at 1550 nm or shorter wavelength at bend radii typical for FTTH installations. For example in some carrier FTTH deployments, bend radii could be as low as 5 mm requiring bend loss to be less than 0.1 dB/turn [53]. As a reference point, the bend loss of standard single-mode fiber at 1550 nm is typically 20 dB/turn at the same bend radius. This implies a bend loss reduction factor of over 200. The second challenge is to meet the requirements of backward compatibility with the standard single-mode fibers imposed by the telecom industry standards. The bending and backward compatibility requirements put severe constraints on the fiber design space.

Corning addressed this difficult problem by exploiting use of a low index trench region in the cladding that was off-set from the high index core region (Fig. 1.12) to design optical fibers with much better bending performance and with other optical parameters compliant with the standards. The bend performance of a fiber with a low index ring in the cladding is determined by the volume of the ring, which is defined as the product of the ring area and the index depression. Increasing the ring volume improves the bend performance. However, the higher ring volume also makes the higher order LP_{11} mode more confined in the core region, which increases the cutoff wavelength. If the ring volume exceeds a certain maximum value, the fiber exceeds the 1260 nm cable cutoff wavelength limit imposed by the G.652 standard. Corning has developed bend-insensitive optical fibers having low index region in the cladding made from both nano-engineered glass and glass doped with conventional index depressing dopants such as fluorine. For a fluorine doped ring, the ring volume is constant in the wavelength range between 1200–1600 nm because the index does not change much with wavelength. For a nano-engineered ring design, the ring volume increases with increasing wavelength. This offers better bend resistance at the more bend sensitive, longer operating wavelengths. At shorter wavelengths the ring volume is reduced, which can keep the cable cutoff wavelength below 1260 nm. As a consequence, the nano-engineered fiber exhibits better bend performance at 1550 nm while retaining complete backwards compatibility with G.652 standard single-mode fibers. To quantify the fiber design

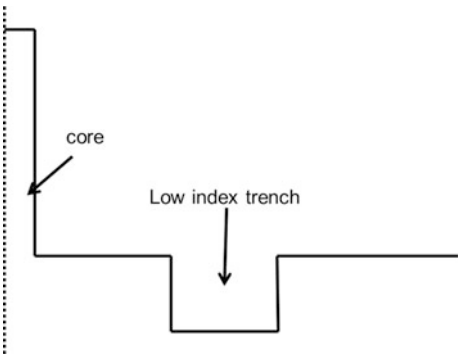

Fig. 1.12 Radial refractive index profile of optical fibers that are bend insensitive and also standards compliant

advantages, the bending loss of nano-engineered and conventional fluorine trench fibers has been calculated using a bend loss model [54]. Both fibers had the same single mode core design. The inner radius and ring thickness of the nano-engineered ring and the fluorine trench were chosen such that the cutoff, mode field diameter (MFD) and dispersion properties were comparable. To get different cutoff wavelengths and different bending losses, the ring width and void fraction were adjusted for the nano-engineered ring and the width and refractive index are changed for the fluorine trench. For illustrative calculations, a bent fiber is transformed into a straight fiber with an equivalent refractive index distribution as suggested in [55],

$$n_{eq}(x, y) = n(x, y) \exp\left(\frac{x}{R}\right) \tag{1.4}$$

where R is the bending radius, and the fiber is bent in the x-axis. The numerical modeling is based on a finite element method solving the fully vectorial Maxwell equations used in a previous study [56]. A circular perfectly matching layer (PML) is implemented at the fiber surface to emulate the effect of an infinite domain in the finite element model. With the PML, the propagation constant β of a mode becomes complex with the real part related to the effective index and the imaginary part related to the bending loss. The bending loss of the fiber (α_B) in a particular mode can be calculated from the imaginary part of the propagation constant β such that,

$$\alpha_B = \frac{20}{\ln(10)} \mathrm{Im}(\beta) \approx 8.686 \mathrm{Im}(\beta) \tag{1.5}$$

Figure 1.13 shows the bending loss at 5 mm radius of the two fibers as a function of cable cutoff wavelength. The cable cutoff wavelength is defined as the wavelength at which the loss of the first higher order mode, LP_{11} mode, has a total attenuation of 19.2 dB for a 22 m long fiber with two 80 mm diameter loops as defined in the TIA/EIA FOTP80. The results in Fig. 1.13 show that the nano-engineered fiber has a bending loss of less than 0.1 dB/turn in the cable cutoff region between 1140 and 1260 nm, which is one tenth of the bend loss of the conventional fluorine doped trench fiber.

Experimental evaluation of the performance of cabled nano-engineered fibers and conventional trench fibers has also been undertaken under extreme deployment conditions, as outlined in [53]. The test conditions are more severe than in typical FTTH deployments and are as follows: 10 × 90° corner bends + 2 bends with 2 kg load + 4 wraps at 10 mm diameter + 30 staples + 10 × 90° corner bend + 1 bend with 14 kg load + 6 wraps at 10 mm diameter + 50 staples + 10 flat staples. For comparison, a conventional trench fiber was tested under the same conditions. Figure 1.14 plots the attenuation increases at 1550 nm for the two fibers. The conventional trench fiber has a total attenuation increase of almost 2.5 dB. On the other hand, the total attenuation of nano-engineered fiber is about 0.25 dB, which is

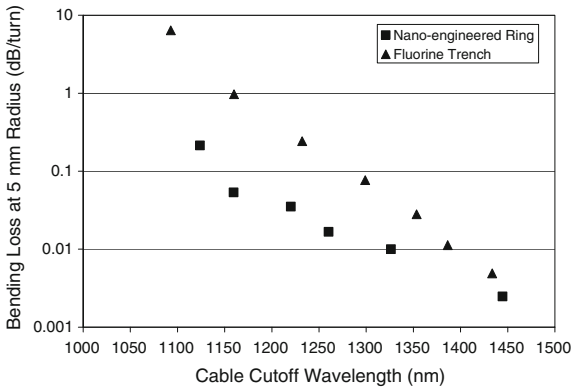

Fig. 1.13 Calculated bending loss at 1550 nm for nano-engineered and conventional trench fibers designs.Reproduced from Tandon et al. [57]

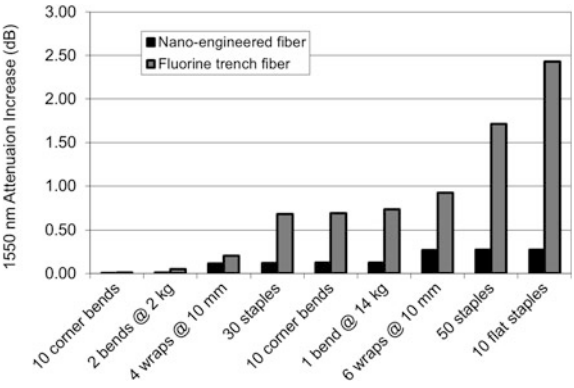

Fig. 1.14 Cabled fiber optical attenuation increases at 1550 nm in FTTH installations described in [53]. Reproduced from Tandon et al. [57]

only one tenth of total attenuation of the conventional fluorine doped trench fiber. This test demonstrates clearly the advantages of nano-engineered bend-insensitive fiber for FTTH deployments. However, Corning has recently developed and commercialized (as ClearCurve® LBL and ZBL fibers) advanced fluorine doped trench profiles with additional unique features (not discussed here) that result in superior bend performance compared to conventional fluorine doped trench fibers and provide bend loss performance that is comparable to that of the nano-engineered fibers [57, 58]. Indeed, these unique features can be combined with the nano-engineered fiber technology to yield even lower bend losses and design standards compliant bend insensitive fibers with super-low bend losses.

For the case of the nano-engineered fibers, optical properties and bending performance are quite sensitive to the void microstructure. The number of voids in the ring and the size distribution are strongly influenced by the process conditions used in glass making and subsequent drawing to fiber. It has been established that the fiber bend performance is significantly improved by having the nano-engineered region comprised of an increased number of smaller voids. In Fig. 1.15 is shown a scanning electron microscrope (SEM) image of a nano-engineered fiber having

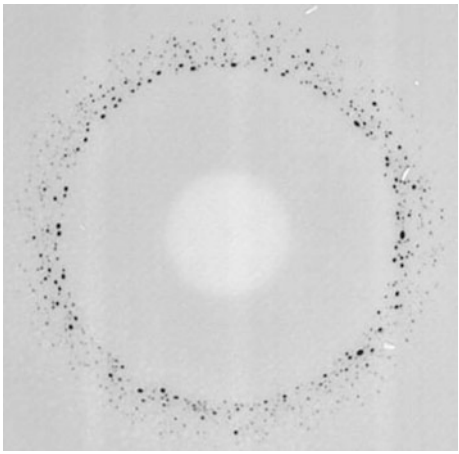

Fig. 1.15 SEM image of a nano-engineered fiber. Reproduced from Tandon et al. [57]

greater than 400 voids with the mean void diameter of ~130 nm. Increasing the void number density in the ring results in tight packing of the voids, resulting in good bend uniformity not only in the azimuthal direction, but also in the axial direction along the length of the fiber. It has also been established that by controlling the void microstructure, the ring volume of the void filled region could be significantly increased compared to the fibers reported in Li et al. [57, 59] and still have cable cutoff wavelength less than 1260 nm, thereby being fully compliant with standard G.652 single mode fibers. Thus, by increasing the void number density (by factor of >2x compared to fibers in Li et al. [57, 59]) and fraction in the fiber, the bend performance of the nano-engineered fibers is significantly improved compared to even the low bend loss values reported in Li et al. [54, 59].

To achieve super-low bend performance, quasi single-mode fibers have been proposed and made with thick rings of nano-engineered voids or fluorine doped trenches. While these fibers do not meet the cut-off requirement of G.652 because of the large trench volumes, they can be used as a single-mode fiber if a restricted launch into the core is used. The advantage of this type of fiber is that the bending loss is even lower than the bending loss of single-mode bend insensitive optical fibers. The bending loss of this fiber is less than 0.01 dB/turn at 5 mm bend radius and less than 0.001 dB/turn at 10 mm bend radius.

Similar to single-mode fibers, bend-insensitive multimode fibers (MMF) are attractive for enterprise network and data-center applications because they offer improved space operating margins, and enable smaller cable, hardware and equipment designs that can deliver space savings, easy handling for frequent changes, better cooling efficiency, and better overall connection and cable management. To design bend-insensitive MMF, a depressed index ring in the cladding similar to designing bend-insensitive single-mode fibers is used. Figure 1.16 shows two bend-insensitive MMF designs. Both designs have alpha graded index core with a low index ring in the cladding. In Design (a) of Fig. 1.16, the alpha-profile extends into the low index ring. Design (b) in Fig. 1.16 has an offset between the

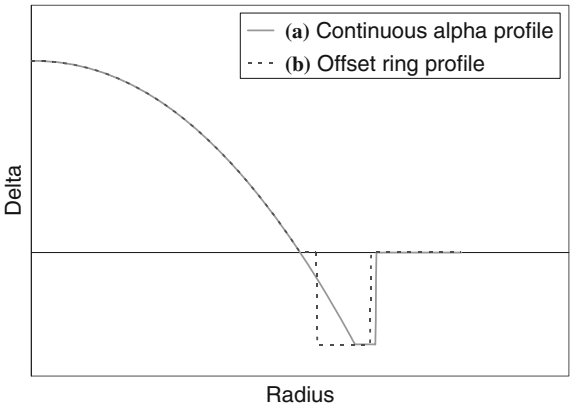

Fig. 1.16 Bend-insensitive MMF profile designs. **a** Continuous alpha profile in the ring, and **b** offset ring profile

core and the low index ring. In both designs, the low index ring reduces the optical power of guided modes in the cladding region outside the ring, thus improving their bend performance. The design task would be simple if only the bend loss requirement was considered. However, other requirements for MMF need to be considered as well such as numerical aperture (NA), optical core diameter (CD) and more importantly the bandwidth (BW), making the design task much more complicated. Care must be taken in designing both the core and the ring to satisfy all these requirements.

Increasing the ring volume will increase the bend performance, but also increase the core NA and CD. In order to keep the NA and CD compatible with the specifications of the standard MMF fiber, the ring volume has to be small enough to allow the unwanted higher order modes to tunnel into the cladding. At the same time, the core delta and core radius need to be adjusted to achieve the design targets. For MMF, bandwidth (BW) is a very important parameter. To achieve high BW, the core profile needs to be carefully designed with the correct alpha value. Any deviation from the optimum alpha profile will result in degradation in fiber BW. For standard MMF without the low index ring, the outermost mode groups tend to have shorter time delays. However these outer mode groups are not observed in a practical fiber as they are bend sensitive and can be easily stripped. For bend-insensitive MMF, the bending loss of these modes is decreased and the profile needs to be carefully designed to correct any delay problem associated with these modes. In Design (a) shown in Fig. 1.16, this problem is solved by extending the alpha profile into the low index ring region. The outer mode groups of the core see an ideal alpha profile and their delays are not affected by the ring. In Design (b) shown in Fig. 1.16, an offset is placed between the core and the ring. If the offset value is properly selected, the outer mode group delays can be corrected. Figure 1.17 shows the effect of offset on time delays at 850 nm wavelength of the outer mode groups. The core delta is 0.936%, the core radius is 24.5 μm, the ring delta is −0.45%, and the ring width 5 μm. For an offset of 1 μm, the two outer mode

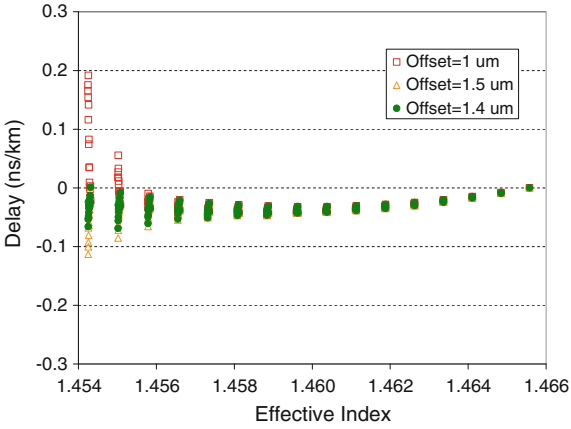

Fig. 1.17 Effects of ring offset on time delays

groups travel slower, but for an offset of 1.5 μm, the two outer mode groups travel faster. The optimum offset value in this case is about 1.4 μm.

Figure 1.18 compares the bend loss of each mode of a standard 50 μm MMF and a bend-insensitive MMF at the wavelength of 850 nm and the bend radius of 8.8 mm. The ring volume for the bend-insensitive fiber is 101%Δ μm^2. It can be seen that the low index ring reduces bend losses of the outer mode groups while the bend losses of the inside mode groups remain the same. As a result, the bend loss of a MMF depends on launch conditions. However, even if only the inner mode groups are excited, discontinuities such as connectors, splices, and small perturbations along the fiber, will cause mode coupling, spreading the power into outer mode groups. A bend-insensitive fiber will show benefits in these practical deployment conditions. Figure 1.19a plots calculated overall bend loss at 850 nm as a function of bend radius for a standard MMF and a bend-insensitive MMF under an encircled flux launch (EFL) condition by using a 2 m length of standard MMF with a 25 mm diameter mandrel in the middle. It's clear that the bend-insensitive MMF has a bend loss more than 10 times lower compared to standard MMF in the bend radius range studied. Figure 1.19b shows measured bend loss for a bend-insensitive fiber compared to a standard MMF. The bend loss of the bend-insensitive MMF is more than 10 times lower than the standard MMF, which is in excellent agreement with the modeling results shown in Fig. 1.19a. In addition to the excellent bend performance, the bend-insensitive fiber is fully compatible with the MMF standard. In particular the bandwidth can meet the OM3 and OM4 requirements (as detailed in ISO/IEC 11801), suitable for high data rate applications.

1.4.3 State of the Art in Bend-Resistant Optical Fibers

The fibers disclosed in the section above represent the "best in category" fibers for single-mode, quasi-single mode and multi-mode applications. For the case of

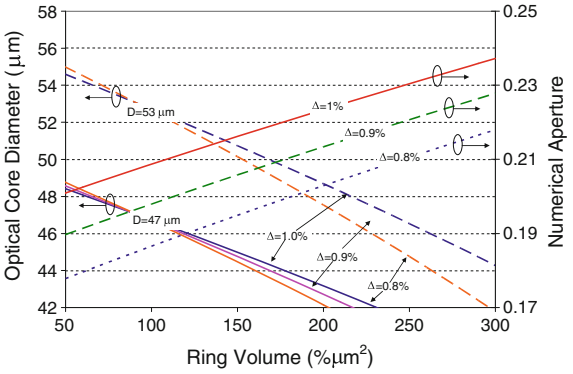

Fig. 1.18 Design diagram for numerical aperture and optical core diameter. The ring delta is between −0.5 and −0.3%

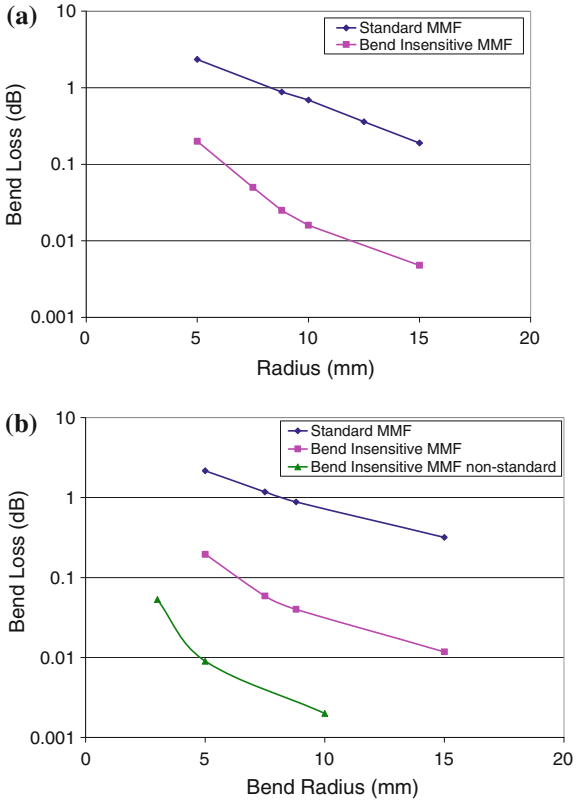

Fig. 1.19 **a** Calculated bending loss for standard and bend-insensitive MMF. **b** Comparison of bending performance of standard and bend-insensitive MMF

single-mode bend-insensitive fibers, as outlined above, Corning exploiting the nanoStructures® technology was one of the first fiber manufacturers to introduce nano-engineered bend-insensitive fibers that exhibited very low bend loss even at 5 mm bend radius. It has since developed and successfully commercialized

(ClearCurve® LBL and ZBL optical fibers) all solid fluorine-doped trench fibers that are standards compliant and have bend performance that is comparable to nano-engineered fibers. The unique all-solid trench assisted bend-insensitive fiber designs developed at Corning using fluorine doped trenches have the advantage of being readily compatible with conventional connectorization/splicing technologies and recipes, while at the same time delivering bend performance comparable to nano-engineered fibers.

Similarly, bend-insensitive ClearCurve® multi-mode fibers having fluorine doped negative index trench in the cladding are being extensively used for data centers and enterprise applications, allowing for efficient space utilization and cable/connection management. The unique fiber designs for these fibers are able to deliver ultra-low bend loss performance and yet have optical properties such as bandwidth, Numerical Aperture, optical core diameter that are standards compliant and comparable to standard multi-mode fibers.

1.4.4 Future Needs in Bend-Resistant Optical Fibers

There continues to be a need for bend-insensitive fibers with even lower bend losses. The fiber design principles developed for the current bend-insensitive products, along with the unique manufacturing processes, can be used for making next generation of low bend-loss products. For some of the ultra-low bend loss applications, quasi-single mode fibers are attractive as they deliver very low bend losses and yet functionally behave as single-mode fibers by choosing appropriate launch conditions. For the bend-insensitive single-mode fibers, optical fiber designs having low bend performance for mode field diameter matched to standard single mode fibers and for smaller coated fiber diameter would be important for installation of these fibers beyond FTTH. Low bend loss fibers with high NA are also starting to be commercialized and find applications in consumer and Very Short Distance Network (VSDN) applications.

1.5 Skills and Talents

Corning has many projects going on today that are similar to the innovations presented here, and we continue to draw upon all of the competencies presented in Fig. 1.1. We will continue to need people with backgrounds in physics (particularly optical physics), chemistry, materials science (especially glass science, ceramics, and polymer science), biological sciences, math, and computer science. We also need people who can take inventions and make them into practical embodiments that can actually be manufactured, so people from the same disciplines but with engineering backgrounds are especially important. And because many of our products are made using specialized processes that we invent, we usually have to

design our own machines to manufacture them. We need people with a range of skills in developing and running those special machines, including mechanical engineers, electrical engineers, software engineers, robotics experts, etc.

With so many opportunities, what skills should an aspiring student acquire to tackle such grand challenges in materials science? The answer lies at the intersections of disciplines. While it is common to find people skilled in modeling, mechanical properties, characterization, or processing, it is rare to find people skilled in two or more areas especially when one of those areas is glass composition. These hybrid disciplines are likely to bear fruit since they are not often studied nor fully understood. For example a person skilled in both mechanical properties and glass composition would be well suited to find a glass that doesn't break (or at least is much harder to break). A young inexperienced hybrid professional may not be able to instantly solve the problem, but can instantly serve as a bridge between mechanical property experts and composition experts to get the ball rolling and then likely contribute breakthrough research of their own as they learn more from their more experienced teammates. Even at conferences different groups tend to silo themselves into different sessions with few bridges to link key findings in one are with those in another.

Just examine the innovations presented in this chapter to see that intersections of disciplines are where the fruit lies. ClearCurve® fiber was at the intersection of physics (optical waveguides) and material processing. The Epic® sensor was at the intersections of biology, optics, and surfaces. Gorilla® Glass is the result of glass composition, ion exchange, chemistry, mechanical properties, material interaction (materials science) and glass processing. No one person could have done it all, but it required smart curious people in all areas who were willing to push the limits. Many of us were not initially experts, but we quickly became so as we learned from others via collaboration, internal reports, literature, and/or conversations. Thus the ability to work as part of team and learn from others are critical skills. Finally all these contributors were extremely passionate about their work and their internal pull of curiosity and science far eclipsed any external push from management to get the job done. So we encourage young scientists and engineers to find a field they love and passionately sink their teeth into it.

References

1. *Devitrification* is the glass manufacturing term for crystallization—small crystals form in the glass, leading to opacity and mechanical degradation. Avoiding devitrification is one of the main goals in glassmaking. Devitrification can occur when the temperature of the glass goes below the *liquidus temperature*, defined as the lowest temperature at which crystals can be in equilibrium with their surrounding liquid—see C. Bergeron, S. Risbud, *Introduction to Phase Equilibria in Ceramics*, The American Ceramic Society, Columbus, OH (1984), p. 22. The *liquidus viscosity* is the viscosity of the glass at the liquidus temperature, and determines what forming processes can be used to make molten glass into useful objects such as bottles, bulbs, or precision sheet. If any static interface in the glass manufacturing system is in contact with

molten glass at a temperature below the liquidus temperature, crystals will grow on that interface and pollute the pristine glass with crystalline inclusions. Above the liquidus temperature only the liquid phase is stable and the glass will never experience devitrification
2. J.E. Shelby, *Introduction to Glass Science and Technology* (The Royal Society of Chemistry, Cambridge, 2005), p. 191
3. J. Olcott, Chemical strengthening of glass: After more than 70 years of research, glasses can now be made strong enough to be bent sharply. Science **140**(3572), 1189–1193 (1963)
4. R. McMaster, D. Shetterly, A. Bueno, Annealed and tempered glass, in *Engineered Materials Handbook*, ed. by S. Schneider. Ceramics and Glasses, vol. 4 (ASM International, Ohio, 1991), pp. 453–459
5. W. Dumbaugh, Laminated glass, in *Engineered Materials Handbook*, ed. by S. Schneider. Ceramics and Glasses, vol 4 (ASM International, Ohio, 1991), pp. 423–426
6. E. Berger, Unbreakable and malleable glass. Naturwissenschaften **25**, 79 (1924)
7. R. Bartholomew, Ion-exchange, in *Engineered Materials Handbook*, ed. S. Schneider. Ceramics and Glasses, vol. 4 (ASM International, Ohio, 1991), pp. 460–463
8. G. Schulze, Experiments relating to the diffusion of silver into glass. Ann. Phys. **40**, 335–367 (1913)
9. S.D. Stookey, New high strength ion-exchange glass-ceramics. Corning Internal Report R-1990 June 29, 1960
10. S.D. Stookey, J.S. Olcott, H.M. Garfinkel, D.L. Rothermel, Ultra-high-strength glasses by ion exchange and surface crystallization. *Technical Papers of the Sixth International Congress on Glass*, Washington, D.C., 1962, pp. 397–411
11. S.S. Kistler, J. Phys. Chem. **34**, 52 (1932)
12. P. Acloque, J. Tochon, Measurement of mechanical resistance of glass after reinforcement, in *Symposium sur la resistance mecanique du verre et les moyens de l'ameliorer (Colloquium on Mechanical Strength of Glass and Ways of Improving It)*, pp. 687–704, Florence, Italy, 25–29 Sept 1961,. Published by Union Scientifique Continentale du Verre, Charleroi, Belgium, 1962. 1044 pp.; Ceram. Abstr., 1963, January, p. 31i
13. S.S. Kistler, J. Am. Ceram. Soc. **45**(2), 59–68 (1962)
14. M.E. Nordberg, E. Mochel, H.M. Garfinkel, J.S. Olcott, Strengthening by ion exchange. J. Am. Ceram. Soc. **47**(5), 215–219 (1964)
15. M.B.W. Graham, A.T. Shuldiner, *Corning and the Craft of Innovation* (Oxford University Press, Oxford, 2001), pp. 260–267
16. An *isopipe* is a trough made from refractory material that is used in the fusion down draw process pioneered by Corning—molten glass overflows both sides of the trough, forming a pristine sheet of glass underneath
17. A. Ellison, I.A. Cornejo, Glass substrates for liquid crystal displays. Int. J. Appl. Glass Sci. **1** (1), 87–103 (2010)
18. A. Ellison, S. Gomez, Down-drawable, chemically strengthened glass for cover plate. United States Patent No. 7,666,511
19. J.E. Shelby, *Introduction to Glass Science and Technology* (The Royal Society of Chemistry, Cambridge, 2005), p. 4
20. S. Rekhson, Viscoelasticity of Glass. in *Glass: Science and Technology*, ed. by D.R. Uhlmann, N.J. Kreidl, vol. 3 (Academic Press, New York, 1986), p. 4
21. M. Dejneka, A. Ellison, S. Gomez, Ion exchanged, fast cooled glasses. United States Patent No. 8,232,218
22. R. Doremus, *Glass Science* (Wiley, New York, 1973), p. 237
23. M.J. Dejneka, S. Gomez, Fining agents for silicate glasses. United States Patent No. 8,114,798
24. M.J. Dejneka, S. Gomez, Fining agents for silicate glasses. United States Patent No. 8,158,543
25. M. Dejneka, R. Morena, S. Gomez, A. Ellison, Glasses having improved toughness and scratch resistance. United States Patent No. 8,652,978
26. K.L. Barefoot, M.J. Dejneka, N. Shashidhar, S. Gomez, T.M. Gross, Crack and scratch resistant glass and enclosures made therefrom. United States Patent No. 8,586,492

27. M. Dejneka, A. Ellison, J. Mauro, Zircon compatible, ion exchangeable glass with high damage resistance. United States Patent No. 8,951,927
28. W. Höland, G.H. Beall, *Glass Ceramic Technology,* 2nd edn. (Wiley, Hoboken, 2012)
29. D.C. Swinney, J. Anthony, How were new medicines discovered? Nat. Rev. Drug Discov. **10**, 507–519 (2011)
30. K. Strebhardt, A. Ullrich, Paul Ehrlich's magic bullet concept: 100 years of progress. Nat. Rev. Cancer **8**, 473–480 (2008)
31. F. Pammolli, L. Magazzini, M. Riccaboni, The productivity crisis in pharmaceutical R&D. Nat. Rev. Drug Discov. **10**, 428–438 (2011)
32. M. Rask-Andersen, M.S. Almén, H.B. Schiöth, Trends in the exploitation of novel drug targets. Nat. Rev. Drug Discov. **10**, 579–590 (2011)
33. A.L. Hopkins, Network pharmacology: the next paradigm in drug discovery. Nat. Chem. Biol. **4**, 682–690 (2008)
34. M. Pacholec, J.E. Bleasdale, B. Chrunyk, D. Cunningham, D. Flynn, R.S. Garofalo et al., SRT1720, SRT2183, SRT1460, and resveratrol are not direct activators of SIRT1. J. Biol. Chem. **285**, 8340–8351 (2010)
35. H. Hu, H. Deng, Y. Fang, Label-free phenotypic profiling identified D-luciferin as a GPR35 agonist. PLoS ONE **7**, e34934 (2012)
36. G.D. Luker, K.E. Luker, Optical imaging: current applications and future directions. J. Nucl. Med. **49**, 1–4 (2008)
37. Y. Fang, Label-free cell-based assays with optical biosensors in drug discovery. Assays Drug Dev. Technol. **4**, 583–595 (2006)
38. R.A. Copeland, D.L. Pompliano, T.D. Meek, Drug-target residence time and its implications for lead optimization. Nat. Rev. Drug Discov. **5**, 730–739 (2006)
39. G. Li, A.M. Ferrie, Y. Fang, Label-free profiling of endogenous G protein-coupled receptors using a cell-based high throughput screening technology. JALA **11**, 181–187 (2006)
40. A.M. Ferrie, Q. Wu, Y. Fang, Resonant waveguide grating imager for live cell sensing. Appl. Phys. Lett. **97**, 223704 (2010)
41. Y. Fang, A.M. Ferrie, N.H. Fontaine, J. Mauro, J. Balakrishnan, Resonant waveguide grating biosensor for living cell sensing. Biophys. J. **91**, 1925–1940 (2006)
42. Y. Fang, Troubleshooting and deconvoluting label-free cell phenotypic assays in drug discovery. J. Pharmacol. Tox. Methods **67**, 69–81 (2013)
43. Y. Fang, Label-free drug discovery. Front. Pharmacol. **5**, 52 (2014)
44. A.M. Ferrie, Q. Wu, O. Deichmann, Y. Fang, High frequency resonant waveguide grating imager for assessing drug-induced cardiotoxicity. Appl. Phys. Lett. **104**, 183702 (2014)
45. A.M. Ferrie, H. Sun, Y. Fang, Label-free integrative pharmacology on-target of drugs at the β_2-adrenergic receptor. Sci. Rep. **1**, 33 (2011)
46. F. Verrier, S. An, A.M. Ferrie, H. Sun, M. Kyoung, Y. Fang, S.J. Benkovic, GPCRs regulate the assembly of a multienzyme complex for purine biosynthesis. Nat. Chem. Biol. **7**, 909–915 (2011)
47. A.M. Ferrie, C. Wang, H. Deng, Y. Fang, Label-free optical biosensor with microfluidics identifies an intracellular signalling wave mediated through the β_2-adrerengic receptor. Integr. Biol. **5**, 1253–1261 (2013)
48. N. Orgovana, B. Kovacs, E. Farkas, B. Szabó, N. Zaytseva, Y. Fang, R. Horvath, Bulk and surface sensitivity of a resonant waveguide grating imager. Appl. Phys. Lett. **104**, 083506 (2014)
49. A.M. Ferrie, O.D. Deichmann, Q. Wu, Y. Fang, High resolution resonant waveguide grating imager for cell cluster analysis under physiological condition. Appl. Phys. Lett. **100**, 223701 (2012)
50. Y. Fang, Label-free whole cell phenotypic diagnostics for cancer, in *Biosensors for Healthcare: Hot Topics, Future Medicine* (2013), pp. 54–67
51. N. Zaytseva, W. Miller, V. Goral, J. Hepburn, Y. Fang, Microfluidic resonant waveguide grating biosensor system for whole cell sensing. Appl. Phys. Lett. **96**, 163703 (2011)

52. D.J. Bornhop, J.C. Latham, A. Kussrow, D.A. Markov, R.D. Jones, H.S. Sørensen, Free-solution, label-free molecular interactions studied by backscattering interferometry. Science **317**, 1732–1736 (2007)
53. D.Z. Chen, W.R. Belben, J.B. Gallup, C. Mazzali, P. Dainese, T. Rhyne, Requirements for Bend Insensitive Fibers for Verizon's FiOS and FTTH Applications. Paper NTuC2, OFC/ NFOEC2008, San Diego, California, 2008
54. M.-J. Li, P. Tandon, D.C. Bookbinder, S.R. Bickham, M.A. McDermott, R.B. Desorcie, D.A. Nolan, J.J. Johnson, K.A. Lewis, J.J. Englebert, Ultra-low Bending Loss Single-Mode Fiber for FTTH. J. Lightwave Technol. **27**(3), 376–382 (2009)
55. M. Heiblum, J.H. Harris, Analysis of curved optical waveguides by conformal transformation. IEEE J. Quantum Electron. **QE-11**, 75–83 (1975)
56. M.J. Li, X. Chen, D.A. Nolan, G.E. Berkey, J. Wang, W.A. Wood, L.A. Zenteno, High bandwidth single polarization fiber with elliptical central air hole. J. Lightwave Technol. **23**, 3454–3460 (2005)
57. P. Tandon, M.J. Li, D. Bookbinder, S. Logunov, E. Fewkes, Nano-engineered optical fibers and application. J. Nanophotonics **2**(5–6), 383–392 (2013)
58. D.C. Bookbinder, M-J. Li, P. Tandon, Low bend loss optical fiber. United States Patent No. 8,385,701
59. M.-J. Li, P. Tandon, D.C. Bookbinder, S.R. Bickham, M.A. McDermott, R.B. Desorcie, D.A. Nolan, J.J Johnson, K.A. Lewis, J.J. Englebert, Ultra-low bending loss single-mode fiber for FTTH. OFC/ NFOEC2008, Paper PDP10, San Diego, California, 24 Feb 2008

Chapter 2
IRradiance Glass: Technology Transfer from University to Industry

J. David Musgraves, Jennifer McKinley and Peter Wachtel

Abstract An overview of IRradiance Glass, Inc. and our development process for advanced chalcogenide glasses for infrared optics are presented. The physical and optical properties of chalcogenide glasses are reviewed, and some topics in infrared sensing are introduced to the reader. The impact of gradient refractive index (GRIN) materials on the functionality of optical elements is discussed, and the IRradiance Glass GRIN materials are described, explaining the technical challenges faced in moving this technology from the laboratory to the manufacturing floor. The chapter ends with a discussion of the technology transfer process, whereby intellectual property developed in a university setting is licensed to commercial entities for development. Future directions in both GRIN optics and technology transfer processes are discussed.

2.1 Introduction

This chapter describes the technology transfer process, i.e. making commercial products from technology developed at universities, from a company's point of view. Most of the other examples in this book describe the process of moving a company's product idea from in-house R&D to the manufacturing line. But sometimes, the best research idea isn't internally supported—it comes from federally-funded university research, as is the case for a technology IRradiance Glass is in the process of commercializing. So instead of giving a technical review of several different products, this chapter will focus on only one technology, but

This chapter is Approved for Public Release, Distribution Unlimited.

J.D. Musgraves (✉) · J. McKinley · P. Wachtel
IRradiance Glass Inc, 3267 Progress Drive, Orlando, FL 32826, USA
e-mail: musgraves@irradianceglass.com

L.D. Madsen and E.B. Svedberg (eds.), *Materials Research for Manufacturing*, Springer Series in Materials Science 224,
DOI 10.1007/978-3-319-23419-9_2

examine both the technical aspects as well as the business aspects of the university-to-corporation technology transfer process.

The technology being transferred in this case is a method for forming advanced optical lenses using glass ceramic materials. IRradiance Glass (pronounced as "irradiance" and abbreviated as IRG) specializes in the design and production of infrared-transparent chalcogenide glasses, and we want to use a technology for selectively forming nanocrystals in these glasses that will allow us to create chalcogenide glass lenses with advanced optical functionality, able to focus light in ways other lenses cannot. Some of the scientific background of this technology, as well as some of the preliminary results demonstrated by the university partners, are discussed below in this section, as well as in Sect. 2.2 of this chapter.

Section 2.3 describes the current legal and institutional status of the technology transfer process, and how these issues impact the commercial development process. The advent of technology transfer as a codified and encouraged process is fairly recent, with the passage of the Bayh-Dole Act in 1980. One of the primary impacts of the passage of this law was to allow universities to obtain legal ownership over technologies developed on their campuses, even though the research itself was directly funded with federal grant dollars. These changes in legal policy overlapped with the business trend of reducing the scale of internal R&D efforts, leading to the dramatic reduction of intellectual property-generating business units such as Bell Laboratories. The result of this confluence of policy and commercial changes has led to a dramatic rise in the use of technology transfer as a legitimate extra-mural source of R&D.

The chapter closes with some perspectives on future directions in both advanced infrared optics as well as in the technology transfer process. Lots of exciting potential exists in both areas.

2.1.1 An Overview of IRradiance Glass

IRradiance Glass, Inc. (IRG), headquartered in Orlando, Florida, specializes in the compositional design of infrared-transparent glasses for use in cutting-edge optical systems. IRG was founded in 2012 by a group of four scientific researchers and entrepreneurs with the goal of providing low-cost, high-quality chalcogenide glasses for an expanding broad-based commercial market. IRG has developed chalcogenide glass products to provide infrared solutions for customers ranging from small startups to large Tier-1 defense contractors.

Unlike many of the larger manufacturers in the field of IR-transparent materials, which generally force their customers to select from a narrow, standardized palette of material offerings, IRG prides itself on being able to offer developers a much wider array of materials from which to choose to best fit their own specific needs.

So, if the application's demands are simple and straightforward, then through its IRRADIANCE™ CLASSIC line, IRG can produce cost effective, high quality, industry-standard materials of the sort the customer can get from any of the larger suppliers in this area.

However, for those customers whose product design needs demand something beyond a simple, "off-the-shelf" selection, IRG expands the toolbox available to the optical design community by offering its IRRADIANCE™ CUSTOM lines featuring small to medium-scale boules of compositions that are individually-designed for customers interested in research or glass product prototypes with specific mechanical, optical, and other material property requirements. These products may be fabricated for requirements such as rare earth doping, restriction of hazardous substances (RoHS) compliance, and advanced optical functionality. For these sorts of demanding applications, IRG's team of experienced glass scientists will work with the customer to tailor a formulation custom designed to meet those specialized demands. Some of the range of glass compositions and forms created by IRG are shown in Fig. 2.1.

The IRRADIANCE™ SELECT line of glasses represents IRG's efforts to address specific market needs that are intended to be offered on a larger scale. These applications may include products with increased mechanical stability, improved glass molding properties, and additional attention to environmental hazards.

With its nimble, customer-centric approach, IRG is positioning itself to be at the forefront of what it expects to be the widespread commercialization of IR technologies as they transition from the highly specialized realm of high-end military and industrial applications into much more traditional commercial applications such as cell phones [1], home entertainment [2], and automobiles [3].

In addition to its regular commercial activities, through its ongoing involvement in grant-funded programs and its close affiliation with the highly regarded College of Optics and Photonics of the University of Central Florida, IRG is continually striving to be at the cutting edge of developments in glass science and technology to enable it to help bring those advancements to its customers.

2.1.2 General Principles of Chalcogenide Glasses

Chalcogenide glasses are amorphous semiconductors containing the chalcogen elements sulfur, selenium, and/or tellurium, but excluding oxygen. Shown in Fig. 2.2, these glasses are differentiated from their crystalline counterparts (Fig. 2.2a) by the disorganized nature of their network structures (Fig. 2.2b). While crystals are constrained to have single composition and associated physical and optical properties, the amorphous nature of the chalcogenide glass network makes it possible to change the composition of the network off of the stoichiometric standard, and achieve new and interesting physical properties. This process is shown in Fig. 2.2c, where some of the arsenic atoms have been replaced with germanium atoms in the glass network. This substitution gives rise to a host of changes in the physical properties, and is responsible for the optical changes shown in Fig. 2.1c. Chalcogenide glasses exhibit several unique optical and structural properties that make them ideal material candidates for infrared optics and photonics in bulk, fiber as well as thin film forms (Fig. 2.2):

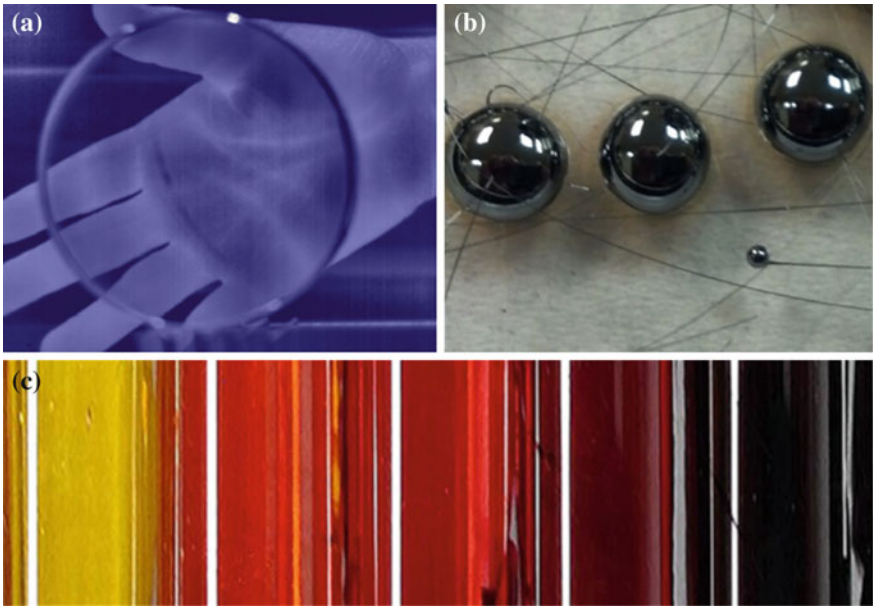

Fig. 2.1 Photographs above show several examples IRG's chalcogenide glasses: **a** shows an industry-standard arsenic selenide glass plate, four inches in diameter. **b** Shows the same glass formed from the melt as spheres for molding. The glasses shown in (**c**) are in the Ge–As–S ternary glass family. The bandgap of the material has been tuned by changing the ratios of the constituent elements, giving glasses that move from clear and yellow in the visible region of the spectrum to black and opaque, all while remaining fully transparent in the infrared

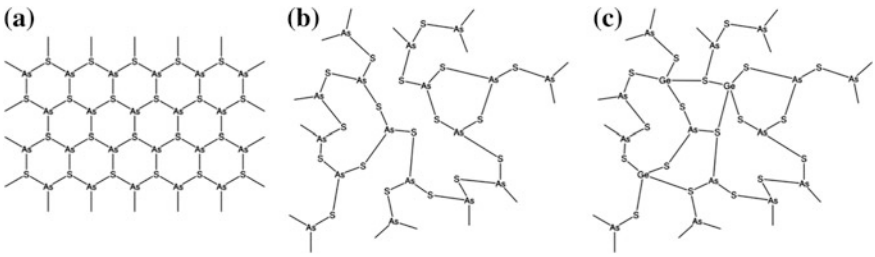

Fig. 2.2 Network-level structure of several chalcogenide compounds: **a** $As_{50}S_{50}$ crystal, **b** $As_{40}S_{60}$ glass, and **c** Ge-doped $As_{40}S_{60}$ glass

(1) *Low phonon energy*, which accounts for chalcogenide glass's wide optical transparency windows with an infrared cut-off wavelength deep into the long-wave IR regime (up to 25 μm wavelength [4–7], while typical silicate glasses are opaque beyond 5 μm wavelength);

(2) *High refractive indices*, up to 3.5 [8], allowing the fabrication of high-index-contrast optical devices such as strongly confined optical waveguides,

high-efficiency diffractive optics, micro-lens arrays with low spherical aberration, and broadband grating reflectors;

(3) *Property tailoring via composition alloying*, a property benefitting from chalcogenide glass's broad glass forming region, permits continuous tuning of glass optical and thermal properties over a large range [9–11]. This feature is critical to applications such as optical bonding [12] and retroreflector designs [13], which require precise refractive index matching. Beside composition alloying, we have recently shown that chalcogenide glass-polymer hybrid materials can be derived from a common amine-based solution, and refractive indices of the resulting solution-processed hybrid materials can be continuously tuned across the entire organic-inorganic composition range, further broadening the accessible refractive index range in the material system [14];

(4) *Processing versatility*, Bulk chalcogenide glasses can be synthesized using the well-established melt-quenching method or microwave sintering as a low-cost alternative [15], and chalcogenide glass thin films can be prepared using vapor and solution deposition methods at a low substrate temperature (<200 °C) [16–19]. The amorphous nature of chalcogenide glasses, coupled with their low deposition temperature, facilitates monolithic integration with virtually all technically important substrate materials including plastic substrates, enabling the creation of inorganic-organic hybrid flexible photonic circuits [20, 21].

In addition to their superior optical properties, chalcogenide glasses also exhibit thermo-mechanical characteristics that are drastically different from oxide glasses and are suitable for shaping via molding. Chalcogenide glasses typically have lower glass transition (T_g) and softening temperatures, which enables molding of photonic components at reduced temperatures [22]. The low molding temperature contributes to decreased thermal stress, reduced surface degradation and adhesion to molds, as well as the use of elastomer stamps for molding on nonplanar and flexible substrates.

2.1.3 Applications of Infrared Optics

Chalcogenide glasses (ChGs) are well known for their high infrared (IR) transparency and amenability to fabrication in fiber and thin film forms, which makes them attractive candidates for mid-IR optical chemical and biological sensors, in addition to infrared imaging applications. This section describes recent advances in the production of sensing devices from a variety of thin film and fiber structures, highlighting the critical materials parameters needed for achieving low loss, high detectivity operation.

Optical chalcogenide glass fibers have undergone tremendous development since the first draws were reported in the mid 1960s [23]. With the advent of photonic crystal fibers, they have now found numerous applications including the fields of IR light-wave propagation [24], dispersion tailoring [25], supercontinuum generation [26], medical endoscopy [27], temperature monitoring and imaging [28–30],

all-optical switching [31], and Raman gain engineering [32]. In addition ChG fiber-based sensor devices have proven to be excellent candidates for remote quantitative detection and quantification of organic and biological species. Some of the key attributes of these sensors are their mechanical flexibility, length and surface area, portability, water and corrosion resistance, low environmental impact, immunity from electromagnetic fields, safety, and low fabrication cost.

The standard sensing mechanism in these applications is based on IR fiber evanescent wave spectroscopy, which consists of measuring the modulation in the evanescent electric field of the sensor fiber when in contact with an external absorbing species. Compared with oxide or fluoride glasses, IR-transmitting ChG fibers offer a much broader wavelength region available for remote spectroscopy, up to 20 μm for the telluride-based materials. This wide spectral window in the mid-IR region overlaps the highly specific vibrational modes of most of organic chemicals and biomolecules, between 400 cm^{-1} (25 μm) and 4000 cm^{-1} (2.5 μm). A plethora of systems have been investigated using ChG-based fiber sensors, including aqueous and non-aqueous solutions, gaseous species, as well as solids.

In contrast to fiber optic sensors, integrated optical sensors use on-chip components such as waveguides and resonators to perform molecular detection. Compared to conventional sensors based on bench-top instruments, integrated planar sensors feature a small footprint and low-power consumption, require minimal amount of analyte, and their manufacturing is potentially compatible with standard semiconductor microfabrication process flow [33–35]. ChGs are uniquely poised as an attractive material candidate for on-chip optical sensors: these glasses possess high refractive indices (typically n = 2–3), which enable strong optical confinement and compact on-chip integration, their amorphous structure facilitates monolithic planar integration on different substrates, and their broad IR transparency window overlaps with the spectral fingerprints of most chemical and biological species.

These advantages of chalcogenide materials were well recognized even in the very early days of glass waveguide development [36]. Integrated ChG waveguides were first demonstrated in the 1970s on $LiNbO_3$ substrates. Spectroscopic sensing applications of planar ChG waveguide devices, although remained unexplored until the last decade, are rapidly becoming a field of intensive scientific investigation in recent years [4], largely spurred by the rapid progress of mid-IR laser sources (quantum cascade lasers [37–39], and interband cascade lasers [40, 41]), uncooled detectors [42], and mid-IR optical fibers [43].

2.2 Gradient Refractive Index (GRIN) Optics

Gradient-index (GRIN) optics are materials in which the refractive index (i.e. the speed of light in the material) varies spatially within the piece. This is in stark contrast to traditional lenses, in which the refractive index is constant throughout the glass or crystal, and the "bending" of the light performed by the lens is obtained

through the curvature of the lens surface. GRIN lenses have potential to provide incredible new functionality to existing optical systems, as well as opening up new avenues in optical system design [44]. The reason for this potential is that control over the refractive index gradient is typically not something that an optical designer is allowed. Optical engineers, who design lens systems to accomplish specific imaging or sensing objectives, typically have control over three main lens characteristics: the thickness, the curvature, and the refractive index of the material they are designing with. The additional control over the design provided by the GRIN allows optical designers to produce lenses with completely new optical functionality [45] as well as to optimize the behavior of previous, non-GRIN designs [46–48].

2.2.1 Examples of GRIN Optics

Figure 2.3 shows two embodiments of the GRIN approach, an axial GRIN lens and a radial GRIN fiber optic core. The axial GRIN lens is used to eliminate spherical aberrations from an optical imaging system. Mass-produced lenses are almost always created with spherical front surfaces; this fact arises from a manufacturing consideration, namely that spherical surfaces can easily be obtained through an automated grinding and polishing system. One difficulty imposed by the spherical surface is the problem of spherical aberration: light rays passing through the lens at different lens diameters are focused to slightly different spots along the optical axis

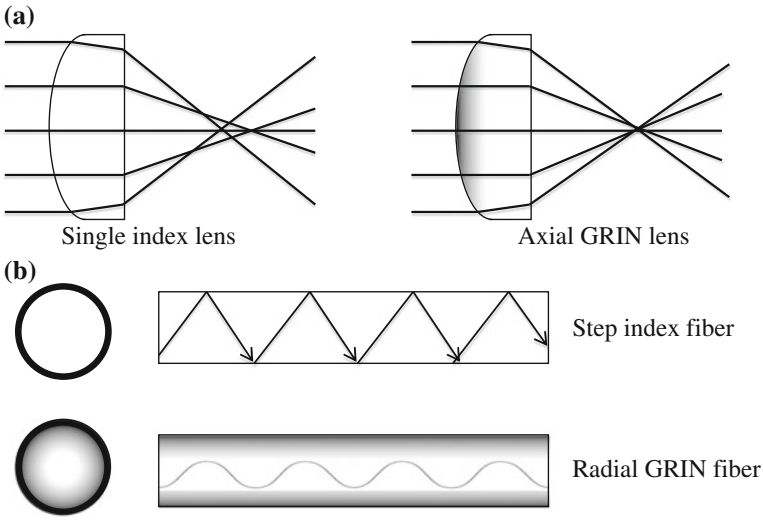

Fig. 2.3 **a** The impact of an axial refractive index gradient on the focusing properties of a spherical lens, elimination of spherical aberration and **b** the impact of a radial refractive index gradient on the light propagation behavior of a fiber optic

(Fig. 2.3a, left). The problem of spherical aberration could be corrected by grinding and polishing aspheric lenses, but this presents severe manufacturing automation difficulties; currently, aspheric optics are formed by single point diamond turning, or precision glass molding. An alternative to these more complex manufacturing techniques is to instead form a traditional spherical lens shape, but from a material that has an axial refractive index gradient along the direction of the optical rays. This style of GRIN lens is shown in Fig. 2.3a, right, and is sold commercially under such trade names as GRADIUM [49].

Figure 2.3b shows the application of the GRIN idea to fiber optic materials. In a typical step index core-clad fiber optic structure, shown in the top portion of Fig. 2.3b, the light ray experiences reflection at the core/clad interface due to the lower index of the cladding layer compared to that of the core. This step-index reflection is the basis for fiber optics, but as in the case of the spherical lens discussed above, the simplicity of the system leads to minor distortions that can play a large role in imaging. The step index fiber, when operating in a multi-mode configuration, exhibits modal dispersion, meaning that different modes propagating through the fiber travel at slightly different velocities. Because fiber optics have kilometers of optical path length for the light to travel through, even slight differences in mode velocity can add up to create serious problems. GRIN fiber optics minimize the problem of modal dispersion because the radial refractive index gradient in the core of the fiber causes the light to move in a sinusoidal path, constantly re-focusing the light back to the center of the core.

2.3 Description of the IRradiance Glass GRIN Approach

Figure 2.4 shows a schematic view of the IRG GRIN approach,[1] originally invented by the university partners, and the subject of the technology transfer process described in Sect. 2.4. Rather than subject the glass to an ion diffusion process, typical for creating GRIN structures in oxide glasses, the refractive index gradient is created by selectively growing a high index crystal phase into the low index glass matrix. This approach to forming GRIN structures presents a very interesting materials science and manufacturing challenge: controlled crystallization. Most of the history of glass manufacturing has been the quest to find glass compositions that *do not* crystallize; crystallization during window glass manufacture would cause windows that were visibly “foggy”, a product of light scattering off of the crystals in the glass matrix. However, growing a small crystal phase into the glass matrix (assuming it can be controlled) has been widely used to form the glass-ceramic composite materials used in everything from stovetops to cellphones [50, 51]. In the

[1]The effort depicted in this Section was sponsored by the Defense Advanced Research Projects Agency.

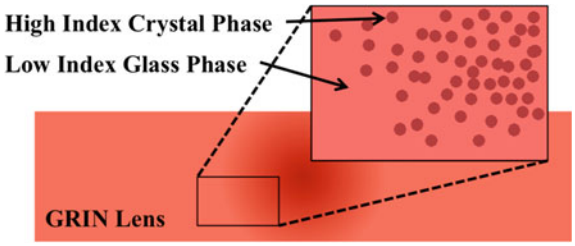

Fig. 2.4 Schematic of the IRG GRIN technology; the refractive index gradient is created by forming high index nanocrystals in the low index bulk glass

case of the optical GRIN devices, the goal is to form a very tightly controlled volume fraction of crystals with well-defined, monodispersed sizes. If the crystals remain small relative to the wavelength of the light, then the light will experience an "effective refractive index" which is a weighted average of the refractive index of the low-index glass and of the high-index crystal, with the indices weighted by the volume fractions of glass and crystal in a given optical volume.

One of the promising features of this controlled crystallization approach is that, in theory, it can be used to generate an arbitrary GRIN profile within an optical element. Currently deployed technologies for producing GRIN profiles such as neutron irradiation, chemical vapor deposition, and ion exchange techniques can be used to create either an axial or a radial index gradient within the material, but the GRIN is constrained to a single direction due to the processing conditions.

Figure 2.5 shows transmission electron micrographs of the heat-treated base glass. The small dark regions in Fig. 2.5a are the high-index crystals formed during the heat treatment on the base glass material. The heat supplied during the treatment is just enough to begin growing the crystals from the glass matrix; the goal is to have enough control over the heat distribution within the material during treatment that the crystals are forced to grow in a well-defined region of the optic.

Figure 2.6 shows a proof-of-concept demonstration of the controlled-crystallization GRIN approach. The goal of this experiment was to demonstrate that a 1D refractive index gradient could be obtained in the material through a simple heating process. One end of a glass rod was held at a temperature above the crystallization temperature of the high-index crystals. The other end of the rod was held at room temperature, and the glass rod was allowed to come to a steady-state condition, where there was a constant rate of heat flow from the hot end of the glass rod to the cold end. After the glass rod was exposed to these thermal processing conditions, it was cut into ten separate slices, and the refractive index of each slice was measured by spectroscopic ellipsometry. It was found that the refractive index varied almost linearly across the length of the rod, meaning that a 1D axial GRIN, similar to that shown in the lens in Fig. 2.3a, had been formed through simple thermal processing.

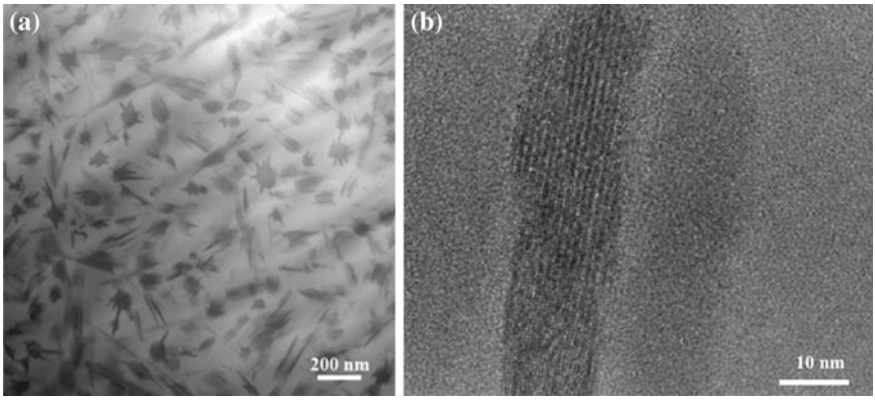

Fig. 2.5 **a** Low resolution and **b** high resolution transmission electron micrographs showing the high index crystal phase precipitating out of the glass matrix

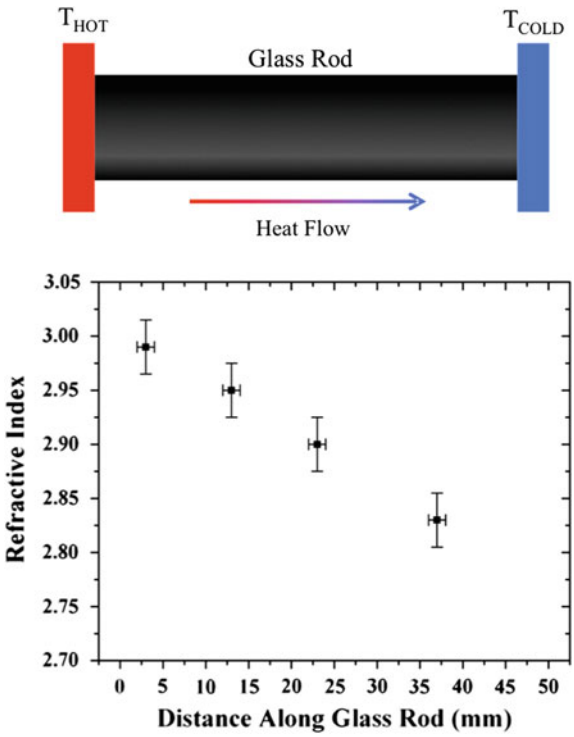

Fig. 2.6 Proof-of-concept demonstration of the IRG GRIN process. *Above* The glass rod is held at steady state between a hot and cold end, generating a constant heat flow. *Below* The steady state heat flow leads to an almost linear change in refractive index in the rod

2.3.1 Remaining Technical Challenges

Though the production of the 1D proof-of-concept was a definitive step forward in the development of the controlled crystallization GRIN approach, much work remains to be done before this can be exploited in a viable commercial product. Among the technical challenges still facing the team are: (1) true 3D GRIN development, (2) direct mapping between processing conditions and optical performance, and (3) production-scale fabrication. The issue of producing 3D GRIN structures in the glass via controlled crystallization is now one of determining how to create the desired 3D thermal profile throughout the material during processing. The same simple thermal boundary conditions used to create the axial GRIN shown in Fig. 2.6 can be used to create a radial GRIN structure in the material: namely, the edges of the rod or disc of glass can be held at one temperature and the center at a different temperature to set up the steady state heat flow. Based on the proof-of-concept results, this approach is expected to supply a radial GRIN similar to that exhibited by the fiber optic in Fig. 2.3b. However, the question remains as to how to best create a complex 3D thermal profile in the material in order to produce more complex GRIN structures. Currently, the team is exploring using laser processing as a tool to create local "hot spots" in the glass in order to achieve the needed geometries.

The process that creates GRIN structures via controlled crystallization is complex, with several intermediate stages between the application of the heat flow and the resulting graded index. It is important to keep the diameter of the crystals very small, as larger crystals, greater than 1/10th of the wavelength of the light will lead to scattering in the system. Because of the complex nature of the crystal growth process, a direct mapping of the processing conditions to the resultant effective refractive index is required. Finally, the chosen processing route needs to be scaled up so that optical elements may be produced at a competitive price, otherwise the technical advantages of the GRIN approach will remain outside the reach of consumers.

2.4 Technology Transfer

Most of the examples in this book describe the process of moving a company's product idea from in-house R&D to the manufacturing line. But sometimes, the best research idea is not internally supported—it's from federally-funded university research, as is the case for the technology IRradiance Glass is in the process of commercializing.

The mechanism to move these ideas from universities to industry is called technology transfer. This section covers the legislative history that has encouraged an era of increased technology transfer activity, an overview of the process from lab to initial commercialization efforts, and a glimpse of future trends of industrial innovation.

2.4.1 History of the Passage of Bayh-Dole

Before 1980, all federally-funded research that resulted in a patent had the rights retained by the U.S. government—whether the institution that did the research was public or private. Very few license agreements were ever pursued, since only non-exclusive licenses were negotiated, and the process was burdensome. This set-up, of course, reduced any industry incentive to commercialize products based on government-owned patents [52, 53].

After the 1940s, the United States was considered unmatched in economic and political power. Yet by the 1970s it was clear that the country was losing its competitive edge to countries in Europe and Asia. A way to invigorate the U.S. economy was required, and Congress debated about the best way forward in the management of the research dollars awarded each year as well as a new strategy for revision of the government's intellectual property policies. Limited exceptions to the government's patent policy could be attained by universities with the only mechanism for these institutions to acquire patent rights from the government—the Institutional Patent Agreement. Unfortunately, these were not issued from every federal agency, so if an important discovery was made using funds from an agency that did not set up these agreements, the university could not take title to the patent. Viable patents and important research with societal and economic benefits languished [54].

In 1978, a bill was introduced by Senator Birch Bayh (D. IN) and Senator Robert Dole (R. KS) that was intended to assist both universities and small businesses who wished to commercialize federally-funded research. The main intent was to encourage the commercialization and industrious use of inventions resulting from federal R&D funding. When the bill was introduced, Senator Bayh stated:

> A wealth of scientific talent at American colleges and universities—talent responsible for the development of numerous innovative scientific breakthroughs each year—is going to waste as a result of bureaucratic red tape and illogical government regulations…
>
> The problem, very simply, is the present policy followed by most government agencies of retaining patent rights to inventions.
>
> Government sponsored research is often basic rather than applied research. Therefore, many of the resulting inventions are at a very embryonic stage of development and require substantial expenditures before they actually become a product or applied system of benefit to the public.
>
> It is not government's responsibility—or indeed, the right of government—to assume the commercialization function. Unless private industry has the protection of some exclusive use under patent or license agreements, they cannot afford the risk of commercialization expenditures. As a result, many new developments resulting from government research are left idle.

The bill's legislative history to ultimate passage is fascinating—stories of animated hearing testimony, last-minute staffer meetings, tales of outstanding senatorial courtesy unheard of today, and reminders of the special rules for Presidential signatures on bills during lame duck sessions have been documented. In short, the Bayh-Dole was signed by President Carter (who had just been defeated by Ronald Reagan, as was the outgoing Senator Bayh by Senator Dan Quayle) on December

12, 1980. The Bayh-Dole Act became law—by amending Title 35 of the United States Code, chapter 30 on Patents—on the last day possible before inaction would have resulted in a pocket veto. Although with that battle won, the final victory not declared until President Reagan supported the Bayh-Dole approach in his Presidential Memorandum on Patent Policy of 1982, and clashes over the legislative regulations were not settled until 1984 [54].

The Bayh-Dole legislation specifically addressed the following:

(1) Permitted universities, not-for-profits, and small businesses to obtain title to inventions developed with governmental support.
(2) Provided early-on intellectual property rights protection of invention descriptions from public dissemination and Freedom of Information Act (FOIA).
(3) Allowed government-owned, government-operated (GOGO) laboratories to grant exclusive licenses to patents.

This piece of legislation along with the Technology Innovation Act of 1980 (the Stevenson-Wydler Act—required establishment of budgets and technology transfer offices at government funded institutions), the Small Business Innovation Development Act of 1982 (established the Small Business Innovation Research (SBIR) program), and the Federal Technology Transfer Act of 1986 (allowed federal laboratories to enter into cooperative research agreements with industrial partners and negotiate patent licensing agreements) has arguably had the biggest economic impact on entrepreneurial ventures in the United States, and created a strong infrastructure for technology transfer [53].

2.4.2 Overview of the Technology Transfer Process

The technology transfer process from a university to industry consists of a sequence of steps that proceeds towards commercialization of federally-funded technology by private industry. These stages include *invention disclosure* to the research institution by faculty who may envision a commercial application to their research, *intellectual property applications* by university Offices of Technology Transfer (OTT) for disclosures that have potential for valid patents (or other forms of intellectual property) and licensing, and *license and option agreements* between the university and the company to pursue commercialization and of the research. While this may appear to be a straightforward process, the path is lined with various pitfalls and complications that can derail even the most economically viable idea [55, 56].

2.4.3 Disclosure and Patenting

When researchers invent a product or process using the institution's resources, that technology is owned by the University. The inventor is encouraged to disclose in a timely manner and before publication of results the non-confidential details of the invention. This disclosure is reviewed by OTT staff or other institutional committee, and a preliminary decision is made about commercial potential and patentability. If the University decides to take title to the invention and pursue a patent application, the university is then free to license the invention to those companies that are interested in pursuing commercialization [56].

In the case of the technology described in this chapter, co-inventorship of the technology was determined to be attributed to both academic and industrial development partners, and therefore the disclosure and decision to pursue the patent process occurred at all of the involved institutions. An Inter-institutional Agreement (IIA) between these entities lays out the guidelines for working together and sharing royalties as this technology is commercialized.

2.4.4 Interfacing with Technology Transfer Office and the University Research Group: Relationships, Intellectual Property (IP) Ownership and Conflict of Interest

From a company's point of view, there are many ways to find suitable ideas for product development, including patent searches and journal publications. Yet the most important element of this discovery phase of innovation possibilities appears to be the relationships that are established between university research groups and industrial partners. By encouraging the development of these personal contacts through alumni relationships or technical conferences, industrial R&D staff can be aware of the latest research in their area of interest. In many cases, new companies are started based on original university research [56, 57].

Many times, industrial funding is a part of the sponsored-research invention process. In this era of industry-funded research and increasing consulting interaction between faculty and private companies, universities should have strong intellectual property policies and confidentiality agreements in place. These policies establish the determination of ownership rights of faculty, staff, and students and any industrial partners to clearly define what are considered University resources used to develop the idea and who holds inventorship. Faculty would do well to clearly define these policies to incoming students who may not be familiar with the requirements to maintain confidentiality for certain projects in an environment where free exchange of information is the norm. Acknowledging this tension

between the academic pursuit of knowledge and the desire to attract funding resources or potential license agreements from industry (that have profit goals dependent upon secrecy of development) is an important real-world instructional distinction to make.

An additional complication, apparent in the case of IRradiance Glass, is where a faculty member may benefit financially from the transfer of the technology to the company and may additionally hold equity in the company. Universities typically have explicit conflict of interest policies in place to manage these situations where there may be monetary gain from faculty activity outside of their prescribed duties. Of course, in the case of federally-funded research, these policies flow down from the federal government's regulations on conflict of interest, and there most likely are state regulations that govern these situations as well.

In institutions where entrepreneurial activity of faculty is encouraged (in fact, sometimes up to 20% of a faculty member's time may be spent on outside, revenue-generating activities), these conflicts can be managed, but compliance can be rigorous. Potential conflicting activities must be approved under the direction of the Office of Sponsored Research and the Office of Compliance in a document updated periodically. These conflicts can be managed successfully, as long as there are clear mitigation strategies to maintain an ethical commitment to objective research and the duties of employees to taxpayer-supported research institutions. It is entirely possible to take this compliance challenge on, but it should be stated that is can prevent timely progress on additional commercial development of the research idea.

2.4.5 Licensing University-Generated Technology

Once there is a connection between a company that is interested in a particular University-owned invention or technology and the OTT at that institution, conflict of interest issues have management plans, and intellectual property protection is in place, the process of commercialization may begin. The OTT engages in license agreement, license option, and terms negotiations with the interested company for use of the invention or the ability to continue research. The university typically will ask for details of development and milestones to ensure that the technology is developed and will not just sit idle. If the company is a start-up and unable to fund the terms of the license, the university may include the option to take equity in the company in exchange for license fees or legal expenses. Royalty payments may be between 3–6% of net sales or a minimum payment after a period of time. Licensing terms are unique (and negotiable!) to each case and may depend upon the details of the cost to develop the invention, size of the market, or stage of the development [56]. These steps in the company's process of licensing another entities' intellectual property is summarized in Fig. 2.7.

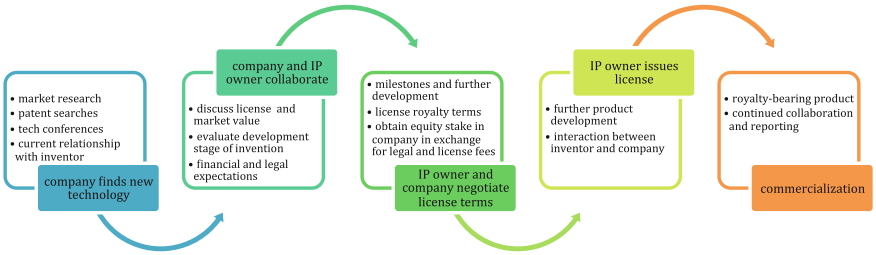

Fig. 2.7 Company point of view of the licensing process from other entity

2.5 Future Directions in GRIN Optics and Technology Transfer

> Prediction is very difficult, especially if it's about the future.
>
> —Neils Bohr

2.5.1 GRIN Optics

The utility of the GRIN approach is not new to science: James Clerk Maxwell demonstrated a theoretical refractive index gradient lens as early as 1854. However, it has not been until the last 20–30 years that materials scientists have begun addressing the technical challenges in producing such materials. Lenses from materials such as GRADIUM, or the use of chemical vapor deposition to produce GRIN fiber optics represent particular success stories. However, development of the theoretical foundations for these optics still far outpaces the technology to create the real life materials. In particular, a huge hurdle still to be overcome is the inability of manufacturers to produce arbitrary GRIN profiles. As discussed above, axial and radial gradients are obtainable through straightforward, though delicate, processing routes. But just as the axial gradient provides an excellent solution to the problem of spherical aberration, the ability to produce arbitrary 3D, rather than purely 1D axial, gradients will open up vast new capabilities for optical designers.

Another challenge for the materials scientists and optical designers tackling these problems are the issues of quality control and post-processing. The issue of quality control reduces quickly to the question: "how do you measure an index gradient in a finished piece?" Interferometric measurements have been utilized to characterize materials such as GRADIUM, but these measurements are non-trivial to extend to the infrared spectral region. In the realm of post-processing, a major question revolves around how to effectively coat these materials. An Anti-Reflective (AR) coating is required for almost every IR-transparent optic, due to the large Fresnel Reflection loss exhibited by the material (in turn, due to their high refractive

index). But this begs the question: "How does one accurately AR coat a surface that does not have a constant refractive index?"

2.5.2 Open Innovation and Trends in R&D Commercialization

In the past, companies internally funded large R&D departments to carry out both basic and applied research and product development. Now, without large internal R&D budgets (or well-defined revenue streams in regulated monopolies like AT&T Bell Labs), companies have to creatively find new ways to become leaders in innovation and bring research ideas to market. Companies can no longer exclusively look to closed models of internal innovation where all the intellectual property is performed and controlled by the company. Licensing agreements, research partnerships with universities, and joint ventures can be robust channels that lead to a new era of open innovation and increased potential of idea commercialization [58, 59].

2.5.3 Skills and Talents for Tomorrow's Scientists at IRG

As of this writing in late 2014, IRradiance Glass employs less than ten people, but is expanding rapidly to meet the demands of some of the large commercial and defense contracts it has secured. As such, IRG has a need for a wide range of talented researchers, engineers, and technicians to help grow the company to its full potential. Interdisciplinary research and collaboration is a critical part of what we do at IRG, aspiring students or technicians are recommended to focus as much on their soft skills, such as teamwork and communication, as they are on the harder disciplines of chemistry, physics, optics, and material science. IRG has the corporate vision of rising to meet the challenges presented to us by our customers rather than relying only on what we already know how to do perfectly. Because of this vision, we are looking for people who are excited, engaged, and ready to tackle challenges they had never even considered.

References

1. http://www.flir.com/flirone/. Accessed June 2014
2. http://www.xbox.com/en-US/xbox360/accessories/kinect. Accessed June 2014
3. http://www.audi.co.uk/new-cars/a8/a8/driver-assistants/night-vision.html. Accessed June 2014
4. B.J. Eggleton, B. Luther-Davies, K. Richardson, Chalcogenide photonics. Nat. Photonics **5**, 141–148 (2011)

5. Z. Yang, P. Lucas, Tellurium-based far-infrared transmitting glasses. J. Am. Ceram. Soc. **92**, 2920–2923 (2009)
6. S. Danto, P. Houizot, C. Boussard-Pledel, X. Zhang, F. Smektala, J. Lucas, A family of far-infrared-transmitting glasses in the Ga-Ge-Te system for space applications. Adv. Funct. Mater. **16**, 1847–1852 (2006)
7. S. Maurugeon, C. Boussard-Pledel, J. Troles, A.J. Faber, P. Lucas, X.H. Zhang, J. Lucas, B. Bureau, Telluride glass step index fiber for the far infrared. J. Lightwave Technol. **28**, 3358–3363 (2010)
8. V. Tikhomirov, D. Furniss, A. Seddon, J. Savage, P. Mason, D. Orchard, K. Lewis, Glass formation in the Te-enriched part of the quaternary Ge-As-Se-Te system and its implication for mid-infrared optical fibres. Infrared Phys. Technol. **45**, 115–123 (2004)
9. A. Zakery, S. Elliott, Optical properties and applications of chalcogenide glasses: a review. J. Non Cryst. Solids **330**, 1–12 (2003)
10. G. Yang, H. Jain, A. Ganjoo, D. Zhao, Y. Xu, H. Zeng, G. Chen, A photo-stable chalcogenide glass. Opt. Express **16**, 10565–10571 (2008)
11. W. Li, S. Seal, C. Rivero, C. Lopez, K. Richardson, A. Pope, A. Schulte, S. Myneni, H. Jain, K. Antoine, A. Miller, Role of S/Se ratio in chemical bonding of As-S-Se glasses investigated by Raman, x-ray photoelectron, and extended x-ray absorption fine structure spectroscopies. J. Appl. Phys. **98**, 053503 (2005)
12. E.J. McBrearty, P. Mason, D. Orchard, M. Harris, K. Lewis, Optical bonding of high refractive index semiconductors using index matched chalcogenide glass. SPIE Proc. **5250**, 462–470 (2004)
13. B. Bernacki, N.C. Anheier, K. Krishnaswami, B.D. Cannon, K.B. Binkley, Design and fabrication of efficient miniature retroreflectors for the mid- and long-range infrared. SPIE Proc. **6940**, 69400X (2008)
14. N. Carlie, A solution-based approach to the fabrication of novel chalcogenide glass materials and structures, Ph.D. Thesis, Clemson University (2010)
15. K. Sivakumaran, C.K.S. Nair, Rapid synthesis of chalcogenide glasses of Se-Te-Sb system by microwave irradiation. J. Phys. D-Appl. Phys. **38**, 2476–2479 (2005)
16. S. Ramachandran, S.G. Bishop, Low loss photoinduced waveguides in rapid thermally annealed films of chalcogenide glasses. Appl. Phys. Lett. **74**, 13–15 (1999)
17. T. Kohoutek, T. Wagner, M. Frumar, A. Chrissanthopoulos, O. Kostadinova, S.N. Yannopoulos, Effect of cluster size of chalcogenide glass nanocolloidal solutions on the surface morphology of spin-coated amorphous films. J. Appl. Phys. **103**, 063511 (2008)
18. M. Waldmann, J.D. Musgraves, K. Richardson, C.B. Arnold, Structural properties of solution processed Ge23Sb7S70 glass materials. J. Mater. Chem. **22**, 17848–17852 (2012)
19. Y. Zou, H. Lin, O. Ogbuu, L. Li, S. Danto, S. Novak, J. Novak, J.D. Musgraves, K. Richardson, J. Hu, Effect of annealing conditions on the physio-chemical properties of spin-coated As2Se3 chalcogenide glass films. Optical Materials Express **2**, 1723–1732 (2012)
20. L. Li, H. Lin, S. Qiao, Y. Zou, S. Danto, K. Richardson, J.D. Musgraves, N. Lu, J. Hu, 3-D integrated flexible glass photonics. Nat. Photon. (2014). doi:10.1938/nphoton.2014.138
21. L. Li, Y. Zou, H. Lin, J. Hu, X. Sun, N. Feng, S. Danto, K. Richardson, T. Gu, M. Haney, A fully-integrated flexible photonic platform for chip-to-chip optical interconnects. J. Lightwave Technol. **31**, 4080–4086 (2013)
22. B. Bureau, X.H. Zhang, F. Smektala, J.L. Adam, J. Troles, H.L. Ma, C. Boussard-Pledel, J. Lucas, P. Lucas, D. Le Coq, M.R. Riley, J.H. Simmons, Recent advances in chalcogenide glasses. J. Noncryst. Solids **345**, 276–283 (2004)
23. N.S. Kapany, R.J. Simms, Recent developments in infrared fiber optics. Infrared Phys. **5**, 69 (1965)
24. J.D. Shephard, W.N. MacPherson, R.R.J. Maier, J.D.C. Jones, D.P. Hand, M. Mohebbi, A.K. George, P.J. Roberts, J.C. Knight, Single-mode mid-IR guidance in a hollow-core photonic crystal fiber. Opt. Express **13**, 7139–7144 (2005)

25. T.D. Engeness, M. Ibanescu, S.G. Johnson, O. Weisberg, M. Skorobogatiy, S. Jacobs, Y. Fink, Dispersion tailoring and compensation by modal interactions in OmniGuide fibers. Opt. Express **11**, 1175–1196 (2003)
26. J. Hu, C.R. Menyuk, L.B. Shaw, J.S. Sanghera, I.D. Aggarwal, Maximizing the bandwidth of supercontinuum generation in As(2)Se(3) chalcogenide fibers. Opt. Express **18**, 6722–6739 (2010)
27. Z. Wang, N. Chocat, Fiber-optic technologies in laser-based therapeutics: threads for a cure. Curr. Pharm. Biotechnol. **11**, 384–397 (2010)
28. T. Ueda, K. Yamada, T. Sugita, Measurement of grinding temperature of ceramics using infrared radiation pyrometer with optical fiber. J. Eng. Ind. Trans. ASME **114**, 317–322 (1992)
29. M. Saito, M. Takizawa, S. Sakuragi, F. Tanei, Infrared image guide with bundled as-s glass-fibers. Appl. Opt. **24**, 2304–2308 (1985)
30. J. Nishii, T. Yamashita, T. Yamagishi, C. Tanaka, H. Stone, Coherent infrared fiber image bundle. Appl. Phys. Lett. **59**, 2639–2641 (1991)
31. M. Asobe, T. Ohara, I. Yokohama, T. Kaino, Low power all-optical switching in a nonlinear optical loop mirror using chalcogenide glass fibre. Electron. Lett. **32**, 1396–1397 (1996)
32. R.E. Slusher, G. Lenz, J. Hodelin, J. Sanghera, L.B. Shaw, I.D. Aggarwal, Large Raman gain and nonlinear phase shifts in high-purity As2Se3 chalcogenide fibers. J. Opt. Soc. Am. B-Opt. Phys. **21**, 1146–1155 (2004)
33. B. Kuswandi, Nuriman, J. Huskens, W. Verboom, Optical sensing systems for microfluidic devices: a review. Analytica Chimica Acta **601**, 141–155 (2007)
34. P.V. Lambeck, Integrated optical sensors for the chemical domain. Meas. Sci. Technol. **17**, R93–R116 (2006)
35. S.-S. Kim, C. Young, B. Mizaikoff, Miniaturized mid-infrared sensor technologies. Anal. Bioanal. Chem. **390**, 231–237 (2008)
36. R.M. Klein, Chalcogenide glasses as passive thin-film structures for integrated optics. J. Electron. Mater. **3**, 79–99 (1974)
37. Y. Bai, S. Slivken, S.R. Darvish, M. Razeghi, Room temperature continuous wave operation of quantum cascade lasers with 12.5% wall plug efficiency RID C-6716-2011 RID B-7273-2009 RID B-7265-2009. Appl. Phys. Lett. **93**, 021103 (2008)
38. C. Gmachl, F. Capasso, D.L. Sivco, A.Y. Cho, Recent progress in quantum cascade lasers and applications. Rep. Prog. Phys. **64**, 1533–1601 (2001)
39. C. McDonagh, C.S. Burke, B.D. MacCraith, Optical chemical sensors. Chem. Rev. **108**, 400–422 (2008)
40. M. Kim, C.L. Canedy, W.W. Bewley, C.S. Kim, J.R. Lindle, J. Abell, I. Vurgaftman, J.R. Meyer, Interband cascade laser emitting at lambda = 3.75 μm in continuous wave above room temperature RID A-9426-2009. Appl. Phys. Lett. **92**, 191110 (2008)
41. I. Vurgaftman, W.W. Bewley, C.L. Canedy, C.S. Kim, M. Kim, C.D. Merritt, J. Abell, J.R. Lindle, J.R. Meyer, Rebalancing of internally generated carriers for mid-infrared interband cascade lasers with very low power consumption. Nature Communications **2**, 585 (2011)
42. A. Rogalski, Infrared detectors: status and trends. Prog. Quantum Electron. **27**, 59–210 (2003)
43. J.S. Sanghera, L.B. Shaw, I.D. Aggarwal, Chalcogenide glass-fiber-based mid-IR sources and applications. IEEE J. Sel. Top. Quantum Electron. **15**, 114–119 (2009)
44. D.T. Moore, Gradient-index optics: a review. Appl. Opt. **19**, 1035–1038 (1980)
45. R.K. Luneburg, *Mathematical Theory of Optics* (University of California Press, Berkeley, 1966)
46. G.J. Tearney, S.A. Boppart, B.E. Bouma, M.E. Brezinski, N.J. Weissman, J.F. Southern, J.G. Fujimoto, Scanning single-mode fiber optic catheter-endoscope for optical coherence tomography. Opt. Lett. **21**, 543–545 (1996)
47. E.B. Grann, M.G. Moharam, D.A. Pommet, Optimal-design for antireflective tapered 2-dimensional subwavelength grating structures. J. Opt. Soc. Am. A **12**, 333–339 (1995)
48. A. De Leebeeck, L.K.S. Kumar, V. de Lange, D. Sinton, R. Gordon, A.G. Brolo, On-chip surface-based detection with nanohole arrays. Anal. Chem. **79**, 4094–4100 (2007)
49. http://www.lightpath.com/gradium-lenses.html. Accessed June 2014

50. http://www.us.schott.com/hometech/english/products/ceran/. Accessed June 2014
51. http://www.corninggorillaglass.com/. Accessed June 2014
52. J. Allen, A long, hard journey: from bayh-dole to the federal technology transfer act. Tomorrow's Technol. Transf. **1**, 21–32 (2009)
53. W.D. Swearingen, T.F. Slaper, Economic impacts of technology transfer: two case studies from the U.S. department of defense. les Novelles, (2012)
54. A.J. Stevens, The enactment of Bayh–Dole. J. Tech. Trans. **29**, 93–99 (2004)
55. J.G. Thursby, M.C. Thursby, Who is selling the ivory tower? Sources of growth in university licensing. Manag. Sci. **0**, 1–15 (2001)
56. B. Bastani, E. Mintarno, D. Fernandez, *Tools of the Technology Transfer Trade–Licensing Intellectual Property from University to Industry* (Tech Monitor, May-Jun, 2004)
57. J.G. Thursby, M.C. Thursby, Industry perspectives on licensing university technologies: sources and problems. AUTM J. **XII**, (2000)
58. H.W. Chesbrough, The era of open innovation. MIT Sloan Manag. Rev. April 2013
59. T. Hockaday, Phases of growth in university technology transfer, les Novelles, Dec 2013

Chapter 3
General Electric Company: Selected Applications of Ceramics and Composite Materials

Gregory Corman, Ram Upadhyay, Shatil Sinha, Sean Sweeney, Shanshan Wang, Stephan Biller and Krishan Luthra

Abstract The General Electric Company (GE) is a global technology company involved in a broad range of businesses relying heavily on advanced materials and manufacturing technologies. This chapter focuses on three advanced technologies: (i) ceramic matrix composites (CMCs), a revolutionary materials technology for aircraft engines and industrial gas turbines, (ii) polymer matrix composite (PMC) fan blades for aircraft engines, primarily for weight reduction, and (iii) NaMx batteries that rely very heavily on ceramics for their efficient operation.

3.1 Introduction

GE is a global technology company that has more than 307,000 employees working in 170 locations around the world. With $147 billion in revenues, GE encompasses several business units, including Aviation, Power and Water, Energy Management, Oil and Gas, Transportation, Healthcare, Appliances and Lighting, and Capital. We manufacture everything from power generation turbines and energy management products that generate and deliver much of the world's electricity to aircraft engines that power some of the biggest commercial airliners. GE also manufactures world-class medical imaging and diagnostics equipment found in hospitals across the globe, appliances and lighting in countless homes and buildings, and locomotives and other rail products that carry freight and goods safely all of over the world from North America to Asia.

Each GE business has its own research organization. In addition, GE has a Global Research organization with over 2500 employees that is headquartered in Niskayuna, NY with centers in Detroit (Michigan), San Ramone (California), Houston (Texas), Bangalore (India), Shanghai (China), Munich (Germany), and Rio de Janeiro (Brazil). The GE Global Research organization performs research

G. Corman · R. Upadhyay · S. Sinha · S. Sweeney · S. Wang · S. Biller · K. Luthra (✉)
General Electric Global Research, 1 Research Circle, Niskayuna, NY 12309-1027, USA
e-mail: luthra@ge.com

L.D. Madsen and E.B. Svedberg (eds.), *Materials Research for Manufacturing*, Springer Series in Materials Science 224,
DOI 10.1007/978-3-319-23419-9_3

and development for all GE businesses. The focus of the research at GE Global Research is primarily on technology feasibility and demonstration in a laboratory environment (Technology Readiness Level (TRL) 2–4), whereas the focus of R&D at the businesses is on technology demonstration in relevant environments and product development (TRL 5 and 6), although significant overlap often exists. Materials and manufacturing are critical to GE's success, and relevant research at Global Research is performed within the Manufacturing, Chemical and Materials Technologies (MCMT) organization.

The MCMT organization performs research on a wide range of materials, including ceramics, metals, electronic materials, coatings of various kinds, systems like solid oxide fuel cells (SOFCs), and a wide range of manufacturing technologies, including additive manufacturing. For this chapter, we have chosen three technologies: (i) ceramic composites, a revolutionary new technology that has broad applications in aircraft engines and industrial gas turbines, (ii) polymer matrix composites for aircraft engines fan blades, and (iii) NaMx batteries, a new product within the Power and Water business. These three technologies were chosen because they represent a broad spectrum of materials and manufacturing challenges. Ceramic composites is a new technology that is now being scaled up for production; polymer matrix composite (PMC) fan blades are an existing technology that has been used extensively at GE for over 20 years and still offers opportunities for growth; and NaMx batteries that depend on critical ceramic materials and processes, and have just recently gone into production. Both the PMC and battery factories have heavily leveraged analytics to improve manufacturing systems performance.

Ceramic matrix Composites (CMCs) are attractive for gas turbine and aircraft engines because of their higher temperature capability in comparison to metals. Currently the super-alloys used in the turbine industry are nickel-based or cobalt-based. For long-term applications these classes of materials are useful for temperatures up to $\sim$1100 °C, very close to their incipient melting temperature of $\sim$1200 °C. Consequently there is a strong interest in using ceramic matrix composites, which offer the potential to be used at much higher material temperatures. CMCs have the added advantage that they are $\sim$1/3 the density of superalloys so that the weight of CMC components are greatly reduced relative to the metallic components they are replacing. In this chapter we cover the history of CMC development over 25 years at GE, followed by material properties, coatings for long life, and testing and commercialization plans of CMC components.

The need for polymer composite fan blades for aircraft engines is primarily driven by weight. These materials have a density of roughly 1.5–1.7 g/cm^3 compared to aluminum at 2.7 g/cm^3 and steels at $\sim$7–8 g/cm^3. In the PMC fan blade section we discuss the history of PMC development, followed by materials development, and the use of modeling and other productivity tools including analytics.

GE's NaMx Durathon™ batteries are useful for high energy density applications. The NaMx battery is reliant on several materials technologies, in particular ceramic electrolytes and ceramic-to-ceramic and ceramic-to-metal seals, as well as various manufacturing technologies for production and assembly of all the various components.

In this chapter we focus on one of the key ceramics technologies, the production of β″-alumina electrolyte tubes, and the use of manufacturing analytics to improve factory systems performance.

3.2 Ceramic Matrix Composites (CMCs)

General Electric has developed a class of CMCs, so called Melt Infiltrated (MI) CMCs, which are made by a silicon melt infiltration process, and consist of a SiC–Si matrix reinforced with SiC fibers that are coated with a multi-layer fiber coating based on boron nitride. These composites were originally developed mostly under the Department of Energy (DOE)-funded, cost shared Continuous Fiber Ceramic Composites (CFCC) program [1, 2]. Further development was done under GE funding, and the application of the composite system to industrial gas turbine hardware has been done under a combination of DOE [3] and GE funding. GE has publicly announced the commercial introduction of these composites for aircraft engines [4, 5].

The performance benefit of CMCs relative to current superalloys is shown schematically in Fig. 3.1. The trend in evolutionary superalloy development since 1960 has been roughly an improvement of ~30 °C per decade in material temperature capability, whereas CMC materials are a revolutionary technology that allows for a much more rapid improvement. To our knowledge, oxide dispersion strengthened (ODS) alloys and intermetallics with a capability of ~1150 °C are not being commercialized. CMCs represent an advantage of 100–200 °C in comparison to the metals currently in use.

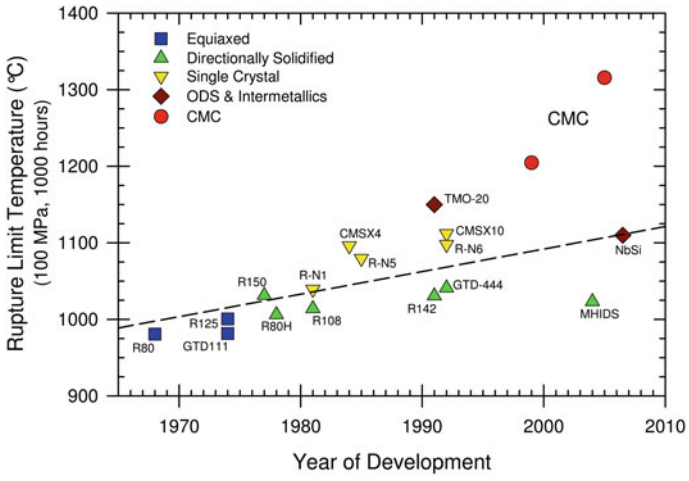

Fig. 3.1 Historical progression in superalloy temperature capability, as represented by the creep rupture temperature limit, compared to MI-CMC materials

3.2.1 History of CMC Development

The term "composite," in its most general sense, can be used to describe any mixture of materials and/or phases. We will use a more restrictive definition limited to structures having continuous (>5 cm) reinforcing fibers distributed within a continuous matrix phase. Ideally the orientation, distribution and volume fraction of fibers within the matrix will be controlled by the fabrication processes used.

The range of continuous fibers that are both suitable for use in CMCs and are commercially available is very limited. The fibers need to withstand not only the intended use temperature, but also any thermal excursion or physical abuse that may occur during the CMC fabrication process. Consequently there are only three classes of fibers currently available that are suitable for use in CMCs: carbon, SiC-based (including non-stoichiometric variations such as Si–N–C or Si–C–B–N–O), and alumina-based (including aluminosilicates such as mullite).

After the fiber, the most critical part of a CMC material is the fiber-matrix interface. By themselves the fibers and matrix of a CMC are brittle materials. All of the mechanisms that provide the CMC with macroscopic toughness (such as crack deflection, fiber-matrix debonding, multiple matrix cracking and fiber pull-out) rely on the presence of a weak, low toughness interface between the fiber and matrix. Since such interfaces are not prone to form naturally, a coating is generally applied to the fibers to engineer the interface behavior. Unfortunately, the list of proven fiber coating materials is limited to just carbon and boron nitride. There has been exploratory work into alternate coating materials, such as monazite ($LaPO_4$), β-alumina or complex mica-like silicates, or even just porosity. In limited cases such coatings have been shown to deflect cracks along interfaces in model systems, but none has been demonstrated to be effective or robust enough to generate tough behavior in multi-filament composites used at high temperatures for extended times.

3.2.1.1 Early Carbon Fiber Composites

The pace of development for most composite systems, and certainly for CMCs, has been limited by the availability of suitable structural fibers. Early glass and organic fibers simply were not thermally stable enough for consideration as reinforcements in ceramic matrices. However, the commercial introduction of carbon fiber in the early 60s directly led to numerous early attempts at incorporating this fiber into ceramic matrices, most of which failed. The two successful exceptions were carbon-carbon and carbon fiber-glass matrix composites [6, 7].

The main problems with utilizing carbon fiber for CMC materials are (i) the very low and anisotropic coefficient of thermal expansion (CTE) of carbon fiber, (ii) the difficulty of producing a dense matrix surrounding a non-densifying network of fibers, and (iii) the inherent oxidation limitations of carbon. The first problem is circumvented by using low CTE glass matrices or by allowing the matrix to microcrack as in carbon-carbon. The second problem is generic to all CMCs.

Carbon-glass composites utilize the viscous flow of the glass to enable matrix densification, but this typically limits shape capability. With C–C composites densification is accomplished by using resin impregnation and pyrolysis (RIP) and/or chemical vapor infiltration (CVI), but neither forms fully-dense matrices. As for the third problem, that of oxidation of carbon, no adequate solution has been found despite over 60 years of research. Consequently, neither of these systems, C–C or C–glass, is suitable for use at the temperatures and times needed for gas turbine applications.

3.2.1.2 SiC Fiber Composites

The next major progression in the development of CMC materials was the introduction of continuous "silicon carbide" fibers in the mid-70s. Pioneered by Yajima in Japan [8], SiC fibers were first introduced commercially by Nippon Carbon Co. under the trade name of Nicalon™. More detailed reviews of SiC fiber processing and properties can be found in [9–11].

The introduction of these new SiC fibers enabled a growth in CMC development throughout the late 1970s and 1980s [12–14]. During this time many of the fundamentals of successful CMC material systems and fabrication processes were determined, such as the effectiveness of BN as a fiber-matrix debond coating [15]. A summary of the CMC fabrication approaches that existed in the early 1990s, and their relative merits and challenges, is shown in Table 3.1. Although work on CMC materials has continued steadily throughout the 1990s and 2000s, there has been no fundamentally new fabrication process developed for CMCs over the past 20 years. Consequently, the 1991 list of fabrication processes and their relative rankings are

Table 3.1 Comparison of various processes for capability of producing CMC materials with SiC fiber capable of utilization in a gas turbine engine

Process	Near net shape	Low matrix porosity	Matrix type	Oxidation resistance	Thermal conductivity
Sintering	o	o	Oxides	− to o	−
Pressure-assisted sintering (hot press, HIP, SPS)	−	+	Oxides	− to o[a]	−
	−	+	SiC or Si_3N_4	+	+
Sol–Gel	+	—	Oxides	−[a]	−
Polymer impregnation and pyrolysis	+	—	SiC, Si_3N_4	o	o
Chemical vapor infiltration	+	—	SiC	o	o
Melt oxidation	+	o[b] to +	Al/Al_2O_3	o	o
Glass-ceramic processing	+	+	Oxides	− to o	−
Gas-solid reaction (RBSN)	+	−	Si_3N_4	− to o	o
Silicon melt infiltration	+	+	SiC/Si	+	+

[a]Primarily based on interface coating oxidation
[b]Dependent on whether the residual metal is extracted

still valid today. In this table a plus sign indicates that the combination of process and matrix is able to meet the desired criteria, a "o" means the process does not meet the criteria by a small margin or barely meets it for only some applications, and a negative sign means the system misses the criteria by a large margin.

3.2.1.3 Alumina Fiber Composites

Around the same time that the first SiC fibers became available there was also a surge in the development of oxide fibers. Numerous fine oxide fibers, mostly based on Al_2O_3 or aluminosilicate compositions, have been developed [16], but none have had the inherent thermal stability (i.e. resistance to grain growth and resultant strength degradation) and sufficient creep resistance for long-term use at or above 1200 °C. The possible exception would be single crystal oxide fibers, such as sapphire or YAG, which are produced via pulling from the melt. Consequently these fibers have relatively large diameters (typically >120 μm) with only moderate strength, making them difficult to handle during composite processing and incapable of forming small radii features in components. They also have very high production costs, roughly 100–1000 times that of comparable lengths of multifilament tow.

Oxide fibers are generally utilized with similar composition matrices (i.e. alumina matrices with alumina-based fibers, etc.) due to the poor CTE match of most of the fibers with SiC. A fundamental problem with such oxide–oxide CMCs is that there are no robust fiber coatings identified. While C or BN will work in the short term, oxygen diffusion through any oxide matrix is sufficiently fast above ~1200 °C that these phases oxidize quite readily. For instance, dispersed carbide and silicide phases within a variety of oxide matrices were found to oxidize at rates 2.5–5 orders of magnitude faster than monolithic SiC [17, 18]. Various attempts have been made at developing oxide debond coatings, such as monazite ($LaPO_4$) [19], β-alumina, or sheet-like silicates similar to mica, but with only limited success on a very small scale. Consequently oxide composites generally do not utilize a fiber coating, but instead rely on having very weak, porous matrices to promote toughness. Unfortunately the high porosity in the matrix also means that the composites have low thermal conductivity and poor interlaminar properties. Such oxide composites also have limited high temperature stability due to sintering of the matrix to the fibers and consequent embrittlement above ~1100 °C.

3.2.2 GE's Prepreg Melt Infiltrated (MI) Composite Development

The various problems with the other CMC materials and processes, as discussed in the previous sections, led GE to focus on using reactive melt infiltration for the fabrication of SiC-based CMC materials. The term "Silcomp" refers to GE's trade

name for Reaction-Bonded SiC (RBSC) originally developed in the early 1970s [20]. Various companies had already commercialized reaction bonded SiC materials at the time, but GE's innovation was to utilize carbon fiber during the fabrication of the preform shapes, thus enabling the utilization of standard polymer composite fabrication techniques. Although the Silcomp material was a composite in its broadest sense since it consisted of two separate SiC and Si metal phases, the carbon fiber was consumed by reaction with Si during processing so that it was not a fiber-reinforced ceramic by conventional standards. Consequently the material was brittle and tended to fail catastrophically. Nevertheless, the silicon reaction bonding process has several advantages over other CMC fabrication processes in that it is near net shape, the densification step is relatively fast, the matrix produced has a good CTE match to SiC fiber, and the final material is fully dense.

The initial breakthrough to developing MI SiC composites was the demonstration that BN fiber coatings would survive the melt infiltration process and provide suitable fiber-matrix debonding in this system [21]. The early work on MI-CMCs utilized the Textron SCS type SiC monofilament fibers [20, 22] since the finer tow-based SiC fibers of the day, namely CG-Nicalon™, would not survive the silicon melt infiltration process due to the presence of oxygen in the fiber. This early MI CMC was often referred to as "Toughened Silcomp."

The second breakthrough was thus the development of fine diameter, tow based SiC fiber that was relatively free of oxygen (i.e. Hi-Nicalon™). Without the oxygen impurities this fiber was able to survive exposure to the melt infiltration temperature.

Much of the early-to-mid 1990s was spent on the third major breakthrough, that of developing CVD fiber coating technology for coating continuous lengths of such tow. Coating tow prior to shaping the fiber into a cloth or preform was a deviation from most previous CMC process approaches; however, this was intentionally done so that the coatings on the fiber would nominally remain independent of each other. A consequence of weaving, braiding, or otherwise forming the fiber into shape prior to interface coating was that the coating tended to overcoat, or "can", the entire tow such that all of the fiber coatings throughout the part were interconnected. Such interconnected coatings compromise the composite oxidation resistance.

By the late 1990s the entire process of fiber coating, slurry prepregging, ply layup and lamination, binder burn-out and melt infiltration had been developed and demonstrated [2]. This overall fabrication process is shown schematically in Fig. 3.2. Material made by this process came to be known as "prepreg MI CMC" in order to differentiate it from another MI CMC that utilized a combination of CVI and MI technologies (aka "slurry cast" MI CMC as described in [23, 28]). It has been shown that the relatively straight and independent fibers that are achieved through tow coating and unidirectional tape prepregging improve the effectiveness of the fiber for providing toughness and strength relative to systems using woven or braided reinforcement. This better utilization of the fiber reinforcement in turn allows for composites with comparable in-plane tensile properties, and better interlaminar properties, than cloth-based composites while having a lower overall fiber volume fraction.

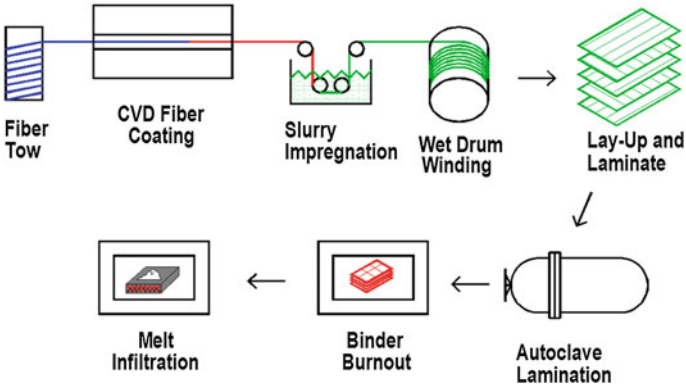

Fig. 3.2 Schematic representation of GE's prepreg MI CMC (aka HiPerComp) fabrication process

3.2.3 Material Properties

The mechanical, physical and thermochemical properties of GE's prepreg MI CMC material, also known under the trade name HiPerComp™,[1] have been previously described [2, 3, 20, 24–27]. The in-plane tensile fracture response of HiPerComp CMCs is typically characterized by a stress-strain curve as shown in Fig. 3.3. The stress-strain response can be divided into four sections as shown by the dotted lines in Fig. 3.3. The first section represents the simple linear elastic loading of the composite. As the stress increases multiple matrix cracks are generated in the composite and the fibers bridging the cracks are shear debonded from the matrix (Sect. 2). It is this matrix cracking and fiber-matrix debonding that are primarily responsible for the "pseudoplastic" behavior and high toughness of these types of CMCs. Eventually the crack density saturates and the bridging fibers become completely debonded in the regions between the matrix cracks, such that continued loading (Sect. 3) represents the elastic response of the bridging fibers. At still higher loads fiber fracture begins to occur (Sect. 4), which often leads to a slight leveling of the stress-strain curve just before ultimate failure.

The important fracture parameters that are determined from the stress-strain curves include the initial modulus, proportional limit stress, ultimate strength and strain to failure, as illustrated in Fig. 3.3. It is often very difficult to determine unambiguously the stress at which the first matrix crack occurs, so the proportional limit stress, i.e. the stress at which the strain deviates by 0.005% from linear loading, is more commonly used to characterize this important stress level.

The temperature dependence of the tensile stress-strain behavior of Prepreg HiPerComp CMC reinforced with Hi-Nicalon fiber is shown by the plots in Fig. 3.4. Both the initial modulus and proportional limit are relatively constant up

[1]Trademark of the General Electric Company.

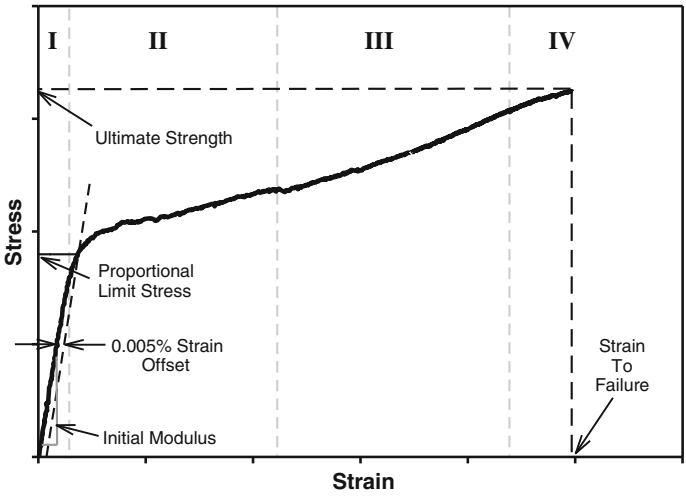

Fig. 3.3 Typical tensile stress-strain behavior of a prepreg MI CMC material and the parameters used to characterize the behavior

to ~1200 °C and then start to slowly decrease at higher temperatures. The ultimate strength shows a near linear reduction with increased temperature. Strain to failure is the most sensitive parameter to test temperature, but remains above 0.2% even at 1300 °C.

Use of stoichiometric SiC fibers with higher temperature capability, such as Hi-Nicalon™ Type-S, Tyranno™ SA or Sylramic™ fibers, generally has only minor effects on short-term properties, but has a strong influence on long-term thermal stability. For instance, the short term fracture properties for Type-S fiber reinforced HiPerComp composites are shown by the dashed curves in Fig. 3.4, and with the exception of the strain to failure they match the tensile properties of the Hi-Nicalon fiber composites very closely. Data comparing the relative ultimate strength for Hi-Nicalon and Hi-Nicalon Type-S reinforced HiPerComp following extended exposure at 1200–1315 °C in air are shown in Fig. 3.5. At 1200 °C the CMC with Hi-Nicalon reinforcement shows only moderate (<10%) strength loss after 4000 h exposure, but at 1315 °C the degradation is more severe at ~30% reduction in only 1000 h. HiPerComp made with Hi-Nicalon Type-S fiber has similar thermal stability at 1315 °C as the material with Hi-Nicalon fiber at 1200 °C.

The greater thermal stability of the stoichiometric fibers is also reflected in the creep rupture and fatigue responses. For instance, rupture data for prepreg HiPerComp CMC reinforced with Hi-Nicalon or Hi-Nicalon Type-S fiber is shown in Fig. 3.6. The rupture data indicate a >300× increase in life at 140 MPa for the Type-S reinforced composite relative to that reinforced with Hi-Nicalon.

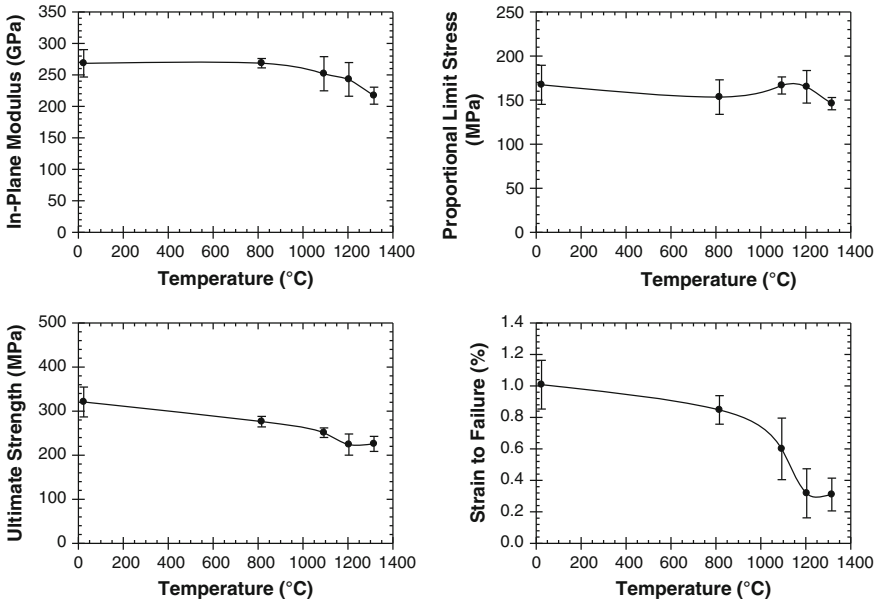

Fig. 3.4 Tensile behavior as a function of test temperature for prepreg HiPerComp reinforced with nominally 24 vol.% Hi-Nicalon fiber in a 0–90 balance layup, shown by the data points and *solid curves*. Similar property trends for HiPerComp reinforced with Hi-Nicalon Type-S fiber are shown by the *dashed curves*

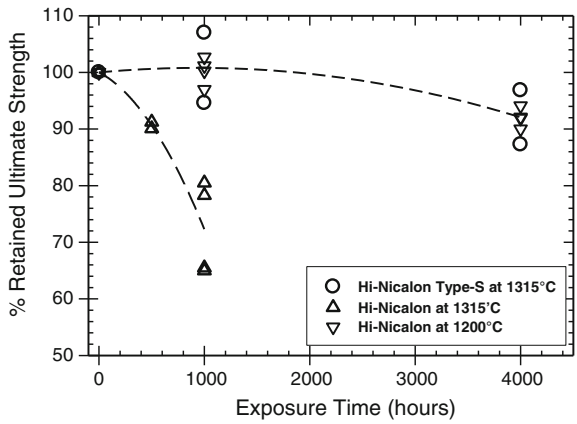

Fig. 3.5 Relative ultimate strength as a function of time at elevated temperature in air for prepreg HiPerComp reinforced with nominally 24 vol.% Hi-Nicalon or Hi-Nicalon Type-S fiber in a 0–90 balanced layup

3.2.4 Recession and Its Abatement

Silicon carbide and silicon, the main constituents of the MI CMC matrix, are known to normally have excellent oxidation resistance due to the formation of a protective silica layer as the oxidation product. At temperatures over ~1100 °C, oxygen

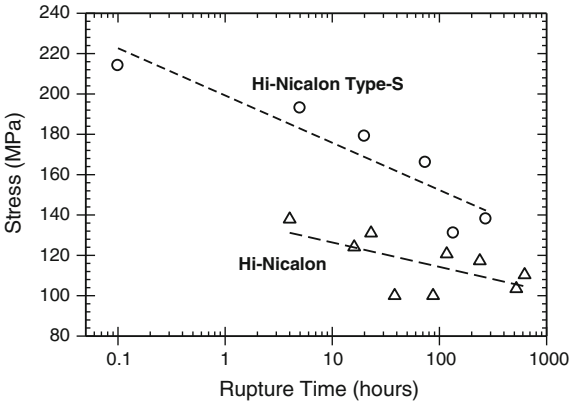

Fig. 3.6 Creep rupture data at 1315 °C in air for prepreg HiPerComp CMC reinforced with nominally 24 vol.% Hi-Nicalon or Hi-Nicalon Type-S fiber in a 0–90 balanced layup

permeability through the silica film is the lowest known amongst all oxides [28]. Consequently, silica-forming materials are attractive for high temperature applications in oxidizing environments. However, during the NASA-funded High Speed Civil Transport (HSCT) program in the mid-1990s, it was recognized that under gas turbine conditions (high temperature, high pressure, high water vapor concentration and high flow) silica reacts with water vapor to form volatile silicon hydroxides. The concurrent oxidation of SiC/Si and volatilization of the silica oxidation product leads to a paralinear loss of the CMC, also known as recession [29–31]. The primary approach developed to deal with this recession problem was to apply oxide coatings, commonly referred to as environmental barrier coatings, or EBCs, that would block the penetration of water vapor to the substrate.

Oxides used for EBCs should have several key characteristics:

- Their coefficient of thermal expansion should be similar to that of the substrate (i.e., $\sim 5 \times 10^{-6}$/°C for SiC-based CMCs). Otherwise the strain mismatch during thermal cycling will cause spallation or cracking of the coating. A dense, uncracked oxide layer has been believed to be necessary to prevent the ingress of water vapor to the substrate and to prevent the recession of the underlying CMC.
- They should be chemically compatible with the thermally grown silica film that forms on the silicon bond coat.
- They should be stable under the water vapor environments present in the turbine for tens of thousands of hours. Typically the thickness of most coatings are of the order of 0.13–0.25 mm, which means that the recession rate of the EBC should be no more than about 6–12 μm per thousand hours.

During the early stages of the HSCT program an exhaustive search was done of the possible compounds that could satisfy these requirements. Two classes of compounds were found to be particularly attractive: alkaline earth aluminosilicates and rare earth silicates. It was also recognized that the oxidation of SiC leads to the formation of CO gas which can destroy the integrity of the dense oxide layers [32]. A silicon bond coat was developed to eliminate the CO formation. The oxidation

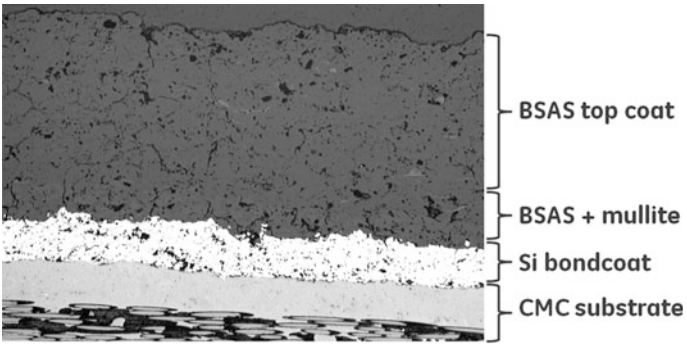

Fig. 3.7 Micrograph showing the layer configuration of the initial EBC system. The improved system utilizes multiple oxide layers including rare-earth silicates

resistance and the thermal expansion coefficient of silicon are similar to that of the CMC substrate.

At GE two EBC systems have been developed, one of which is shown in Fig. 3.7. The initial system was originally developed under the HSCT program in cooperation with NASA and United Technologies, and its processing was further optimized under the DOE-funded CFCC program and under internal GE-funded programs. The improved EBC system was developed under GE funding and the deposition process optimized under the DOE CFCC and Advanced Materials for Advanced Industrial Gas Turbines (AMAIGT) programs. In the improved system rare-earth silicate layers were added due to their improved volatilization resistance relative to barium-strontium alumino-silicate (BSAS).

3.2.5 Engine Testing of CMC Components

Extensive rig and field engine testing of turbine components made by the prepreg MI process were carried out from the late 1990s through the 2000s [2, 3, 20, 24]. Most of this early testing was focused on shrouds and combustor liners for GE Energy applications. Components made from alternate CMC materials, such as CVI SiC/SiC, slurry cast MI and direct metal oxidation (DIMOX), were included in much of this testing, but the performance of the prepreg MI composites was generally superior.

A major step in the commercialization of GE's prepreg MI CMC was the acquisition of the GE Aviation—Newark production facility. Two of the premiere CMC manufacturing organizations in the U.S. in the late 1980s were DuPont, concentrating on CVI SiC composites using technology licensed from SEP, and DuPont-Lanxide Composites, who developed the DIMOX process for making oxide-matrix composites. These two organizations were merged under the DuPont-Lanxide Composites name in 1993, were acquired by Allied Signal (Allied Signal Composites) in 1998, and then acquired by Honeywell (Honeywell

Advanced Composites, Inc.) in 1999 [33]. In 2001 GE acquired the business from Honeywell, after which it has gone through several additional name changes (i.e. GE Power Systems Composites, GE Ceramic Composite Products, and finally GE Aviation—Newark). Transition of the prepreg MI composite technology from GE Global Research to the Newark facility began in 2002, and the material was later commercialized under the trade name HiPerComp™.

Additional process scale-up and refinement took place during the 2000s. Numerous rig and engine tests of CMC components were performed during this period, both to prove the capability of the material system in turbine environments and to validate the material testing, design and lifting methodologies. A timeline showing the major material and process developments along with several of the important engine tests is shown in Fig. 3.8.

Although HiPerComp CMC shroud components have been undergoing field engine tests in industrial gas turbines since 2002, the initial commercial introduction of this material will be as shrouds in the CFM LEAP engine. This engine is scheduled to enter service in 2016, with over 6,000 engines having been sold as of April, 2014 [34]. CMC combustor and other turbine components will also be part of the GE9X engine, which is scheduled to enter service in 2018 [35].

The timeline in Fig. 3.8 highlights the long development time needed to bring revolutionary new materials, such as CMCs, to commercialization, particularly for demanding applications like gas turbine engines. In the particular case of melt-infiltrated CMCs the time from initial conception [21] through material and process development, preliminary component design, rig and engine testing, final component design, qualification and commercialization will have been nearly 30 years.

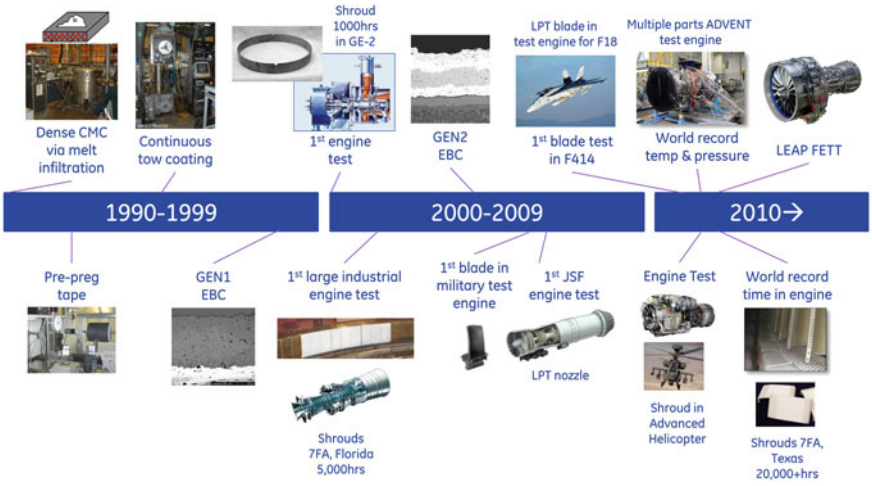

Fig. 3.8 Schematic timeline showing the various early milestones relative to the development of the HiPerComp™ CMC material and process, as well as several of the key engine demonstration milestones for both GE Power and Water and GE Aviation applications

3.2.6 Future Needs

Although HiPerComp is on the verge of commercialization, both material and process development are continuing. The never-ending push for higher turbine engine efficiency puts constant upward pressure on structural material temperature capability. Thus further increases to the temperature capability limits of CMCs are desired. Currently the upper use limit for HiPerComp is defined by the long-term material properties, such as fatigue and creep, in combination with the specifics of the component operating conditions, primarily temperature and stress state. However, there is a hard upper limit to the use temperature of the current MI-CMC and EBC systems of 1410 °C due to melting of the residual silicon in the matrix, as well as in the bond coat of the EBC coating. Removal of free silicon from the system without compromising mechanical properties or environmental resistance is therefore a main thrust for future development.

As with any new materials technology, CMCs are inherently very expensive due to limited production volumes and high manual labor content. Opportunities for cost reduction, such as process scale-up, automation, introduction of in-process monitoring for process control, improved machining, and others, need to be pursued as appropriate for each specific component.

3.3 Polymer Matrix Composite (PMC) Fan Blades

Improving the propulsive efficiency of turbo-fan engines requires larger fans rotating at lower speeds, and the larger fans in modern engines account for an increasing portion of the total engine weight. For example, the CF6-80C2 has a bypass ratio of 5:1 and the fan accounts for 20% of the overall engine weight whereas the newer GEnx-1B engine has a bypass ratio of 10:1 and the fan makes up 30% of the engine weight [36]. Furthermore, a one kg weight increase in the fan leads to additional increases of 1 kg for containment, ½ kg in the rotor, ½ kg in the engine structure and ¼ kg in aircraft structure weight. Thus the larger fans are driving the need for new lighter weight materials.

As noted previously, the primary driver for use of PMC fan blades is weight reduction of the fan structure. Fiber reinforced carbon/epoxy composites offer very high specific modulus and specific strength as compared to metals [37], as shown in Fig. 3.9. The benefits of utilizing such light-weight materials for turbine fan blades are obvious.

3.3.1 History of PMC Fan Blade Development

In June 1967, Rolls-Royce was the first to offer a fan stage built of a new carbon fiber material called *Hyfil* developed at Royal Aircraft Establishment (RAE) at

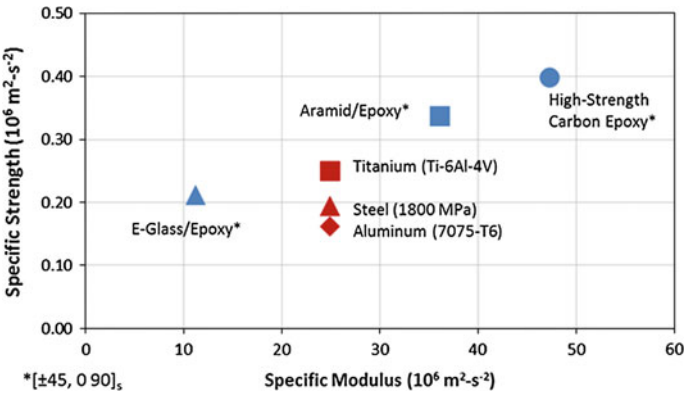

Fig. 3.9 Comparison of specific modulus and specific strength of metals and composites [37]

Farnsborough as part of RB211 engine. In May 1970, after having passed every other test, the fan stage could not pass the bird strike test which shattered the blade into pieces [38]. This failure, although a setback for composites, emphasized the need for a tougher matrix material, and eventually led to development of HexPly® 8551-7, an amine-cured toughened epoxy resin system [39]. A preferred reinforcement for this resin is continuous IM7 graphite fibers, and consequently all current GE PMC fan blades in service have been made from IM7/8551-7 prepreg (pre-impregnated uni-directional ply).

Figure 3.10 shows the history of composite fan blade at GE starting with un-ducted fan blade in 1980. The un-ducted fan concept never went into production, but it provided a good knowledge base for development of the GE-90 fan blade that went in commercial production in 1995. Since then there have been significant improvements in the aerodynamic design and a reduction in number of blades, and we are poised for further advances into the 4th generation. Composite fan blades have set a bench-mark for future developments and further improvements in propulsive efficiency.

Figure 3.11 shows the typical steps of the blade manufacturing process. We start with a solid model of the blade driven by aerodynamic requirements. Blade volume is then divided into 3-D layers, each having the thickness of the prepreg sheet, using a process commonly referred as "peeling the onion". Each layer, referred to as a ply, is then flattened into a 2-D shape and cut from a roll of prepreg with fiber direction being determined by the blade structural requirements. Plies are then laid up in a tool to build the intended volume of the part which is then cured under temperature and pressure.

In the following sections we will look back at the development and commercialization of wide chord fan blades [40] which included the utilization of a tougher matrix material, process modelling techniques, process design methods, and systems for manufacturing producibility. Each of these will be discussed in detail, followed by a summary with lessons learned and prospects for future developments.

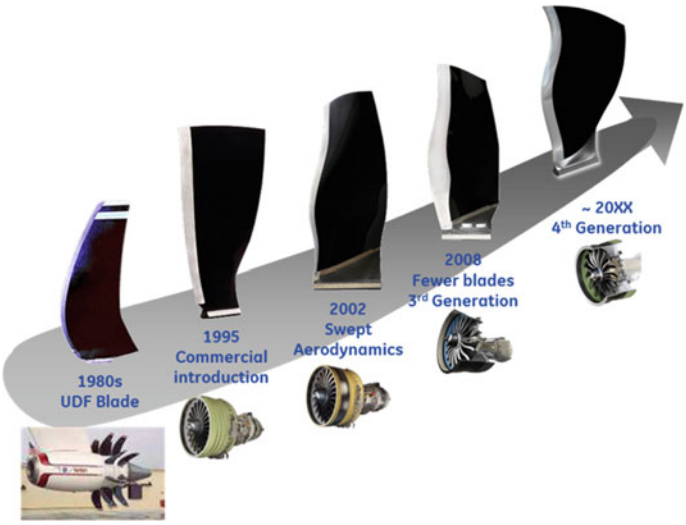

Fig. 3.10 Historic perspective of composite fan blade development at GE

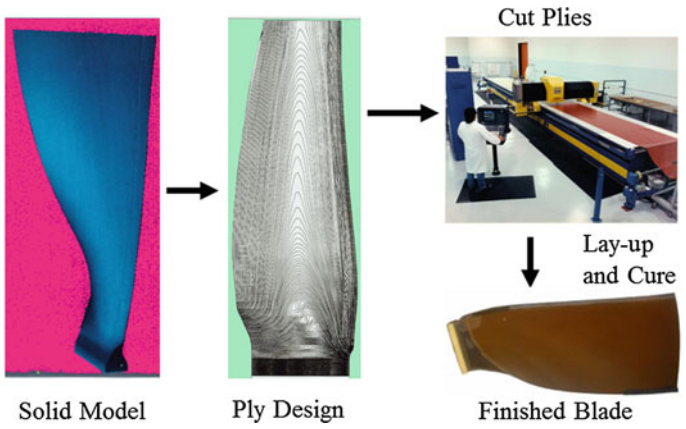

Fig. 3.11 Typical steps in a blade manufacturing process starting from a solid model to finished part

3.3.2 Material Characterization

Understanding of material behavior during the forming process is critical to designing appropriate tooling and a process cycle that avoids producing internal defects. One of the challenges is to identify material properties that drive the quality during the manufacturing process. Characterization of curing, flow and modulus behavior is critical to understanding in situ behavior of the material during the

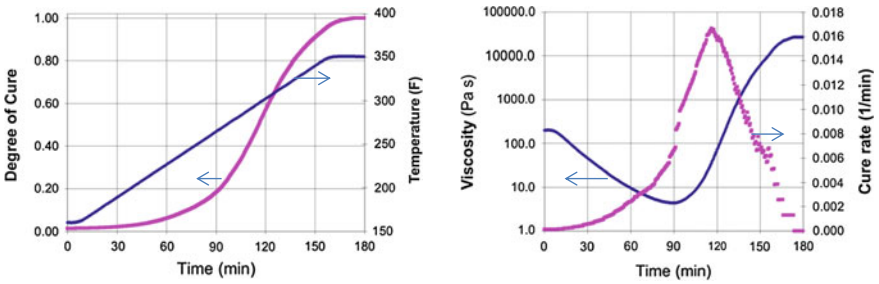

Fig. 3.12 Degree of cure, cure rate and viscosity of Epoxy 8551-7 for a typical heating ramp

consolidation process. We collaborated with research team of Simon et al. [41, 42] at the National Institute of Standards and Technology (NIST) to characterize Epoxy 8551-7, and developed mathematical models that predict the extent of cure and flow for any specified thermal cycle. These models were subsequently used for tooling and process design. Figure 3.12 shows the evolution of the extent of cure and viscosity for a typical temperature cycle.

3.3.3 Process Modeling and Process Cycle Design

Driven by the aerodynamic need for accurate dimensions and surface finish, a matched die mold (referred to as "hard tooling") was initially chosen. It was later shown that this tooling had implications for part internal quality. The molding was done in 1000 ton presses specially designed to control closure to within 2.5 μm accuracy. Instead of a conventional single hydraulic ram there were four independently controlled rams, one for each corner. Internal temperature, pressure, viscosity and flow were simulated using state of the art finite element analysis (FEA) methods, and were then related to part defects like wrinkling, delamination and porosity. One of the major defects was out-of-plane wrinkles, as shown in Fig. 3.13, that significantly reduce the structural properties.

Models and experiments were used to assess the effect of various geometry, thermal/closure and material parameters on wrinkles measured as fiber waviness on tapered specimens with fixed ply layup sequences [43]. Figure 3.14 shows the sensitivity of fiber waviness to various parameters.

Concentrated bulk has a large influence on waviness, but low bulk can lead to lack of consolidation and porosity. Lower root temperature is good for wrinkles but can lead to porosity. Material effects are strongly coupled with process parameters. Nevertheless, higher viscosity or lower flow is better for wrinkles, but can lead to surface quality issues. Based on this and other data, the cure cycle was designed for the blade and the models were extended to the full blade geometry.

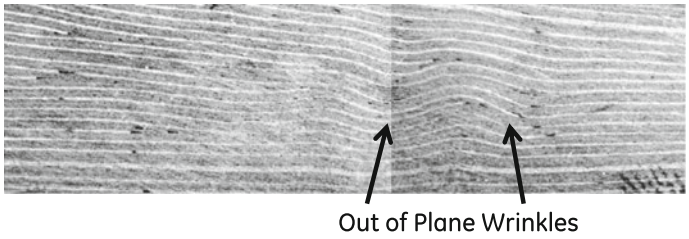

Fig. 3.13 Typical out of plane wrinkles in fan blade

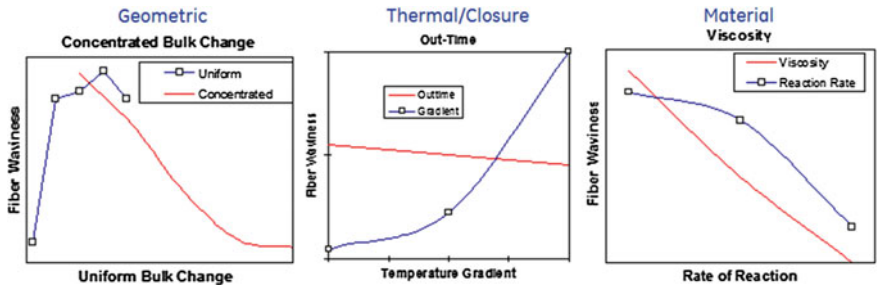

Fig. 3.14 Sensitivity of geometric parameters: uniform and concentrated bulk, thermal parameters: out-time and thermal gradient, and material parameters: viscosity and reaction rate on fiber waviness

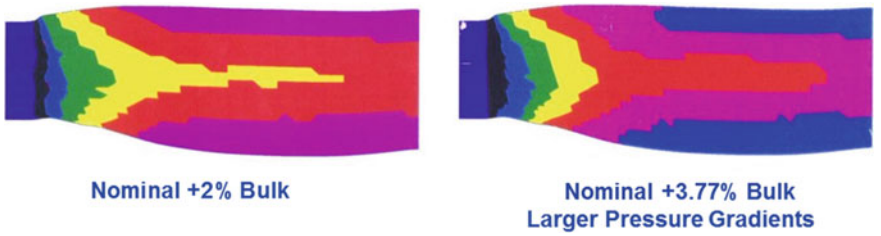

Fig. 3.15 Effect of additional bulk (amount of compaction) on the pressure distribution during consolidation due to higher per ply thickness

Figure 3.15 shows the effect of additional bulk (i.e. the amount of compaction during the consolidation step) due to higher per ply thickness of the prepreg used to build the volume. The models clearly show larger pressure gradients for higher bulks that were found to correlate with an increased degree of wrinkling.

During fabrication the parts were laid up in one tool and then transferred to a mold for consolidation, making it necessary to trim the edges of the layup to fit the mold. Process models were then used to understand internal pressure distribution and develop trimming specifications to minimize wrinkles. The effects of the

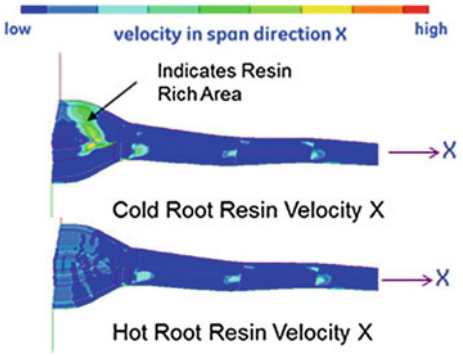

Fig. 3.16 Hot and cold root spanwise resin velocity during consolidation. Higher velocity leads to resin rich areas

thermal boundary conditions were also modelled to set the temperature cycle. The molding press was designed to control individual platen temperatures and root and tip temperatures independently. A typical axial resin velocity distribution during consolidation in the part is shown for cold and hot root conditions in Fig. 3.16 [44]. There is significant difference in the upper root area where higher velocities produced resin rich areas which led to delamination due to resin shrinkage. A cold root temperature difference between the root and platen of $\sim$25 °F was correlated with the occurrence of delamination in root section. Specifications for the temperature cycle were developed based on this analysis.

The temperature/pressure cycle was designed with the intent of minimizing internal defects, which were primarily wrinkles in the root or airfoil regions, porosity or delamination. The dimensions were always within tolerance due to the choice of hard tooling. The complex interaction of material physical and chemical variability, temperature and pressure boundary conditions, and the temperature/pressure cycle made it extremely hard to overcome all defects simultaneously. There was always a tradeoff between wrinkles, porosity and delamination. We learned, after conducting many DOE's and producing 100's of parts, that the inherent entitlement of the process was significantly reduced due to not allowing dimensions to have variation. One of the enduring lessons for composites is that variation in volume due to material must be handled in tool design and accounted for in the process. It is a three-way trade-off between dimensions, internal quality and performance [45].

As a result of low yield entitlement from the hard tooling configuration, we redesigned the tooling so it has an open mold with a flexible caul, referred to as the "soft tooling concept". This tool could accommodate volume variation in the prepreg without creating the large pressure gradients that caused wrinkles. Parts were then cured and consolidated in an autoclave under near-isotropic pressure conditions.

This change of tooling greatly decreased both porosity and delamination, but ply wrinkles were still a major cause of rejects. The wrinkles were both out-of-plane and in-plane at 45° from the reinforcement orientation. Numerous other improvements were required to eliminate these wrinkles, many of which are shown in the timeline in Fig. 3.17. Initial improvements were based on controlling the movement of material within the mold. Additional improvements came from controlling the

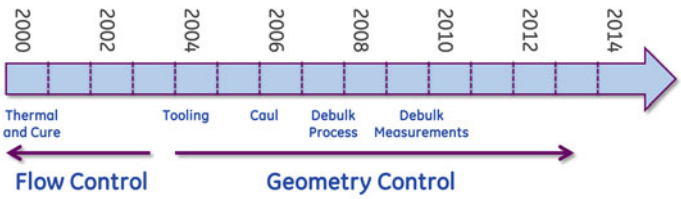

Fig. 3.17 Methods and major historic milestones to eliminate wrinkles in PMC fan blades

various geometric factors of the tooling, and by instituting in-line measurements and volume adjustments to the layup kit in order to adapt for prepreg thickness variation.

3.3.4 Tools for Producibility and Design

As we worked through the tough challenge of understanding the key quality drivers and trade-offs necessary to improve our yield entitlement, it was necessary to develop a platform where we could integrate all material, process and quality data, thereby enabling fast interactive analyses to better understand the underlying process behavior. Figure 3.18 shows the fundamental architecture of the GE Informatics system that is currently being used for fan blade processing and for most other composite components for GE engines. The primary objective of the system is to provide tools and methods to almost automatically integrate all data, convert it into information, generate knowledge in terms of mathematical relationships and enable corrective action. Overall the system minimizes the "Learn and Adapt Time" for a given process.

It is extremely important to develop a feedback mechanism so that important manufacturability data is easily available to the next generation of component designs. Manufacturing provides crucial feedback for design, such as feature producibility and bonded assembly stack-ups. Reductions in the number of geometric measurements needed for airfoil sections are realized by using statistical sampling based on correlations between sections [46]. This information helps designers make robust designs that are producible and at the same time maximize weight reductions without compromising long term performance. The GE Informatics system is starting to make the linkage stronger and is a key piece in the design for manufacturability puzzle.

3.3.5 PMC Summary and Challenges

PMCs represent a mature technology that has been in use for some time, but significant challenges still remain. One of the key challenges is developing design rules

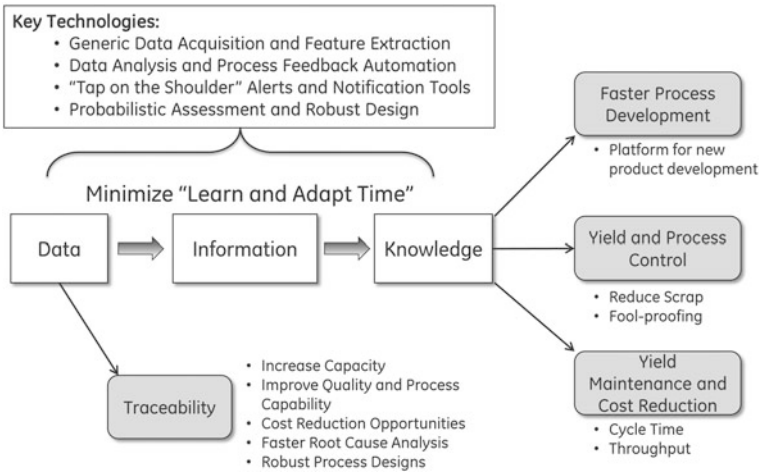

Fig. 3.18 Architecture of the GE informatics system that is being used as a producibility tool and feedback mechanism from manufacturing to design

that allow the inherent trade-off between dimensions, internal quality and performance. We are just now, after decades of application, beginning to build a foundation for manufacturable design. The tools for this are: (i) process models capable of exploring the entire material and process space, (ii) an Informatics system for fast feedback and adaptive control, and (iii) robust feedback to design. Future challenges to introducing new composite components faster is to develop tools for design, manufacturing and testing that can incorporate inherent variation in raw materials and directional placement of reinforcements. This approach requires a fundamental rethinking of design practices that account for composite materials with inherent variation rather than simply replacing metal designs with composite materials.

3.4 NaMx Batteries

GE's NaMx Durathon™[2] batteries, based on a nickel-sodium chloride chemistry, began production in 2011–2012. These batteries are generally most advantageous for applications that require high energy density. Some areas where NaMx batteries can be useful include integration with diesel generators at remote cell phone tower sites for fuel savings, peak smoothing of electricity for the grid, and uninterrupted power supplies [47]. NaMx batteries face certain unique production challenges including manufacture of high quality β″-alumina solid electrolyte (BASE) ceramics with good sodium ion conductivity and strength, production of strong and

[2]Trademark of the General Electric Company.

corrosion-resistant ceramic-to-ceramic glass seals and ceramic-to-metal seals, and efficient integration of the production of various components of a cell and battery for maximum throughput/minimum cost. This chapter will focus on the first step in the production of the BASE ceramic as well as analytics efforts to improve overall battery production throughput.

3.4.1 History of β''-Alumina Solid Electrolyte (BASE) Ceramics

In the 1980s, General Electric worked on the development of sodium-sulfur batteries, that contain sodium-conducting BASE ceramics, ceramic-to-ceramic glass seals and ceramic-to-metal seals similar to those used in NaMx batteries. A good survey of sodium sulfur battery development can be found in the book by Sudworth and Tiley [48]. In 2007, with renewed interest in the so-called "ZEBRA" nickel-sodium chloride battery (now known as the "NaMx" or Durathon battery) GE purchased Beta R&D, Ltd., in order to accelerate GE's technology maturation by utilizing Beta's expertise and experience. GE's NaMx battery plant officially opened at GE's Schenectady, NY site in mid-2012.

The NaMx battery produced by GE, also known as the Durathon battery, contains a cloverleaf-shaped BASE tube to conduct sodium ions between an outer anode compartment containing sodium and an inner cathode compartment containing nickel, sodium chloride, sodium aluminum chloride, and other chemical additives, as shown schematically in Fig. 3.19. In a cell the sodium-conducting BASE ceramic must be sealed to an electrically insulating ceramic. To survive operating temperatures, typically 250–350 °C, this seal is generally made with a glass. The insulating ceramic must also be sealed to a metal to attach the entire ceramic assembly to the cell case with a current collector inside. NaMx batteries generally operate in the temperature range of 250–350 °C because such temperatures are necessary to obtain good sodium ion conduction through the BASE electrolyte. If battery operation were performed at temperatures higher than 350 °C any gains in sodium conductivity would likely be offset by shortened lifetimes due to increased degradation rates of seal and cathode materials, such as by morphological/chemical changes occurring in the cathode chemistry and/or by corrosion.

One particular challenge in making a high quality NaMx battery is making a high quality β″-alumina ceramic sodium conductor. The β″-alumina phase is not present in the Na_2O–Al_2O_3 binary system and requires the presence of a secondary stabilizing dopant such as MgO or Li_2O. A typical composition of lithia-stabilized β″-alumina is 8.8–9 wt% Na_2O, 0.75 wt% Li_2O, and a balance of Al_2O_3. Thus chemical precursors of soda, lithia, and alumina must be mixed to produce β″-alumina.

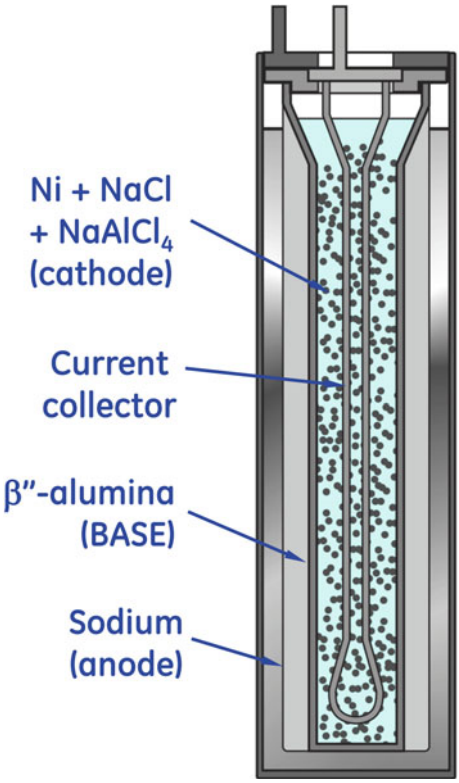

Fig. 3.19 Schematic diagram showing the basic components of a NaMx Durathon™ battery cell

Virkar [49] was one of the first to successfully produce β″-alumina with good ionic resistivity using the so-called "Zeta" process. With three separate mixing and three calcination steps, this process is not particularly amenable to low-cost manufacturing.

Another process not currently used for large-scale production is the Materials and Systems Research, Inc. (MSRI) process, also pioneered by Virkar [50]. In this process α-alumina is mixed with ~30 volume percent of 8 mol% yttria-stabilized zirconia, and these are sintered together into a dense body. This material is then heated with a nearby bed of β″-alumina composition powder so that sodium and oxygen can deposit through the vapor phase, with sodium ions diffusing through the forming β″-alumina phase and oxygen ions diffusing through the zirconia to maintain charge neutrality. β″-alumina on its own is a good conductor of sodium ions but not of oxygen ions, hence the need for an interconnected oxygen-conducting network of zirconia. In this way, macroscopic ceramics can be made as a composite of zirconia and β″-alumina. This process generally yields high strength ceramics with good environmental stability against humidity, but does suffer from ionic resistivities that are at least 50% higher than for BASE made by other processes.

NGK [51] has a commercial process for making magnesia-stabilized BASE, such as with 9.0 wt% Na_2O and 3.8 wt% MgO, starting from α-alumina, sodium carbonate, and magnesium hydroxide. These three components are milled and granulated, formed into a part, and the β″-alumina phase forms within the part during heat treatment and sintering to full density. This process has the advantage of having limited steps and thus lower equipment needs and production times.

3.4.2 GE's BASE Process

The process used by GE to produce lithia-stabilized BASE is similar to that described in Sudworth [52, 53]. Precursors of alumina and sodium and lithium compounds are mixed in a process known as pan granulation. The granulated material is calcined to primarily the β″-alumina phase, milled, granulated as by spray drying, pressed into form, and heat treated. To reduce manufacturing costs, it is desired to maximize yield and throughput without sacrificing quality. The pan granulation process is one step in the process where, in particular, throughput was maximized during startup of the factory.

The pan granulation process involves dry mixing of powder precursors followed by application of water with or without dissolved additives, and mixing until this water becomes evenly distributed through the powder and the powder granulates into spheres generally between a few hundred microns and 10 mm in diameter. Granules that are too small may not flow well and granules that are too large can also exhibit flowability issues due to excess water accumulating over the low specific surface area granules. Granulation, in general, and the pan granulation process, in particular, are described in various references [54–56].

The basics of how pan granulation is believed to work on a microscopic scale are shown schematically in Fig. 3.20. The addition of liquid water to the powder introduces some inhomogeneities in water content of the material, i.e., there are wetter regions surrounded by dryer regions. Upon mechanical mixing, the powder homogenizes, with wetter material coming into contact with dryer material and the excess water from the wetter material being wicked into the pores of the dryer material. Because the water is being wicked into the pores, and therefore does not remain at the surface where the groupings of particles are in contact, the adhesion forces between groupings of particles are minimal, due primarily to Van der Waals forces rather than capillary forces. Thus at this stage clumps of particles can be relatively easily broken up by mechanical agitation. Once the water reaches a certain level of homogeneity in the material such that the pores of most of the powder agglomerates are filled, the slight excess of water present (above what is necessary to fill all the pores) can exist at the surface of the agglomerates without getting wicked away by non-saturated regions of powder that they come into contact with. At this point granulation begins in earnest, with the wet granule surfaces sticking to other wet granule surfaces by capillary cohesive forces. The mechanical mixing and scraping actions of the rotor and blade act to give a normal

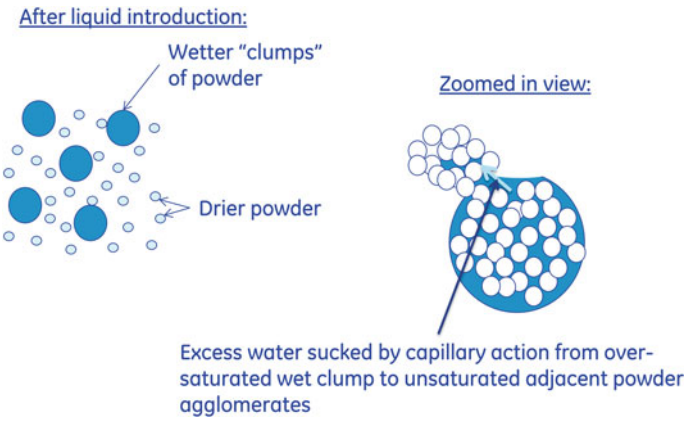

Fig. 3.20 Schematic representation of moisture homogenization that occurs during pan granulation after initial liquid introduction

component of force between these granules so that they can adhere and deform together into larger granules [57].

Two ways to decrease the granulation time in pan granulation involve adding more water and running the rotor faster for more mechanical agitation. Adding more water has the following disadvantages: (1) more energy must be used to remove the water during drying/calcination, (2) granulation can happen so quickly that it becomes difficult to control the granule size, and (3) the extra water may make the granule surfaces wet and sticky such that flowability of the final material is significantly reduced. Increasing rotor speed can increase wear and tear on the equipment and can also make control of granule size difficult. This is shown schematically in Figs. 3.21 and 3.22. Figure 3.21 shows how increasing the rotor speed can decrease the granulation "onset time," when significant granule growth begins. Figure 3.22 shows how the granule growth rate generally increases with rotor speed. Thus higher rotor speeds shorten granulation time but make it more difficult to control the average granule size.

To further complicate the situation, there can be combinations of starting water contents and rotor speeds that never result in granulation of the material. This outcome is because as the water is being mixed into the powder there is heating of the material due to friction and also possibly due to heats of solvation if there are components of the material that dissolve exothermically. As the material heats up, the vapor pressure of water increases and thus significant water can escape from the pan as vapor. Depending on the relative rates of water loss and water homogenization, granulation may never occur. This is shown schematically in Fig. 3.23.

In GE's pan granulation process, the rotor speed and water contents are carefully controlled to give the fastest throughput that results in reasonable consistency of product moving to the next stage of production. One significant challenge where further research may prove fruitful is in understanding how powder variability can

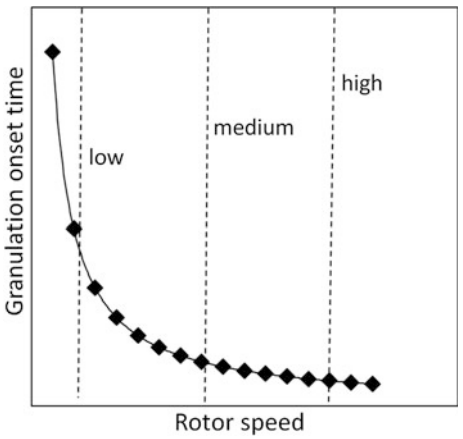

Fig. 3.21 Schematic of the effect of rotor speed on granulation onset time

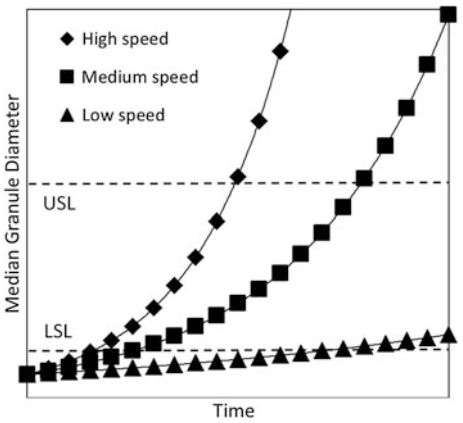

Fig. 3.22 Schematic of the effect of rotor speed upon granule growth rate

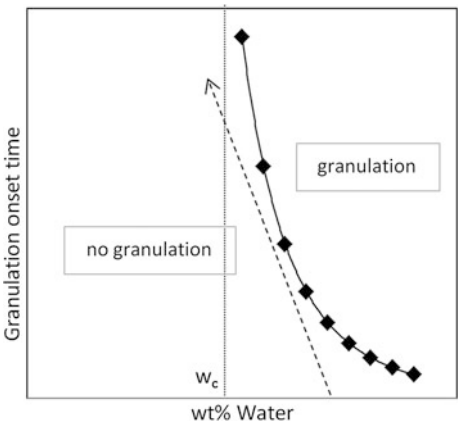

Fig. 3.23 Schematic of granulation onset time versus water content of the granulating material, showing a possible path of water loss with time where granulation may never occur

lead to process and property variability, and how in-line characterization tools may enable real-time compensation/control for these factors. This challenge is compounded by the desire to keep raw material and analysis costs to a minimum and yet produce high strength, high ionic conductivity ceramic components with a high degree of repeatability. Production of high quality, low cost BASE ceramic is, however, only one step in the production of high quality, low-cost NaMx batteries. Optimized production from BASE powder through to batteries can be greatly aided by the use of data analytics.

3.4.3 *Improving Factory Systems Performance Through Manufacturing Analytics*

The generic challenge in any factory is how to improve overall factory performance, i.e. throughput, quality, cost, and order fulfillment. In the past, performance improvements were mostly based on manual data collection and aimed at *long-term* performance improvements. However, with today's factory IT systems (mainly Manufacturing Exceptions Systems and Enterprise Resource Planning) and equipment producing gigabytes of data, the grand challenge is how to integrate and utilize the data to improve performance in real time. We have described this challenge in detail in a previous paper [58] and focus here on its application to the battery plant. In particular, we are addressing math-based capacity planning, throughput improvements and quality improvements through perfect product genealogy.

Facing the challenges of quick production ramp-up needs and the inherent uncertainties of a new production line, the NaMx battery plant adapted data analytics and system modeling methods to help accelerate the learning curve, improving yields, reducing variable costs and increasing plant throughput. Data systems are used to help detect any deviation in "reality" from initial engineering assumptions through the product genealogy. Multi-variable data-driven methods (e.g. decision tree, principal component analysis (PCA), regression) identify key differentiators among the thousands of parameters that are recorded for a product unit. In addition, discrete-event simulation models are used to predict the production throughput and order fulfillment and to identify improvement opportunities.

A manufacturing simulation was built using AnyLogic™. The extendable and Java-based architecture of the software provides a flexible test environment. Changing experiment settings and the simulation initial state, the model can support both long-term steady-state analysis and short-term prediction. The developed model can run as a standalone application or be embedded in a larger system with other real-time data extraction and data visualization tools. Thus, the model is easy to integrate with other manufacturing IT systems for production control.

The combination of advanced data system and simulation models generates powerful results. The data system in the factory tracks the machine information at the most granular level, providing the distribution of key metrics (e.g., cycle times, yield) in real time. The data are fed into a stochastic discrete event simulation.

In one example, the model revealed and quantified a throughput leak due to the dynamic interactions of three neighboring machines. This analysis led to an effective plant and equipment investment decision that increased plant throughput by more than 10%.

The simulation not only helps diagnose the current bottleneck, but also helps predict future obstacles. A ramp-up plan was generated through simulation to guide the plant expansion. The analysis highlighted a series of critical improvement projects identified by targeting the most constrained bottlenecks with single period investments until hitting a fixed throughput level or becoming limited by a subsequent bottleneck, see Fig. 3.24. The simulated improvement path helped managers and engineers plan ahead to remove current and future bottlenecks. The model also helps accurately understand the benefits of projects. For example, doubling the capacity of the bottleneck process may not necessarily double the system throughput as the system can become limited by a new bottleneck.

The capacity simulation is further being developed to become an online operations optimization system. Connecting the model with real-time machine status and factory data, the simulation will be triggered when unplanned events (e.g., downtime) occur. It will evaluate different recovery options and optimally reallocate resources (e.g., staffing) to minimize the disruption to the production plan and to system throughput.

3.4.4 NaMx Battery Summary and Challenges

The Durathon™ NaMx battery is a system that integrates a significant number of materials (ceramics, metals, and glass), components, and process steps into a high

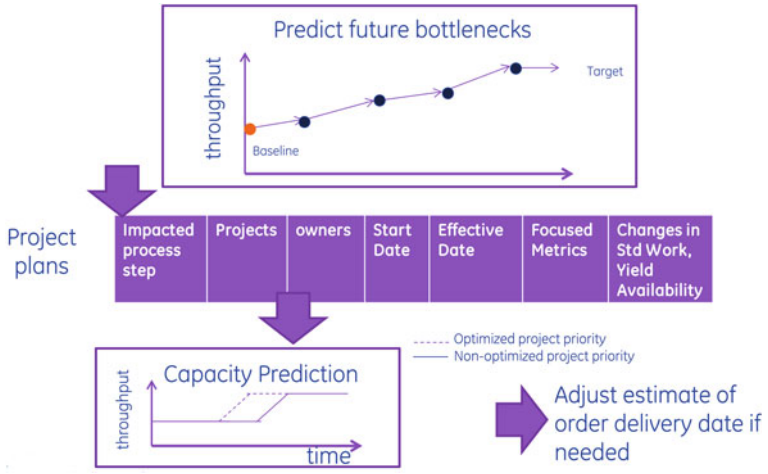

Fig. 3.24 Example ramp-up plan

performance energy storage device. To reduce manufacturing costs and maintain high product quality, the yields and throughputs of the processes can be maximized through a combination of analytics to know where one will gain the most benefit per investment dollar, and engineering to actually make the improvements in the individual process steps. Some of the challenges in increasing performance, decreasing lifetime cost, and thus increasing economical-viability of these batteries to a broader range of applications include understanding the degradation mechanisms of the cathode chemistry with all the complex electrochemical processes that can be occurring there, increasing the robustness of components against corrosion and mechanical stresses to extend the life and reliability of the battery, and automating production as much as possible. Also, the relatively high operating temperatures of 250–350 °C present a particular opportunity for the discovery and implementation of new low cost, high conductivity, corrosion resistant materials that can operate in this temperature range or even enable reduced operating temperatures.

3.5 Educational Recommendations

In general, the skills and educational background required to flourish in a large company, such as GE, have some commonalities with those of entrepreneurs running small companies, but also several significant differences. In both cases there is a desire to move and act quickly in order to beat the competition to market. However, in large companies most of the high-impact projects are not done by individuals, but rather by teams of engineers and scientists having diverse backgrounds. Knowing how to comfortably work with such a team, both by being an active contributor and by being confident and comfortable in trusting others, is very important. Another general skill that is very important is critical thinking is the ability to sort through complex data and identify critical/important variables.

In addition to the general skills, such as "Team Work" and "Critical Thinking," a researcher needs to have strong expertise in their field of choice. Most of the problems addressed within a research organization in a large company, such as GE Global Research, are complex and often require in-depth expertise in very specialized fields to solve. For instance, two particular specialties that played important roles in the development of ceramic composites, as discussed in this chapter, were ceramic processing and high-temperature thermochemistry (thermodynamics and kinetics), two disciplines that have been on the decline in academia for the past 20 years.

The objective of this book is to describe the importance of modelling to materials development. However, an overreliance on modelling, without having the basic physical or mechanical understanding of a system to know when the models are misleading or wrong, can be a huge problem. All process models are necessarily simplifications of very complex systems with many inherent assumptions built in. Acknowledging the limitations of the models and validating the predictions with rigorous experimentation are both key to their successful application.

3.6 Summary and Conclusions

The successful implementation of advanced materials technologies requires a systems approach involving development of advanced materials and manufacturing technologies and their close interaction with system design. This chapter deals with three examples of advanced materials technologies.

CMCs are a revolutionary technology for hot stage components of aircraft engines and industrial gas turbines, where they offer opportunities for huge fuel savings. However, the development and commercialization of revolutionary technologies, such as CMCs, can take over 25 years. Further improvements in their temperature and stress capability and reductions in manufacturing costs would broaden the application of CMCs to other industries.

Polymer Matrix Composite fan blades represent an old technology that has been in use for aircraft engines for over 20 years, but significant challenges still remain in low-cost manufacturing and reducing the cycle time to introduce new components.

The Durathon™ NaMx battery is a complex system, and this chapter focused on β″-alumina solid electrolyte tube production and process analytics. Although already competitive in several applications, to extend the utility of this battery even further, improvements in the performance-to-cost ratio will need to be made based upon improvements in understanding of such things as the effect of powder raw materials variability on process and property variability, degradation mechanisms in the battery chemistry and hardware, and methods for automating and maximizing throughput and yield in production.

Acknowledgments Parts of the early CMC work were sponsored by the U.S. DOE under contracts DE-FC26-92CE41000 and DE-FC26-00CH11047. The authors wish to thank the research teams at GE Global Research, GE Aviation, GE Power & Water, and GE Transportation for numerous contributions to the research described in this chapter.

References

1. G.S. Corman, K.L. Luthra, M.K. Brun, P.J. Meschter, Toughened silcomp composites for gas turbine engine applications. DOE CFCC Program Phase I Final Report, Report #DOE/CE/41000-2, July 1994
2. G.S. Corman, K.L. Luthra, Melt infiltrated ceramic composites (HiPerComp™) for gas turbine engine applications. DOE CFCC Program Phase II Final Report, Report #DOE/CE/41000-3, Jan 2006
3. G.S. Corman, Melt infiltrated ceramic matrix composites for shrouds and combustor liners of advanced industrial gas turbines. DOE Advanced Materials for Advanced Industrial Gas Turbines Program Final Report, contract DE-FC26-00CH11047, OSTI ID 1004879, Jan 2011
4. http://www.aviationweek.com/aw/generic/story.jsp?id=news/avd/2010/09/17/10.xml&headline=New%20GE%20Engine%20Has%20Potential%20For%20Commercial%20Use&channel=mro
5. http://www.asdnews.com/news/19672/GE_Moving_To_Apply_Ceramic_Matrix_Composites_to_Heart_of_Future_Engines.htm

6. P. Morgan, *Carbon Fibers and Their Composites* (CRC Press, Boca Raton, 2005)
7. D.C. Phillips, R.A.J. Sambell, D.H. Bowen, The mechanical properties of carbon fibre reinforced pyrex glass. J. Mater. Sci. **7**, 1454–1464 (1972)
8. S. Yajima, K. Okamura, J. Hayashi, M. Omori, Synthesis of continuous SiC fibers with high tensile strength. J. Am. Ceram. Soc. **59**, 324–327 (1976)
9. M. Takeda, J. Sakamoto, S. Saeki, Y. Imai, H. Ichikawa, High performance silicon carbide fiber Hi-Nicalon for ceramic matrix composites. Ceram. Eng. Sci. Proc. **16**(4), 37–44 (1995)
10. F.S. Gallaso, Chapter 4 in *Advanced Fibers and Composites* (Taylor and Francis, 1989), pp. 59–65
11. J.A. DiCarlo, H. Yun, Non-oxide (silicon carbide) fibers, Chapter 2 in *Handbook of Ceramic Composites*, ed. by N.P. Bansal (Kluwer Academic Publishing, 2005), pp. 33–52
12. T. Mah, M.G. Mendiratta, A.P. Katz, K.S. Mazdiyasni, Recent developments in fiber-reinforced high temperature ceramic composites. Am. Ceram. Soc. Bull. **66**(2), 304–308 (1987)
13. J. Cornie, Y-M.Chang, D.R. Uhlmann, A. Mortensen, J.M. Collins, Processing of metal and ceramic matrix composites. Am. Ceram. Soc. Bull. **65**(2), 293–304 (1986)
14. L.J. Schioler, J.J. Stiglich, Ceramic matrix composites: a literature review. Am. Ceram. Soc. Bull. **65**(2), 289–292 (1986)
15. R.N. Singh, M.K. Brun, Effect of boron nitride on fiber-matrix interactions, GE report 87CRD051 (1987)
16. A.R. Bunsel, Oxide fibers, Chapter 1 in *Handbook of Ceramic Composites*, ed. by N.P. Bansal (Kluwer Academic Publishing, 2005), pp. 3–31
17. M.P. Borom, M.K. Brun, L.E. Szala, Kinetics of oxidation of carbide and silicide dispersed in oxide matrices. Adv. Ceram. Mater. **3**(5), 491–497 (1988)
18. K.L. Luthra, H.D. Park, Oxidation of SiC-reinforced oxide matrix composites at 1375-1575°C. J. Am. Ceram. Soc. **73**, 1014–1023 (1990)
19. K. Keller, T-I. Mah, Development of monazite ($LaPO_4$) coated-fiber reinforced oxide-oxide composites. Presented at the *5th International Conference on High Temperature Ceramic Matrix Composites (HTCMC5)*, Seattle WA, 12–16 Sept 2004
20. G.S. Corman, K.L. Luthra, M.K. Brun, Silicon melt infiltrated ceramic composites—processes and properties, Chapter 16 in *Ceramic Gas Turbine Component Development and Characterization*, ed. by M. vanRoode, M.K. Ferber, D.W. Richerson (ASME Press, 2003), pp. 291–312
21. M.P. Borom, W.B. Hillig, R.J. Singh, W.A. Morrison, L.V. Interrante, Fiber containing composite, U.S. Patent 5,015,540 (1991)
22. K.L. Luthra, R.N. Singh, M.K. Brun, Toughened silcomp composites—process and preliminary properties. Am. Ceram. Soc. Bull. **72**(7), 79–85 (1993)
23. J.A. DiCarlo, H.M. Yun, G.N. Morscher and R.T. Bhatt, SiC/SiC composites for 1200°C and above, Chapter 4 in *Handbook of Ceramic Composites*, ed. by N.P. Bansal (Kluwer Academic Publishing, 2005), pp. 77–98
24. G.S. Corman, K.L. Luthra, Silicon melt infiltrated ceramic composites (HiPerComp™), Chapter 5 in *Handbook of Ceramic Composites*, ed. by N.P. Bansal (Kluwer Academic Publishing, 2005), pp. 99–115
25. R. Nimmer, G. Corman, R. Gilmore, Orthotropic mechanical data characterizing uni-directional and cross-plied HiPerComp™ composite material, in *29th Annual Conference on Composites, Materials, and Structures*, Cape Canaveral, FL, 24–27 Jan 2005
26. D. Dunn, The Effect of Fiber Volume Fraction in HiPerComp™ SiC-SiC Composites, Ph.D. thesis, Alfred University, Sept 2010
27. D. Dunn, G. Kirby, Effect of fiber volume fraction on the creep rupture of HiPerComp™ CMC, in *34th Annual Conference on Composites, Materials, and Structures*, Cape Canaveral, FL, 25–28 Jan 2010
28. E.L. Courtright, J.T. Prater, C.H. Henager, E.N. Greenwell, Oxygen permeability for selected ceramic oxides in the range 1200°C–1700°C, Wright Laboratory Technical Report WL-TR-91-4006 (1991)

29. E.J. Opila, R.E. Hann, Paralinear oxidation of CVD SIC in water vapor. J. Am. Ceram. Soc. **80**(1), 197–205 (1997)
30. E.J. Opila, D.S. Fox, N.S. Jacobson, Mass spectrometric identification of Si-O-H(g) species from the reaction of silica with water vapor at atmospheric pressure. J. Am. Ceram. Soc. **80**(4), 1009–1012 (1997)
31. E.J. Opila, J.L. Smialek, R.C. Robinson, C.S. Fox, N.S. Jacobon, SiC recession caused by SiO_2 scale volatility under combustion conditions: II, thermodynamics and gaseous-diffusion model. J. Am. Ceram. Soc. **82**(7), 1826–1834 (1999)
32. H. Wang, K.L. Luthra, Ceramic with preferential oxygen reactive layer, U.S. Patent No. 6,299,988 (2001)
33. D.J. Landini, A.S. Fareed, H. Wang, P.A. Craig, S. Hemstad, Ceramic matrix composites development at ge power systems composites, LLC, Chapter 14 in *Ceramic Gas Turbine Component Development and Characterization*, ed. by M. vanRoode, M.K. Ferber, D.W. Richerson (ASME Press, 2003), pp. 259–276
34. http://www.cfmaeroengines.com/press/lufthansa-places-1-0-billion-leap-1a-engine-order/745
35. http://www.geaviation.com/press/ge90/ge90_20131119a.html
36. F. Worthoff, System requirements flowdown to components influencing manufacturability, in *Composite Manufacturing Symposium*, GE Global Research, 16 April 2013
37. F.C. Campbell, Introduction to composite materials, Chapter 1 in *Structural Composite Materials*, ASM International (2010)
38. http://en.wikipedia.org/wiki/Rolls-Royce_RB211#cite_note-bird_ingestion-8
39. http://www.hexcel.com/Resources/DataSheets/Prepreg
40. G.C. Murphy, B.J. Furhmann, Wide chord fan blade, US Patent US 5141400 A, Aug 1992
41. S.L. Simon, G.B. McKenna, O. Sindt, Modeling the evolution of the dynamic mechanical properties of a commercial epoxy during cure after gelation. J. Appl. Poly. Sci. **76**, 495–508 (2000)
42. P. Prasatya, G.B. McKenna, S.L. Simon, A viscoelastic model for predicting isotropic residual stresses in thermosetting materials: effects of processing parameters. J. Comp. Mat. **35**, 826–848 (2001)
43. R.K. Upadhyay, R.K. Pandy, Design of manufacturing process for complex composite, in *SEM (Society for Experimental Mechanics) Conference*, 1999
44. R.K. Upadhyay, S. Sinha, W Bushko, B. Kirpatrick, Manufacturing process simulation, Progress Report GE-Boeing collaboration Program, Jan 2006
45. R.K. Upadhyay, Uniqueness of composites from manufacturing perspective, in *Composite Manufacturing Symposium*, GE Global Research, April 16, 2013
46. T. Lednicky, Case study of successful design manufacturing interaction, in *Composite Manufacturing Symposium*, GE Global Research, April 16, 2013
47. www.geenergystorage.com
48. J. Sudworth, A.R. Tiley, *Sodium Sulfur Battery* (Springer, 1986)
49. A.V. Virkar, G.R. Miller, R.S. Gordon, Resistivity-microstructure relations in lithia-stabilized polycrystalline β″-alumina. J. Am. Ceram. Soc. **61**(5-6), 250–252 (1978)
50. A.V. Virkar, J. Jue, K.Z. Fung, Alkali-Metal-β- and β″-alumina and gallate polycrystalline ceramics and fabrication by a vapor phase method, US Patents 6,117,807 (2000), 6,537,940 B1 (2003), 6,632,763 B2 (2003)
51. T. Oshima, M. Kajita, A. Okuno, Development of sodium-sulfur batteries. Int. J. Appl. Ceram. Technol. **1**(3), 269–276 (2004)
52. J.L. Sudworth, P. Barrow, W. Dong, B. Dunn, G.C. Farrington, J.O. Thomas, Toward commercialization of the β-alumina family of ionic conductors. MRS Bull. **25**(3), 22–26 (2000)
53. J.L. Sudworth, The sodium/nickel chloride (ZEBRA) battery. J. Power Sources 149–63 (2001)
54. J.S. Reed, *Principles of Ceramic Processing*, 2nd edn. (John Wiley & Sons Inc, New York, 1995), pp. 379–382
55. S.D. Salman, M. Hounslow, J.P.K. Seville, *Granulation* (Elsevier Science, 2006)

56. D.M. Parikh (ed.), *Handbook of Pharmaceutical Granulation Technology*, 3rd edn. (Informa Healthcare USA Inc, New York, 2010)
57. N. Ouchiyama, T. Tanaka, The probability of coalescence in granulation kinetics. Ind. Eng. Chem., Process Des. Dev. **14**(3), 286–289 (1975)
58. M. Annunziata, S. Biller, The future of work. GE White Paper. http://files.publicaffairs.geblogs.com/files/2014/04/AM_II_FOW_WhitePaper_FINAL-1.pdf. Accessed April 2014

Chapter 4
KEMET Electronics: Breakthroughs in Capacitor Technology

Abhijit Gurav, Xilin Xu, Yuri Freeman and Erik Reed

Abstract With their world-wide production volume exceeding two trillion pieces per year, capacitors account for the majority of the parts mounted on almost any printed circuit board in any application. As electronics continues on its trend of miniaturization, increased functionality and connectivity, the need for high reliability capacitors is growing rapidly in automotive, medical, military, aerospace and industrial electronics. This chapter describes how KEMET Electronics is leading development in these areas with significant innovations in new products for extreme high temperature environments and for high reliability military and aerospace applications.

4.1 Introduction

KEMET Electronics Corporation is a leading global manufacturer of a wide variety of capacitors. Our product offerings include tantalum, multi-layer ceramic, solid and electrolytic aluminum, and film and paper capacitors. KEMET's capacitors are found in various defense and aerospace electronics, automotive electronics, power management systems, communication, computer and data processing systems, cellular phones, and many other electronic devices and systems.

KEMET's operations began in 1919 as a division of Union Carbide Corporation to manufacture component parts for vacuum tubes, and then grew into manufacturing capacitors in the 1950s and 1960s. Over the past several decades, KEMET has led many segments of the capacitor industry due to its strong emphasis on research and development. During fiscal years 2013 and 2014, we shipped 32 billion and 35 billion capacitors, respectively, and during these 2 years, we had

A. Gurav (✉) · X. Xu · Y. Freeman · E. Reed
KEMET Electronics Corporation, 2835 KEMET Way, Simpsonville, SC 29681, USA
e-mail: AbhijitGurav@kemet.com

L.D. Madsen and E.B. Svedberg (eds.), *Materials Research for Manufacturing*, Springer Series in Materials Science 224,
DOI 10.1007/978-3-319-23419-9_4

consolidated net sales of $843.0 million and $833.7 million, respectively. We operate 21 production facilities in Europe, North America and Asia, and employ 9,600 employees worldwide. Our customer base includes most of the world's major electronics original equipment manufacturers ("OEMs") (including Alcatel-Lucent USA Inc., Bosch Group, Cisco Systems, Inc., Continental AG, Dell Inc., Hewlett-Packard Company, IBM Corporation, Intel Corporation, Nokia Corporation, and TRW Automotive), electronics manufacturing services providers ("EMSs") (including Celestica Inc., Flextronics International LTD, Jabil Circuit, Inc. and Sanmina-SCI Corporation) and distributors (including TTI, Inc., Arrow Electronics, Inc. and Avnet, Inc.). In the fiscal year 2014, KEMET capacitor sales into industrial products made up 24% of net sales, followed closely by automotive at 22%, telecommunications at 18%, computers at 15% and defense/medical at 12%. Consumer products remained our smallest sales segment at 9% of net sales.

4.1.1 Recent Trends in Electronics

Capacitors are electronic components that store, filter, and regulate electrical energy and current flow. As an essential passive component used in most circuit boards, capacitors are typically used for coupling, decoupling, filtering, oscillating and wave shaping functions. They are used in communication systems, data processing equipment, personal computers, cellular phones, automotive electronic systems, defense and aerospace systems, consumer electronics, power management systems and many other electronic devices and systems (basically anything that plugs in or has a battery).

The most common trends in electronics are miniaturization, increased functionality and connectivity, which lead to continuing growth of the overall content of electronics in our homes, cars, smart phones, other personal devices, medical instruments, industrial electronics, and so on. The total production volume of capacitors crossed the 1 trillion/year mark in 2007 [1]. Now in 2014, the total world-wide production volume of the three passive components, capacitors, resistors and inductors is estimated at over 3 trillion pieces per year ($\sim$100,000 pieces used per second!), and capacitors contribute a major portion of these at over 2 trillion pieces per year. Within this volume, the biggest share is contributed by the multi-layer ceramic capacitors (MLCC) at well over 90%. Thus, in general, ceramic capacitors account for the majority of the parts mounted on almost any printed circuit board in any application.

4.1.2 Ceramic and Polymer-Tantalum Capacitors

The multi-layer ceramic capacitors (MLCC) consist of alternating layers of ceramic dielectric and metal electrodes (Fig. 4.1). Until the mid- to late-1990s, the most

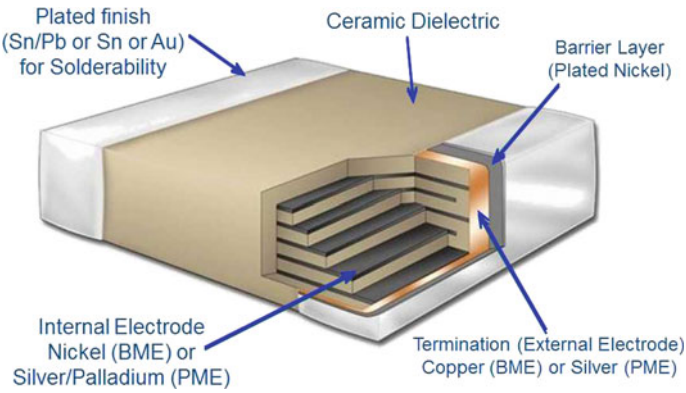

Fig. 4.1 Schematic of a multi-layer ceramic capacitor (MLCC)

common internal electrodes were precious metal electrodes (PME) made of pure palladium (Pd) or a silver-palladium (Ag/Pd) alloy. Due to the rapid increase in the price of palladium in the late 1990s, the ceramic capacitor industry mostly converted to base-metal electrodes (BME) primarily made of nickel (Ni). The manufacturing process starts with fine powders of ceramic dielectric, coating thin layers of the ceramic, then screen printing nickel electrode layers, followed by stacking alternating layers of the ceramic dielectric and metal electrodes to build the capacitor as per its design. This layering is followed by thermal processing to burn off the binders and other organics, and to fire or sinter the capacitors at high temperatures. Next, an end metallization or termination material (e.g., Cu) is applied on the ends of the chips, followed by application of a solderable finish (e.g., nickel/tin). Capacitors then go through electrical testing and followed by reeling and packaging.

The key properties of ceramic dielectrics and capacitors include its dielectric constant (k) and capacitance which are a measure of how much electric charge it can store, its insulation resistance (IR) which is the converse of its leakage current when voltage is applied, and its temperature coefficient of capacitance (TCC) which is a measure of how much the capacitance changes versus temperature. The ceramic dielectrics are classified into different classes and specifications such as Class-I (e.g., C0G) and Class-II (e.g., X7R, X8R), etc., based on their TCC behavior.

The (EIA) Electronics Industries Association specification for X7R dielectrics requires that the capacitance variation ($\Delta C/C$) from its value at room temperature (25 °C) should be within ±15% over the temperature range from −55 to 125 °C. Due to the need for high capacitance values along with such a controlled temperature variation of capacitance, the X7R dielectrics are based on barium titanate, $BaTiO_3$ with addition of suitable dopants to achieve good electrical and reliability properties. Typical dielectric constants (k) for X7R dielectrics are in the range of 2500–3200. In applications where capacitance needs to be precisely controlled over

a wide temperature range, such as digital tuning and timing circuits, the C0G dielectric is an optimum choice in the MLCC. The EIA specification for a C0G dielectric is that the capacitance variation from room temperature should be within 0 ± 30 ppm/°C over the temperature range from −55 to 125 °C. Traditional C0G dielectric materials for precious metal electrodes (PME, such as Pd or Ag/Pd) are typically based on the barium neodymium titanate (BNT). The base metal electrode (BME) C0G dielectrics are $CaZrO_3$-based materials with a dielectric constant (k) of ~31. There are several aspects of judging the reliability of capacitors, but common criteria is based on how stable the insulation resistance (IR) is when voltage and temperatures are applied on a capacitor for a length of time. For example, life tests can be conducted by applying twice the rated voltage on a number of capacitor samples kept at their maximum operating temperature of 125 °C for 1000 h. Certain electrical characteristics, such as capacitance and IR (or leakage), can be measured on the samples before and after the 1000 h test, and the measurements are compared to the specified values for these parameters.

Tantalum capacitors start with a slug of porous, high surface area tantalum metal with an attached tantalum lead wire. The high surface area contributes to the high capacitance of the capacitor. A thin tantalum pentoxide dielectric is conformally electrochemically deposited on the metal. An intrinsically conductive polymer is deposited on the dielectric. This forms the basic Ta Anode/tantalum pentoxide dielectric/conductive polymer capacitor (Fig. 4.2). To make connection to the circuit, first carbon and silver paint layers are applied. The cathode is connected to a lead frame with a conductive adhesive while the anode is connected via welding of the tantalum wire. The assembly is then over molded with an epoxy to form the completed package.

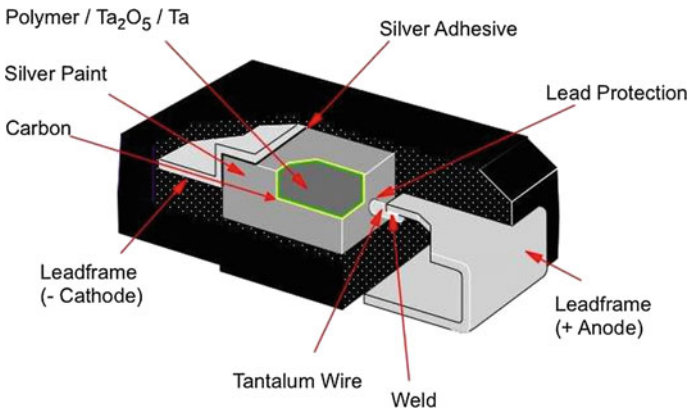

Fig. 4.2 Schematic of a polymer-tantalum capacitor

4.2 Ceramic Capacitors for High Temperature Applications

4.2.1 Growing Need for Electronics for Extreme Environments

For applications in harsh environment conditions, such as down-hole oil exploration, geothermal energy generation, power electronics, automotive under the hood electronics, military devices and avionics, etc., the maximum operating temperature are commonly 175−200 °C or higher [2–4]. These industries need capacitors that are robust and reliable at these high temperatures. However, at these temperatures, dielectric materials either have significant capacitance variation with temperature, or exhibit high dielectric losses, and hence, are not commonly available in the market [5–7]. As the electronics involved in these applications becomes more complex and grow with respect to component density, there is also a trend to minimize cooling for the electronic components involved. Commercial C0G and X7R type ceramic dielectrics are usually designed for applications up to 125 °C, while the X8R type dielectric is designed for applications up to 150 °C. One approach for using the X7R/X8R dielectric at temperatures above their design limit of temperature is by de-rating their rated voltages due to reliability concerns. For example, some X7R dielectrics can be used at 150 °C after 50% voltage de-rating [8]. Similarly, it may be possible to use some X8R type capacitors at temperatures above 150 °C by appropriate voltage de-rating, but this allows only a limited extension of the application temperature range.

Developing a suitable ceramic dielectric for the extreme environments of high temperatures combined with shock and vibration has been a formidable challenge for the capacitor industry. Several capacitor manufacturers have been working towards overcoming these challenges, and a greatly successful solution that became commercially available in the recent years is KEMET's base-metal electrode (BME) C0G Multi-Layer Ceramic Capacitors (MLCC). These BME C0G capacitors typically use a $CaZrO_3$-based dielectric ceramic material, and exhibit excellent reliability at 200 °C and higher. Compared to the Class-II dielectrics such as the X7R/X8R materials, the C0G dielectrics offer many advantages in their electrical characteristics. These C0G capacitors show high stability of capacitance over temperature and voltage, no aging (reduction over time) of capacitance, no micro-phonic (noise) effects, and low dielectric loss (DF). In addition, with the progress in the technology of making and laminating thin layers of ceramic dielectric and nickel electrodes, the maximum capacitance offering as well as the reliability of the BME C0G capacitors are greatly improved compared to the traditional precious metal electrode (PME) C0G MLCC [9, 10]. This section will describe the development and performance of BME C0G MLCC at temperatures up to 200 °C, and compare it with other capacitor solutions such as the PME C0G and BME X8R based MLCCs.

4.2.2 Development of Ceramic Dielectric for High Temperatures

Traditional C0G dielectric materials are mainly based on the barium neodymium titanate (BNT) and are compatible with precious metal electrodes (PME) such as palladium, Pd or a silver/palladium (Ag/Pd) alloy. Due to the high cost of palladium metal, the ceramic capacitor industry has mostly converted from PME to BME (mainly Ni electrodes). The BME C0G dielectric used for these high temperature ceramic capacitor was based on calcium zirconate material ($CaZrO_3$). The dielectric composition, dopant chemistry, ceramic microstructure and the electrode/ceramic interfaces were tailored to achieve stable and high insulation resistance (IR) (or low leakage currents) at high temperatures. The BNT dielectric material in PME C0G capacitors has a dielectric constant (k) of $\sim$70, while the k of $CaZrO_3$-based BME C0G material is $\sim$31. Although the BME-C0G system has a lower dielectric constant (k), due to the advancement of materials and processing technologies, the BME-C0G materials can be processed into MLCC with higher layer counts and thinner layers in order to achieve higher capacitance in the same case size. Thus, for the same case size and voltage rating, BME C0G can offer much higher capacitance than PME C0G capacitors because of its thinner, but high reliability dielectric layers.

4.2.3 Electrical Performance at High Temperatures

4.2.3.1 BME C0G MLCC Versus PME C0G MLCC

In electronics and many other industries, it is common to test and compare reliability of components by using Highly Accelerated Life Test (HALT) methodology. For HALT study of capacitors, the acceleration is accomplished by temperature and voltage stresses in excess of the rating of the capacitors. Longer time-to-failure at rated as well as accelerated conditions of temperature and voltage indicate better reliability. The time-to-failure HALT plot for two sets of samples of 1206 case size 10 nF MLCC rated at 50 V (one is PME C0G and the other is BME C0G) is shown in Fig. 4.3. The dielectric thickness for the BME C0G MLCC was 7.0 μm, and that for the PME C0G was 11.6 μm. These two samples both passed the required quality assurance (QA) life test, which was performed at 125 °C and twice rated voltage for 1000 h. In order to push these samples to failure, HALT test was conducted at 175 °C and 400 V. Figure 4.3 shows that the BME C0G 1206/10 nF sample exhibited markedly longer time-to-failure (TTF) values compared to the PME C0G 1206/10 nF parts. The median time-to-failure (MTTF) at HALT for PME 1206/10nF was 62.6 min, while that for the BME1206/10 nF was 869.6 min, which is more than an order of magnitude of improvement in the MTTF. This HALT result indicates that

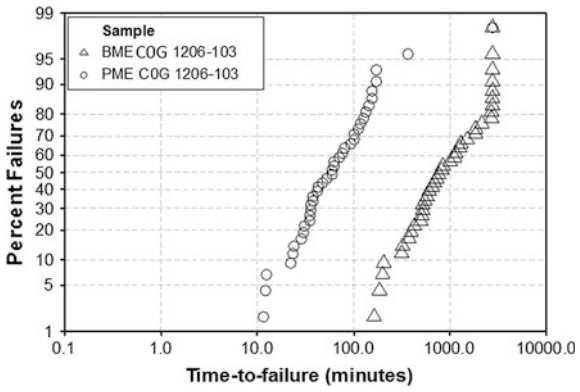

Fig. 4.3 HALT time-to-failure plots for PME and BME C0G 1206/10nF MLCC (HALT conducted at 175 °C and 400 V.)

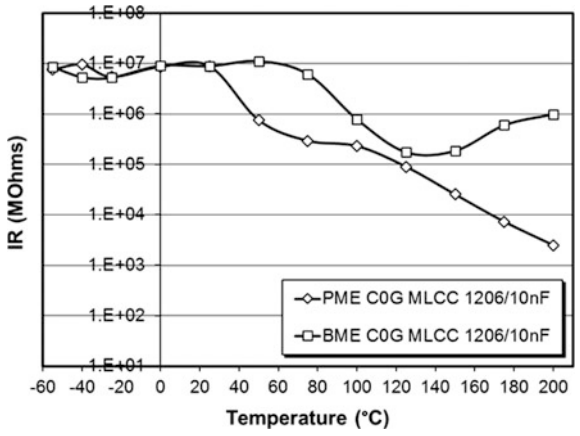

Fig. 4.4 Dependence of IR on temperature with 25 V DC bias for PME and BME C0G MLCC

BME C0G will be a better material for high temperature applications than the PME C0G capacitors.

In capacitors, higher values of insulation resistance (IR) (or lower leakage currents) are desirable, and are indicative of a good, stable dielectric. The insulation resistance (IR) of these two samples of PME and BME C0G 1206/10nF capacitors were also measured over a temperature range from −55 to +200 °C under a DC bias of 25 V, and are plotted in Fig. 4.4. Even with a much thinner dielectric thickness, the BME C0G typically shows higher IR than the PME C0G over the whole temperature range, especially at temperature above 120 °C. Due to its special composition and formulation, the IR of the BME C0G started to increase beyond 120 °C (instead of decreasing), which resulted in more than two orders of magnitude higher IR than that of the PME C0G at 200 °C. This contributes to the robust reliability of the BME C0G at high temperatures.

4.2.3.2 BME C0G MLCC Versus X8R MLCC

The X8R type ceramic capacitors offer another high temperature solution and are rated for 150 °C. The samples used for comparison were KEMET BME C0G MLCC (1206 case size, 100 nF and 25 V rated) and a commercially available X8R MLCC (1206 case size, 220 nF and 50 V rated). The dielectric thickness for the BME C0G MLCC was 2.8 μm, and that for the X8R MLCC was 11.2 μm, which is nearly four times thicker than the BME C0G MLCC.

Figure 4.5 shows the relative capacitance variation with reference capacitance at 25 °C (ΔC/C) versus temperature for BME C0G MLCC and X8R MLCC in the temperature range of –55 to +200 °C. The BME C0G MLCC exhibit extremely flat response over the whole temperature range whether with 25 V DC bias applied or without any DC bias. The maximum temperature coefficient of capacitance (TCC) from –55 to +200 °C is found to be 13.4 ppm/°C, which indicates that this dielectric material is not only compliant with the EIA C0G specification, but also can be extended to the X9G specification (capacitance variation from the reference point of 25 °C should be within 0 ± 30 ppm/°C (or $\Delta C_{Max}/C \leq 0.525\%$) over the temperature range of –55 to +200 °C). The X8R MLCCs hold their capacitance reasonably well below 125 °C. However, at temperatures above 125 °C, their capacitance decreased sharply. This is because at temperatures above the Curie point (125 °C for $BaTiO_3$-based materials), the capacitance (C)–temperature (T) dependence for ferroelectric material follows the Curie-Weiss Law: $C \propto k \propto \Theta/(T\text{-}T_c)$, where k is the dielectric constant, Θ is the Curie constant, and T_c is the Curie temperature. At 200 °C, the capacitance of X8R MLCC dropped by 50.1% without DC bias, and by 52.1% while under 25 V DC bias compared to their capacitance at 25 °C. Hence, the 220 nF X8R MLCC had almost the same effective capacitance at 200 °C as the 100 nF BME C0G MLCC. At temperatures above 200 °C, the capacitance of the X8R MLCC is expected to reduce to values below 100 nF. Thus, for high temperature applications, the actual capacitance under the use conditions needs serious consideration because of the severe capacitance reduction with

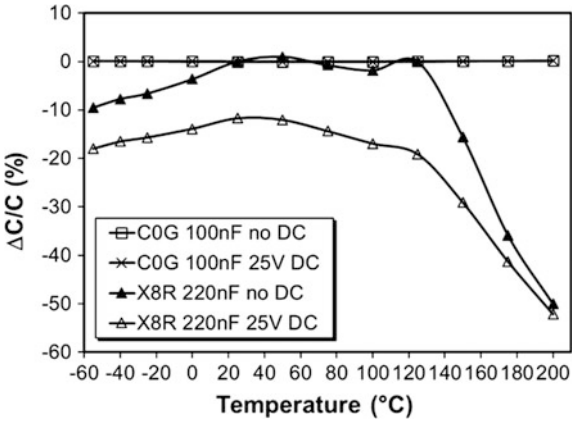

Fig. 4.5 ΔC/C variation with temperature and DC bias for BME C0G MLCC and X8R MLCC

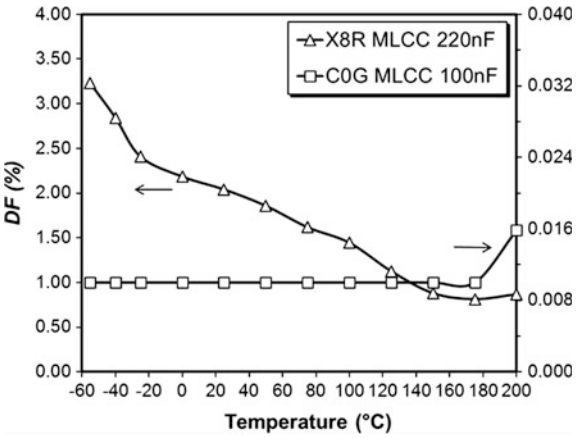

Fig. 4.6 %DF versus temperature without DC bias for BME C0G MLCC and X8R MLCC

temperature (versus considering only the nominal capacitance value at room temperature). Another factor to note is that the actual electric field applied in the BME C0G MLCC was almost 4 times higher than that for the X8R MLCC because of the dielectric thickness difference. If the X8R MLCC were under the same field strength as the BME C0G MLCC, their effective capacitance would have been even lower.

The measured dielectric loss or dissipation factor (*DF*) of the BME C0G and X8R MLCC samples without DC bias in the temperature range of −55 °C to +200 °C is shown in Fig. 4.6. The BME C0G MLCC has a maximum *DF* of 0.016% over the temperature range investigated. The *DF* of the X8R MLCC was 2.04% at 25 °C and decreased with increasing temperature because of the easier rotation of ferroelectric domains at increasing temperatures. However, the X8R MLCC still showed a *DF* of 0.87% at 200 °C.

The comparison of insulation resistance (IR) was quite revealing between the BME C0G and X8R MLCC, as shown in Fig. 4.7. From room temperature to 200 °C, the IR of BME C0G MLCC measured at 25 V changed from 1.22 TΩs to 28.3 GΩs. The X8R MLCC sample used in this study was originally rated at 50 V for applications below 150 °C. In these IR measurements, a voltage of only 25 V DC was applied. Even then, the IR of X8R MLCC decreased more than three orders of magnitude to 6.3 MΩs at 200 °C. This shift results in an R*C product (capacitance times IR) of only 0.67 MΩ μF at 200 °C, which will be of great concern for the majority of high temperature applications. Thus, the X8R MLCC would need to be de-rated in voltage rating for high temperature applications above 150 °C, while the BME C0G capacitors are expected to hold their capacitance, *DF* as well as IR reasonably well over the temperature range of −55 to +200 °C as shown in this study.

The dielectric breakdown strength of the BME C0G and X8R MLCC samples was also investigated, and results are shown in Fig. 4.8. From room temperature to 150 °C, the breakdown strength of BME C0G MLCC only dropped from 233 V/μm

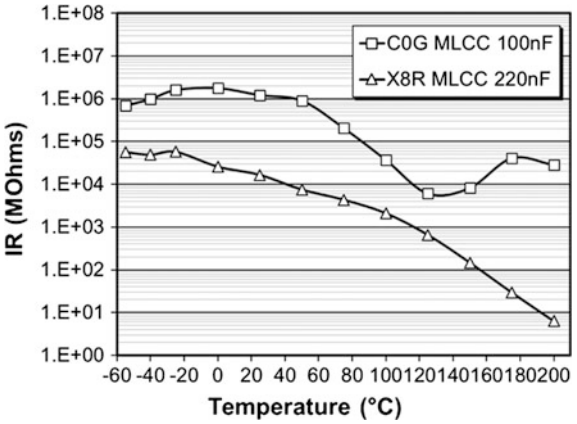

Fig. 4.7 IR with temperature with 25 V DC bias for BME C0G MLCC and X8R MLCC

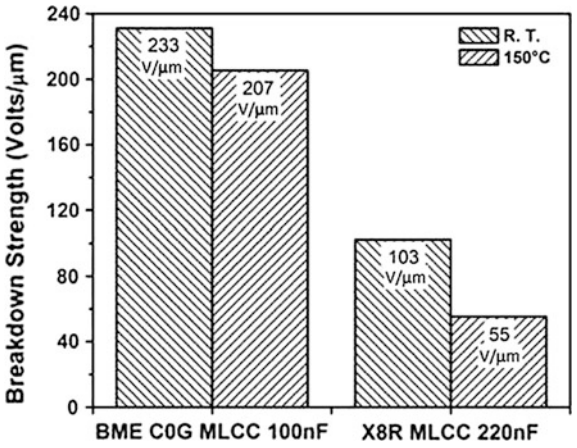

Fig. 4.8 Dielectric breakdown strength at room temperature and 150 °C for BME C0G MLCC and X8R MLCC

to 207 V/µm, while the breakdown strength for the X8R MLCC dropped from 103 V/µm to 55 V/µm, a reduction of 46%. At 150 °C, the breakdown strength of BME C0G MLCC is 3.7 times higher than the X8R MLCC. Breakdown tests for X8R MLCC could not be conducted at temperatures above 150 °C due to its high leakage. The high breakdown strength of BME C0G capacitors make them more attractive for energy storage applications [10–12].

4.2.4 Modeling of Accelerated and Life Test Reliability

One of the key parameters for high temperature applications is the long term reliability. As reported earlier [9, 10], unlike the typical $BaTiO_3$ based BME X7R/X5R dielectric materials, oxygen vacancy is not a concern for reliability in

BME C0Gs based on $CaZrO_3$. In order to estimate the lifetime in high temperatures applications, a highly accelerated life test (HALT) study was used. The HALT data under various temperature and voltage conditions was used to extrapolate the reliability of the capacitors at typical use conditions. The detailed principle and procedures of this kind of study have been well reported [13, 14], and will be only summarized in this chapter. An empirical equation by Prokopowicz and Vaskas (P-V equation), shown in (4.1), is employed to correlate the reliability behavior under accelerated test conditions to operating conditions.

$$\frac{t_1}{t_2} = \left(\frac{V_2}{V_1}\right)^n \exp\left[\frac{E_a}{k}\left(\frac{1}{T_{1_{abs}}} - \frac{1}{T_{2_{abs}}}\right)\right] \tag{4.1}$$

where:

t_i time to failure under conditions i,
V_i voltage under condition i,
n voltage stress exponential,
E_a activation energy for dielectric wear out,
k Boltzmann's constant (8.62×10^{-5} eV/K),
T_i absolute temperature for condition i.

The P-V equation can be simplified to (4.2):

$$t = A\frac{1}{V^n}\exp\left(\frac{E_a}{kT}\right) \tag{4.2}$$

where A is the time constant. Equation (4.2) can also be put into the following form for easy multi-regression analysis of experimental data.

$$Ln[t] = Ln[A] - nLn[V] + \frac{E_a}{kT} \tag{4.3}$$

Typically, the time (t) used for reliability modeling is the median time to failure (MTTF). By running HALT at multiple combinations of voltages and temperatures, the median time to failure data at each combination can be obtained from the time-to-failure data distribution fitting if more than 50% of the parts failed during testing. Using the multi-regression tool in a commercial software package, parameters such as A, n, and E_a can be determined. Thus, from (4.2), a lifetime can be predicted under given use conditions (voltage V and temperature T).

Three BME C0G MLCC part types, 0402-101-50V, 0603-471-50V and 0805-222-50V were tested under HALT conditions at four temperatures (125, 150, 175, and 200 °C) and six voltages (300, 400, 450, 500, 550, and 600 V) for 200 h. The maximum temperature (200 °C) and maximum voltage (600 V) used in this study were limited by the equipment capability. A sample size of 20 pieces was used in each HALT run. HALT time-to-failure (TTF) was recorded when IR at test temperature dropped below 4.28 MΩ.

Figure 4.9 shows the HALT time-to-failure distributions for part type 0805-222-50V under various temperature and voltage conditions. Following the steps described above, a time constant A, voltage exponential n, and the activation energy E_a were obtained by multi-regression and are listed in Table 4.1. The R-Squared of this regression was 94.7%. By substituting values of A, n and E_a parameters back into (4.3), MTTF can be calculated for various use conditions. Some of these use conditions are listed in Table 4.2 as examples. At 150 °C and 50 V, the predicted lifetime is over 52.6 million years, and even at 200 °C and 50 V, the predicted median lifetime is 1.48 million years.

HALT testing was also conducted on part types 0402-101-50V and 0603-471-50V at several combinations of temperatures and voltages. As shown in Fig. 4.10, there were not enough failures under even the most severe HALT conditions used up to 200 h of test time. While this is a strong proof of the robust reliability of these BME C0G capacitors under the accelerated test conditions, these tests still could not cause the required number of failures (50th percentile) needed to model the median-time-to-failure (MTTF) data. Thus, their HALT distribution fitting cannot be performed. This also indicates that it is not necessary to de-rate the

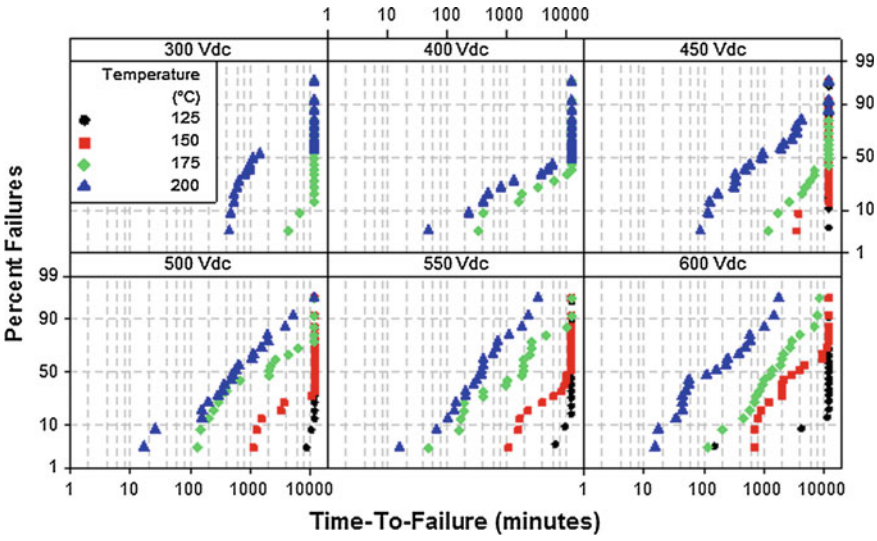

Fig. 4.9 HALT time-to-failure distributions for part type 0805-222-50V

Table 4.1 Multi-regression results for HALT-TTF P-V model for 0805-222-50V

Part type	A (min)	n	*Ea* (eV)	R^2
C0805C222J5GAB	1.30E+14	9.0	1.23	94.7%

Table 4.2 Lifetime prediction from MTTF model for 0805-222-50V

Part type	CAP (nF)	Rated voltage	Application temperature (°C)	Application voltage	MTTF (Years)
C0805C222J5GAB	2.20	50	25	50	7.47E+13
				25	3.91E+16
			125	50	4.39E+08
				25	2.29E+11
			150	50	5.26E+07
				25	2.75E+10
			175	50	7.98E+06
				25	4.17E+09
			200	50	1.48E+06
				25	7.73E+08

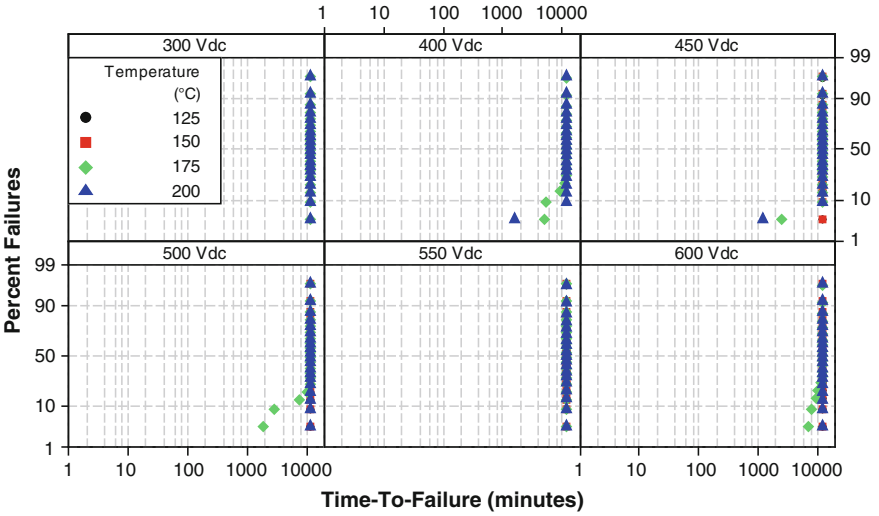

Fig. 4.10 HALT distributions at various test conditions for 0603-471-50V

voltage rating for the BME C0G MLCC tested in this study for high temperature applications, which is a clear advantage over the MLCCs based on X7R/X8R dielectrics. It is important to mention that BME C0G chips of various case sizes, capacitance and rated voltages have been tested through long term life tests at 125 °C (4000 h), 150 °C and 200 °C (2000 h) without any failures or degradation of electrical characteristics such as capacitance, %DF or insulation resistance.

4.2.5 Manufacturing Perspective: Challenges of Scale-up, Testing and Screening

In an industry that manufactures about two trillion pieces world-wide every year, manufacturability and high quality of its products are critical to success. Additionally, the high temperature capacitor products described here are used in electronics that are very expensive to make. Costs associated with shutdown run high in some applications such as down-hole drilling ($50k–$100k per hour), making it critical that the electronics operates without failing through the designed run cycles. Thus, high quality and high reliability of these capacitors need to be assured through design, manufacturing, and 100% testing and screening of the product.

Scale-up from R&D and pilot scale to large scale manufacturing can be very challenging for the advanced capacitor products described here. A number of best practices and process improvements had to be developed and followed in the successful scale-up and manufacturing of the high temperature ceramic capacitors. Design-for-six-sigma (DFSS) and design-of-experiments (DOE) were used extensively to better optimize process parameters during scale-up, and to assure rapid and successful scale-up into manufacturing. It was necessary to use high purity raw materials with tighter control of compositions and other material characteristics. Process steps from dispersion and milling of ceramic dielectric, coating of ceramic layers, lamination and singulation of capacitors (by dicing or cutting) had to be done in a class-1000 (or better) clean room environment. Since the layers involved are only one to a few micro-meters in thickness, many of the processing and handling steps needed to be automated, which already existed in KEMET's manufacturing plants. At every process step, a number of process parameters have to be controlled within tight limits and have to be monitored continuously. Tightly controlled materials and processes, automation, and close monitoring of the processes help minimize variation, and to improve yields as well as reliability of the product. Additional electrical and reliability screening tests were introduced to screen the product effectively. At the end, a happy customer base and growing sales of advanced products are *the testimony* to new product development done right!

4.3 Ceramic Capacitors for High Reliability Space and Military Applications

4.3.1 Trends in the Electronics for Space and Military

The world-wide production volume of multi-layer ceramic capacitors (MLCC) has exceeded 2 trillion pieces per year, making them a key class of hybrid electronic components. The trends of miniaturization, enhanced functionality, connectivity,

and reliability in consumer, industrial, automotive as well as military electronics have helped drive considerable amount of innovation and development in ceramic capacitor technology. Ceramic capacitors have been able to keep up with the trend of miniaturization due to the advent and growth of base-metal electrode technology (BME, e.g., nickel). This section looks at some new and exciting developments in the BME ceramic capacitor technology which are about to catapult the aerospace and military electronics into its next generation.

4.3.2 Paradigm Shift in High Reliability Capacitor Technology

Traditionally, ceramic capacitors for high reliability (Hi-Rel) military and space applications have been made using precious metal electrode (PME) technology and manufactured as per "MIL" specifications such as MIL-PRF-123, MIL-PRF-55681, etc. Several North American capacitor manufacturers (including KEMET) supply these Hi-Rel grade PME ceramic capacitors. Due to the good performance history of the Hi-Rel PME capacitors, until recently, the military and aerospace industry had no pressing need to venture into the use of BME ceramic capacitors. Some of the MIL-specifications (e.g., MIL-PRF-123) had clearly prohibited the use of nickel base-metal electrodes (BME) in Hi-Rel applications. The design rules governing PME capacitors for Hi-Rel applications were established well over three decades ago in the MIL specifications. These design rules, the materials and build-up technology for PME capacitors have not evolved with time. However, in recent years, as the requirements for ceramic capacitors for Hi-Rel applications started to drive towards higher capacitance values in smaller case sizes, it has become increasingly difficult to provide them using the conventional precious-metal electrode (PME) ceramic capacitors.

Concurrently, as the majority of development efforts were focused on BME capacitors, there has been significant advancement in the understanding of the materials, processing, properties and reliability of BME ceramic capacitors. This has led to the rapid growth and acceptance of BME ceramic capacitors in different segments of industry, even in the electronics for automotive and implantable medical devices where long-term reliability is critical. The demonstrated reliability and performance of BME capacitors in automotive and medical applications over the past 10–15 years are helping with a paradigm shift in the Hi-Rel industry which is now receptive to the idea of using BME capacitors in their applications. This section reviews various aspects of design and reliability test data of BME ceramic capacitors, and discusses their potential for high-reliability applications.

4.3.3 *Base Metal Electrode (BME) C0G*

In the previous section, we reviewed the development of Base-Metal Electrode (BME) C0G ceramic capacitors for high temperature industrial electronics such as down-hole and geothermal applications. These applications require a life time of a few to several 100 h at temperatures of 175–200 °C. The high-reliability military and aerospace applications focus on a temperature range of –55 to 125 °C, and require qualification testing through 4000 h life tests at twice the rated voltage at a maximum temperature of 125 °C. Thus, the critical questions to answer are: (1) is this BME C0G dielectric good for the long-term reliability required in Hi-Rel applications, and (2) how can we adapt, screen and modify the BME C0G capacitors for possible Hi-Rel applications.

4.3.3.1 Tailoring the Reliability of BME C0G Capacitors

The BME C0G capacitors typically use a $CaZrO_3$-based dielectric material. In Sect. 2.3 and Fig. 4.4, it was shown that the BME C0G capacitors exhibit higher insulation resistance (IR) or lower leakage currents compared to the corresponding PME C0G capacitors. This high insulation resistance is also stable under accelerated conditions of elevated temperatures and applied voltages during accelerated testing up to 92 h (Fig. 4.3). To insure that the capacitance and IR of BME C0G capacitors stays stable over long-term life test conditions such as 4000 h, it was necessary to modify and tailor the dielectric composition, microstructure and the electrode/dielectric interfaces which control the stability of the leakage behavior (or insulation resistance) and reliability of these capacitors.

The robust reliability of BME C0G is attributed to several factors. Ceramic capacitors using BME technology (Nickel internal electrodes) are typically fired under a reducing atmosphere consisting of $N_2/H_2/H_2O$ at 1100–1300 °C. The dielectric composition starts with high purity raw materials and includes a proprietary dopant package to insure that the mixed oxide dielectric is reduction-resistant when sintered under a reducing atmosphere. After the firing or sintering step, the capacitors are exposed to a well-controlled re-oxidation process to alleviate any oxygen vacancies that might have formed in the dielectric. As a result, the $CaZrO_3$-based formulation is highly reduction resistant and shows clean interfaces free of NiO and secondary phases between the dielectric and nickel electrode. This is evident from extensive studies of transmission electron microscopy (TEM) of the fired dielectric and dielectric/electrode interfaces, as well as from highly accelerated life tests on BME C0G capacitors fired with and without re-oxidation treatment. Figure 4.11 shows typical interfaces between the nickel electrode and BME C0G dielectric which show the clean interfaces without any signs of reduction of the dielectric or any spurious Ni/Ca/Zr-alloy or mixed oxide formation. Figure 4.12 shows insulation resistance of BME C0G 1206/47 nF and 0805/22 nF capacitors (both rated at 50 V) fired with and without the re-oxidation treatment and then

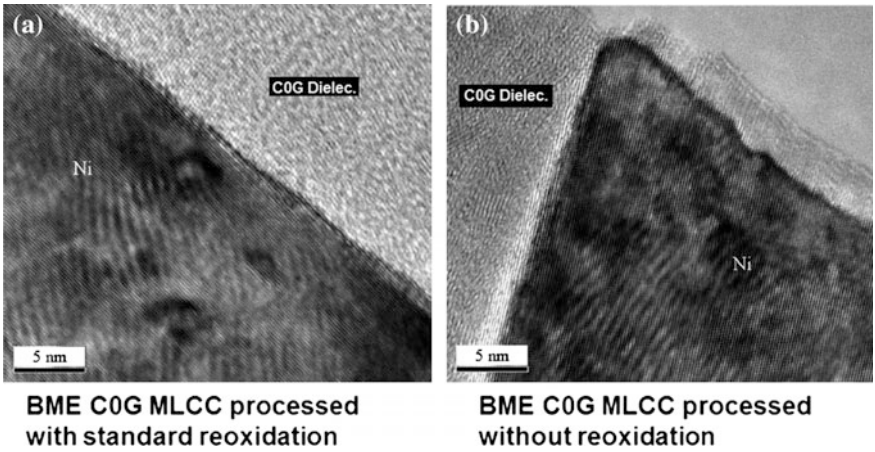

Fig. 4.11 **a**, **b** Typical transmission electron microscopy (TEM) micrographs of electrode/dielectric interfaces in Nickel-BME C0G ceramic capacitors

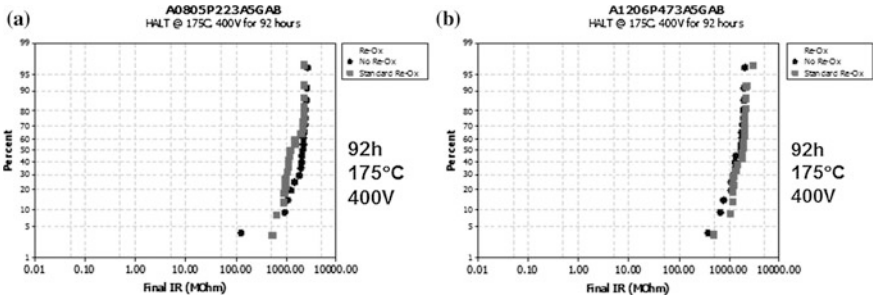

Fig. 4.12 **a**, **b** Insulation resistance of BME C0G capacitors processed with and without reoxidation: HALT at 175 °C and 400 V for 92 h. **a** BME C0G 0805/22nF/rated 50 V. **b** BME C0G 1206/47nF/rated 50 V

HALT tested for 92 h at 175 °C and 400 V. These IR results indicate that this dielectric has robust reliability when processed with or without re-oxidation. In $CaZrO_3$, the oxygen ions are tightly bound in the perovskite crystal structure due to the high affinities of calcium and zirconium ions for oxygen. This factor, along with the reduction resistant formulation and the wide band gap nature of zirconium make this BME C0G highly reduction resistant, and reliable under bias and elevated temperature conditions. The BME C0G capacitors still receive an optimized re-oxidation treatment during their manufacturing. The BME C0G capacitors are also proven to be extremely robust under long term humidity testing at 1 × and 2 × rated voltages as well as under low-voltage humidity testing (1.3–1.5 V) under 85% relative humidity at 85 °C. These 1000 h 85/85 humidity tests are an essential part of qualification testing for Hi-Rel type applications.

4.3.3.2 Long Term Life Testing of BME C0G Chip and Stack Capacitors

As a part of initial qualification of the BME C0G capacitor family for automotive and high temperature applications, a number of part types were tested through HALT studies and qualified through automotive AEC-Q200 qualification protocols and load (bias) life tests for 1000 h and 2000 h at 125 °C, and then at 200 °C. However, it is essential to test the performance of these capacitors through 4000 h life tests as per the criteria of MIL-PRF-123 specification at twice rated voltages at 125 °C to verify potential for high reliability applications. Figure 4.13 shows typical life test results on BME C0G capacitors 0805/10 nF/rated-50V and 1206/22 nF/rated-25 V through 4000 h at twice rated voltages at 125 °C. The plots of insulation resistance verify no failures or degradation of IR occurred through these long-term life tests. Table 4.3 shows a summary of life test results on various part types of BME C0G ceramic capacitors through 4000 h at twice rated voltages at 125 °C. The BME C0G capacitors including part types such as 1210/104/25 V and 0805/103/50 V have performed well through 4000 h life tests with zero failures.

In the field of ceramic capacitors, it is common to achieve higher capacitance by stacking more than one ceramic chip in the form of capacitor stacks by attaching leadframes to the terminations of the chips. Such stacks can be fabricated in various configurations using suitable feeder chips and leadframe designs. It is important to evaluate life test reliability when ceramic chips are formed into ceramic stacks. Life test results on military style BME C0G case-code-4 stack are reported below. First, stacks were built using BME C0G chips based on dimensions recommended for Case Code 4 stacks as per MIL-PRF-49470. Each stack consisted of 5 chips of case code 4 each having a capacitance of 0.5 µF and thickness of 0.1 inch. These Case Code 4 BME C0G stack had a capacitance of 2.5 µF and a rated voltage of 50 V. These stacks passed life test at 125 °C through 4000 h without any failures or degradation of insulation resistance as shown in Fig. 4.14.

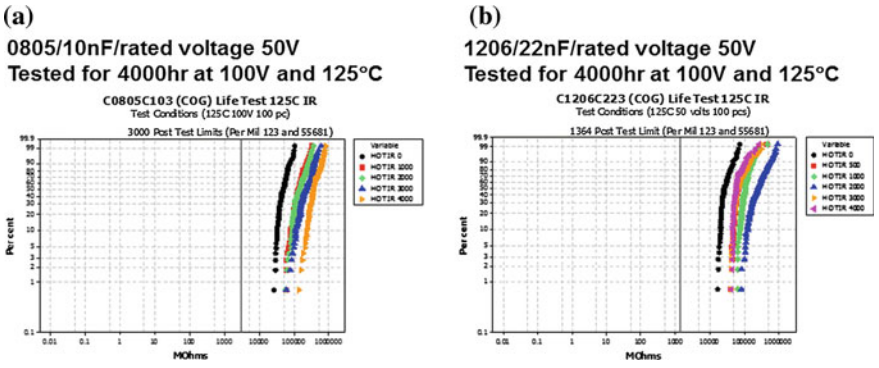

Fig. 4.13 **a**, **b** Life test results on BME C0G 0805/10nF/rated 50 V and 1206/22nF/rated 25 V through 4000 h at twice rated voltages at 125 °C

Table 4.3 Summary of Life Test Results on BME C0G Ceramic Capacitors 4000 h at Twice Rated voltage at 125 °C

Part type	Capacitance (nF)	Volatge to be rated at (V)	Test voltage (V) test temp = 125 °C	1000 h	2000 h	3000 h	4000 h
C 0G 0603/680	0.068	100	200	0/100	0/100	0/100	0/100
C 0G 0603/181	0.18	50	100	0/100	0/100	0/100	0/100
C 0G 0603/391	0.39	50	100	0/100	0/100	0/100	0/100
C 0G 0603/392	3.9	50	100	0/100	0/100	0/100	0/100
C 0G 0603/562	5.6	25	50	0/100	0/100	0/100	0/100
C 0G 0805/103	10	50	100	0/100	0/100	0/100	0/100
C 0G 0805/103	10	25	50	0/100	0/100	0/100	0/100
C 0G 1206/182	1.8	100	200	0/100	0/100	0/100	0/100
C 0G 1206/272	2.7	50	100	0/100	0/100	0/100	0/100
C 0G 1206/183	18	50	100	0/100	0/100	0/100	0/100
C 0G 1206/223	22	25	50	0/100	0/100	0/100	0/100
C 0G 1201/223	22	50	100	0/100	0/100	0/100	0/100
C 0G 1210/104	100	25	50	0/100	0/100	0/100	0/100

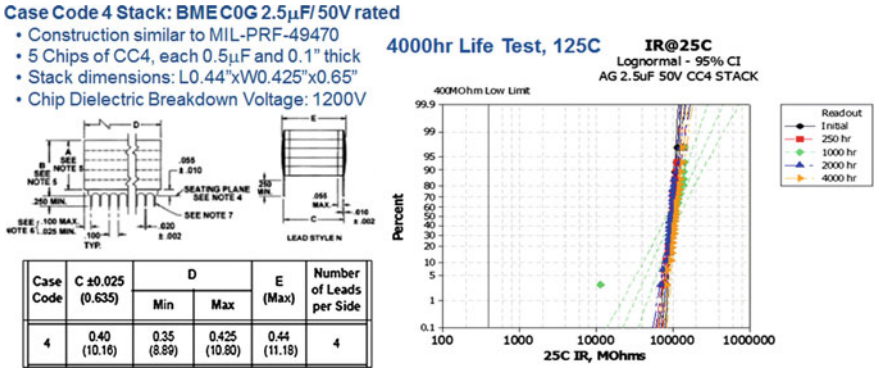

Fig. 4.14 Life test at 125 °C through 4000 h on Case-Code-4 BME C0G stacks 2.5µF/rated 50 V

4.3.4 Base-Metal Electrode (BME) X7R

4.3.4.1 Tailoring the Material and Microstructure Design for High Reliability

During the past two decades, the majority of research and development in the field of ceramic capacitors has focused on understanding and improving BME ceramic capacitors with respect to their raw materials, processing and equipment for superior dispersion, build-up and thermal treatment, as well as to improve their reliability performance. Although some of these efforts were driven by efforts

towards lower cost and large scale manufacturing, they have led to significant knowhow for tailoring the design of ceramic capacitors for high reliability applications. Figure 4.15 demonstrates some of the key improvements in the raw materials and microstructure design employed in the BME X7R ceramic dielectric. Depending on the design thickness of the dielectric, high purity barium titanate ($BaTiO_3$) powders of high crystallinity and narrow particle size distribution are chosen for the dielectric (available down to 150, 200, 250 nm size, etc.). Highly sophisticated milling, dispersion and coating techniques allow molecular- and nanometer-level dispersion of dopant elements and additives within the

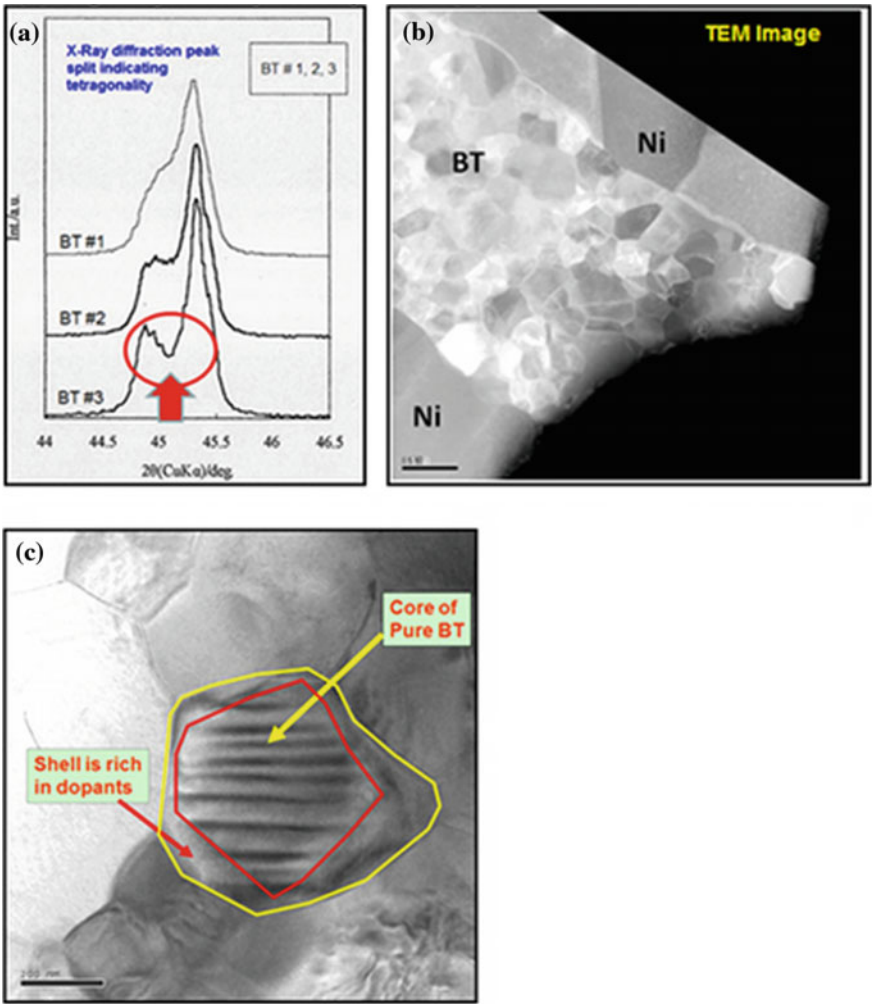

Fig. 4.15 a–c Some of the key material design features for improving the microstructure, performance and reliability of BME MLCC

$BaTiO_3$-based ceramic. This helps to achieve a core-shell type microstructure in the ceramic dielectric with a core of high crystallinity barium titanate, and a uniform grain size within the fired or sintered ceramic dielectric. The dopant package chemistry, processing conditions and microstructure are optimized to achieve the required levels of dielectric constant, insulation resistance and other electrical characteristics.

4.3.4.2 Long Term Reliability of BME X7R Capacitors

In the past, similar to the BME C0G system, a large number of the BME X7R capacitor part types have also been qualified through automotive AEC-Q200 qualification protocols and load (bias) life tests for 1000 and 2000 h at 125 °C. The BME X7R type capacitors have been used successfully in automotive applications for well over 10 years.

Although it is possible to make high capacitance value BME X7R MLCC due to the advancement in materials, processing and testing/screening, a systematic and rigorous approach is required to design and evaluate BME X7R capacitors for high reliability applications. To ensure designing-in the highest levels of reliability in the capacitor parts, many of the raw materials, processing steps and chip-design rules had to be either modified or re-defined. Some examples of the scrutiny and improvements based on material selection and tailoring of ceramic dielectric microstructure were already described above. In addition, detailed part type specific reliability studies using HALT and life testing were conducted to ascertain and optimize various chip design and processing parameters for robust long term reliability of the capacitors. These parameters include dielectric thickness, chip designs and build-up conditions, thermal processing parameters, sintered ceramic grain microstructure, as well as the conditions for electrical testing, screening and burn-in. Finally, it is essential to test the reliability performance through 4000 h load (bias) life tests at twice rated voltages at 125 °C to verify potential for high reliability applications.

Figure 4.16 shows life test results on BME X7R capacitors 1206/1μF/rated voltage 50 V tested at 100 V and 1206/2.2 μF/rated voltage 16 V tested at 32 V through 4000 h at 125 °C. The plots of insulation resistance verify that no failures or degradation of IR occurred through these life test conditions. Table 4.4 shows a summary of life test results on various part types of BME X7R ceramic capacitors through 4000 h at twice rated voltages at 125 °C. It is interesting to note that high capacitance part types such as 1210/4.7 μF and 1206/2.2 μF (both rated at 25 V) have performed very well through 4000 h life tests with zero failures. Thus, the $BaTiO_3$-based BME X7R dielectric offers great options for extending capacitance ranges in BX/X7R dielectric family for high reliability applications. Work continues to include additional batches and part types in this evaluation.

An important takeaway here is that the Hi-Rel BME capacitors allow increase in capacitance by a factor of 10 to 100 in the same case sizes while still maintaining excellent long-term reliability compared to the values currently available in Hi-Rel grade PME ceramic capacitors rated at 50 and 100 V. At lower voltage ratings, the

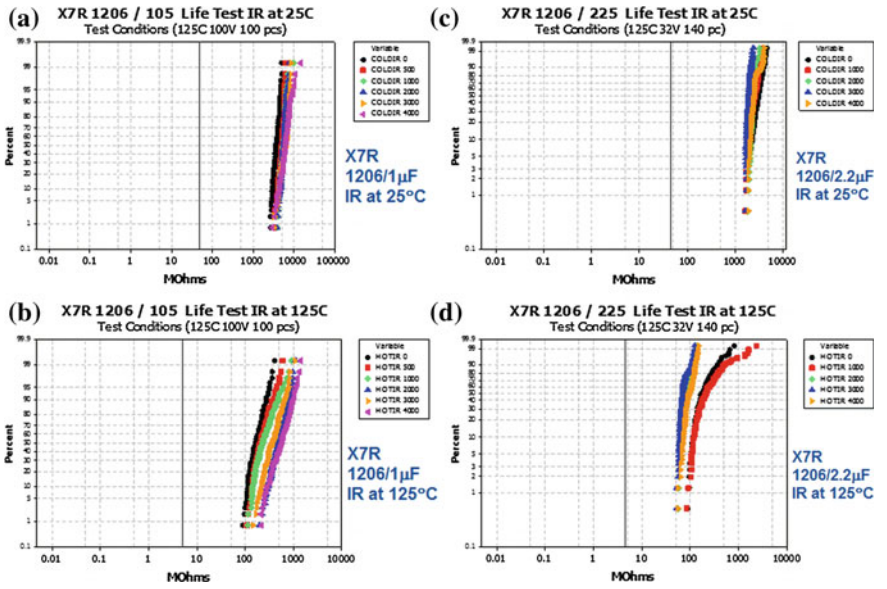

Fig. 4.16 **a**–**d** Insulation Resistance Plots at 25 °C (**a** and **c**) and 125 °C (**b** and **d**) of BME X7R capacitors 1206/1µF/Vr50 V tested at 100 V and 1206/2.2µF/Vr16 V tested at 32 V through 4000 h at 125 °C

capacitance offerings will increase by 2–3 orders of magnitude. This can obviously allow significant opportunities for reductions in chip sizes, and hence, in the weight and volume of the electronics. Typical hardware in satellites, military electronics, avionics, radar systems, etc., uses hundreds to many thousands of capacitors. The increase in the volumetric efficiency (capacitance per unit volume) offered by BME capacitors can allow significant weight reductions, increased functionality, power savings (longer battery life), and can completely revolutionize the Hi-Rel electronics going forward.

4.3.5 Manufacturing Considerations

Several comments about considerations for scale-up and manufacturing were included in the previous section on ceramic capacitors for high temperature applications. The best practices based on the use of clean rooms, automation, extensive in-process testing and monitoring, etc., described there also apply to the manufacturing of BME capacitors for Hi-Rel applications. In addition, it is important to note that the performance of capacitors in Hi-Rel applications is mission critical. High reliability and quality must be designed-in, and then these capacitors must be tested and screened by the toughest possible criteria to remove any weaker parts from the population. Accordingly, a “burn-in” step was included

Table 4.4 Summary of life test results on BME XR7 ceramic capacitors 4000 h at twice rated voltage at 125 °C

Part type	Capacitance (μF)	Voltage to be rated at (V)	Test voltage (V) test temp = 125 °C	1000 h	2000 h	3000 h	4000 h
X7R 0603/154	0.15	16	32	0/100	0/100	0/100	0/100
X7R 0603/154	0.15	25	50	0/100	0/100	0/100	0/100
X7R 0603/224	0.22	10	20	0/100	0/100	0/100	0/100
X7R 0603/224	0.22	10	20	0/100	0/100	0/100	0/100
X7R 0603/224	0.22	16	32	0/100	0/100	0/100	0/100
X7R 0805/684	0.68	25	50	0/100	0/100	0/100	0/100
X7R 0805/105	1	10	20	0/77	0/77	0/77	0/77
X7R 0805/105	1	16	32	0/77	0/77	0/77	0/77
X7R 0805/105	1	10	20	0/140	0/140	0/140	0/140
X7R 0805/105	1	10	20	0/140	0/140	0/140	0/140
X7R 0805/225	2.2	6.3	13	0/77	0/77	0/77	0/77
X7R 1206/684	0.68	50	100	0/200	0/200	0/200	0/200
X7R 1206/105	1	50	100	0/100	0/100	0/100	0/100
X7R 1206/105	1	25	50	0/100	0/100	0/100	0/100
X7R 1206/105	2.2	16	32	0/140	0/140	0/140	0/140
X7R 1206/105	2.2	25	50	0/100	0/100	0/100	0/100
X7R 1206/225	2.2	16	32	0/140	0/140	0/140	0/140
X7R 1210/475	4.7	10	20	0/77	0/77	0/77	0/77
X7R 1210/475	4.7	16	32	0/77	0/77	0/77	0/77
X7R 1210/475	4.7	25	50	0/77	0/77	0/77	0/77
X7R 1812/475	4.7	10	20	0/100	0/100	0/100	0/100
X7R 1812/475	4.7	16	32	0/100	0/100	0/100	0/100
X7R 1812/475	4.7	25	50	0/100	0/100	0/100	0/100

to screen 100% of the chips at twice rated voltages for 96 to 236 h (typically 168 h) at 125 °C to remove infant mortal and early failure type defects. Similar to the criteria outlined in specifications for MIL-level and Space-level parts (MIL-PRF-123, MIL-PRF-55691, NASA-S311-P829, etc.), the testing plans also include acoustic screening to detect internal voids or cracks, and testing of various electrical parameters in 100% of the parts in every batch of capacitors. A review committee and working group (called the "BME Industry Forum") comprising of representatives from a number of the Hi-Rel industries and some of the capacitor manufacturers was formed in 2013 to develop a detailed specification for the testing and qualification of BME ceramic capacitors for military and space level Hi-Rel applications. This committee meets every week to scrutinize data and various possible testing protocols to include in the specification for BME capacitors. A first draft of this specification is expected to be completed by the end of 2015. The authors firmly believe that BME technology will find increasing use in high-reliability applications as data and experience with these products grows in the coming years.

4.4 High Reliability Polymer Tantalum Capacitors

4.4.1 Introduction

Electrolytic tantalum (Ta) capacitors are broadly used in modern electronics due to their high volumetric efficiency, stability, and reliability. These capacitors consist of a Ta anode sintered in vacuum with a fine Ta powder, an anodic oxide film of Ta employed as a dielectric, and a cathode which can be either a liquid electrolyte (wet Ta Capacitors), manganese dioxide (solid Ta/MnO_2 capacitors), or a conductive polymer (polymer Ta capacitors). Poly(3,4-ethylenedioxythiophene) (PEDOT) and Polypyrrole (PPy) are commonly used as the cathode material in polymer Ta capacitors [15–17]. The high conductivity of these materials in comparison to the conductivity of manganese dioxide provides a low equivalent series resistance (ESR) for polymer Ta capacitors, making them attractive for high frequency applications. The conductive polymer cathode was initially developed in 1990s for aluminum capacitors and later applied to tantalum capacitors to satisfy demands of the fast growing computer and telecommunication industries for miniaturization, low ESR, and high ripple current operation [18]. Another feature of polymer Ta capacitors is their non-ignition failure mode, which is an important safety feature, especially in low ESR circuits.

Since their introduction to the market and until recently, the working voltages of polymer Ta capacitors have been limited to 25 V, while the working voltages of wet Ta capacitors available in the market are up to 150 V and those for solid Ta/MnO_2 capacitors are 63 V or even higher. Also, direct current leakage (DCL) in polymer Ta capacitors was about 10 times higher than DCL in wet and solid Ta capacitors. These limitations have made applications of polymer Ta capacitors impossible in high voltage, high reliability circuits, where the combination of low ESR and DCL combined with non-ignition failure mode are the most critical. Traditionally, the working voltages of Ta capacitors are increased by using a higher formation voltage to grow a thicker Ta_2O_5 dielectric film. Since the thickness of the anodic oxide film is directly proportional to the formation voltage, a higher formation voltage results in a thicker dielectric and, thereby, results in a greater breakdown voltage (BDV) and working voltage for Ta capacitors [19]. However, as the formation voltage increased in polymer Ta capacitors with PEDOT cathodes, the BDV increased to approximately 50 V and then leveled off, even though the dielectric thickness continued to grow [20]. This “saturation” of the BDV limited the ultimate working voltage of polymer Ta capacitors since the working voltage should be no larger than 50% of the BDV in order to provide long term stability to the capacitors. To overcome these limitations, significant changes in the traditional technology of polymer Ta capacitors was needed, especially in manufacturing of Ta anodes and conductive polymer cathodes.

4.4.2 Breakthroughs in Technology

Traditional manufacturing of Ta anodes includes the mixing of Ta powder with an organic lubricant to improve the powder flow and density uniformity in finished anodes, pressing of Ta powder into pellets with embedded Ta lead wire, de-lubricating of pressed pellets by heating in vacuum at relatively low temperatures to decompose and evaporate organic lubricant, and sintering of the pellets in vacuum at temperatures ranging from about 1200 °C for the finest Ta powders to 2150 °C for the coarsest Ta powders. Press density and sintering temperature are optimized for every type of Ta powder to achieve sufficient mechanical strength and maximum surface area in the sintered anodes. This step provides stability towards mechanical stress and high capacitance in the finished capacitors [21, 22].

The drawback of the traditional technology is contamination of the sintered anodes with carbon and oxygen during anode manufacturing. The carbon dissolves in Ta from decomposed organic lubricant during thermal de-lubrication. The oxygen dissolves in Ta from native oxide on Ta surface during heating in vacuum to sintering temperature and remains in Ta when sintering temperature is equal to or below 1870 °C [23]. During sintering, Ta reacts with dissolved carbon and oxygen forming inclusions of crystalline tantalum carbide Ta_2C and tantalum oxide Ta_2O_5. In case of carbide inclusions, strong bonds between tantalum and carbon suppress normal growth of anodic oxide of Ta, resulting in local thinning areas and craters in anodic oxide film [24]. Figure 4.17a shows anodic oxide film of Ta formed on sintered Ta anodes with high carbon content [25].

Crystalline inclusions of Ta oxide on the surface of Ta anodes act as seeds for crystallization of amorphous matrix of anodic oxide film of Ta [26–28]. During manufacturing, testing and field application they continue to grow, gradually increasing mechanical stress and eventually causing disruption of the dielectric and failure of the capacitor. Figure 4.17b demonstrates cracks in anodic oxide of Ta formed on the surface of Ta anode with high oxygen content [25].

To eliminate these defects in the dielectric, flawless technology (F-Tech) was developed incorporating de-carbonizing and de-oxidizing steps in anode manufacturing [29, 30]. An image of the flawless dielectric formed on F-Tech Ta anode is shown in Fig. 4.17c. Implementation of Ta anodes manufactured with F-Tech processes resulted in improvement of the DCL and BDV in polymer Ta capacitors; however, to achieve major breakthrough, a change in traditional manufacturing of polymer cathode was also needed.

Traditionally, PEDOT cathode in polymer Ta capacitors is manufactured by an in situ chemical reaction between monomer 3,4-ethylenedioxythiophene and oxidizer iron (III) toluenesulfonate with monomer/dopant ratio 3:1 [17]. There should be 5–6 cycles of in situ polymerization to provide full coverage of the oxide dielectric inside porous Ta anode with the PEDOT cathode. To remove byproducts of the in situ chemical reaction, washing with organic solvents is performed after each cycle of the in situ polymerization. However, due to the very small pore size in sintered and formed Ta anodes and gradual filling of these pores with polymer

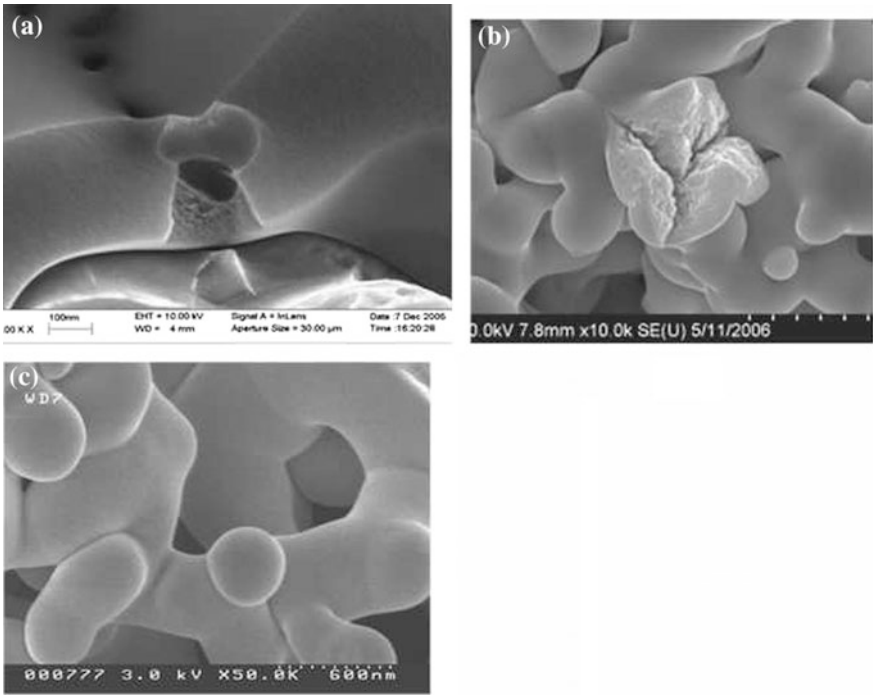

Fig. 4.17 **a**–**c** SEM Images of 200 nm anodic oxide films formed on Ta anodes with high carbon content (**a**), high oxygen content (**b**) and F-Tech (**c**)

cathode, washing process becomes less efficient after every cycle of the in situ polymerization. As a result, by-products of the chemical reaction accumulate in PEDOT cathode, including its interface with the oxide dielectric.

The new process of manufacturing of PEDOT cathodes in polymer Ta capacitors addressed this issue. In this process sintered and formed Ta anodes were dipped into a water-born dispersion of the nano-scale PEDOT particles (slurry) and subsequently dried in air at room temperature and then at 150 °C [31, 32]. In contrast to the in situ polymerization, applying of the pre-polymerized PEDOT slurry doesn't require in situ chemical reaction and, thereby, does not leave any byproducts of this reaction in PEDOT cathodes of polymer Ta capacitors.

A combination of F-Tech Ta anode and PEDOT slurry cathode resulted in radical change in I-V characteristic of polymer Ta capacitors in comparison to these in capacitors with in situ PEDOT cathode [25]. As an example, Fig. 4.18 shows I-V characteristics of polymer Ta capacitors with F-Tech anodes, 200 nm anodic oxide films, and either in situ or pre-polymerized PEDOT cathodes. As one can see, the Ta capacitors with pre-polymerized PEDOT have nearly ideal diode-like I-V characteristics, with very low current at normal polarity (+on Ta anode) and rapid current increase at reverse polarity (–on Ta anode). In comparison, the Ta capacitors

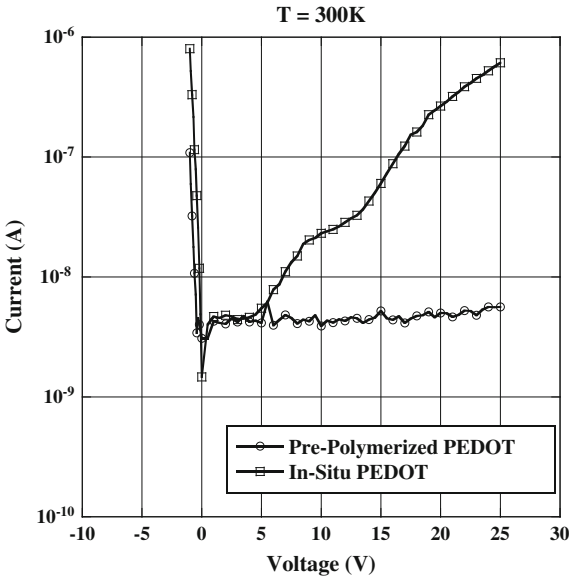

Fig. 4.18 I-V characteristics of polymer Ta capacitors with F-Tech anodes, 200 nm anodic oxide of Ta, and either in situ or pre-polymerized PEDOT cathodes

with in situ PEDOT have significantly higher current at normal polarity, while very little difference in the currents at reverse polarity is observed.

These I-V characteristics can be explained within classical metal-insulator-semiconductor (MIS) theory where in this case M stands for Ta anodes, I stands for Ta_2O_5 insulator, and S stands for p-type semiconductor PEDOT cathode [25]. According to this theory broadly used in physics of semiconductor devices, current flow through the Ta/Ta_2O_5/PEDOT structure under normal conditions can be caused by field and temperature induced emission of current carriers from the semiconductor into the insulator. A potential energy barrier at the Ta_2O_5/PEDOT interface limits the emission. This barrier effectively increases with applied voltage, which keeps the current low and nearly constant in the case of flawless dielectric, while pores and cracks filled with conductive polymer shunt the dielectric and make inefficient the potential barrier on the Ta_2O_5/PEDOT interface.

In the case of in situ PEDOT cathode, residuals of the chemical reaction between oxidizer and monomer cause surface charge at the Ta_2O_5/PEDOT interface. This surface charge "pins" the potential barrier at the IS interface, preventing its increase with applied voltage at normal polarity, which results in a higher current and a lower BDV at normal polarity. Increasing the number of in situ polymerization cycles results in a higher density of surface charge and, thereby, in even higher DC leakage current and lower BDV. These differences in the Ta_2O_5/PEDOT interface can explain the differences in I-V characteristics between the polymer Ta capacitors with F-Tech anodes and either in situ or pre-polymerized PEDOT cathodes.

4.4.3 Outstanding Performance

Combination of F-Tech anodes and slurry PEDOT cathodes provides outstanding performance to polymer Ta Capacitors, including very low DCL in broad range of operating temperatures [33]. Low DCL with weak dependence on voltage allowed record high BDV and working voltages up to 125 V never seen before on any type of solid Ta capacitors (Fig. 4.19) [34].

To achieve long-term DCL stability in polymer Ta capacitors with a hermetic design, a controlled amount of moisture was added to these capacitors before hermetization [35]. In this case moisture acts as a plasticizer, maintaining stability of the potential barrier on IS interface and suppressing anomalous transitional and DC currents in polymer capacitors [25, 36]. With these manufacturing techniques, all the electrical parameters including capacitance, dissipation factor, ESR and DCL remained practically unchanged during 10,000 h of life test at 85 °C and rated voltage [37]. Besides that, low and stable ESR with weak dependence on temperature provided outstanding stability of capacitance in broad range of operating temperatures and frequencies. For example, capacitance of polymer Ta capacitors with rating 100 μF–60 V remained within 20% tolerance when temperature was reduced from room temperature to −55 °C and frequency was increased from 120 Hz to 10 kHz. At the same conditions, capacitance of the wet Ta capacitor with the same size and rating reduced below 90% of its initial value. This means that at low temperatures and high frequency 6–20 wet Ta capacitors are needed to provide the same capacitance as one polymer Ta capacitor.

Additional factors providing outstanding stability and reliability to polymer Ta capacitors are special methods of testing and screening of these capacitors including simulated breakdown screening (SBDS) [38, 39]. Using SBDS allows removal of potentially unreliable capacitors with small hidden defects in the dielectric, like the

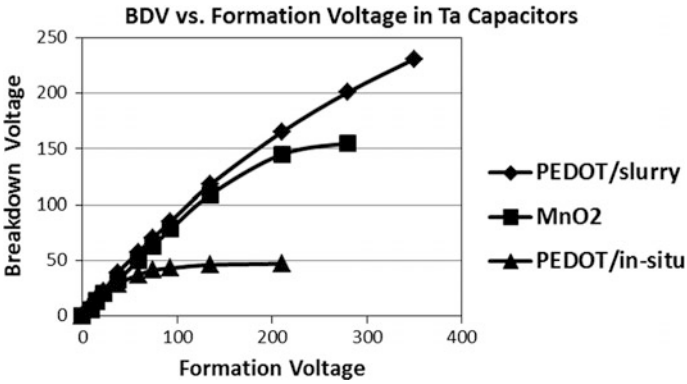

Fig. 4.19 BDV versus formation voltage in Ta capacitors with F-Tech anodes and either PEDOT/slurry, MnO_2 or PEDOT/in situ

crystalline seeds, not detectable by traditional DCL testing. These seeds can progress during field application and cause catastrophic failure of the capacitor.

4.4.4 Testing and Screening

Tantalum-polymer capacitors offer many performance advantages over the incumbent MnO_2-cathode technology. Among these advantages are much lower ESR (and higher ripple current limits), better stability of capacitance and ESR over the full operating temperature range, more uniform dielectric robustness that can provide superior reliability, and a more benign failure mode (no transient thermal event upon failure). It is not surprising that engineers who design high-reliability systems want to use these capacitors in their designs.

While almost all claims of superior parametric performance can be quickly demonstrated in the test laboratory, claims of superior reliability are not so easily proven. While almost all capacitors demonstrate very high reliability, some may not. It is important that manufacturers have testing and screening techniques available that allow them to identify individual capacitors or whole lots of capacitors that are poorly suited for high-reliability applications.

MnO_2-cathode technology has been in use for half a century and much is known about its strengths and weaknesses. Standard test protocols exist that stress capacitors in almost all of the ways that tantalum capacitors are known to fail. One summary of such testing can be made by inspecting the contents of MIL-PRF-55365, a US Department of Defense specification for tantalum capacitors [40].

Manufacturers also develop proprietary test and screening methods to supplement the standard industry methods. An example of a proprietary screening method is simulated breakdown voltage screening (SBDS). This is a patented technique that estimates the likely breakdown voltage of individual capacitors by examining their charging characteristics at voltages well above rated voltage while carefully avoiding dielectric damage in parts that pass the screen. The statistical distribution of the resulting breakdown voltage estimates is analyzed, and out-of-population devices are removed from the lot. SBDS allows detection of less-robust capacitors, even when their normally-measured parameters are not statistically out of population, and the removed capacitors have been demonstrated to have a much higher failure rate than the remainder of the population.

An example of a popular "standard" reliability assessment method is the Weibull failure rate grading method described in MIL-PRF-55365. For MnO_2-cathode tantalum capacitors, this technique allows a manufacturer to assign one of several failure rates to a lot of tantalum capacitors. Two failure rates of interest to the high-reliability community are Weibull "C" which is 0.01%/1000 h and Weibull "D" which is 0.001%/1000 h. A customer specifies the desired failure rate and the manufacturer grades lots per the MIL-PRF-55365 method and only ships lots to the customer that meet the specified reliability level.

The basis of Weibull grading is knowledge that when MnO_2-cathode capacitors are tested under accelerated conditions, there are many early failures. But the failure rate falls quickly with time as the weak capacitors are culled from the population. If the rate of failures falls quickly enough during the allotted test time, the surviving capacitors can be assigned the desired failure rate. MIL-PRF-55365 provides the practical test details which include a voltage acceleration formula, maximum allowed accelerated voltage, critical test times, a procedure for plotting the cumulative probability distribution of failures, and formulas for calculating failure rate versus time from the probability distribution.

Figure 4.20 contains representative Weibull grading data for a suitable population of tantalum capacitors. The upper graph shows individual data points which are the times-to-failure of 11 of 267 capacitors tested at 1.4 times rated voltage. The test was conducted at 85 °C and lasted for 1000 h. The data are plotted on a specially scaled graph that linearizes the Weibull cumulative distribution statistical function and allows quick estimation of key Weibull distribution parameters. Several straight lines are fit to these data points. The line specified by MIL-PRF-55365 is the heavy solid line drawn between the first failure and a point at 40 h whose y-axis value is the same as that of the last failure occurring before 40 h. Other lines include the heavy

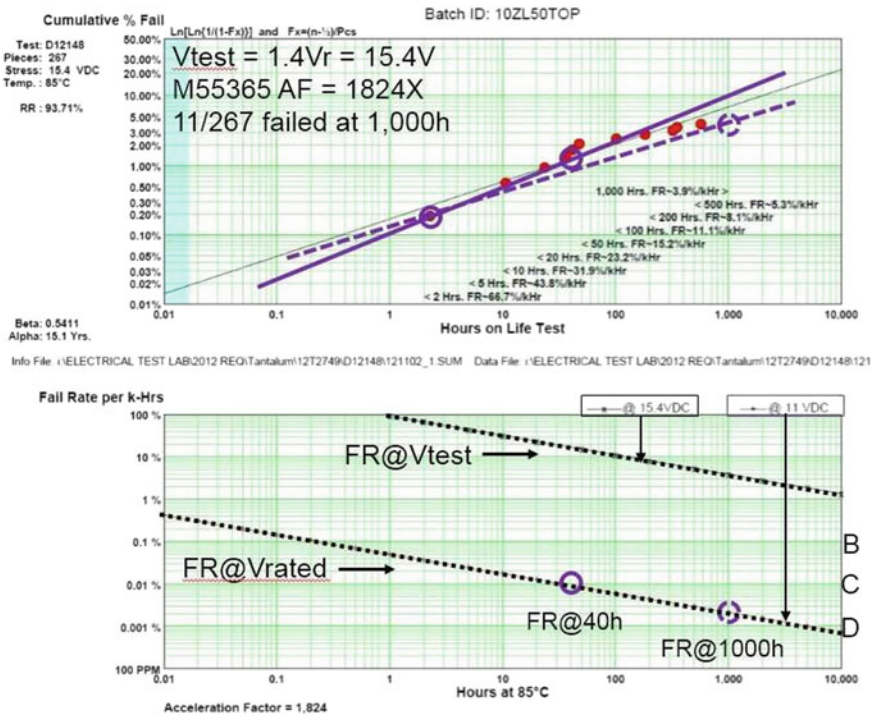

Fig. 4.20 Representative Weibull Time-to-failure data plotted both as cumulative fraction failed versus time and failure rate versus time

dashed line drawn between the first failure and a point at 1000 h whose y-axis value is the same as that of the last failure occurring before 1000 h. Finally, the thin line is a least-squares fit to all the failures. There are additional possibilities and much debate regarding which is most representative of the true lot behavior.

It is the slope of the fitted line (the Weibull β parameter) plus the cumulative fraction failed at a given time that provide the information needed to calculate failure rate versus time. Calculated failure rate estimates appear in the lower graph of Fig. 4.20. The top line estimates the failure rate at the test voltage (1.4Vr) while the bottom line estimates the failure rate at rated voltage.

The vertical spacing between the lines reflects the acceleration factor (1,824 at 1.4Vr per MIL-PRF-55365). It can be seen that the failure rate falls to 0.01%/1,000 h near 40 h, but won't reach 0.001%/1000 h until after more than 4000 h. These capacitors comfortably grade to the Weibull C failure rate, but would not likely be graded to Weibull D because of the associated delay and expense.

There is ongoing debate regarding the precision of the MIL-PRF-55365 acceleration formula, some poor choices of notation in the formulas, and the possible consequences of imprecision in the plotting procedure. But the MIL-PRF-55365 method is used by all major tantalum capacitor manufacturers and the end results have been generally satisfactory from the customers' perspective.

For this reason, when tantalum polymer capacitors were suggested for use in high-reliability applications, customers asked that the capacitors be Weibull-graded to a desired failure rate per the MIL-PRF-55365 method. But for many tantalum polymer capacitors, the Weibull grading procedure fails because the resulting time-to-failure data are more like the data of Fig. 4.21 than the data of Fig. 4.20.

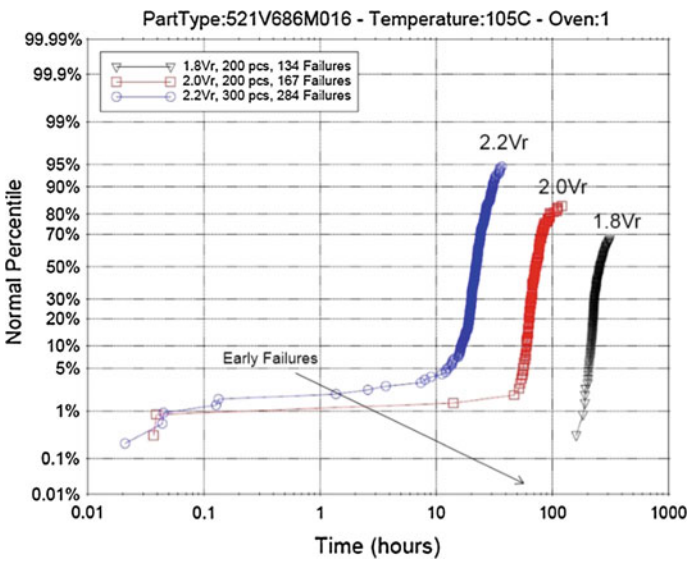

Fig. 4.21 Cumulative fraction failed distributions for representative tantalum polymer capacitors

For the capacitors of Fig. 4.21, the early failures necessary for Weibull grading do not occur until test voltages greater than 1.8 Vr are employed, and MIL-PRF-55365 does not allow more than 1.52 Vr. Also, if 2.0Vr were actually used to force the needed early failures, almost all of the useful life of the capacitors would be consumed during the required 40 h of testing. A different reliability assessment method is needed that better fits the reliability characteristics of the new polymer technology.

Another shortcoming of the Weibull grading method is that it is performed on capacitors that are not soldered to a circuit board. It is known that reflow soldering can damage some mechanically weak capacitors. It is recommended to perform any alternative reliability assessment test on reflow-soldered capacitors to account for this potential vulnerability.

KEMET's solution to this problem was to develop an accelerated life test protocol that demonstrates that a large enough sample of capacitors can survive enough test hours at a total acceleration of 10,000X to validate the failure rate desired by the customer. Such a test would require 100 capacitors to last for 100 h at an acceleration of 10,000X with no more than one failure permitted to validate an observed constant failure rate of 0.001%/1,000 h (Weibull D). We call this test the polymer capacitor reliability assessment test (PCRAT).

Before starting the PCRAT, the samples are soldered to test boards with two solder reflows to account for possible vulnerability to reflow stress. Also in contrast to the MIL-PRF-55365 method, the test acceleration is accomplished with both voltage and temperature acceleration. Finally, rather than use a fixed acceleration formula for all designs, specific acceleration properties are determined for each capacitor design, in advance, via laboratory testing.

The results of this new reliability assessment test are excellent. An example of success with a major customer is presented in the next section.

4.4.5 Validation in Customer Testing

A high-reliability customer approached KEMET with a problem. They were building a circuit board that carries thousands of MIL-PRF-55365 MnO_2 tantalum capacitors—all connected in parallel across the power source. In spite of dividing the capacitors into separate banks and using fuses, occasional failures would result in damage to the circuit boards that prevented rework. Failures would also frighten the final users of the system. Our customer thought that tantalum polymer capacitors might have a more benign failure mode, but wanted assurance from us that the polymer capacitors would have reliability at least as good as the legacy parts.

We designed a testing program that includes many of the standard tests and screens of MIL-PRF-55365. We also included our proprietary SBDS (described earlier) and PCRAT on every lot. About 75% of lots passed the PCRAT at 0.001%/1000 h maximum failure rate and of those, many had no failures.

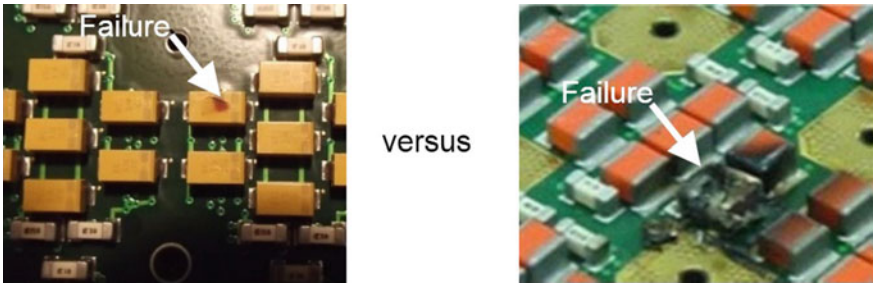

Fig. 4.22 appearance of customer circuit boards after production test failures (polymer vs. MnO_2)

After some time passed, we received a *report card* on the success of our efforts. The capacitors passed the customer's stringent internal qualification program. After qualification, failures observed during production testing fell from 0.14 to 0.01% (a 14 times improvement!) As *icing on the cake*, the few capacitors that did fail did not damage their circuit boards which allowed cost-effective rework (see Fig. 4.22). The customer is delighted with these results.

4.5 Future Directions

4.5.1 R&D and Capacitor Product Development

The trends of miniaturization, increased functionality and connectivity are expected to continue in the field of electronics. The overall content of electronics continues to grow in our homes, cars, smart phones, other personal devices, medical instruments, and practically, in everything with a battery or an electrical cord. This growth can be sustained and complimented only through continuing R&D and new product development. Some thoughts on specific areas of focus and strategies for future R&D are given below.

As seen in the three example projects in this chapter, the key areas of focus in capacitors are:

(1) *Miniaturization*: Achieve more capacitance per unit volume and develop capacitors with smaller footprints and lower heights (thickness).
(2) *Improved reliability*: This is a rather obvious one, but more specifically, the needs for capacitors with excellent reliability for electronics in military, aerospace, implantable medical as well as automotive electronics are growing rapidly.
(3) *Improved robustness*: This aspect is somewhat related to (2) above, but encompasses the mechanical, electrical and thermal robustness of capacitors during handling, mounting and in their applications. Increasing number of capacitors are being used in harsh environments of temperature extremes,

mechanical shock and vibration, and are expected to survive increased levels of mechanical, thermal and voltage stresses during handling and in applications without cracking or failing.

There can be a few other specific areas or types of capacitors that will come up for development, but in general, the development will mostly fall within the three focus areas listed above. At this point, it is also important to address what skillsets and tools are necessary to support R&D and innovation in the capacitor industry and a few key fundamental challenges that the research community should help address.

As is evident from the discussions so far, the field of capacitor development requires multi-disciplinary expertise. Although our industry provides ample opportunity for training and learning by running designed experiments and projects, it is always looking for researchers and engineers with advanced level education in chemical engineering and materials science. A strong background in chemistry and physics of materials and processes, keen analytical abilities and an aptitude for problem solving are highly desirable.

4.5.2 R&D and Innovation in the Changing Times

It is often said that in advanced technology industries, companies that do not innovate, tend to fall behind rapidly (or cease to exist). In the 21st century so far, we have seen two severe economic downturns (during the periods of 2001–2002 and 2008–2010), and with the rapid growth of manufacturing in Asia and the intense competition coming from there, most industries in the U.S. have been facing diminishing funds and resources for R&D along with growing time pressures to stay competitive. To succeed through these circumstances, many industries have had to undergo a paradigm shift with respect to their organization structures and how they manage R&D and innovation. The days of heavily funded central R&D organizations creating a few innovations every few years—which may or may not be useful for their company, are gone. Rather than relying entirely on internal ideas at central and local R&D groups, smart organizations have learned to benefit from "open innovation" and outside collaborations which leverage combinations of internal and external sources for ideas [41]. Collaborating with universities and outside companies to combine expertise and to co-innovate is proving to be efficient and economical. Programs such as the National Science Foundation's Grant Opportunities for Academic Liaison with Industry (GOALI) to obtain research grants are greatly beneficial to conduct research on fundamental and scientific challenges involved in applied R&D, while collaborating with universities and graduate researchers [42]. Furthermore, rapid innovation is possible in spite of the limited funding, if R&D organizations are managed as groups of smaller innovation teams that collaborate within and outside, take calculated risks, go after smaller bets, run projects via rapid experimentation, failing fast—and yet, avoiding

expensive or long-lasting mistakes, and overall, maintain a flexible system of project management [43–45]. Each organization has to ascertain the best set of strategies that work for them, and adapt or modify these as needed. This approach is proving to be successful in our company over the past 7–8 years.

4.5.3 Challenges for the Research Community

With the constraints of reduced internal funding for R&D and innovation, it is essential for industry to learn from and collaborate with universities and other research organizations for fundamental developments and breakthroughs. Some such challenges are outlined below.

1. **Study of Defect Interactions and Interfaces in Dielectrics**
   Electronics applications for geothermal, down-hole oil exploration and certain avionics are already in the 200–250 °C range. With the arrival of SiC-based semiconductor devices, the application temperatures are expected to rise to 350 °C and above. The time horizon for these developments is expected within the next 3–6 years. As the temperature and voltage stresses rise and layer thicknesses of dielectrics and electrodes are reduced, the reliability of capacitors heavily depends on the defect interactions and interfaces within the devices. The evolution of and transport equilibria between point defects and interfaces between the dielectric and electrodes, grain boundaries and domain boundaries govern the reliability of capacitors in extreme environments. Development of various analytical tools for direct or indirect observation and monitoring of the point defects, their interactions with the various interfaces and the mechanisms behind degradation and breakdown of the interfaces are needed to develop ways to engineer these materials and interfaces for robust reliability under extreme environments. There is also an urgent need to develop new compositions and even novel families of materials with the highest possible dielectric constants to be used as dielectric materials for capacitors for high temperatures, and for energy storage and pulse applications.
2. **Development of BME Dielectrics Without the Need for Rare-Earth Oxide Additives**
   It is common knowledge that BME capacitors are fired (sintered) under a reducing atmosphere due to the presence of nickel electrodes. In order to make the dielectric resistant to reduction and to achieve good reliability, it is common to include rare-earth oxide additives in the dielectric formulations. However, over 97% of the ores for rare-earth oxides come out of China. During the past six to 7 years, China has repeatedly announced restrictions on the export of the rare-earth oxide ores which resulted in artificial shortages of these materials and subsequent price increases. This puts the American capacitor industry at a disadvantage, and clearly poses a strategic threat. It is, therefore, very important to develop pathways to BME dielectrics using only a small amount or none of

the rare earth oxide additives. This task requires some breakthroughs in materials because it may require careful manipulation of the crystal chemistry of the $BaTiO_3$. But, this is well within the expertise of the research community in the U.S.A., since most of the pioneering work on the development of $BaTiO_3$ and ceramic dielectrics was indeed done in our country back in the late 1940s through the 1970s.

3. **Development of Pb-Free Ceramic Dielectrics and Piezoelectric**
   The dielectrics materials described in the previous sections of this chapter were all Pb-free, and KEMET has diligently worked on the development of ceramic dielectrics without the use of lead (Pb) for use in ceramic capacitors. However, in the light of the July 2017 deadlines of the EU RoHS (Restriction of Hazardous Substances) and WEEE (Waste Electrical and Electronic Equipment) directives which restrict the use of certain hazardous substances (e.g., Pb) in electrical and electronic equipment, and from the standpoint of the whole ceramic piezoelectric and dielectric industry, there is an urgent need to convert entirely to Pb-free materials.

References

1. Ceramic Capacitors: World Markets, Technologies and Opportunities Report, 2012–2017 (Paumanok Publications, Inc., Cary, NC 27519)
2. R. Kirschman, Present and future needs in high temperature electronics for the well logging industry, pp. 132–133, High Temperature Electronics, IEEE (1998)
3. M.R. Werner, W.R. Fahrner, Review on materials, microsensors, systems and devices for high-temperature and harsh-environment applications. IEEE Trans. Ind. Electron. **48**(2), 249–257 (2001)
4. R.W. Johnson, J.L. Evans, P. Jacobsen, J.R. Thompson, M. Christopher, The changing automotive environment: high-temperature electronics. IEEE Trans. Electron. Packag. Manuf. **27**(3), 164–176 (2004)
5. E.F. Alberta, W.S. Hackenberger, C.A. Randall, T.R. Shrout, High temperature ceramic multilayer capacitors, pp. 69–72, in *Proceedings of the 24th Symposium for Passive Components* (CARTS USA 2004), San Antonio, TX, USA, 2004
6. C.J. Stringer, N.J. Donnelly, T.R. Shrout, C.A. Randall, E.F. Alberta, W.S. Hackenberger, Dielectric characteristics of perovskite structured high temperature relaxor ferroelectrics. J. Am. Ceram. Soc. **91**(6), 1781–1787 (2008)
7. C.A. Randall, et al., High temperature and high energy density dielectric materials, pp. 346–351, Pulsed Power Conference, PPC '09, IEEE (2009)
8. Product bulletin, http://www.epcos.com/inf/20/10/ds/MLCC__Chip__MLSC__X7R.pdf
9. A. Gurav, X. Xu, P. Pinceloup, A. Tajuddin, M. Sato, C. Randall, G.Y. Yang, Characteristics of CaZrO3-based BME C0G dielectric, pp. 359–362, in *Proceedings of the 13th US-Japan Seminar on Dielectric and Piezoelectric Ceramics*, Awaji Island, Hyogo, Japan, 2007
10. X. Xu, M. Niskala, A. Gurav, M. Laps, K. Saarinen, D. Montanari, E. Boni, Advances in Class-I C0G MLCC and SMD Film Capacitors. pp. 449–461, in *Proceedings of the 28th Symposium for Passive Components* (CARTS USA 2008), Newport Beach, CA, USA (2008)
11. N.H. Fletcher, A.D. Hilton, B.W. Ricketts, Optimization of energy storage density in ceramic capacitors. J. Phys. D Appl. Phys. **29**, 253–258 (1996)

12. M.D. Waugh, F.J. Toal, M. Pan, T.R. Shrout, C.A. Randall, Structure-property investigation of a modified PbHfO3 composition for high energy storage, in *Ceramic Transactions*, vol. 90, Manufacturing of Electronic Materials and Components, eds. by A. Ghosh, B. Hiremath, S. Sumita. The American Ceramic Society (1998) pp. 153–163
13. T. Prokopowicz, A. Vaskas, Research and development, intrinsic reliability, subminiature ceramic capacitors, Final Report, ECOM-9705-F, 1969 NTIS AD-864068
14. J.L. Paulsen, E.K. Reed, Highly accelerated life testing of KEMET base metal electrode (BME) ceramic chip capacitors, pp. 265–270, CARTS USA 2001
15. S. Kirchmeyer, K. Reuter, J. Mat. Chem. **15**, 2077 (2005)
16. N. Koch, A. Vollmer, A. Elschner, Appl. Phys. Lett. **90**, 043512 (2007)
17. K. Ueno, L. Dominey, R. Alwitt, in *211th Meeting of The Electrochemical Society–B1-Electrochemistry of Novel Electrode Materials for Energy Conversion and Storage*, 6–10 May 2007
18. Y. Kudoh et al., Synth. Met. **41–43**, 1133–1136 (1991)
19. L. Young, *Anodic Oxide Films* (Academic Press, New York, 1961)
20. J. Young, J. Qiu, R. Hahn, in *Proceedings of the 28th Symposium for Passive Electronic Components*, Newport Beach, CA, 241–251, (2008)
21. Y. Freeman, *Passive Component Industry*, January/February 2005, 6
22. Y. Freeman, P. Lessner, *Passive Component Industry*, July/August 2008, 22
23. B. Boiko, V. Kopach, S. Melentyev, Y. Pozdeev, V. Starikov, Thin Solid Films **229**, 207 (1993)
24. D.A. Vermilyea, J. Electr. Soc. **104**, 542 (1957)
25. Y. Freeman, W. Harrell, I. Luzinov, B. Holman, Ph Lessner, J. Elechtrochem. Soc. **156**(6), G65 (2009)
26. R.E. Powell, J.J. Campbell, J. Electrochem. Soc. **111**, 1230 (1964)
27. N. Jackson, J. Appl. Electrochem. **91**, 3 (1973)
28. Y. Pozdeev-Freeman, Y. Rozenberg, A. Gladkikh, M. Karpovsli, A. Palevski, J. Mater. Sci. : Mater. Electron. **9**, 309 (1998)
29. B. Melody et al., US Patent 6,319,459 B1
30. W. Albrecht et al., US Patent 4,537,641
31. Y. Qiu, R. Hahn, K. Brenneman, US Patent 7,563,290 B2
32. U. Merker et al. US Patent Application Publication No: US 2007/0064376 A1
33. Y. Freeman, Y.Qiu, S. Hussey, P. Lessner, US Pat. No. 8,310,815 B2
34. Y. Freeman, G. Alapatt, W. Harrell, P. Lessner, J. Electrochem. Soc. **159**(10), A1646–1651 (2012)
35. Q. Chen, Y. Freeman, S. Hussey, US Patent No. 8,379,371 B2
36. Y. Freeman, G. Alapatt, W. Harrell, I. Luzinov, P. Lessner, J. Qazi, ESC J. Solid State Sci. Technol. **2**(11), N197–N204 (2013)
37. Y. Freeman, J. Chen, R. Fuller, S. Hussey, E. Jones, T. Kinard, P. Lessner, M. Maich, T. McKinney, in *Proceedings of the CARTS-Europe, Munch, Germany,* Nov 2010, p. 143
38. Y. Freeman, US Pat. No. 7,671,603 B2
39. J. Paulsen, E. Reed, Y. Freeman, US Pat. No. 8,441,265 B2
40. http://www.landandmaritime.dla.mil/Downloads/MilSpec/Docs/MIL-PRF-55365/prf55365.pdf
41. H. Chesbrough, "Open Innovation," Harvard Business School Press, 2006
42. NSF Grant Opportunities for Academic Liaison with Industry (GOALI) grants, http://www.nsf.gov/funding/pgm_summ.jsp?pims_id=504699
43. P. Sims, *Little Bets—Breakthrough Ideas from Small Discoveries* (Free Press, New York, 2011)
44. Kim E. Ruyle, *Lessons from a CEO's Journal* (Inventive Talent Consulting, LLC, Coral Gables, FL, 2014)
45. S.H. Thomke, *Experimentation Matters* (Harvard Business School Press, Boston, 2003)

Chapter 5
American Superconductor: Second Generation Superconductor Wire—From Research to Power Grid Applications

Srivatsan Sathyamurthy, Cees Thieme and Martin W. Rupich

Abstract American Superconductor Corporation (AMSC) is the leader the development, manufacturing and deployment of high temperature superconducting (HTS) wire. The company's HTS wire, called Amperium HTS wire, is the result of decades of a research and development effort on texturing of metals, epitaxial growth of complex oxides and innovative roll-to-roll manufacturing techniques. AMSC is also a leader in developing HTS wire based products that are being deployed in the power grid around the world. In this chapter we provide an overview of the high temperature superconducting materials, describe the challenges overcome in converting these materials into useful wires and summarize the major markets for the Amperium wire.

5.1 Introduction

American Superconductor Corporation (AMSC) was established in 1987, shortly after the discovery of the cuprate based high temperature superconductors, with the goal of developing these newly discovered materials for use in commercial applications. Since its founding, AMSC has been a world leader in the development and manufacturing of HTS (high temperature superconducting) wire for a broad range of commercial and military applications. While AMSC focused on the development of HTS wire, it evolved into a broad-based energy company that supplies innovative products and services to the both the wind and power grid markets. AMSC's focus is now on providing the world with cleaner, greener and more secure energy solutions based on both conventional and innovative HTS-based technologies. AMSC's HTS wire remains a core company technology and as it matures, it is being incorporated into a growing range of products providing innovative solutions to increase the power grid's capacity, reliability, security and efficiency.

S. Sathyamurthy (✉) · C. Thieme · M.W. Rupich
Materials R&D, AMSC, 64 Jackson Road, Devens, MA 01434, USA
e-mail: Srivatsan.Sathyamurthy@amsc.com

L.D. Madsen and E.B. Svedberg (eds.), *Materials Research for Manufacturing*, Springer Series in Materials Science 224,
DOI 10.1007/978-3-319-23419-9_5

5.1.1 Cuprate-Based High Temperature Superconductors

Over a quarter of a century after the discovery of the cuprate based (RE)$Ba_2Cu_3O_{7-x}$ ((RE)BCO where RE = rare earth) HTS materials with superconducting transition temperatures (T_c) above liquid nitrogen temperature (77 K), the first commercial applications of HTS wires are beginning to be realized. Although their discovery in 1987 was accompanied by vast excitement and visions of near-term applications, it was soon realized that the materials were complex oxides that would require a formidable research and development effort to understand and transform them into usable conductors for real-world applications. Today, after extensive development effort, American Superconductor Corporation (AMSC) and a number of other manufacturers are producing the HTS wire, typically referred to as 2G or second generation HTS wire, in continuous lengths with the performance level required for these initial commercial applications, as shown in Fig. 5.1. (First generation or 1G HTS wire is based on the BiSrCaCuO-based materials described below [1].) These wires are now being used in fault current limiters (FCL's) that are being deployed in the electrical grid and in a number of cable projects around the world [2–5]. The first 2G HTS wire-based cable installed in an actual electrical grid, a 500 m long DC cable produced by Cable Systems and the Korean Electric Power Company (KEPCO) using AMSC 2G HTS wire, was energized on Jeju Island, Korea in September 2014 [6]. This will be followed by longer cables projects currently being installed or planned in Korea and the United States.

Within months of the material discovery, the first (RE)$Ba_2Cu_3O_{7-x}$ wire was initially fabricated by Jin at Bell Labs using an oxide-powder-in-tube (OPIT) approach [7]; however, it carried a critical current density, J_c, of only 175 A/cm^2 (77 K, self-field), orders of magnitude lower than required for practical conductors. Early studies of the (RE)BCO materials found the low critical current in polycrystalline samples, such as used in Jin's first wire, arose from the fundamental physics of the cuprate materials; specifically, a short coherence length and the correlated character of their electron systems made them extremely sensitive to the

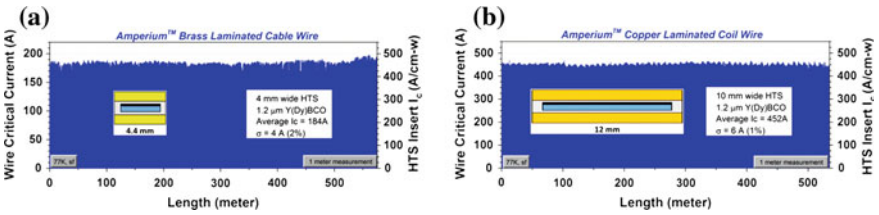

Fig. 5.1 Critical current as a function of length for 2G HTS wire manufactured by AMSC. The 2G HTS cable wire (**a**) is brass laminated with dimensions of 4.4 mm × 0.3 mm and the 2G HTS coil wire (**b**) is copper laminated with dimensions of 12 mm × 0.4 mm (courtesy of AMSC). Other manufacturers are also producing wire with comparable properties

grain boundary misorientations. Since epitaxial $YBa_2Cu_3O_{7-x}$ films had critical current densities of over 10^6 A/cm^2 at 77 K, it was thought that the manufacture of long length (RE)BCO based wires would require km-length single crystals, a challenge with no clear solution. Thus within 3 years of their discovery, reports began to appear stating that (RE)BCO was inherently incapable of carrying enough current to be useful and that development of (RE)BCO wire faced insurmountable obstacles [8, 9].

As a result, wire development efforts turned to the BiSrCaCuO-based materials (i.e., $Bi(Pb)_2$–$Sr_2Ca_2Cu_3O_x$) which could be uni-axially textured (*c*-axis grain alignment only) through thermo-mechanical processing using powder-in-tube methods [10]. Although there was no alignment of the *ab*-planes in the BSCCO materials, the wire, typically referred to as the first generation or 1G wire, carried significantly higher critical current due to a brick-wall type stacking of the platelet-shaped grains that produced a large effective grain boundary area that compensated for the weak linked grain boundaries [11, 12].

AMSC and Sumitomo Electric Industries (SEI) pursued this 1G technology and were instrumental in establishing the technical viability of HTS wires for various applications in the electrical power industry and rotating machinery by the mid 1990s [13]. Meanwhile, researchers around the world continued studying the (RE) $Ba_2Cu_3O_{7-x}$ materials, searching for innovative ways to overcome their fundamental limitations and routes around the seemingly insurmountable obstacles to practical long-length conductors.

5.2 (RE)BCO Structure and Properties

The (RE)BCO-based high temperature superconductors have a perovskite-type crystal structure, as shown in Fig. 5.2 (where RE = Y), in which two CuO_2 layers surround the RE atom separate CuO chains are oriented along the *b*-axis in another layer. Superconductivity occurs in the CuO_2 planes, while the CuO chains are

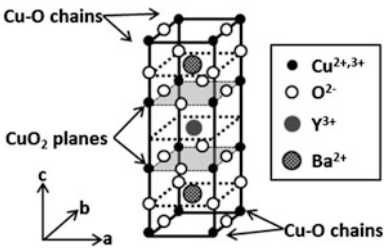

Fig. 5.2 Unit cell crystal structure of the (RE)$Ba_2Cu_3O_{7-x}$ cuprate superconductor. The RE atom is located between the two CuO_2 planes. Superconductivity is confined to the CuO_2 planes while the CuO chains, which are oriented along the *b*-axis serve as charge reservoirs providing carriers to the CuO_2 planes

principally charge reservoirs providing carriers to the CuO_2 planes depending on the oxygen content, expressed by (7 − x) in the chemical formula of (RE) $Ba_2Cu_3O_{7-x}$. A low oxygen content (large x), produces an electrically insulating tetragonal structure while a higher oxygen content (x < 0.65) converts the material into a superconducting orthorhombic structure, with a peak superconducting transition temperature (T_c) occurring at x ∼ 0.07. This planar CuO_2 structure produces a large anisotropy in the superconducting properties of the (RE)BCO materials, resulting in the supercurrent in the *a-b* plane being much greater than along the *c*-axis [14, 15].

As mention earlier, the coherence length, (ξ), which can be described in simple terms as the spatial distance over which the paired superconducting electrons interact, is small in the (RE)BCO materials—1 to 4 nm in the *ab*-plane and less than 1 nm along the *c*-axis [16] (for comparison the ξ in pure elemental type-I superconductors is ∼1000 nm and in the type II superconductors such as NbTi is ∼5 nm). Consequently small disruptions in the lattice periodicity, such as high angle grain boundaries, appear as planar defects that drastically restrict the supercurrent flow from grain to grain.

A study of the effect of grain boundary misorientation on supercurrent flow, by Dimos, Chaudhari and Mannhart in 1990, found that the critical current density (J_c) across a grain boundary is nearly unaffected for grain boundary misorientations of less than 4°, but decreases exponentially for a misorientation angle greater that 4° [17, 18], as shown in the Fig. 5.3. In addition, they established that the J_c across grain boundaries was independent of the type (twist, tilt) of grain misorientation.

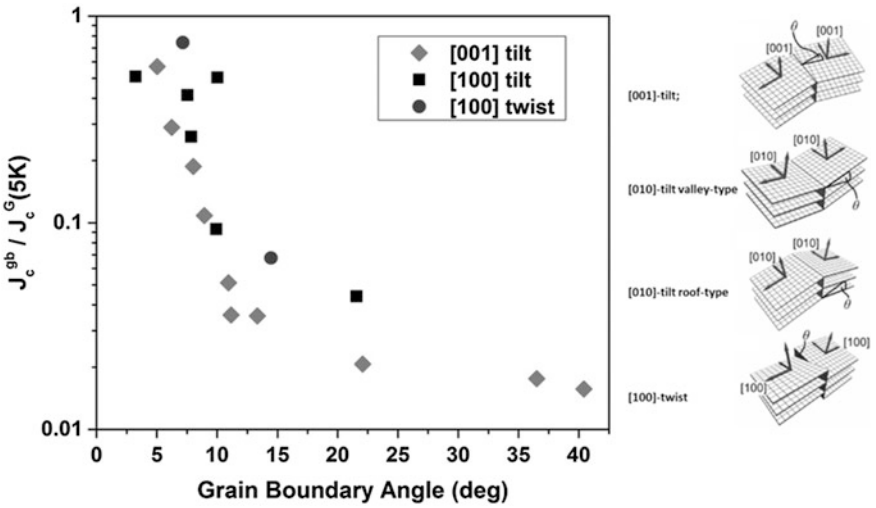

Fig. 5.3 The study by Dimos et al. [17] of YBCO films on bi-crystals showed the effect of **a** grain boundary misalignment and **b** grain boundary type, in the (RE)BCO materials and helped stimulate the development of textured templates for (RE)BCO coated conductors

These fundamental properties indicated that in order to carry high critical currents, the (RE)BCO materials would need to be textured with very clean grain boundaries and for fabricating practical conductors, this would need to be accomplished over lengths of 100s–1000s of meters.

A solution to the grain boundary issue was first developed by Iijima et al. at Fujikura, in 1991, when it was discovered that oxides, such as yttria-stabilized zirconia (YSZ), could be grown with biaxial texture on untextured substrates by focusing an argon-ion beam at a select angle to a substrate during the vapor phase deposition process [19–21]. The resulting bi-axially textured films had single crystal-like properties and supported the subsequent growth of epitaxial YBCO films with low grain boundary misorientations, enabling high J_c's. This ion beam assisted deposition (IBAD) process was used for the deposition of biaxially textured YSZ films on flexible metal tapes using a roll-to-roll process, demonstrating the first potential route to manufacturing continuous lengths of a highly textured YBCO films. This discovery reignited research efforts around the world and marks the real beginning of the 2G HTS wire development. The ensuing research rapidly identified alternate paths for producing textured templates and multiple methods for depositing the HTS layer.

5.3 2G HTS Wire—Architecture and Manufacturing Options

The fundamental properties and in-plane texture requirements of the (RE)BCO materials dictate that the conductors be fabricated in the form of a tape rather than a round wire. Thus all second generation wire today is based on a composite tape architecture comprised of a flexible textured template onto which an epitaxial film of (RE)$Ba_2Cu_3O_{7-x}$ is deposited, as shown in Fig. 5.4. A normal metal surrounds the composite tape to provide a low resistance electrical contact with the (RE)BCO

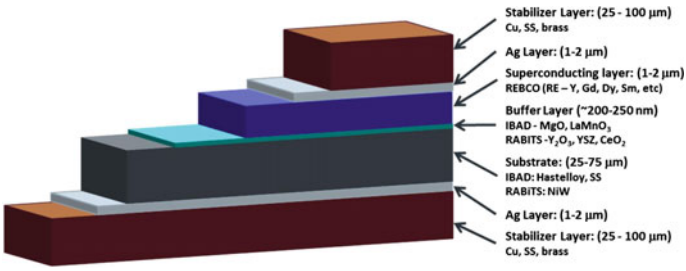

Fig. 5.4 2G HTS wires are manufactured with a composite architecture containing a metal substrate, biaxially textured oxide buffer layers, a biaxially textured (RE)BCO layer, a Ag contact layer and a metallic stabilizer layer (not to scale). Specific materials, formulations and thickness of the individual layers vary from manufacturer to manufacturer (courtesy of AMSC)

and electrical and thermal stabilization for the wire. The template consist of a flexible metallic substrate coated with a series of biaxially textured oxide layers that prevent reaction of the metal substrate with the (RE)BCO and provide a highly textured, single crystal-like surface for the epitaxial nucleation and growth of the (RE)BCO. All commercial 2G HTS wires have this basic composite architecture; however, manufacturers have chosen different technologies to produce the biaxially textured substrates, deposit the HTS layer and stabilize the wire, resulting in variations in the specific materials and architectures of their wires [22].

5.3.1 Template Technologies

The template controls the nucleation and biaxial grain alignment of the (RE)BCO and is the key component that allows roll-to-roll (also referred to as reel-to-reel or R2R) manufacturing of today's 2G HTS wire. In addition to enabling the growth of the biaxial (RE)BCO, the template must also be chemically compatible with the (RE)BCO, stable at the (RE)BCO growth conditions, amenable to formation into tapes and provide sufficient mechanical stability to the thin (RE)BCO films. The three processing technologies used today include the rolling-assisted-biaxially-textured-substrate (RABiTS^{TM}), IBAD and inclined substrate deposition (ISD) processes as illustrated in Fig. 5.5.

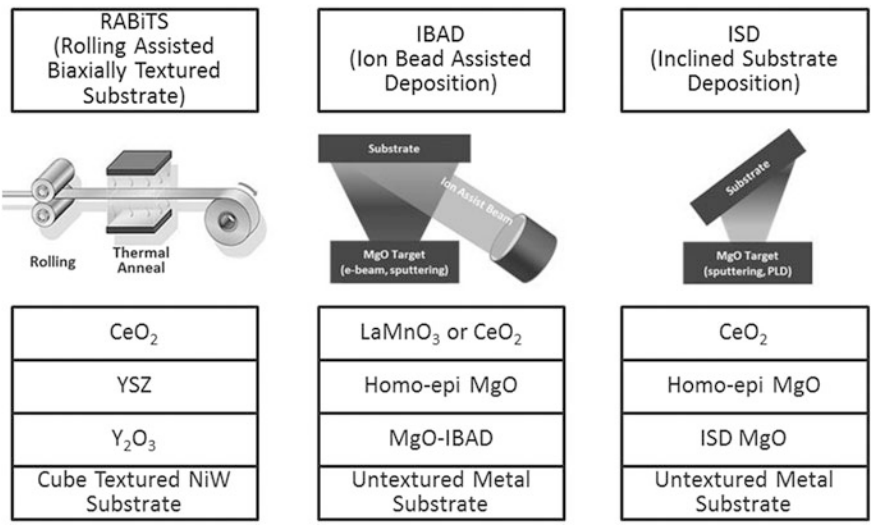

Fig. 5.5 Three basic fabrication methods, **a** RABiTS, **b** IBAD and **c** ISD have been developed for producing templates with high degree of in-plane grain alignment needed high performance and amenable to R2R processing over long continuous lengths

The RABiTS technology (described in greater detail later in the chapter) is based on generating a $\{001\}\langle 100\rangle$ cube texture in a metal substrate by conventional rolling deformation and recrystallization techniques, as the metal is converted into a thin tape [23–25]. Although many cubic metals or alloys can be textured, face-centered cubic (FCC) materials such as Cu and Ni are the materials of choice since the thermo-mechanical deformation generates a sharp texture in which the cube plane is oriented parallel to the tape plane and a cube edge parallel to the rolling direction. Since the (RE)BCO is not chemically compatible with the metal substrate, it is necessary to deposit a series of epitaxial oxide layers, typically Y_2O_3/YSZ/CeO_2, on the substrate that replicate the substrate texture, provide a metal diffusion barrier and promote the nucleation and growth of the (RE)BCO film [25].

The IBAD process is based on the bombardment of an oxide film during its vapor phase deposition by an off-normal ion beam which sputters away unfavorable grain orientations, promoting the growth of a highly oriented, biaxially textured oxide film on the untextured substrate. Early efforts focused on YSZ [26] and $Gd_2Zr_2O_7$ films [27, 28]; however, the texture evolution was slow, requiring the deposition of thick films resulting in long processing times and low throughput. Most manufacturers using the IBAD process today deposit MgO films in which the biaxial texture develops rapidly, achieving a constant texture within the first 10 nm [26, 29–32]. The IBAD MgO layer is generally capped with a thin homo-epitaxial MgO layer and then either a $LaMnO_3$ or CeO_2 layer which serves as the nucleation layer for the (RE)BCO [33].

The ISD technology, developed by Hasegawa et al. of Sumitomo Electric Industries (SEI) [34], is based on the deposition of an oxide film, typically MgO, at an angle slightly tilted from the plane of the substrate. The texture develops due to a shadowing effect which promotes preferential growth of the MgO along the [001]-axis at an angle tilted slightly from the substrate normal [35, 36].

5.3.2 Superconductor Layer Deposition

Four different deposition technologies are currently used for the superconducting layer: (a) metal organic deposition (MOD), (b) metal organic chemical vapor deposition (MOCVD), (c) pulsed laser deposition (PLD), and (d) reactive co-evaporation (RCE). In addition, a variety of chemical formulations are used for the (RE)BCO layer in order to enhance deposition rates, growth conditions or J_c for each specific deposition technique. A variety of dopants such as RE_2O_3 or $BaZrO_3$ are also frequently added to generate nano-scale defect structures (typically nano-particles or nano-rods) which enhance flux pinning and thus increase the current the (RE)BCO film carries in the presence of a magnetic field [37, 38].

MOD is an ex situ, chemical deposition technique in which a solution-based precursor is coated onto the template and then converted into the (RE)BCO film [39–44]. This process is described in more detail later.

PLD is a vacuum-based, in situ growth process that utilizes a high power excimer laser (KrF or XeCl) to vaporize a (RE)BCO target that deposits from the plasma onto the template as a thin film. The PLD process has produced some of the thickest, highest I_c (RE)BCO films (1400 A/cm-w at 75 K, self-field) reported to date [45, 46].

MOCVD is an in situ deposition process based on the injection of a precursor material into a reactor chamber where it vaporizes and undergoes a pyrolysis reaction as it deposits as a thin film on a substrate [47]. Early MOCVD efforts used solid phase 2,2,6,6-tetramethyl-3,5-heptanedionates as the precursor sources; however, these have been replaced by single source liquid precursors, based on RE, Ba and Cu tetramethyl heptanedionates (tmhd) which have enabled higher rate deposition and improved stability and uniformity [48].

RCE is a thermal evaporation technique developed for the deposition of the epitaxial, multi-component oxide HTS films [49]. The deposition is carried out either by sequential evaporation of a thin layer of the metal components onto the substrate in a low pressure zone followed by oxidation in a high oxygen pressure zone [50–52] or alternately by the co-evaporation of the entire metal film in a single step, forming an amorphous, glassy sub oxide film which is then converted ex situ to the superconducting (RE)BCO phase [53].

5.3.3 Roll-to-Roll Processing

2G HTS wire, which consists of a superconductor thin film on a long length flexible substrate, is ideally suited to industrial R2R processing. A major advantage of the R2R manufacturing is the ability to process wide webs of material which can be slit to the final product width at the end of the process. Although R2R processing is a widely used low-cost, high-volume manufacturing technology, it had not been used for manufacturing of flexible electrical materials, especially ones with the stringent biaxial texture requirements of 2G HTS wire. Thus, in addition to developing the basic deposition technologies, the 2G engineering community also had engage equipment manufacturers to design and build R2R tools that could be adapted to the epitaxial deposition processes.

For cost reasons, it was necessary to maximize the process (or deposition) zone area in order to maximize throughput (m^2/h). Two similar, but distinct approaches were developed for the R2R manufacturing of 2G HTS wire. The first is the wide-web process, pioneered by AMSC and the second is a narrow-web, helix process developed by SuperPower, as illustrated in Fig. 5.6. The wide-web process uses a wide substrate (46–100 mm) which is slit to individual wires (up to 24 individual 4 mm wide wires from a 100 mm web) at the end of the process. This wide web approach is advantageous with the RABiTS template technology which can be produced in wide widths and solution based deposition processes which utilize low-cost ovens with long process zones (10 m or greater) enabling high

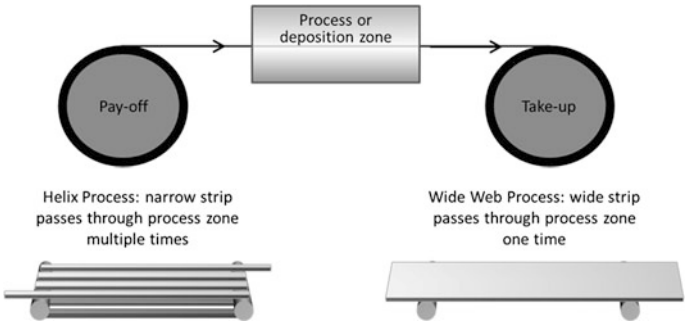

Fig. 5.6 2G HTS wire is manufactured using a R2R process employing either **a** a wide web (50–100 mm) which passes through the deposition or process zone once or **b** a narrow-web (10–12 mm) which passes through a helix deposition or process zone multiple times (courtesy of AMSC)

throughput (m^2/h) compared to PVD systems in which deposition zones are generally restricted to around 1 m.

The narrow-web, helix approach starts with a narrower (10–12 mm wide) strip that is slit into fewer individual wires at the end of the process, or is used without slitting. In order to increase the throughput, the narrow tape passes through the deposition zone multiple times by means of a helix configuration, effectively increasing the length of the process zone. An advantage of the helix system is that inhomogeneities across the width of the deposition zone are averaged out, making it useful for the IBAD template technology and other small deposition area PVD processes such as PLD and RCE depositions.

5.4 AMSC's Selection of the RABiTS/MOD Process Technology

In the early stages of the 2G wire development, it was uncertain whether any template process could achieve the required texture over the hundreds of meter length required for commercial manufacturing or could be done at a cost that would enable a commercial market. In order to identify the preferred manufacturing approaches, AMSC established collaborations through a multi-organizational association called the Wire Development Group (WDG). The makeup of the WDG collaboration varied over the years, but included scientists from Los Alamos National Laboratory, Oak Ridge National Laboratory, Argonne National Laboratory, the University of Wisconsin, the University of California Berkeley, Massachusetts Institute of Technology, Florida State University and Industrial

Research Laboratory (in New Zealand). The WDG collaborators generally focused on a fundamental understanding and the technical capabilities of the different template and HTS technologies, while AMSC scientists and engineers focused on the manufacturability, scalability and cost of the various approaches.

Ultimately AMSC chose the combination of the RABiTS technology for the template and the MOD process for the HTS layer. The primary advantage of the RABiTS/MOD approach is the ability to carry out the entire R2R process using a wide strip which is slit into multiple wires of the desired width at the end of the process. AMSC's current process is designed around a 46 mm wide strip; however, its manufacturing equipment is designed to process strips up to 100 mm wide. A key requirement of the wide-web approach is maintaining uniform properties across the substrate width. Thus in the early 2000s, AMSC focused its early manufacturing development efforts on processing width rather than length, while others, using the narrow-web approach, focused on length. However, once the cross-web uniformity was established on short length strips ($\sim$100 m), AMSC rapidly extended the length to 500–600 m, which is sufficient for most applications.

In addition to the template and HTS deposition technologies, AMSC uses a lamination process, previously developed for 1G HTS wire, to fabricate the 2G HTS as a robust commercial wire (conductor) for use in a variety of cable and coil applications. In this process, a metal foil is bonded to each side of the slit strip (referred to as the insert wire) and the edges are sealed with solder fillets. The lamination process also provides the flexibility to customize the normal-state electrical or mechanical properties of the final wire for specific applications.

5.4.1 AMSC's RABiTS/MOD Wire Manufacturing Process

AMSC has established a 2G HTS wire manufacturing plant in its Devens, Massachusetts facility based on the RABiTS/MOD process [54]. The facility, designed as a wide-web, R2R process is currently the largest 2G manufacturing plant in the world. Figure 5.7 illustrates the major process steps for the template fabrication, superconductor deposition and wire fabrication. This production line was the result of years of R&D focused on both optimizing the performance of the RABiTS/MOD process and reducing the materials and processing costs. The following sections describe the selected technology in more detail and highlight some of the challenges overcome in its successful development.

5.4.2 The RABiTS Substrate

The RABiTS process was developed by Goyal, et al. at Oak Ridge National Laboratory (ORNL) in the early 1990s and subsequently developed by AMSC into a cost-effective template for 2G wire manufacturing [54, 55]. The basis of the

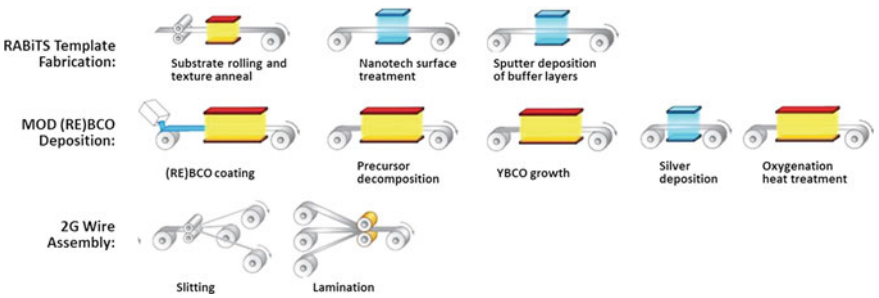

Fig. 5.7 Schematic diagram illustrating basic process steps AMSC uses for the: (1) RABiTS template fabrication, (2) MOD superconductor deposition and (3) final wire 2G wire assembly (*courtesy* AMSC)

RABiTS process is the creation of a thin metallic substrate, with a sharp cube texture, that supports the growth of epitaxial buffer layers [25, 56]. Early R&D at AMSC and ORNL focused on high purity Ni substrates which can be produced with near 100% cube texture. However, pure Ni is very weak when annealed, making the high temperature R2R processing a challenge. In addition, Ni is ferromagnetic, resulting in a hysteretic power loss making it less attractive for alternating current applications. Thus research efforts rapidly focused on identifying suitable nickel alloys that would meet the following substrate requirements:

1. A sharp cube texture in a thin substrate,
2. Non-magnetic,
3. Sufficient yield strength at RT and elevated temperatures, and
4. Oxidation resistance (no native oxide formation at conditions for buffer deposition).

Texture FCC metals with a medium stacking fault energy (SFE) such as Cu or Ni tend to form very sharp, nearly single-crystal like $\{001\}\langle 100\rangle$ foils when rolled to high reductions ($\sim$95–99% cube) followed by a high temperature anneal. Although this phenomenon had been known since 1929 [57], it was generally considered a metallurgical curiosity—research often focused on inhibiting texture formation in order to allow isotropic deformation. The capability to form a highly cube textured substrate requires a small grain size at the start of the deformation process, a high deformation strain before final anneal, and a sufficiently high SFE. There are a number of nickel alloys with a medium SFE which are able to develop a cube texture and are oxidation resistant. Figure 5.8 shows the stacking fault probability α ($\alpha = K \cdot \rho/\gamma$), where K is a constant; ρ the dislocation density and γ the SFE, as a function of the concentration of various elements, X, in Ni(X) solid solution alloys [58]. Assuming a constant dislocation density, the data show the inverse SFE has an inverse dependence on X. Trends in Fig. 5.8 were confirmed in a recent modeling study [59].

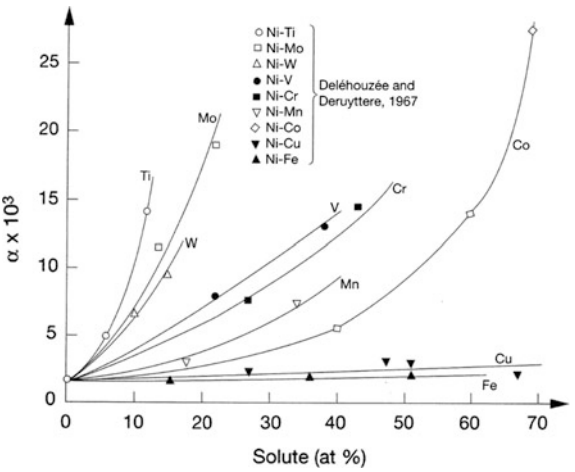

Fig. 5.8 Stacking fault probability α in Ni(X) solid solution alloys as a function of [X]. $\alpha = K \cdot \rho/\gamma$; K: constant; ρ: dislocation density; γ: SFE. After Gallagher [58]

In Fig. 5.8, the alloys fall roughly into three categories: (1) NiX alloys (Cu and Ni) with a complete or very high solubility and an α nearly independent of composition; (2) NiX alloys (Co, V, Cr, Mn, W and Mo) with a an extensive solubility in Ni and an α that varies with X; and (3) NiX alloys (Ti) with a very low solubility and limited ability to form a sharp cube texture. While Fig. 5.8 shows a gradual decrease of the SFE of these alloys, the ability to form a sharp cube texture does not follow this same dependency. Experience shows that Ni(Cr) forms an excellent cube texture at [Cr] ≤ 13 at.%, Ni(V) at [V] ≤ 9 at.%, and Ni(W) at [W] ≤ 5–6 at.%. However, when [X] exceeds these concentrations, the ability to form a cube texture rapidly deteriorates even though there is only a small additional decrease in γ.

It is also desirable that the RABiTS substrate is non-magnetic (or at least weakly ferro-magnetic) and strong enough to withstand mechanical deformation and damage during high temperature R2R processing. Alloying Ni with metals such as W, Cr, Mo or V significantly increases the strength of the alloy and reduces the Curie temperature. The reduction in Curie temperature in Ni(X) is virtually linear with both [X] and its valency [60], with Cr being nearly 3 times and W nearly 5 times more effective than Cu. For the substrate to be non-magnetic at low temperatures (<20 K), requires approximately 13 at.%Cr, 9 at.%V or 9.3 at.% W.

Oxidation resistance of the alloy needs to be sufficient to withstand processing, in an a high temperature, oxidizing environment in subsequent steps, with minimal oxide scale formation. Although elements such as Al provide excellent oxidation protection via the formation of an oxide film (i.e., Al_2O_3), the oxide its formation prior to the buffer deposition will disrupt the epitaxial growth of the buffer layers (this is discussed in more detail in the following section). Other alloying elements that can meet this requirement include W, Mo and Cr.

Based on these requirements and suitability for supporting the epitaxial buffer growth, NiW was identified as the best choice for development of the RABiTS substrate. The cube texture forms at W concentrations of up to ≈5.5 at.% even

though the change in SFE is gradual over the entire 0–10 at.% W. However, at [W] > 6% the cube texture rapidly decreases. The reason for this abrupt decrease in texture in alloys with lower γ was poorly understood. Thus, although the Ni–5 at.% W is weakly ferromagnetic, AMSC and others chose to work with the Ni–5 at.% W composition since this was initially thought to be minor disadvantage to final wire properties. However, since the competing IBAD template technology is based on a non-magnetic substrate, 2G wire based on Ni–5 at.%W was at a competitive disadvantage in ac cable applications where the ferro-magnetism contributes to enhanced ac losses. As a result, AMSC and others [61] began to study the deformation mechanisms in the lower γ alloys This multi-year research effort eventually led to the development of a proprietary thermo-mechanical process to that produces an excellent cube texture in the non-magnetic Ni–9 at.% W alloy that matches that in the Ni–5 at.% W composition.

Detailed studies of the microstructure development in both the Ni–5W and Ni–9W alloys showed them to be similar to those of FCC alloys with a medium SFE [62]. After an initial stage of deformation banding, highly distorted lamellae develop and evolve into a structure of nearly horizontal but wavy, in-plane lamellae, as shown in the transmission electron microscopy (TEM) micrograph in Fig. 5.9.

Figure 5.10 shows the texture components M_i for substrates rolled to final thickness ($\eta = 3.9$) (prior to the final thermal anneal) for Ni–5W and Ni–9W, with the standard and the modified thermo-mechanical process, respectively. Ni–5W texture components are similar to that of pure copper.

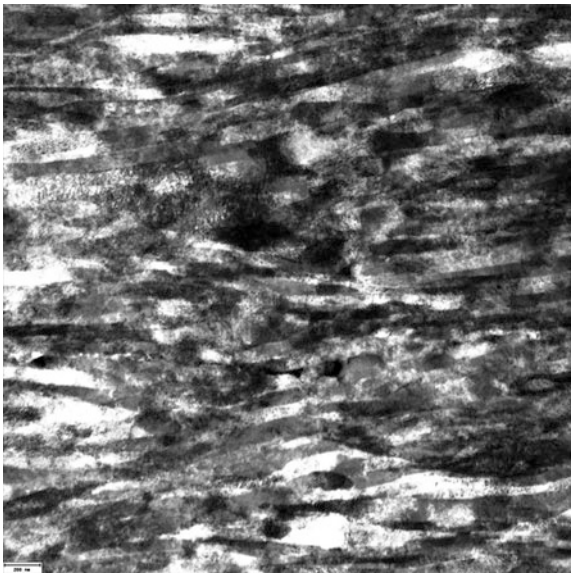

Fig. 5.9 TEM image of rolled Ni–9W, thickness is 0.076 mm. Longitudinal view, rolling direction is horizontal; Bar in *left corner* 200 nm. V. Svetchnikov and C. Tretiatchenko, Institute for Metal Physics, Kiev

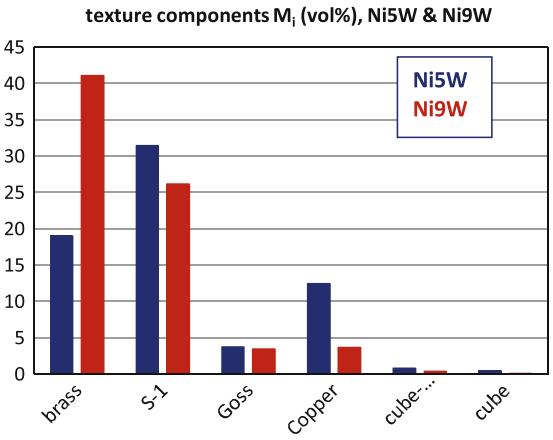

M_i	orientation
brass	{110} <1-12>
S	{132} <6-43>
Goss	{110} <001>
copper	{112} <11-1>
cube	{001} <100>

Fig. 5.10 Texture components M_i (vol.%) for Ni–5W and Ni–9W at final thickness (FWHM: 10°)

As seen in Fig. 5.10, the S texture {132}⟨6–43⟩ is the strongest component in the Ni–5W composition, followed by the brass orientation {110}⟨1–12⟩, copper {112}⟨11–1⟩ and Goss {110}⟨001⟩. The {001}⟨100⟩ cube and cube-Goss {025}⟨100⟩ components are 1% or less. In contrast the Ni–9W composition shows a very different picture with the brass texture being the dominant component, followed by S, Goss and a relatively low copper component. In both compositions Cube and Cube-Goss textures are well below 1%. However, despite these quite dissimilar M_i (% texture component) values the final textures for the Ni–5W and Ni–9W are very similar (97–98% cube).

Figure 5.10, in which the final desired cube orientation is nearly absent, does not foretell the formation of a near 100% cube texture during the final anneal in any way. This example illustrates the difficulty in pin-pointing the exact stabilization and growth mechanisms for the few existing cube lamellae in the final substrate. For a review of the theory (and historical background) of cube recrystallization texture see for example Humphreys and Hatherley [63]. It is generally believed that high angle boundaries combined with strain-induced boundary movement (SIBM) is essential in cube growth. Already existing, stable cube lamellae grow into the neighboring lamellae with a different texture, in which particular grain boundary orientations can assist in this growth. The low concentration of cube lamellae, as found in NiW can be advantageous, since higher levels can block growth when cube growth bands “collide” leading to orientation pinning as has been observed, for example, in Al. However, to track this process in Ni–9W and be more precise about the growth of the cube texture extensive high resolution scanning electron microscopy (HRSEM)/TEM combined with electron backscatter diffraction (EBSD) analysis is still required at various stages of the growth process.

Long Length RABiTS Substrate Manufacturing AMSC worked closely with collaborators at ORNL to scale the RABiTS process from the initial short sample demonstration to a wide-web R2R process. The major effort focused on developing the appropriate deformation and annealing paths to insure a sharp and uniform cube texture was generated over both the width and length of the substrate. With the optimized deformation and annealing process, a cube texture of 96–98% is achieved over the length and width of the substrate. The cube texture is determined from the integrated area of the (200) or (111) X-ray pole figures and full width at half-maximum (FWHM) values for in-plane ($\delta\phi$) and out-of-plane ($\delta\chi$ and $\delta\omega$) texture.

The measured in-plane texture, $\delta\phi$, values, which are averaged over a large area, are between 6.5–7°. Although this is larger than the 4° grain boundary mis-orientation that Dimos showed caused a precipitous drop in supercurrent, these substrates support currents in the (RE)BCO layer of >4 MA/cm^2. One reason for the higher than predicted J_c is an improvement of the in-plane texture, $\delta\phi$, of the initial Y_2O_3 buffer layer. This sharper Y_2O_3 texture is inherited by the subsequent YSZ barrier and CeO_2 cap layer (see later section). Secondly, in the MOD (RE)BCO layer the grain boundaries are typically slanted and meandering, enhancing the total grain boundary (GB) area available for current transport [64].

It is also critical to prevent the formation of other texture components which can appear as obstacles to the super current flow. For example, annealing twins form high angle grain boundaries with the cube texture grains and abnormal grains, which can reach 200–300 μm in size, and appear as obstacles to the supercurrent flow.

In the early development, texture uniformity was examined by scanning the length and width of the substrate using a R2R x-ray analysis system at ORNL. However, the best indicator of texture homogeneity is the local and long-length uniformity of the supercurrent along the length of each individual wire produced from the RABiTS substrate.

The initial development efforts used small (∼20 lb.), high purity, laboratory scale Ni–5 at.% W ingots which can prepared with precisely controlled compositions, typically within 0.1 at.%. However, a commercial manufacturing operation requires multi-ton quantities with the same purity and homogeneity requirements. AMSC worked closely with metal suppliers to develop a production scale process based on a conventional melt of high purity Ni and W followed by a second melt to remove volatile impurities. The melting process is followed by a homogenization treatment, a hot deformation step and cold rolling to desired thickness, with anneal steps at critical stages. This process routinely yields high purity, compositionally homogeneous Ni-W coils which can be used for precise rolling to final thickness, and slitting to desired width. A similarly scaled process has now also been demonstrated for the non-magnetic Ni–9W alloy, on which superconductors have been demonstrated in length, and with critical currents approaching those on Ni–5W.

5.4.3 *Epitaxial Growth of Oxide Buffer Layers on NiW Substrates*

Buffer layers play several key functions on the RABiTS template including:

(1) Transfer of texture from the metal substrate to the (RE)BCO layer,
(2) A chemically inert surface for the nucleation and growth of the (RE)BCO,
(3) A barrier to prevent metal diffusion from the substrate to the (RE)BCO layer during the high temperature growth,
(4) A barrier to prevent oxidation of the metal substrate during processing, and
(5) Provide mechanical stability and adhesion of the (RE)BCO layer to the substrate.

To accomplish all these functions, the buffer layers must be matched as closely as possible in both the lattice parameters and the coefficient of thermal expansion to the alloy substrate and the (RE)BCO film. The buffer layers also need to be continuous, smooth, crack-free and dense, to provide effective chemical separation between the alloy substrate and the HTS film. Any contamination of the (RE)BCO layer with the elements from the substrate can degrade the superconductivity of the (RE)BCO materials. For instance, as little as 3% Ni substitution in the Cu site in YBCO reduces the critical temperature to below 77 K [65].

AMSC and collaborators at ORNL explored a variety of materials that would meet all of the buffer layer requirements and ultimately settled on a three layer combination of Y_2O_3/YSZ/CeO_2 deposited by physical vapor deposition (PVD), in particular by reactive magnetron sputtering. A cross-section TEM image of the buffer stack in a fully processed conductor is shown in Fig. 5.11, along with a table of typical values of the full width at half-maximum (FWHM) of the out-of-plane texture, $\Delta\chi$ and in-plane texture, $\Delta\phi$ peaks illustrating the sharpness of the texture in each of the layers. In this stack, each layer performs a distinct function. The Y_2O_3 layer deposited directly on the Ni-W substrate acts as a seed layer that replicates the texture of the Ni-W substrate, the YSZ functions as a barrier layer to prevent the diffusion of Ni and W to the (RE)BCO and CeO_2 serves as a "cap" layer which provides an optimized surface for the nucleation and growth of MOD-(RE)BCO. As shown in the table in Fig. 5.11, the Y_2O_3 seed layer has a significant sharpening of the texture over that observed in the Ni-W substrate, and this sharpness carries through to the YSZ and the CeO_2 layers. The texture sharpening, which is unique to the PVD Y_2O_3 layer is believed to arise from lattice strain introduced during the deposition process.

A variety of deposition techniques were explored for the epitaxial deposition of the buffer layers on the NiW RABiTS substrate. These include vacuum based processes such as PLD [66, 67], electron beam evaporation [68], MOCVD [69], rf and reactive sputtering [70–73], etc., and non-vacuum processes such as chemical solution deposition [74, 75]. Among these synthesis methods, chemical solution deposition is the most cost-effective, but sputtering yields the best quality film at reasonable rates to make it manufacturing-friendly.

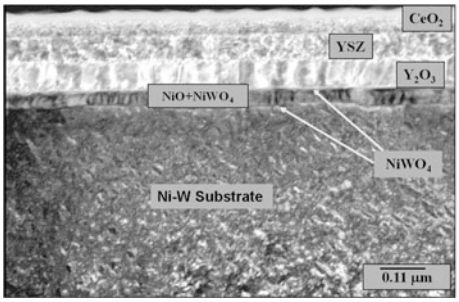

Layer	$\Delta\chi$	$\Delta\phi$
CeO_2	3.4	5.4
YSZ	2.9	5
Y_2O_3	2.9	5.3
Ni-W	7.2	6.3

Fig. 5.11 Cross-section TEM of fully buffered RABiTS after (RE)BCO processing showing the three layer buffer architecture along with a thin layer of adherent native Ni-W-Oxide formed during (RE)BCO processing. The *table* shows typical texture (FWHM) of the substrate and the three buffer layers

In the early R&D development, AMSC used rf-sputtering to deposit the oxide buffer layers. Although rf-sputtering of metal oxides produces highly textured, dense, films with excellent stoichiometry control and is applicable to a wide range of material compositions, the deposition rates are low since the low thermal conductivity of the oxide targets limits the plasma energy that can be used [25]. To circumvent this rate limiting problem, AMSC used reactive sputtering for the manufacturing process. In the reactive sputtering process, thin films of compounds are deposited on substrates by sputtering from metal targets in the presence of a reactive gas (H_2O, oxygen or nitrogen) usually mixed in with the process gas (such as Ar). Careful control of the reactive gas pressure in the sputter atmosphere is critical to controlling the film stoichiometry and the sputtering rates. While the stoichiometry control and the film densities for reactive sputtering are slightly inferior to rf-sputtering of oxide targets, the enhanced deposition rates accommodated by reactive sputtering make it a very attractive industrial process.

Deposition of Seed Layer One of the biggest materials challenges in the RABiTS template development was the deposition of the seed layer on the textured Ni-W alloy substrate. The primary role of the seed layer is to provide an ideal surface for the nucleation and growth of subsequent oxide layers while providing a perfect transfer of the biaxial texture in the Ni-W alloy. The vapor phase deposition of the metal oxide seed layer such as Y_2O_3 by reactive sputtering is typically carried out at a high temperature in the presence of oxygen, conditions which favor the formation of the native oxides of the Ni-W substrate.

A clear understanding of the stability regimes of these oxides relative to those of the oxides of Ni and W is essential. The Ni in the substrate oxidizes at a pO_2 higher than 10^{-12} mTorr, and the W oxidizes at a pO_2 higher than 10^{-14} mTorr. Any oxidation of the substrate disrupts the epitaxial nucleation of the seed layer leading to a degraded or random texture which propagates through the next layers. Hence, one of the key requirements of materials choice for a seed layer is the ability to nucleate and grow as a stoichiometric oxide at oxygen pressures where the substrate

components are thermodynamically stable. Y_2O_3 or CeO_2 are typically grown in a H_2O/H_2 atmosphere that produces an effective pO_2 in which Ni and W are stable against oxidation but the Ce and Y oxides are stable. In contrast, these materials cannot be grown on NiCr substrates since the Cr oxides are stable at much lower oxygen pressures than the Y and Ce oxides.

Based on the initial success in depositing epitaxial layers of CeO_2 or Y_2O_3 on Ni-based substrates, AMSC began developing the full buffer stack. However, it was found that occasionally, Y_2O_3 layers would nucleate *c*-axis oriented but with multiple in-plane textures. Around the same time, Cantoni et al. showed that the formation of a sulfur superstructure on the metal alloy surface promoted the formation of a single in-plane texture with these seed layer materials [76–78]. Using reflection high energy electron diffraction (RHEED) to monitor the nucleation and growth of epitaxial oxide films on textured Ni-substrates, they observed the formation of a c(2 × 2) sulfur superstructure on the textured Ni surface, prior to the nucleation of the epitaxial oxide as illustrated in Fig. 5.12. The c(2 × 2) type superstructure was found to provide a template which promoted the a single in-plane nucleation of the oxide seed layer as schematically illustrated for YSZ nucleation in Fig. 5.12. This c(2 × 2) superstructure, identified by Cantoni, formed as sulfur impurities in the Ni diffused to the surface as the substrate was heated in the PVD deposition process. Since the impurity level of S varies in the starting Ni material, this explained the variation AMSC observed in the early development work.

This groundbreaking work by Cantoni clearly showed the critical role the nano-scale substrate surface structure plays in controlling the epitaxial nucleation of these oxide layers. Such precise control of the surface structure posed a challenging

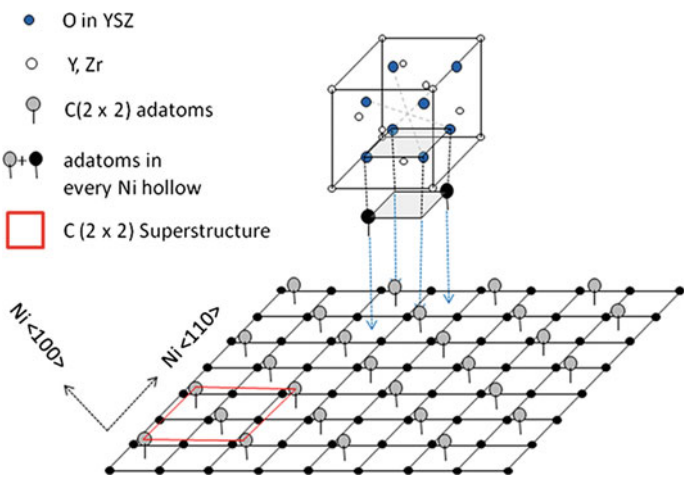

Fig. 5.12 Schematic illustration of a c(2 × 2) superstructure formed by adatoms mediating epitaxial growth of YSZ on (001) Ni surface (Based on model proposed by Cantoni et al. (based on Fig. 4 in [76])

problem in the R2R deposition process in which the nano-structure needs to be controlled over hundreds of square meters of substrate. The solution was a precise control of the impurity levels in the starting substrate material and development of a proprietary process that promotes a controlled, highly reproducible surface structure during the sputtering process over long lengths.

Once the importance of the nano-surface structure of the substrate was fully understood and processes were developed to precisely control c(2 × 2) super-structure, development of the YSZ barrier and CeO_2 cap layers were straight forward processes.

5.4.4 Epitaxial Growth of Thick YBCO Films

AMSC chose to develop the trifluoroacetate-based (TFA) MOD process rather than a vacuum-based approach for the superconductor layer since solution-based routes are significantly less expensive, the precursors are inexpensive with utilization rates of nearly 100% and the process can be readily scaled for a wide-web process. The TFA precursor was selected since the intermediate formation of BaF_2 during the processing prevents the formation of $BaCO_3$ which collects at grain boundaries, limiting the current in the final HTS film. Although solution-based coating processes are widely used in industry (i.e., photographic film, papers, etc.), they had never been used for the continuous deposition of thick, epitaxial, high quality electronic ceramic films over flexible, kilometer-length substrates. Thus, AMSC faced significant technical challenges to both develop the process and design the equipment necessary for low-cost manufacturing. AMSC's implementation of these processes is described below.

Precursor The TFA-based precursor was originally developed by Gupta et al. [39], and later refined by McIntyre et al. [40, 42], to avoid the formation of the stable $BaCO_3$ during the pyrolysis of the organic components. During the pyrolysis process, the thermodynamically stable barium oxyfluoride phase is formed rather than the detrimental $BaCO_3$, which is converted to the oxide by reaction with H_2O.

The original precursor was based on a methanol solution of the Y, Ba and Cu trifluoroacetate salts; however, AMSC made modifications, as discussed below, to increase the film thickness and reduce the processing time. In addition, composition changes were made to promote the formation of nanoparticles throughout the film and increase the flux pinning. AMSC's current precursor consists of a proprietary alcohol-based solution of Y, Dy, Ba and Cu trifluoroacetates and carboxylates along with a stabilizer.

Coating and Pyrolysis A standard industrial slot-die coating process was developed for coating the precursor on the RABiTS template. In the slot-die technique, a metered amount of precursor is dispensed on a moving template which is then passed into a low temperature oven to remove the solvent. This technique produces

a film with excellent thickness and compositional uniformity over the length and width of the template and excellent control of run-to-run variability.

The organic components of the dried film are removed in a separate pyrolysis process carried out in a moist oxygen atmosphere at a temperature around 400 °C, leaving a film comprised of copper oxide and RE-Ba oxyfluoride ((RE)BaOF) phases. The pyrolysis reduces the film thickness by over 50%, and generates extreme stress in the film which can lead to cracking and delamination. Additionally, gas evolution can also lead to blistering and film failure. In order to eliminate these defects, the original decomposition process, developed by McIntyre et al. [40, 42], required over 15 h to produce a 200 nm thick film on a small ($\sim 1 \times 1$ cm) single crystal substrate without defects.

Such long processing times and thin films are not compatible with high-rate, low-cost R2R manufacturing of high performance (thicker) films on long length flexible substrates. Thus AMSC focused on understanding the stress formation mechanisms throughout the pyrolysis process and subsequently modified the copper and rare earth chemistries to mitigate the stress, control gas evolution and accelerate the process time [41, 79–84]. These changes in the chemistry have enabled the routine deposition of films with a thickness of 1.2 μm (effective thickness of a 100% dense (RE)BCO film)) with a total pyrolysis time of less than 1 h.

Reaction The decomposed metal oxyfluoride film is converted to the (RE)BCO phase by reaction with H_2O and O_2 according to (5.1) and (5.2):

$$RE_nBa_mO_xF_y \xrightarrow{H_2O} (0.5n)RE_2O_3 + (m)BaF_2 + (y - 2m)HF(g) \tag{5.1}$$

$$0.5RE_2O_3 + 2BaF_2 + 3CuO \xrightarrow{H_2O/O_2} (RE)Ba_2Cu_3O_{7-x} + 4HF(g) \tag{5.2}$$

Since the (RE)BCO film must grow epitaxially, it is necessary that the initial nucleation occur at the textured template (CeO_2) surface within a narrow temperature range. The epitaxial growth then proceeds through the thickness as illustrated in Fig. 5.13 [81, 85]. During the growth process, untextured rare earth based nanoparticles, which are important for pinning (see below), must also form uniformly throughout the film thickness without disrupting the epitaxial (RE)BCO growth. As observed in the SEM images in Fig. 5.13, the film thickness reduces over 50% during this process. In order to insure the proper epitaxial growth, it is necessary to precisely control the (RE)BCO nucleation and growth kinetics, which depends on the equilibrium $K_{eq} \triangleq [HF]^4/[H_2O]^2$. Achieving a uniform growth rate requires precise control of the $H_2O(g)$ and HF(g) concentrations at the tape surface along both the length and width of the tape. With a short, stationary sample this is a relatively easy process; however, in a wide-web, R2R process it is a more challenging issue since the HF evolution changes along the length of the furnace and mixes with the process gas as it flows through the furnace [41]. If the [HF(g)] varies across the width of the web, the nucleation and growth rate will be affected,

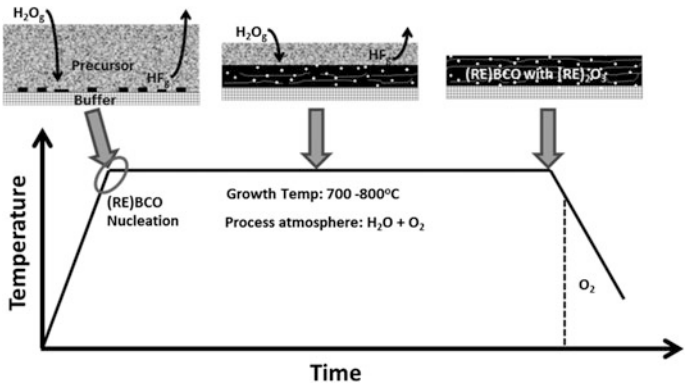

Fig. 5.13 Schematic illustration of the nucleation and growth of the (RE)BCO phase and RE_2O_3 nanoparticle formation as a function of temperature and process gas

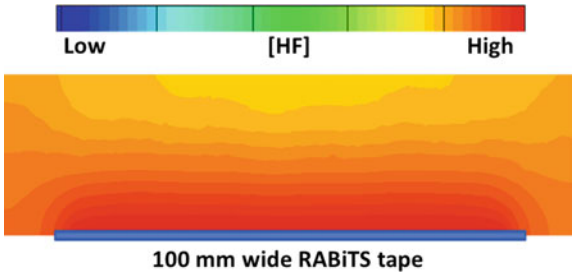

Fig. 5.14 Computational fluid dynamic model showing the HF(g) concentration across the width of a 100 mm wide MOD coated (RE)BCO RABiTS tape in the nucleation zone of the (RE)BCO growth process

resulting in an inhomogeneous (RE)BCO grain structure and subsequently large variations in the I_c of the HTS film. The solution to this challenge was a detailed study of the nucleation and growth kinetics and the use of computational fluid dynamic modeling, to design a 10 m long furnace in which the O_2, H_2O and HF concentrations can be independently and precisely controlled over both the width and length of the moving tape. Figure 5.14 shows the uniformity in the calculated [HF] concentration across the width of a 100 mm wide tape in the nucleation zone of a 10 m furnace. This approach has allowed the design of production scale furnaces that achieve growth rates exceeding 10 Å/s over the entire width of the wide-web RABiTS templates.

MOD has some advantages in the way grain-growth occurs, particularly when high angle grain boundaries are present in the RABiTS template. Unlike the vacuum-based growth processes, which have a columnar type growth of the (RE)

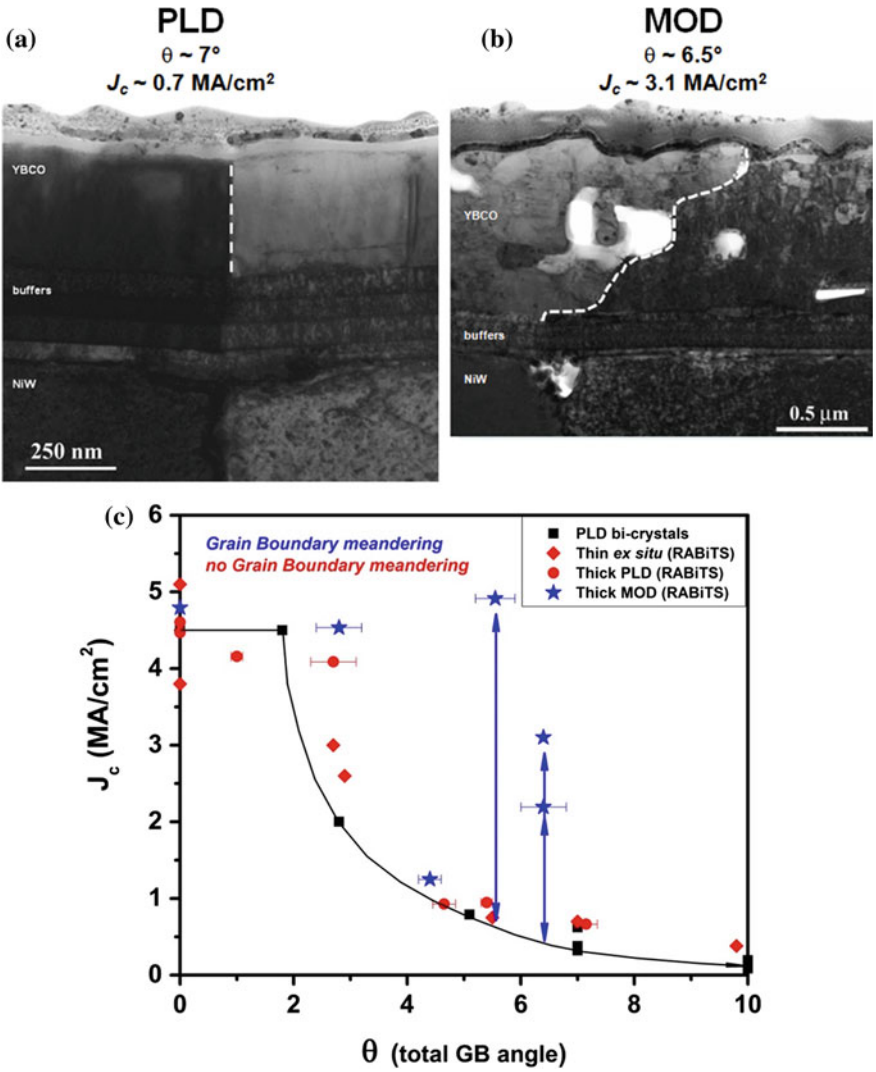

Fig. 5.15 TEM image of the growth modes of **a** PLD and **b** MOD (RE)BCO films across high angle boundaries and **c** the benefit of meandering grain boundaries on J_c [64]

BCO, the MOD process has a laminar type growth (as shown in Fig. 5.15a, b) [64]. This laminar growth allows the (RE)BCO grains to meander over the template grain boundaries, particularly as the film thickness increases. Figure 5.15c shows that the meandering grain boundary of the MOD (RE)BCO at least partially negates the current blocking effect of the high angle RABiTS template grain boundary, whereas the PLD (RE)BCO with the columnar grains shows a significant decrease in J_c across a similar grain boundary as predicted by the Dimos plot [17].

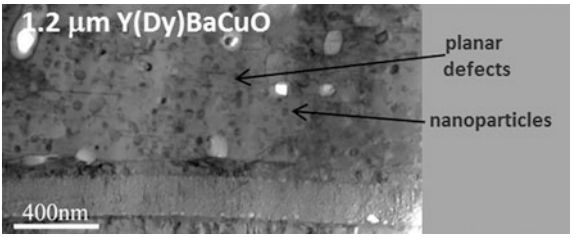

Fig. 5.16 Cross-sectional TEM micrograph of a 1.2 μm thick Y(Dy)BCO film deposited by the MOD process developed by AMSC

After the formation of the (RE)BCO phase, a thin Ag layer is deposited on the YBCO surface to provide passivation and a low resistance electrical contact, and then the (RE)BCO film is heated in an O_2 atmosphere to oxygenate the (RE)BCO, thereby forming the orthorhombic superconducting phase.

The final HTS layer, shown in the TEM image in Fig. 5.16 consists of a (RE)BCO matrix containing a uniform distribution of rare earth-based nanoparticles which pin magnetic flux lines and so enhance the critical current in the presence of magnetic fields oriented perpendicular to the tape surface, and also a distribution of planar defects that enhance the critical current in magnetic fields oriented in the plane of the tape.

5.4.5 Wire Fabrication

The last step in the 2G HTS wire manufacturing process is to convert the wide web into individual narrow wires. This is done by roll slitting (Fig. 5.6) the wide strip into multiple strips of generally 4–10 mm width, depending on the application. These individual strips are then laminated (Fig. 5.6) between two metal strips to form a robust, hermetically sealed composite wire architecture, shown in Fig. 5.17, that is impervious to environmental degradation; electrically stable during quenches and mechanically strong enough to withstand the rigors of the cable and coil fabrication processes, repetitive cooling and heating cycles, and the stresses experienced in application [86].

The lamination process also provides the flexibility to customize the electrical or mechanical properties of the final wire depending on the material chosen for the metal strips. Typically, high conductivity copper is used for wire intended for conduction-cooled lower temperature coil applications, while brass and stainless steel are favored in liquid nitrogen ac applications such as cables and resistive fault current limiters [87], respectively. In AMSC's 2G HTS wire, which uses a Ni–5 at.% W or Ni–9 at.% W substrate, the mechanical properties are predominantly determined by the properties of the lamina and solder fillet dimensions.

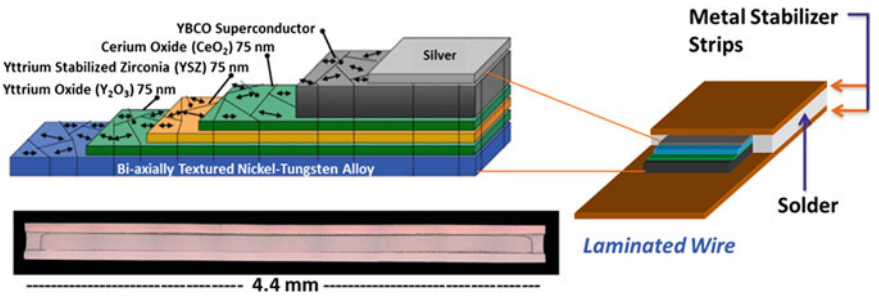

Fig. 5.17 Schematic illustrations of AMSC's 2G insert and laminated wire architectures. A TEM micrograph of the insert cross-section is shown in the *upper right* and an optical micrograph of a cable wire transverse cross-section is shown in the *bottom left* (*courtesy* AMSC)

5.5 On-Going R&D

The performance of today's 2G HTS wire is suited for several applications, but broad market penetration of this technology necessitates that the cost associated with these materials be reduced. Therefore, most of the R&D focus at AMSC revolves around various approaches to reduce the effective wire cost or price-performance metric, measured in $/kA-m (dollars per kiloampere-meter). The main areas of focus include increasing capacity (to drive down manufacturing cost through volume production), increasing performance and developing more cost-effective deposition technologies.

With an eye toward high capacity manufacturing, right from the outset of this technology, AMSC has focused on a wide-web manufacturing approach. In the early days of scaling up the RABiTS process, AMSC's R&D focused not only on processing longer strips, but also wider strips. This approach lends itself to capacity expansion without significantly increasing the equipment footprint or capital equipment cost. The AMSC process has moved from the initial 1 cm wide strips, which are still used by some manufacturers, to the current 4.6 cm wide strips which are slit to the required wire widths. The next step in this scale-up will be a 10 cm wide strip for which all the process equipment currently in use is designed to handle, and long term R&D will focus on increasing the strip width further. The increased capacity provides a pathway to meet the demands of large projects that require large quantities of wire, and as the quantities of wire being used increases, the cost will naturally come down.

Any improvement in critical current directly affects the effective cost of the 2G HTS wire to the customer, as it reduces the amount of wire required to build a device. The improvements are not focused just on the 77 K sf I_c but also at the operating temperatures in the 4–50 K range in a few tesla magnetic field. In the last

few years, significant improvements have been achieved in the performance of commercial long length wires with the I_c more than doubling in the 4–50 K range. Additional increases in performance will come from a combination of enhanced pinning through skillful engineering of the pinning microstructure, and increases in thickness of the HTS layer.

Most of the improvements in pinning in all the different superconductor deposition methods have resulted from the introduction of correlated defects, oriented along the *c*-axis, and point defects. These have been accomplished using introduction of twin boundaries, addition of nanoparticles in the HTS layer, introduction of *ab*-planar defects, and in situ growth of $BaZrO_3$ or $BaHfO_3$ nano-columns [88]. These approaches to engineer the pinning microstructure have been particularly effective to enhance properties at low temperatures and high fields, with wire performance approaching 1000 A/cm-width in magnetic fields (H//c) around 2T at 30 K. Controlling these nano-scale engineered pinning microstructures over kilometer lengths of wire processed is still a manufacturing challenge.

While these recent advances are being transferred to the manufacturing lines, other avenues for additional flux pinning enhancement are continuously being explored. One area that has shown promise is irradiation by ions ranging from protons to gold [89]. Recent work has shown that such irradiation processes can more than double the critical current of 2G HTS production wire at temperatures and fields relevant to rotating machines, while adding minimal cost to the wire [90].

Another potential area of cost reduction is the development of solution-based buffer layers for the RABiTS substrates. Solution processing is an inherently high volume low-cost approach which is compatible with the wide-web manufacturing used at AMSC. The process offers significant advantages over the PVD processes currently in use, such as 100% material utilization, fast coating rates, uniform coating thickness over large widths, and no need for expensive high vacuum equipment. The feasibility of this approach has already been demonstrated with reasonable success for the barrier layer using lanthanum zirconate [91]; however, the development of a solution-based seed and cap layers is still at a very early stage. In case of the seed layer, the PVD Y_2O_3 seed layer shows an enhancement in texture over the metal substrate. The fundamentals of epitaxial nucleation that contribute to this phenomenon are not fully understood at the current time. The challenge for a solution-based process would be to produce similar texture improvements, and that has only been partially demonstrated with lanthanum niobate and lanthanum tantalate films [92]. In case of the cap layer, the PVD CeO_2 has been tailored to be ideally suitable for the nucleation and growth of the MOD-HTS layer. The solution processed CeO_2 layer, while epitaxial, has yet to demonstrate that kind of suitability. Additional R&D is required to fill these rather large gaps in understanding for solution buffers to become a viable cost-cutting alternative in 2G wires.

5.6 2G HTS Wire Manufacturers, Wire Market and Needs

Over 25 years after the discovery of the HTS materials, 2G HTS wire is ready to be deployed in the first commercial applications and begin to fulfill the promise of a revolution in the way electricity is generated, delivered and consumed. Although the development of the HTS wire technology has been a long path, it is similar to other revolutionary, high-risk material-based technologies, such as optical fibers and semiconductors, which required two or more decades to move from the laboratory to the commercial market.

Today there are around 10 commercial companies involved in manufacturing of 2G HTS wire, as shown in Fig. 5.18. AMSC and SuperPower (now fully owned by Furukawa) have established manufacturing facilities and have produced most of the 2G HTS wire used to date. The other companies are either in the early stages of establishing manufacturing facilities or still developing the processes.

The applications for which 2G HTS wires are targeted can be separated into two groups. The first includes existing applications, such as cables, motors, generators, transformers and magnets, where 2G HTS wire replaces conventional resistive copper conductors. The second group encompasses new technologies that cannot be addressed with conventional conductors, such as superconducting fault-current limiters (SFCLs), superconducting magnetic energy storage (SMES) and certain defense applications. Penetrating an existing market is challenging and requires that the 2G HTS wire has both a performance and economic advantage over the established conventional technologies. Although today's 2G HTS wire can meet or exceed the performance requirements for many applications, the cost of the wire

Fig. 5.18 2G HTS wire manufacturing is being pursued by companies in the United States, Europe and Asia. Most commercial wire has been produced by AMSC and SuperPower, while the other companies are either in the early stages of establishing manufacturing facilities or still developing the manufacturing processes

still leaves it at an economic disadvantage in many cases. However, as the manufacturing capacity ramps up, manufacturing capability improves and performance continues to increase, this economic difference is beginning to decrease.

In contrast, new applications, for which there are no conventional solutions, are less sensitive to cost concerns and are likely to be the first products accepted in the commercial market. As these markets evolve, they will help drive down the cost of the 2G HTS wire to a level where it can compete with established technologies.

AMSC has chosen to focus in the near-term on providing wire to applications in the electric utility and defense areas where the value-proposition of the HTS system is compelling. Brief descriptions of the major applications AMSC is pursuing are described below.

5.6.1 Fault Current Limiters

Current surges or fault currents in the electrical grid are becoming more common and destructive, particularly in urban areas, as new power generation sources are added to meet the world's growing energy demands. As the severity of these fault currents increases, they are approaching levels that exceed the safe operating limits of conventional circuit breakers and other grid equipment.

The unique properties of 2G HTS wire have allowed the development of a SFCL technology that effectively addresses this problem [93–96]. In the "resistive" SFCL (the most common design), a fault current (one exceeding the critical current) instantly forces the HTS wire to transition to a very high resistance state, effectively shunting the current into a higher resistance layer, thereby reducing the amplitude of the fault current. Once the fault current is cleared, the 2G HTS wire-based SFCL returns to its normal superconducting state and is ready for the next fault. AMSC manufactures a customized FCL wire that utilizes a high resistance stainless steel laminate to optimize the wire's overall resistance and its capacity to absorb heat generated during the fault. Alternate SFCL designs, based on inductive concepts are also being developed.

Although SFCL's not are a huge volume market for 2G HTS wire, they are anticipated to be one of the first products installed in the commercial electrical grid. Currently SFCL systems, based on AMSC's 2G HTS wire, are available from Nexans [97].

5.6.2 Cables

Compact, high-efficiency, HTS-based power cables are envisioned as an important new technology for boosting grid capacity and transmitting large amounts of electrical power over long distances and represent one of the largest potential commercial markets for 2G HTS wire. The engineering critical current density (J_c) of today's 2G HTS wire is nearly 100 times greater than that of conventional copper

conductors; thus HTS power cables can carry several times as much power as conventional copper cables of the same size. Additionally, since HTS-based cables do not produce the resistively generated heat or strong electromagnetic fields associated with conventional copper cables, they can be readily installed in compact spaces near other underground infrastructures. For this reason, 2G HTS cables are viewed as a near-term, cost-effective solution for delivering power over short distances in congested urban areas where the right-of-way is limited and siting and installation of conventional cables is expensive and difficult.

The technical feasibility and reliability of HTS-based cables has been demonstrated in a number of government supported projects around the world over the past decade, with the longest being a 1 km, 10 kV, 40 MVA cable, based on 1G HTS wire, installed by Nexans, Karlsruhe Institute of Technology and RWE in Essen Germany and energized in May 2014 [98–103].

AMSC, Southwire, Consolidated Edison and ORNL, with support from the U.S. Department of Homeland Security, have developed a novel fault-current limiting cable technology that combines the high current capacity of a HTS cable with inherent FCL functionality [104, 105]. This unique technology provides a means to increase the resiliency of the electric grid to disruptive faults (from either natural causes or intentional acts of vandalism). This technology is currently being deployed in the Consolidated Edison grid in New York, and a 3 mile long cable system is planned for installation in Commonwealth Edison's Chicago grid [106].

5.6.3 Rotating Machines

Another potentially large market for 2G HTS wire is in rotating machines, such as motors and generators. Typically these HTS machines are designed with HTS rotor field coils, which operate with dc currents, while the stator coils, which experience high ac currents, are made of copper. A major advantage of these HTS-based machines is that they can generate a very high torque in a compact size, allowing the design of high efficiency, light-weight, compact machines.

The first large-scale demonstration of such a HTS-based machine was a 36.5 MW HTS ship propulsion motor (based on 1G HTS wire) produced by AMSC and Northrop-Grumman, in 2009, for the US Navy, which has a long-term goal of converting to an all-electric fleet. The motor, which is less than half the size of a conventional motor, would reduce a ship's weight by over 200 metric tons. Such compact, efficient electric propulsion systems will enable flexibility in ship design and more efficient integration of a ship's energy-usage. This will allow an increase in the cargo or passenger space or, in the case of the military, additional or more powerful weapon systems. Additionally, the elimination of rotor losses leads to higher efficiency, especially under partial-load conditions, resulting to longer cruising ranges and greater fuel economy.

The need for clean, carbon-free renewable energy has fueled rapid growth of wind power and large off-shore wind farms. The economics of off-shore wind farm

installations favor wind turbines with the highest possible power ratings. However, higher power ratings increase the size and weight of conventional turbines, making installation more difficult and costly. Thus there is a growing interest in the development of HTS-based generators that can be used in off-shore wind turbines rated at 10 MW and greater. The first demonstration of a full-scale HTS-based wind turbine is a number of years off, with current activities focused on testing of sub-scale designs, verification of the cryogenic cooling systems and most importantly reducing the total wire cost through improvements in performance to reduce the amount of wire needed and through reduction in manufacturing costs.

5.6.4 Other Applications

2G HTS wire is also being developed for a variety of defense applications including power and degaussing cables, motors and generators. Although these applications do not represent a large market, they are performance rather than cost driven and will likely be among the first uses of 2G HTS wire. Other applications, which AMSC considers longer-term or niche markets, include medical or industrial MRI's and NMR's, high field research magnets, magnetic levitation, transformers, superconducting magnetic energy storage (SMES), fusion, directed energy weapons and current leads.

5.7 Summary

The discovery of the HTS materials in the late 1980s provided the foundation for today's superconductor wire technology. This initial discovery rapidly lead to the basic research focused on understanding the vortex physics that controls the critical current density of the HTS materials, and the complex chemistry and material science of the (RE)BCO film growth. This basic science research slowly evolved into the applied research and development directed at innovative manufacturing technologies; the development of high-performance, robust, long length conductors; the development of concepts for the use of these new HTS materials and finally the design for HTS-based electric power equipment. Now after nearly three decades of research and development, the HTS wire technology has achieved the maturity level where it can start to be deployed in the "real-world" applications. As the commercialization of this revolutionary technology progresses we may finally see the broad impact envisioned at the time of its discovery.

The successful development of this technology at AMSC required assembling a diverse team of scientists and engineers who thought "out-of-the-box" and were not confined by conventional thinking. The ASMC team was built around key people with backgrounds in chemistry, physics, material science, mathematics, ceramics,

geology, computer modeling, mechanical and electrical engineering. This combination of scientists and engineers was able to address the fundamental science of the materials, develop innovative manufacturing processes and equipment and identify applications and develop product specifications. The successful development of such challenging technologies requires contributors who are experts in specific scientific or engineer disciplines, but can also effectively work in related fields.

References

1. M.W. Rupich, E.E. Hellstrom, Bi-Ca-Sr-Cu-O HTS Wire, in *100 Years of Superconductivity*, eds. by H. Rogalla, P.H Kes (CRC Press, Boca Raton, 2012), Chap. 11.4
2. http://ir.amsc.com/releasedetail.cfm?ReleaseID=725019
3. http://ir.amsc.com/releasedetail.cfm?ReleaseID=736299
4. S.H. Sohn, J.H. Lim, B.M. Yang, S.K. Lee, H.M. Jang, Y.H. Kim, H.S. Yang, D.L. Kim, H. R. Kim, Y.J. Won, S.D. Hwang, Design and development of 500 m long HTS cable system in the KEPCO power grid, Korea. Physica C: Superconduct. **470**, 1567 (2010)
5. C. Ryu, H. Jang, C. Choi, Y. Kim, H. Kim, Current status of demonstration and commercialization of HTS cable system in grid in Korea, in *Proceedings of 2013 IEEE International Conference on Applied Superconductivity and Electromagnetic Devices*, Beijing, China, 25–27 Oct 2013, ID3231, p. 539
6. http://www.lscns.com/pr/news_read.asp?idx=2953&pageno=1&kType=&kWord
7. S. Jin, R.C. Sherwood, R.B. van Dover, T.H. Tiefel, D.W. Johnson Jr, High T_C superconductors-composite wire fabrication. Appl. Phys. Lett. **51**, 203 (1987)
8. Superconductivity: Is the Party Over? Science, **244**, 914 (1989)
9. http://www.nytimes.com/1989/06/06/us/superconductors-showing-a-flaw-that-dims-hope.html
10. T. Hikata, K. Sato, H. Hitotsuyanagi, Ag-sheathed Bi-Pb-Sr-Ca-Cu-O superconducting wires with high critical current density. Jpn. J. Appl. Phys. **L28**, 82 (1989)
11. L.N. Bulaevskii, J.R. Clem, L.I. Glazman, A.P. Malozemoff, Model for the low-temperature transport of *Bi*- based high-temperature superconducting tapes. Phys. Rev. B **45**, 2545 (1992)
12. L.N. Bulaevskii, L.L. Daemen, M.P. Maley, J.Y. Coulter, Limits to the critical current in high-T_c superconducting tapes. Phys. Rev. B **48**, 13798 (1993)
13. K. Sato, Bismuth-based oxide (BSCCO) high-temperature superconducting wires for power grid applications: properties and fabrication, in *Superconductors in the Power Grid*, ed. by C. Rey (Elsevier, Amsterdam, 2015), Chap. 3
14. S.L. Cooper, K.E. Gray, in *Physical Properties of High Temperature Superconductors*, ed. by D.M. Ginsberg (World Scientific, Singapore, 1994), vol. IV, p. 61
15. Y. Jia, U. Welp, G.W. Crabtree, W.K. Kwok, A.P. Malozemoff, M.W. Rupich, S. Fleshler, J.R. Clem, Microstructure dependence of the c-axis critical current density in second-generation YBCO tapes. J. Appl. Phys. **110**(8), 083923 (2011)
16. M. Tinkham, *Introduction to Superconductivity*, 2nd edn. (McGraw-Hill, New York, 1996)
17. D. Dimos, P. Chaudhari, J. Mannhart, Superconducting transport properties of grain boundaries in $YBa_2Cu_3O_7$ bicrystals. Phys. Rev. B **41**, 4038 (1990)
18. H. Hilgenkamp, J. Mannhart, Grain boundaries in high-T_c superconductors. Rev. Mod. Phys. **74**, 485 (2002)
19. Y. Iijima, N. Tanabe, Y. Ikeno, O. Kohno, Biaxially aligned $YBa_2Cu_3O_{7-x}$ thin film tapes. Physica C: Superconduct. **185**, 1959 (1991)
20. Y. Iijima, N. Tanabe, O. Kohno, Y. Ikeno, In-plane aligned $YBa_2Cu_3O_{7-x}$ thin films deposited on polycrystalline metallic substrates. Appl. Phys. Lett. **60**, 769 (1992)

21. Y. Iijima, K. Kakimoto, M. Kimura, K. Takeda, T. Saitoh, Reel to reel continuous formation of Y-123 coated conductors by IBAD and PLD method. IEEE Trans. Appl. Superconduct. **11**, 2816 (2001)
22. M.W. Rupich, Second-generation (2G) coated high-temperature superconducting cables and wires for power grid applications, in *Superconductors in the Power Grid*, ed. by C. Rey (Elsevier, Amsterdam, 2015), Chap. 4
23. D.P. Norton, A. Goyal, J.D. Budai, D.K. Christen, D.M. Kroeger, E.D. Specht, Q. He, B. Saffian, M. Paranthaman, C.E. Klabunde, D.F. Lee, B.C. Sales, F.A. List, Epitaxial $YBa_2Cu_3O_7$ on biaxially textured nickel (001): an approach to superconducting tapes with high critical current density. Science **274**, 755 (1996)
24. E.D. Specht, A. Goyal, D.F. Lee, F.A. List, D.M. Kroeger, M. Paranthaman, R.K. Williams, D.K. Christen, Cube-textured nickel substrates for high-temperature superconductors. Superconduct. Sci. Technol. **11**, 945 (1998)
25. M.P. Goyal, U. Schoop, The RABiTS approach: using rolling-assisted biaxially textured substrates for high-performance YBCO superconductors. MRS Bull. **29**, 552 (2004)
26. P.N. Ardent, S.R. Foltyn, Biaxially textured IBAD-MgO templates for YBCO-coated conductors. MRS Bull. **29**, 543 (2004)
27. Y. Iijima, K. Kakimoto, Y. Yamada, T. Izumi, T. Saitoh, Y. Shiohara, Research and development of biaxially textured IBAD-GZO templates for coated superconductors. MRS Bull. **29**, 564 (2004)
28. T. Kato, Y. Iijima, T. Muroga, T. Saitoh, T. Hirayama, I. Hirabayashi, Y. Yamada, T. Izumi, Y. Shiohara, Y. Ikuhara, TEM observations of $Gd_2Zr_2O_7$ films formed by the ion-beam-assisted deposition method on an Ni-based alloy. Physica C: Superconduct. **392–396**, 790 (2003)
29. C.P. Wang, K.B. Do, M.R. Beasley, T.H. Geballe, R.H. Hammond, Deposition of in-plane textured MgO on amorphous Si_3N_4 substrates by ion-beam-assisted deposition and comparisons with ion-beam-assisted deposited yttria-stabilized-zirconia. Appl. Phys. Lett. **71**, 2955 (1997)
30. X. Xiong, S. Kim, K. Zdun, S. Sambandam, A. Rar, K.P. Lenseth, V. Selvamanickam, Progress in high throughput processing of long-length, high quality, and low cost IBAD MgO buffer tapes at SuperPower. IEEE Trans. Appl. Superconduct. **19**, 3319 (2009)
31. K.P. Ko, H.S. Ha, H.K. Kim, K.K. Yu, R.K. Ko, S.H. Moon, S.S. Oh, C. Park, S.I. Yoo, Fabrication of highly textured IBAD-MgO template by continuous reel-to-reel process and its characterization. Physica C: Superconduct. **463–465**, 564 (2007)
32. S. Hanyu, C. Tashita, T. Hayashida, Y. Hanada, K. Morita, Y. Sutoh, N. Nakamura, H. Kutami, M. Igarashi, K. Kakimoto, Y. Iijima, T. Saitoh, Long-length IBAD-MgO buffer layers for high performance RE-123 coated conductors by a large ion beam source. Physica C: Superconduct. **470**, 1227 (2010)
33. M. Paranthaman, T. Aytug, D.K. Christen, P.N. Arendt, S.R. Foltyn, J.R. Groves, L. Stan, R. F. DePaula, H. Wang, T.G. Holesinger, Growth of thick $YBa_2Cu_3O_{7-\delta}$ films carrying a critical current of over 230 A/cm on single $LaMnO_3$-buffered ion-beam assisted deposition MgO substrates. J. Mater. Res. **18**, 2055 (2003)
34. K. Hasegawa, K. Fujino, H. Mukai, M. Konishi, K. Hayashi, K. Sato, S. Honjo, Y. Sato, H. Ishii, Y. Iwata, Biaxially aligned YBCO film tapes fabricated by all pulsed laser deposition. Appl. Superconduct. **4**, 487 (1996)
35. M. Dürrschnabel, Z. Aabdin, V. Große, M. Bauer, G. Sigl, W. Prusseit, O. Eibl, Growth of biaxially-textured MgO buffer layers by inclined substrate deposition. Phys. Procedia **36**, 1546 (2012)
36. M. Bauer, R. Metzger, R. Semerad, P. Berberich, H. Kinder, Inclined substrate deposition by evaporation of magnesium oxide for coated conductors. MRS Proc. **585**, 35 (1999)
37. N.M. Strickland, N.J. Long, E.F. Talantsev, P. Hoefakker, J.A. Xia, M.W. Rupich, W. Zhang, X. Li, T. Kodenkandath, Y. Huang, Nanoparticle additions for enhanced flux pinning in YBCO HTS films. Current Appl. Phys. **8**, 372 (2008)

38. Y. Chen, V. Selvamanickam, Y. Zhang, Y. Zuev, C. Cantoni, E. Specht, M.P. Paranthaman, T. Aytug, A, Goyal, D. Lee, Enhanced flux pinning by $BaZrO_3$ and $(Gd,Y)_2O_3$ nanostructures in metal organic chemical vapor deposited GdYBCO high temperature superconductor tapes. Appl. Phys. Lett. **94**, 062513 (2009)
39. R.J. Gupta, E.I. Cooper, E.A. Giess, J.I. Landman, B.W. Hussey, Superconducting oxide films with high transition temperature prepared from metal trifluoroacetate precursors. Appl. Phys. Lett. **52**, 2077 (1988)
40. P.C. McIntyre, M.J. Cima, M.F. Ng, Metalorganic deposition of high-Jc Ba2YCu3O_{7-x} thin films from trifluoroacetate precursors onto (100) $SrTiO_3$. J. Appl. Phys. **68**, 4183 (1990)
41. M.W. Rupich, D.T. Verebelyi, W. Zhang, T. Kodenkandath, X. Li, Metalorganic deposition of YBCO films for second-generation high-temperature superconductor wires. MRS Bull. **29**, 572 (2004)
42. P.C. McIntyre, M.J. Cima, Heteroepitaxial growth of chemically derived *ex situ* $Ba_2YCu_3O_{7-x}$ thin films. J. Mater. Res. **9**, 2219 (1994)
43. M. Yoshizumi, T. Nakanishi, J. Matsuda, K. Nakaoka, Y. Sutoh, T. Izumi, Y. Shiohara, Crystal growth of YBCO coated conductors by TFA–MOD method. Physica C: Superconduct. **468**, 1531 (2008)
44. X. Obradors, T. Puig, S. Ricart, M. Coll, J. Gazquez, A. Palau, X. Granados, Growth, nanostructure and vortex pinning in superconducting $YBa_2Cu_3O_7$ thin films based on trifluoroacetate solutions. Superconduct. Sci. Technol. **25**, 123001 (2012)
45. D. Dijkkamp, T. Venkatesan, X.D. Wu, S.A. Shaheen, N. Jisrawi, Y.H. Min-Lee, W.L. McLean, M. Croft, Preparation of Y-Ba-Cu oxide superconductor thin films using pulsed laser evaporation from high Tc bulk material. Appl. Phys. Lett. **51**, 619 (1987)
46. S.R. Foltyn, H. Wang, L. Civale, Q.X. Jia, P.N. Arendt, B. Maiorov, Y. Li, M.P. Maley, J.L. MacManus-Driscoll, Overcoming the barrier to 1000 A/cm width superconducting coatings. Appl. Phys. Lett. **87**, 162505 (2005)
47. H.M. Manasevit, Single-crystal Gallium Arsenide on insulating substrates. Appl. Phys. Lett. **12**, 156 (1968)
48. V. Selvamanickam, G. Carota, M. Funk, N. Vo, P. Haldar, U. Balachandran, M. Chudzik, P. Arendt, J.R. Groves, R. DePaula, B. Newnam, High-current Y–Ba–Cu–O coated conductor using metal organic chemical-vapor deposition and ion-beam-assisted deposition. IEEE Trans. Appl. Superconduct. **19**, 3379 (2001)
49. P. Berberich, B. Utz, W. Prusseit, H. Kinder, Homogeneous high quality $YBa_2Cu_3O_7$ films on 3″ and 4″ substrates. Physica C: Superconduct. **219**, 497 (1994)
50. S.S. Oh, H.S. Ha, H.S. Kim, R.K. Ko, K.J. Song, D.W. Ha, T.H. Kim, N.J. Lee, D. Youm, J. S. Yang, H.K. Kim, K.K. Yu, S.H. Moon, K.P. Ko, S.I. Yoo, Development of long-length SmBCO coated conductors using a batch-type reactive co-evaporation method. Superconduct. Sci. Technol. **21**, 034003 (2008)
51. T. Ohnishi, J.-U. Huh, R.H. Hammond, W. Jo, High rate in situ $YBa_2Cu_3O_7$ film growth assisted by liquid phase. J. Mater. Res. **19**, 977 (2004)
52. J.L. MacManus-Driscoll, A. Kursumovic, B. Maiorov, L. Civale, Q.X. Jia, S.R. Foltyn, H. Wang, $YBa_2Cu_3O_7$ Coated conductor grown by hybrid liquid phase epitaxy. IEEE Trans. Appl. Superconduct. **17**, 2537 (2007)
53. S.H. Moon, Recent progress of 2G superconducting wire at SuNAM. Presentation at the International Workshop on coated Conductors for Applications 2014, Jeju, Korea, 2 Dec 2014
54. M.W. Rupich, X. Li, S. Sathyamurthy, C.L.H. Thieme, K. DeMoranville, J. Gannon, S. Fleshler, Second generation wire development at AMSC. IEEE Trans. Appl. Superconduct. **23**, 6601205 (2013)
55. X. Li, M.W. Rupich, C.L.H. Thieme, M. Teplitsky, D. Buczek, E. Siegal, D. Tucker, J. Schreiber, K. DeMoranville, J. Inch, R. Savoy, S. Fleshler, The development of second generation HTS wire at American superconductor. IEEE Trans. Appl. Superconduct. **19**, 3231 (2009)

56. J.B. Goyal, D.M. Kroeger, D. Norton, E.D. Specht, D.K. Christen, Preparing biaxially textured metal alloy article; superconductors, United States Patent No. 5,741,377 (1998)
57. V. Goler, G. Sachs, Walz und Rekristallizationstextur regular-flachenzentrierter Metalle III, IV. Z. Angew. Phys. **59**, 477 (1929)
58. P.C.J. Gallagher, The influence of alloying, temperature and related effects on the stacking fault energy. Met. Trans. **1**, 2429 (1970)
59. S.L. Shang, C.L. Zacherl, H.Z. Fang, Y. Wang, Y. Du, Z.K. Liu, Effects of alloying element and temperature on the stacking fault energies of dilute Ni-base superalloys. J. Phys: Condens. Matter **24**, 505403 (2012)
60. R.M. Bozorth, *Ferromagnetism* (D. van Nostrand, New York, 1951)
61. R. Huhne, J. Eickemeyer, V.S. Sarma, A. Guth, T. Thersleff, J. Freudenberger, O. de Haas, M. Weigand, J.H. Durrell, L. Schultz, B. Holzapfel, Application of textured highly alloyed Ni–W tapes for preparing coated conductor architectures. Superconduct. Sci. Technol. **23**, 034015 (2010)
62. L. Delannay, Observation and modelling of grain interactions and grain subdivision in rolled cubic polycrystals. Ph.D. Thesis, Catholic University, Leuven, May 2001
63. F.J. Humphreys, M. Hatherley, *Recrystallization and Related Annealing Phenomena*, 2nd edn. (Elsevier, Oxford, 2004), Chap. 12
64. D.M. Feldmann, T.G. Holesinger, R. Feenstra, C. Cantoni, W. Zhang, X. Li, M. Rupich, A. Malozemoff, A. Gurevich, D.C. Larbalestier, Grain orientations and grain boundary networks of $YBa_2Cu_3O_{7-\delta}$ films deposited by metalorganic and pulsed laser deposition on biaxially textured Ni–W substrates. J. Mater. Res. **21**, 923 (2006)
65. J.M.S. Skakle, Crystal chemical substitutions and doping of $Yba_2Cu_3O_x$ and related superconductors. Mater. Sci. Eng. **R23**, 1 (1998)
66. G.D.P. Norton, J.D. Budai, M. Paranthaman, E D. Specht, D.M. Kroeger, D.K. Christen, Q. He, B. Saffian, F.A. List, D.F. Lee, P.M. Martin, C.E. Klabunde, E. Hartfield, V.K. Sikka, High critical current density superconducting tapes by epitaxial deposition of $YBa_2Cu_3O_x$ thick films on biaxially textured metals. Appl. Phys. Lett. **69**, 1795 (1996)
67. Q. He, D.K. Christen, J.D. Budai, E.D. Specht, D.F. Lee, A. Goyal, D.P. Norton, M. Paranthaman, F.A. List, D.M. Kroeger, Deposition of biaxially-oriented metal and oxide buffer-layer films on textured Ni tapes: new substrates for high-current, high-temperature superconductors. Physica C: Superconduct. **275**, 155 (1997)
68. M. Paranthaman, D.F. Lee, A. Goyal, E.D. Specht, P.M. Martin, X. Cui, J.E. Mathis, R. Feenstra, D.K. Christen, D.M. Kroeger, Growth of biaxially textured RE_2O_3 buffer layers on rolled-Ni substrates using reactive evaporation for HTS-coated conductors. Superconduct. Sci. Tech. **12**, 319 (1999)
69. M.N. Molodyk, S. Street, L. Castellani, A. Ignatiev, All-MOCVD technology for coated conductor fabrication. IEEE Trans. Appl. Superconduct. **21**, 3175 (2011)
70. F.A List, A. Goyal, M. Paranthaman, D.P Norton, E.D Specht, D.F Lee, D.M Kroeger, High Jc YBCO films on biaxially textured Ni with oxide buffer layers deposited using electron beam evaporation and sputtering. Physica C: Superconduct. **302**, 87 (1998)
71. D.P. Norton, A. Goyal, J.D. Budai, D.K. Christen, D.M. Kroeger, E.D. Specht, Q. He, B. Saffian, M. Paranthaman, C.E. Klabunde, D.F. Lee, B.C. Sales, F.A. List, Epitaxial $YBa_2Cu_3O_7$ on biaxially textured nickel (001): an approach to superconducting tapes with high critical current density. Science **274**, 755 (1996)
72. T. Aytug, M. Paranthaman, B.W. Kang, S. Sathyamurthy, A. Goyal, D.K. Christen, La0.7Sr0.3MnO3: A single, conductive-oxide buffer layer for the development of $YBa_2Cu_3O_{7-\delta}$ coated conductors. Appl. Phys. Lett. **79**, 2205 (2001)
73. T. Aytug, J.Z. Wu, C. Cantoni, D.T. Verebelyi, E.D. Specht, M. Paranthaman, D.P. Norton, D.K. Christen, R.E. Ericson, C.L. Thomas, Growth and superconducting properties of $YBa_2Cu_3O_{7-\delta}$ films on conductive SrRuO3 and $LaNiO_3$ multilayers for coated conductor applications. Appl. Phys. Lett. **76**, 760 (2000)
74. S. Sathyamurthy, M. Paranthaman, H.Y. Zhai, S. Kang, T. Aytug, C. Cantoni, K.J. Leonard, E.A. Payzant, H.M. Christen, A. Goyal, X. Li, U. Schoop, T. Kodenkandath, M.W. Rupich,

Chemical solution deposition of lanthanum zirconate barrier layers applied to low-cost coated-conductor fabrication. J. Mater. Res. **19**, 2117 (2004)
75. K. Knoth, R. Hühne, S. Oswald, L. Schultz, B. Holzapfel, Highly textured $La_2Zr_2O_7$ buffer layers for YBCO-coated conductors prepared by chemical solution deposition. Superconduct. Sci. Tech. **18**, 334 (2005)
76. C. Cantoni, D.K. Christen, R. Feenstra, A. Goyal, G.W. Ownby, D.M. Zehner, D.P. Norton, Reflection high-energy electron diffraction studies of epitaxial oxide seed-layer growth on rolling-assisted biaxially textured substrate Ni(001): The role of surface structure and chemistry. Appl. Phys. Lett. **79**, 3077 (2001)
77. C. Cantoni, D.K. Christen, D.K. Heatherly, M.M. Kowalewski, F.A. List, A. Goyal, G. Ownby, D.M. Zehner, B.W. Kang, D.M. Kroeger, Quantification and control of the sulfur c (2 × 2) superstructure on {100}⟨100⟩ Ni for optimization of YSZ, CeO_2 and $SrTiO_3$ seed layers texture. J. Mat. Res. **17**, 2549 (2002)
78. C. Cantoni, D.K. Christen, A. Goyal, L. Heatherly, F.A. List, G.W. Ownby, D.M. Zehner, H. M. Christen, C.M. Rouleau, Growth of oxide seed layers on Ni and other technologically interesting metal substrates: issues related to formation and control of sulfur superstructures for texture optimization. IEEE Trans. Appl. Superconduct. **13**, 2646 (2003)
79. Y. Tokunaga, T. Honjo, T. Izumi, Y. Shiohara, Y. Iijima, T. Saitoh, T. Goto, A. Yoshinaka, A. Yajima, Advanced TFA-MOD process of high critical current YBCO films for coated conductors. Cyrogenics **44**, 817 (2004)
80. H. Fuji, R. Teranishi, Y. Kito, J. Matsuda, K. Nakaoka, T. Izum, Y. Shiohara, Y. Yamada, A. Yajima, T. Saitoh, Progress on TFA-MOD coated conductor development. Physica C: Superconduct. **426–431**, 938 (2005)
81. K. Tada, J. Yoshida, N. Mori, K. Yamada, R. Teranishi, M. Mukaida, T. Kiss, M. Inoue, Y. Shiohara, T. Izumi, J. Matsuda, K. Nakaoka, Growth process of Ba-poor YBCO film fabricated by TFA-MOD process. Physica C: Superconduct. **468**, 1554 (2008)
82. J. Yoshida, K. Tada, T. Tanaka, N. Mori, K. Yamada, R. Teranishi, M. Mukaida, T. Kiss, M. Inoue, Y. Shiohara, T. Izumi, K. Nakaoka, J. Matsuda, Effect of calcination conditions on microstructures and Jc of YBCO films fabricated by TFA-MOD method. Physica C: Superconduct. **468**, 1550 (2008)
83. C.S. Li, Y.F. Lu, P.X. Zhang, Z.M. Yu, B.W. Tao, J.Q. Feng, L.H. Jin, Study of modified TFA-MOD method for YBCO film growth. Physics Procedia **36**, 1620 (2012)
84. M.W. Rupich, X. Li, S. Sathyamurthy, C.L.H. Thieme, K. DeMoranville, J. Gannon, S. Fleshler, Second generation wire development at AMSC. IEEE Trans. Appl. Superconduct. **23**, 6601205 (2013)
85. M.W. Rupich, X. Li, S. Sathyamurthy, C. Thieme, S. Fleshler, Advanced development of TFA-MOD coated conductors. Physica C: Superconduct. **471**, 919 (2011)
86. D.W. Hazelton, Advances in 2G HTS conductor for high field applications, presented at the *Low Temperature High Field Superconductivity Workshop*, St. Petersburg, FL Nov. 5, 2013: http://www.superpower-inc.com/system/files/2013_1105+LTHFSW+SuperPower+FINAL.pdf
87. W. Schmidt, H.-P. Kraemer, N.-W. Neumueller, U. Schoop, D. Verebelyi, A.P. Malozemoff, Investigation of YBCO coated conductors for fault current limiter applications. IEEE Trans. Appl. Superconduct. **17**, 3471 (2007)
88. V. Selvamanickam, Y. Yao, Y. Chen, T. Shi, Y. Liu, N.D. Khatri, J. Liu, C. Lei, E. Galstyan, G. Majkic, The low-temperature, high-magnetic-field critical current characteristics of Zr-added (Gd, Y)Ba2Cu3Ox superconducting tapes. Superconduct. Sci. Tech. **25**, 125013 (2012)
89. Y. Jia, M. LeRoux, D.J. Miller, J.G. Wen, W.K. Kwok, U. Welp, M.W. Rupich, X. Li, S. Sathyamurthy, S. Fleshler, A.P. Malozemoff, A. Kayani, O. Ayala-Valenzuela, L. Civale, Doubling the critical current density of high temperature superconducting coated conductors through proton irradiation. Appl. Phys. Lett. **103**, 122601 (2013)
90. M. W. Rupich, S. Sathyamurthy, S. Fleshler, Q. Li, V. Solovyov, T. Ozaki, U. Welp, W. K. Kwok, M. Leroux, A. E. K., D. J. Miller, K. Kihlstrom, L. Civale, S. Eley, A. Kayani,

Engineered Pinning Landscapes for Enhanced 2G Coil Wire. IEEE Trans. on App Supercond. (in press)
91. L. Heatherly, H. Hsu, S.H. Wee, J. Li, S. Sathyamurthy, M. Paranthaman, A. Goyal, Slot die coating and conversion of LZO on rolling assisted biaxially textured Ni-W substrates with and without a very thin seed layer in low vacuum. IEEE Trans. Appl. Superconduct. **17**, 3417 (2007)
92. M.S. Bhuiyan, M. Paranthaman, S. Sathyamurthy, Chemical solution-based epitaxial oxide films on biaxially textured Ni–W substrates with improved out-of-plane texture for YBCO-coated conductors. J. Electron. Mater. **36**, 1270 (2007)
93. N.-W. Neumueller, W. Schmidt, H.-P. Kraemer, A. Otto, J. Maguire, J. Yuan, D. Folts, W. Romanosky, B. Gamble, D. Madura, A.P. Malozemoff, N. Lallouet, S.P. Ashworth, J.O. Willis, S. Ahmed, Development of resistive fault current limiters based on YBCO coated conductors. IEEE Trans. Appl. Superconduct. **19**, 1950 (2009)
94. J.B. Na, D.K. Park, S.E. Yang, Y.J. Kim, K.S. Chang, H. Kang, T.K. Ko, Experimental verification of non-inductive wound solenoid coil for large transport currents. Physica C: Superconduct. **469**, 1754 (2009)
95. T. Yazawa, K. Koyanagi, M. Takahashi, K. Toba, H. Takigami, M. Urata, Y. Iijima, T. Saitoh, N. Amemiya, Y. Shiohara, T. Ito, Development of 6.6 kV/600 A superconducting fault current limiter using coated conductors. Physica C: Superconduct. **469**, 1740 (2009)
96. P. Tixador, N.T. Nguyen, Design of ReBaCuO-coated conductors for FCL. Superconduct. Sci. Technol. **25**, 014009 (2012)
97. http://www.amsc.com/library/SAFCL_BRO_0812.pdf
98. H. Yumura, Y. Ashibe, H. Itoh, M. Ohya, M. Watanabe, T. Masuda, C.S. Weber, Phase II of the Albany HTS cable project. IEEE Trans. Appl. Superconduct. **19**, 1698 (2009)
99. Super3C Project news release, 17 March 2009. http://www.bruker-est.com/super3c.html
100. M. Ohya, Y. Ashibe, M. Watanabe, T. Minamino, H. Yumura, T. Masuda, T. Kato, Development of RE-123 superconducting cable. IEEE Trans. Appl. Superconduct. **19**, 1766 (2009)
101. S. Mukoyama, M. Yagi, T. Masuda, N. Amemiya, A. Ishiyama, N. Kashima, S. Nagaya, Y. Aoki, M. Yoshizumi, Y. Yamada, T. Izumi, Y. Shiohara, Development of (RE)BCO cables for HTS power transmission lines. Physica C: Superconduct. **469**, 1688 (2009)
102. J.F. Maguire, F. Schmidt, S. Bratt, T.E. Welsh, J. Yuan, Installation and testing results of Long Island transmission level HTS cable. IEEE Trans. Appl. Superconduct. **19**, 1692 (2009)
103. J. Maguire, D. Folts, J. Yuan, D. Lindsay, D. Knoll, S. Bratt, Z. Wolff, S. Kurtz, Development and demonstration of a fault current limiting HTS cable to be installed in the Con Edison grid. IEEE Trans. Appl. Superconduct. **19**, 1740 (2009)
104. C.M. Rey, R.C. Duckworth, J.A. Demko, A. Ellis, D.R. James, M.J. Gouge, E. Tuncer, Test results for a 25 meter prototype fault current limiting HTS cable for project Hydra. AIP Conf. Proc. **1218**, 453 (2010)
105. J. Maguire, D. Folts, J. Yuan, N. Henderson, D. Lindsay, D. Knoll, C. Rey, R. Duckworth, M. Gouge, Z. Wolff, S. Kurtz, Status and progress of a fault current limiting HTS cable to be installed in the Con Edison grid. AIP Conf. Proc. **1218**, 445 (2010)
106. http://ir.amsc.com/releasedetail.cfm?ReleaseID=860164

Chapter 6
Trans-Tech: Perspectives on the Development Process for New Microwave Dielectric and Magnetic Ceramics

Michael D. Hill

Abstract Trans-Tech is a company, specializing in the manufacture of ceramic dielectric and magnetic components to support the wireless communication infrastructure business. The company has about 200 employees and is a wholly-owned subsidiary of Skyworks Solutions Inc. Trans-Tech's products are developed internally and this chapter focuses on the process of that development from using scientific concepts to invent the material and put it into production. Emphasis is placed on specific case studies for dielectric and magnetic materials, the necessity of designing and adapting to raw material price fluctuations and the importance parallel activities in intellectual property development.

6.1 Practice of Material Development

Trans-Tech, Inc. is a wholly-owned subsidiary of Skyworks Solutions, Inc. that provides complementary state-of-the-art RF/microwave ceramic products. For 50 years, the company has been designing and manufacturing a complete line of RF and microwave components to address the demands of today's commercial markets including GaAs monolithic microwave integrated circuit and integrated components, RF and microwave semiconductor devices, and integrated multifunction sub-systems. Expertise is focused across the spectrum from tightly controlling processes from raw materials, to forming, firing, finishing, assembling and testing,

M.D. Hill (✉)
Research and Development, Trans-Tech Inc. (Division of Skyworks Solutions Inc.), 5520 Adamstown Rd., Adamstown, MD 21710, USA
e-mail: Mike.Hill@skyworksinc.com

L.D. Madsen and E.B. Svedberg (eds.), *Materials Research for Manufacturing*, Springer Series in Materials Science 224,
DOI 10.1007/978-3-319-23419-9_6

6.1.1 Driving Force

At Trans-Tech, most of the new material research and development projects start as the result of one of three needs:

(1) A major customer has a need for a new material to enable their wireless infrastructure platform
(2) A raw material in a current product has dramatically risen in price so as to necessitate a lower cost substitute material to be developed
(3) Based on a market analysis within, Trans-Tech, a material is developed to meet a perceived unmet need.

Cases 1 and 2 involve R&D being reactive to market conditions while Case 3 involves R&D being pro-active to market conditions. For material developments that fall within Cases 1 or 2, there is a guaranteed market for the product that effort was put into to develop. On the other hand, for Case 3, there is market risk in developing a product to meet a perceived need rather than as a result of a direct customer request. With this risk is the potential for failure of for very large rewards; failure if the market does not want the new product, large rewards if the market wants this new product. This position is enhanced further if the material is patented, putting the manufacturer of this hypothetical product in a powerful single-source position.

6.1.2 Procedure

Research in industry often starts at the point where research in universities or government labs ends. Let's take for example, a hypothetical microwave dielectric. Often, there are published results in the literature detailing the composition and crystal structure. This information serves as a starting point for the R&D research. Only a large company has the resources to scour hundreds of chemical systems looking for crystal structures which may serve the purpose of this hypothetical microwave dielectric. Therefore, our starting point is published phase diagrams, crystal structure determinations and the technical literature detailing the microwave properties. Much of the initial active R&D starts with selecting the crystal structure (solid state compound), investigating substituents to enhance particular properties, looking at the influence of stoichiometric variations, examining fluxing agents to optimize sintering schedules to individual kilns and small proprietary additives to optimize properties or the sinterability of the material. Of particular use are the 'Phase Diagrams for Ceramists' publications [1] which is a compilation of Ceramics-based Phase Diagrams gathered from numerous references over the years. Many microwave dielectrics are two phase mixtures, since the desired properties may not be attained with a single phase but rather a composite of two different phases. The phase diagrams provide a map of what materials may chemically coexist with one another in a ceramic system. In addition, new phases discovered

during the investigation of phase diagrams may have useful properties for microwave material design. Additionally, references such as Acta Crystallographica and the Journal of Solid State Chemistry which detail the specifics of crystal structures are helpful as well. The sharp-eyed microwave materials researcher is always interested in publications presenting structural motifs such as octahedrally-coordinated titanium atoms, even if it is in a publication dealing with a topic as seemingly unrelated as inorganic phosphors.

Modern research methods include the use of mathematical modeling and combinatorial synthesis. Although it is without question, that these are valuable and effective techniques and composition selection is guided by literature results derived from these techniques, materials development at Trans-Tech typically proceeds using an iterative empirical approach. Essentially, a series of materials are made (typically a statistically designed matrix of compositions looking at stoichiometry variations and interactions with the minor additives above). The powders are processed, formed into green bodies, fired as a ceramic in either R&D or production kilns and evaluated electrically. Based on the results, the process is narrowed and repeated until an optimal composition is selected.

The composition is selected to fit the process of standard solid state diffusion induced reaction of powders to form the desired crystal structure. The steps in manufacturing would be in this order, weighing the components (typically raw oxides or carbonates), blending the materials, pre-sintering the blend to induce the solid state reaction to the desired phase or phases, milling the material in water to reduce the particle size, spray drying the material with binder to aid in the forming process, forming and finally firing the ceramic. More detail will be presented later on the production version of this process. There may be post firing machining required on some customer designs but this will not be treated here. In R&D the process for synthesizing the test ceramic parts (50–150 g) is designed to mimic as much as possible the final sequence of manufacturing steps need to produce thousands of parts from these materials.

In the manufacturing world, the easier part is to design the material in the lab. It is more difficult to design a process to fit the large scale manufacturing equipment available. There are instances where investment in equipment to fit a material needs to happen, but these instances tend to be infrequent and it is much more common to attempt to modify existing equipment to accommodate a process designed to produce a new material.

With this short introduction to the basics of R&D processes, we will turn our attention to the types of products to be produced. Microwave dielectric materials will be introduced initially and developments associated with Case 1 will be highlighted. This occurs when a customer requests the development of a new material to align with their own R&D process as occurred with “Super Q” Ceramic Materials. Further research led to an instance where Case 3 is highlighted in which an R&D team developed a material on their own to satisfy a perceived market need. Following this discussion, magnetic materials will be discussed where Case 2 will be highlighted in which raw material market conditions forced an R&D effort to change the composition to less costly materials.

6.2 Wireless Infrastructure and the Use of Ceramic Materials

6.2.1 Historical Info

In the late 1980s, the electronic ceramics world had been focused on high temperature superconductive materials with hundreds of papers presented on this subject, with the end goal being the achievement of loss-less power transmission and levitating trains. Although levitating trains between Boston and New York never became a reality, one tangible benefit of the explosion of research in this area was a greater appreciation in the United States, in the universities, government labs and in industry, of the intricacies of processing electronic ceramics. Prior to this, the field had been dominated by large Japanese companies such as Murata, Kyocera and NGK Spark Plug.

At this time, microwave magnetic and dielectric materials were typically used for military applications such as phased array radars. In fact, Trans-Tech began in 1955 as a stand- alone company supplying ferrite and dielectric based ceramics for the military radar market. The 1990s saw the advent of these materials being used for commercial applications such as patch antennas for GPS systems, monoblock filters for, at that time, bulky cellular handsets, and components for cellular base stations.

6.2.2 Auto-tune Combiners

Microwave dielectrics have been commercially available for nearly 25 years for applications from 700 MHz to 3 GHz range. These materials are typically placed in a cavity resonator or used as metalized coaxial resonators. As cavity resonators, the materials find applications in auto-tuned combiners (ATCs) for 2G applications as well as in high power transmit filters for 3G applications. Ceramic loaded cavities have an inherent advantage over air cavities in having greater frequency selectivity and smaller size. The chief disadvantage of ceramic loaded cavities is a higher cost relative to air cavities. The division of the frequency spectrum into smaller bands favors the use of ceramic-based ATCs and filters.

6.2.3 Transverse Magnetic (TM) Mode Filters

Starting with 3G and 4G long-term evolution (LTE) designs, there has been a shift from resonators operating in the transverse–electric (TE) resonant mode to the transverse-magnetic (TM) resonant mode. TE mode resonators generally had required much higher quality (Q) values than TM mode resonators. Many TM mode designs require smaller cavities. These will drop the achievable Q value considerably and therefore expensive high Q materials are not required. Cost and size become the key driving forces when designing with TM mode filters. This forces

the design of materials with lower cost raw materials as well as creating a push to remove extra costs such as post fired machining.

6.2.4 Magnetics for Isolators and Circulators

Ferrite materials are used in isolators and circulators for cellular base stations. These are typically assemblies of disks of magnetic non-conducting oxide compounds of iron and other metallic elements (known as ferrites, usually based on yttrium iron garnet) and a biasing magnet. These devices utilize gyromagnetic polarization splitting to direct the RF signal and prevent RF power from leaking into unwanted areas. These devices can be operated either above or below the gyromagnetic resonance of the ferrite material with the frequency determined by the saturation magnetization, size and bias of the ferrite. Insertion loss and intermodulation products are issues which need to be addressed in circuit design. To reduce intermodulation effects, the outer diameter of the ferrite disk is often glued to or co-fired with a non-magnetic dielectric ring to prevent interaction with its steel enclosure. As miniaturization is always required, higher dielectric constant ferrite materials are an active area of R&D research.

6.3 Basics of Microwave Dielectrics

6.3.1 Relevant Material Parameters

There are three critical material parameters that need to be considered in the design of a microwave dielectric material. The first, the dielectric constant (ε), can be derived by summing the ionic polarizabilities of the individual ionic components and dividing by the molar volume [2]. Shannon has derived a series of polarizabilities that is an excellent predictor of the dielectric constant of a large number of ceramic systems. However, although the Shannon polarizabilities provide an excellent start for predicting the dielectric properties of many ceramic oxides, there are numerous crystal chemical phenomena which cause very large deviations from the predicted values. Paraelectic/ferroelectric behavior (as in titanates) or the inclusion of ions with lone pairs (such as Pb^{2+}, Bi^{3+} etc.) serve to cause the dielectric constant to be higher than predicted by polarizability sums. This is significant from an application standpoint, since the dielectric constant of a material determines the size of the resonator used for a particular frequency according to the relation with k denoting a constant [3].

$$\text{Diameter} = k\varepsilon^{-1/2} \tag{6.1}$$

For example, to design with a smaller ceramic component at a particular frequency, a system designer would choose a resonator material with a higher dielectric constant.

This is especially significant in some TM mode resonator or dielectric antenna miniaturization for a variety of applications.

The second parameter is the quality factor, or Q. The Q of the material is defined as the inverse of the loss tangent. The loss tangent is a measure of the response of a material to an applied frequency. In atomistic terms, the materials with atoms which respond out of phase with the applied frequency show an increased loss tangent. Materials which show electronic or polaron conduction, or have weakly bound atoms tend to have large loss tangents and low Q values. In microwave applications, the cavity size as well as the intrinsic loss tangent will affect the Q of the material in a cavity resonator. The Q of the material is measured by looking at the bandwidth 3 dB below the peak of the primary resonant mode [4]. A higher Q material will have a sharper resonance with an extremely narrow bandwidth leading to sharp cutoffs in filters and the ability to stuff many more channels into a single auto-tuned combiner. A crude rule of thumb for materials is that the product of the Q and the resonant frequency (Qf) is a constant [3]. This means that the higher the frequency, the lower the Q value. While the Q does decrease with frequency, the "Qf product rule" is rarely obeyed and the Qf product tends to increase with frequency.

The third factor, the τ_f, describes the temperature behavior of the resonator, defined as the temperature coefficient of resonant frequency, measured in parts per million per degrees C. This parameter is a combination of the thermal expansion coefficient of the ceramic as well as the temperature coefficient of the dielectric constant by the relation:

$$\tau_F = (-1/2)\tau_K - \alpha \tag{6.2}$$

where τ_F = the temperature coefficient of the resonant frequency, τ_K is the temperature coefficient of the dielectric constant and α is the thermal expansion coefficient of the ceramic material. The temperature coefficient of the dielectric constant is a material property intimately associated with chemical and crystallographic parameters [5, 6]. Filter and combiner designers often require the ceramic component to have a τ_F (or temperature drift) to balance out the intrinsic thermal drift in the metal cavity. That is why in developing dielectric systems, it is important to offer the customer a very large range of available τ_F options (including custom materials, as is often the case.)

6.3.2 Classical Materials

6.3.2.1 Magnesium Calcium Titanate (MCT) Based Materials

Among the earliest microwave dielectric materials are two phase mixtures of magnesium titanate ($MgTiO_3$) and calcium titanate ($CaTiO_3$). The phase diagram [7] clearly indicates compatibility between these two distinct phases (illustrating the usefulness of this reference in ceramic materials design). Magnesium titanate has a dielectric constant of 16, a τ_F of −30 and Qf products near 20,000 [8].

Calcium titanate has a dielectric constant of 180, a very positive $\tau_F > 500$ and modest Qf products on the order of 2000. However, since the phases are chemically compatible, two phase mixtures of $MgTiO_3$ and $CaTiO_3$ may be obtained where the τ_F is close to zero and can be tailored by adjusting the relative volume percent of $MgTiO_3$ of $CaTiO_3$ [8]. This is a rather classical example of a frequently used technique for microwave materials design where two phases with τ_F values of opposite sign are put together in a two phase ceramic to obtain temperature coefficients close to 0. In this case, the MCT ceramics have temperature coefficients close to 0 at a dielectric constant of 20. Mixing rules for dielectric constant goes as the logarithm of the volume fraction of the two phases while mixing rules for the τ_F are linear with the volume fractions.

6.3.2.2 $Ba_2Ti_9O_{20}$ and $BaTi_4O_9$ Based Materials

Including the MCT system, many of the earliest microwave dielectric materials were crystalline ceramics featuring tetravalent titania in octahedral coordination. O'Bryan [9] thoroughly studied the titania rich region of the $BaO–TiO_2$ system and identified two compounds which have been staple materials for microwave dielectrics up to this day. Barium tetratitanate ($BaTi_4O_9$) and barium nonatitanate ($Ba_2Ti_9O_{20}$) each have dielectric constants between 36 and 38 with slightly positive temperature coefficients [10]. The Q values are modest (Qf = 30,000) by today's standards but still useful for a large number of applications The temperature coefficients approach zero for a two-phase mixture of the components for reasons yet to be clearly established. Figure 6.1 [11] depicts the relationship between the temperature coefficient of the resonant frequency (τ_F) and the relative contents of barium nonatitanate and barium tetratitanate. Further improvements in the Q values [12] have been made by a coupled substitution of Zn^{2+} and Nb^{5+} or Ta^{5+} for Ti^{4+} in this material.

6.3.3 Rutile and $ZrTiO_4$ Type Materials

Another system containing Ti^{4+} in octahedral coordination is the $ZrO_2–TiO_2$ system and specifically the compound $ZrTiO_4$ with the alpha-lead oxide structure. Sn^{4+} doped $ZrTiO_4$ ($Zr_{1-z}Sn_zTiO_4$) was one of the earliest microwave dielectrics used with a dielectric constant of 36 [13, 14]. Qf products above 40,000 were obtained around 1 GHz in this material. For the Sn^{4+} doped system, there is a substitution limit above which other cations cannot go into the alpha-PbO structure. Above this limit, a second phase rutile forms with the τ_F and the ε increasing dramatically. Sn^{4+} substitution decreases the dielectric constant and temperature coefficient for the $ZrTiO_4$ material while enhancing the Q [15]. By adjusting the atomic percent of the zirconia substituent, the temperature coefficient may be tuned. Coupled substitutions such as $1/3\ M'^{2+} + 2/3\ M''^{5+}$ (where M′ is a divalent ion such as Mg^{2+}, Ni^{2+} or Zn^{2+} and M″ is a pentavalent ion such as Nb^{5+} or Ta^{5+}) may serve a similar role to the Sn^{4+} and such

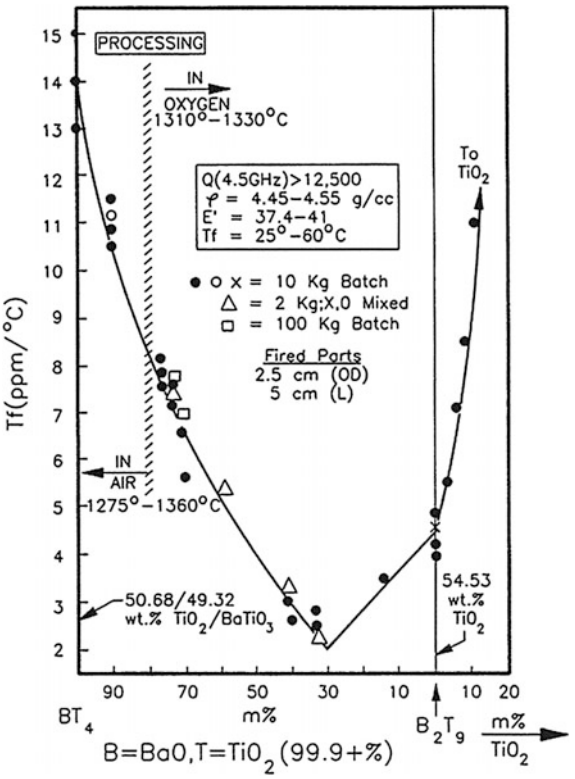

Fig. 6.1 Temperature coefficient of resonant frequency as a function of the relative contents of barium tetratitanate and barium nonatitanate (from [11])

combinations have been shown to increase the dielectric constant of $ZrTiO_4$ based systems [16].

6.3.4 Perovskite-Based Titanates

A third commercially available titanate based ceramic is a perovskite based on a solid solution of lanthanide aluminates with either calcium or strontium titanate. The temperature coefficient can be tuned by varying the relative concentrations of the lanthanide aluminate and alkaline earth titanate content. These materials show dielectric constants between 39 and 44 depending on the choice of the lanthanide and alkaline earth element [17]. Qf products for commercially available materials range from 40,000 for the neodymium aluminate-calcium titanate system to 50,000 for the lanthanum titanate–strontium titanate system [18]. Reaney [19] has showed that the maximum Qf product depends on the distribution of ionic sizes on the A site (lanthanide ion, calcium or strontium) and the B site (titanium, aluminum or gallium). The highest Q values reported were on a lanthanum gallate-strontium

titanate solid solution where the differential ionic size between the A-site cations (lanthanum and gallium) and the B-site cations (titanium and gallium) is minimized.

6.3.5 Titanate Processing

One ceramic processing issue with the titanate-based dielectrics is the tendency to form a black core in the body center of ceramic parts. This "coring" phenomenon is due to localized thermal reduction of the Ti^{4+} to Ti^{3+} during high temperature sintering [11]. At temperatures below the sintering temperature (1000–1150 °C) Ti^{4+} is stable relative to Ti^{3+} and re-oxidation occurs. However, during cooling if the surface of the ceramic is sintered to near theoretical density, it is difficult for oxygen to be transported through the material to re-oxidize the titanium. Therefore, the result is a residue of the thermally reduced Ti^{3+} and a low Q ceramic body with a dark core. Ironically, impurities settling at grain boundaries can serve to help transport oxygen into the center of the ceramic body. It was reported [11] that impurities such as phosphorus and alkali metals improve the grain boundary oxygen conductivity, preventing coring. Another engineering approach to preventing coring is to add an acceptor ion such as manganese to prevent titanate reduction [20, 21].

Titanates, although showing acceptable Q values, are not capable of exhibiting the highest Q values of the "Super-Q" ceramic materials. This is due to their susceptibility to reduce to the Ti^{3+} state as well as their tendency toward incipient ferroelectricity when in the octahedral coordination [22]. Incipient ferroelectricity is associated with a displacement in the position of titanium ions from the center of the octahedron toward one of the oxygen ions. This displacement is simultaneously responsible for the advantage of the large dielectric constants exhibited in ceramic titanates along with the disadvantage of the limitation on their achievable Q values.

Finally, the binary oxide TiO_2 with the rutile structure is an anomaly in that it has a very high dielectric constant (close to 100) with a Qf product close to 40,000. All other known microwave dielectric materials with dielectric constants above 60 exhibits much lower Q values (or higher loss tangents) [23]. Unfortunately, rutile exhibits an extremely high τ_F (>+500) rendering it useless as a viable commercial microwave dielectric material.

6.4 Technology Trends Necessitating Material Development

6.4.1 Original Equipment Manufacturer (OEM) Push to Super Q Dielectrics

In the case of original equipment manufacturer (OEM) driven R&D, there are usually several groups from competitive suppliers, appraised of the technical

requirements, who are independently working on the materials. This serves to both increase the probability of a solution to the technical challenge as well as to ensure that there are multiple suppliers. In this case there is little risk that R&D dollars would be spent on an item that has no market. However, there is the risk of being beaten to the solution by a competitor who sets the specification ranges, effectively requiring all second sources to have to modify their material to conform to the first material to market. Like many industries, being first to be designed in has tremendous advantages in material development as well.

For example, in the mid-1990s there was interest in deploying infrastructure capable of processing digital as well as analog signals through cellular base stations at frequencies close to 2 GHz. This specification required very sharp frequency selectivity and, as a result, very high Q requirements (>40,000 at 2 GHz) for the ceramic used in the auto-tuned combiner. Titanates were unable to meet the Q requirements, because of their tendency to reduce to Ti^{3+} and to show incipient ferroelectric behavior. Dielectric constants in crystalline oxide systems tend to be enhanced when a d^0 cation (a transition metal in an oxidation state where all of the d electrons are removed) in octahedral co-ordination is a part of the structure. In addition to Ti^{4+}, $Zr^{4+,}$ Nb^{5+}, Ta^{5+}, Mo^{6+} and W^{6+} are candidate ions for enhanced dielectric constant oxide based ceramics [22].

At that time, the best Q values known were for the complex ordered perovskites barium magnesium tantalate $Ba_3MgTa_2O_9$ (BMT) and barium zinc tantalate $Ba_3ZnTa_2O_9$ (BZT). BMT was especially tantalizing in that Matsumoto et al. [24] reported Qf products in excess of 200,000 for 10 GHz resonators with a dielectric constant of 25. These materials had the perovskite structure with multiple cations on the B-site. The B-site cations are ordered in consecutive planes in the 111 direction as shown in Fig. 6.2 [25]. There are two consecutive rows of Ta^{5+} ions followed by a row of divalent metal ions (Zn^{2+} or Mg^{2+}). These complex structures yield a very high Qf product, often greater than 100,000 with dielectric constants of 25 (for BMT) and 30 (for BZT). The τ_f values of these are slightly positive but close enough to zero to be tunable with moderate amounts of substituent cations [24]. The Q value is directly correlated with the degree of ordering in these materials [26].

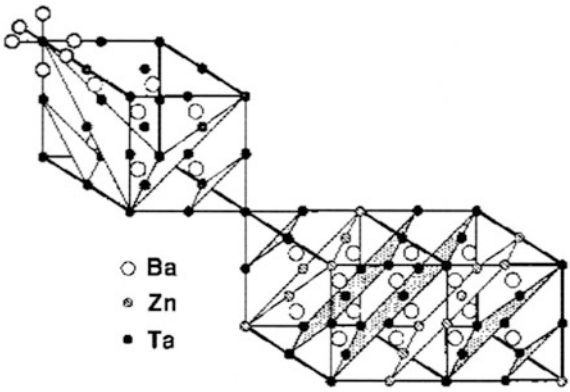

Fig. 6.2 Schematic of 2:1 ordered arrangement in complex high Q $Ba_3ZnTa_2O_9$ perovskites (adapted from [25])

Perovskites with randomly distributed B-site cations show very low Q values as compared to the ordered variants. Above a critical temperature (the order-disorder transformation temperature) the material reverts to the disordered structure. It is desirable to sinter ceramic bodies of ordered perovskite materials below the order disorder transformation temperature, if possible. Fortunately, the order-disorder temperature in BMT and BZT is well above 1600 °C [27], leaving a wide temperature window for ceramic processing.

One Japanese company produced a patented material based on barium zinc tungstate with a dielectric constant of 21. The relatively low dielectric constant necessitated a larger resonator than a material made from one of the tantalite-based materials (24–30 dielectric constants). However, in this case, the patent served as a double-edged sword. With the infrastructure manufacturer requiring two sources and the dielectric 21 material patented (and with an odd dielectric constant), the customer designed their combiner using the higher dielectric constant (29) solution which has multiple suppliers.

6.4.2 Origins of High-Q Behavior

There has been a great deal of study regarding the origin of the high Q values in these complex ordered perovskites. Intuitively, it would be expected that simple structures would show the highest Q values. However, this has not shown to be true. Simple perovskites such as barium zirconate and barium hafnate do not have the Q values of the complex perovskites, even though the zirconate and hafnate materials do not show the predilection toward reduction (coring) or for off-center octahedral displacements (incipient ferroelectricity) that Ti^{4+} does. Additionally, there is no differential in the ionic size to contend with as discussed above with the titanate-aluminate perovskites. A probable reason for the Q limitation in simple structures may be related to the second law of thermodynamics. A simple structure would contain some individual point defects which are inevitable due to entropy considerations. These defects include impurity substituents, vacant lattice sites, interstitial ions, Frenkel pairs, etc. which may disrupt the lattice periodicity. This disruption in the lattice periodicity will lead to out of phase lattice vibrations, broad resonant peaks and reduced Q values.

More complex structures (such as the 2:1 ordered perovskite) may result in lower loss tangent materials because there are regions for such naturally occurring defects to “hide” and be less disruptive to the overall Q. The nature of the defects in complex structures is radically different from those in simpler pervoskites such as barium zirconate and barium hafnate. In addition to grain boundaries, lattice vacancies and substituent cations, complex structures may also show anti-phase domain boundaries as well [28]. For example, in the 2:1 ordered perovskites referred to above, the 2:1 ordering is a nucleation and growth phenomena within a particular grain. If there are multiple nucleation sites within a particular grain, there may be several potential orientations for the 2:1 ordering. An anti-phase domain

boundary (APB) is formed where two different orientations of the 2:1 ordering meet. In this case, there is a large excess positive charge at the APB if there are four consecutive Ta^{5+} containing planes. This excess positive charge leads to lattice distortions which decrease Q. The stabilization of these APBs is the essential process in obtaining high Q ceramics of 2:1 ordered perovskites. Point defects may be swept to the APBs to reduce this excess positive charge. In essence the two types of effects will effectively neutralize each other's negative effect on the Q.

6.4.3 *Stabilization of Anti-phase Domain Boundaries and Production of a Super Q Material*

An attempt to synthesize 2 GHz resonators out of barium magnesium tantalate illustrates the danger of universally applying "technical guidelines" like the Qf product rule. Despite extremely high Qf products at 10 GHz, all attempts to produce a material with a Q > 40,000 met with failure. At the time, it was uncertain what was happening at 2 GHz, although it is hypothesized that the reason may be the poor stabilization of APBs. Attention then turned to the barium zinc tantalate material.

There are two known methods of stabilizing APBs in barium zinc tantalate. Chai and Davies [29] observed that the addition of modest Q barium zirconate greatly improved the Q of barium zinc tantalate. This apparent anomaly was explained by Davies in which he noted that the ionic size of Zr^{4+} was intermediate between that of Zn^{2+} and Ta^{5+} [25]. Looking at the APBs using transmission electron microscopy, he observed regions of 1:1 ordering at the APB. In 1:1 ordering, the 2+ and 5 + cations are arranged in the rock salt structure. The 1:1 ordering removes the excess positive charge at the anti-phase domain boundary and enhancing the Q value. This method of stabilizing APBs applies in barium magnesium tantalate (BMT) as well where barium stannate is added to BMT since the ionic size of Sn^{4+} was intermediate between that of Mg^{2+} and Ta^{5+} [24, 29]. However, this mechanism, while effective at high frequencies, did not appear to be effective in the 2 GHz range.

The second method of stabilizing anti-phase domains involves the solid solution addition of B-site cation deficient hexagonal perovskites. The parent compounds have the perovskite crystal structure with several layers of face sharing octahedral and hence regions of hexagonal close packing. Small amounts of B-site deficient compounds like $Ba_5Ta_4O_{15}$ may dissolve in the BZT structure to form 8-layer hexagonal perovskites of the formula $Ba_8ZnNb_6O_{24}$ [30]. Upon formation of the APB, the B-site vacancies migrate to the APB to counteract the excess positive charge, stabilizing the Q. Figure 6.3 shows a micrograph of a hexagonal perovskite crystallite nucleating at the APB in the pseudocubic main phase. It is interesting to note that Mg does not form a hexagonal $Ba_8MgNb_6O_{24}$ type phase and this may be the reason for the poor low frequency Q values in the BMT based systems [31].

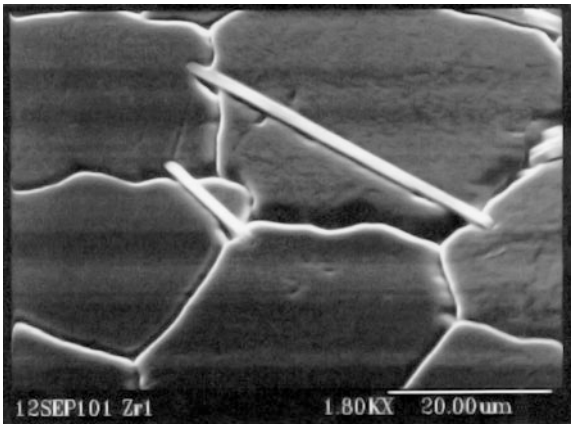

Fig. 6.3 Microstructure of hexagonal perovskite needles growing from anti-phase domain boundaries in BZCN crystals (courtesy of M. Hill and D. Phelps, Trans-Tech)

By contrast, BZT based materials stabilized by 1:1 ordered and hexagonal perovskites were a mainstay material, supplied by multiple sources, for 2 GHz auto-tuned combiners for several years.

6.5 Development of a New Perovskite

Barium zinc niobate is a 2:1 ordered perovskite isostructural with the corresponding tantalate. A solid solution with barium cobalt niobate produces a material ($Ba_3Zn_{1-x}Co_xNb_2O_9$ called BZCN) with a dielectric constant of 34 and a τ_F close to zero. The high dielectric constant means that at a given frequency, the niobate based ceramic resonator will be smaller than its tantalate based counterpart [32]. However, the BZCN material has an order-disorder transformation temperature near 1400 °C, which is below the typical sintering range of 1450–1550 °C [33]. This necessitates complicated processing and heat treatments including a lengthy annealing to obtain the high Q ordered configuration. In 1999, there was a demand for materials with dielectric constants in the 35–40 range for 3G high power transmit filters and WiMAX applications. As a result, the decision was made to embark on an R&D project aimed at producing a high Q material with a dielectric constant in the mid to high 30 s. It is also an advantage that niobium is significantly cheaper than tantalum. This is an example of Case 3 from above, where a material is pro-actively developed to meet a market need rather than prompted as a reaction to external events.

Many of the lessons learned regarding the stabilization of domain walls in the tantalate ceramics apply also to these niobate based ceramics. The hexagonal phases $Ba_8ZnNb_6O_{24}$ and $Ba_8CoNb_6O_{24}$ form readily in these niobates and, indeed, the image in Fig. 6.3 is actually of the niobate-based material. Significant additions of the hexagonal phases adjust the temperature compensation point ($\tau_F = 0$) to a

dielectric constant of 35 and the 2 GHz Qf product was greater than 80,000. In an ironic twist, because of these high Q values and the fact that niobium is much cheaper than tantalum, the largest market for this material ended up being re-designed auto tuned combiners, a market for which the material was not designed. By 2005, tantalum based resonators for this application became obsolete and the niobate version dominated the 3G auto tune combiner designs.

6.6 Basics of Microwave Magnetics

6.6.1 Magnetic Oxides

Oxide materials have been known for centuries for their magnetic properties. Lodestone, used by mariners in the Middle Ages as a compass is actually magnetite or Fe_3O_4 with the spinel structure [34]. Oxide materials have the advantage of being insulating so that there are no eddy current losses due to free electrons as in metals. While metals show ferromagnetic behavior due to the electron spin effects caused by the direct interaction between neighboring metal atoms, insulating oxides show ferrimagnetic interactions in which the non-magnetic oxygen ion mediates the magnetic interaction between second nearest neighbor cations. As a result, the magnetic properties of most oxides are diluted relative to metals. (Metal magnets show much higher Curie Temperatures; the temperature at which thermal energy breaks down the magnetic interaction).

There are four major structural families of magnetic oxide materials of technological importance: the spinels, garnets, hexagonal ferrites, and perovskites. Perovskites have not been historically useful for their magnetic properties (although recently there has been a flurry of interest in bismuth ferrite due to the simultaneous occurrence of ferrimagnetism and ferroelectricity in its perovskite structure) [35]. Hexagonal ferrites show a wide range of useful applications including permanent magnets and absorbers but, because of their high anisotropy, have not been widely used for microwave magnetic applications [36]. Spinels were the earliest ferrite based materials studied and are very useful for a wide range of applications from the kHz range to the 10 s of GHz [34, 37]. However, most of the activity for microwave magnetic materials centers on the garnet structure and yttrium iron garnet ($Y_3Fe_5O_{12}$ or YIG) based materials.

6.6.2 Magnetic Garnets

YIG was synthesized by Geller et al. [38] in the late 1950s and Geller and other groups observed that there were a large number of other cations which can easily

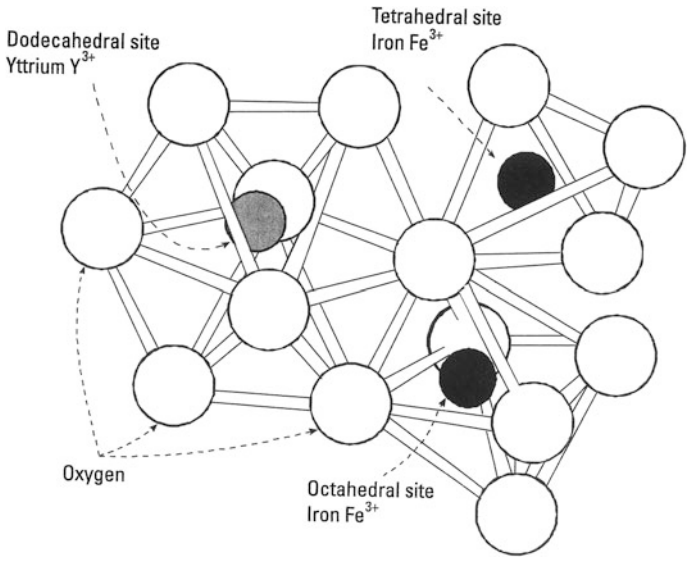

Fig. 6.4 Schematic diagram of crystallographic sites in the garnet structure after Cruickshank [41]

substitute for yttrium or iron making available materials with a wide range of commercially useful magnetic properties [39, 40]. The garnet structure has three distinct cation sites as shown in Fig. 6.4 [41]. First, there is the dodecahedral (or 8 coordinate) site where the larger yttrium ions reside. There are three of these sites per formula unit of garnet. Second, there is the octahedral (6 coordinate) site where two out of five of the iron atoms in the basic formula unit reside. Finally, there is the tetrahedral (4 coordinate) site where the remaining three iron atoms in the formula unit reside. The magnetic response in garnets is due to the ferromagnetic interaction between the tetrahedral iron sites and octahedral iron sites of opposite spins (3 Fe↑−2 Fe↓) which leaves a net magnetization of 1 Fe↑. Since each Fe^{3+} ion has five unpaired electrons, there is still a significant amount of net magnetization in YIG. That saturation magnetization can be adjusted down by substituting non-magnetic ions in the tetrahedral site (such as Al^{3+}) or up by substituting non-magnetic ions in the octahedral site (such as In^{3+}), for example [41, 42].

One of the real advantages of YIG and YIG-derivative ceramics is the lack of magnetic anisotropy in this structure. Because YIG is a cubic crystal structure and there is very little difference in the magnetic response of single crystal YIG based on the direction of an externally applied magnetic field relative to its crystallographic orientation, randomly oriented polycrystalline ceramics of YIG will show a sharp gyromagnetic resonance. By contrast, hexagonal ferrites show a large change in the magnetic response due to the orientation of the crystal and as a result polycrystalline hexagonal ferrites show a very broad gyromagnetic resonance. Without getting bogged down in the physics, because the garnet structure behaves

the same way regardless of orientation, all of the resonances from each individual grain overlap at the same frequency, leading to a sharp resonance and low magnetic losses at frequencies close to the resonant peak. Other materials have resonances that span decades in the microwave spectrum and are very lossy materials, unsuitable for microwave applications.

Much like the microwave dielectrics, most of the interest in garnets prior to about 1990 was for military applications. Substituting various ions into YIG led to materials suitable for temperature-stable latching phase shifters for radar applications.

6.6.3 Magnetic Applications and Narrow Linewidth Garnets

With the interest in cellular communication and the development of base station towers to cover the landscape with cellular access, there was a need for isolators and circulators to direct the RF signals in only the desired direction. These isolators and circulators required insulating magnetic materials with very narrow gyromagnetic resonances.

In many cases for this application, pure YIG would work. However, in some instances, there was a need for extremely narrow resonant linewidth materials. Concurrently, there is also a need to tune the magnetization of the material to accommodate a range of resonant frequencies. Pure YIG has a saturation magnetization close to 1780 gauss. For the requirement of narrowing the resonant linewidth further than in YIG, Van Hook [43] and later Winkler [44] had observed that substituting an ion with a larger ionic radius than Fe^{3+} for iron in the octahedral site would reduce the magnetic anisotropy even further than in pure YIG. In^{3+} (0.94 Å) was nearly the ideal size for this requirement substituting for Fe^{3+} (0.69 Å). For the second requirement, pentavalent vanadium (V^{5+}) was used to substitute for iron in varying amounts on the tetrahedral sites to generate a suite of narrow resonance linewidth garnets with magnetizations varying from 1850 to 800 gauss. Vanadium was chosen because it is unique among non-magnetic ions in being able to substitute for iron without drastically reducing the Curie temperature (and therefore the temperature performance of outdoor mounted isolators and circulators within cellular base stations) [45]. Because vanadium is a pentavalent ion substituting for a trivalent ion, charge compensation was achieved by substituting two Ca^{2+} ions for Y^{3+} on the dodecahedral site. Since neither yttrium nor calcium is a magnetically active ion, this charge compensation scheme had a negligible effect on the magnetic properties.

So in the mid-80s, Trans-Tech produced a series of narrow resonance linewidth polycrystalline garnets with the general formula of $Y_{3-2x}Ca_{2x}In_yV_xFe_{5-x-y}O_{12}$ and then in 2003, the price of indium skyrocketed.

6.7 Development for Cost Reduction and the Use of Critical Materials

6.7.1 Price Erosion

The economics of semiconductor based electronics has cast a long shadow on the pricing expectations in many other technology industries. Price erosion has been the rule for semiconductor chips due to advances in technology to miniaturize circuits and allow more components to be placed onto a single chip. As a result, the price of electronic items in which these chips serve as the brains drops from one generation to the next, while the functionality increases. Many customers are demanding similar price erosion for electronic ceramics components as well. Some of this price erosion can be accommodated by cost savings due to process improvements for materials already in production. These improvements include removing post-firing machining steps by moving to an as-fired ceramic process, having a capable process that reduces material testing and completing the production ramp up to full volumes where economies of scale apply. However, unlike the semiconductor industry, the raw material cost in electronic ceramics is a greater fraction of the total cost. As a result there is a price floor at which the production of ceramics does not become profitable.

At this point, the only remaining price lever is to reduce the cost of raw materials. Some of this effort involves finding ways to utilize less pure (and expensive) grades of raw materials without sacrificing the electrical performance of the finished product. However, there are instances where a cost reduction in the raw materials is offset by extra processing steps (for example, annealing) required to produce high quality ceramics with the less expensive materials. A more extreme and disruptive way to reduce the raw material costs is to reformulate using less expensive elements. As large as an effort can be, many R&D efforts at Trans-Tech have involved just such reformulations. Typically this is driven by economic forces, resulting in large increases in the price of particular raw materials.

6.7.2 Critical Materials

One of the realities in the industrial materials business is fluctuations in the cost of raw materials. There can be order of magnitude jumps in the cost of a critical raw material which may change the competitive landscape significantly if one particular supplier uses this raw material while competitors do not. These raw material fluctuations tend to be economic in nature and not a case of the earth running out of ore. Even for gold, there is still enough material in the earth's crust to last over five million years even if the demand skyrocketed [46]. Nonetheless, the distribution and concentration of the ore, and the access to processing facilities have a significant effect on the raw material price. For example, ores concentrated in politically

unstable parts of the world may show a dramatic increase in the price in the case of war breaking out in that nation.

Less dramatic but also potentially problematic is the case where an ore is mined as a by-product of the mining of another mineral [47]. For example, Indium is obtained as a by-product of zinc mining. If the demand for zinc drops significantly, there can be a severe shortage of indium since there are fewer mines producing the material. The fact that there are no international metal exchanges for many of the less common elements means that production quantities, and therefore raw material prices, may be dependent on one or two isolated purchase agreements [47].

Additionally, prices may increase when there is a demand for a critical material in another industry. Vanadium and niobium increased during 2006–2008 due to the demand for these elements as carbide formers in steel for China's booming infrastructure build. Furthermore, if either the mining or the processing of a particular ore is confined to one country, there is a danger of that government putting an excise tax on the export of those materials to allow internal manufacturing operations to have a competitive advantage. This happened when the Chinese government both limited the export of, and imposed an excise tax on, yttrium and the lanthanide ions in 2010 and 2011.

There can be hypothetical cases where the raw material costs of two competitor's materials will flip flop over time. If Company A has a dielectric containing rare earths and a Company B produces a dielectric rich in niobium, company B may suffer when the price of niobium skyrockets due to an increasing demand for specialty steels. However, at another time, the situation may reverse itself if, due to the actions of foreign governments, rare earth prices skyrocket, or material becomes unavailable. Industrial R&D teams always have to be cognizant of raw material prices and make every effort to avoid scarce or expensive raw materials in new designs and look for opportunities to replace expensive raw materials in existing designs.

6.7.3 Indium in Garnets

With the indium containing garnets in 2003, the skyrocketing price of indium forced R&D team to look into less expensive substituents that may have a similar effect. Winkler [44] reported that having a larger ion than Fe^{3+} in the octahedral site of the garnet structure would reduce the anisotropy of the magnetic response in each garnet grain (The technical term for this is magnetocrystalline anisotropy energy). Winkler had looked at the elements In^{3+} (0.94 Å), Zr^{4+} (0.86 Å), Sn^{4+} (0.83 Å), and Ti^{4+} (0.75 Å) with steadily decreasing ionic radii and showed that the critical parameter (the linewidth at 3 dB below resonance) broadened as the ionic radius of the substitute ion decreased. Therefore, although indium was the optimum substitution, research began to look at the addition of the much less expensive zirconium in these garnet materials. Recall that Zr^{4+} additions will require Ca^{2+} to be added onto the dodecahedral site for compensation and suddenly the formulas of the

narrow linewidth garnets began to look dramatically different. It took 18 months of dedicated R&D and manufacturing process adjustment but after it was completed, a suite of zirconium substituted materials replaced the indium containing materials.

6.7.4 Tantalum Free

Although the niobate based material was not intended to replace the tantalum based material for the high Q combiner application, the price of tantalum skyrocketed around 2000 forcing some changes in the material set used in the auto-tuned combiners. The tantalum demand was driven by the market for electrolytic capacitors and its scarcity became so acute, that wars were fought in the eastern part of the Democratic Republic of Congo to obtain the coltan (short for columbite–tantalite) ore from which tantalum was derived [48]. At this point, the OEMs demanded reduced tantalum dielectric products for the auto-tuned combiners. However, despite the very high Q values shown by the niobate based perovskite derivative, the dielectric constant was too high and would necessitate a thorough redesign of the combiner to accommodate the smaller sized niobate-based puck. After several years of largely fruitless efforts to find a reduced tantalum combiner material that would serve as a "drop-in replacement" for the tantalum containing material, the base station manufacturers finally yielded and adjusted the design to accommodate the higher dielectric constant niobate-based materials.

6.8 Transition from R&D into Production

6.8.1 Intellectual Property

One area of particular focus is the transition of a new product from research and development into production. This is the one of the most difficult parts of the entire R&D process. Obtaining a 100 g ceramic sample from a controlled lab kiln is one thing; developing a process to manufacture hundreds of thousands of consistent parts in a tunnel kiln while minimizing scrap is another challenge altogether.

The first issue to be dealt with is the protection of intellectual property rights. An interesting material has been synthesized in the R&D lab. The first question is whether to patent or keep as a trade secret. In general, it is best to patent if a competitor's potential infringement can be easily detected. New material chemistries should always be patented as infringement can be detected by a chemical analysis of the competitor's material. On the other hand, it may be best to keep processing techniques a trade secret since the method of manufacture of a particular ceramic cannot be easily deduced from an examination of the competitor's material.

In 2013, U.S. patent laws changing from a first-to-invent basis to a first-to-file basis [49]. It is therefore imperative to prepare a case for filing a provisional or utility patent prior to disclosing the material to a customer or any outside agency. In the past "first-to-invent" era, it was important to keep detailed and dated lab records that may be used as evidence in a potential court case that, in fact, the material was first invented here. In a "first-inventor-to-file" world, if an invention was obtained independently by two different organizations, the first of the inventing organizations to file at the U.S. patent office will be awarded the patent, even if the second, non-filing, organization invented the product first.

Since original equipment manufacturers always prefer to have at least two suppliers of a given product, they are often threatened by a supplier obtaining exclusive rights to produce an invention. There have been cases of OEMs refusing to design in innovations in order to prevent them from being subject to a single source supply situation. In other cases, some large companies will fund universities to perform research in a key area with the aim of having the university publish innovations and putting them into the public domain to prevent patents. In any case, the issue of intellectual property transcends the technical aspects of R&D and crosses into business decisions on how much to spend on legal fees and international filings as well as sales-based decisions on what relationship a company will have with its customers.

6.8.2 New Product Development Process

Assuming a business decision is made regarding intellectual property issues, the next step is to define a new product introduction process. This is in accordance with the ISO-9001 standards which include defining a market for the material, setting up specifications for the material, as well as the technical approach to the pre-production [50]. In most cases, the R&D portion of the technical approach for a new product introduction into production involves two facets:

(1) Adapting a small scale R&D process into existing (or purchased) large scale manufacturing equipment
(2) Understanding the processing science associated with volume manufacturing operations.

These elements go hand in hand, but typically it is important to understand the process limits for a new material to be placed in production. For example, what are the high and low temperature limits for sintering a material within specifications, what is the maximum time and minimum time at the sintering temperature to produce conforming product, what is the optimal binder content and if the binder is not completely removed prior to sintering, and what is the effect of reduced oxygen pressures during sintering due to the presence of these combustion products such as carbon monoxide and hydrocarbon vapors. From a powder processing standpoint, it

is also critical to know the compositional limits for which material meeting the specifications may be made.

6.8.3 Movement to Production Scale Equipment

To affect the transfer into production, many companies set up a new product introduction team which is composed of both R&D and production personnel to orchestrate the movement into production. The effort is usually divided into four phases: powder manufacture, forming, firing, and post-firing.

In general, the effort begins with the powder preparation, largely because, if the powder is bad, then it is unlikely that any process further downstream will be able to correct for poorly made powder. The output of the powder process is to produce a solid state reacted material with the proper particle size and powder surface area for optimal sintering, the proper binder composition and granule size for forming, and the proper chemistry and phase content to ensure that the magnetic and electrical properties are in specification after sintering. The first step is the choice and characterization of raw materials. This stage goes more smoothly if R&D uses the same raw materials as production. The blending step is extremely important as well as a poor blend can lead to disastrous results in cases where unintended kinetically stable intermediate phases form and cannot be removed by re-processing. Moving from lab scale ball mills to production scale vibratory mills can be a challenge since the slurry composition (in terms of the amount of water, non-aqueous medium, dispersant, etc.) is likely to have to be engineered from scratch. Typically blending is done in a fluid media necessitating a drying step as well.

After blending is the pre-sintering (or calcining) step. This step is necessary to react the oxide components to form the desired phase. In the case of yttrium iron garnet, the thermally driven reaction would be:

$$3Y_2O_3 + 5Fe_2O_3 \rightarrow 2Y_3Fe_5O_{12}$$

The powder should be homogenous and a fine enough particle size to drive the solid state reaction. Additional considerations include understanding the thermal profile of the kiln as well as determining what containers the powder is to be in contact with during the heat treatment. The heat treatment temperature has to be optimized as well. Too low and the reaction would be incomplete, too high and some sintering will accompany the calcinations necessitating vigorous post-calcine particle size reduction and the concomitant danger of extensive contamination from this process. After the pre-sintering comes the comminution step where the reacted particles are milled to reduce the particle size to a level optimal for later sintering. Binder is typically added during milling and the slurries are spray-dried into soft deformable granules suitable for pressing.

For the forming process, the binder content needs to be optimized as well as the green (packed powder) density. For the firing process, the thermal profile has to be

determined and whether the new product will be fired in a periodic kiln or a tunnel kiln. The thermal variation throughout the kiln needs to be monitored and the sintering atmosphere optimized to meet the need to produce consistent product throughout the kiln, for partial or full kiln loads.

In general, the pre-production step may take anywhere from six months to a year or more. As technical challenges manifest themselves during the ramp-up, R&D performs parallel experiments to understand the science behind these process variations and therefore help tighten down the process. After certain phase-gate criteria are met, the process is formally transferred to production.

6.8.4 Marketing New Material Products

Most medium-sized companies do not have the luxury of using precious resources for high market- risk or high technical-risk research. Material development is a time consuming process and often requires enabling technologies to be present for the material to be a viable commercial success. For example, Teflon development took 31 years and it took 17 years from the development of Kevlar until the product reached 50% of its eventual annual sales volume [51]. As a result, organic R&D tends to focus on known market or markets adjacent to known markets. In addition, it is important to work with the largest companies who drive the technology in a given space. Technological innovations occur rapidly and there are often many ways to solve a particular technological problem. By working with the largest companies with the deepest pockets, one has some level of assurance that years of R&D effort will not be wasted because some other technical solution is adopted in the market.

6.9 Emerging Directions in Microwave Materials Research

6.9.1 Low Dielectric Constant Microwave Dielectrics

Although there is an excellent suite of commercially available materials in the 20–45 dielectric constant range, there is a demand for new materials in the low and high dielectric constant range for new applications. Super-Q materials with a low dielectric constant are in demand for high frequency (>10 GHz) applications such as collision avoidance [52]. A low dielectric constant is necessary to have a resonator of a manageable size at these frequencies. Current microwave materials with low dielectric constants include aluminum oxide with $\varepsilon' = 10$ [53], magnesium aluminate spinel with an $\varepsilon' = 10$ [54], forsterite ($\varepsilon' = 6$) [55], cordierite ($\varepsilon' = 4$) [56], and magnesium aluminum titanate ($\varepsilon' = 12-20$) [57]. These materials may show

very respectable Q values (Qf > 100,000 for pure aluminum oxide). There is also research into looking into high Q materials with dielectric constants lower than 10 such as Willemite (Zn_2SiO_4) [57] which has a dielectric constant of 6.6, a Qf product of 219,000 and a τ_F of −61 ppm/°C. Much of the research effort on this material is focused on tuning the τ_F to values closer to 0. Another active area of research is for low dielectric constant materials based on the corundum structure such as $Mg_4(Nb,Ta)_2O_9$ [58] with a dielectric constant of 12 and Qf values of up to 347,000 reported. Again, the τ_F is an unmanageable −70 ppm/°C [58] and all efforts to tune this material to a τ_F closer to 0 have decreased the Q.

6.9.2 High Dielectric Constant Materials and the Physical Origins of the Dielectric Constant

There appears to be a limit to the Q values attainable for ceramics with a dielectric constant greater than 50 since the same incipient ferroelectric behavior leading to the high dielectric constants lead to reduced Q values as well. The industry standard material with a dielectric constant in the 70–90 range is the $Ba_{6-x}Ln_{8+2/3x}Ti_{18}O_{54}$ system (Ln = La through Gd) with the tetragonal tungsten bronze structure [59]. This material is temperature compensated, and with chemical modifications, can show Qf products in the 10,000–12,000 range at both 1 GHz and above [60]. There are numerous applications for high dielectric constant materials including dielectric antennas and co-axial resonators. The chief advantage of such high dielectric constant materials is for component miniaturization. Since many of these applications involve metal in direct contact with the ceramic body, the Q requirement is not as stringent. However, temperature compensation is required for many applications so titanium oxide (dielectric constant = 100, τ_F > +500) is not a viable option. There are numerous chemical systems being researched that may be of interest for such high dielectric constant applications. These include the $(Li_{1/2}Nd_{1/2})TiO_3$–$CaTiO_3$ system [61] with dielectric constants near 120 and the bismuth niobate pyrochlores with dielectric constants in the 150–200 range [62]. An especially intriguing system is the $AgNbO_3$–$AgTaO_3$ system which has been reported to show dielectric constants near 400 [63]. However, this solid solution has an extremely non-linear temperature dependence of the dielectric constant making design with materials in this system problematic.

6.9.3 Current Research into Magnetic Materials

In a similar fashion to dielectrics, there are significant advantages to increasing the dielectric constant for garnets used in circulator and isolator applications. Reduced

ferrite disk size leads to reduced isolator sizes and smaller footprints for these components in the base station. Yttrium iron garnet and many of its narrow resonant linewidth substitutes have a dielectric constant close to 15. However, the substitution of Bi^{3+} for Y^{3+} leads to materials with enhanced dielectric constant due to the "lone pair" effect previously mentioned. However, because of the larger ionic radius of Bi^{3+} (compared with Y^{3+}) and its asymmetrical nature due to the lone pair, there is a limit to which Bi may substitute for yttrium. For an 1850 gauss material, 1.4 formula units of yttrium may be substituted with bismuth. As a result, the garnet material has a dielectric constant of 30 and the area of individual ferrite disks within an isolator or circulator is reduced by 50% [64, 65].

An additional effort is underway with materials suitable for self-biasing circulators [66]. In this case, hexagonal ferrites, mentioned previously are used for high frequency application where a metallic biasing magnet is not needed. Some hexagonal ferrite materials based on $BaFe_{12}O_{19}$ have such strong magnetic anisotropies that individual grains have a built-in bias mechanism. There are still some technical challenges associated with the self-biasing circulators such as obtaining a magnetically aligned (textured) microstructure as well as dealing with the very high magnetic losses associated with hexagonal ferrites.

6.9.4 Special Applications for Microwave Materials

Another active area of ceramic materials research involves low-temperature co-fired ceramics (LTCC) materials and their potential compatibility with Silicon in semiconductors. LTCCs are ceramic components that are integrated into the chip structure. To be co-fired with semiconductors, they must be able to densify in the range of 800–1100 °C (Ag melts at 962 °C and Cu melts at 1064 °C) [67, 68]. Because of their direct contact with conducting materials, the Q requirements are less stringent for these materials. Initially LTCC materials were glass-ceramic composites where classical microwave dielectrics were blended with a low melting frit to form an LTCC material. However, there are disadvantages with this design including poor mechanical reliability and the tendency for the glass to react with the metal conductors [68]. As a result, there is a great deal of research into glass-free LTCC materials. There are two approaches to designing materials glass-free materials for LTCC applications. First, the designer can take a classical bulk microwave dielectric such as $BaTi_4O_9$ and add a sintering aid such as CuO or B_2O_3 to reduce the firing temperature [69, 70]. A second approach is to search for new materials among some low melting oxides such as Li_2O, Bi_2O_3, and even TeO_4 [71–73]. There is a good deal of research on perovskite tellurites as well as on the Li–Ti–Nb–O system in an effort to find good properties in a low firing microwave dielectric material.

6.10 Future Challenges

6.10.1 Low Cost Foreign Competition

With a new product, there is typically a development time, followed by a ramp-up to volume production when the market has adopted the product (in this case, a new ceramic material) [74, 75]. At the beginning of the volume production phase, the new product may command the highest price. With some markets like the medical and military market, this price may be stable and extend for a very long time (due to the very high barrier to entry for competitors being designed in due to lengthy qualification processes). However, for many other commercial markets, price erosion kicks in and competitive solutions are quickly developed (or the patent expires and the virtual monopoly disappears). As margins decline, the material becomes a commodity if new, improved, products are not developed. With relatively few players in this market, even as commoditization occurred, margins could still be maintained due to the process improvements. In fact, for years, the main players in microwave magnetics were in the United States, Japan, and France and in microwave dielectrics in the United States, United Kingdom, Japan, and somewhat in South Korea. However, in the last few years several companies have appeared in China producing both microwave magnetic and dielectric materials. These companies are a serious threat to the established players for two reasons:

(1) Labor costs for manufacturing are typically lower in China
(2) Chinese companies have ready access to a variety of indigenous raw materials without being subject to availability restrictions or excise taxes. This gives them a huge advantage in terms of the cost of raw materials.

In addition, many Chinese universities work directly with Chinese factories, supplying technical support and in some cases transferring their own inventions to their "partner" factories. It is only a matter of time before competitors appear in other nations, with similar advantages.

6.10.2 Staying Ahead of the Curve

How can a company continue to compete in this environment? The best plan is to invent and patent. This is much easier said than done and requires some risk. However, it starts with having a thorough knowledge of the target markets and anticipating customer needs, involves having an R&D team capable of developing innovative products to meet these needs, and requires a company vision that is focused on developing the intellectual property portfolio and filing for patent protection in the United States as well as in foreign patent offices. Patents eventually expire, so the R&D team has to continue to invent and stay ahead of the

curve. This is not a low risk proposition. However, errors in any one of the steps may lead a company with limited resources to make time-wasting errors on the use of these resources. For example, if a market need is misread, there can be fruitless efforts developing a material that nobody wants. Or if a market is accurately read, there is no guarantee that the R&D team will be able to be the first to arrive at the solution. Typically, an R&D team will consist of one or more Ph.D. level individuals in materials science, materials engineering, chemistry or physics. Relevant skills include ceramic processing, ceramic science, phase equilibria and crystal chemistry for the R&D group. It is important to have an engineer of M.S. level that understands ceramic processing to ease the transition of new products from the R&D group into production. There are talented people throughout the world and in the 21st century materials developers will be competing with many more of them than they have in the past. However, in this environment of fast- paced technological change and global competition, the importance of effective, pro-active R&D teams cannot be over-emphasized.

Acknowledgments The author wishes to acknowledge the valuable discussions with Dave Cruickshank, Dan Tipsord, and Mark Wolf of Trans-Tech as well as the synthesis and measurements gifts of Connie Griffith and Jeff Shunkwiler (also of Trans-Tech) and of Davin Phelps (DuPont).

References

1. Phase Diagrams for Ceramists, Joint Publication of NIST and the American Ceramic Society
2. R.D. Shannon, J. Appl. Phys. **73**, 348 (1993)
3. K. Wakino, T. Nishikawa, Y. Ishikawa, H. Tamura, Br. Ceram. Trans. J. **89**, 39 (1990)
4. K. Wakino, T. Nishikawa, H. Tamura, T. Sudo, Microwave J. **1987**, 133 (1987)
5. I.M. Reaney, E.L. Colla, N. Setter, Jpn. J. Appl. Phys. **33**, 3984 (1994)
6. M. Maeda, T. Yamamura, T. Ikeda, Jpn. J. Appl. Phys. **26**, 76 (1987)
7. L.W. Coughenour, R.S. Roth, S. Marzullo, F.E. Sennett, J. Res. Nat. Bur. Standards **54**, 153 (1955)
8. K. Wakino, Ferroelectrics **91**, 69 (1989)
9. H.M. O'Bryan, J. Thomson Jr, J.K. Plourde, J. Amer. Ceram. Soc. **57**, 450 (1974)
10. P. Davies, R.S. Roth, J. Solid State Chem. **71**, 490 (1987)
11. T. Negas, G. Yeager, S. Bell, R. Amren, NIST Spec. Publ. **804**, 21 (1990)
12. T. Negas, G. Yeager, S. Bell, N. Coates, I. Minis, Am. Ceram. Soc. Bull. **72**, 80 (1993)
13. G. Wolfram, H.E. Goebel, Mat. Res. Bull. **16**, 1455 (1981)
14. D. Houivet, J. El Fallah, B. Lamagnere, J. Hausomme, J. Eur. Ceram. Soc. **21**, 1727 (2001)
15. S. Hirano, T. Hayashi, A. Hattori, J. Am. Ceram. Soc. **74**, 1320 (1991)
16. P. RiaziKhoei, F. Azough, R. Freer, J. Am. Ceram. Soc. **89**, 216 (2006)
17. J. Moon, H.M. Jang, H.S. Park, J.Y. Shin, H.S. Kim, Jpn. J. Appl. Phys. **38**, 6821 (1999)
18. J. Bancar, D. Suvarov, M. Valant, G. Drazic, J. Eur. Ceram. Soc. **23**, 1391 (2003)
19. I.M. Reaney, D. Iddles, J. Am. Ceram. Soc. **89**, 1 (2006)
20. S. Nomura, Ferroelectrics **49**, 61 (1983)
21. R.J. Cava, J. Mater. Chem. **11**, 54 (2001)
22. J.K. Burdett, Inorg. Chem. **20**, 1959 (1981)
23. A. Templeton, X. Wang, S. Penn, S. Webb, L. Cohen, N. Alford, J. Am. Ceram. Soc. **83**, 95 (2000)

24. H. Matsumoto, H. Tamura, K. Wakino, Jpn. J. Appl. Phys. **30**, 2347 (1991)
25. P. Davies, J. Tong, T. Negas, J. Am. Ceram. Soc. **80**, 1727 (1997)
26. E.S. Kim, K.H. Yoon, Ferroelectrics **133**, 187 (1992)
27. C.H. Lu, C.C. Tsai, J. Mater. Res. **11**, 1219 (1996)
28. D.J. Barber, K.M. Moulding, J. Zhou, M. Li, J. Mater. Sci. **32**, 1531 (1997)
29. L. Chai, P. Davies, J. Am. Ceram. Soc. **80**, 3193 (1997)
30. V. Tolmer, G. Desgardin, J. Am. Ceram. Soc. **80**, 1981 (1997)
31. T. Vanderah, Provate Communication
32. H. Endo, J. Am. Ceram. Soc. **78**, 534 (1995)
33. A. Akbas, P. Davies., MRS Special Publication 432. Solid State Chem. Mater. 45 (1998)
34. M. Sugimoto, J. Am. Ceram. Soc. **82**, 269 (1999)
35. T. Rojac, A. Bencan, B. Malic, G. Tutuncu, J.L. Jones, J.E. Daniels, D. Damjanovic, J. Am. Ceram. Soc. **97**, 1993 (2014)
36. R.C. Pullar, Prog. Mater Sci. **57**, 1191 (2012)
37. A. Broese Van Groenou, P.F. Bongers, A.L. Stuyts, Mater. Sci. Eng. **3,** 317 (1968–1969)
38. Geller and Gilleo, J. Phys. Chem. Solids **3**, 30 (1957)
39. S. Geller, J. Appl. Phys. **31**, 30S (1960)
40. G. Winkler, P. Hansen, P. Holst, Philips Res. Repts. **27**, 151 (1972)
41. D. Cruickshank, *Microwave Materials for Wireless Applications*, Artech House (2011)
42. G.R. Harrison, L.R. Hodges, J. Amer. Ceram. Soc. **44**, 214 (1961)
43. H.J. Van Hook, J.J. Green, F. Euler, F.R. Czerlinsky, J. Appl. Phys. **39**, 730 (1968)
44. G. Winkler, IEEE Trans. Mag. **MAG-7**, 773, (1971)
45. V.M. Yudin, S.A. Poltinnikov, O.B. Proskuryakov, N.N. Parfenova, Phys. Lett. **28A**, 483 (1969)
46. Hague Center for Strategic Studies, Scarcity of Materials Report (2010)
47. H. Wouters, D. Bol, Material Scarcity, An M2i Study (2009)
48. Hague center for Strategic Studies, Coltan, Congo and Conflict (2013)
49. Leahy-Smith America Invents Act, Public Law 112–29 (2011)
50. International Organization for Standardization, ISO-9001 Quality Management Systems Requirements. American Society for Quality (2008)
51. E. Maine, E. Garnsey, Res. Policy **35**, 375 (2006)
52. H. Ohsato, Mat. Res. Soc. Symp. Proc. Vo. **833**, 241 (2005)
53. S. Penn, N. McN, A. Alford, X. Templeton, M. Wang, M.Reece Xu, K. Schrapel, J. Am. Ceram. Soc. **80**, 1885 (1997)
54. T. Sugiyama, T. Tsunooka, K. Kakimoto, H. Ohsato, J. Eur. Ceram. Soc. **26**, 2097 (2006)
55. T. Okamura, T. Kishing, Jpn. J. Appl. Phys. **37**, 5364 (1998)
56. Z. Wing, J. Halloran, Q. Zhang, P. McGinn, J. Am. Ceram. Soc. **89**, 456 (2006)
57. Y. Guo, H. Ohsato, K. Kakimoto, J. Eur. Ceram. Soc. **26**, 1827 (2006)
58. H. Ogawa, A. Kan, S. Ishihara, Y. Higishida, J. Eur. Ceram. Soc. **23**, 2485 (2003)
59. D. Suvarov, M. Valant, D. Kolar, J. Mater. Sci. **32**, 6483 (1997)
60. US Patent 8,318,623 (2012)
61. X. Chen, W. Zhang, B. Zalinska, I. Sterianou, S. Bai, I.M. Reaney, J. Am. Ceram. Soc. **95**, 3207 (2012)
62. X. Wang, H. Wang, Z. Yao, J. Am. Ceram. Soc. **80**, 2745 (1997)
63. M. Valant, D. Suvarov, A. Meden, J. Am. Ceram. Soc. **82**, 81 (1999)
64. US Patent 8,696,925 (2014)
65. D. Cruickshank, M. Hill, *Plenary Presentation at the MMA-2014 Conference* (Boise, ID, 2014)
66. V.G. Harris, IEEE Trans. Mag. **48**, 1075 (2012)
67. H. Birol, T. Maeder, P. Ryser, J. Eur. Ceram. Soc. **26**, 1937 (2006)
68. M.T. Sebastian, H. Jantunen, Int. Mater. Rev. **53**, 57 (2008)
69. M. Kim, Y. Jeong, S. Nahm, H. Kim, H. Lee, J. Eur. Ceram. Soc. **26**, 2139 (2006)
70. J. Lee, J.H. Lee, J.J. Kim, J. Eur. Ceram. Soc. **26**, 2111 (2006)
71. A. Borisovich, P. Davies, J. Eur. Ceram. Soc. **21**, 1719 (2001)

72. M. Valant, D. Suvarov, J. Am. Ceram. Soc. **84**, 2900 (2001)
73. G. Subodh, M.T. Sebastian, J. Am. Ceram. Soc. **90**, 2266 (2007)
74. T. Levitt, Harvard Bus. Rev. **43**, 81 (1965)
75. G. Day, J. Mark. **45**, 60 (1981)

Chapter 7
Catalytic Materials: Nanofibers—From Research to Manufacture

Nelly M. Rodriguez and R. Terry K. Baker

Abstract Graphene nanofibers are materials that display extraordinary properties suitable for a number of advanced energy storage devices as well as chemical processes. These solids offer the most direct route for the manufacture of bulk quantities of high quality graphene. The cost of producing these materials on a commercial scale presents a major challenge, which we have sought to overcome via the use of natural gas as a source of carbon. The key breakthrough in the process has been the design of a catalyst system that is capable of generating high purity graphene nanofibers and hydrogen in a very efficient manner.

7.1 Introduction

Catalytic Materials, LLC was founded in 1995. This company owns intellectual property for the most advanced technology for the manufacture of high purity graphene nanofibers, multiwalled carbon nanotubes and carbon nanochips. The focus has been on the architecture and design of nano-carbon materials. Design and engineering of carbon nanostructures has required the understanding of the interfacial phenomena at carbon surfaces as well as control over the morphological characteristics of metal catalyst particles. These parameters have been elucidated from dynamic studies performed by in situ transmission electron microscopy (TEM). It is from this foundation of knowledge and years of experience that the journey from research of graphene nanofibers to their manufacture is laid out.

N.M. Rodriguez (✉) · R.T.K. Baker
Catalytic Materials, 325 Heartland Drive, Pittsboro, NC 27312, USA
e-mail: rodriguez@catalyticmaterials.com

L.D. Madsen and E.B. Svedberg (eds.), *Materials Research for Manufacturing*, Springer Series in Materials Science 224,
DOI 10.1007/978-3-319-23419-9_7

7.1.1 Background

In the past few years a tremendous explosion has been taken place in the research and development activities surrounding nanotechnology. While workers in heterogeneous catalysis have appreciated the extraordinary properties displayed by nano-sized metal particles for decades, the recognition that such behavior can be extended to all materials is generating immense excitement in all fields of science and engineering. Indeed, research on the effect of metal particle size and crystallographic orientation on activity and selectivity has been the central theme of many catalytic studies. The notion of using nanotechnology to build molecules atom by atom presents some fascinating opportunities to generate a variety of unusual structures and devices. In this respect, the use of nano-structured materials, particularly those based on carbon that possess a combination of high surface area and high electrical conductivity, is likely to exert an enormous impact in numerous applications. It should be stressed that when one moves into the realm of nano-structured materials, dramatic changes in the intrinsic properties are observed compared to those encountered on the bulk scale. For example, nano-sized metal particles exhibit pseudo liquid-like behavior at temperatures of half their bulk melting point in (K). Tammann [1] first reported this phenomenon in 1932; however, its significance with regard to the catalyzed formation of carbon nano-materials was not realized until about 1970. Indeed, it is this property that allows for the solubility of carbon species in metal catalysts at temperatures around 600 °C, one of the key steps in the carbon nano-material growth pattern that is followed by diffusion and eventually precipitation in the form of a fiber to proceed.

Interest in nanostructured materials has grown following the discovery of the Buckminster fullerene molecule, a new form of carbon produced by arc discharge and laser ablation of graphite [2, 3]. Research in this area also led to the identification of other related structures, which are considered to be an extension of the C_{60} and C_{70} molecules namely, multi-walled carbon nanotubes. It was shown that carbon nanotubes consist of concentric sheets of graphite arranged in a tubular form. Contrary to popular belief, the detailed structure of multi-walled carbon nanotubes was first reported by Baird and coworkers in 1971 [4]. During this period the materials were known as carbon filaments. Since that time there have been numerous papers and patents describing the production of these materials via the metal catalyzed decomposition of carbon-containing gases. Hyperion Catalysis International, Bayer Materials and Arkema use the metal catalyzed decomposition of ethylene or acetylene to generate multi-walled carbon nanotubes (MWCNT) in their commercial processes. In recent years, global research activity has been focused on graphene, a compound that is currently being publicized as the new wonder material with exceptional mechanical, electrical, thermal and optical properties. Figure 7.1 shows a schematic rendition of a sheet of graphene where it the two distinct faces, “armchair” and “zig-zag” are highlighted.

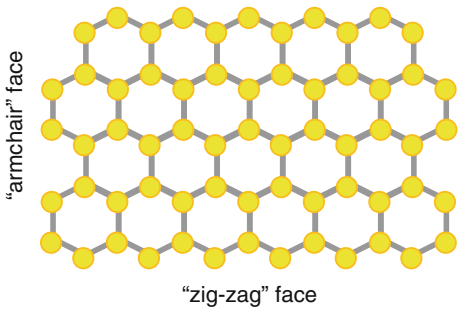

Fig. 7.1 Schematic representation of a graphene sheet

7.1.2 Graphene Nanofibers

While carbon nanotubes have attracted considerable attention, an analogous material, graphene nanofibers, a more recently discovered solid, offers a unique set of properties that have been the target of researchers for over 50 years. These structures are highly crystalline in nature and exhibit relatively high surface areas ($\sim$100 m^2/g) that are two orders of magnitude higher than that of traditional graphite. Furthermore, they possess an extraordinary surface architecture that offers distinctive crystallographic arrangements for deposited metal and metal oxides particles. The presence of edges in the graphite nanofiber conformations allows one to build a variety of chemical functionalities onto the regions that allows for interaction with solids, liquids and gases. As a consequence, one finds that these types of structures can be readily dispersed in both aqueous and organic liquids. Furthermore, graphene nanofibers exhibit good mechanical strength and stability when utilized in a liquid reactant. Structural modifications of the graphene nanofibers can be achieved by heating in an inert gas at high temperatures. This treatment results in a sealing action of one set of edge sites and is found to produce a new material that exhibits remarkable behavior in a variety of applications. One of the most important features of graphene nanofibers is that due to their small cross-sectional area they can be readily cleaved to provide a source of very high purity nano-graphene.

Catalytic Materials LLC has developed a several processes for the synthesis of graphene nanofibers (GNF), which are produced from the decomposition of either carbon monoxide or hydrocarbons over selected metal surfaces at temperatures over the range 600–750 °C [5]. It has been found that by judicious choice of the catalyst and control of the parameters involved in the synthesis, it is possible to manipulate the morphology and the crystallinity of the structure [6, 7]. In this Chapter we shall trace the pathway of the development, manufacture and commercial applications of a unique material, graphene nanofibers.

7.2 Fundamental Aspects of Graphene Nanofibers

7.2.1 The Catalyst

Synthetic graphite is manufactured by the thermal treatment of carbonaceous precursors and it requires temperatures in excess of 3000 °C. On the other hand, via the use of suitable catalysts it is possible to generate graphite at temperatures as low as 600 °C. The selection of the catalyst is crucial since at high temperature and in the presence of a reactant gas, metal particles undergo reconstruction and adopt a shape that ultimately determines the type and orientation of the graphene layers that are deposited. The "herringbone" type is formed when metal catalyst particles adopt a flat diamond-like morphology. In this case, two faces are capable of adsorbing and dissociating the reactant gas and four faces precipitate graphene (Fig. 7.2a). In contrast, when the metal particle acquires a pillbox shape, decomposition of the reactant gas occur on four faces and graphene formation on only two faces (Fig. 7.2b).

7.2.2 Growth Mechanism

The growth mechanism leading to the formation of graphene nanofibers has been studied by many different groups and has been a source of debate, particularly with respect to the chemical state of the active catalyst species and the driving force for the reaction. Studies by Baker and co-workers at Harwell in 1972 employed the sophisticated technique of controlled atmosphere electron microscopy to directly follow the manner by which small metal particles generated graphene nanofibers via the catalyzed decomposition of hydrocarbons [8, 9]. From the detailed analysis of the recorded videotape sequences it was possible to determine the growth rates of the nanofibers and establish some of the kinetic parameters involved in the process.

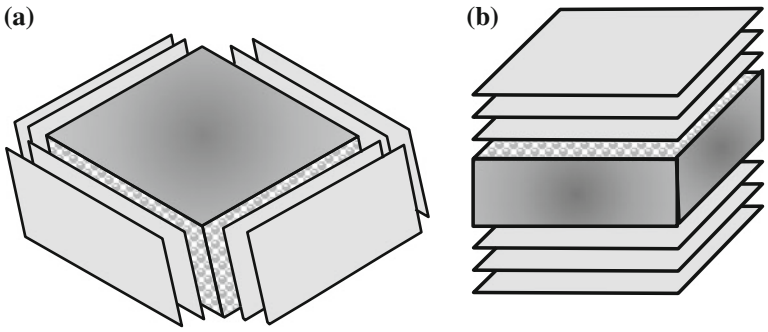

Fig. 7.2 Schematic diagram showing the architecture of **a** "herring-bone" and **b** "platelet" graphene nanofibers and the respective catalyst particle shapes

Based on these investigations, they proposed a growth mechanism that was later refined to include the following steps: (i) adsorption and decomposition of the reactant hydrocarbon or CO molecule at a certain set of metal crystallographic faces, (ii) dissolution and diffusion of carbon species through the metal particle, and (iii) precipitation of carbon at a different set of crystallographic faces to form the nanofiber structure. They claimed that diffusion of carbon through the metal catalyst particle was the rate-controlling step. This assertion was corroborated by the close agreement between the measured activation energies for nanofiber growth and the corresponding value for carbon diffusion through the respective metals that were used as catalysts in the process.

The chemical state of the metal catalyst, the reaction temperature and the composition of the reactant gas were shown to control the morphology and degree of crystalline perfection displayed by the nanofiber. Figure 7.3a–c is a schematic series designed to highlight the key features of the growth steps involved in the production of platelet graphene nanofibers. Initially, the hydrocarbon or CO molecules are chemisorbed on two identical faces of the metal particle (A). The interaction between the gas and metal results in the generation of carbon species, which then dissolve in the particle and proceed to follow two equal and opposite diffusion paths through the catalyst particle (B), finally leading to the precipitation of carbon in the form of graphene sheets at two other sets of identical faces (C) of the particle. The nanostructure assumes "platelet" architecture similar to that of a "deck of cards". As long as the heat balances are preserved in the reaction system, the carbon structure continues to develop and only ceases when perturbations occur in the chemistry of the active faces of the metal catalyst particle. Under these circumstances, carbon builds up at this interface and deactivation occurs. It is believed that a carbon concentration gradient across the particle is responsible for the driving force for diffusion step.

7.2.3 Synthesis of Graphene Nanofibers

Graphene nanofibers can be prepared in relatively large quantities using a variety of metals preferably in a powdered form as the catalytic entities. We have adopted the following protocol for the synthesis of platelet graphene nanofibers. The metal catalyst is dispersed in a uniform manner across the base of a ceramic boat that is positioned in the center of a horizontal tube furnace and reduced in hydrogen at 600 °C. Following this step, the temperature is brought to the desired reaction condition. A predetermined hydrocarbon/hydrogen or CO/hydrogen reactant mixture is passed over the catalyst and the reaction allowed to proceed for periods of up to five hours. Immediately following the growth sequence the reactant gas is replaced with helium and the sample cooled to room temperature. By following this procedure one can generate as much as 20 g quantities of nanofibers from a 100 mg of catalyst powder.

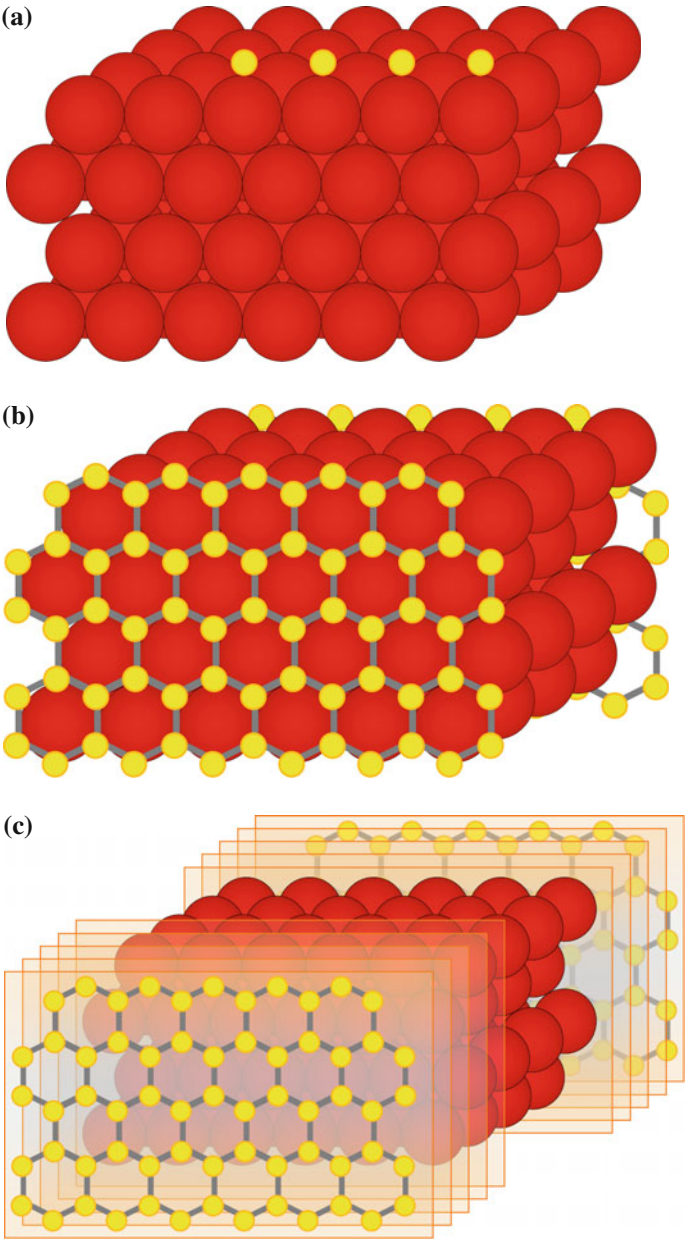

Fig. 7.3 Steps **a**–**c** involved in the growth mechanism of "platelet" graphene nanofibers

The use of bimetallic powders has been found to exert a dramatic impact on the behavior of the catalyst system towards the growth of graphene nanofibers. It is often found that when copper is added to one of the iron transition metals there is a substantial enhancement in the yield of the solid carbon product and furthermore, the morphology and degree of crystalline perfection of the nanofibers is altered to a significant extent [10]. When either pure copper or iron powders were heated in the presence of an ethylene/hydrogen mixture at 600 °C, the metals exhibited little or no ability to catalyze the formation of carbon nanofibers. In sharp contrast, when a small amount of one of these metals was mixed with the other component then, on subsequent treatment under the same reaction conditions, prolific growth of this form of solid carbon was achieved. It was claimed that the enhancement in catalytic activity was due to electronic perturbations in the iron, induced by the presence of copper. This effect resulted in changes in the adsorption characteristics and subsequent decomposition of C_2H_4 on the catalyst surface.

We have used the iron-copper catalyst system for the generation of graphene nanofibers from the decomposition of CO/H_2 mixtures at 600 °C. It was found that whilst the yield of nanofibers was only marginally higher than that achieved by using a pure iron catalyst for the reaction, the degree of crystallinity of the material was significantly higher when the reactant was passed over an Fe–Cu (7:3) catalyst. Other features that were established from this series of experiments included the finding that the optimum solid carbon yields were obtained with a CO/H_2 (9:1) mixture [11]. Another finding was that as the reaction temperature was raised from 600 to 700 °C, a dramatic change in the nanofiber structure occurred from a "platelet" to a "tubular" architecture. It was argued that this transformation was directly linked with the α-Fe to γ-Fe phase change that is known to occur over this temperature range. During this phase transformation the crystal structure of the metal transforms from body-centered cubic (BCC) to face-centered cubic (FCC), and there are major changes in the carbon solubility and diffusion characteristics through iron.

In an alternative approach to producing graphene nanofibers, we a developed a method based on the use of methane as the reactant and capitalizing on previous knowledge acquired by the authors many years ago to design a unique catalyst capable of decomposing this extremely stable hydrocarbon. We have found that a copper-nickel-magnesium oxide catalyst was capable of maintaining its activity towards the decomposition of methane at high levels for relatively long periods of time at 665–725 °C to generate CO free hydrogen and solid carbon [12]. Under these conditions the solid carbon product consisted exclusively of graphene nanofibers possessing a platelet structure. It was interesting to find that when nickel, copper or nickel-copper powders were heated in methane under the same reaction conditions as those stated above, then no conversion of methane was observed. Furthermore, if Ni/MgO or Cu/MgO were reacted with the methane, little or no reaction ensued. We believe that the unexpected activity of a catalyst containing the three components is related to the tendency to form very small nickel-copper alloy particles on the magnesium oxide surface during the initial hydrogen reduction step.

The degree of crystalline perfection of the solid carbon product is controlled by a number of factors including the chemical nature of the catalyst particle, the composition of the gaseous reactant and the reaction temperature. We have established that the graphitic nature of the nanofibers is dictated in large measure by the wetting properties that exist between the metal faces where precipitation of carbon takes place and graphite, i.e. a strong interaction exists between these two components. It has been demonstrated that in order for dissolved carbon to be precipitated in a highly crystalline form, there must be a registry between the interstitial spacing of the metal atoms at this interface and the atomic spacing of the carbon atoms in graphene. Surface science studies indicate that specific crystallographic faces of a metal favor precipitation of dissolved carbon in the form of graphene sheets, whereas less ordered forms of carbon are deposited from other faces [13].

In addition to determining the degree of crystalline order exhibited by the nanofibers, the orientation of the crystallographic faces present at the metal-carbon interfaces are responsible for imposing the particular geometric arrangement of the graphene sheets with respect to the direction of the nanofiber growth axis. Examples of two arrangements, "platelet" and "herringbone" are shown in the high-resolution transmission electron micrographs, 4a and 4b. Both types of nanofibers share a number of common characteristics, including the fact that the width of the structures is the same as that of the associated catalyst particle. Another feature is that the nanofibers are relatively straight, indicating that the carbon diffusion pathways through the catalyst particle are symmetrical (Fig. 7.4).

7.2.4 Characterization Studies

The morphology and other structural features of the graphene nanofibers were determined by the use of several techniques including high-resolution transmission electron microscopy (HRTEM), temperature programmed oxidation in CO_2 (TPO), surface area analysis using nitrogen adsorption (SA) and X-ray diffraction (XRD). The TEM studies were performed in a JEOL 2000EXII instrument (lattice resolution 0.18 nm). Transmission specimens were prepared by ultrasonic dispersion of samples of the solid carbon product in iso-butanol and then applying a drop of the

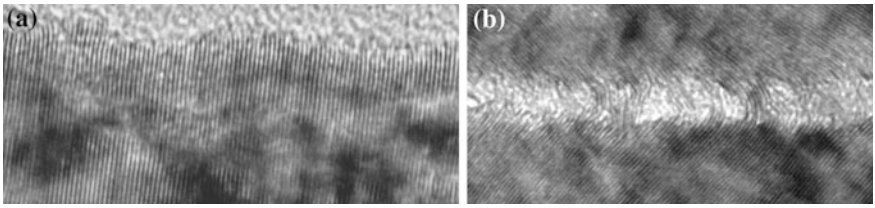

Fig. 7.4 High resolution transmission electron micrographs of **a** "platelet" and **b** "herring-bone" graphene nanofibers

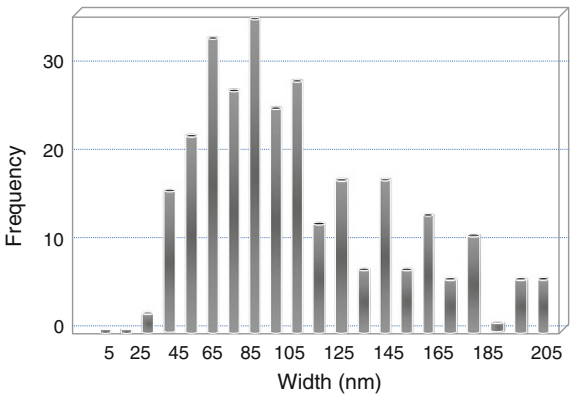

Fig. 7.5 Size distribution of "platelet" graphene nanofibers from the decomposition of CO/H_2 (4:1) over a Fe–Cu (7:3) catalyst at 600 °C

resulting suspension on to a holey carbon support grid. Low magnification inspection of many different areas of such specimens allows one to determine the sizes of the nanofibers produced from a given experiment. In order to gain a meaningful size distribution, it is essential to make measurements of over 300 nanofibers. Figure 7.5 shows the distribution, of "platelet" graphene nanofibers from the decomposition of CO/H_2 (4:1) over a Fe–Cu (7:3) catalyst at 600 °C. From this type of procedure it was evident that the average width of the nanofibers was about 80 nm with typical lengths of 5–10 μ.

The characteristics of controlled oxidation of carbonaceous solids in CO_2 provide a very sensitive method of establishing the structural perfection of such materials. We have compared the gasification profiles of the catalytically generated nanofibers to that of two forms of carbon that possess extreme structural order: high purity single crystal graphite (highly crystalline material) and active carbon (amorphous in nature). These studies were performed in the presence of a CO_2/Ar (1:1) gas mixture using a Cahn 2000 microbalance at a heating rate of 5 °C/min. Under these conditions the onset of gasification of the active carbon sample was observed at 550 °C, whereas the corresponding temperature for graphite was found to be 860 °C. From a comparison of the gasification profiles of these two forms of carbon with that of the uncharacterized sample it is a simple task to gain an insight into the structural perfection of the latter material. In order to overcome any problems associated with the participation of metal impurities in the gasification process, the samples must be initially demineralized by treatment in 1 M hydrochloric acid to remove the catalyst particles. Failure to perform this step in a thorough manner will result in an erroneous gasification profile. Figure 7.6 shows the temperature programmed oxidation profile for nanofibers formed from the interaction of Fe–Cu (7:3) powder with CO/H_2 (4:1). It can be seen that the nanofibers generated at 600 °C exhibit gasification characteristics that are very close to that of single crystal graphite.

A Rigaku Multiflex X-ray diffractometer with monochromatic Cu Kα radiation was used for the X-ray determinations. Three samples of "as-grown" and

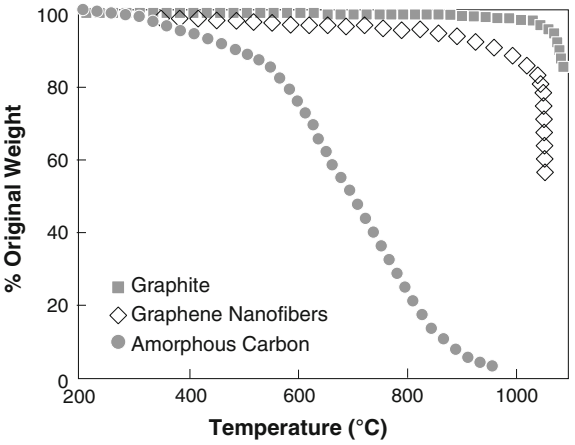

Fig. 7.6 Comparison of the temperature programmed oxidation profile in CO_2 for graphene nanofibers formed from the interaction of Fe–Cu (7:3) powder with CO/H_2 (4:1) with those of active carbon and graphite

Table 7.1 Characteristics of "platelet" graphene nanofibers as a function of treatment conditions

Treatment temperature (° C)	Surface area (m^2/g)	d-spacing (nm)	L_c002 (nm)	L_a110 (nm)
As grown	80.0	0.3369	30.3	14.8
1800	48.0	0.3366	33.5	15.1
2300	38.0	0.3363	35.4	17.7
Graphite	1.0	0.3359	–	–

L_a crystal size; L_c stacking height

heat-treated nanofibers were examined at a scanning rate of 1°/min within the 2Θ values 34° to 84°. Inspection of the X-ray diffraction patterns of the three samples of nanofibers samples revealed the progressive enhancement in the degree of crystalline perfection achieved by a heating treatment in argon, Table 7.1. For example, the sample treated at 2300 °C showed separated (100) and (101) peaks, while the other two GNF samples exhibited a broad and coupled peak between 42° and 45°. The separation of (100) and (101) has been a criterion for evaluating the crystallinity of synthetic graphite. Crystallite sizes obtained from the (110) peak, L_a110 showed the existence of a significant increase (about 20%) after the treatment at 2300 °C. All these features suggest that while the "as-grown" "platelet" graphene nanofibers possessed a well-developed graphitic structure, the degree of crystalline perfection could be further enhanced by heat treatment at high temperatures in argon. Also included in Table 7.1 for comparison purposes, are the data obtained from a sample of high purity graphite.

Brunauer–Emmett–Teller (BET) surface area measurements were carried out in a Coulter Omnisorb 100CX unit with nitrogen at −196 °C using the static method. Values for "as-prepared" and "heat-treated" graphene nanofibers along with pure graphite are presented in Table 7.1.

7.2.5 *Properties of Graphene Nanofibers*

HRTEM has revealed that these materials consist of extremely small graphene platelets that are separated at a minimum distance of 0.342 nm and held together by van der Waals forces. Scanning electron microscopic observations indicate that the cross section of a "platelet" graphene nanofiber is not cylindrical, but either rectangular or rhombohedra. Whereas the basal plane is the main face revealed in conventional graphite materials, the edge sites are the only faces exposed in these types of nanofibers. The unique configuration adopted by graphene nanofibers endows the material with a rare set of properties; a high electrical conductivity combined with a large fraction of active sites that correspond to the exposed edge of the platelet architecture. These regions are available for chemical and physical interactions with a variety of species. Perhaps one of the most unexpected findings is that these highly graphitic materials can exhibit relatively high surface areas that can be activated to a level of around 250 m^2/g.

A further factor to be taken into account is the chemical functionality that exists at the edge regions of the nanofibers. When graphene nanofibers are in their pristine state and free of surface oxygen groups they are hydrophobic in nature. Following normal activation procedures, such as oxidation in CO_2, the materials acquire a certain degree of hydrophilic character. It has been demonstrated that following treatment in an oxygen plasma, acidic groups are introduced onto the surface, while nitrogen and ammonia plasmas produce basic functionalities. The possibility of controlling the acid-base properties of the graphene nanofiber surface will have a significant impact on a variety of applications involving adsorption and separation of liquids.

Table 7.2 shows the transmittance criteria used to rank the dispersion characteristics of graphene nano-materials in various liquids. It is evident that the "as-grown" and "heat-treated" samples exhibited superior dispersion behavior in all the liquid media compared to the performance of MWCNT. Pre-treatment of all the nano-carbon materials in H_2O_2, O_3 and H_2O_2/O_3 appeared to improve the dispersion in water as shown in Table 7.3. This behavior supports the claim that such treatments result in the conversion of unstable –O–O–O– groups present on the as grown surface of the carbonaceous solids into stable –COOH–, –CO– and –OH

Table 7.2 Transmittance index criteria used to rank the dispersion of carbon nanomaterials in various liquids

Dispersion index	Transmittance index criteria description
5	Very dark supernatant/no precipitates
4	Very dark supernatant/trace amount precipitate
3	Dark supernatant/some precipitate
2	Dark supernatant/substantial amount precipitate
1	Light dark supernatant/heavy black precipitate
0	Clear supernatant//all black precipitate

Table 7.3 Dispersion of carbon nanomaterials after sonication for 30 min in various liquids

Treatment/solvent	GNF as grown		GNF HT 3000C		MWCNT	
	a	b	a	b	a	b
Immersion in H_2O	4	3	4	3	2	1
30% H_2O_2 and then immersion in H_2O	4	4	5	4	2	1
O_3 and then immersion in H_2O	4	4	4	3	2	1
O_3 followed by 30% H_2O_2 and then immersion in H_2O	4	4	4	2	3	3
Oxidation at 450 °C and then immersion in 2-butanol	5	4	5	4	3	1
Oxidation at 450 °C and then immersion in acetone	4	3	5	4	2	1
Oxidation at 450 °C and then immersion in dimethyl formamide	5	4	5	4	1	0

First and second values refer to the dispersion indexes (a) immediately following sonication for 0.5-h and (b) 24-h later, respectively

hydrophilic functionalities. A further rationale that should be taken into consideration is the possibility that the nanofiber materials readily undergo exfoliation following the pre-treatments and as a consequence, dispersion is enhanced. When the same set of carbon nano-materials were initially pre-oxidized in air at 450 °C prior to sonication in various organic media then once again the graphene nanofiber samples exhibited much higher dispersion characteristics than MWCNT. Indeed, we have found that treatment in a concentrated HNO_3/H_2SO_4 mixture at 90 °C for several hours is required in order to disperse the latter materials in water.

7.2.6 *Heat Treated Graphene Nanofibers*

We have found that when "platelet" graphene nanofibers are subjected to a high temperature treatment from 1100 to 3000 °C in an inert gas environment, certain edge regions of such materials undergo a reaction that produces the fusion of adjacent layers that results in a "sealing action" of up to 10 neighboring graphene layers. These structures form folds of two, four, six, eight or ten walls. The modified "platelet" graphene nanofibers can be subsequently cleaved into smaller sections resulting 'chips" or slabs with cross-sectional dimensions in the range 40–120 nm, and spacing between graphene layers of 0.33–3.02 nm. It should be stressed that the lower limit width is significantly smaller than that of traditional SWCNT. The average thickness of the "chips" is dependent upon the temperature at which the precursor "platelet" graphene nanofibers are treated. On the other hand, the distance between the inner adjacent walls of the "nanochips" is fixed at a distance of 0.342 nm, which is narrower than any other known carbon nanostructure. Consequently, these new materials are anticipated to exhibit a set of unique chemical, physical and electronic properties.

The impact of the high temperature treatment can be seen in the high-resolution micrograph, Fig. 7.7. The formation of loops resulting from a sealing action of the edge regions is clearly visible. It was evident that as the treatment temperature was raised so there was a progressive increase in the number of walls associated with a given set of sealed sections. From inspection of the micrographs it was possible to measure the number of walls in a given set of carbon nanochips and these data are presented in Table 7.4. These measurements were based on at least fifty different

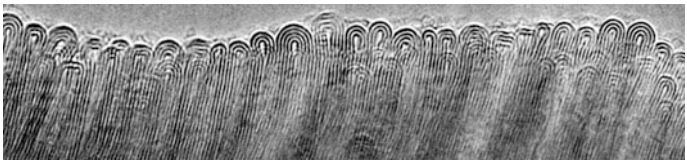

Fig. 7.7 High-resolution transmission electron micrograph showing the formation of loops at the "armchair" faces of "platelet" graphene nanofibers following high temperature treatment in argon

Table 7.4 Effect of heating platelet graphene nanofibers (P-GNF) at various temperatures in flowing argon

Material	Average number of looped walls in nanochips
P-GNF1100	2
P-GNF 1800	2
P-GNF 2330	6
P-GNF 2800	10
P-GNF 3000	10

structures at each temperature. It is evident that, as the treatment temperature increased, there was a progressive increase in the number of loops associated with the nanofibers. As the temperature was raised from 1100 to 3000 °C, the average number of sealed walls in a given chip increased from two to ten. Similar observations were reported by Murayama and Maeda [14] from treatment of graphene nanofibers in argon at 2800 °C.

It is evident that the treatment of P-GNF in argon at temperatures up 3000 °C imposes major modifications on both the structural and chemical properties of the material. Since the adjacent layers are physically locked together the intercalation properties will tend to become more selective in nature and ingress of large ions and molecules may be restricted. It should be stressed, however, that the sealing action may be limited to a certain set of graphene faces, possibly the "armchair" arrangement whilst the "zig-zag" faces remain in their initial active state. Despite this structural transformation it is significant that the spacing between the graphene layers is unchanged and slightly greater than that associated with high purity graphite. This apparent disparity can be rationalized according to the notion that at the nanoscale level bulk thermodynamics need to be adjusted and the forces between adjacent layers of P-GNF are weakened. Under these conditions one can expect to observe significant differences in absorption, adsorption and cleaving characteristics compared to those exhibited by bulk graphite. It should be appreciated that both natural and synthetic graphite will have been subjected to temperatures of at least 3000 °C and, as a consequence, a similar linking of a set neighboring edges might have occurred. These looped regions appear to offer a different reactivity to those of unsealed edges. In contrast to the harsh conditions required for bulk graphite, it is a relatively simple task to cleave the purified P-GNF structure into discrete sheets of graphene.

7.2.7 Graphene

Methods for the preparation of samples consisting of a few graphene layers have been known for about 50 years [15]. The procedure developed by Hennig involved the cleaving of crystals of natural single graphite obtained from Ticonderoga, New York. Successive layers were removed from the bulk graphite crystals using Scotch

tape until an optically transparent section remained. Such specimens varied in thickness from about 1 to 5 nm. In later years, Baker [16] at Exxon Mobil Corp. used the same procedure to prepare specimens that were used for controlled atmosphere electron microscopy dynamic studies of metal catalyzed gasification of graphite.

One of the most important features of graphene nanofibers is that due to their small cross-sectional area they can be readily cleaved to provide a source of very high purity nano-graphene and this compound is currently being publicized as the new wonder compound with exceptional mechanical, electrical, thermal and optical properties [17]. In this regard it is significant that Japanese workers [18] have claimed that following supercritical fluid exfoliation graphene nanofibers underwent a progressive decrease in the number of layers to produce nano-graphene.

Natural and synthetic graphites have been exposed to temperatures in excess of 3000 °C and as such, one may safely assume that the structure at the edge regions is identical to that exhibited by graphene nanofibers heat treated at comparable temperatures, Fig. 7.7. It would have been impossible to observe this feature by TEM given the thickness of the material. It has been reported that preparative methods of graphene from either natural or artificial graphite precursors require aggressive oxidation treatments that involve the use of a mixture of concentrated sulfuric and nitric acids in order to separate the layers. It is not surprising, since we have conclusively demonstrated in this chapter that when graphene nanofibers are heated to temperatures in excess of 2400 °C, linking of adjacent layers to form loops takes place. In contrast, graphene nanofibers are synthesized a temperatures no higher than 700 °C and under such conditions there is no formation of loops. We can therefore assert that the most direct route to graphene is via delamination of graphene nanofibers that have not been "graphitized".

7.3 Applications of Graphene Nanofibers

7.3.1 Use of Graphene Nanofibers as Catalysts

Conventional heterogeneous catalyst systems consist of a metal phase dispersed on a powdered or pelleted carrier and while these classical designs have provided a satisfactory means of supporting small metal particles there is a need for major innovations in this area. The emergence of new nano-fibrous materials with diverse structures affords one with the opportunity of exploiting the potential of such solids as novel catalyst entities. The networked structure of these materials allows for easy access of both liquid and gaseous reactants. As a consequence, more efficient interaction between the active sites and reactant molecules is achieved and problems associated with mass transport limitations are minimized.

Dehydrogenation of organic molecules is a rapidly expanding area of catalysis in which the synthesis of styrene from ethylbenzene is a major commodity. The major

route for the production of styrene is from the catalytic dehydrogenation of ethyl benzene [18, 19]. This process is carried out in an adiabatic fixed dual-bed system at atmospheric pressure and temperatures between 600 and 660 °C. The traditional commercial catalyst used for the reaction is prepared by a co-precipitation protocol to give a composition of 88 wt% Fe_2O_3, 2.5% wt% Cr_2O_3 and 9.5 wt% K_2O. The following set of reactions occurs simultaneously giving an overall conversion level of 50–65%. Although there is a high initial selectivity to styrene, about 90%, the current catalyst systems rapidly lose activity.

$$C_6H_5CH_2CH_3 \rightarrow C_6H_5CH = CH_2 + H_2$$

$$C_6H_5CH_2CH_3 \rightarrow C_6H_6 + C_2H_4$$

$$C_6H_5CH_2CH_3 + H_2 \rightarrow C_6H_5CH_3 + CH_4$$

The current commercial catalyst system suffer from a number of drawbacks that are associated with various deactivation phenomena, including excessive coke formation, migration of the potassium promoter, transformation of the iron oxide component and physical degradation. Furthermore, traditional catalysts contain constituents such as chromium that are considered to be environmental hazards and as a consequence, present disposal problems. The potential to carry out the reaction at lower temperatures and at the same time achieve high selectivity towards the desired product would result in significant energy savings and a reduction in greenhouse gas emissions.

Recent studies have demonstrated that certain carbon materials exhibit significant catalytic activity for various reactions, including the oxidative dehydrogenation of ethyl benzene [20]. Graphitic materials appear to exhibit superior catalytic performance than that displayed by active carbon samples [21]. At this time, however, it is not clear as to whether the catalytic activity is enhanced by interaction of the hydrocarbon with the basal plane regions or by chemisorption at the edges sites. The use of high surface area carbon would be desirable as it is expected that higher reactivity could be achieved. The important criterion is that in order to realize the full potential of the material, there must be edge sites associated with the nanofiber.

In order to evaluate the performance of both pristine and heat-treated graphene nanofibers as catalysts for the oxidative dehydrogenation of ethyl benzene (EB), experiments were carried out for extended periods of time with various reactant mixtures at temperatures ranging from 450 to 650 °C. The reaction conditions were as follows: mole ratio O_2/EB = 1.4, EB flow rate = 9.33×10^{-6} mol/min, He = 9.8 cc/min, catalyst weight = 40 mg. In each case, the data were taken after 22 h on stream. The latter material was generated by treatment of P-GNF at 2330 °C in argon for 30 min. Inspection of the results given in Table 7.5 reveals that the highest styrene selectivity and yield was obtained at 545 °C when pristine graphene nanofibers were used as the catalyst. On the other hand, the data presented in Table 7.6 shows that when heat-treated graphene nanofibers were used as the

Table 7.5 Effect of reaction temperature on the catalytic performance of as-grown graphene nanofibers for the conversion of ethylbenzene to styrene

Temperature (°C)	EB conversion (%)	ST selectivity (%)	ST yield (%)
515	29.0	98.1	28.4
545	39.8	93.9	37.0
575	30.4	88.1	27.0

Table 7.6 Effect of reaction temperature on the catalytic performance of heat-treated (2330 °C) graphene nanofibers for the conversion of ethylbenzene to styrene

Temperature (°C)	EB conversion (%)	ST selectivity (%)	ST yield (%)
450	23.5	100.0	23.7
475	34.3	93.6	32.1
500	47.7	92.8	44.2
547	69.6	76.5	53.3
575	73.7	78.2	57.7
600	80.7	69.9	56.4
625	76.9	70.1	53.8
650	76.4	61.6	47.1

catalyst the maximum activity for the conversion of EB was achieved at 600 °C and the optimum selectivity to the desired product, styrene (ST) being obtained at 450 °C and the maximum yield of styrene occurs at 575 °C. This difference in the temperature at which highest catalytic activity is achieved is most probably related to the surface structure and degree of crystalline perfection of the two materials.

A further series of experiments was conducted to assess the activity maintenance and selectivity pattern of the two types of nano-carbon catalysts for the EB oxidative dehydrogenation reaction as a function of time. The reaction conditions selected were as follows: mole ratio O_2/EB = 0.86, EB flow rate = 9.33×10^{-6} mol/min, He = 9.8 cc/min, reaction temperature 545 °C and catalyst weight = 40 mg. A comparison of the plots presented in Figs. 7.6 and 7.7 shows that the catalytic activity of pristine nanofibers declines over the reaction period while the selectivity pattern remains unchanged. In contrast, it is apparent that following an induction period of about 5 h, the catalytic activity of the heat-treated analogs for EB conversion actually increases with time and maintains a very high selectivity towards the formation of the desired product, styrene for an extended period of time. Clearly the performance of this latter system is significantly enhanced following the high-temperature treatment.

The data given in Table 7.7 shows the comparison of the performance of various materials, including the current commercial system based on Fe, Cr, K oxides, for the catalyzed oxidative dehydrogenation of ethyl benzene at 500 °C. Other reaction conditions were as follows: mole ratio O_2/EB = 0.86, EB flow rate = 9.33×10^{-6} mol/min, He = 9.8 cc/min, catalyst weight = 40.5 mg. The data were taken 17 h after the start of the reaction.

Table 7.7 Comparison of various catalysts for the conversion of methylbenzene to styrene at 500 °C

Catalyst	(%) EB conversion	(%) ST selectivity	(%) ST yield	S.A. (m^2/g)	Pore size (nm)
GNF2330	47.7	94.8	44.2	38	13.2
GNF1800	36.2	94.4	36.7	48	11.8
P-CNF	35.1	94.1	33.0	80	6.3
Carbon black (XC-72)	34.6	75.5	29.3	230	5.2
Fe, Cr, K oxides	6.9	75.9	5.2	4.4	4.0

An examination of the results shows some major differences in catalytic behavior of the five systems and highlights the superior performance of the graphene nanofibers that had been treated in argon at 2330 °C, which is significantly better than that of the same type of material that had been heated to 1800 °C. While both of these materials exhibited a 100% selectively towards styrene, it is the generation of a higher pore size in the former material that appears to be the critical factor. On the other hand, the magnitude of the surface area of the materials does not exert such a profound effect on the catalytic behavior. Indeed, when one considers all the data, there appears to be a direct correlation between pore size and catalytic performance.

The inter-conversion of CO_2 and CO, and possible transformation of these gases into value-added products play a key role in many of the world's current energy problems. Processes involving the sequestration or chemical conversion of CO_2 are topics of intense research activity since the gas has been identified as a greenhouse gas and are ultimately responsible for global warming. A particularly appealing system involves the hydrogenation of CO_2 into CO and steam via the reverse water-gas shift (RWGS) reaction followed by the catalytic decomposition of CO to form highly tailed graphene nanofibers. This concept is of interest not only from an environmental standpoint, but also economically attractive, since CO_2 is readily available as a cheap and plentiful by-product from oil and coal-based power plants.

Catalytic hydrogenation of CO_2 has some major advantages compared with other traditional methods of disposal. When the reaction is carried out over certain supported metal catalysts it is possible to convert CO_2 into a variety of useful products such as methanol and hydrocarbons. Unfortunately, the high cost and regeneration/disposal operations make these systems unattractive for commercial applications. We have found that graphene nanofibers function as catalysts for the RWGS reaction without the presence of an active metal. Conditions at which the hydrogenation reaction can be performed include temperatures of about 400 to 475 °C at a CO_2:H_2 ratio of about 1:2.

A comparison was made of the catalytic performance of "platelet" and "herringbone" graphene nanofibers with two other commercial carbon materials, Carbon Black XC-72 from Cabot Corp. and Darco G-60 active carbon for the RWGS reaction at 475 °C. Examination of the results shown in Table 7.8 reveals

Table 7.8 Effect of various types of carbon on the CO_2 to CO conversion at 475 °C

Catalyst	Reaction time (h)	%CO_2 conversion
H-GNF	0.5	33.0
	3.0	37.0
	6.0	38.0
	22.0	37.6
P-GNF	0.5	39.0
	1.0	41.0
	4.0	41.0
	23.0	42.0
Carbon black (XC-72)	0.4	0.0
	16.0	0.0
Darco G-60	0.5	0.0
	16.0	0.0

Table 7.9 Comparison of the performance of 10 wt% silver dispersed on various support media for ethylene epoxidation after 100 h at 220 °C

Catalyst	% Conv. C_2H_4	% C_2H_4O selectivity	% C_2H_4O yield
Ag/P-GNF	8.00	49.90	3.98
Ag/HT P-GNF	25.48	39.57	10.08
Ag/α-alumina	10.10	30.60	2.67
Ag/Graphite	4.52	22.94	1.04

that catalytic activity was only achieved when using the graphene nanofibers as the catalytic entities. Furthermore, the "platelet" type appeared to exhibit the highest catalytic activity, which is consistent with the fact that this structure exposes the highest percent of edge sites (Table 7.9).

7.3.2 Use of Graphene Nanofibers as Catalyst Supports

The heterogeneous partial oxidation of ethylene to ethylene oxide is a fully developed technology that is based on the conversion of the olefin/oxygen reactant mixture over an α-alumina supported silver catalyst at between 200 and 250 °C. The key function of the catalyst is to limit the supply of oxygen to the olefin, thereby generating the desired product, as indicated in the following scheme:

$$CH_2 = CH_2 + \frac{1}{2}O_2 \rightarrow CH_2OCH_2$$

If the reaction is allowed to proceed to completion then formation of undesired products occurs, as shown:

$$CH_2 = CH_2 + 3O_2 \rightarrow 2CO_2 + 2H_2O$$

We have investigated the potential of using graphene nanofibers as a support medium for silver metal particles for the epoxidation of ethylene. Experiments were carried out with 10% silver dispersed on pristine and heat-treated graphene nanofibers, single crystal graphite and α-alumina, respectively. These reactions were performed at atmospheric pressure and the C_2H_4/O_2 (1:4) mixture was passed over the catalysts at 220 °C for 100 h. From the data presented in Fig. 7.8 and Table 7.10 it can be seen that at the conditions used in this study both the pristine and heat-treated graphene nanofiber supported silver catalysts gave a higher selectivity towards ethylene oxide formation than the current commercial system. Furthermore, inspection of the plots shows that the selectivity of graphene nanofiber supported metal catalysts continues to rise as a function of reaction time, whereas that of the corresponding alumina supported system exhibits a steady decline over

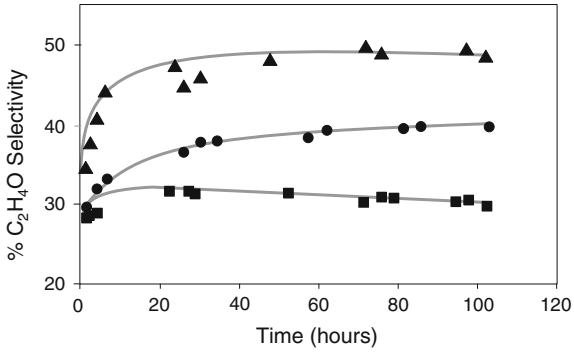

Fig. 7.8 Comparison of the selectivity to ethylene oxide for the C_2H_4/O_2 (1:4) over various supported 10 wt% Ag catalysts as a function of time at 220 °C. *Filled triangle* Heat-treated GNF, *filled circle* α-alumina, *filled square* platelet GNF

Table 7.10 Charging and discharging data and efficiency for various carbons over the range 0–2.0 V

Anode	Electrolyte	Capacity (mAh/g)		Efficiency	
		70 (mA/g)	350 (mA/g)	3rd cycle	10th cycle
P-GNF(1)	EC+DEC	355.1	341.9	96.3	98.1
	EC+PC	347.3	336.7	96.9	98.1
	PC	344.9	335.1	97.2	97.5
P-GNF(2)	EC+DEC	346.3	336.6	97.2	98.3
	EC+PC	346.2	332.9	96.2	97.1
	PC	344.4	332.1	96.4	97.3
Graphite	EC+DEC	318.0	288.1	90.6	93.8
	EC+PC	263.8	244.6	92.7	93.5
	PC	0	0	0	0

the same period. When one combines the activity and selectivity after a given reaction time it is possible to derive the values of yields of ethylene oxide (Table 7.10). It is evident that the highest yields are obtained with catalysts where the silver is dispersed on graphene nanofibers. As stated the current experiments were performed at atmospheric pressure and as such, cannot be directly compared to the commercial operation, which is generally conducted at high pressures (10–30 atm). Under the latter conditions the selectivities towards ethylene oxide formation will be considerably higher than those measured in this work,

Nitrous oxide (N_2O) accounts for about 6% of the greenhouse gases and has an impact on global warming that is 300 times exhibited by CO_2. Emission of N_2O arises from several sources including agricultural, transportation and is generated from industrial activities such as the production of adipic acid, which is used in the production of nylon fiber. The thermal decomposition of N_2O commences at 625 °C and although a number of metal oxides have been found to catalyze the reaction, activity is not maintained for long periods of time. We have investigated the use of copper dispersed on graphene nanofibers as a catalyst for the N_2O decomposition reaction. In order to maintain copper in the metallic state and circumvent the gasification of the carbon support it is necessary to conduct the decomposition reaction in the presence of a reducing agent such as CO according to the scheme:

$$N_2O + CO \rightarrow N_2 + CO_2$$

In this series of experiments we compared the catalytic performance of 5 wt% copper dispersed on "platelet" and "herring-bone" graphene nanofibers (P-GNF and H-GNF) with that where the same metal loading was introduced onto pitch based carbon fibers (PF) for the above reaction. Reactions were carried out in a custom designed fixed bed micro-reactor system using an equimolar mixture of N_2O and CO. The data presented in Fig. 7.9 shows the variation in the activity of the three

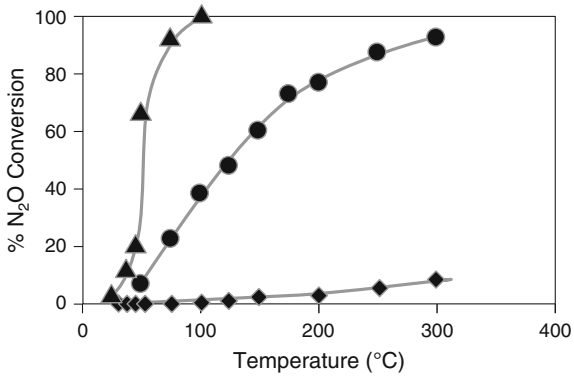

Fig. 7.9 Effect of the carbon support on the copper catalyzed decomposition of N_2O in the presence of CO as a reducing agent. *Filled diamond* Cu/PF; *filled circle* Cu/GNF-P; and *filled triangle* Cu/GNF-H

carbon supported copper catalysts as a function of reaction temperature. A very low conversion of N_2O was achieved when the reaction was carried out over 5 wt% Cu/PF and only reached a level of 10% at 300 °C. In sharp contrast, when the metal was dispersed on graphene nanofibers, extremely high activities were observed. Indeed, when the 5 wt% Cu/H-GNF system was employed, 100% conversion was achieved at temperatures of around 100 °C. While the Cu/P-GNF system does not exhibit the same degree of activity, conversion of N_2O reaches a level of about 95% at 300 °C.

Since the topography of the exposed carbon atoms in the "armchair" and "zig-zag" edge regions of the graphene nanofibers is different, it is known that the deposited metal particles will adopt specific crystallographic orientations depending upon the structure of their surface location sites. Indeed, it was demonstrated that when nickel particles were dispersed on graphene nanofibers, only those metal particles that were in contact with the "zig-zag" faces exhibited catalytic activity [22]. These observations are consistent with the findings that silver particles dispersed on heat-treated "platelet" graphene nanofibers displayed the highest activity, since in this case the "armchair" regions are sealed. Mention should also be made of studies carried out by other researchers who have reported on the remarkable performance of graphene nanofibers as catalyst support media not only for gas phase, but also for liquid phase reactions [23–26].

7.3.3 Use of Graphene Nanofibers in Lithium Ion Batteries

The ability to intercalate lithium ions into the carbon structure of the anode is a major factor in determining the behavior of the Li ion battery. The performance of lithium ion secondary batteries, such as the charge/discharge capacity, rate capability and cyclic stability strongly depend upon the structural characteristics of the carbon material used to fabricate the anode [27]. Types of carbonaceous materials that have been investigated for use in lithium ion batteries include graphitic carbons [28] and non-graphitic carbons, such as semi-coke and glass-like carbons [29]. Soft carbons (synthetic graphites) have received the most attention because of their desired high volumetric reversible capacity and their low electrochemical potential relative to that of lithium metal.

With regard to Li ion battery experiments it is well established that the so-called irreversible loss in capacity during the first few cycles of the unit is associated with a formation of a passivation layer, termed as solid electrolyte interface (SEI). This process is associated with the decomposition of salts and organic solvent species on the graphite edge sites. The formation of SEI consumes lithium ions from the cathode of the battery, leaving an irreversible loss between 10 to up to 70% and a lowering the overall energy density of battery. It has been reported that the irreversible loss or charge/discharge efficiency depends upon such aspects as the nature of the exposed carbon surface and the surface area [30]. Since the reaction takes place on the surface of anode, the surface area of the carbon and/or graphite anode

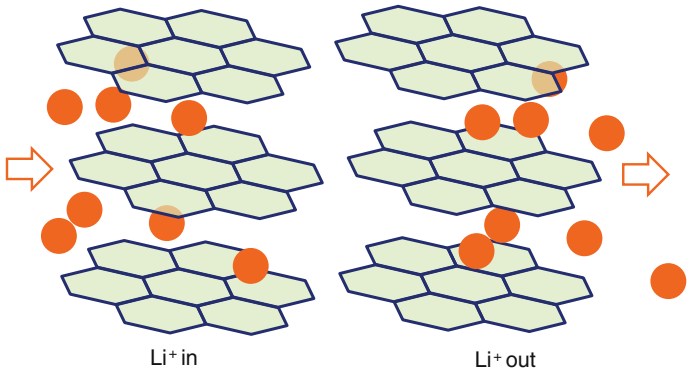

Fig. 7.10 Schematic diagram showing the charging and discharging of lithium ions into and out of the graphene layers

might be proportional to the irreversible loss. Therefore, carbon or graphite materials such as natural or synthetic graphite with a low surface area are usually selected for the use in Li Ion battery as the anode material.

On the other hand, high surface area nano-carbon materials offer certain advantages in battery performance. The battery performance is highly dependent upon the ion transportation within the electrode and/or the electrode material. The successful design of the electrode must also take into consideration the nature of the porosity of the carbon material since this is a critical issue in determining the efficiency of ion transportation within the structure. In contrast, the low surface area of carbon is favorable with respect to the lowering of the irreversible loss during the first few cycles. High surface area, however, will be beneficial for the overall battery performance when one considers aspects such as rate capability, cyclability, and energy density. It is evident therefore that the ideal carbon structure for this application would be one that combines a high surface area with a high degree of chemical inertness. Our experimental data confirms that the deposition of a very thin layer of amorphous carbon on the exposed surfaces of P-GNF achieves this criterion and results in a dramatic improvement in the performance of the material. Figure 7.10 is a schematic rendition of the function of the graphene nanofiber electrode during charging and discharging of lithium.

The evaluation of two P-GNF samples coated with a thin layer of amorphous carbon as an anode for a rechargeable Li Ion battery was carried out in an electrochemical cell. Electrodes were prepared by mixing the P-GNF with 7 wt% of polymeric binder (polytetrafluoroethylene) then coated onto a piece of copper exmet (size = 1 × 1 cm^2). The coated carbon electrode was then dried at 120 °C under vacuum for at least 12 h before use. A thin lithium foil was used as the counter and reference electrodes for charge/discharge test between 0 to 2.0 V versus Li/Li^+. The charge/discharge cycle testing was carried out in three different electrolyte systems, e.g. 1 M $LiClO_4$ dissolved in (a) a 1:1 mixture of ethylene carbonate (EC) and diethyl carbonate (DEC), hereafter, EC + DEC; (b) a 1:1 mixture

of ethylene carbonate (EC) and propylene carbonate (PC), hereafter, EC + PC: and (c) propylene carbonate (PC) alone. Two charge/discharge rates, 70 and 350-mA/g, were applied to the electrochemical cell. The electrochemical performance of P-GNF was assessed based on capacities at different rates, rate capability, capacities and efficiency at different cycles. As a comparison, a graphitic material from Hitachi Chemical was used as control. All the electrochemical experiments were performed at ambient temperature in a glove box filled with argon (99.999%).

The data presented in Table 7.9 illustrates the electrochemical performance of the two samples of P-GNF in a Li ion rechargeable battery. The capacity of GNF is superior to that exhibited by a commercial graphite material at two charge/discharge rates of 70 and 350-mA/g. For instance, the capacities of P-GNF (1) and P-GNF (2) in EC + DEC and EC + PC solvent systems at charge/discharge rate of 70-mA/g are 346–355-mAh/g, give a 15% improvement over the traditional graphite anode with capacities of 264–318-mAh/g. Such an improvement becomes more significant at a high charge/discharge rate of 350-mA/g, the P-CNF samples deliver a capacity range of 332–342-mAh/g, while the traditional graphite anode gives 245–288-mAh/g. The capacity improvement at the high rate is up to 26%. Material with a high rate capability is highly desirable for improving the overall performance of Li Ion battery.

It should be stressed that the traditional graphite anode could not be tested when PC was used as the solvent of electrolyte, no capacity being obtained. The electrolyte decomposition on the surface of graphite electrode was so bad that no lithium ion intercalation/de-intercalation occurred. In sharp contrast, the P-GNF samples exhibited high capacities of around 345-mAh/g at a low rate of 70-mA/g, and more than 332-mAh/g at high charge/discharge rate of 350-mA/g. Since lithium batteries with PC electrolytes exhibit excellent discharge performance under high current density, these results demonstrate the great potential of P-GNF for applications in high performance lithium batteries. It also implies that the structural characteristics of P-GNF are unique for Li Ion battery application, the electrolyte (PC) co-intercalation and interlayer exfoliation, which is a common phenomenon for traditional graphite materials in a PC electrolyte, are not observed with the amorphous coated nanofiber materials. Moreover, the PC electrolyte can function over a wide range of temperature, −40 to 80 °C, a necessary criterion for many applications.

7.3.4 *Use of Graphene Nanofibers in Polymer Electrolyte Membrane (PEM) Fuel Cells*

Recent global events have focused attention on the importance and dependence of the industrialized nations on foreign oil. Since ∼80% of the electricity in the US is generated from fossil fuels, the development of alternative generation systems to solve the increasing demand for energy is imperative. Among the various options, fuel cells offer distinct advantages, because in these devices direct conversion from

chemical to electrical energy is realized [31]. The efficiency of the operation can be approximately three times that achieved using the conventional thermal generation process. The overwhelming advantage of this technology is that the energy source, hydrogen, is one of the most abundant elements found in nature and that the product of the process is water. Furthermore, the system can easily be regenerated therefore constituting a true renewable energy source. Unfortunately, the commercial implementation of such technology has been fraught with problems, one of which being the high cost and mediocre performance of the catalyst. Platinum supported on XC-72 carbon black is the most widely used catalyst system for this application. It has been established that the main functions of the carbon support are (i) dispersion of the Pt catalyst, (ii) provide numerous micropores to the electrode, and, (iii) increase the electrical conductivity of the catalyst layer [32]. In order to achieve a reasonable performance however, the loading of the metal must reach a value of between 30 to 40 wt%.

The utilization of platinum in the current electrode formulation has serious disadvantages, since the metal exhibits a low tolerance to CO and is subject to poisoning, a condition that ultimately leads to high over-potentials [33]. A problem associated with the catalyst is the low reaction rate of the cathode oxygen reduction reaction [34]. It is therefore essential to develop new catalyst systems that exhibit higher activity for both hydrogen oxidation and oxygen reduction reactions and are less sensitive to the presence of a few ppms CO in the fuel. In this regard the use of some of the recently developed carbon nano-materials that do not contain sulfur impurities would appear to offer major advantages over the current technology. Sulfur is known to make the Pt catalyst inactive by blocking reaction sites in a process known as "poisoning".

We have tested the potential of "platelet" graphene nanofibers (GNF), as an electrode for fuel cell applications using the electrochemical oxidation of methanol at 40 °C as a probe reaction [35]. It was found that catalysts consisting of 5-wt% platinum supported on highly electrically conductive nanofibers exhibited activities comparable to those observed with a 25-wt% Pt on Vulcan carbon. In addition, GNF supported Pt particles were less susceptible to CO poisoning. The improvement in performance over that of the commercial catalyst system was attributed to the specific crystallographic orientations that the metal particles adopted when dispersed on the highly tailored GNF structures. This aspect is illustrated in the electron micrographs, Fig. 7.11a, b. In contrast, the Pt particles supported on

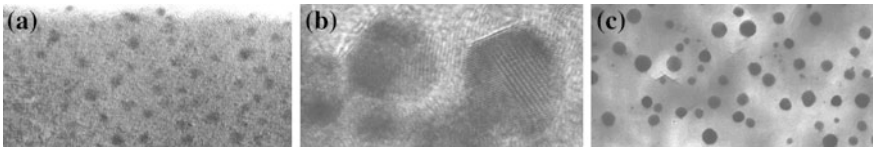

Fig. 7.11 Transmission electron micrograph of **a** Pt particles on GNF support, **b** high resolution TEM micrograph of Pt/GNF showing the thin facetted conformation of the particles and **c** Pt on a XC-72 support

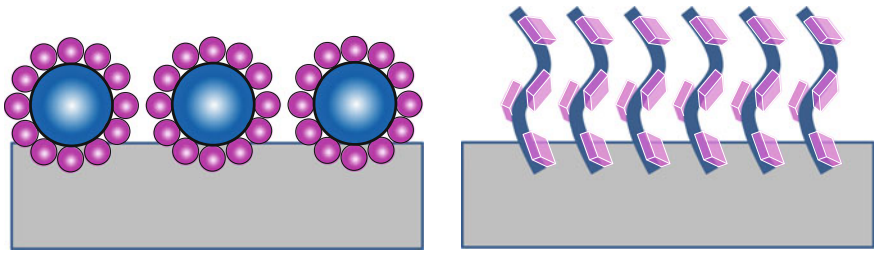

Fig. 7.12 Schematic diagram showing the morphology of Pt particles supported on the globular XC-72 carbon (*left*) and the GNF system (*right*)

Table 7.11 Properties of carbons containing polymers

Filler	Filler surface area (m^2/g)	% carbon	Resistivity (Ω cm)
Carbon black (XC-72)	285	1	1 × 1012
Graphene nanofibers	80	1	1 × 106

Vulcan carbon were found to adopt a more dense globular morphology, suggesting that in this case there was a relatively weak interaction between the metal and support (Fig. 7.11c). We also believe that this material would exhibit a superior performance as the support for the cathode catalyst compared to that achieved with XC-72 carbon black.

Figure 7.12 highlights the major physical differences of two electrodes; one consisting of Pt supported on globular XC-72, where the metal particles (pink) exhibit a weak interaction with the carbon and adopt a globular geometry. In contrast, Pt crystallites supported on GNF establish a strong metal-support interaction and undergo a spreading action to form thin flat particles. The narrow size of GNF will also facilitate gas diffusion processes. A further aspect that marks the difference between these two types of electrodes is the electrical conductivity. Table 7.10 shows data of the electrical resistivity of polymers containing a small fraction of XC-72 compared to that obtained with "platelet" GNF. It is evident that the architecture of carbon nanostructures is much more efficient in achieving a lower electrical resistivity. As a consequence, even if the Pt crystallite loses contact with the GNF support, electron-tunneling effects can maintain catalytic activity of the isolated particle. Under these circumstances, the utilization of the deposited Pt phase can be expected to reach almost 100%. Other workers have reported on the finding of high activity from the use of Pt–Ru particles dispersed on 'herring-bone" graphene nanofibers when used as the electrode for a direct methanol fuel cell [36, 37] (Table 7.11).

7.4 Commercial Production of Graphene Nanofibers

Prior to embarking on the large-scale production phase for graphene nanofibers with the help of Dawnbreaker, a commercialization company, we undertook the task of developing a Business Plan for the operation. From this exercise we discovered that the major hurdle that had to be overcome in order to develop a competitive manufacturing process for the production of these materials was the price of carbon monoxide. This gas had initially been used for the growth of "platelet" graphene nanofibers in the laboratory scale studies. It was imperative therefore that if the commercial operation was going to be viable, an alternative cheaper reactant gas was required. This situation caused us to examine the possibility of using methane as a source of carbon and led to the realization that the cheapest source of this reactant was either natural gas or biogas. Fundamental studies were mounted on the quest to find an efficient catalyst to break down this extremely stable hydrocarbon molecule. Based on our earlier research we were able to develop an inexpensive proprietary catalyst system that is capable of decomposing methane into carbon and hydrogen at temperatures of 650–750 °C.

Graphene nanofibers are being produced in a fluidized bed reactor that allows for a semi-continuous batch operation. The catalyst is supplied into the top of the reactor, natural gas is introduced at a pre-determined flow rate that allows for the particles to be suspended and undergo contact with the reactant gas. Although the diameter of the reactor tube determines the volume of GNF that can be manufactured in a given cycle, heat transfer factors limit the use of a very wide reactor tube. In addition, due to both high temperature and reactivity, most metal alloys are unsuitable for this process. Indeed, since Fe and Ni are catalysts for the formation of other forms of carbon, a search was launched to select a suitable material from which to construct the reactors. In the laboratory studies the reactor tubes were built of quartz, but this arrangement is impractical for mass production. The service temperature of stainless steel is below that at which the reaction is carried out and furthermore, contains constituents that catalyze the formation of undesirable forms of carbon. The notion of using high temperature alloys such as Hastelloy proved to be an encouraging route to follow. After a suitable reaction time has elapsed and either the catalyst is deactivated or the reactor is filled to capacity with GNF, the material is removed and the process repeated. Using a 12″ diameter reactor in a semi-continuous operation we can produce over 3 tons of graphene nanofibers per reactor in a year.

7.5 Conclusions

The manufacture of graphene from naturally occurring or synthetically produced graphite presents a major challenge from the industrial point of view. In order for graphite to reach a high degree of crystallinity it is necessary to expose the material

to temperatures in excess of 3000 °C. This treatment results in the fusion of the edges of consecutive layers and in order to produce graphene it is required to treat graphite with strong acids in order to cleave the multilayers that are present. Such treatment makes the process very expensive and results in a damaged product. We have developed a novel approach for the generation of graphene nanofibers from the catalyzed decomposition of natural gas at temperatures of 725 °C. Under these conditions adjacent layers are not bonded to each other and as a consequence, can readily be separated by a shear force.

7.6 Future Needs and Challenges

In order to increase the scale of production level of graphene nanofibers to 100 tons/year, there are a number of practical and financial issues that need to be addressed:

(a) It is essential that the graphene nanofiber production be made into a continuous process. This is not a simple operation to accomplish, since this is a very unusual catalytic reaction system. The desired product being a solid deposit containing dispersed metal catalyst particles and the by-product, hydrogen, a potentially dangerous gas to handle. Furthermore, it is necessary to separate hydrogen from unconverted methane via a pressure swing adsorption unit.

(b) The scaling up of the production of graphene nanofibers presents one with a dilemma with regard to the reactor material, size and number of units required for this task. The selection of the material to be used in the furnace/reactor zones is a critical aspect in the design of the process. Since the reaction is conducted at a relatively high temperature, ceramic reactors would seem to be the obvious choice, however, their tendency to crack upon temperature cycling creates a safety issue. Inconel 625 appears to exhibit the best set of properties for our applications. In particular, it has a very low iron and high chromium contents. The former could present problems as iron catalyzes undesirable carbon deposition. On the other hand, chromium is likely to segregate to the tube surface and form an oxide coating, which is inactive towards carbon deposition. Inconel 625 has a relatively high thermal conductivity and heat transfer coefficient, which favors heat transfer across the reactor. In this regard, the thermal conductivity coefficient of quartz is about 20 times lower and therefore heat transfer across the catalyst bed is very poor. Since graphene nanofibers exhibit high thermal conductivity one can expect the thermal transport properties of the system to remain quite high.

The dimensions and number of the reactors required to produce 100 tons of graphene nanofibers per year are further aspects to be determined. The current reactor is 12″ diameter, however, if the heat transfer properties exhibited with the Inconel 625 tubes are as good as predicted, then one should certainly consider a 24″ diameter reactor for the large scale manufacturing process as it

is possible to obtain 8X as much product in the same reaction time with the larger diameter tube. Under these circumstances the number of reactors required would be significantly lowered.

(c) For some applications of graphene nanofibers, it is not essential to remove entrained catalyst particles from the carbon nanostructures. On the other hand, it may be a useful exercise to examine the economics of retrieving the deactivated catalyst via treatment of the "as produced" graphene nanofibers in dilute mineral acid. The cost of this operation has to be compared with that for the production of fresh catalyst powders.

(d) It should be stressed that there is a crucial need to be cognizant of safety issues and to this end it is imperative to bring onboard a Control Specialist whose responsibilities will include focusing on any potential hazards. In addition to the problems encountered with the handling of hydrogen one must also be aware of the need to provide a cooling jacket for the GNF collection unit.

(e) Throughout these phase of the operation we shall be searching for suitable financial investment and business partners in order to raise the required capital for the commercial venture. Ideally such a partner would provide the marketing and sales capability for the commercialization of this type of product. Catalytic Materials LLC has acquired a strong patent portfolio that includes both processes and applications of graphene nanofibers. We are aware that changes in technological requirements may have a dramatic impact on the viability of using graphene nanofibers for a particular application and must be ready to change directions. As a consequence, we shall continue to explore other potential uses of the material and endeavor to obtain patent coverage in such areas.

(f) As the company manufacturing activities expands we shall be looking to increase our workforce. In this regard, professionals with chemical engineering and materials science expertise will be at the top of the list along with personnel who have experience in the marketing and sales area.

References

1. G. Tammann (1932) *Lehrbuch der Metallkunde : Chemie u. Physik d. Metalle u. ihrer Legierungen* [*Textbook of Physical Metallurgy: Chemistry and Physics and metals and their alloys*] (in German). Leipzig: L. Voss. Retrieved 2010-09-12
2. W. Krätschmer, L.D. Lamb, K. Fostiropoulos, D.R. Huffman, C60: a new form of carbon. Nature **347**(6291), 354–358 (1990)
3. R.E. Smalley, Process for making fullerenes by the laser evaporation of carbon. US Patent 5,300,203 (1994)
4. T. Baird, J.R. Fryer, B. Grant, Structure of fibrous carbon, pp. 329–330 (1971)
5. N.M. Rodriguez, A review of catalytically grown carbon nanofibers. J. Mater. Res. **8**(12), 3233–3250 (1993)
6. N.M. Rodriguez, A. Chambers, R.T.K. Baker, Catalytic engineering of carbon nanostructures. Langmuir **11**(10), 3862–3866 (1995)

7. O.C. Carneiro, M.S. Kim, J.B. Yim, N.M. Rodriguez, R.T.K. Baker, Growth of graphite nanofibers from the iron-copper catalyzed decomposition of CO/H_2 mixtures. J. Phys. Chem. B **107**(18), 4237–4244 (2003)
8. R.T.K. Baker, M.A. Barber, P.S. Harris, F.S. Feates, R.J. Waite, Nucleation and growth of carbon deposits from the nickel catalyzed decomposition of acetylene. J. Catal. **26**(1), 51–62 (1972)
9. R.T.K. Baker, P.S. Harris, R.B. Thomas, R.J. Waite, Formation of filamentous carbon from iron, cobalt and chromium catalyzed decomposition of acetylene. J. Catal. **30**(1), 86–95 (1973)
10. N. Krishnankutty, N.M. Rodriguez, R.T.K. Baker, Effect of copper on the decomposition of ethylene over an iron. J. Catal. **158**(1), 217–227 (1996)
11. N. Krishnankutty, C. Park, N.M. Rodriguez, R.T.K. Baker, The effect of copper on the structural characteristics of carbon filaments produced from iron catalyzed decomposition of ethylene. Catal. Today **37**(3), 295–307 (1997)
12. H. Wang, R.T.K. Baker, Decomposition of methane over a Ni-Cu-MgO to produce hydrogen and carbon nanofibers. J. Phys. Chem. B **108**(52), 20273–20277 (2004)
13. D.W. Goodman, R.D. Kelley, T.E. Madey, J.T. Yates Jr, Kinetics of the hydrogenation of CO over a single crystal nickel. J. Catal. **63**(1), 226–234 (1980)
14. H. Murayama, T. Maeda, A novel form of filamentous graphite **345**, 791–793 (1990)
15. G.R. Hennig, Electron microscopy of reactivity changes near lattice defects in graphite. Chem. Phys. Carbon **2**, 1–49 (1966)
16. R.T.K. Baker, In situ electron microscopy studies of particle behavior. Cataly. Rev. Sci. Eng. **19**(2), 161–209 (1979)
17. S. Park, R.S. Ruoff, Chemical methods for the production of s. Nat. Nanotechnol. **4**(4), 217–224 (2009)
18. T. Tomai, Y. Kawaguchi, I. Honma, Production from platelet carbon nanofiber by supercritical exfoliation. Appl. Phys. Lett. **100**, 233110–233114 (2012)
19. F. Cavani, F. Trifiro, Alternative processes for the production of styrene. Appl. Catal. A **133** (2), 219–239 (1995)
20. G.C. Grunewald, R.S. Drago, Oxidative dehydrogenation of ethylbenzene to styrene over carbon-based catalysts. J. Mol. Catal. **58**(2), 227–233 (1990)
21. G. Mestl, N.I. Maksimova, N. Keller, V.V. Roddatis, R. Schlögl, Carbon nanofilaments in heterogeneous catalysis: an industrial application for new carbon materials? Angew. Chem. Int. Ed. **40**(11), 2066–2068 (2001)
22. C. Park, R.T.K. Baker, Catalytic behavior of graphite nanofiber supported nickel particles. 3. the effect of chemical blocking on the performance of the system. J. Phys. Chem. B **103**(13), 2453–2459 (1999)
23. V.B. Fenelonov, L.B. Avdeeva, O.V. Goncharova, L.G. Okkel, P.A. Simonov, A.Y. Derevyankin, V.A. Likholobov, Catalytic filamentous carbon as adsorbent and support. Stud. Surf. Sci. Catal. **91**, 825–832 (1995)
24. C. Pham-Huu, N. Keller, G. Ehret, L.J. Charbonniere, R. Ziessel, M.J. Ledoux, Carbon nanofiber supported palladium for liquid-phase reactions: an active and selective for hydrogenation of cinnamaldehyde into hydrocinnamaldehyde. J. Mol. Catal. A: Chem. **170** (1), 155–163 (2001)
25. T.G. Ros, D.E. Keller, A.J. Van Dillen, J.W. Geus, D.C. Koningsberger, Preparation and activity of small rhodium metal particles on fishbone carbon nanofibres. J. Catal. **211**(1), 85–102 (2002)
26. Z. Paal, D. Teschner, N.M. Rodriguez, R.T.K. Baker, L. Toth, U. Wild, R. Schlögl, Rh/GNF catalysts: characterization and catalytic performance in methylcyclopentane reactions. Catal. Today **102**, 254–258 (2005)
27. J.R. Dahn, T. Zheng, Y. Liu, J.S. Xue, Mechanisms for lithium insertion in carbonaceous materials. Science **270**(5236), 590–593 (1995)
28. T. Iijima, K. Suzuki, Y. Matsuda, Electrodic characteristics of various carbon materials for lithium rechargeable batteries. Synth. Met. **73**(1), 9–20 (1995)

29. K. Sato, M. Noguchi, A. Demachi, N. Oki, M. Endo, A mechanism of lithium storage in disordered carbons. Science **264**(5158), 556–558 (1994)
30. R. Fong, U. von Sacken, J.R. Dahn, Studies of lithium intercalation into carbons using nonaqueous electrochemical cells. J. Electrochem. Soc. **137**(7), 2009–2013 (1990)
31. B.D. McNicol, D.A.J. Rand, K.R. Williams, Direct methanol–air fuel cells for road transportation. J. Power Sources **83**(1), 15–31 (1999)
32. L.J. Blomen, M.N. Mugerwa (eds.) *Fuel cell systems* (Springer, 1993)
33. H.A. Gasteiger, N.M. Markovic, P.N. Ross Jr, Electrooxidation of CO and H_2/CO mixtures on a well-characterized Pt3Sn electrode surface. J. Phys. Chem. **99**(22), 8945–8949 (1995)
34. A.K. Shukla, M. Neergat, P. Bera, V. Jayaram, M.S. Hegde, An XPS study on binary and ternary alloys of transition metals with platinized carbon and its bearing upon oxygen electroreduction in direct methanol fuel cells. J. Electroanal. Chem. **504**(1), 111–119 (2001)
35. C.A. Bessel, K. Laubernds, N.M. Rodriguez, R.T.K. Baker, Graphite nanofibers as an electrode for fuel cell applications. J. Phys. Chem. B **105**(6), 1115–1118 (2001)
36. E.S. Steigerwalt, G.A. Deluga, D.E. Cliffel, C.M. Lukehart, A Pt-Ru/graphitic carbon nanofiber nanocomposite exhibiting high relative performance as a direct-methanol fuel cell anode. J. Phys. Chem. B **105**(34), 8097–8101 (2001)
37. W. Li, C. Liang, J. Qiu, W. Zhou, H. Han, Z. Wei, Q. Xin, Carbon nanotubes as support for cathode of a direct methanol fuel cell. *Carbon*, *40*(5), 791–794 (2002)

Chapter 8
Dow Chemical: Materials Science Contributions to Membrane Production

Abhishek Shrivastava, Ian A. Tomlinson, Abhishek Roy, Jon E. Johnson, Steven Jons, Caleb V. Funk, Luke Franklin and Martin Peery

Abstract In this chapter, authors present a review of technical developments in reverse osmosis membranes and module technology and ultrafiltration membranes and module technology. State of the art of these technologies, potential future research opportunities and impact areas are also discussed.

8.1 Introduction to Membrane Processes in Water Purification

Dow Chemical has been in business for more than century. Its goal has been to create value through a diversified, market-driven portfolio of specialty products in the chemical, advanced materials, agrosciences and plastics areas. It strives to leverage cost advantage, scale and geographic presence—together with close customer collaboration and industry-leading R&D expertise—to deliver differentiated solutions that address unmet market needs. In this chapter, Dow's approach to one major world issue, water purification, is described.

Water scarcity is one of the most critical issues that we will face in the near future. By 2025, more than two thirds of the world's population will be living in water stressed regions [1]. With rising population, climate change and rapid industrialization, freshwater resources are diminishing along with an increase in the ratio of rate of water withdrawal to water availability [2].

A. Shrivastava (✉)
Dow Energy and Water Solutions, The Dow Chemical Company, 1215 Chrysler Drive, Menlo Park, CA 94025, USA
e-mail: AShrivastava@dow.com

I.A. Tomlinson
Dow Energy and Water Solutions, The Dow Chemical Company, 1821 Larkin Center Drive, Midland, MI 48674, USA

A. Roy · J.E. Johnson · S. Jons · C.V. Funk · L. Franklin · M. Peery
Dow Energy and Water Solutions, The Dow Chemical Company, 7600 Metro Blvd, Minneapolis, MN 55439, USA

L.D. Madsen and E.B. Svedberg (eds.), *Materials Research for Manufacturing*, Springer Series in Materials Science 224,
DOI 10.1007/978-3-319-23419-9_8

A quantitative breakdown of global fresh water consumption [3, 4] shows that more than 70% of global water consumed is used in agriculture, next is the power industry that consumes approximately 20% [5], and the remaining is used for household purposes. Treatment of water is also important to sustain fracking and oil and gas exploration [6]. The manufacturing industry also relies on good quality water as a critical part of processes. The numbers can vary based on geographies and economies but the water-energy-food nexus, the nexus between the key sustainability pillars has become increasingly important as our energy [7] and water footprint has been growing [8] (Fig. 8.1).

With diminishing freshwater resources and rising water demand, and given the importance of water for sustenance and its critical role in the water-energy-food nexus, it is imperative that we work towards ensuring a sustainable water future. Desalination and water reuse are both major parts of the solution along with a need to conserve water and focus on technologies and industrial processes and manufacturing that have lower water footprint.

Desalination is a term that is broadly used to describe processes involving purification of water from salt water feeds and removal of other impurities of the ionic size ranges. Depending on the concentration of salt in water feed it can be further classified as sea water desalination (typically 2% salt concentration or above) or brackish water desalination (less than 2% salt concentration, typically 500–5000 ppm). Major desalination technologies that are currently used are thermal distillation and membrane desalination.

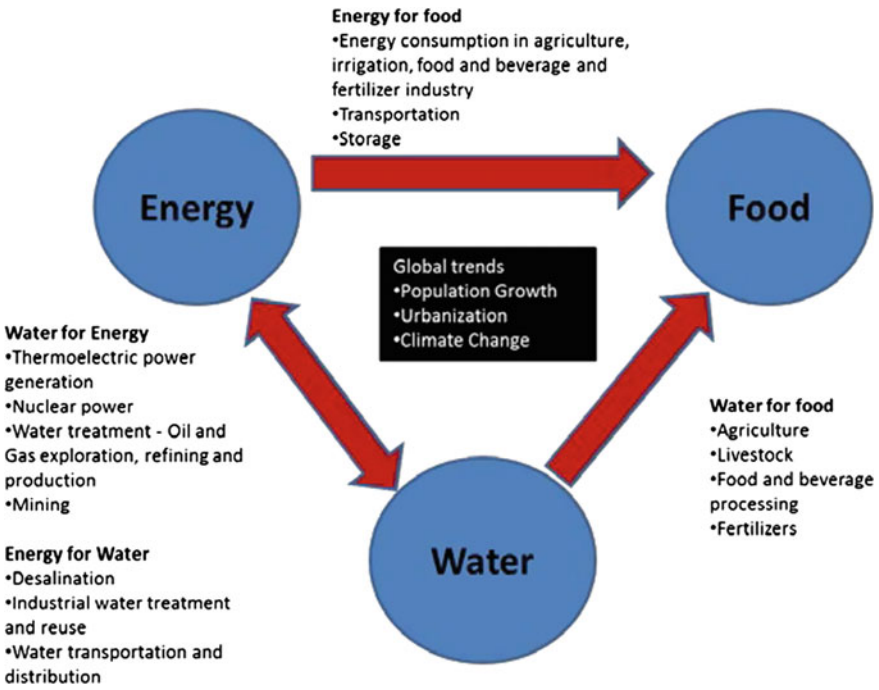

Fig. 8.1 Water–Energy–Food Nexus. Water serves as a critical pillar in the nexus. Adapted from [9]

Membrane desalination is further classified into thermal membrane desalination and reverse osmosis. In the last 50 years, advances in reverse osmosis have resulted in more than ten-fold enhancement in its energy efficiency [10] and as a result it is at least 5–10 times more energy efficient than traditional thermal desalination [11, 12]. Thermodynamically, it is proven that currently a state of the art optimized seawater reverse osmosis desalination plant [9, 10, 13, 14] is close to the practical achievable efficiency limit for energy efficiency for salt water separation. This limit is independent of the technology used and hence implies that membrane desalination via reverse osmosis, in addition to being the most energy efficient desalination technology available, is also proving to be the technology that can provide the best possible practical energy efficiency for water purification.

A layout of a typical reverse osmosis desalination plant is presented in Fig. 8.2. Pretreatment comprises of chemical pretreatment like addition of flocculants, coagulants, anti-scalants and separation of particulates, bacteria, colloidal impurities using microfiltration and ultrafiltration membranes. This is followed by separation of ionic impurities using desalination membranes depending on the application. These can be nanofiltration membranes (for selectively separating multivalent ions), brackish water reverse osmosis membranes and sea water reverse osmosis membranes. In the case of a typical seawater desalination plant, energy recovery devices are used to recover the pressure energy from the concentrate as the feed streams are highly pressurized (>800 psi). Also where high purity of permeate is needed a second pass reverse osmosis (RO) operation is utilized. These steps are followed by post treatment processes to obtain the final purity and composition of water.

Key technologies used in a desalination or water treatment plant are ultrafiltration for pretreatment and reverse osmosis for separation of water from ionic impurities. In both these technologies, membranes are used to separate impurities from water. The separation phenomena are size-based for ultrafiltration membranes and permeability-based for reverse osmosis membranes [15, 16]. Advances in materials science, manufacturing, widescale adoption and energy efficiency of reverse osmosis and ultrafiltration membranes have led to a significant reduction in

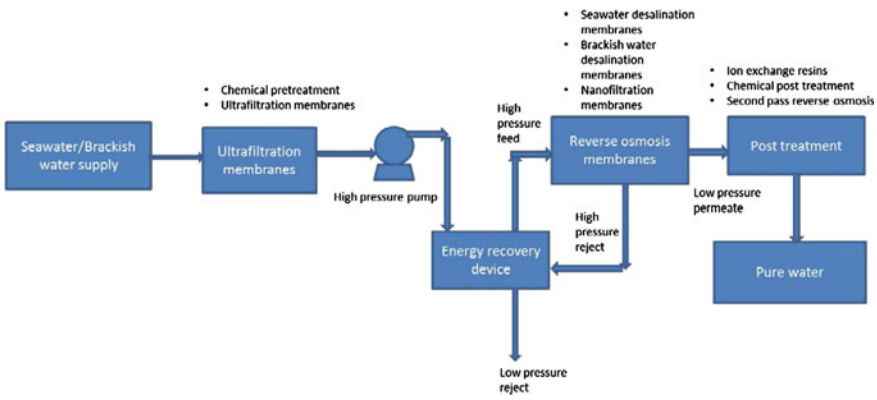

Fig. 8.2 Layout of a typical desalination plant

the total cost of water for desalination using these technologies. For example, reverse osmosis based desalination the total cost of water has decreased by a factor of three in the last 40 years to its current value of 0.5–1.2 $/m^3 [12, 17]. In the rest of the chapter, a state of the art review and some key recent technical accomplishments in both these technologies will be discussed.

8.2 Recent Developments in Membrane and Module Technology

8.2.1 Reverse Osmosis Membranes

8.2.1.1 Reverse Osmosis and Nanofiltration Membrane Chemistry

The structure of a thin film composite membrane comprises three layers, a non-woven backing layer (typically poly(ethylene) terephthalate) for mechanical strength, a polysulfone asymmetric membrane layer (ultra-filtration) for porosity and finally a polyamide discrimination layer which is so named because it is responsible for the rejection of ions and small molecules while allowing water to pass. The advantage of this structural approach for high performance reverse osmosis (RO) and nanofiltration (NF) membranes is that each of the layers can be individually optimized for performance, which is usually measured in terms of salt rejection and water flux. The bottom layer, which provides reinforcement and mechanical strength to the membrane sheet, is typically a non-woven fabric. The most commonly used fabric is a non-woven polyethylene terephthalate, however, some membranes are produced with non-woven polypropylene or non-woven polyacrylonitrile, particularly when improved stability to pH extremes is desired.

The central layer of the thin film composite structure of both reverse osmosis membranes and nanofiltration membranes is an ultrafiltration membrane. The role of this membrane is to provide a good porous non-selective support for the highly selective discrimination layer. The preparation of this ultrafiltration membrane layer is a phase inversion process which results in an asymmetric membrane with a porous skin on the surface and progressively larger interconnected pores at the face adjacent to the non-woven fabric.

As described in a recent review [18] there are four common techniques for achieving this phase inversion: immersion precipitation, thermally induced phase precipitation, evaporation induced phase separation and vapor induced phase separation. Immersion precipitation is the technique most often used in the production of RO and NF membranes, where the polymer of choice is first dissolved into a suitable solvent, coated as a thin film onto the fabric backing and immediately immersed into a non-solvent coagulation bath (typically water). Precipitation occurs as a result of the exchange of solvent from the polymer solution and the non-solvent. For this process to occur efficiently, the two solvents must be miscible and the resulting porosity both at the surface and in the bulk can be controlled by

optimizing the relative rate at which the solvent diffuses into the coagulation bath and the non-solvent (water) diffuses into the polymeric cast film [19, 20]. This process can be optimized by choice of polymer, solvents and non-solvents and the incorporation of additives. The precipitation time and the bath temperature can also have an effect on the morphology of the resulting membrane. For commercial thin film composite reverse osmosis and nanofiltration membranes the most common polymers used for the ultrafiltration (UF) support are polysulfone (1) and polyethersulfone (2) (Fig. 8.3).

The final layer of the thin film composite membrane is the discrimination layer. This layer is most commonly a highly crosslinked polyamide, and the standard reaction for the production of reverse osmosis membranes is the interfacial polymerization reaction between 1,3,5-trimesoyl chloride (TMC) and *meta*-phenylenediamine (MPD) (Fig. 8.4), as was first described by Cadotte [21]. During the manufacturing process the polysulfone layer is imbibed with an aqueous solution of the MPD, excess liquid is removed from the surface of the membrane and the membrane is pulled across a heated reaction table to provide sufficient time at temperature for the interfacial reaction to occur. At the beginning of the reaction table a solution of TMC in a high boiling hydrocarbon solvent is brought into contact with the moving film. A thin layer forms and the two monomers react together at the interface.

The growing cross-linked network is not particularly soluble in the hydrocarbon solvent and rapid precipitation occurs forming a thin film of polyamide on the surface of the polysulfone. The MPD, which is believed to have a higher affinity for the growing polymer than for the hydrocarbon solvent, thus continues to diffuse into the polyamide matrix providing sufficient monomer available for reaction to produce a high integrity cross-linked polyamide discrimination layer on the top surface of the membrane. Once the polyamide layer is formed and a sufficiently thick film has been achieved to ensure a high integrity coating, the excess TMC solution is recovered and the membrane enters a series of rinsing steps. The purpose of the rinses is for the neutralization of excess carbonyl chloride groups and the extraction of the residual reactants and solvent out of the membrane. Following this extraction process, the membrane can be optionally coated with a hydrophilic polymer, dried and rolled to provide a finished membrane suitable for fabrication into membrane elements. All of the major membrane manufacturers today produce their membrane flat sheet using a similar process to the one described above.

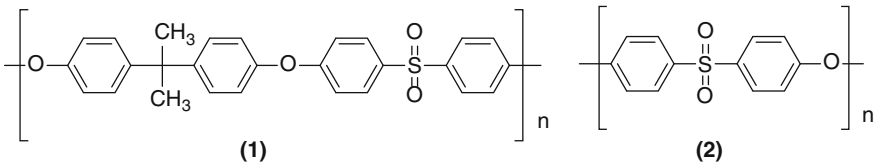

Fig. 8.3 Polymers used in the manufacture of thin film composite membranes

The performance characteristics of the resulting reverse osmosis membrane, either brackish water membrane (e.g., for water with a salt concentration of 2000 mg/L, achieving 99.5% salt rejection, 1.67 m^3/h at 16 bar) or sea water membrane (e.g., for water with a salt concentration of 32,500 mg/L, achieving 99.7% salt rejection, 0.95 m^3/h at 55 bar) can be varied by optimization of the concentrations of the two monomers and reaction conditions for the interfacial polymerization. The overall structure of the cross-linked network as described in Fig. 8.4 tends to have an excess of free carboxylic acids over free amines, particularly at the surface. This is to be expected with the way the reaction is performed such that prior to quenching, reactive amines are in the presence of a large excess of TMC near the surface of the polyamide. The excess carboxylic acids are typically in the salt form during operation which results in an improvement in salt rejection resulting from the Donnan Effect of ionic repulsion [22].

Polyamide thin film composite membranes are known to be susceptible to oxidation by aqueous bleach at pH 8 and above, a property which is unfortunate because chlorine is broadly used to pre-treat the water to reduce biofilm formation in the membrane element. One desirable effect at moderate bleach concentrations is the partial hydrolysis and oxidation of amide linkages, to produce an excess of carboxylic acids and a modestly more open cross-linked network. This results in an initially higher performance specification for the membrane, higher flux and higher salt rejection. There is also an associated reaction in which ring chlorination occurs [23, 24], described in Fig. 8.5, which is often referred to as the Orton Rearrangement. This process, which involves chlorination of the amide nitrogen followed by ring chlorination, results in a membrane which is more susceptible to hydrolysis during operation and membrane cleaning operations.

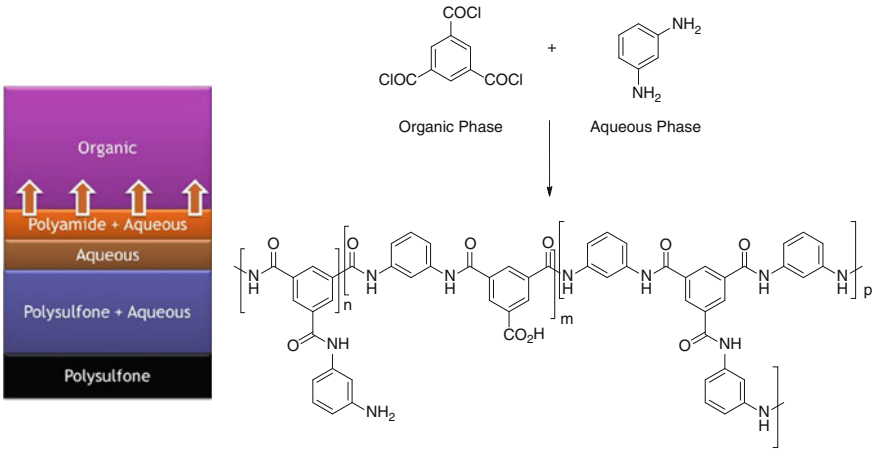

Fig. 8.4 Crosslinked polyamide layer formed by an interfacial polymerization between trimesoyl chloride and *meta*-phenylenediamine

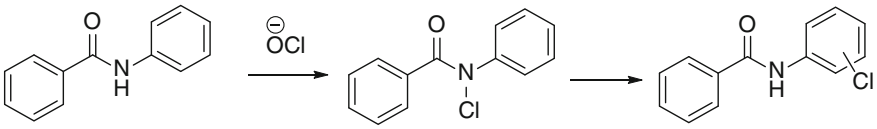

Fig. 8.5 Proposed Orton Rearrangement during bleach treatment of the polyamide layer (N-chlorination followed by intermolecular rearrangement, representative example of benzanilide)

Over the years membrane developers have looked for ways to manufacture higher flux and higher rejection membranes. There are a number of instances where additives have been mixed either with the TMC in the organic phase or with the MPD in the aqueous phase in an attempt to positively influence the interfacial polymerization. The addition of polar aprotic solvents such as N-methyl pyrrolidone, dimethyl formamide, sulfolane, dioxane, pyridine, or triethylphosphite into the aqueous phase with the amine and an optional acid acceptor was reported by Chau [25] to produce membranes with increased flux. Similarly, the use of polar alcohols, ketones, ethers, esters and halogenated hydrocarbons within a specific solubility range, introduced in either the organic or aqueous phase, have been reported to improve the performance of polyamide membranes [26]. Treatment of the preformed polyamide with strong base [27] or with strong mineral acid followed by treatment with a rejection enhancing agent [28] such as colloids or water soluble polymers to plug defects in the membrane resulting from the acid treatment have also been reported to improve membrane performance.

Two techniques for improving the membrane flux and the salt rejection are typically practiced today. In the 1990s Dow was successful in enhancing both the salt rejection and the flux of reverse osmosis membranes by incorporation of phosphate derivatives (e.g., trialkyl phosphates) into the interfacial reaction [29]. The advantages of this process for the production of the polyamide discriminating layer is that the effect occurs during the synthesis of the polyamide, no weakening of the structure occurs and the resulting membrane shows excellent durability. The second process frequently practiced in the industry is a deliberate post treatment with chlorine bleach [30]. As described above, exposure of a polyamide membrane to chlorine bleach typically results in the cleavage of some of the amide linkages, generating a higher level of free carboxylic acids and a more open structure. The benefits are higher water flux and a lower initial salt passage. The challenge with this process is that the portion of the membrane which becomes chlorinated, most likely in the ortho position to the nitrogen of the amide, as a result of the Orton rearrangement (Fig. 8.5) is activated towards hydrolysis. This results in membranes which are less durable, which undergo further hydrolysis during regular cleaning of the membrane and a steady loss of separation performance.

The other form of membrane utilized in water purification is the nanofiltration (NF) membrane. Frequently described as “loose RO”, NF is widely used in applications where it is important to remove or significantly reduce the level of divalent ions, such as calcium (Ca^{+2}), magnesium (Mg^{+2}), or sulfate (SO_4^{-2}), but where it is not essential to remove all of the monovalent ions such as sodium (Na^{+})

and chloride (Cl^-). These membranes are used in softening applications and have been very successful in the oil industry for the removal of sulfate from sea-water used for secondary oil recovery. Elimination of dissolved sulfate provides benefits, both from reduced scaling (esp. $BaSO_4$ and $SrSO_4$) and reduced souring (caused by sulfate-reducing bacteria).

As compared to RO, there is an even wider range of chemistries commercially employed for nanofiltration. Both ceramic and polymeric membranes used. Polymeric membranes have been formed by phase inversion, polymer coating, loosening of existing RO, and by interfacial polymerization. The majority of NF membranes used in water separations are made by replacing the MPD with piperazine (Fig. 8.6).

The final step in the manufacture of membranes is frequently the coating of the polyamide with a polymer coating. There are multiple purposes for the coating of membranes with an additional polymer and a broad range of polymers have been studied. Typically, the polymers used are hydrophilic in order to have the least impact possible on water passage through the membrane. Coating provides improved processing during the manufacturing of the membranes and fabrication of elements, since the polymer provides protection for the delicate polyamide layer during membrane module production. Coatings are also frequently utilized for performance benefits. There is a vast body of literature [31–34] looking at the benefits of various polymer coatings (physically adsorbed or covalently attached to

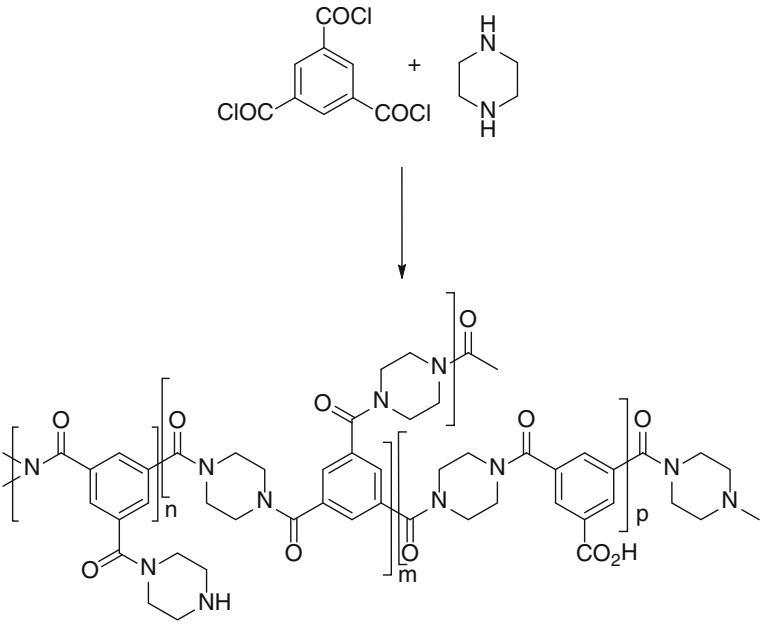

Fig. 8.6 Crosslinked polyamide layer formed by an interfacial polymerization between trimesoyl chloride and *piperazine*

the surface of the membrane) for their anti-fouling properties and also to improve the rejection of salts and neutral solutes during operation.

8.2.1.2 Structure Property Relationships

The above section outlines the main chemistry behind the interfacial polymerization reaction of the polyamide membrane. In this section a brief overview will be provided on the membrane structure and composition and how finally it affects the polymer structure.

Morphology

Figure 8.7 represents a TEM (transmission electron microscopy) image of a typical polyamide membrane. As evident from the image, the surface is not only rough but the layer is also very thin.

Freuger et al. [35] did a similar investigation with TEM technique and discussed on the heterogeneity of polyamide structure. They proposed a double-layer structure, in which the outer layer is negatively charged and is separated from an inner positively charged dense layer. They commented on the inability of other techniques, for example streaming potential and X-ray electron spectroscopy over TEM to differentiate the fine structure from the overall heterogeneous structure.

Chemical Composition

Based on the chemistry, the final polymer structure is expected to have amine and COOH functional groups as end groups. The concentration of those groups is a

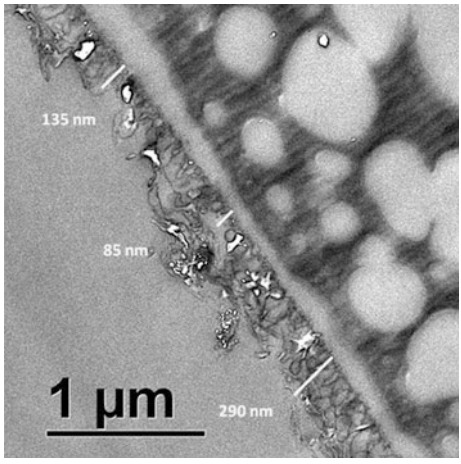

Fig. 8.7 Transmission electron micrograph of polyamide membrane supported on asymmetric polysulfone matrix

function of the monomer conversion and relative sol-gel fraction of the final structure. In the last decade, a significant amount of research has been done in quantifying the amount of these end groups and how the end groups control the transport properties. The most common technique for measuring membrane charge has been zeta potential measurement [36]. The technique is widely used to understand the role of surface charge on ionic rejection and fouling. The two most important parameters that are widely studied are the absolute zeta potential of the membrane at an application pH and the corresponding iso-electric point. The iso-electric point of the membrane is typically defined as the pH where the negative charge resulting from the COOH groups equals the positive charge from the amine groups. Above the iso-electric point the membrane is negatively charged and below it is positively charged. The iso-electric point has significant implications in controlling ionic rejection.

Although zeta potential is routinely measured and studied for polyamide membrane research, it is a surface sensitive technique and fails to quantify the total COOH and amine content of the bulk polymer. Coronell et al. [37–43] made significant progress in the last few years to develop a Rutherford backscattering (RBS) technique to measure both the bulk ionizable COOH functional groups and amine functional groups. The technique involves titrating the membrane with silver nitrate solution to form the corresponding Ag salt of the COOH groups and then measuring the Ag^{+} content through He ion backscattering. For amines, the authors selected barium chloride as the titrant and the corresponding Ba^{2+} was determined. They studied several commercial membranes from different suppliers and provided an in-depth summary of ionizable COOH and amine content for various membranes. The COOH content was found to vary within 0.2–0.4 mmoles/g of the polyamide membranes. The study was extended over a wide range of pH which allowed for estimation of the bulk iso-electric point.

Elimelech reported the of use of different probes, for example uranyl acetate and toluidine blue O dye to bind with COOH groups, and then later quantifying the relative content using liquid scintillation for uranyl and visible light spectroscopy for the toluidine dye to estimate the COOH content [44]. Their paper also provides a good comparison of the different quantification techniques underlying the advantages and disadvantages of the individual techniques.

Viscoelastic and Mechanical Properties

Real time operation of an RO membrane involves cross flow of water over the membrane surface with a net driving pressure ranging from below 50 psi to above 500 psi. A typical RO membrane is expected to last at least 5 years. It is to be expected that the performance over time will be a function of the viscoelastic and mechanical property of the polyamide layer itself. A recent publication from Stafford et al. introduced a wrinkle-cracking methodology for measuring static mechanical properties for RO membranes [45]. The method allows one to measure elastic modulus, strength and fracture strain. The authors studied mechanical

properties as a function of chlorine exposure time. The authors concluded that modulus of the membranes increased exponentially with time of chlorination while both fracture strength and onset of fracture strain decreased continuously with time of exposure. The results suggest a fundamental change in membrane structure with chlorination which is consistent with the expectations outlined above in the discussion of membrane chemistry.

Alternative to the wrinkle-crack methodology, Greenberg et al. [46, 47] reported the use of pendant drop mechanical analysis to measure the viscoelastic and mechanical properties of RO membranes. In a typical experiment, interfacially polymerized films formed over mPD drops were deformed and the decrease in internal pressure due to stress relaxation was monitored with time. The measurement provided an insight on the nature of crosslinking and branching as function of mPD and TMC concentrations. Crosslinking was found to be more sensitive to TMC concentrations than that of mPD concentrations.

Polymer Structure and Transport

Unlike gas separation membranes where literature suggests that the transport of fluid across the membrane is a function of polymer free volume, no clear correlation has been observed between the free volume of interfacially polymerized polyamide and water/solute transport across an RO membrane. The primary reason has been in the difficulties of measuring free volume or related properties under hydrated conditions. Furthermore, the RO membrane is highly cross-linked, made evident by the broad glass transition temperature range (140–190 °C) measured through the atomic force microscopy (AFM)-based nano thermal technique [48]. Significant research and progress has been made in these areas, but still it remains as one of the major challenges behind developing structure-property relationships.

Lee et al. in a recently reported a water absorption study for an aromatic polyamide layer and correlated with free volume/cavity size as measured by positron annihilation lifetime spectroscopy (PALS) technique [49]. The PALS data suggested the cavity size to be larger than the size of a water molecule. However, no evidence of free water was observed, indicating the size of the clusters is still small. The authors also reported the PALS measurement under varying relative humidity, which most likely will open up new areas of research and fundamental understanding of water transport under hydrated conditions. Similar insight on water transport was reported using a quartz microbalance technique by Zhang et al. [50]. The authors studied the water absorption as a function of water activity and estimated the self-diffusion coefficient of water to be 2–3 times lower than free water. The authors found a fractional free volume of 0.25 based on the free volume and group contribution model. The diffusion coefficient of water estimated from that calculated free volume was in accordance with that calculated from the solution diffusion model and experimentally measured value. Besides PALS and quartz crystal microbalance (QCM) techniques, nuclear magnetic resonance (NMR) has been also leveraged to understand salt and water transport. Kirkpatrick et al.

reported the study of water and Na ion transport in polyamide membrane through ^{23}Na NMR technique [51]. RBS [52] and impedance [53] techniques have also been used to understand the partitioning of salt within the membrane.

8.2.1.3 Potential Future Research Directions

The above sections provide a brief overview of the different characterization tools and insight into the RO membrane structure. From an industry standpoint the authors believe that there is significant value in continuation of advanced structure-property research. Outlined below are some thoughts on the opportunities and challenges for the next generation of membrane characterization research.

1. Diffusivity versus Solubility—Development of high throughput characterization techniques will help to decouple these two important parameters and understand the role of polymer composition versus structure on final properties. This would definitely revolutionize the next generation polyamide chemistry research towards new monomers and structures
2. Spacing between functional groups/charge density—In the recent years there has been significant amount of work in quantifying the COOH content in RO membranes. Along with the quantification, insight on the spacing of these groups in these membranes will help to understand the role of the Donnan exclusion principle in controlling salt rejection to a greater extent.
3. Accelerated ageing test—One of the biggest challenges the industry faces is to predict long term membrane performance in different application spaces. Typically one has to wait until a membrane fails to evaluate the root cause and then take countermeasures. The failure mode could be due to chemical degradation, polymer modification or viscoelastic relaxation of the polymer itself. Research to predict these failure modes, either computational or experimental, would help to improve reliability and sustainability of RO membranes.
4. Modeling of 3D structure—There is always an incentive to develop computational models to predict membrane performance as a function of polymer structure and composition. The lack of knowledge on free volume, density and other viscolelastic properties has slowed down the progress of computational modeling. However, with recent progresses in analytical capability development the authors expect more research will take place in the coming years towards developing a comprehensive structure-transport model for RO membranes.

Further advances in membrane chemistry are also desirable, with the focus changing to improvement in performance across a broad range of water types around the world rather than the historical driver of reducing the energy required for reverse osmosis and hence the cost of water produced. As water becomes more scarce and increased recovery and recycling is practiced the quality of the source water has become increasingly challenging. This results in opportunities to design new novel membrane chemistries which provide the performance of the current polyamide layer while improving the fouling resistance of the membrane.

Two major areas of research where breakthroughs are sought, (a) novel coating polymers which can be covalently bound to the membrane surface without significant loss in water flux and with improved resistance to chemical and biological fouling, (b) membranes with a new polymer discrimination layer which is resistant to degradation by continuous exposure to low levels of chlorine used for disinfection of the source water.

8.2.2 Reverse Osmosis Membrane Module

8.2.2.1 Spiral Wound Modules for Reverse Osmosis

Most of the world's commercial reverse osmosis installations rely upon spiral wound modules made from flat-sheet RO membrane. The spiral wound configuration represents a useful compromise between competing performance objectives that are sometimes at odds. Those objectives include high membrane packing density, low pressure drop from feed to concentrate, high mixing or mass transfer within the feed channel, as well as cleanability, durability, chemical compatibility, and low cost. The spiral module was developed in the late 1960s [54, 55] and has benefitted from more than four decades of improvements in materials, design, and fabrication technique. The most common sizes are sufficiently standardized to permit interchangeability regardless of manufacturer. Large-scale industrial and municipal reverse osmosis relies upon a module that is 8 in. in diameter and 40 in. in length.

Spiral wound modules are generally formed by winding at least one feed spacer and at least one membrane envelope about a central permeate tube. The membrane envelope is a sandwich of two membrane sections surrounding a permeate spacer, with glue lines sealing the three edges of the envelope away from the permeate tube. The cut-away view in depicts key components of this device.

The list of components in Fig. 8.8 will guide the following discussion of spiral wound module innovation. The patent literature of the last 10 years will be drawn upon to provide an overview of technical challenges and proposed solutions relating to each component. The patents cited do not represent the earliest or even the most well-known solutions in each area, and many claimed benefits have not been independently validated, but the documents shed light on current research and development within academia and industry.

Permeate Tube

The permeate collection tube receives fluid from the attached sheets of permeate spacer and provides communication with adjacent modules or collection points. The interface between the stacked layers of the membrane scroll and the rigid tube is an area of special concern. Compression of the layers at this interface can restrict permeate flow into the side-holes of the collection tube, and it is common to provide

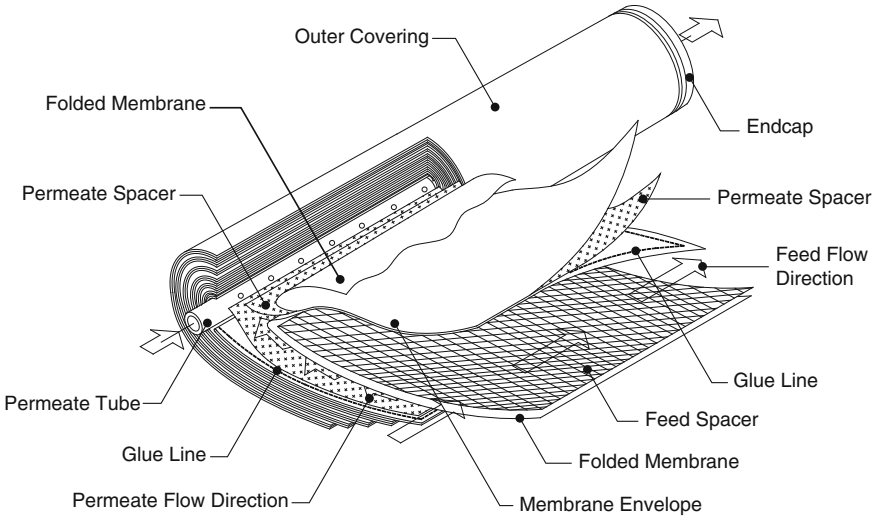

Fig. 8.8 Spiral wound membrane module

one or more wraps of spacer material about the tube. Alternatively, several concepts have been presented that create recessed flow passages on the exterior of the tube [56–58]. In addition to improving hole access, a complex extrusion also provided side holes without the need for drilling [58]. Finally, it has also been noted that the tube is an excellent location for deploying permeate flow control features. A check valve prevented back-flow which can damage RO membranes [59], and an axially-varying side-hole distribution reduced the upstream permeate flux so that foulants were distributed more evenly within the element [60].

Feed Spacer

The most common feed spacer configuration used in RO modules is the biplanar extruded net [61]. The feed spacer has two functions. It provides an open channel for the flowing feed water by maintaining separation between the membrane sheets. It also promotes mixing within the feed channel, moving salt and other rejected substances away from the membrane surface (Fig. 8.9).

While most feed spacers are extruded from polypropylene, polymer enhancements have been proposed to combat fouling, such as antimicrobial agents [62, 63], treatments to reduce hydrophobicity [64], and ion exchange structures to capture hardness and reduce scaling potential [65].

Modifications to the traditional axial feed flow configuration have been made to increase crossflow velocity and reduce fouling. Concepts include axial inflow and outflow with serpentine flow paths defined by special gaskets or blockages in the feed channel [66–68], as well as more radically revised element configurations with

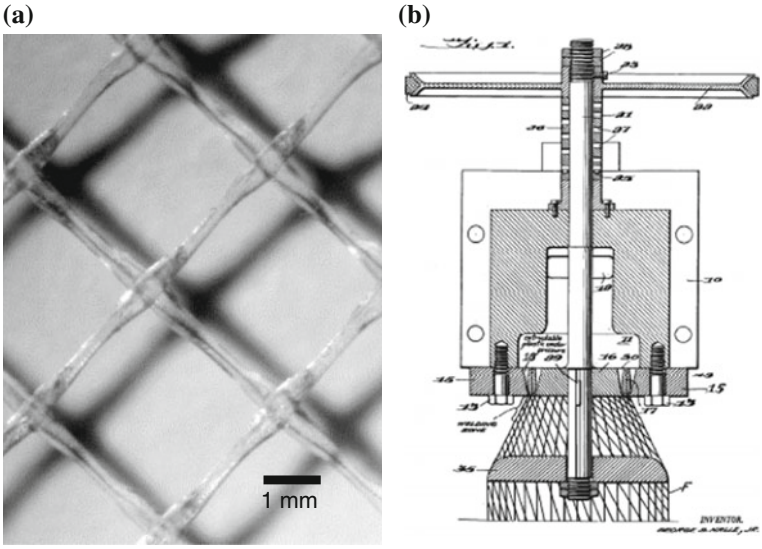

Fig. 8.9 **a** Biplanar extruded netting is comprised of two intersecting sets of parallel, extruded strands. **b** An early patent was obtained by Nalle [61]

redefined entry and exit points [69]. In most cases, the revised flow path is longer and narrower than the original, or tapers in the flow direction to maintain velocity.

Spacerless channels have been made by adhering small structures directly to the membrane [70–72], and by creating patterns of varying elevation within the membrane [72–76]. These eliminate one of the spacers required during module fabrication, and also facilitate thinner feed channels with low pressure drop, improved mass transfer, and increased packing factor. In another case, dots of adhesive applied the membrane simplified construction and increase module strength by binding the scroll together [77].

Fifty years after its development, optimization of extruded biplanar netting is ongoing for the purposes of reduced pressure drop, improved mass transfer and less fouling [78–85]. Flat sheets with embossed or applied protrusions appear to be a highly manufacturable alternative [86–90]. However, many performance-enhancing configurations may be too costly to manufacture on a large scale [91, 92].

Permeate Spacer

The permeate spacer provides a conduit for the collection and transport of permeate from the membrane to the permeate tube. Woven polyester fabric is the most common spacer in commercial use. The tricot weave offers a useful combination of the sought-after characteristics of thinness, low pressure drop, and uniformly and closely spaced support points for the membrane sheet. Development of improved

tricot and other knitted fabrics is a work in progress [93–97]. Tricot fabrics are asymmetric, having a rough side and a smooth side. Using two sheets of fabric with their rough sides together provided a smoother composite that more uniformly supported the membrane [98].

In order to positively shift the tradeoff between thinness and low pressure drop, novel webs made from embossed films [99] and perforated extrusions [100] have been proposed. Varying the web cross-section to provide extra thickness near the permeate tube where the flow is highest is intuitively appealing [101, 102]. Applying the feed spacer directly to the back side of the membrane, using resins that solidify by cooling or chemical reaction, promises to reduce thickness and simplify module assembly [103–106].

Finally, the permeate spacer has been manipulated to meet larger operational objectives. Additives such as antimicrobials [107], activated carbon [108], and wetting agents [109] provided enhanced functionality. A few developers proposed to use normally-unwanted permeate spacer pressure drop for operational advantage. In order to reduce fouling and increase module longevity, they segmented the spacer to cause greater permeate backpressure near the feed end of the element, where fluxes are highest [60, 110–112].

Endcap and Coupler

The ends of the module are typically fitted with an injection-molded plastic endcap. The endcap is present to protect, contain, and prevent axial movement of layers within the scroll, but secondary functions such as *mixing* and *interconnecting* are motivating current development.

Permeate fluxes tend to be slightly higher in close proximity to the central collection tube, which can lead to enrichment of solutes in this region. Endcaps with special mixing features were proposed in order to increase turbulence or redistribute solutes/particles prior to entering the module [113–116].

The permeate tubes of adjacent modules deployed in series are connected, often with the help of a small, insertable coupler. O-rings on the coupler are prone to leakage, and development has aimed to eliminate the coupler, reduce the number of o-ring seals, and improve seal reliability. Endcap modifications have emphasized locking connections between adjacent elements to prevent the relative axial movement that leads to o-ring abrasion [117–120]. Sometimes, the locking endcaps include an integral seal [121, 122]. The couplers, which are usually molded from glass-filled polymer, have been modified to reduce permeate pressure drop [123], reduce o-ring wear through restricted movement [124], and interface more reliably with the pressure vessel [125].

The RO pressure vessel is a demanding environment, and endcap development must consider the mechanical loads present. Increased strength [126], reduced weight [127], and improved adhesion between endcap and outer shell [128, 129] were addressed with new molded-in features. Conduits were added to better manage the pressure in the annulus surrounding the module [130].

Brine Seal

The bypass of feed water around the modules installed inside a pressure vessel impacts performance by reducing the crossflow needed to move solutes and foulants away from the membrane surface. While the problem is normally addressed by fitting the end of each module with a large-diameter rubber seal, several new concepts promise to ease module handling by reducing friction [131–134]. Other concepts manipulate bypass to gain advantage. A controlled bypass stream was designed to continuously flush the annulus surrounding the module [135] using a porous seal. By installing a check valve in parallel with a rubber brine seal, annulus flow in the forward direction was blocked while reverse flow through the annulus during cleaning episodes was permitted [136].

Adhesive

In the spiral module of Fig. 8.8, an adhesive forms an envelope by joining the back side of adjacent membranes sheets together along three edges. A variety of materials may theoretically be used, including hot melts, UV-cured polymers, and epoxies. In practice, a two-part urethane is almost exclusively used commercially. Most commonly, the adhesive applied along the periphery of a membrane sheet penetrates the permeate spacer in the area of the glue line during rolling and also wicks into both adjacent membrane sheets. To the extent that adhesive does not penetrate through both the membrane backing and support layers, there can be an open path for fluid passage in the narrow region between penetrated adhesive and the membrane barrier layer. Deformation of the support (under heat and/or pressure) reduces void volume and limits this passage. A backing layer with a specific range of pore sizes (8–12 μ) was asserted to promote full penetration of the support layer [137]. Also related to imperfect penetration of adhesive into the support layer, blisters in the membrane can be formed following changes in feed solution when an otherwise-sealed void region is in contact with the barrier layer and an osmotic pressure differences across the membrane barrier causes water to flow into the void. A sealant applied to the barrier layer surface has been used to avoid blisters [138].

Adhesion of urethane glue is not a problem in most cases. However, in the cases of rapid feed pressure changes, there is greater potential for back glue lines to fail, and this circumstance has been addressed with wider glue lines at the back of a membrane leaf than near the tube [139]. At the other end of the leaf, roughening the permeate tube has been used to improve adhesion there [98]. Similarly, roughening the back surfaces of membranes has been proposed so that glue lines may be narrowed and retain strength [140]. An optimal cured hardness value (Shore D45–60) was suggested to generally provide sufficient glue strength without being prone to cracking [141].

One common area for defects is the insertion point, where the module scroll face abuts the permeate tube. During fabrication, small movements of a membrane leaf near the tube can result in a path through the adhesive at this location, allowing feed

water to enter the permeate tube. After cutting the scroll face, slow curing urethanes and hot melts have historically been used to patch this region. This area has been treated with a fast curing adhesive (e.g., UV) to facilitate a more automated approach [142]. A collar has been placed around tube at this location for the same purpose [143]. A similar approach is taken in [144], but the collar additionally is fastened by a rapidly curing adhesive.

Outer Covering

Reverse osmosis modules are most typically coated with a shell comprising glass fibers and epoxy resin. Several alternative reinforced composites have been proposed [145–147]. Whereas large modules are typically fiberglassed, small and mid-size module modules are usually only tape wrapped [148, 149]. Molded materials, heat shrinkable covers, and fused bands have also been proposed [150–152]. In still other applications (e.g., sanitary operations, where regions of stagnant flow are not acceptable), it is important to maintain a level of controlled bypass. One common option is a full-fit, where a mesh-like outer wrap is porous and fills the vessel tightly. A hard shell surrounded by external threads of exacting dimensions is also commercially used to create desired flow around the module [153, 154]. A variety of other options have been proposed to achieve controlled bypass through modifications to the shell [155–157].

8.2.2.2 Potential Future Directions

One recent change has been the commercialization of larger diameter modules by several membrane manufacturers. While modules larger than 8″ in diameter had been constructed by different manufacturers before, and potential cost reductions from improved economies of scale had been previously identified [158], the lack of a standard module size and reduced ability for competitive bidding had been identified as important barriers to end-user adoption. In 2006, a consortium, including several membrane manufacturers, was formed to determine the extent to which the use of a larger diameter module could improve the economics of RO plants and to establish a standard diameter [159]. The consensus was for standardization upon a 16-in. diameter module for both brackish and seawater applications. The study estimated that total construction costs could be reduced by 18–25% for brackish ground water and 7–12% for seawater desalination. One outcome of this effort was that the world's largest (624,000 m^3/day) desalination plant (in Sorek, Israel) was commissioned in 2013 with 16-in. modules split between Dow and Hydranautics.

The vast majority of commercial reverse osmosis spiral wound modules use the design previously described and illustrated in Fig. 8.8, where feed propagates axially across the module and permeate travels radially to the tube. However, several alternative designs instead use counter-current feed and permeate flows, the

feed propagating from a region near the permeate tube towards the periphery of a membrane leaf. In one variant promoted for high recovery residential modules, feed enters both sides of the module and exits from a porous outer surface [160]. In others, feed flow follows a serpentine flow path away from the tube [68, 161, 162]. These geometries can suppress scaling by avoiding coincidence of regions where feed concentration is highest with those having either low feed velocity or high permeate flux. Another different set of alternative designs have been proposed to reduce permeate pressure drop in a long membrane leaf. For instance, permeate may be taken off one side or through alternative paths, so that the differences in permeate pressure (and thus membrane flux) are kept relatively low across the membrane [111, 163–166]. Finally, a more balanced flux in the conventional spiral wound geometry may also be achieved by using membranes with different permeabilities across the sheet [167]. Any of these approaches could potentially provide the opportunity to operate at higher concentrations without scaling or fouling.

There have recently been several suggestions to enable individual modules to better communicate information with end users. Indicators within the module for later examination may take the form of chemical sensors, such as those for determining exposure to halogen-type oxidizing agents [168] or high temperature [169]. An module with electronic recording medium provided inside of the permeate tube has been described [170]. Several documents describe incorporating an RFID tag, antenna, and sensors within the module, so that information might be immediately provided information about the module location and performance [171, 172]. This could facilitate implementation of loading maps, monitoring system performance, on-line probing, and replacement of defective modules. Alternatively, a detachable sensor for feed or permeate fluid may be located in a coupler between modules [173, 174]. In these situations, power for sensors and electronics may come from a battery, it may supplied by wire, it may be collected by an antenna incorporated within the module, or it may be generated by liquid flow within the module [175]. It has also been proposed that multiple sensors may be located down a vertical-oriented vessel (e.g., in permeate tube) [176]. In light of recent progress at Sorek, near-term implementation of large-scale, continuous monitoring may be reasonable.

8.3 Ultrafiltration Membrane and Module

8.3.1 Ultrafiltration Membranes

8.3.1.1 Background and Classification

Ultrafiltration (UF) is a valuable separations process with the capability to remove impurities $\sim$1 nm in size and above, and applications range from removal of silt and bacteria to viruses and high molecular weight organic molecules [177]. Polymeric UF membranes can be classified in several ways, such as their module construction, material of construction, and formation mechanism. UF membranes

are commercially available in flat sheet and hollow fiber format. Flat sheet UF membranes are typically produced in a spiral wound format similar to RO elements. More common, however, is the hollow fiber configuration used by Dow (see Fig. 8.10). As with a spiral design, high membrane surface area can be packed into relatively small volume. However, hollow fibers can be more easily backflushed, and the individual mobility of fibers enables effective cleaning through agitation by air sparging. UF is a very valuable pretreatment operation in reverse osmosis applications, due to its ability to remove various potential foulants from feed water.

The most common polymers used to make UF hollow fibers are poly(vinylidene fluoride) (PVDF) and poly(ether sulfone) (PES), due to their excellent mechanical strength and chemical resistance. Manufacturers such as Dow, General Electric (GE), Pall, and Toray use PVDF for their main fiber offering, while BASF and Pentair use PES. Other polymers, such as the poly(vinyl choride) used by Litree and the polyacrylonitrile used by Pall, are also important in the UF industry; the former selected due to low cost and durability [178], and the latter due to hydrophilicity [179]. Organic and biological foulants are known to be much less of a problem in UF when a hydrophilic polymer is used, although concessions on durability and chemical resistance must be made. Periodic cleaning cycles are employed to maintain a high sustainable flux in UF, and these cleanings often require an aggressive pH or oxidizers to remove foulants. A customer's choice of UF membrane material must take into account the cleaning protocols required for the foulants in their feed stream.

Narrowing the discussion further to only PVDF membranes, there are two sub classifications within commercial UF hollow fibers—those made by thermally induced phase separation (TIPS), and those made via diffusion induced phase separation (DIPS). Membranes made via TIPS, such as those made by Pall, begin with the dissolution of polymer and additives in a diluent that is a solvent at high temperature, but a non-solvent for the polymer at low temperature. Typical diluents

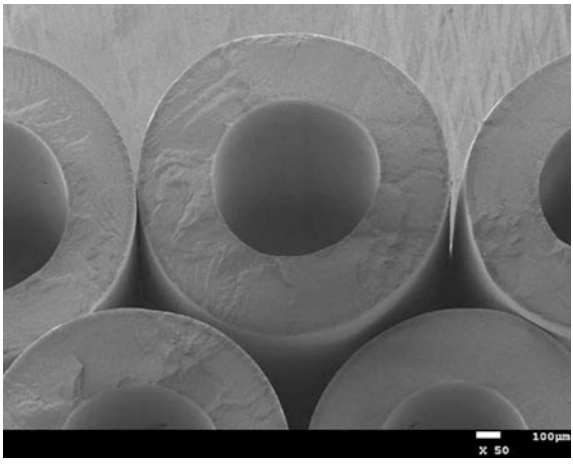

Fig. 8.10 Cross section of a Dow UF fiber

for PVDF include diphenyl carbonate [180] and mixtures of phthalates, such as dibutyl and diethylhexyl phthalate [181]. These must be manufactured at high temperatures, and most often require non-aqueous means of diluent extraction. Benefits of these membranes include excellent mechanical strength, due to the ability to maintain high permeability at high bulk membrane density, and high flux, due to large pore sizes in the range of 100–300 nm. On the other hand, DIPS is used with PVDF to make a very different membrane structure. These are formed by dissolving the polymer and additives in a solvent (e.g., dimethylformamide, dimethylacetamide, N-methylpyrrolidinone, or triethylphosphate) at a much lower temperature and extruding through a die into an aqueous quench bath. Here water, a non-solvent for PVDF, diffuses into the polymer solution to induce PVDF precipitation. The resulting structure is an asymmetric fiber; that is, the surface pore size is very small (usually 10–40 nm) while the underlying structure is much more open. The membranes are designed to provide as little resistance to water flow as possible within the underlying structure. A bore fluid is selected to provide stability to the fiber during quenching by slowly inducing phase separation and precipitation of the PVDF, while at the same time forming a low resistance interior wall [177].

8.3.1.2 Challenges and Recent Development

Ultrafiltration membrane development faces a seemingly infinite array of potential foulants in feed waters. Performance modeling (and thus material development) for reverse osmosis membranes can focus on the flux and rejection of individual solutes and predict with good accuracy because certain pre-treatment steps (e.g., ultrafiltration, chlorination/dechlorination, and anti-scalants) are taken to protect the membrane; however, ultrafiltration feed water typically contains a combination of inorganic particulates, bacteria, organic molecules, dissolved scalants, and other contaminants. Thus, developing a single product that can be used in a wide range of applications is not a trivial task. Specific UF membranes have been developed for low fouling, high water flux applications that would be unsuitable for virus removal applications [182]. Conversely, membranes have been developed with good molecular weight cutoffs that do not provide flux sufficient for economic viability in RO pretreatment [183, 184]. Therein lies a key challenge in UF membrane manufacturing: being able to focus on a single technology type (e.g., DIPS vs. TIPS, or PVDF vs. PES) to avoid an unnecessarily complex manufacturing strategy while maintaining the flexibility to address multiple applications and markets. Dow's approach to this challenge was to produce a PVDF DIPS fiber with a unique set of characteristics, designed to best meet the world's water purification needs. Its consistent surface pore structure and good water productivity are largely products of a process-controlled asymmetric structure, while its durability and excellent chemical resistance are attributable to the polymer selection (PVDF) and the proprietary spinning solution recipe.

While the first challenge of fiber development is simply developing a process that can, in less than a second, turn a low viscosity fluid into a hollow fiber strong

enough to withstand the tensile and compressive forces of a high speed fiber spinning line, a much more difficult feat is to develop a recipe that best meets customer needs. The key to developing a DIPS fiber is to understand the complexities of phase separation and growth kinetics. Targeting the need for a high strength fiber, Dow scientists first selected PVDF as the fiber material, and sought to develop a structure free of large ($\sim$50–200 μm) interior voids, referred to as macrovoids in the membrane industry [185, 186]. While a consensus on the exact mechanism of macrovoid formation has not been reached, they are generally formed by an in-flux of nonsolvent during phase separation, possibly by an osmotic pressure gradient, and growth of a solvent-nonsolvent pocket away from the advancing gelation front. Because macrovoids can be avoided when the advancing gelation front moves more quickly than the growth rate of a macrovoid, it is important to control the phase separation and gelation processes through recipe. To do this, Dow scientists developed a solvent-nonsolvent mixture into which the PVDF would be dissolved that placed the system teetering on the edge of phase separation before quenching in an aqueous bath. That is, to avoid macrovoid formation, the polymer solution was made predisposed to rapid phase separation and solidification. Furthermore, control of the quench bath composition maintains an osmotic pressure gradient that is less favorable for macrovoid initiation (Fig. 8.11).

Phase diagram generation is a logical first step in any membrane development process; however, PVDF does not allow phase diagram generation by traditional means, where increasing amounts of nonsolvent are added to a polymer solution until the solution becomes cloudy or solidifies. PVDF undergoes an additional phase transition uncharacteristic of other UF polymers like PES, one that is most often overlooked in the UF literature. In addition to the liquid–liquid demixing transition (also known as a cloud point) and the crystallization transition responsible for PVDF hollow fiber strength, PVDF can undergo a slow association-induced gelation at water concentrations below that required for the

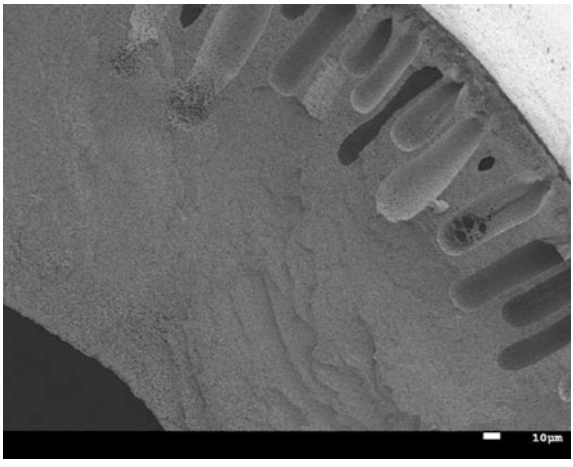

Fig. 8.11 Cross sectional SEM image of a PVDF hollow fiber containing macrovoids

other transitions [187, 188]. This forms micro-gel domains, thickens the polymer solution, and prevents liquid-liquid demixing unless water is introduced more quickly than the gelation can occur—at rates higher than are possible for a phase diagram measurement. Therefore, meticulous experimental design was employed to determine where the phase separation boundary lies by spinning fibers—not by actually measuring it in a laboratory. Generic phase diagrams for PVDF under different water diffusion rates are shown in Fig. 8.12. Fortunately, since the development of the Dow fiber, a proprietary method has been developed to measure the point of association induced gelation within the applicable range of polymer concentrations. This will aid in future recipe development as new solvents, additives, or polymers are investigated.

Asymmetry is an important aspect of Dow UF fiber, and the selection of a diffusion induced phase separation process is the most important avenue to such a structure. However, processing conditions are nearly as important, and further research had to be undertaken to optimize the temperatures at which phase separation would occur and to control the rate of water diffusion. Temperature is a key parameter in manipulating solubility, and therefore is paramount to controlling phase separation. At a higher temperature, the polymer solution is more stable, more water is required to precipitate PVDF, and a different phase separated structure will result since the solvent-nonsolvent mixture is more water-rich at the point of demixing. In the case of PVDF, a spinodal decomposition results near the surface of the fiber where the water moves quickest, resulting in a dense, lacy structure that provides the fiber's selectivity. This surface structure is highly dependent upon the solvent content in the aqueous quench, since it also affects the rate of water diffusion into the nascent fiber. Further into the fiber wall, however, where water moves more slowly, a nucleation and growth mechanism leads to lower density cellular structure that is important for maintaining a high water flux while imparting sufficient mechanical strength [189]. This is a difficult phenomenon to model for a polymer capable of strong interchain interactions like PVDF, and extensive experimentation must be done to arrive at an optimum set of processing

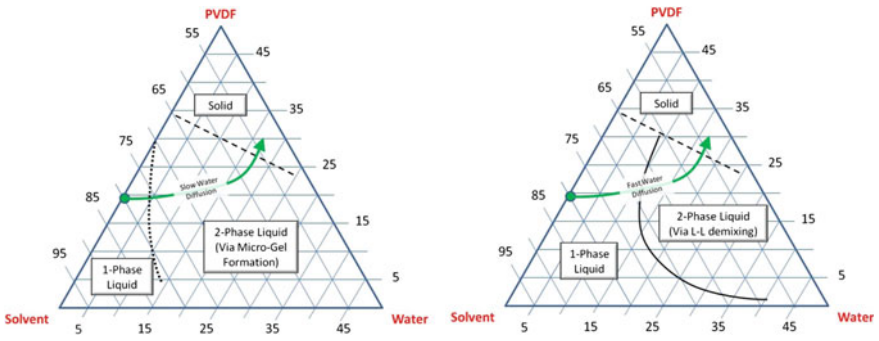

Fig. 8.12 Generic phase diagrams for PVDF diffusion induced phase separation membranes made (*left*) with a slow water diffusion rate and (*right*) a fast water diffusion rate

conditions for a given fiber recipe. When designing the manufacturing process, it was important to take into account the need for tight control on flow rates, temperature, and concentration, as these become more and more important as line speed increases. That is, since the feedback time on fiber performance is so long, it is important that variability be minimized to avoid large amounts of scrap material.

In summary, Dow has met a need in the ultrafiltration membrane market by designing a fiber with good durability and chemical resistance that also combines excellent water permeability with a 30 nm surface pore size. This unique set of characteristics makes the Dow UF fiber valuable in a variety of applications that provide synergy with its already market-leading reverse osmosis membrane business. At the same time, Dow developed a technology basis for a wide range of future UF products, and a manufacturing asset with the flexibility needed for such future development.

8.3.2 Ultrafiltration Modules

8.3.2.1 Background

Upon developing a membrane with the desired characteristics for a given application, packaging it into a module is a critical next step in enabling the membrane to perform at its full potential. Broad reviews on the current state of UF technology have been compiled by Zeman and Zydney, Kubota et al., Kennedy et al., and Cheryan [190–193]. Subject specific reviews that discuss the role of UF module design and operation have also been complied on gas sparging or air scouring [194, 195], fouling [196–198] and concentration polarization [199].

Pictured in Fig. 8.13 is a cutaway drawing of a typical hollow fiber UF module. Although UF membrane is also manufactured in flat sheet and tubular form, hollow fiber has emerged as the dominant geometry for large scale applications spanning desalination pretreatment, surface water purification, paint recovery, select food/dairy processes, and medical/pharmaceutical purification [190]. The fibers are contained within a cylindrical module in a tube and shell arrangement. Kubota et al. notes this geometry enables the largest membrane area per unit volume [192]. Hollow fiber membrane geometry is also important to overall module design through its effective participation in flushing, air scouring, and backwash processes. An outside-in flow direction through the membrane is frequently, but not exclusively, used to encourage efficient removal of foulants during these processes.

The primary module components are shown in Fig. 8.13. The module housing contains the membrane and creates a flow channel through which the pressurized feed water passes. At the process inlet of the housing, the inlet structure comprises an endcap, an inlet or feed port, a flow distribution channel, a flow diffuser, and auxiliary ports. The feed port introduces the feed stream into the housing, via the feed channel and flow diffuser. These features are designed to evenly distribute the feed stream around the circumference of the housing before the flow travels axially

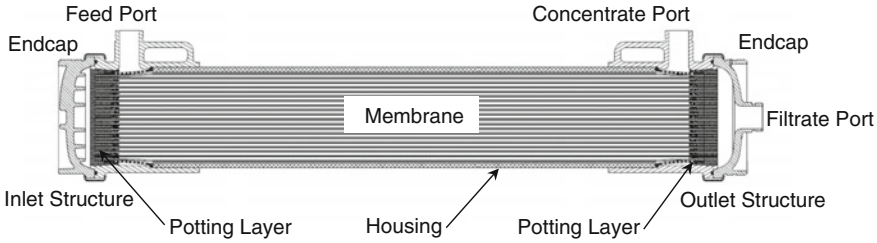

Fig. 8.13 Typical hollow fiber ultrafiltration module

through the module to the membrane surface. Auxiliary ports incorporated into the inlet structure are intended as connection ports for air scouring and chemical cleaning (CIP) processes. At the process exit, or concentrate end of the module, an outlet structure exists containing the concentrate port. In water treatment for potable water or RO pretreatment, the module is not generally used in a continuous cross flow filtration mode, therefore the concentrate port does not see continuous water flow. More commonly, this port is only used during flushing, backwash, and cleaning cycles. Operating in a dead-end filtration mode allows UF processes to maintain very high recoveries, on the order of 90–98%. A filtrate or permeate port is also generally found within the outlet structure, but can be located on both of the ends of the module. This port is often molded into a separate endcap that is fastened to the inlet or outlet structure in a final manufacturing step. The need for a separate endcap arises from manufacturing requirements for casting potting resin around the fibers in the inlet and outlet structure and then trimming the potting layer to open a permeate path for the filtered liquid to exit. The potting resin is a critical component that fully seals both inter-fiber voids and the fiber bundle to the module. Common potting materials include epoxies and polyurethanes.

The most important characteristics of the UF module are those intended to address mechanical, hydrodynamic, and economic requirements [193]. Examining first mechanical requirements, the module design and materials of construction are selected to endure pressures on the order of 5 bar with frequent pressure cycling. Although transmembrane pressure (TMP) ranges are typically less than 3 bar, the module is designed to handle significantly higher pressures. For example the Dow IntegraFlo™ module lists a TMP specification of <2.1 bar, but a maximum module pressure specification of 4.75 bar. This ensures the user can maintain a reasonable permeate pressure as well as handle pressure pulsations during air scouring, backwashing, and flushing. With backwash cycle times on the order of twenty to sixty minutes common in operation, module components can be subjected to hundreds of thousands of pressure oscillations between 5 bar and ambient pressure in a typical five year design life. Special attention must be given to fatigue resistance of a design as well as static integrity. Polymers offering good mechanical strength, chemical resistance, and manufacturability at a low cost are excellent candidates for construction of UF module components. GE, Dow, and Inge (BASF) all manufacture UF module housings from polyvinylchloride (PVC), with the latter

two examples employing the same material for module inlet/outlet structures and end caps. Polyethylene is also used as a module housing material by Toray. Acrylonitrile butadiene styrene (ABS) and Polystyrene blended polyphenylene oxide (Noryl) are used in inlet/outlet structures and endcaps by Toray and GE respectively. Manufacturing processes common to the above thermoplastics include extrusion and injection molding.

Hydrodynamic and economic requirements of the UF module are generally closely coupled from the end user point of view. Developing a model for a UF module requires consideration of pressure losses through the membrane (trans-membrane pressure or TMP) and pressure losses due to the filtrate flow down the narrow lumen, or inner diameter, of the fiber. Both of these pressure losses are major contributors to UF module operating expenses [200]. Packing density of the fibers and fiber diameter are also known to effect flow properties around the fiber OD leading to an effect on backwash and cleaning frequency [201, 202]. The module designer is required to obtain the highest active membrane area in the module while ensuring the fibers also have adequate freedom for agitation during air scouring and flushing. Considering the above works, an optimum fiber diameter and packing density can be predicted for a corresponding module length and a particular set of operating conditions.

8.3.2.2 Challenges and Recent Development

Recent innovations in Dow's UF module design have focused on three important aspects of module performance which contribute to mechanical, hydrodynamic, and economic benefits. The first two areas of development, energy consumption and fiber breakage, are related to interactions between the feed water and the membrane within the module. The third area of research, module implementation, considers the use of UF modules within the entire water treatment system.

Energy Consumption

In addition to trans-membrane pressure (TMP) and lumen pressure drop, pressure loss due to flow entrance and distribution are also common to UF modules. TMP is purely a function of membrane characteristics and will not be addressed here. However the design of the module directly contributes to entrance and lumen side pressure loss. Advances in the geometry of Dow's newest generation of UF modules have made strides at addressing these losses. Pressure drop through the inlet port and inlet structure geometry was initially quantified, then optimized via computational fluid dynamics. Then prototypes were constructed and experimentally verified to reduce inlet and distribution losses by 15% at high operating fluxes over previous generation modules. This development leads directly to end user savings through reduced electrical power requirements.

Fiber breakage

A significant problem in UF membrane integrity arises from the hollow fiber geometry that is most well suited for this type of filtration. Within a UF module there are as many as 12,000 small fibers, roughly 0.5–1.5 mm in diameter. These fibers are commonly unsupported along the module axis, secured only by potting resin at each end of the module. This configuration results in significant opportunity for fiber breakage, especially during air scouring events where the fibers are agitated to remove foulants. In addition to membrane materials research, module design is an effective tool to help control the conditions the fibers are exposed to. Figure 8.14 shows the diffuser that makes up the inner diameter of the inlet structure on a Dow IntegraFlo™ UF module. The perforated diffuser was designed to allow unrestricted flow of feed water into the module housing; however, the portion directly adjacent to the feed port is solid in order to protect the hollow fibers from high velocity flow. Additionally, the air scouring ports are oriented to impact the same impenetrable position on the diffuser.

Module Implementation

Advances in module development also address the implementation and function of the UF module within the water treatment plant. A recent development has been the addition of integral handling features to aid in module installation and removal [203]. Due to typical UF module size, handling during installation is a significant concern of many end users. For example a Dow IntegraFlo™ IW102-1100 module is more than 2 m long and has a shipping mass of 70 kg, making installation and removal challenging, especially in confined locations.

Additional work has gone into developing products that streamline the plant design and construction process. With the intent of significantly reducing piping and mounting hardware, the Dow IntegraPac™ system can be composed of 6–22 modules that connect to scalable connection manifolds giving the end user a field

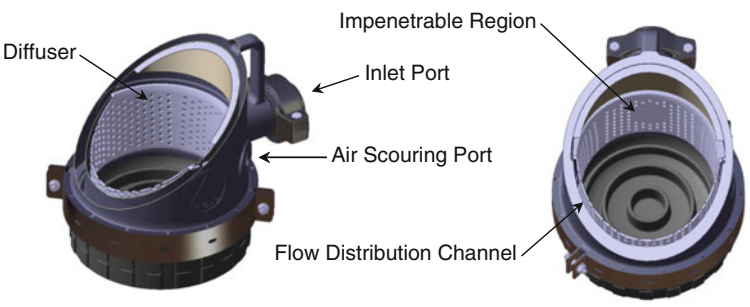

Fig. 8.14 Inlet structure of a Dow IntegraFlo™ UF module

assembled ultrafiltration skid. Feed and concentrate ports have been designed to easily connect to adjacent modules thus eliminating much of the previous required piping [204]. Modular permeate and air manifolds are also incorporated into the design.

8.3.3 *Unmet Needs in Ultrafiltration*

The most important unmet need for ultrafiltration membranes is a low-cost fiber material that is permanently hydrophilic while maintaining the durability and chemical resistance of PVDF. Typical UF operation might involve a cleaning cycle frequency of every 0.5–2 h. During the cleaning cycles, fibers are back-flushed with water, air is used to agitate the fibers, and/or chemicals are fed to the module to remove foulants, but no clean water is produced. Thus, the frequency of cleaning directly affects the output of the module over time. Hydrophilicity is extremely valuable when treating biologically active feed streams, as the contaminants, such as bacteria and proteins, would be less likely to adhere to such a surface. As a result, a hydrophilic PVDF membrane would require less frequent cleanings and lower chemical consumption.

Additives such as polyvinylpyrrolidone and poly(methyl methacrylate) are often combined with PVDF to improve hydrophilicity, but these cannot withstand the harsh cleaning cycles of UF membranes. Other polymers or modifications, such as surface grafting or copolymerization, lack either the mechanical strength or the chemical resistance afforded by PVDF, or are too costly to be economically feasible [205]. The development of inexpensive copolymers able to reduce the fouling tendency of UF membranes in harsh operating environments will be critical to future development.

Although UF offers very high recoveries, on the order of 90–98%, efforts to increase the energy efficiency of the module design are ongoing. Future designs may utilize dual end permeation in an effort to reduce lumen side pressure loss by effectively cutting both permeate path length and flow in half within each fiber. A summary of studies that illustrate the advantages of dual end permeation is given by Serra et al. [206]. Dual end permeation products do exist, however they have yet to be thoroughly tested and widely accepted in the industry. In order to properly quantify the advantages of a dual end permeating UF module, the capital cost of a second permeate port, fittings, valves, piping, etc., and additional manufacturing steps must be compared with the savings in operating expenses associated with the lumen pressure losses.

Opportunities also exist in the development of high speed manufacturing operations for assembling UF modules. Assembling membrane modules comprising thousands of hollow fibers marks a notable deviation from the flat sheet handling practices familiar to many manufacturers experienced in RO and NF flat sheet membranes. Fiber handling and trimming, module potting, and component assembly share few parallels with analogous flat sheet operations, leaving manufacturers to develop these process from scratch.

8.4 Conclusion

In the recent years, there has been a significant amount of effort focused on novel membrane materials. These advanced materials [207–222] pose a great opportunity for membranes for water purification. However advanced manufacturing and economy of scale needs to be implemented before these can become cost competitive with incumbent desalination technologies which are already very energy efficient [9, 10] as they are approaching the thermodynamic limit of salt-water separation [9, 10, 13].

Water is a critical sustainability pillar and it is imperative that as we plan for a sustainable water future we focus on technologies that can lead to more cost and energy efficient water purification. Cost efficiency has to come from manufacturing more energy efficient membranes that are fouling resistant so that the energy efficiency is sustainable over the life time of the membrane [31, 32, 223–226]. In order to optimize these properties, research needs to continue to improve understanding of the structure property relationships for existing and novel membrane materials. Along with membranes, modules and system design also play a significant role in the overall energy efficiency and cost efficiency of water purification applications [9, 14]. Novel materials, manufacturing methods and designs for modules as discussed in this chapter are key in realizing the full potential of membranes in our effort to secure a sustainable water future.

References

1. Service, R.F., Desalination freshens up. Science **313**(5790), 1088–1090 (2006)
2. T. Oki, S. Kanae, Global hydrological cycles and world water resources. Science **313**(5790), 1068–1072 (2006)
3. Water Crisis. [cited 2014 06/11/2014]. http://www.worldwatercouncil.org/library/archives/water-crisis/
4. UNESCO water facts and figures. [cited 2014 06/11/2014]. http://www.unesco.org/new/en/natural-sciences/environment/water/wwap/facts-and-figures/
5. Energy Demands on Water Resources (20060
6. T. Younos, R. Hill, H. Poole, Water dependency of energy production and power generation systems. Water Resour. Impact **14**(1), 9–12 (2012)
7. S. Chu, A. Majumdar, Opportunities and challenges for a sustainable energy future. Nature **488**(7411), 294–303 (2012)
8. P. Hanlon, R. Madel, K. Olson-Sawyer, K. Rabin, J. Rose, K. Demaline, L. Hatfield, C. Hunt, K. Sweetman, Food, Water Energy. 2013
9. A. Shrivastava, S. Rosenberg, M. Peery, Maximizing seawater reverse osmosis energy efficiency with high permeability membranes and system design, in *International Desalination Association World Congress on Desalination and Water Reuse 2013* (IDA, Tianjin, 2013)
10. M. Elimelech, W.A. Phillip, The future of seawater desalination: energy, technology, and the environment. Science **333**(6043), 712–717 (2011)
11. R. Semiat, Energy issues in desalination processes. Environ. Sci. Technol. **42**(22), 8193–8201 (2008)

12. J.E. Miller, *Review of Water Resources and Desalination Technologies* (Sandia National Laboratories, Albuquerque, 2003)
13. E.L. Cussler, B.K. Dutta, On separation efficiency. AIChE J. **58**(12), 3825–3831 (2012)
14. C. Liu, K. Rainwater, L. Song, Energy analysis and efficiency assessment of reverse osmosis desalination process. Desalination **276**(1–3), 352–358 (2011)
15. J. Wijmans, R. Baker, The solution-diffusion model: a review. J. Membr. Sci. **107**(1), 1–21 (1995)
16. D.R. Paul, Reformulation of the solution-diffusion theory of reverse osmosis. J. Membr. Sci. **241**(2), 371–386 (2004)
17. N. Ghaffour, T.M. Missimer, G.L. Amy, Technical review and evaluation of the economics of water desalination: current and future challenges for better water supply sustainability. Desalination **309**, 197–207 (2013)
18. B.S. Lalia, V. Kochkodan, R. Hashaikeh, N. Hilal, A review on membrane fabrication: Structure, properties and performance relationship. Desalination **326**, 77–95 (2013)
19. P. Radovanovic, S.W. Thiel, S.-T. Hwang, Formation of asymmetric polysulfone membranes by immersion precipitation. Part I. Modelling mass transport during gelation. J. Membr. Sci. **65**(3), 213–229 (1992)
20. P. Radovanovic, S.W. Thiel, S.-T. Hwang, Formation of asymmetric polysulfone membranes by immersion precipitation. Part II. The effects of casting solution and gelation bath compositions on membrane structure and skin formation. J. Membr. Sci. **65**(3), 231–246 (1992)
21. J.E. Cadotte, M.M.N.U.S., Interfacially synthesized reverse osmosis membrane. US4277344A (1981)
22. J. Wang, D.S. Dlamini, A.K. Mishra, M.T.M. Pendergast, M.C.Y. Wong, B.B. Mamba, V. Freger, A.R.D. Verliefde, E.M.V. Hoek, A critical review of transport through osmotic membranes. J. Membr. Sci. **454**, 516–537 (2014)
23. A. Antony, R. Fudianto, S. Cox, G. Leslie, Assessing the oxidative degradation of polyamide reverse osmosis membrane—accelerated ageing with hypochlorite exposure. J. Membr. Sci. **347**(1–2), 159–164 (2010)
24. J. Glater, S.-K. Hong, M. Elimelech, The search for a chlorine-resistant reverse osmosis membrane. Desalination **95**(3), 325–345 (1994)
25. M.M. Chau, S.D.C.A.U.S., High flux semipermeable membranes. US4950404A (1990)
26. M. Hirose, S.J.P., S.J.P. Ito Hiroki, S.J.P. Tanaka Kazuo, Osmosis membrane. US5989426A (1999)
27. W.E. Mickols, M.M.I.U.S., Method of treating polyamide membranes to increase flux. US5755964A (1998)
28. J.E. Cadotte, M.M.N.U.S., K.G.B., D.R. Walker, Polyamide membranes useful for water softening. US4765897A (1998)
29. W.E. Mickols, C.M.N., Composite membrane and method for making the same. US6337018B1 (2002)
30. S.D. Jons, E.P.M.N.U.S., M.M.I.U.S., K.J. Stutts, M.M.I.U.S., M.S. Ferritto, C.M.N.U.S., W.E. Mickols, Treatment of composite polyamide membranes to improve performance. US5876602A (1999)
31. A.C. Sagle, E.M. Van Wagner, H. Ju, B.D. McCloskey, B.D. Freeman, M.M. Sharma, PEG-coated reverse osmosis membranes: desalination properties and fouling resistance. J. Membr. Sci. **340**(1–2), 92–108 (2009)
32. E.M. Van Wagner, A.C. Sagle, M.M. Sharma, Y.-H. La, B.D. Freeman, Surface modification of commercial polyamide desalination membranes using poly(ethylene glycol) diglycidyl ether to enhance membrane fouling resistance. J. Membr. Sci. **367**(1–2), 273–287 (2011)
33. J. Wu, A.E. Contreras, Q. Li, Studying the impact of RO membrane surface functional groups on alginate fouling in seawater desalination. J. Membr. Sci. **458**, 120–127 (2014)
34. L. Zhao, P.C.Y. Chang, C. Yen, W.S.W. Ho, High-flux and fouling-resistant membranes for brackish water desalination. J. Membr. Sci. **425–426**, 1–10 (2013)

35. V. Freger, Nanoscale heterogeneity of polyamide membranes formed by interfacial polymerization. Langmuir **19**(11), 4791–4797 (2003)
36. M. Elimelech, W.H. Chen, J.J. Waypa, Measuring the zeta (electrokinetic) potential of reverse osmosis membranes by a streaming potential analyzer. Desalination **95**(3), 269–286 (1994)
37. L.A. Perry, O. Coronell, Reliable, bench-top measurements of charge density in the active layers of thin-film composite and nanocomposite membranes using quartz crystal microbalance technology. J. Membr. Sci. **429**, 23–33 (2013)
38. B.X. Mi, O. Coronell, B.J. Marinas, F. Watanabe, D.G. Cahill, I. Petrov, Physico-chemical characterization of NF/RO membrane active layers by Rutherford backscattering spectrometry. J. Membr. Sci. **282**(1–2), 71–81 (2006)
39. O. Coronell, X. Zhang, M.I. Gonzalez, D.G. Cahill, B.J. Marinas, Quantification of functional groups in FT30 (RO) membrane and modeling of their acid/base behavior, in *Abstracts of Papers, 235th ACS National Meeting*, p. ENVR-119, New Orleans, LA, United States, 6–10 Apr 2008
40. O. Coronell, B.X. Mi, B.J. Marinas, D.G. Cahill, Modeling the effect of charge density in the active layers of reverse osmosis and nanofiltration membranes on the rejection of Arsenic(III) and potassium iodide. Environ. Sci. Technol. **47**(1), 420–428 (2013)
41. O. Coronell, B.J. Marinas, X.J. Zhang, D.G. Cahill, Quantification of functional groups and modeling of their ionization behavior in the active layer of FT30 reverse osmosis membrane. Environ. Sci. Technol. **42**(14), 5260–5266 (2008)
42. O. Coronell, B.J. Marinas, D.G. Cahill, Depth heterogeneity of fully aromatic polyamide active layers in reverse osmosis and nanofiltration membranes. Environ. Sci. Technol. **45**(10), 4513–4520 (2011)
43. O. Coronell, I. Marinas Benito, G. Cahill David, Accessibility and ion exchange stoichiometry of ionized carboxylic groups in the active layer of FT30 reverse osmosis membrane. Environ. Sci. Technol. **43**(13), 5042–5048 (2009)
44. A. Tiraferri, M. Elimelech, Direct quantification of negatively charged functional groups on membrane surfaces. J. Membr. Sci. **389**, 499–508 (2012)
45. J.Y. Chung, J.-H. Lee, K.L. Beers, C.M. Stafford, Stiffness, strength, and ductility of nanoscale thin films and membranes: a combined wrinkling-cracking methodology. Nano Lett. **11**(8), 3361–3365 (2011)
46. V.P. Khare, A.R. Greenberg, W.B. Krantz, Investigation of the viscoelastic and transport properties of interfacially polymerized barrier layers using pendant drop mechanical analysis. J. Appl. Polym. Sci. **94**(2), 558–568 (2004)
47. V.P. Khare, A.R. Greenberg, W.B. Krantz, Development of pendant drop mechanical analysis as a technique for determining the stress-relaxation and water-permeation properties of interfacially polymerized barrier layers. J. Appl. Polym. Sci. **90**(10), 2618–2628 (2003)
48. S.H. Maruf, D.U. Ahn, A.R. Greenberg, Y.F. Ding, Glass transition behaviors of interfacially polymerized polyamide barrier layers on thin film composite membranes via nano-thermal analysis. Polymer **52**(12), 2643–2649 (2011)
49. J. Lee, C.M. Doherty, A.J. Hill, S.E. Kentish, Water vapor sorption and free volume in the aromatic polyamide layer of reverse osmosis membranes. J. Membr. Sci. **425–426**, 217–226 (2013)
50. X. Zhang, D.G. Cahill, O. Coronell, B.J. Mariñas, Absorption of water in the active layer of reverse osmosis membranes. J. Membr. Sci. **331**(1–2), 143–151 (2009)
51. X. Xu, R.J. Kirkpatrick, NaCl interaction with interfacially polymerized polyamide films of reverse osmosis membranes: a solid-state 23Na NMR study. J. Membr. Sci. **280**(1–2), 226–233 (2006)
52. X. Zhang, D.G. Cahill, O. Coronell, B.J. Marinas, Partitioning of salt ions in FT30 reverse osmosis membranes. Appl. Phys. Lett.**91**(18), 181904/1–181904/3 (2007)
53. V. Freger, S. Bason, Characterization of ion transport in thin films using electrochemical impedance spectroscopy. J. Membr. Sci. **302**(1+2), 1–9 (2007)
54. T. Bray Donald, Reverse osmosis purification apparatus. US3417870A (1968)

55. C. Westmoreland Julius, Spirally wrapped reverse osmosis membrane cell. US3367504A (1968)
56. K.V. Larsen, D.K.M.D.K., Permeate tube|permeatrohr|tube de permeat. EP1807179B1 (2011)
57. Y. Uda, O.J.P., O.J.P. H. Toshimitsu, O.J.P. C. Shinichi, Spiral separation membrane element, perforated hollow tube, and method of producing the same. US20130087499A1 (2013)
58. P.T. Goebel, N.H.M.N.U.S., Spiral wound membrane element product water tube with external flow grooves. US8529762B2 (2013)
59. H. Kang Sang, R/O type purifier including in reverse flow preventing function|reverse osmosis-typed water purifier with a backflow preventing function, comprising backflow preventing units installed in water collecting holes of a water collecting pipe|The reverse osmotic pressure type water-cleaner in which the inverse current preventing function is equipped. KR2009056618A (2009)
60. Y. Uda, M. Beppu, S. Jizo, Separation membrane element|Separation-membrane element. JP2010264420A (2010)
61. G.S. Nalle, Jr., Die head for extruding plastic netting and method of extruding such netting. US3067084A (1962)
62. I. Shelby, S.D.C.A.U.S., S.D.C.A.U.S. B.C. Roger, Cross-flow filtration apparatus with biocidal feed spacer. US20090314713A1 (2009)
63. Y. Uda, I.-s.J.P., I.-s.J.P.K. Naoki, I.-s.J.P.Y. Yuuji, I.-s.J.P.M. Kouji, I.-s.J.P.K. Takahisa, Feed side passage material and spiral separation membrane element. US20110168623A1 (2011)
64. Z. Cai, C.N., C.N. S.-M. Liang, C.N. J. Tao, C.N. Y. Jin, C.N. G.-Y. Xu, C.N. Z. Wu, Method for improving anti-pollution performance of reverse osmosis membrane element| A kind of the reverse osmosis membrane element anti-pollution performance of method. CN102941019A (2013)
65. S.Y. Lee, K. Kim Youn, Membrane filter capable of reducing dissolved solid| Membrane filter capable of the removal of a hard material for installing a hardness material eliminating unit| The membrane filter capable of the removal of the harden property material. KR2010109156A (2010)
66. C.U. Hardwicke, S.S.C.U.S., H.T.X.U.S. A.J. Avagliano, C.P.N.Y.U.S. G.R. Chambers, D. N.Y.U.S. S.F. Rutkowski, F.P.A.U.S. E.J. Hall, Reverse osmosis membrane and membrane stack assembly. US20090139650A1 (2009)
67. Y. Tayalia, S.S.G., B.I.N. P.R. Dontula, S.A.Z.U.S. U.J. Bharwada, Feed spacers for spiral wound membrane element. US20130146531A1 (2013)
68. B. Wood, P.K.Y.U.S., Spiral wound filter. US8236177B1 (2012)
69. P.P. Beauchamp, R.N.Y.U.S., L.K.Y.U.S. R. Thiyagarajan, B.I.N. A. Kumar, N.N.Y.U.S. T. A. Anderson, Separation module. US20120103892A1 (2012)
70. A.B. Minick, U.S., U.S. M.F. Buser, Fluid separation system with reduced fouling| Fliud separation system with reduced fouling. CN102333582A (2012)
71. H. Hirozawa, J.P., J.P.M. Koiwa, J.P.H. Yamada, J.P.K. Takagi, J.P.Y. Okamoto, J.P.T. Hamada, J.P.K. Oto, J.P.M. Kimura, Separation membrane and separation membrane element| Membrane de séparation et élément de membrane de séparation. WO2013125505A1 (2013)
72. N. Harada, A. Ko, K. Ishii, O. Hayashi, A. Mizuike, Y. Kawaguchi, Sheet-like separation membrane and separation membrane element| A sheet-like separation membrane and a separation-membrane element. JP2010125418A (2010)
73. N. Harada, A. Ko, Sheet-like composite semi-permeable membrane and manufacturing method therefor| A sheet-like composite semi-permeable membrane and its manufacturing method. JP2010099590A (2010)
74. H. Hirozawa, M. Kimura, Y. Suzuki, K. Takagi, Separation membrane and separation membrane element| A separation membrane and a separation-membrane element. JP2012066239A (2012)

75. M. Koiwa, M. Kimura, K. Takagi, Separation membrane element| Separation-membrane element. JP2012055817A (2012)
76. K. Takagi, S.J.P., S.J.P. M. Kimura, S.J.P. M. Koiwa, S.J.P. H. Hirozawa, Separation membrane element. US20130334128A1 (2013)
77. M. Koiwa, K. Takagi, H. Hirozawa, M. Kimura, Spiral type separation membrane element and method for producing the same| A spiral-type separation-membrane element and its manufacturing method. JP2012139615A (2012)
78. The supply side flow-path material used for a spiral-type separation-membrane element, and its manufacturing method. JP04684783B2 (2011)
79. M. Beppu, Y. Uda, Spiral type separation membrane element| Spiral type|mold separation-membrane element. JP2007209956A (2007)
80. Y. Uda, N. Kurata, Y. Yamashiro, K. Maruyama, T. Konishi, Spiral separating membrane element| Spiral type|mold separation-membrane element. JP2009028714A (2009)
81. M. Beppu, Spiral separation membrane element| Spiral type|mold separation-membrane element. JP2009050759A (2009)
82. S. Jizo, T. Hamada, M. Beppu, Y. Uda, M. Takada, Spiral membrane element| Spiral type|mold film element. JP2009195870A (2009)
83. M. Beppu, O.J.P.O.J.P.S. Chikura, Spiral separation membrane element. US8303815B2 (2012)
84. A.J. Kidwell, M.M.N.U.S., Membrane filtration using low energy feed spacer. US20130341264A1 (2013)
85. K.-K. Tung, J.T.W., J.T.W.Y.-L. Li, T.C.T.W.M.-Y. Lu, T.C.T.W.J.-Y. Lai, Feed spacer for spiral-wound membrane module. US7459082B2 (2008)
86. P.R. Dontula, B.I.N., S.S.G.Y. Tayalia, S.A.Z.U.S.U.J. Bharwada, Feed spacer for spiral wound membrane element. US20130146532A1 (2013)
87. H.-Y. Hong, C.N., C.N.G. Chen, C.N.J.-F. Bao, Coil type membrane component with vertical-horizontal wide flow channels | Roll-type membrane module with vertically and horizontally wide flow channels. CN202151550U (2012)
88. M.K. McCague, E.C.A.U.S., S.D.C.A.U.S.W.G. Light, High density filtration module| Hochdichtes Filtrationsmodul| Module de filtration à haute densité. EP1707254A1 (2006)
89. G. Popa, R.D.E., S.-G.-e.-L.F.R.J. Suidureau, H.D.E.P. Johannsen, K.D.E.G. Reinhold, Spacer for filter modules. US20080290031A1 (2008)
90. A. Zounek, W.D.E., I.-W.D.E.U. Meyer-Blumenroth, Spacer for filtration devices| Abstandshalter für filtrationsvorrichtungen| Espaceur pour dispositifs de filtration. EP2544802A2 (2013)
91. T. Melin Prof. Dr, A.G.V.N.L., A.D.E.C. Bayer, A.D.E.C. Fritzmann, Membrane device with turbulence promoting spacers| Membranvorrichtung mit Abstandshalterelementen zur Strömungsvergleichmäßigung| Dispositif de membrane avec éléments espaceurs pour l'augmentation de la turbulence. EP2143480B1 (2013)
92. O. Tozawa, Spiral type separation membrane element| Spiral type|mold separation-membrane element. JP2006305556A (2006)
93. Spiral-type separation-membrane element. JP04488431B2 (2010)
94. K. Kono, Spiral type liquid separation element| Spiral-type liquid isolation|separation element. JP2010094659A (2010)
95. Y. Odaka, O.J.P., I.-g.J.P.T. Katayama, O.J.P.T. Kitagawa, Liquid separation device, flow channel material and process for producing the same. US8388848B2 (2013)
96. H. Im Ki, Y. Kim Duk, M. Yeo Sang, G.U.N.S. Kim, Tricot permeate channel for reverse osmosis membrane filter| Tricot permeate channel used for a reverse osmosis membrane filter for minimizing generation of harmful components to human body. KR704383B1 (2007)
97. Y. Odaka, J.P., J.P.T. Katayama, J.P.T. Kitagawa, Liquid separation device, flow channel material and process for producing the same| The separation of liquid device, and the fluid path ash and a manufacturing method thereof. KR1353830B1 (2014)

98. H. Ando, T. Katayama, Spiral type fluid separation element and method for manufacturing the same| A spiral-type fluid isolation|separation element and its manufacturing method. JP2013103182A (2013)
99. T. Nishioka, Y. Odaka, Liquid separating element, reverse osmosis apparatus using it and reverse osmosis membrane treatment method| A liquid isolation|separation element and a reverse osmosis equipment using the same, a reverse osmosis membrane processing method. JP2006247453A (2006)
100. K.V. Larsen, S.E., A spacer for membrane modules, a membrane module and uses thereof. CN101128252A (2008)
101. A separation membrane and a separation-membrane element. JP2014064973A (2014)
102. S. Jizo, T. Hamada, M. Beppu, Y. Uda, M. Takada, Spiral membane element| Spiral type|mold film element. JP2009195871A (2009)
103. H. Hirozawa, S.J.P., S.J.P.M. Koiwa, S.J.P.K. Takagi, S.J.P.Y. Okamoto, S.J.P.H. Yamada, S.J.P.Y. Seike, S.J.P.T. Hamada, S.J.P.M. Kimura, Separation membrane, separation membrane element, and method for producing separation membrane| Trennmembran, trennmembranenelement und verfahren zur herstellung der trennmembran| Membrane de séparation, élément de membrane de séparation et procédé de fabrication d'une membrane de séparation. EP2730331A1 (2014)
104. K. Iwai, S. Furuno, Y. Otaka, K. Komori, Separation membrane element, and membrane module| A separation-membrane element and a membrane module. JP2013208519A (2013)
105. Y. Okamoto, J.P., J.P.M. Koiwa, J.P.H. Yamada, J.P.K. Takagi, J.P.H. Hirozawa, J.P.T. Hamada, J.P.M. Kimura, Separation membrane element | Elément de membrane de séparation. WO2014003170A1 (2014)
106. K. Takagi, J.P., J.P.M. Kimura, J.P.M. Koiwa, J.P.H. Yamada, J.P.H. Hirozawa, Separation membrane and separation membrane element| Membrane de séparation et élément de membrane de séparation. WO2014021133A1 (2014)
107. Y. Jung, D.O.O., P.Y.O.S. Hong, S. Im Hee, Y. Koo Ja, Antimicrobial tricot permeate channel, manufacturing method thereof and spiral wound membrane module using the same| Antimicrobial tricot permeate channel made of sterilizer containing sheath-core type complex fiber, a manufacturing method of the same, a spirally wound membrane module including the same| The antibiotic tricote permeated water fluid path, and the manufacturing method thereof and spiral wound membrane module including the same. KR2012137890A (2012)
108. S.-Y. Lee, S.K.R., S.K.R.D.-W. Han, S.K.R.Y.-K. Kim, S.K.R.H.-J. Ahn, S.K.R.E.-J. Moon, S.K.R.S.-Y. Lee, Spiral wound type filter cartridge. US8506807B2 (2013)
109. P.R. Dontula, B.I.N., S.S.G.Y. Tayalia, S.A.Z.U.S.U.J. Bharwada, B.I.N.J.S. Radhakrishnan, B.I.N.M. Patnam, Spiral wound membrane element and permeate carrier. US20130098829A1 (2013)
110. A. van der Padt, A.N.L., B.N.L.T. Jongsma, Spiral wound filter assembly. US20100326910A1 (2010)
111. J.A. Bair, C.N.Y.U.S., H.N.Y.U.S.T.J. Fendya, I.N.Y.U.S.M.F. Hurwitz, T.N.Y.U.S.T. ul Haq, C.N.Y.U.S.S.A. Geibel, Fluid treatment arrangements and methods. US8043512B2 (2011)
112. K. Saito, T.J.P., T.J.P.T. Sano, Spiral-type filtration module, and liquid treatment method and device employing the same. US20120318736A1 (2012)
113. W. Graham, G.s.B.Z.A., Flow distributor plate for the treatment of water by reverse osmosis. US8715500B2 (2014)
114. S. Chikura, J.P., J.P.Y. Uda, J.P.T. Hamada, End member for spiral separation membrane element, spiral separation membrane element and separation membrane module | The part for the spiral separation film element, and the spiral separation film element and separating film module. KR2014047149A (2014)
115. Spiral-type fluid isolation|separation element. JP05181917B2 (2013)
116. A spiral-type film|membrane element and a spiral type membrane module. JP05179230B2 (2013)

117. M. Beppu, I.J.P., I.J.P.Y. Uda, I.J.P.S. Chikura, K.J.P.K. Yamamoto, Spiral membrane module. US8034241B2 (2011)
118. Y. Uda, T. Hamada, M. Beppu, S. Chikura, N. Tahara, M. Takata, Separation membrane element and separation membrane module using the same| Separation film element and separating film module using the same. KR1290463B1 (2013)
119. D.M. Colby, M.M.A.U.S., E.C.A.U.S.F.K. Lesan, S.D.C.A.U.S.A.M. Franks, C.M.A.U.S. C.-L. Hsieh, T.O.K.U.S.A.K. Mukherjee, Filtration element and method of constructing a filtration assembly. US7387731B2 (2008)
120. Y. Uda, T. Hamada, S. Jizo, M. Beppu, H. Yamane, M. Takada, K. Yoshida, Spiral membrane module| Spiral type membrane module. JP2012066184A (2012)
121. D. Bonta, S.P.M.N.U.S., M.M.I.U.S.M.M. Hoagland, End cap assembly adapted for interconnecting filtration elements. US8425773B2 (2013)
122. Y. Kim, J.A.E., H. Ryu Sang, H.W.A.S. Hwang, I.L.S. Lee, P.Y.O.S. Hong, Y. Koo Ja, Connecting assemblies for a filtering module capable of rapidly separating and combining a filtering module by mounting a pair of connecting assemblies at both end parts of the filtering module| The connecting assembly for the filtration module. KR1273573B1 (2013)
123. Y. Tayalia, S.S.G., B.I.N.P.R. Dontula, S.A.Z.U.S.U.J. Bharwada, Interconnector for filtration apparatus with reduced permeate pressure loss. US20120228208A1 (2012)
124. Y.-Z. Hou, C.N., C.N.S.-Y. Li, Reverse osmosis membrane element center pipe connector| Connector for central tube of the reverse osmosis membrane element. CN201079733Y (2008)
125. Spiral type|mold membrane module. JP04152246B2 (2008)
126. Y. Odaka, H. Matsumoto, H. Kanamori, Spiral type fluid separation element| Spiral type|mold fluid isolation|separation element. JP2009189947A (2009)
127. H. Ando, T. Katayama, Telescope prevention plate and spiral type fluid separating element| A telescope prevention plate and a spiral-type fluid isolation|separation element. JP2013208522A (2013)
128. M. Beppu, I.-s.J.P., I.-s.J.P.T. Hamada, Edge member for membrane element and membrane element equipped with same. US20120037562A1 (2012)
129. M. Beppu, J.P., J.P.T. Hamada, Edge member for film element and film element equipped with same | The end member for the film element and the film element equipped with this. KR1308837B1 (2013)
130. A. Katayama, T. Katayama, T. Seki, Fluid separation element and fluid separation apparatus | A fluid isolation|separation element and a fluid separation apparatus. JP2011152538A (2011)
131. C.J. Elwell, E.C.C.A.U.S., E.C.A.U.S.F.K. Lesan, S.A.U.V. Verbeek, S.M.C.A.U.S.P. J. Metcalfe, Radial split ring seal for filtration systems. US8728213B2 (2014)
132. F.K. Lesan, U.S., U.S.N. Kordani, Seal plate for membrane separation device| Plaque d'étanchéité pour dispositif de séparation membranaire. WO2013033616A1 (2013)
133. I. Shelby, S.D.C.A.U.S., S.D.C.A.U.S.C.R. Bartels, V.C.A.U.S.D. Dewinter, Brine seal for a filtration device. US8388842B2 (2013)
134. M. Taniguchi, J.P.J.P.T. Maeda, Separation membrane module and replacement method for separation membrane element| Module membrane de séparation et procédé de remplacement d'un élément de membrane de séparation. WO2013129283A1 (2013)
135. D.B. Weber, M.G.M.N.U.S., S.V.C.A.U.S.K.J. Knebel , Energy saving spiral element. US20090200237A1 (2009)
136. J.E. Johnson, U.S., U.S.M.D. Mittag, Spiral wound element and seal assembly | Élément en spirale et ensemble joint d'étanchéité. WO2013015971A1 (2013)
137. A. Hiro, I.J.P., I.J.P.H. Fujioka, I.J.P.A. Koumoto, Spiral reverse osmosis membrane element, method of manufacturing the same, and its use method. US8608964B2 (2013)
138. S. De La Cruz, V.C.A.U.S., Blister protection for spiral wound elements. US7303675B2 (2007)
139. M. Beppu, A spiral-type film|membrane element and its manufacturing method. JP04936435B2 (2012)

140. T. Okuno, T. Ogurisu, T. Hashimoto, Spiral pattern membrane element and its manufacturing method| A spiral type|mold film element and a method of manufacturing the same. JP2006247629A (2006)
141. K. Higashi, T. Katayama, A. Ogiwara, Spiral type fluid separation element| Spiral-type fluid isolation|separation element. JP2012176345A (2012)
142. A.O. Larson, R.M.N.U.S., E.P.M.N.U.S.S.D. Jons, L.M.I.U.S.P.I. Moody, Insertion-point seal for spiral wound module. US8142657B2 (2012)
143. H. Inoue, Spiral type membrane module. JP04704791B2 (2012)
144. K. Ishii, A spiral-type separation-membrane element and its manufacturing method. JP04485410B2 (2010)
145. D.D. Marschke, M.M.N.U.S., Reinforcement element. US20130161253A1 (2013)
146. S. Chikura, A spiral-type film|membrane element and its manufacturing method. JP05204994B2 (2013)
147. S. Chikura, I.J.P., I.J.P.K. Ishii, I.J.P.H. Matsuda, I.J.P.M. Beppu, I.J.P.H. Fujioka, I.J.P.Y. Uda, Spiral membrane element and process for producing the same. US7998348B2 (2011)
148. R.P. McCollam, R.M.N.U.S., Method for applying tape layer to outer periphery of spiral wound module. US8142588B2 (2012)
149. Q. Wang, C.N., C.N.Y. Hou, C.N.S. Li, Process for manufacturing spirally wound reverse osmosis membrane element| Procédé pour la fabrication de module membranaire d'osmose inverse spiralé. WO2014012519A1 (2014)
150. M.D. Huschke, E.P.M.N., L.E.M.N.G.W. Peterson, B.M.N.M.S. Koreltz, fluid filter assemblies with integral fluid seals. US6299772B1 (2001)
151. K. Buecher, W.D., I.D.B.U. Meyer, B.C.D.K. Noll, N.D.T. Reus, Membrane element and process for its production. US20020070158A1 (2002)
152. K. Ishii, O.J.P., O.J.P.S. Chikura, O.J.P.H. Matsuda, O.J.P.M. Beppu, O.J.P.H. Fujioka, O.J.P.Y. Uda, Spiral membrane element. US20090065426A1 (2009)
153. P.H. Knappe, S.B.C.A.U.S., V.C.A.U.S.M. Tanner, Sanitary spiral wound filtration cartridge. US8668828B2 (2014)
154. P.H. Knappe, S.B.C.A.U.S., V.C.A.U.S.D.F. Quigg, G.C.A.U.S.R.P. Magnani, Sanitary rigid shell spiral wound element. US5985146A (1999)
155. D.D. Marschke, E.P.M.N.U.S., Axial bypass sleeve. **US20130161257A1** (2013)
156. D.D. Marschke, M.M.N.U.S., C.M.N.U.S.M.J. Madsen, *Sanitary brine seal.* US20130161258A1 (2013)
157. J.H. Moon, D.K.R., D.K.R.S.K. Kim, G.-d.K.R.K.S. Park, G.-d.K.R.S.H. Ryu, Tubular molded body capable of full-wrapping membrane module and industrial filter assembly using the same. US20120223007A1 (2012)
158. T.I. Yun, Performance and economic evaluation of a 16-inch-diameter reverse osmosis membrane for surface water desalting, in *AWWA Membrane Conference* 2001
159. C., B., B.R., H.M.J., H.L., K.P., J. Lozier, M.P., P.M., , S.I, Industry consortium analysis of large reverse osmosis and nanofiltration element diameters. Desalination and Water Purification (2004)
160. Y. Hou, S.C.N., Spiral wound reverse osmosis membrane element. US8337698B2 (2012)
161. P.R. Dontula, B.I.N., S.S.G.Y. Tayalia, S.A.Z.U.S.U.J. Bharwada, System and process for treating water and spiral wound membrane element. US20130146540A1 (2013)
162. Y. Hou, S.C.N., S.C.N.Q. Wang, Reverse osmosis membrane element. US20140042080A1 (2014)
163. C.R. Bartels, U.S., U.S.C.M. Cummings, U.S.A.M. Franks, High flow high recovery spirally wound filtration element|element de filtration enroule en spirale a recuperation elevee et a haut debit. WO2000027511A1 (2000)
164. K. Shimizu, Spiral type membrane module. JP05136738B2 (2013)
165. M. Hirota, The operating method of a membrane separator.JP03900623B2 (2007)
166. Y. Nishida, S. Ishihara, Spiral separation membrane element| Spiral type|mold separation-membrane element. JP2005305324A (2005)

167. S.D. Jons, E.P.M.N.U.S., L.M.N.U.S.A.R. Marsh Iii, Spiral wound module including membrane sheet with regions having different permeabilities. US8496825B1 (2013)
168. T. Onishi, Separation membrane element|Separation-membrane element. JP2013202445A (2013)
169. A.R. Marsh, E.P.M.N.U.S., B.M.N.U.S.R. Schaffenberg, E.P.M.N.U.S.S.D. Jons, M.M.I.U. S.R.A. Davis, *Package assembly for piperazine-based membranes.* US7156997B2 (2007)
170. T. Uete, S. Goto, Spiral-type separation membrane element and production method and administration method for separation membrane module| The manufacturing method and the management method of a spiral type| Mold separation-membrane element and a separation-membrane module. JP2009119333A (2009)
171. N. Ikeyama, O.C.A.U.S.S.D.C.A.U.S.M. Wilf, Filtration devices with embedded radio frequency identification (RFID) tags. US7481917B2 (2009)
172. N. Ikeyama, O.J.P.S.D.C.A.U.S.M. Wilf, Reverse osmosis filtration devices with RFID tag-powered flow and conductivity meters. US8617397B2 (2013)
173. K. Kobayashi, O.J.P., O.J.P.T. Konishi , O.J.P.M. Kobuke, Separation membrane module and coupling member. US20140027370A1 (2014)
174. T. Konishi, O.J.P., O.J.P.K. Kobayashi, O.J.P.M. Kobuke, *Separation membrane module.* US20130334124A1 (2013)
175. T. Konishi, O.J.P., O.J.P.K. Maruyama, O.J.P.T. Kouno, O.J.P.K. Hirano, O.J.P.A. Ootani, O.J.P.H. Yoshikawa, O.J.P.N. Ikeyama, Spiral type membrane filtering device and mounting member, and membrane filtering device managing system and membrane filtering device managing method using the same. US20110114561A1 (2011)
176. B. Liberman, T.A.I.L., K.S.I.L.M. Faigon, H.I.L.Y. Pinhas, T.A.I.L.M. Ilevicky-Ozel, Z.I.L. Y. Ben-Yaish, E.H.I.L.E. Reuveni, Desalination system and elements thereof. US8480894B2 (2013)
177. G.R. Guillen, Y. Pan, M. Li, E.M.V. Hoek, Preparation and characterization of membranes formed by nonsolvent induced phase separation: a review. Ind. Eng. Chem. Res. **50**, 3798–3817 (2011)
178. J. Xu, Z.-L. Xu, Poly(vinyl chloride) (PVC) hollow fiber ultrafiltration membranes prepared from PVC/additives/solvent. J. Membr. Sci. **208**, 203–212 (2002)
179. K. Nouzaki, M. Nagata, J. Arai, Y. Idemoto, N. Koura, H. Yanagishita, H. Negishi, D. Kitamoto, T. Ikegami, K. Haraya, Preparation of polyacrylonitrile ultrafiltration membranes for wastewater treatment. Desalination **144**, 53–59 (2002)
180. Y. Lin, Y. Tang, H. Ma, J. Yang, Y. Tian, W. Ma, X. Wang, Formation of a bicontinuous structure membrane of polyvinylidene fluoride in diphenyl carbonate diluent via thermally induced phase separation. J. Appl. Polym. Sci. **114**, 1523–1528 (2009)
181. G.-L. Ji, C.-H. Du, B.-K. Zhu, Y.-Y. Xu, Preparation of Porous PVDF membrane via thermally induced phase separation with diluent mixture of DBP and DEHP. J. Appl. Polym. Sci. **105**, 1496–1502 (2007)
182. D. Vial, G. Doussau, The use of microfiltration membranes for seawater pre-treatment prior to reverse osmosis membranes. Desalination **153**(1–3), 141–147 (2003)
183. S.F.E. Boerlage, M.D. Kennedy, M.R. Dickson, D.E.Y. El-Hodali, J.C. Schippers, The modified fouling index using ultrafiltration membranes (MFI-UF): characterisation, filtration mechanisms and proposed reference membrane. J. Membr. Sci. **197**(1–2), 1–21 (2002)
184. J. Lowe, M.M. Hossain, Application of ultrafiltration membranes for removal of humic acid from drinking water. Desalination **218**(1–3), 343–354 (2008)
185. C.A. Smolders, A.J. Reuvers, R.M. Boom, I.M. Wienk, Microstructures in phase-inversion membranes. Part 1. Formation of macrovoids. J. Membr. Sci. **73**, 259–275 (1992)
186. S.A. McKelvey, W.J. Koros, Phase separation, vitrification, and the manifestation of macrovoids in polymeric asymmetric membranes. J. Membr. Sci. **112**, 29–39 (1996)
187. S. Mal, A. Nandi, Gelation mechanism of thermoreversible Poly(vinylidene fluoride) gels in glyceryl tributyrate. Polymer **30**, 6301–6307 (1998)
188. S. Mal, P. Maiti, A. Nandi, On the gelation rates of thermoreversible Poly(vinylidene fluoride) gels. Macromolecules **28**, 2371–2376 (1995)

189. A. Akthakul, W.F. McDonald, A.M. Mayes, Noncircular pores on the surface of asymmetric polymer membranes: evidence of pore formation via spinodal demixing. J. Membr. Sci. **208**, 147–155 (2002)
190. M. Cheryan, *Ultrafiltration Handbook* (Technomic Publishing Co. Inc, Lancaster, 1986)
191. M.D. Kennedy, J. Kamanyi, S.G.S. Rodríguez, N.H. Lee, J.C. Schippers, G. Amy, Water treatment by microfiltration and ultrafiltration, in *Advanced Membrane Technology and Applications* (Wiley, New York, 2008), pp. 131–170
192. N. Kubota, T. Hashimoto, Y. Mori, *Microfiltration and Ultrafiltration*, in *Advanced Membrane Technology and Applications* (Wiley, New York, 2008), pp. 101–129
193. L.J. Zeman, A.L. Zydney, *Microfiltration and Ultrafiltration: Principles and Applications* (Marcel Dekker, Inc, New York, 1996)
194. Z.F. Cui, S. Chang, A.G. Fane, The use of gas bubbling to enhance membrane processes. J. Membr. Sci. **221**(1–2), 1–35 (2003)
195. R. Ghosh, Enhancement of membrane permeability by gas-sparging in submerged hollow fibre ultrafiltration of macromolecular solutions: role of module design. J. Membr. Sci. **274** (1–2), 73–82 (2006)
196. A.G. Fane, C.J.D. Fell, A review of fouling and fouling control in ultrafiltration. Desalination **62**, 117–136 (1987)
197. W. Gao, H. Liang, J. Ma, M. Han, Z.-L. Chen, Z.-S. Han, G.-B. Li, Membrane fouling control in ultrafiltration technology for drinking water production: a review. Desalination **272** (1–3), 1–8 (2011)
198. N. Hilal, O.O. Ogunbiyi, N.J. Miles, R. Nigmatullin, Methods employed for control of fouling in MF and UF membranes: a comprehensive review. Sep. Sci. Technol. **40**(10), 1957–2005 (2005)
199. S.S. Sablani, M.F.A. Goosen, R. Al-Belushi, M. Wilf, Concentration polarization in ultrafiltration and reverse osmosis: a critical review. Desalination **141**(3), 269–289 (2001)
200. H.M. Yeh, H.P. Wu, J.F. Dong, Effects of design and operating parameters on the declination of permeate flux for membrane ultrafiltration along hollow-fiber modules. J. Membr. Sci. **213** (1–2), 33–44 (2003)
201. S. Chang, A.G. Fane, The effect of fibre diameter on filtration and flux distribution—relevance to submerged hollow fibre modules. J. Membr. Sci. **184**(2), 221–231 (2001)
202. S. Yoon, H. Kim, I. Yeom, Optimization model of submerged hollow fiber membrane modules. J. Membr. Sci. **234**(1–2), 147–156 (2004)
203. S.T. Burr, M.M.I.U.S., M.M.I.U.S.M.D. Mittag, L.M.I.U.S.M.J. Turpin, W.M.I.U.S.D.D. Vogel, Fluid filter module including handle. US8261919B2 (2012)
204. S.T. Burr, M.M.I.U.S., M.M.N.U.S.M.J. Hallan, M.M.I.U.S.M.D. Mittag, L.M.I.U.S.M. J. Turpin, W.M.I.U.S.G.D. Vogel, Fluid filter module including sealed boss. US8173018B2 (2012)
205. F. Liu, N.A. Hashim, Y. Lui, M.R.M. Abed, K. Lin, Progress in the production and modification of PVDF membranes. J. Membr. Sci. **375**, 1–27 (2011)
206. C. Serra, M.J. Clifton, P. Moulin, J.-C. Rouch, P. Aptel, Dead-end ultrafiltration in hollow fiber modules: module design and process simulation. J. Membr. Sci. **145**(2), 159–172 (1998)
207. K. Gethard, O. Sae-Khow, S. Mitra, Water desalination using carbon-nanotube-enhanced membrane distillation. ACS Appl. Mater. Interfaces **3**(2), 110–114 (2011)
208. W.-F. Chan, H.-Y. Chen, A. Surapathi, M.G. Taylor, X. Shao, E. Marand, J.K. Johnson, Zwitterion functionalized carbon nanotube/polyamide nanocomposite membranes for water desalination. ACS Nano **7**(6), 5308–5319 (2013)
209. P.S. Goh, A.F. Ismail, B.C. Ng, Carbon nanotubes for desalination: performance evaluation and current hurdles. Desalination **308**, 2–14 (2013)
210. A.T. Nasrabadi, M. Foroutan, Ion-separation and water-purification using single-walled carbon nanotube electrodes. Desalination **277**(1–3), 236–243 (2011)
211. D. Konatham, J. Yu, T.A. Ho, A. Striolo, Simulation insights for graphene-based water desalination membranes. Langmuir **29**(38), 11884–11897 (2013)

212. E.N. Wang, R. Karnik, Water desalination: graphene cleans up water. Nat Nano **7**(9), 552–554 (2012)
213. M.A. Shannon, P.W. Bohn, M. Elimelech, J.G. Georgiadis, B.J. Marinas, A.M. Mayes, Science and technology for water purification in the coming decades. Nature **452**(7185), 301–310 (2008)
214. X. Li, R. Wang, F. Wicaksana, C. Tang, J. Torres, A.G. Fane, Preparation of high performance nanofiltration (NF) membranes incorporated with aquaporin Z. J. Membr. Sci. **450**, 181–188 (2014)
215. H.L. Wang, T.-S. Chung, Y.W. Tong, K. Jeyaseelan, A. Armugam, H.H.P. Duong, F. Fu, H. Seah, J. Yang, M. Hong, Mechanically robust and highly permeable Aquaporin Z biomimetic membranes. J. Membr. Sci. **434**, 130–136 (2013)
216. Y. Zhao, C. Qiu, X. Li, A. Vararattanavech, W. Shen, J. Torres, C. Helix-Nielsen, R. Wang, X. Hu, A.G. Fane, C.Y. Tang, Synthesis of robust and high-performance aquaporin-based biomimetic membranes by interfacial polymerization-membrane preparation and RO performance characterization. J. Membr. Sci. **423–424**, 422–428 (2012)
217. M. Kumar, W. Meier, J. Zilles, Aquaporin based triblock copolymer membranes for water purification. Polym. Prepr. (Am. Chem. Soc., Div. Polym. Chem.) **52**(2), 1060–1061 (2011)
218. W. Choi, J. Choi, J. Bang, J.-H. Lee, Layer-by-layer assembly of graphene oxide nanosheets on polyamide membranes for durable reverse-osmosis applications. ACS Appl. Mater. Interfaces **5**(23), 12510–12519 (2013)
219. A.K. Mishra, S. Ramaprabhu, Functionalized graphene sheets for arsenic removal and desalination of sea water. Desalination **282**, 39–45 (2011)
220. J.-G. Gai, X.-L. Gong, W.-W. Wang, X. Zhang, W.-L. Kang, An ultrafast water transport forward osmosis membrane: porous graphene. J. Mater. Chem. A **2**(11), 4023–4028 (2014)
221. D. Cohen-Tanugi, J.C. Grossman, Water desalination across nanoporous graphene. Nano Lett. **12**(7), 3602–3608 (2012)
222. E.N. Wang, R. Karnik, Water desalination: graphene cleans up water. Nat. Nanotechnol. **7**(9), 552–554 (2012)
223. S.A. Avlonitis, K. Kouroumbas, N. Vlachakis, Energy consumption and membrane replacement cost for seawater RO desalination plants. Desalination **157**(1–3), 151–158 (2003)
224. G.-D. Kang, Y.-M. Cao, Development of antifouling reverse osmosis membranes for water treatment: a review. Water Res. **46**(3), 584–600 (2012)
225. S. Lee, J. Cho, M. Elimelech, Influence of colloidal fouling and feed water recovery on salt rejection of RO and NF membranes. Desalination **160**(1), 1–12 (2004)
226. D.C. Sioutopoulos, A.J. Karabelas, Correlation of organic fouling resistances in RO and UF membrane filtration under constant flux and constant pressure. J. Membr. Sci. **407–408**, 34–46 (2012)

Chapter 9
American Process: Production of Low Cost Nanocellulose for Renewable, Advanced Materials Applications

Kim Nelson, Theodora Retsina, Mikhail Iakovlev, Adriaan van Heiningen, Yulin Deng, Jo Anne Shatkin and Arie Mulyadi

Abstract Nanocellulose has proven to be a versatile material with a vast array of potential commercial applications including composites and foams for automotive, aerospace, and building construction, viscosity modifiers for cosmetics and oil drilling fluids, and high performance fillers for paper, packaging, paints, plastics, and cement. In addition to material performance properties like gelation, shear thinning, exceptionally high strength, and light weight, nanocellulose has a strong sustainability profile. Being made from biomass, it is renewable, biodegradable, compostable, and designed for the environment with a sustainable life cycle carbon footprint. American Process Inc.'s (API's) American Value Added Pulping (AVAP)® technology offers commercial-scale production of nanocellulose with flexibility in final product morphology (rod shaped nanocrystals and fiber shaped nanofibrils) and surface properties (hydrophilic or hydrophobic) to service the wide variety of emerging end-use market segments. The novel hydrophobic lignin-coated variety of AVAP nanocellulose can be incorporated into plastics. This achievement overcomes a well-known barrier to commercial utilization of nanocellulose. AVAP nanocellulose will also be low cost, with commercial selling prices anticipated to be comparable to competing petroleum-based polymers.

9.1 About American Process Inc.

American Process Inc. (API) focuses on pioneering renewable materials, fuels and chemicals from biomass and develops proprietary technologies and strategic alliances in this field to be scaled industrially throughout the world. The company was founded by Theodora Retsina in 1995, initially as an engineering consulting company specializing in energy use optimization for the forest products industry.

K. Nelson (✉) · T. Retsina · M. Iakovlev · A. van Heiningen · Y. Deng · J.A. Shatkin · A. Mulyadi
American Process Inc., 750 Piedmont Ave. NE, Atlanta, GA 30308, USA
e-mail: knelson@americanprocess.com

L.D. Madsen and E.B. Svedberg (eds.), *Materials Research for Manufacturing*, Springer Series in Materials Science 224,
DOI 10.1007/978-3-319-23419-9_9

Since then, API has completed over 500 energy integration and water reuse studies within the industry and identified annual energy savings opportunities of billions of dollars. API has worked with Pinch technology, a methodology for minimizing energy consumption of chemical processes by calculating thermodynamically feasible energy targets (or minimum energy consumption) and achieving them by optimizing heat recovery systems, energy supply methods and process operating conditions. API boasts the world's largest experience list for the application of Pinch technology to industry. In 2005, API began developing technologies for the conversion of biomass into cellulosic sugars to be used in the production of biofuels and biobased chemicals. American Process owns two distinct patented cellulosic technologies, Green Power+® and American Value Added Pulping (AVAP®) and operates demonstration plants for each within the US. The Green Power+technology is demonstrated at the "Alpena Biorefinery" in Alpena, MI which can produce up to 1 million gallons per year of cellulosic ethanol along with a low carbon footprint, biobased potassium acetate deicer co-product. In April 2014, the Alpena Biorefinery sold the nation's first commercial quantities of cellulosic ethanol generated from woody biomass under the Environmental Protection Agency's Renewable Fuels Standard (RFS) program. Under the Energy Independence and Security Act of 2007 (EISA), the RFS program requires renewable fuel to be blended into transportation fuel in increasing amounts each year, where each renewable fuel must emit lower levels of greenhouse gases relative to the petroleum fuel it replaces. The Alpena Biorefinery was partially funded with a $22 million grant from the Department of Energy and a $4 million grant from the State of Michigan. API's AVAP technology is demonstrated at the "AVAP Biorefinery" in Thomaston, GA. The AVAP Biorefinery produces specialty cellulose products for advanced materials applications and exceptionally pure lignocellulosic sugars for on or off-site conversion into biobased fuels and chemicals. The plant can process three tons of biomass feedstock (dry basis) per day. Beginning in 2012, API has developed an innovative process based on the AVAP technology to produce commercially scalable, low cost nanocellulose. Nanocellulose is a material composed of high-strength nanosized cellulose crystalline rods known as cellulose nanocrystals (CNC) or longer crystalline and amorphous cellulose nanofibrils (CNF). API's nanocellulose has flexibility in final product morphology and surface properties (hydrophilic or hydrophobic) that can service the wide variety of emerging end-use market segments, including composites and foams for automotive, aerospace, and building construction, viscosity modifiers for cosmetics and oil drilling fluids, and high performance fillers for paper, packaging, paints, plastics, and cement. In addition to material performance properties like gelation, shear thinning, exceptionally high strength, and light weight, nanocellulose has a strong sustainability profile. Being made from biomass, it is renewable, biodegradable, compostable, and designed for the environment with a sustainable life cycle carbon footprint.

API's nanocellulose process and products are protected by granted patents (such as U.S. Patent Nos. 8,030,039, 8,038,842, 8,268,125, 8,585,863, and 8,685,167) and pending patents (such as U.S. Patent App. Pub. Nos. 2014/0154756, 2014/0154757, and 2014/0155301 and patent cooperation treaty (PCT) publications

WO 2014/085729 and WO 2014/085730) as well as proprietary know-how and trade secrets. In total, API has over 15 issued patents and over 130 patents pending in the biorefinery field. API is currently installing a nanocellulose pilot line at the AVAP Biorefinery for production of the full range of AVAP nanocellulose products by the second quarter of 2015. API has a research and development group composed of engineers and materials scientists that are dedicated to advancing nanocellulose processing and products. The company also partners internationally with industry, academia, and government for nano-scale characterization and development of commercial applications. University and government partners include the US Department of Agriculture's Forest Products Laboratory, the National Institute of Standards and Technology, Georgia Institute of Technology, the Renewable Bioproducts Institute, Clark Atlanta University, University of Maine, University of Alberta and Swinburne University. API's in-house expertise includes technology, product, and process development, engineering, procurement, plant installation, construction, operations, scale-up and commercialization.

In April 2013, the Brazilian company, GranBio, became a shareholder in API. GranBio is a 100% Brazilian-owned company, founded in June of 2011, and is known as an industrial pioneer in biomaterials, biofuels and biochemicals. The Brazilian National Development Bank (BNDESpar) is one of its shareholders.

9.2 About Nanocellulose

Cellulose $(C_6H_{10}O_5)_n$ is a polysaccharide consisting of a linear chain of several hundred to many thousands of D-glucose units. Cellulose is the most abundant natural organic compound on Earth, comprising at least one-third of all vegetable matter. It is tasteless, odorless, hydrophilic, insoluble in water and most organic solvents, and biodegradable. It's also renewable, non-toxic, carbon neutral, and exceptionally strong. The microfibrils in biomass have high tensile strength that support the cell walls. The microfibrils are composed of cellulose chains held firmly together in a side-by-side arrangement as multiple hydroxyl groups on glucose from one cellulose chain form hydrogen bonds with oxygen atoms on the same or on neighboring cellulose chains. As shown in Fig. 9.1, microfibrils can be broken down into smaller nano-scale particles including cellulose nanofibrils (CNF) and cellulose nanocrystals (CNC). CNF and CNC can be extracted from biomass and utilized with existing technologies to create renewable-based materials that may compete in performance and price with petroleum-derived plastics and metals in various applications. CNCs are rod-shaped particles (3–5 nm wide, 50–500 nm in length) and highly crystalline. CNFs have a longer structure (5–50 nm wide, 500 to several microns in length) and contain both amorphous and crystalline regions.

Figure 9.2 shows that CNF and CNC have lengths similar in size to viruses and bacteria, respectively.

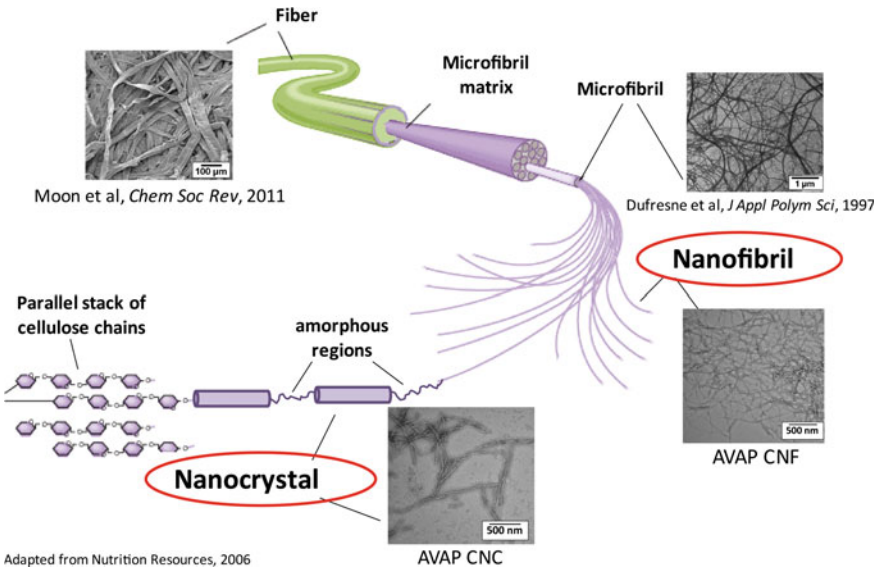

Fig. 9.1 Hierarchal structures in biomass

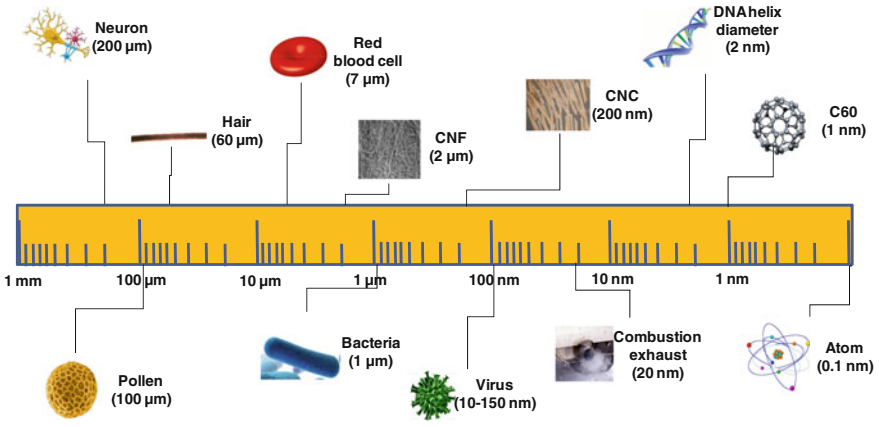

Fig. 9.2 Relative sizes of cellulose nanofibrils and nanocrystals

CNCs have high axial stiffness ($\sim$150 GPa), high tensile strength (estimated at 7.5 GPa), low coefficient of thermal expansion ($\sim$1 ppm/K), thermal stability up to $\sim$300 °C, high aspect ratio (10–100), low density ($\sim$1.6 g/cm^3), lyotropic liquid crystalline behavior, and shear thinning rheology in aqueous suspensions. The exposed –OH groups on CNC surfaces can be readily modified to achieve different surface properties and have been used to adjust CNC self-assembly and dispersion for a wide range of suspensions and matrix polymers and to control interfacial

properties in composites. This unique set of characteristics results in new capabilities compared to more traditional cellulose based particles (pulp fibers, etc.) and the development of new composites that can take advantage of CNCs' enhanced mechanical properties, low defects, high surface area to volume ratio, and engineered surface chemistries [1].

CNFs have unique properties such as high aspect ratio (100–150), large specific surface area (100–200 g/m^2), high strength and stiffness, good elastic properties, tendency for gel formation at low consistency, and shear thinning behavior. Potential applications include strength enhancement additives in packages and lightweight composites, rheology modifiers in coatings, paints, food, cosmetics barrier materials in food contact materials, and as porous and absorbent materials for various purposes [2].

9.3 Nanocellulose Commercial Applications

With its versatility, low toxicity, carbon-neutrality, biodegradability, and abundancy (with an annual production in the biosphere of about 90 billion tons) cellulose is gaining significant global interest for the production of advanced materials, biofuels, and biochemicals. Increased concern about the environment and a consumer and market push for greater sustainability in the use of products and services are making the development and use of renewable materials and products one of the central priorities of this and coming decades. Resource constraints are driving a push toward bio-based products. Increased recognition of global climate change and its effects is behind a shift toward greater carbon neutrality associated with human economic endeavors, including manufacturing, transportation, and energy generation. In particular, concerns about the impacts of plastics and their additives have led to a search for safe and more sustainable alternatives. The use of woody biomass material contributes to a lower carbon economy because trees absorb carbon dioxide and become sinks for carbon. Managed forests, one of the largest sustainably-managed biomass sources in the United States, can reduce U.S. greenhouse gas emissions and foreign fossil fuel dependency by conversion of forest materials into novel materials and products [3].

A global research effort has shown that nanocellulose in particular can displace petroleum-based packaging, metallic components, and other non-renewable materials. For example, cellulosic nanomaterials have strong promise for use as reinforcements in polymer matrix composites due to their light weight, high tensile strength and modulus, and comparably low cost. As shown in Fig. 9.3, CNC potentially offers the lowest cost for specific strength and stiffness when compared to common polymer reinforcement materials [4]. Recent nanocellulose manufacturing advances by American Process Inc. have significantly lowered the production cost such that both CNF and CNC are anticipated to be cost competitive with petroleum based polymers and polymer additives.

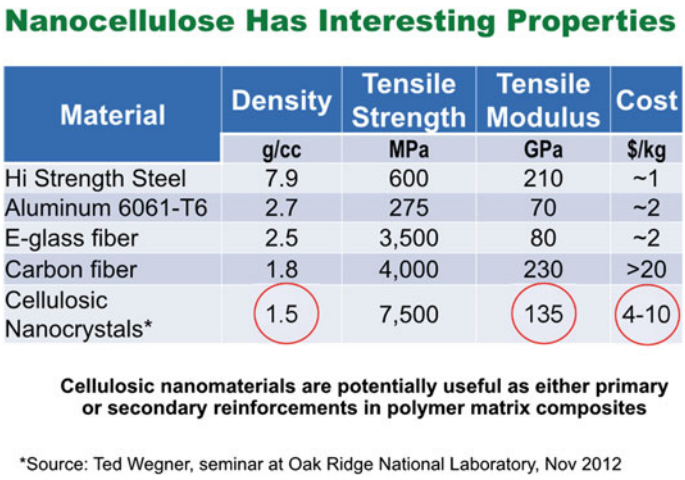

Fig. 9.3 Comparison between cellulose nanocrystals and common polymer reinforcement materials

A recent exploration of potential applications for nanocellulose funded by the United State's Department of Agriculture's (USDA's) Forest Service estimated nanocellulose to have an annual U.S. market potential volume of 6.4 million metric tons and an estimated global market potential of 35 million metric tons [5]. As shown in Table 9.1, the applications identified as having the largest potential volume for nanocellulose include paper and paper packaging, textiles, cement, automotive polymer composite components, and hygiene and absorbent products like diapers. Smaller volume applications include rheology modifiers, cosmetics, construction materials, aerospace applications, pharmaceuticals, and paint additives. In the future, additive manufacturing (3D printing) may become a large volume user of cellulose nanomaterials for toys, architectural models, automobile parts, etc. Researchers at the US Department of Energy's (DOE's) Oak Ridge National Laboratory are currently evaluating nanocellulose as a 3D printing substrate.

API envisions the commercialization timeline for nanocellulose products to be similar to that of plastics. One hundred years after the development of the first fully synthetic plastic in 1907, plastics impact every aspect of our lives. Similarly, we expect nanocellulose materials to be fully integrated into society and commerce within one hundred years of the first nanocellulose gel developed in 1977. Figure 9.4 provides our estimated global production curve for nanocellulose assuming growth rates by decade to be similar to that of plastics [6]. This curve predicts that the USDA's global market size estimate for nanocellulose will be achieved around 2045. Commercial sustainability drivers and global environmental concerns may accelerate the production timeline beyond our conservative estimate.

Table 9.1 Potential markets for nanocellulose

High volume applicatIONS	Low volume applications	Novel and emerging applications
Automotive body	Aerospace interiors	Sensors—medical, environmental, industrial
Automotive interior	Aerogels for the oil and gas industry	Reinforcement fiber—construction
Cement	Aerospace structure	Water filtration
Hygiene and absorbent products	Insulation	Air filtration
Packaging coatings	Paint-architectural	Viscosity modifiers-miscellaneous
Packaging filler	Paint-OEM applications	Purification
Paper coatings	Paint-special purpose	Cosmetics
Paper filler	Wallboard facing	Excipients
Plastic film replacement		Organic LED
Replacement-plastic packaging		Flexible electronics
Textiles for clothing		Photovoltaics
		Recyclable electronics
		3D printing
		Photonic films

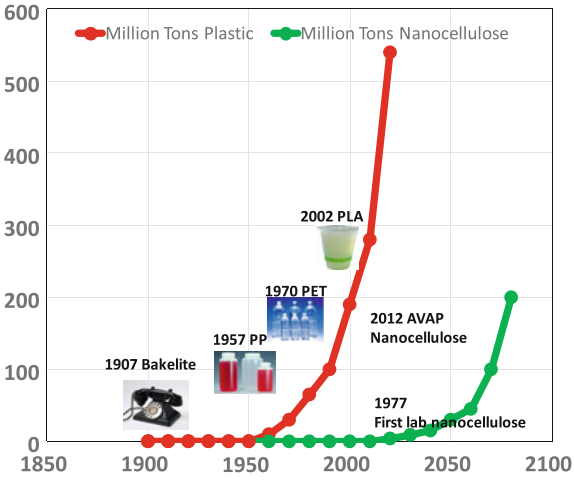

Fig. 9.4 Estimated nanocellulose global production curve

9.3.1 Nanocellulose Polymer Composites

The relatively low cost of cellulose nanomaterials creates an opportunity to use them as reinforcing fibers in composite materials with wide scale structural applications [7]. One auto manufacturer indicated it could create so many components

out of such materials—from body panels to interior trim—that it could shave 340 kg off the weight of its cars [8]. The demand for lightweight composite materials in vehicles is driven by fuel efficiency standards for vehicles. In the near term, adoption will most likely be in applications already using composite materials, while steel replacement is an additional, longer term potential application. Others are investigating the use of nanocellulose based polymers for fire retardant coatings [9].

Such applications include reinforcing (bio-) polymers to create promising, environmentally safe, lightweight construction materials for the car industry. CNC improves the prospects for using bio-plastics in interior automotive parts [10].

Although the mechanical properties of nanocellulose vary depending on the average molecular weight, chemical and thermal treatment, tensile strengths in the range of 80–240 MPa with 3–15 GPa elastic modulus and 3–20% strain-to-failure has been reported for neat nanocellulose films [11–14], as shown in Fig. 9.5 [13]. In addition, the crystalline region of nanocellulose is predicted to have a tensile strength and modulus in the range of 7.5–7.7 and 78–220 GPa [13, 15, 16], respectively.

As a filler reinforcement material, nanocellulose has shown to improve the overall mechanical properties of various hydrophilic polymeric matrices. Using a solution casting method, addition of 10 wt% CNF to a chitosan nanocomposite showed an increase in tensile strength and modulus of 20 and 25%, respectively [17]. Similarly, a 25% increase in strength and 18% increase in modulus were found when only 1 wt% of CNF was used in poly(ethylene oxide) matrices [18]. Poly(vinyl alcohol) reinforced with 6.6 wt% of CNF was also demonstrated to enhance tensile strength and modulus by 140% using the electrospinning process [19].

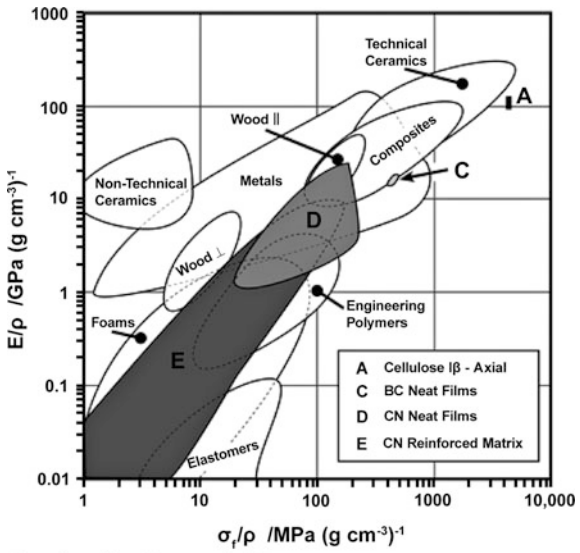

Reproduced from Moon et. al., 2011

Fig. 9.5 Ashby plot of specific modulus (E/ρ) and specific strength (σf/ρ) for various materials

Incompatibility between the hydrophilic surface of nanocellulose and hydrophobic polymers has historically limited the performance of nanocellulose in a wide variety of polymers. Polycaprolactone (PCL) film reinforced CNF is an example that showed a decrease in tensile strength of 25 MPa as a neat PCL film to approximately 13–17 MPa after addition of 3 wt% nanocellulose [20, 21]. The hydroxyl groups on the surface of nanocellulose create high surface energy leading to insufficient wetting and weak interfacial adhesion with hydrophobic polymers [22–24]. Weak interfacial adhesion between CNF and a polymer matrix gives less effective stress transfer leading to low nanocomposite strength [25]. As discussed below, advances by API in creating hydrophobic, lignin-coated CNC and CNF appear to have overcome this well-known grand challenge.

9.3.2 Nanocellulose Concrete Composites

Studies have shown that the high aspect ratio of nanocellulose may facilitate an increase in fracture toughness for cement composites. Preliminary results showed enhancement of fracture energy by up to 50% with the addition of 3 wt% of a mixture of cellulose micro- and nanofibers [26]. Recent work also demonstrated that an additional 20% flexural strength relative to the unreinforced cement paste could be achieved using 0.2 vol.% CNC [27]. The nanoscale fibers appear to fill small pores within concrete, thereby increasing its toughness and flexibility. Utilization of nanocellulose as a high-performance cement filler may reduce the volume of cement needed for a project, thereby lowering material and labor costs, and bringing the added benefit of reduction in associated greenhouse gas emissions.

9.3.3 Nanocellulose Aerogels

Aerogels are extremely low density solid materials with a highly porous surface area composed of up to 99.98% air by volume. As a result of good dimensional stability and mechanical properties, Nanocellulose-based aerogels have been considered for packaging applications to substitute polystyrene-based foam and thermal insulation. There is also strong interest in using nanocellulose-based aerogels as porous templates for advanced materials, because of specific properties like water absorbency, selective separation of oils and organic solvents, CO_2 capture, heavy metal removal, and electrical conductivity. Superior water absorbency of 104 g water per g of dried mass with reusability for at least 20 times has been demonstrated for TEMPO-oxidized CNF aerogels [28]. In recent works, selective separation of oils and organic solvents such as dodecane from contaminated water can be effectively achieved using silane modified nanocellulose aerogels [29–31] or titanium dioxide modified nanocellulose aerogels [32]. Similarly, using aminosilane treatment, modified CNF aerogels have been developed for the capture of carbon

dioxide from air [33]. Rapid and effective removal of hexavalent chromium has also been developed using CNF aerogels functionalized with quaternary ammonium [34]. Controlled drug delivery was reported using nanocellulose aerogels from CNF and bacterial cellulose, as carriers [35]. Both CNF and bacterial cellulose aerogels have also been engineered to achieve flexible and highly conductive material for electronic products [36, 37].

Aerogels also offer advantages for insulation materials. Recent advancements have been made towards creating cheaper, thinner, more breathable insulating materials with higher R-values [38]. This novel material has the lowest bulk density of any known porous solid, as well as significant insulating qualities. Cellulose nanomaterials can create insulating materials using little material and low energy inputs, offering advantages in the fast growing green building sector [5].

Aergoels prepared from 2,2,6,6-tetramethylpiperidine-1-oxyl radical (TEMPO) cellulose nanofibrils (discussed in more detail below) gave low densities in the range of 0.01–0.26 g cm^{-3} with surface areas up to 485 m^2 g^{-1} [13]. High Brunauer–Emmett–Teller (BET) surface areas have also been reported for CNC aerogels with densities in the range of 0.078–0.155 g cm^{-3} [13]. Specific surface areas as high as 605 m^2 g^{-1} and a density of 0.078 g cm^{-3} have been achieved with CNC using supercritical CO_2 drying [39].

9.3.4 Nanocellulose Barrier Films and Packaging

Neat nanocellulose films have been demonstrated to have high water vapor absorption with low oxygen permeability [13, 40]. Several factors, such as the type of nanocellulose, degree of crystallinity, film entanglement and porosity, as well as physical and chemical treatment, play a major role in determining water vapor transmittance rate (WVRT) and oxygen transfer rate (OTR) [40]. As shown in Fig. 9.6, OTR values in the range of 4–18 mL m^{-2} day^{-1} have been reported for nanocellulose [40, 41]. Given that the recommended OTR value for modified atmosphere packaging (i.e. food storage and distribution) is in the range of less than 10–20 mL m^{-2} day^{-1} [40, 42], nanocellulose films show promise for use in oxygen barrier applications within the packaging industry.

In addition to superior oxygen barrier properties, preliminary work indicates that the dense structure of nanocellulose films has certain oil resistance capabilities [43]. CNF-coated paper reduces ink absorption levels into paper as CNF acts as an inkjet pigment binder at the surface [44]. In another work, reinforcing poly(vinyl alcohol) with carboxylated CNC shows an improvement in trichloroethylene resistance [13].

Nanocellulose films may also offer novel alternative filtration technologies. They have also been shown to have barrier properties that control the permeability of other gases, solvents, and charged species. Preliminary results suggest that the membrane performance of CNF films for organic solvent filtration can be tailored by simply controlling the concentration and dimensions of nanofibrils [45]. TEMPO-oxidized CNF films also have excellent hydrogen gas permeation selectivity [46], while films

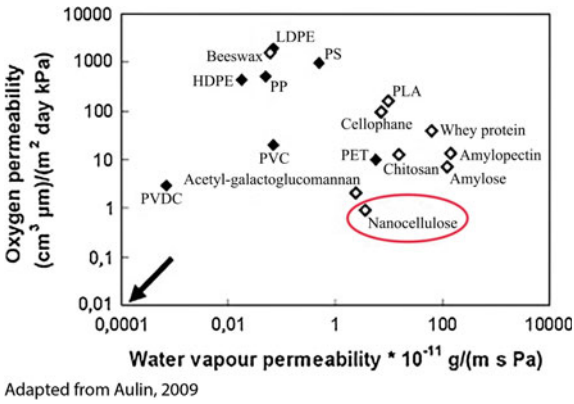

Fig. 9.6 Oxygen and water vapor permeability of various materials

formed using negatively charged CNC are shown to exclusively adsorb positively charged species [47].

9.3.5 Nanocellulose Viscosity Modifiers

Nanocellulose suspensions form thixotropic, or shear thinning, gels [48, 49] that can be used as thickeners and suspension stabilizers for both solid and oil-water emulsions [48–51]. Nanocellulose has been tested as a rheology modifier in food products, cosmetics, paints, aircraft anti-icing fluid and oil recovery [49, 52]. In food products, the addition of flavoring ingredients for salad dressing into 2 wt% CNF suspensions in water showed a stable suspension for more than 6 months [48, 49]. For oil recovery, fracturing fluids from CNF suspensions were shown to generate a stable suspension of 10 wt% fine sand in 2 wt% CNF at elevated temperature of 100 °C for 3 months [48, 49]. The water solubility of nanocellulose allows easy addition for modifying the viscosity of water-based paints and coatings, [49, 53] and has been demonstrated to improve the durability of water-based polyurethane varnishes and paints, reportedly improving finish durability, and protecting paints and varnishes from wear caused by UV radiation [54].

9.4 Nanocellulose Manufacturing Challenge: Production Cost

While cellulose nanocrystals and nanofibrils have strong commercial promise, their commercialization has been limited to date due to material availability and estimated commercial sales price. As discussed below, start-up of API's 0.5 ton per day (dry basis) nanocellulose production line in the first quarter of 2015 at our existing Biorefinery in Thomaston, Georgia will overcome these challenges.

9.4.1 Conventional Cellulose Nanocrystals Production

While CNC has been produced in lab quantities since the 1950s, it first became commercially available in 2012 when CelluForce started up a 1 ton per day demonstration plant in Windsor, Québec. However, as of September 2014, the plant has been idle [55]. In March 2015, CelluForce announced an investment into the company by Schlumberger, the world's leading supplier of technology, integrated project management and information solutions for the global oil and gas industry. Otherwise, CNCs are produced at pilot scale at the U.S. Forest Service's Nanocellulose Facility located at the Forest Products Laboratory (FPL) in Madison, Wisconsin. The pilot plant started in 2012 and can produce up to 50 kg CNC aqueous suspension per week as a 5–10% solids suspension.

The preparation of CNCs from biomass generally occurs in two primary stages. The first stage is a purification of the biomass to remove most of the non-cellulose components in the biomass such as lignin, hemicelluloses, extractives, and inorganic contaminants. This is typically done by conventional pulping and bleaching. The second stage uses an acid hydrolysis process to deconstruct the "purified" cellulose material into its crystalline components. This is accomplished by removing the amorphous regions of the cellulose microfibrils. The resulting rod-shaped particles (3–20 nm wide, 50–2000 nm long) are ~100% cellulose, and are highly crystalline (62–90%, depending on cellulose source material and measurement method). The variations in CNC characteristics (e.g., particle morphology, surface chemistry, percent crystallinity, etc.) are strongly linked to the cellulose source material and the acid hydrolysis processing conditions [1].

FPL's CNC production process is based on the nonproprietary concentrated sulfuric acid hydrolysis method published by Grey et al. [56]. Typically, machine-dried prehydrolysis Kraft rayon-grade dissolving wood pulp is shredded, placed under nitrogen atmosphere, and heated to 45 °C. Sulfuric acid (64 wt%) at 45 °C is sprayed over the top of the shredded pulp strips and the mixture is stirred at 45 °C for 90 min. The reaction is quenched by diluting ~10-fold with water and hypochlorite solution (household Clorox) is added to remove color formed during the reaction. The use of dissolving pulp as a starting material gives less color than with bleached Kraft pulp. The CNC suspension is then neutralized by slow addition of 5–8% wt% NaOH, diluted ~4-fold, and allowed to settle. The salt/sugar solution is then decanted from the solids, which are diluted a second time. At this point, the sodium sulfate concentration drops to about 1 wt% and the CNC particles begin to disperse in the solution. The CNC is then circulated through a tubular ultrafiltration membrane system where the salt/sugar solution passes through the membrane and the CNCs are retained. Reverse osmosis water (RO) is added as needed to maintain the CNC concentration to 1 wt%. Diafiltration is continued until the residual salt concentration is reduced to about 8 μM (requiring about 24 h and 20,000L RO dilution water). The colloidal CNC suspension is filtered using a 20 μm cartridge-style filter to remove dirt and concentrated to at least 5 wt% solids using the tubular ultrafiltration system. The cellulose yield is about 50% based on the

starting bleached pulp. Each bath of CNC requires about 8 h for CNC reaction and neutralization, 24–48 h for settling and initial purification, and 24 h membrane filtration for final salt removal. Current production is 25 kg per batch, with up to two batches per week [57]. One advantage of this process is that it is based on a well-known laboratory method whose CNCs are used as standards throughout the world. Disadvantages of the process include long processing/batch cycle times, high chemical costs due to the high sulfuric acid charge that is not recycled, and large water consumption. The Technical Association of the Pulp and Paper Industry (TAPPI) Nanocellulose Division estimates the commercial sales price of CNC produced from this method to be $10–50/lb.

9.4.2 Conventional Cellulose Nanofibrils Production

While production of CNF gels was first demonstrated in the lab using a milk homogenizer by ITT Rayonier in 1977, today the University of Maine if the only known producer of commercial quantities of mechanically-derived CNF. Their Cellulose Nanofiber Pilot Plant is capable of producing up to one ton per day (dry basis) CNF. Several other small scale CNF pilot plants with capacities of several hundred lbs. per day are operated throughout the world by Nippon Paper (Japan), Borregaard (Norway), Innventia (Sweden), Namicell (France) and Oji Paper (Japan).

CNF is generally manufactured by mechanical treatment using a refiner, grinder, homogenizer, or fluidizer. The resulting material consists of fibrils of many different sizes with the width of the smaller fibrils or aggregates being around 20–40 nm, while their length can be several μm. The fibrils are highly branched and flexible. The high energy consumption of mechanical treatments may be reduced with different chemical or enzymatic pretreatments that facilitate the fibrillation of fibers during mechanical treatment. Several different pretreatments for obtaining cellulose nanofibrils have been published including mild enzyme pretreatment using endogluconase, carboxy-methylation, and TEMPO (2,2,6,6-tetramethylpiperidine-1-oxly radial) mediated oxidation [2]. Particularly in Japan there has been considerable exploration of applications with CNF that has been modified by TEMPO-oxidation. TEMPO is a tetramethyl-piperidine compound that is used as a catalyst in oxidizing cellulose microfibrils which introduces carboxyl groups on the surface of the fibrils. CNF produced by the TEMPO process can be quite uniform, with a diameter as small as 4 nm.

The University of Maine's CNF pilot plant was funded through a joint venture with the USDA's Forest Service. Typically, machine-dried Northern Bleached Softwood Kraft pulp is blended with water to 3 wt% solids before sending to a mechanical disc refiner. The pulp is refined using a series of progressively finer plates until a nanofibril gel is formed and the target particle size range is reached. This series of specific mechanical treatments significantly lowers the energy required to produce the nanofibrillated cellulose ($\sim$2,000 kWhr/MT) compared to

prior art mechanical methods like homogenizers and grinders. Refining is carried out with recirculation to provide nominally 30 passes through the refiner. The pilot plant is equipped with a spray dryer with the capacity to dry several pounds of nanocellulose per day. Advantages of this process include simplicity and low cost compared to chemical methods. Disadvantages of the process include high energy consumption and a large distribution in particle size compared to chemical treatment methods like TEMPO. The TAPPI Nanocellulose Division estimates the commercial sales price of CNC produced from this method to be $4/lb.

The USDA's Forest Products Laboratory nanocellulose pilot plant also produces TEMPO-pretreated cellulose nanofibrils at the 2–3.5 kg scale. Using machine-dried market pulp, the yield of nanocellulose on original pulp is ~90% when using sodium hypochlorite at the primary oxidant. The method is based on laboratory work by Saito et al. [58] who demonstrated that the energy required to produce a nanoscale fibrillated product was reduced by TEMPO pretreatment. The pilot method alters the method by Saito by using a sodium carbonate buffer to control the pH to 10. Typically, commercial machine-dried eucalyptus bleached Kraft pulp is blended with water and then pretreated by mixing at 2 wt% solids, pH 2, and 2 wt% sodium chlorite ($NaClO_2$) on pulp. The mixture is stirred overnight at room temperature, then filtered and washed to collect the pulp. Pretreated pulp is combined with sodium carbonate and stirred for an hour at room temperature. Sodium bicarbonate, sodium bromide, and TEMPO are added and the reaction is heated to 30 °C. Sodium hypochlorite (NaClO) solution is added and the reaction stirred overnight at 30 °C. The treated pup is filtered, washed, diluted to 2 wt% and refined using a disc refiner. Refining is carried out with recirculation and run long enough to provide nominally 25 passes through the refiner. A heat exchanger is included in the recirculation loop to control the temperature near 50 °C. After refining, the pulp is diluted to 0.1 wt% in water and treated with an ultrasonic probe for 6 s with an energy input of 300 W, passed through a centrifuge operating at 12,500 G and concentrated to at least 0.5 wt% solids using a tubular ultrafiltration system with a 200,000-MW cutoff membrane. Final clarification is performed by passing the material twice through a homogenizer (Microfluidics M-110EH-30) equipped with series 200 and 87 μ orifices [59]. A notable advantage of this process is the production of thin nanofibrils with a more uniform particle size distribution that produces transparent gels and films. The principle disadvantage of the process is the high cost of TEMPO which is not recycled. The TAPPI Nanocellulose Division estimates the commercial sales price of CNF produced from this method to be $100/lb.

9.4.3 AVAP Nanocellulose Production

American Process Inc. has developed a single, cost-effective process for production of both cellulose nanocrystals (CNC) and cellulose nanofibrils (CNF) along with novel, hydrophobic, lignin coated versions of each. API's AVAP® technology

offers commercial-scale production of nanocellulose with flexibility in final product morphology and surface properties (hydrophilic or hydrophobic) that can service the wide variety of emerging end-use market segments. The novel hydrophobic lignin-coated variety of AVAP nanocellulose can be incorporated into plastics. This achievement overcomes a well-known barrier to commercial utilization of nanocellulose. Furthermore, AVAP nanocellulose is anticipated to be cost competitive with petroleum-based polymers as well as polymer additives. This break-through technology can help achieve the USDA's future global market size estimate for nanocellulose of 34 million tons per year [59]. In April 2015, API started up a nanocellulose production line at our existing AVAP Biorefinery in Thomaston Georgia for production of the full range of AVAP nanocellulose products for sale under the BioPlus™ trade name. The biorefinery currently demonstrates the AVAP pretreatment process for production of cellulose, cellulosic sugars and cellulosic ethanol from 3 bone dry tons per day of biomass. The biorefinery started in March 2013 and is the site of supply chain integrated alliances with downstream sugar and cellulose converters into chemicals, fuels, and other biobased materials. The facility is situated on 8 acres and includes 41,000 square feet of manufacturing space along with API's fully equipped corporate laboratory.

Figure 9.7 provides a simplified process flowsheet for API's nanoceullose process. The AVAP chemical pretreatment step uses sulfur dioxide (SO_2) and ethanol to remove hemicelluloses, lignin, and the amorphous regions of cellulose from biomass. Sulfur dioxide acts a delignifying agent, effectively freeing cellulose and hemicelluloses from lignin. Ethanol acts as a solvent, aiding penetration of SO_2 into the wood, dissolving resins and extractives, and reducing degradation of crystalline cellulose. The strong lignosulfonic acids created during delignification hydrolyze the amorphous regions of cellulose. The final nanocellulose product morphology (CNF, CNC, or a novel mixture of CNF and CNC) is controlled by the time and temperature (i.e. severity) of the pretreatment step. The dissolved sugars extracted

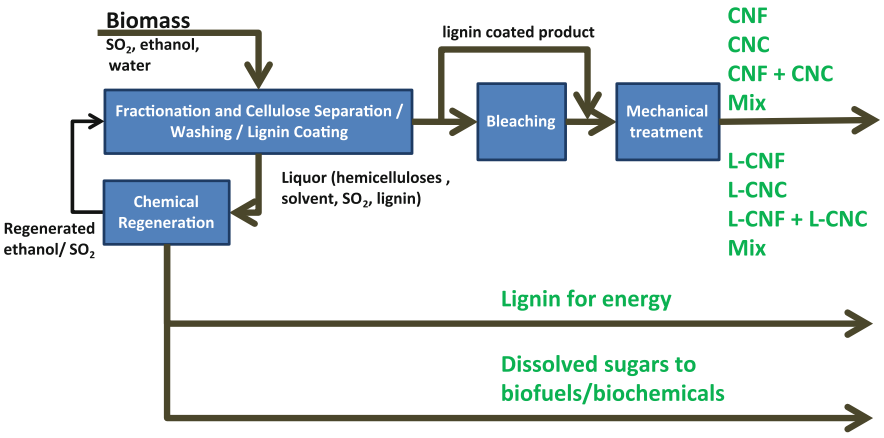

Fig. 9.7 A simplified process flow diagram of the AVAP nanocellulose process

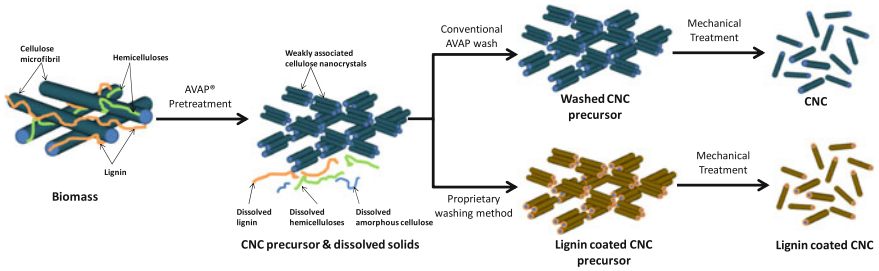

Fig. 9.8 AVAP process routes for traditional CNC and hydrophobic, lignin coated CNC

during pretreatment can be fermented into a cellulosic ethanol or other biochemical co-products for additional revenue. Lignin is removed from the process and burned, making the process self sufficient in energy use or a net energy (power) exporter, depending on the biomass feedstock. The pretreatment chemicals are recycled with high recovery rates in an energy efficient manner for reuse.

Following pretreatment, the chemically-fibrillated cellulose pulp is washed to remove the dissolved lignin and sugars. The pulp is then bleached to obtain pure cellulose. Alternatively, the cellulose is treated using a proprietary method that deposits lignin onto the surface of the fibrils or crystals. Following treatment of brown cellulose or optional bleaching, minimal mechanical energy is applied to the cellulose to liberate the individual nanocellulose particles (see Fig. 9.8) [6].

The AVAP nanocellulose process uses low cost raw biomass and pretreatment chemicals, a small number of process steps, and standard unit operations, which lead to low operating and capital cost requirements. In addition, the unique pretreatment chemicals (SO_2 delignifying agent and ethanol penetrating solvent) make the process suitable for all biomass feedstocks including spruce, red pine, Jack pine, loblolly pine, balsam fir, Douglas fir, larch, birch, beech, aspen, poplar, sugar maple, bark, corn cobs, corn stover, switchgrass, energy cane, eucalyptus, miscanthus, sugar cane straw, wheat straw, oil palm empty fruit bunches, forest residues, bamboo, and kenaf (a *Hibiscus cannabinus* plant that grows similar to bamboo) [60–66].

Figures 9.9 and 9.10 highlight the advantages of the AVAP process for making CNC and CNF over the conventional methods discussed above.

The key to the AVAP nanocellulose process is the "tunability" of the pretreatment step. For a given feedstock, the pretreatment conditions (time and temperature) can be selected that give the desired levels of fibrillation and removal of amorphous cellulose, as indicated by cellulose degree of polymerization (DP). As shown in Fig. 9.11, API has shown, using eucalyptus, softwood and cane straw, that two unique DP targets exist for production of CNF and CNC after mechanical treatment. Between the two targets, a mixture of CNF and CNC is produced.

The unique kinetics of the AVAP pretreatment step is an equally important attribute for nanocellulose production. In the acidic AVAP process the amorphous regions of cellulose are more fully hydrolyzed and dissolved while the crystalline cellulose is less accessible due to the non-swelling nature of the ethanolic cooking

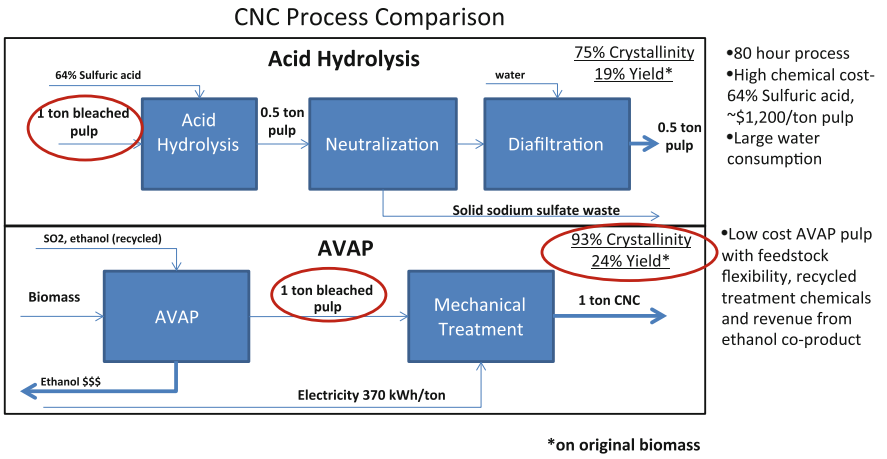

Fig. 9.9 Comparison between the AVAP nanocellulose processing method and the sulfuric acid method

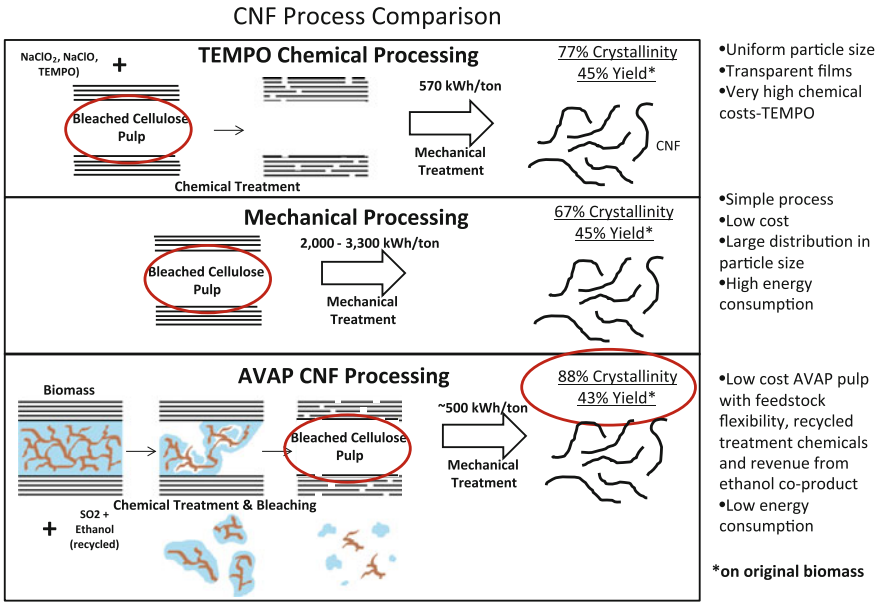

Fig. 9.10 Comparison between the AVAP cellulose nanofibrils processing method and conventional methods

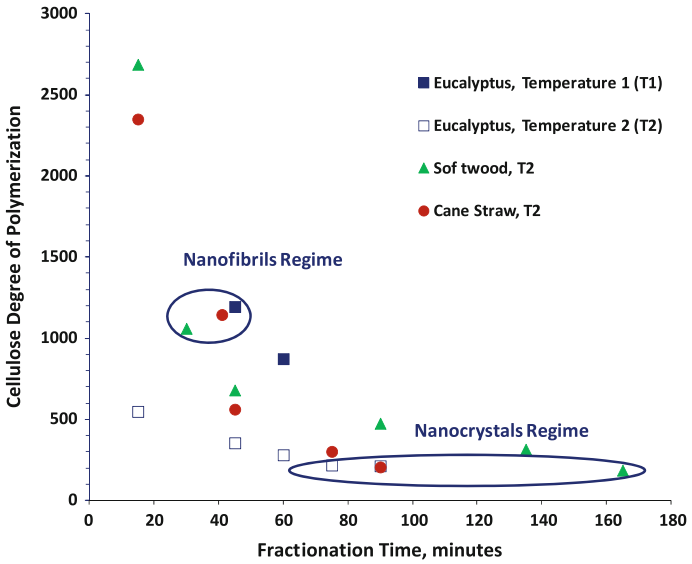

Fig. 9.11 Tunability of AVAP pretreatment step from different biomass feedstocks

liquor compared to that of other processes (e.g. the alkaline Kraft process). As a result, the crystallinity of both AVAP CNF and CNC are exceptionally higher than that produced by competing methods (see Table 9.2). Anticipated benefits of the high crystallinity include higher thermal stability and films and composites with higher strength and improved barrier properties.

As shown in Fig. 9.12, AVAP CNFs from Eucalyptus have a high aspect ratio (5–200 nm wide, 500 nm to several microns in length). AVAP CNCs from Eucalyptus are rod-shaped (4–5 nm wide, 50–500 nm in length) [6].

9.4.4 AVAP Nanocellulose Process Chemistry

As discussed above the AVAP® process utilizes a mixture of ethanol and water with dissolved SO_2 to rapidly fractionate all types of woody biomass into its principal components—pure cellulose (about 40%), hemicelluloses (about 35%) and lignin (about 25%) [67, 68]. Hemicelluloses are hydrophilic polymers, called xylan and glucomannan, consisting of about 100–200 linearly-linked sugar units of xylose and glucose plus mannose, respectively. Xylan and glucomannan also have other sugars as side groups such as arabinose, glucuronic acid and galactose, while some of the hydroxyl groups on the linear hemicelluloses chain are acetylated. Lignin is a hydrophobic amorphous polymer network of phenylpropane units. The components are arranged in woody biomass in a dense structure where the space between the hemicelluloses coated microfibrils is filled with lignin and hemicelluloses which are partly chemically bound to each other, as illustrated in Fig. 9.13.

Table 9.2 Comparison between crystallinity of AVAP CNF and CNC and conventional nanocellulose

	Crystallinity from XRD (%)
CNF, AVAP from eucalyptus chips	88
CNC, AVAP from eucalyptus chips	93
CNF, Mechanical from northern bleached softwood kraft pulp, from UMAine pilot	67
CNF, TEMPO ($NaClO_2$) from eucalyptus bleached kraft pulp, from FPL pilot	77
CNC, Sulfuric acid hydrolysis from spruce pre-hydrolysis rayon grade dissolving pulp, from FPL	75

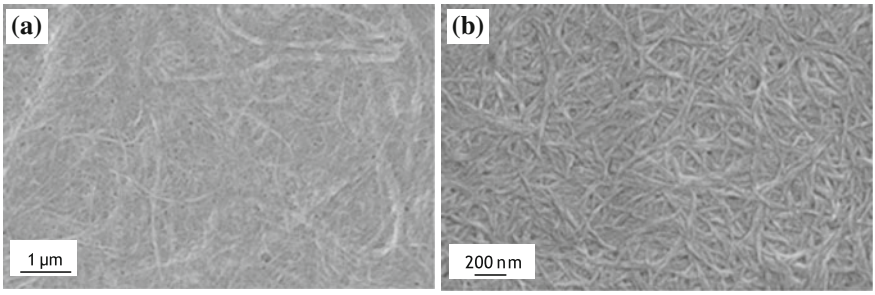

Fig. 9.12 AVAP Cellulose **a** Nanofibrils and **b** nanocrystals from eucalyptus

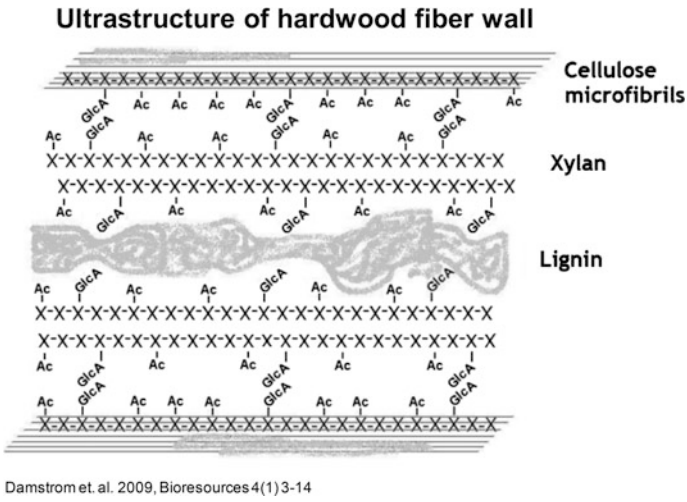

Fig. 9.13 Ultrastructure of harwood fiber wall

This complex composite morphology is nature's answer to create a material with great strength and microbiological protection properties needed for sustained, tall vertical growth. It also explains the difficulty to find a fractionation process which is able to deconstruct lignocellulosic biomass cleanly into its separate components. The unique chemistry of the AVAP® process arises from the presence of both SO_2 and ethanol in the aqueous fractionation chemicals. SO_2, a strong nucleophile, allows for efficient lignin removal, "delignification", of various feedstocks at relatively mild conditions (temperatures of 130–165 °C). SO_2 is responsible for lignin dissolution through sulfonation and depolymerisation. Hemicelluloses are dissolved through hydrolytic cleavage by SO_2 solvates (pK_{a1} for $SO_2{\cdot}H_2O$ in water of about 3.5 at 150 °C [69]) and especially lignosulfonic acids (pK_a in water close to 1 [70]). The major functions of ethanol are: (1) Fast transport of SO_2 to the reaction sites (α-carbons in lignin), (2) moderating the acidity of the reaction system, and (3) dissolution of lignin at relatively low degree of sulfonation [71, 72]. The fast penetration of ethanol into the biomass allows rapid impregnation of SO_2. This avoids impregnation times of one or several hours as customary for traditional biomass fractionation methods, or "pulping methods", such as the Kraft process or the acid sulfite process. The chemical impregnation efficiency of the AVAP process is evident by a low rejects content of the cellulose solids product ("pulp") even at relatively high lignin content and the fact that the process is not affected by variations in moisture content of the biomass feedstock [61]. After fractionation, the dissolved hemicelluloses are present in the liquid phase as monomers and oligomers in approximately equal amounts [71]. Lignin is produced in two fractions—a low-sulfonated fraction, obtained by precipitation after ethanol evaporation from the spent liquor, and more conventional lignosulfonates which can isolated from the liquid stream after sugar utilization (e.g. after fermentation).

The AVAP process has proven optimal for production of various conventional and novel cellulose-based products, as well as biofuels, biomaterials and chemicals. For example, good quality papermaking [73] and dissolving pulp for rayon textiles [74, 75] as well as nanofibrillated cellulose and cellulose nanocrystals [76] have been demonstrated. Also, well-delignified cellulose from the AVAP process can easily be hydrolysed to glucose followed by conversion with or without coprocessing of the conditioned hemicelluloses monosugars to various biofuels and chemicals [77–79] like ethanol and butanol through fermentation of the sugars [64, 80–83].

There are several cost and operating advantages of AVAP® cooking over commercial Kraft and acid sulfite pulping and ethanol-based organosolv pulping (ALCELL). Because cellulosic fibers liberated by conventional pretreatment methods still contain most of the original lignin as well as a significant amount of hemicelluloses, they are not suited for high performance cellulose grades, like nanocellulose. Also extensive lignin condensation and hemicelluloses degradation are typical for conventional processes which makes the resulting products unusable except for low-value combustion for energy production. The capital cost of conventional processes is also significantly higher than AVAP because of their complex recovery cycles.

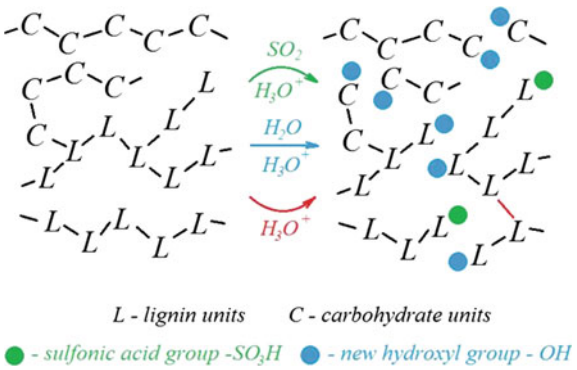

Fig. 9.14 Schematic of the four principal reactions during AVAP® fractionation

The principal chemical reactions in AVAP fractionation are lignin sulfonation, carbohydrate hydrolysis, lignin hydrolysis and lignin condensation reactions. The first three are positive for fractionation since they result in lower molecular weight and more hydrophilic lignin and carbohydrate polymers. The latter reaction increases the degree of polymerization of lignin and can be controlled to produce novel products like lignin-coated cellulose. The four reactions are schematically shown in Fig. 9.14.

As cooking proceeds, SO_2 is consumed in reactions with lignin and in side reactions. However, the highest measured amount of bound sulfur corresponds to only 1.1% on spruce wood with the remainder recoverable as SO_2. Therefore the concentration of SO_2 may be assumed essentially constant during cooking and equal to that of the fresh fractionation chemicals [72].

Pretreatment acidity is determined by the concentrations of SO_2, the formed strong lignosulfonic acid groups and ethanol. It has been shown that the acidity inside the fibers is the same as that in the external liquor [72]. Delignification is governed by chemical reaction rather than by diffusion, as can be inferred from the high values of the activation energies of the fractionation rates [61]. Biomass particle size has no significant effect on the delignification rate in the process [84].

In addition to the reactions leading to cleavage and dissolution of lignin, reactions between different lignin units, called condensation, are possible which form non-cleavable carbon-carbon bonds that prevent lignin removal from the biomass. Condensation is promoted by high acidity and temperature [85].

Like sulfite pulps, AVAP pulps are brighter and exhibit higher bleachability compared to Kraft pulps [73]. The reason for higher brightness of AVAP pulps in comparison with Kraft pulps is absence of strong chromophores such as quinones and stilbenes which are present in Kraft pulps. Better bleachability of AVAP and sulfite pulps in comparison with Kraft pulps is explained by lower amount of lignin-carbohydrate bonds which are mostly hydrolyzed in acidic conditions. Also hexenuronic acids, which are not present in AVAP or acid sulfite pulps, consume high amounts of bleaching chemicals when fully bleached Kraft pulps are produced.

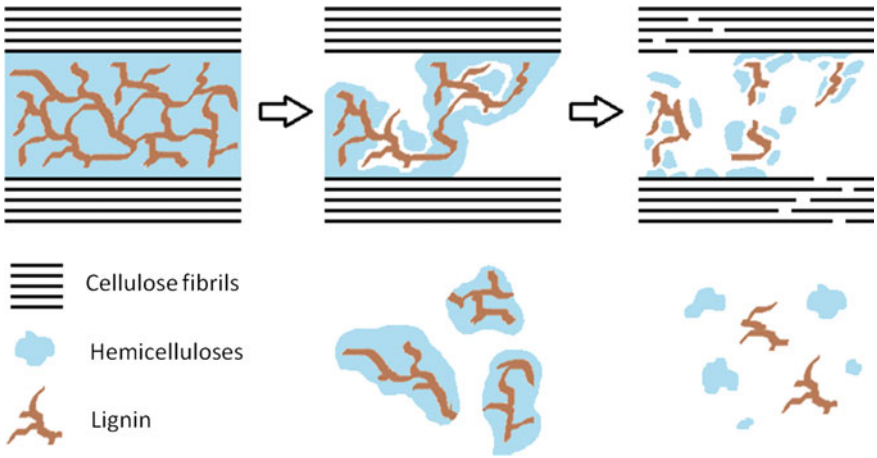

Fig. 9.15 Pictorial schematic of the two phases of AVAP® fractionation

The kinetics of AVAP delignification occurs in two phases. In the first phase, some lignin is removed while still being chemically bound to hemicelluloses as so-called lignin-carbohydrate complexes (LCC), which increases the void space between the cellulose microfibrils. In the second phase, most of the remaining LCCs and residual lignin and hemicelluloses are further sulfonated/hydrolyzed and removed as soluble separate fragments. Due to the removal of LCCs, cellulose chains become accessible to hydrolytic attack resulting in a decrease in the degree of polymerization. A pictorial representation of this delignification scheme is shown in Fig. 9.15.

Hemicelluloses hydrolyse and dissolve at acidic AVAP fractionation conditions. Hemicelluloses removal proceeds essentially in two phases—*initial* and *bulk*. More than half of hemicelluloses are removed in the *initial*, relatively short, phase. In this phase hemicelluloses are likely removed together with lignin as lignin-carbohydrate complexes (LCCs) [72]. During the second phase (called "*bulk*" phase) the removal is substantially slower and is first order in mannan and xylan. The lower removal rate of spruce glucomannan and xylan during the *bulk* phase may be related to the morphology of this residual fraction. Specifically this fraction of glucomannan is closely associated with cellulose in the original wood and is "crystallized" onto cellulose during the *initial* phase [72]. Also in the course of the *initial* phase most of the labile side units of the wood polysaccharides as well as pectins are removed [71].

Glycosidic bonds in cellulose are randomly hydrolyzed at the acid conditions of the AVAP process, leading to a decrease in average Degree of Polymerization (DP) of cellulose. However, for conventional pulps the DP is still higher than 1,000 and cellulose is retained in high (or full) yield in the fibrous residue. For cellulose nanocrystals production, hydrolysis is extended to the third stage (see below). The higher cellulose yield of the AVAP process for conventional pulps compared to alkaline processes is related mostly to the absence of peeling reactions in the former.

When subjected to heterogeneous acid hydrolysis, cellulose exhibits a very fast initial hydrolysis rate which is attributed to the presence of so-called "weak links", attributed to inductive effects of electrophilic substituents (e.g. carboxylic groups) or to physical strains at the folds of cellulosic microfibrils. In the slower second stage, hydrolysis of the "regular" glycosidic bonds takes place in the amorphous regions. After the amorphous cellulose is hydrolysed, the cellulose hydrolysis enters a third, slower stage during which the DP approaches the so-called levelling-off DP value that correspond to the length of the cellulose crystallites.

Similarly to acid sulfite pulps, AVAP pulps have a considerably higher cell-wall pore volume (i.e. fiber swelling) and lower cell-wall cohesion compared to Kraft pulps which explains the fact that AVAP® pulps refine to fibrils much faster [73]. Another explanation for the lower refinability of Kraft pulp accord is that paracrystalline regions of cellulose become amorphous during cooking in a cellulose-swelling medium, e.g. alkaline solutions [86]. On the contrary, acid sulfite and AVAP® liquors are non-swelling agents for cellulose. The higher fraction of amorphous cellulose in Kraft pulp leads to higher energy absorption during beating and thus to less fracture.

The high energy needed to break fibers into fibrils is of great concern for the production of cellulose nanofibrils. However, because of their low refining energy consumption, AVAP pulps are highly suitable for nanocellulose production. In addition, increased fiber swelling (internal fibrillation) also leads to easier rupture of the loosened internal fiber wall structure into fibrils [73]. Evidence for the lower energy required to produce nano/microfibrillar cellulose from AVAP pulps is provided in a recent fundamental study by Morales et al. 2014 [87]. In this study AVAP® fibers were subjected to shear forces that broke up the cell wall structure and produced lignocellulose nanofibrils (LCNF) as a gel-like dispersion. Ten passes through the microfluidizer were sufficient to yield nanofibrils with diameters of less than 20 nm. This represents a significant reduction in energy consumption compared to nanofibrillation of other lignocellulosic materials that required more than 20 passes to attain similar results [88]. Research related to differences in energy consumption upon nanofibrillation of softwood fibers with various lignin contents have been reported [89, 90]. However a most important finding by Morales et al. 2014 is that AVAP fibers obtained at widely different fractionation conditions allowed the production of LCNFs at similar energy costs despite the significant differences in cell wall composition [87].

9.5 Manufacturing Challenge: Hydrophobic surface modification for Incorporation into Plastics

Since cellulose is hydrophilic, nanocellulose does not disperse well in hydrophobic materials such as oils, solvents, or polymers such as polyethylene (PE), polypropylene (PP) or polylactic acid (PLA). As such, an active area of research has

been the chemical modification of the reactive surface CH_2OH components of nanocellulose to make the surface hydrophobic and compatible with hydrophobic media. The hydrophobic surface modification is used to improve not only the distribution of nanocellulose in polymers, plastics, or resins during composite processing, but also interfacial compatibility between the particles and matrices. By limiting hydrogen bonding that contributes to polar character of the nanocellulose, lower degree of hydrophilicity of nanocellulose can be anticipated [24, 91–94].

As discussed below, hydrophobic surface modification of nanocellulose has been successfully performed using various chemical treatments. However the laboratory methods demonstrated are not expected to be economically feasible at large scale due to the use of exotic and expensive solvents and grafting chemicals. API's low cost solution to this challenge is also presented below after a review of current methods.

Two primary approaches are most often demonstrated for the chemical surface modification of nanocellulose: physical adsorption and covalent bonding. For the physical adsorption approach, surfactant and polyelectrolyte solutions are used to tune the surface properties of nanocellulose [13, 91, 93, 95, 96]. Modifying the surface with surfactants improved particle/matrix interactions and dispersion quality [97, 98]. However, migration of the adsorbed moieties from modified nanocellulose surface into the matrix is the main drawback for this approach [91, 93]. The added surfactant or polyelectrolyte could induce weakness in strength leading to lower overall mechanical performance of polymer composite even though nanocellulose compatibility is improved [97]. Surface chemical reaction is introduced to form stable covalent bonding on the hydroxyl groups of nanocellulose.

Covalently bonded hydrophobic surface modification methods of nanocellulose are mainly molecule grafting or polymer grafting [13, 91–93, 96, 99]. Molecule grafting involves esterification where reagents containing carboxylic acid, acid anhydride, or acyl chlorides are used to perform esterification. The resulting nanocellulose ester derivatives, such as acetylated nanocellulose [41, 100–103], facilitate an increase in the degree of hydrophobicity indicated by higher water contact angle. The change in contact angle value varies depending on the degree of substituted hydroxyl groups of nanocellulose. Contact angle values up to 115° have been reported for acetylated nanocellulose using acetic anhydride in pyridine medium [100, 101]. Similarly, hydrophobization of nanocellulose with contact angle value of approximately 105° can also be achieved using alkylketene dimers (AKD)in the cellulose solvent 1,3-dimethyl-2-imidazolidinone/lithium chloride (DMI/LiCl) [104]. Recently, alternative esterifications using environmentally friendly approaches that minimize toxic solvent (or reagents) or solvent exchange process are proposed. Esterifications of various anhydrides, including acetic, butyric, hexanoic and alkenyl succinic anhydrides, and fatty acids chlorides, such as hexanoyl and stearoyl chloride, under ionic liquid have been successfully reported to give contact angle values in the range of 80–104° [103, 105]. Gas-phase esterification through a vapor mixture of trifluoroacetic acid anhydride and acetic acid can also reduce the hydrophilicity of nanocellulose [106]. AKD nano-emulsion exhibits water-based esterification with a contact angle value of 105.8° [107].

Another common molecule grafting method for nanocellulose surface hydrophobization is silylation. Surface silylation with chlorodimethyl isopropylsilane in toluene exhibits improved contact angle values in the range of 117–146° [108]. Similarly, silane treatments in acetone medium using 3-aminopropyltriethoxysilane and 3-glycidoxypropyltrimethoxysilane increase contact angle values to 90 and 64°, respectively [109]. Other coupling agents, such as titanate modifier (Lica 38), also demonstrate hydrophobic surfaces with contact angles of 110° [109].

Hydrophobization surface modifications can also be achieved by polymer grafting. The grafted polymers decrease the polar character of the nanocellulose and considerably increase their apolar character. Polymer grafting generally proceeds either through "grafting from" or "grafting onto". The "grafting from" approach involves growing polymer chains from the active sites of cellulose, while "grafting to" involves attaching pre-formed polymer chains onto the cellulose backbone [93, 95, 96, 110–113].

The "grafting to" approach is typically mediated by a coupling agent to attach the high molecular weight hydrophobic polymer to the surface of nanocellulose [93, 96, 112]. Coupling agents like isocyanate, peptide, or anhydride moieties have been reported to effectively perform chemical surface modification on nanocellulose [95, 96, 112, 113]. The time scale for activation and grafting steps in this method is very rapid compared to that of "grafting from" [114]. The grafting density, however, is expected to be low due to steric hindrance of long polymer chains [93, 95, 110, 112, 115].

The "grafting from" approach is introduced in order to achieve high grafting density. Common methods include conventional free-radical graft polymerization, direct oxidation, ionic graft polymerization, and ring opening polymerization [95, 111, 113, 114]. Various free-radical initiators such as dibenzoyl peroxide (BPO), azobis(isobutyronitrile) (AIBN), potassium persulfate, potassium permanganate, and Fenton's reagent, can be applied for conventional free-radical graft polymerization [114, 116], while direct oxidation typically utilizes transition metal ions like ceric ammonium nitrate to initiate free-radical exclusively on the cellulose backbone [111, 114, 116]. Monomer solubility in the solvent, monomer concentration, swelling properties of cellulose in solvent, generation of free radicals in the presence of the solvent, and the role of additives play important role in graft copolymerization [114, 117]. Several studies on nanocellulose polymer grafting based on ring opening polymerization have been reported for the grafting of ε-caprolactone and L-lactic acid [113]. The most commonly accepted mechanism for this method requires stannous octoate, $Sn(Oct)_2$, as the catalyst [113, 118]. Molecular weight of grafted polymer can be controlled based on the ratio of alcohol groups to monomers [118].

Major drawbacks of the "grafting from" method include inability to control the polydispersity and molecular weight distribution of the polymers [110, 111, 114, 119, 120]. Controlled polymerization methods can be achieved using living polymerization methods. These methods utilize no chain breaking mechanism, such as chain transfer or irreversible termination, as the polymer grows. Living polymerization methods, including atom transfer radical polymerization (ATRP), nitroxide

mediated polymerization (NMP), and reversible addition fragmentation chain-transfer (RAFT), have been successfully introduced to modify nanocellulose [110, 111, 114, 119, 120]. However, these treatments are currently very costly [110].

API's low cost method of precipitating the lignin that was dissolved from biomass during the AVAP pretreatment step onto the surface of the cellulose nanoparticles makes a fully hydrophobic surface that has been shown to be compatible with hydrophobic polymers. As shown in Fig. 9.16, thin films of lignin coated nanocellulose have significantly higher water contact angles compared to the pure cellulose varieties.

As shown in Fig. 9.17, API's freeze-dried lignin coated cellulose nanocrystals (L-CNC)were easily dispersed in highly hydrophobic silicone. The optical translucency of the composites confirms that the nanoparticles were dispersed as individual particles without agglomerations. Freeze-dried and spray dried L-CNC has also been dispersed effectively in other polymers including poly lactic acid, polyhydroxybutyrate, polypropylene, polystyrene, and polyethylene.

Figure 9.18 illustrates that a good distribution and dispersion of nanoparticles within a composite matrix is critical for composite quality and strength advancement. Other factors impacting polymer composite quality that are offered by API's lignin-coated nanocellulose include high aspect ratio and interfacial compatibility between fiber surface and polymer matrix (i.e. wetting).

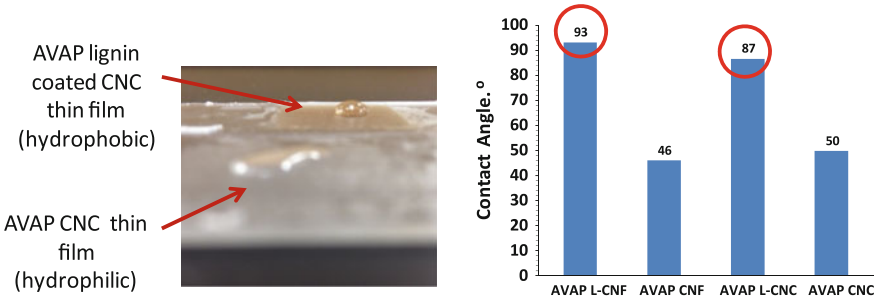

Fig. 9.16 Water contact angle of lignin coated and pure cellulose AVAP nanocellulose

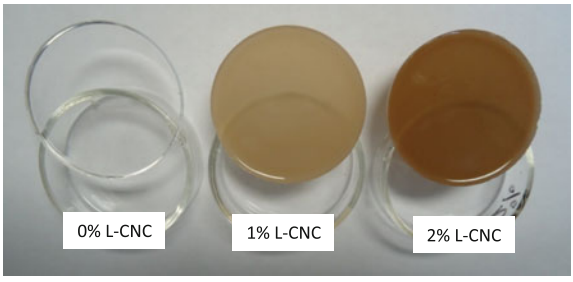

Fig. 9.17 Lignin coated cellulose nanocrystals dispersed in silicone

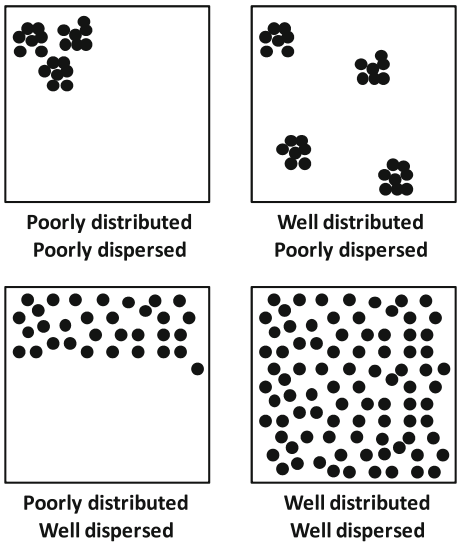

Fig. 9.18 Quality of distributed and dispersive mixing of nanoparticles in a composite matrix

9.6 Other Nanocellulose Manufacturing Grand Challenges

There are a few grand challenges that remain to be solved in the field of nanocellulose manufacturing to ensure rapid utilization and commercialization including:

- Economical drying of nanocellulose suspensions and preservation of discrete nanocellulose particle morphology during drying for effective re-dispersion during end-use
- Development of international standards along the supply chain
- Development of rapid, low cost characterization methods for process and product quality control

9.6.1 Drying

Shipping high water content nanocellulose gels (90–97 wt% water) to their end-use destination is costly and impractical at large volumes and long distances. A nanocellulose drying method must be developed that is scalable, low cost, and that maintains product quality and particle morphology. The most common drying technologies for nanocellulose reported in the literature are freeze drying and spray drying. However, researchers have shown that drying methods can have a negative impact on nanocellulose properties including crystallinity, thermal stability, and irreversible inter-particle aggregation/bonding, known as hornification [121–123].

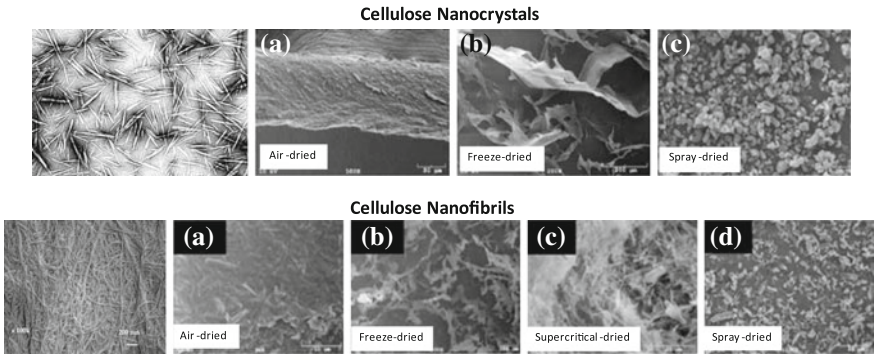

Fig. 9.19 Cellulose nanomaterials obtained from different drying technologies

As shown in Fig. 9.19, cellulose hornification into large agglomerated structures that lose the individual nanoparticle morphology is a significant challenge across all conventional drying methods for both CNF and CNC [124].

Recently, Missoum et al. showed freeze drying to be a good method to prepare dried CNF that maintains discrete particle morphology by adding inorganic salt to a CNF suspension before drying. They indicated that the salt separates the CNF during the drying process so that aggregation and bonding of the particles during drying could be avoided [125]. The salt acts as an inter-particle "hydrogen bonding blocker". As a result, the dried CNF could be redispersed in water as individual nanoparticles. Disadvantages of the method include that the large amount of salt used had to be removed by dialysis in water before end-use and that the method is not applicable for dispersion of nanocellulose in hydrophobic polymers or solvents.

API is actively involved in technology development for scalable, low cost drying of both lignin-coated nanocellulose and pure, hydrophilic nanocellulose. As discussed in the previous section, freeze-drying of API's lignin-coated nanocellulose maintains individual nanoparticle morphology, as demonstrated by uniform redispersion in silicone. The lignin coating appears to function as a separator to prevent the hydrogen bond formation between cellulose during drying. Transmission electron microscriopy (TEM) images support this conclusion (not shown). Development of a low cost, hydrogen bonding blocker for freeze-drying of conventional pure nanocellulose that maintains original surface properties and color/transparency is ongoing.

9.6.2 International Standards

The development of standards is critical for commercialization of new technologies. Standards represent agreed upon performance characteristics, technical criteria, measurement and reporting requirements, and importantly, terminology. For example, fibrillated cellulosic material is often referred to under a variety of names

including cellulose nanofibrils, cellulose microfibrils, cellulose microfibers, microfibrillar cellulose, nano-fibrillated cellulose, and refined pulp. This diversity and lack of precision in terminology creates confusion in the market about the relationship of characteristics and performance properties to name. As with most nanostructured materials, CNF and CNC are a mixture of fibrous materials with a distribution of sizes in terms of length, diameter, and level of aggregation. Sound, agreed upon definitions and requirements are critical for successful business interactions.

Recognizing this need, several organizations are working toward the development of international voluntary standards for nanomaterials and nanotechnology. The Nanotechnology Division of the Technical Association of the Pulp and Paper Industry (TAPPI) has held annual workshops since 2011 on the development of standards for nanocellulose and published a roadmap describing the planned activities under the International Nanocellulose Standards Coordination Committee (INSCC) [126]. Their efforts are coordinated with the American National Standards Institute (ANSI) Nanotechnology Standards Panel, and the International Standards Organization (ISO) Technical Committee 229. TAPPI is working toward terminology, measurement and standards for environmental health and safety (EHS) for forms of nanocellulose. At the time of writing, the Canadian Standards Authority has proposed an ISO Standard for characterization of cellulose nanocrystals based on a standard reference material developed by the National Research Council of Canada to measure particle morphology, purity and surface properties. The ISO TC 229 has developed about 40 standards relating to the measurement and evaluation of EHS of nanomaterials. However, few of these are specific to certain nanomaterials. Nanomaterials are challenging to assess because of measurement issues related to their small size, and different surface to volume characteristics. Nanocellulose adds to the challenge because it is an organic molecule with a high aspect ratio.

9.6.3 Rapid, Low Cost Characterization Methods

Another challenge to the large-scale economical manufacture of nanocellulose is converting the expensive, high-tech characterization methods employed within the field of nanotechnology to rapid methods for the operating floor. With this goal in mind, the U.S. National Institute of Standards and Technology (NIST) in conjunction with TAPPI held a workshop in June 2014 entitled “Measurement Needs for Cellulose Nanomaterials”. Invited representative manufacturers, researchers and product development stakeholders shared their metrology needs and efforts along the end-product value chain. Dr. Kim Nelson presented API’s measurement needs from a manufacturer’s perspective which includes [127]:

- Particle size distribution (current method: scanning electron microscopy (SEM), transmission electron microscopy (TEM)
- Lignin content (tedious wet chemistry)

- Crystallinity (X-ray diffraction (XRD))
- Thermal stability (thermal gravimetric analysis (TGA))
- Purity (inductively coupled plasma atomic emission spectroscopy (ICP-OES))

The principle disadvantages of the existing methods above are capital cost (~$1.4 million total), length of time required for sample preparation and measurement (up to several hours), high level of technical expertise required, and high facility construction costs due to special environmental requirements for many of the instruments in terms of acoustic and mechanical vibrations, electromagnetic fields etc. API and other manufacturers desire methods that can be performed on the operating floor or in a standard process control laboratory, and that have low associated costs, short characterization and test times (minutes) and require minimal training and expertise. Development of these methods will require collaboration between academia, government, industry, and equipment suppliers.

9.6.4 Hiring and Education Needs

The technology, process development, and scale-up of versatile, economical nanocellulose materials require strong skills in chemical engineering with a preferred background in biomass chemistry and processing. The development of commercial end-use applications across a wide variety of industries requires candidates with multidisciplinary focus and skills across materials science, nanotechnology, and polymer processing and chemistry. Luckily, nanocellulose and nanotechnology are popular research topics at universities throughout the world. Recruiting in this field has not been a challenge. Our efforts to commercialize this new material requires members of our team to interact productively with colleagues from diverse fields including R&D and technology development, engineering, operations, marketing and business development, and finance. We seek individuals who are intellectually rigorous, creative, enthusiastic, energetic, and curious and who are committed to our company's mission of fostering adaptation of renewable bio-based materials. We find these traits ensure effective collaborative and team work throughout our business.

References

1. R.J. Moon, S. Beck, A.W. Rudie, Cellulosic nanocrystals—a material with unique properties and many potential applications, in *Production and Applications of Cellulose Nanomaterials*, ed. by M.T. Postek, et al. 2013 (TAPPI Press, Peachtree Corners, GA), pp. 9–12
2. H. Kangas, Cellulose nanofibrils—a class of materials with unique properties and many potential applications, in *Production and Applications of Cellulose Nanomaterials*, ed. by M.T. Postek, et al. 2013 (TAPPI Press, Peachtree Corners, GA)

3. R.W. Malmsheimer et al., Forest management solutions for mitigating climate change in the United States. J. Forest. **106**(3), 115–173 (2008)
4. C. Eberle, S. Ozcan, Nanocellulose reinforced polymers, in *Cellulosic Nanomaterials Workshop* 2014 (Oak Ridge National Laboratory, Washington, DC)
5. J.A. Shatkin et al., Market projections of cellulose nanomaterial-enabled products—Part 1: applications. Tappi J. **13**(5), 9–16 (2014)
6. K. Nelson, T. Retsina, Innovative nanocellulose process breaks the cost barrier. Tappi J. **13** (5), 19–23 (2014)
7. P. Gatenholm, *Building body parts using nanocellulose*, (2010). http://www.nanotech-now.com/news.cgi?story_id=36457. Accessed 20 May 2014
8. *Ford develops carbon fibre technology that could deliver more fuel-efficient vehicles*. http://corporate.ford.com/news-center/press-releases-detail/pr-ford-develops-carbon-fibre3720. Accessed 22 May 2014, (Press Release) Oct 2012
9. D.M. Fox et al., Flame retarded poly(lactic acid) using POSS-modified cellulose. 1. Thermal and combustion properties of intumescing composites. Polym. Degrad. Stab. **98**(2), 590–596 (2013)
10. B. Lyne, *Market Prospects for NanoCellulose* (The Royal Institute of Technology, Alberta Biomaterials Development Centre, Edmunton, AB, Canada, 2013)
11. M. Henriksson et al., Cellulose nanopaper structures of high toughness. Biomacromolecules **9**(6), 1579–1585 (2008)
12. W. Gindl, J. Keckes, All-cellulose nanocomposite. Polymer **46**(23), 10221–10225 (2005)
13. R.J. Moon et al., Cellulose nanomaterials review: structure, properties and nanocomposites. Chem. Soc. Rev. **40**(7), 3941–3994 (2011)
14. I. Siró, D. Plackett, Microfibrillated cellulose and new nanocomposite materials: a review. Cellulose **17**(3), 459–494 (2010)
15. W. Hamad, On the development and applications of cellulosic nanofibrillar and nanocrystalline materials. Can. J. Chem. Eng. **84**(5), 513–519 (2006)
16. J. Lee, Y. Deng, The morphology and mechanical properties of layer structured cellulose microfibril foams from ice-templating methods. Soft Matter **7**(13), 6034–6040 (2011)
17. H.M.C. Azeredo et al., Nanocellulose reinforced chitosan composite films as affected by nanofiller loading and plasticizer content. J. Food Sci. **75**(1), N1–N7 (2010)
18. X. Xu et al., Cellulose nanocrystals vs. cellulose nanofibrils: a comparative study on their microstructures and effects as polymer reinforcing agents. ACS Appl. Mater. Interfaces **5**(8), 2999–3009 (2013)
19. E.S. Medeiros et al., Electrospun nanofibers of poly (vinyl alcohol) reinforced with cellulose nanofibrils. J. Biobased Mater. Bioenergy **2**(3), 231–242 (2008)
20. G. Siqueira, J. Bras, A. Dufresne, Cellulose whiskers versus microfibrils: influence of the nature of the nanoparticle and its surface functionalization on the thermal and mechanical properties of nanocomposites. Biomacromolecules **10**(2), 425–432 (2008)
21. H. Lönnberg et al., Synthesis of polycaprolactone-grafted microfibrillated cellulose for use in novel bionanocomposites-influence of the graft length on the mechanical properties. ACS Appl. Mater. Interfaces **3**(5), 1426–1433 (2011)
22. L. Fang et al., Influence of silane surface modification of veneer on interfacial adhesion of wood–plastic plywood. Appl. Surf. Sci. **288**, 682–689 (2014)
23. A. Dufresne, M.N. Belgacem, Cellulose-reinforced composites: from micro-to nanoscale. Polímeros **23**(3), 277–286 (2013)
24. Y. Xie et al., Silane coupling agents used for natural fiber/polymer composites: a review. Compos. A Appl. Sci. Manuf. **41**(7), 806–819 (2010)
25. S.-Y. Fu et al., Effects of particle size, particle/matrix interface adhesion and particle loading on mechanical properties of particulate–polymer composites. Compos. B Eng. **39**(6), 933–961 (2008)
26. S.J. Peters et al., Nanocellulose and microcellulose fibers for concrete. Transp. Res. Rec.: J. Transp. Res. Board **2142**(1), 25–28 (2010)

27. Y.W. Cao, W. Jason, J. Youngblood, R. Moon, P. Zavattieri, Performance-enhanced cementitious materials by cellulose nanocrystal additions, in *Production and Applications of Cellulose Nanomaterials*, ed. by M.T. Postek, et al. 2013 (TAPPI press, Peachtree Corners, GA), p. 135–136
28. F. Jiang, Y.-L. Hsieh, Super water absorbing and shape memory nanocellulose aerogels from TEMPO-oxidized cellulose nanofibrils via cyclic freezing-thawing. J. Mater. Chem. A **2**(2), 350–359 (2014)
29. Z. Zhang et al., Ultralightweight and flexible silylated nanocellulose sponges for the selective removal of oil from water. Chem. Mater. **26**(8), 2659–2668 (2014)
30. S.T. Nguyen et al., Advanced thermal insulation and absorption properties of recycled cellulose aerogels. Colloids Surf., A **445**, 128–134 (2014)
31. N.T. Cervin et al., Ultra porous nanocellulose aerogels as separation medium for mixtures of oil/water liquids. Cellulose **19**(2), 401–410 (2012)
32. J.T. Korhonen et al., Hydrophobic nanocellulose aerogels as floating, sustainable, reusable, and recyclable oil absorbents. ACS Appl. Mater. Interfaces **3**(6), 1813–1816 (2011)
33. C. Gebald et al., Amine-based nanofibrillated cellulose as adsorbent for CO_2 capture from air. Environ. Sci. Technol. **45**(20), 9101–9108 (2011)
34. X. He, et al., Aerogels from quaternary ammonium-functionalized cellulose nanofibers for rapid removal of Cr(VI) from water. Carbohydr. Polym. (2014)
35. H. Valo et al., Drug release from nanoparticles embedded in four different nanofibrillar cellulose aerogels. Eur. J. Pharm. Sci. **50**(1), 69–77 (2013)
36. D.O. Carlsson et al., Electroactive nanofibrillated cellulose aerogel composites with tunable structural and electrochemical properties. J. Mater. Chem. **22**(36), 19014–19024 (2012)
37. H.-W. Liang et al., Highly conductive and stretchable conductors fabricated from bacterial cellulose. NPG Asia Mater. **4**, e19 (2012)
38. FPL, *Forest Products Laboratory: Restoring America's Forests Through the Wise Use of Wood* (USDA Forest Products Laboratory, Madison, WI, USA, 2013), p. 13
39. L. Heath, W. Thielemans, Cellulose nanowhisker aerogels. Green Chem. **12**(8), 1448–1453 (2010)
40. N. Lavoine et al., Microfibrillated cellulose—its barrier properties and applications in cellulosic materials: a review. Carbohydr. Polym. **90**(2), 735–764 (2012)
41. G. Rodionova et al., Surface chemical modification of microfibrillated cellulose: improvement of barrier properties for packaging applications. Cellulose **18**(1), 127–134 (2011)
42. K. Syverud, P. Stenius, Strength and barrier properties of MFC films. Cellulose **16**(1), 75–85 (2009)
43. C. Aulin, M. Gällstedt, T. Lindström, Oxygen and oil barrier properties of microfibrillated cellulose films and coatings. Cellulose **17**(3), 559–574 (2010)
44. W.T. Luu, D.W. Bousfield, J. Kettle, Application of nano-fibrillated cellulose as a paper surface treatment for inkjet printing, in *2011 PaperCon Conference* 2011, TAPPI
45. A. Mautner et al., Nanopapers for organic solvent nanofiltration. Chem. Commun. **50**(43), 5778–5781 (2014)
46. H. Fukuzumi et al., Selective permeation of hydrogen gas using cellulose nanofibril film. Biomacromolecules **14**(5), 1705–1709 (2013)
47. W. Thielemans, C.R. Warbey, D.A. Walsh, Permselective nanostructured membranes based on cellulose nanowhiskers. Green Chem. **11**(4), 531–537 (2009)
48. T. Lindström, et al., Microfibrillated cellulose, in *Encyclopedia of Polymer Science and Technology* (John Wiley & Sons, Inc, 2002)
49. A.F. Turbak, F.W. Snyder, K.R. Sandberg, Microfibrillated cellulose, a new cellulose product: properties, uses, and commercial potential. J. Appl. Polym. Sci. **37**, 815–827 (1983)
50. K. Xhanari, K. Syverud, P. Stenius, Emulsions stabilized by microfibrillated cellulose: the effect of hydrophobization, concentration and o/w ratio. J. Dispersion Sci. Technol. **32**(3), 447–452 (2011)

51. A. Lif et al., Fischer-Tropsch diesel emulsions stabilised by microfibrillated cellulose and nonionic surfactants. J. Colloid Interface Sci. **352**(2), 585–592 (2010)
52. Y. Boluk, L. Zhao, *Aircraft anti-icing fluids formulated with nanocrystalline cellulose*, Alberta Innovates—Technology Futures (2013)
53. K. Dimic-Misic, P.A.C. Gane, J. Paltakari, Micro- and nanofibrillated cellulose as a rheology modifier additive in CMC-containing pigment-coating formulations. Ind. Eng. Chem. Res. **52**(45), 16066–16083 (2013)
54. VTT. *Innovation and Competitiveness from Nanocellulose*, (2011). http://www.vtt.fi/news/2011/01192011nano.jsp?lang=en. Accessed 21 May 2014
55. J. Moreau, Driving innovation to market. cellulose nanomaterials—a path to commercialization, in *Cellulosic Nanomaterials Workshop* 2014, CelluForce, Washington, DC
56. X. Dong, J.-F. Revol, D. Gray, Effect of microcrystallite preparation conditions on the formation of colloid crystals of cellulose. Cellulose **5**(1), 19–32 (1998)
57. R.S. Reiner, A.W. Rudie, Process scale-up of cellulose nanocrystal production to 25 kg per batch at the forest products laboratory, in *Production and Applications of Cellulose Nanomaterials*, ed. by M.T. Postek, et al. 2013 (TAPPI Press, Peachtree Corners, GA), pp. 21–24
58. T. Saito et al., Cellulose nanofibers prepared by TEMPO-mediated oxidation of native cellulose. Biomacromolecules **8**(8), 2485–2491 (2007)
59. R.S. Reiner, A.W. Rudie, Pilot plant scale-up of TEMPO-pretreated cellulose nanofibrils, in *Production and Applications of Cellulose Nanomaterials*, ed. by M.T. Postek, et al. 2013 (TAPPI Press, Peachtree Corners, GA), pp. 177–178
60. M. Iakovlev, H. Sixta, A. van Heiningen, SO_2-ethanol-water (SEW) pulping: II. Kinetics for spruce, beech, and wheat straw. J. Wood Chem. Technol. **31**(3), 250–266 (2011)
61. M. Iakovlev et al., SO_2-ethanol-water (SEW) fractionation of spruce: kinetics and conditions for paper and viscose-grade dissolving pulps. RSC Adv. **4**(4), 1938–1950 (2014)
62. S.F. Primakov, Delignification of various wood species with aqueous-alcoholic solutions. Nauchn. Tr. Vses. Nauchn.-Issled. Inst. Tsellyulozn.-Bumazhn. Prom. **47**, 69–75 (1961)
63. R.J. Puumala, *Organosolv Pulping and a Preliminary Vapor-liquid Equilibrium Study of a Sulfur Dioxide, Ethanol, Water System* (Michigan Technological University, 1991)
64. E. Sklavounos et al., Oil palm empty fruit bunch to biofuels and chemicals via SO_2–ethanol–water fractionation and ABE fermentation. Bioresour. Technol. **147**, 102–109 (2013)
65. M. Yamamoto, M. Iakovlev, A. van Heiningen, Total mass balances of SO_2-ethanol-water (SEW) fractionation of forest biomass. Holzforschung **65**(4), 559–565 (2011)
66. M. Yamamoto, M. Iakovlev, A. van Heiningen, Kinetics of SO_2–ethanol–water (SEW) fractionation of hardwood and softwood biomass. Bioresour. Technol. **155**, 307–313 (2014)
67. T. Retsina, V. Pylkkänen, Back to the biorefinery: a novel approach to boost pulp mill profits, in *Paper 360*2007. pp. 18–19
68. T. Retsina, V. Pylkkänen, *Method for the production of fermentable sugars and cellulose from lignocellulosic material* (American Process, Inc, 2011)
69. S.A. Rydholm, *Pulping Processes* (John Wiley & Sons Inc., London, 1965)
70. S.S. Vishnevskaya, R.K. Boyarskaya, M.N. Tsypkina, Sulfonation and dissolution of lignin in sulfite pulping. 2. Factors determining the dissolution of lignin. Koksnes Kimija **1**, 23–28 (1981)
71. M. Iakovlev, A. van Heiningen, Efficient fractionation of spruce by SO_2-ethanol-water treatment: closed mass balances for carbohydrates and sulfur. ChemSusChem **5**(8), 1625–1637 (2012)
72. M. Iakovlev, A. van Heiningen, Kinetics of fractionation by SO_2-ethanol-water (SEW) treatment: understanding the deconstruction of spruce wood chips. RSC Adv. **2**(7), 3057–3068 (2012)
73. M. Iakovlev, E. Hiltunen, A. van Heiningen, Paper technical potential of spruce SO_2-ethanol-water (SEW) pulp compared to kraft pulp. Nord. Pulp Pap. Res. J. **25**(4), 428–433 (2010)

74. M. Iakovlev et al., SO_2–ethanol–water (SEW) fractionation process: production of dissolving pulp from spruce. Cellulose **21**(3), 1419–1429 (2014)
75. H. Sixta et al., Novel concepts of dissolving pulp production. Cellulose **20**(4), 1547–1561 (2013)
76. K. Nelson, Low cost co-production of cellulose nanofibrils and/or cellulose nanocrystals with biofuels using the AVAP biorefinery technology, in *NWBC 2014—the 5th Nordic Wood Biorefinery Conference*, 2014. Stockholm, Sweden
77. M. Yamamoto, M. Iakovlev, A. van Heiningen, The effect of chemical and physical characteristics of spruce SEW pulps on enzymatic hydrolysis. Cellulose **21**(5), 3395–3407 (2014)
78. M. Yamamoto et al., Enzymatic hydrolysis of hardwood and softwood harvest residue fibers released by sulfur dioxide–ethanol–water fractionation. Bioresour. Technol. **167**, 530–538 (2014)
79. M. Yamamoto et al., The effect of bark on sulfur dioxide–ethanol–water fractionation and enzymatic hydrolysis of forest biomass. Bioresour. Technol. **167**, 390–397 (2014)
80. E. Sklavounos et al., Conditioning of SO_2-ethanol-water spent liquor from spruce for the production of chemicals by ABE fermentation. Holzforschung **65**(4), 551–558 (2011)
81. E. Sklavounos, M. Iakovlev, A. van Heiningen, Study on conditioning of SO_2–ethanol–water spent liquor from spruce chips/softwood biomass for ABE fermentation. Ind. Eng. Chem. Res. **52**(11), 4351–4359 (2013)
82. E. Sklavounos et al., Comparison of two conditioning schemes for detoxifying SO_2-ethanol-water hydrolysate from lignocellulosics for ABE fermentation. Nord. Pulp Pap. Res. J. **29**(3), 370–382 (2014)
83. S.A. Survase et al., Continuous acetone–butanol–ethanol fermentation using SO_2–ethanol–water spent liquor from spruce. Bioresour. Technol. **102**(23), 10996–11002 (2011)
84. M. Iakovlev, T. Pääkkönen, A. van Heiningen, Kinetics of SO_2-ethanol-water pulping of spruce. Holzforschung **63**(6), 779–784 (2009)
85. N.A. Rozenberger, Rapid sulfite pulping. Bumazhnaya Promyshlennost **36**(12), 3–7 (1961)
86. D.H. Page, The origin of the differences between sulfite and kraft pulps. Canadian J. Pulp Paper **9**(1), 15–20 (1983)
87. L.O. Morales et al., Effects of residual lignin and heteropolysaccharides on the bioconversion of softwood lignocellulose nanofibrils obtained by SO_2–ethanol–water fractionation. Bioresour. Technol. **161**, 55–62 (2014)
88. J.Y. Zhu, R. Sabo, X. Luo, Integrated production of nano-fibrillated cellulose and cellulosic biofuel (ethanol) by enzymatic fractionation of wood fibers. Green Chem. **13**(5), 1339–1344 (2011)
89. K.L. Spence et al., A comparative study of energy consumption and physical properties of microfibrillated cellulose produced by different processing methods. Cellulose **18**(4), 1097–1111 (2011)
90. I.C. Hoeger et al., Mechanical deconstruction of lignocellulose cell walls and their enzymatic saccharification. Cellulose **20**(2), 807–818 (2013)
91. M.A. Hubbe et al., Cellulosic nanocomposites: a review. BioResources **3**(3), 929–980 (2008)
92. H. Abdul Khalil, A. Bhat, A. Ireana Yusra, Green composites from sustainable cellulose nanofibrils: a review. Carbohydr. Polym. **87**(2), 963–979 (2012)
93. K. Missoum, M.N. Belgacem, J. Bras, Nanofibrillated cellulose surface modification: a review. Materials **6**(5), 1745–1766 (2013)
94. D.J. Gardner et al., Adhesion and surface issues in cellulose and nanocellulose. J. Adhes. Sci. Technol. **22**(5–6), 545–567 (2008)
95. Y. Habibi, L.A. Lucia, O.J. Rojas, Cellulose nanocrystals: chemistry, self-assembly, and applications. Chem. Rev. **110**(6), 3479–3500 (2010)
96. S. Rebouillat, F. Pla, State of the art manufacturing and engineering of nanocellulose: a review of available data and industrial applications. J. Biomater. Nanobiotechnol. **4**(2) (2013)

97. J. Kim et al., Dispersion of cellulose crystallites by nonionic surfactants in a hydrophobic polymer matrix. Polym. Eng. Sci. **49**(10), 2054–2061 (2009)
98. N. Ljungberg et al., New nanocomposite materials reinforced with cellulose whiskers in atactic polypropylene: effect of surface and dispersion characteristics. Biomacromolecules **6**(5), 2732–2739 (2005)
99. S. Kalia et al., Nanofibrillated cellulose: surface modification and potential applications. Colloid Polym. Sci. **292**(1), 5–31 (2014)
100. M. Jonoobi et al., A comparison of modified and unmodified cellulose nanofiber reinforced polylactic acid (PLA) prepared by twin screw extrusion. J. Polym. Environ. **20**(4), 991–997 (2012)
101. M. Jonoobi et al., Preparation of cellulose nanofibers with hydrophobic surface characteristics. Cellulose **17**(2), 299–307 (2010)
102. N. Lin et al., Surface acetylation of cellulose nanocrystal and its reinforcing function in poly (lactic acid). Carbohydr. Polym. **83**(4), 1834–1842 (2011)
103. L.C. Tome et al., Surface hydrophobization of bacterial and vegetable cellulose fibers using ionic liquids as solvent media and catalysts. Green Chem. **13**(9), 2464–2470 (2011)
104. Y. Yoshida, L. Heux, A. Isogai, Heterogeneous reaction between cellulose and alkyl ketene dimer under solvent-free conditions. Cellulose **19**(5), 1667–1676 (2012)
105. M. Granstrom et al., Highly water repellent aerogels based on cellulose stearoyl esters. Polym. Chem. **2**(8), 1789–1796 (2011)
106. G. Rodionova, et al., Surface modification of microfibrillated cellulose films by gas-phase esterification: Improvement of barrier properties, in *Proceedings of the 2010 TAPPI International Conference on Nanotechnology for the Forest Product Industry,* Espoo, Finland, 2010
107. K. Missoum et al., Effect of chemically modified nanofibrillated cellulose addition on the properties of fiber-based materials. Ind. Crops Prod. **48**, 98–105 (2013)
108. M. Andresen et al., Properties and characterization of hydrophobized microfibrillated cellulose. Cellulose **13**(6), 665–677 (2006)
109. J. Lu, P. Askeland, L.T. Drzal, Surface modification of microfibrillated cellulose for epoxy composite applications. Polymer **49**(5), 1285–1296 (2008)
110. E. Malmström, A. Carlmark, Controlled grafting of cellulose fibres–an outlook beyond paper and cardboard. Polym. Chem. **3**(7), 1702–1713 (2012)
111. D. Roy et al., Cellulose modification by polymer grafting: a review. Chem. Soc. Rev. **38**(7), 2046–2064 (2009)
112. B. Peng et al., Chemistry and applications of nanocrystalline cellulose and its derivatives: a nanotechnology perspective. Can. J. Chem. Eng. **89**(5), 1191–1206 (2011)
113. Y. Habibi, Key advances in the chemical modification of nanocelluloses. Chem. Soc. Rev. **43**(5), 1519–1542 (2014)
114. A. Bhattacharya, B. Misra, Grafting: a versatile means to modify polymers: techniques, factors and applications. Prog. Polym. Sci. **29**(8), 767–814 (2004)
115. S. Pavlidou, C.D. Papaspyrides, A review on polymer–layered silicate nanocomposites. Prog. Polym. Sci. **33**(12), 1119–1198 (2008)
116. G. Gürdağ, S. Sarmad, Cellulose graft copolymers: synthesis, properties, and applications, in *Polysaccharide Based Graft Copolymers*, ed. by S. Kalia, M.W. Sabaa (Springer Berlin Heidelberg, 2013), pp. 15–57
117. K. Littunen et al., Free radical graft copolymerization of nanofibrillated cellulose with acrylic monomers. Carbohydr. Polym. **84**(3), 1039–1047 (2011)
118. A. Carlmark, E. Larsson, E. Malmström, Grafting of cellulose by ring-opening polymerisation—a review. Eur. Polymer J. **48**(10), 1646–1659 (2012)
119. M. Barsbay et al., Verification of controlled grafting of styrene from cellulose via radiation-induced RAFT polymerization. Macromolecules **40**(20), 7140–7147 (2007)
120. D. Roy, J.T. Guthrie, S. Perrier, Graft polymerization: grafting poly (styrene) from cellulose via reversible addition-fragmentation chain transfer (RAFT) polymerization. Macromolecules **38**(25), 10363–10372 (2005)

121. Y. Peng, et al. Drying cellulose nanocrystal suspensions, in *International Conference on Nanotechnology for Forest*. 2013. Stockholm, Sweden
122. Y. Peng, D.J. Gardner, Y. Han, Drying cellulose nanofibrils: in search of a suitable method. Cellulose **19**(1), 91–102 (2012)
123. Y. Peng et al., Influence of drying method on the material properties of nanocellulose I: thermostability and crystallinity. Cellulose **20**(5), 2379–2392 (2013)
124. Y. Peng, et al., Drying cellulose nanocrystal suspensions, in *Production and Applications of Cellulose Nanomaterials*, ed. by M.T. Postek, et al. 2013 (TAPPI Press, Peachtree Corners, GA), pp. 31–34
125. K. Missoum, J. Bras, M.N. Belgacem, Water redispersible dried nanofibrillated cellulose by adding sodium chloride. Biomacromolecules **13**(12), 4118–4125 (2012)
126. W.L.-S. Nieh, et al., *Roadmap for the Development of International Standards for Nanocellulose* (TAPPI, 2011)
127. K. Nelson, *Measurement Needs for Cellulose Nanomaterials* (2014)

Chapter 10
The Procter and Gamble Company: Current State and Future Needs in Materials Modeling

Russell H. DeVane, Matthew S. Wagner and Bruce P. Murch

Abstract New material development and commercial application is often quite complex due to the material properties and multiple transformations materials undergo in the supply chain, manufacturing process, and distribution of the finished product. In the fast-moving consumer goods industry of personal and household care products, these complexities are particularly acute due to the focus on and use of "commodity" materials that, at times, have significant variability in material properties. These materials are often formulated into complex liquids or assembled products, which undergo multiple transformations during making and can further undergo additional changes during distribution and use by the consumer (some desired, some not). At each stage of development, manufacturing, and distribution, materials models can be tremendously helpful in material and process selection and optimization. This chapter provides an overview of the current state-of-the-art in materials modeling as applied to the soft materials typically used in household and personal care products, with particular focus on modeling tools that span the length and time scales most relevant for modeling. We review the tools and methods in materials modeling and provide several examples where these tools have been used to guide the development of new materials. We conclude with commentary on additional advancements needed to drive practical application of these modeling tools more broadly for material development.

10.1 Introduction

Procter & Gamble is one of the largest consumer goods company in the world, with annual net sales at the time of this writing in excess of $70 billion. P&G started much more humbly in 1837 as a soap and candle-making company in Cincinnati, OH, due to the specific material resource available at that time: fats that resulted

R.H. DeVane (✉) · M.S. Wagner · B.P. Murch
The Procter & Gamble Company, 8256 Union Centre Blvd., West Chester, OH 45069, USA
e-mail: devane.rh@pg.com

L.D. Madsen and E.B. Svedberg (eds.), *Materials Research for Manufacturing*, Springer Series in Materials Science 224,
DOI 10.1007/978-3-319-23419-9_10

from the livestock industry in the area. This naturally derived material formed the feedstock of P&G's businesses and innovations for many years. As the business grew and product lines expanded, new feedstocks (both petroleum-based and plant-based) began to form the basis of P&G products. The design and optimization of critical raw materials such as surfactants and polymers had their origins in the company's early innovations in the use of fats and oils to create value-added products. Formulation of common consumer products such as shampoos and laundry detergents or fabrication of assembled products such as diapers all require significant understanding of material properties to design products with continually improving performance and value.

Our company's product and process engineering relies on our ability to use 'commodity' materials. While common in name, these are complex materials with varying specifications arising from supplier origin. Such variation arises from molecular weight distributions, chain branching, additives and impurities. Analytical descriptions are an incomplete starting point for modeling. Thus, we need to start with materials property measurements, and base modeling tactics on this reference. This rationale applies to performance in product context, where process history generates microstructural detail beyond conventional analytical measures. Semi-solid materials are typically not in thermodynamic equilibrium; rather they are trapped in non-equilibrium states. In the transitions from liquid to solid, local order formation phenomena happens faster than polymer reptation. Thus nano- to micro-scale ordered domains are tethered together by amorphous soft or glassy domains. Specific microstructural features are dependent on cooling rates and flow in the spinning of fibers or casting of films.

In recent years, high performance computing has emerged as a key new tool in the material design and optimization process for P&G. Advancements in the field of modeling over the past 15 years have transformed our ability to computationally represent and simulate complex, multi-scale formulated liquid and assembled products. These modeling tools have been applied to a diverse range of problems relevant to the consumer products industry. Self-assembly, phase behaviors, and properties of surfactant systems have been studied using molecular dynamics methods at both the atomistic and coarse-grained scales [1–10], Monte Carlo [11], and constitutive [12] models have also been used to study the adsorption behavior of molecules onto surfaces. In polymer development, molecular dynamics have been used to understand the structure of bulk polymer materials [13] and larger length scale finite element [14] and constitutive [15] models have been used to understand bulk behavior of polymer systems. Similarly, larger scale numerical models have been used to understand the disintegration of bulk materials in waste treatment [16] and fluid flow in absorbent materials [17, 18]. Modeling has become an increasingly important tool in particle and powder processing [19–29] as well as understanding particle properties [30–34] and studying microcapsule systems [35]. Beyond computational models for studying structural and bulk behaviors, computational methods for quantitative structure-activity relationship (QSAR) modeling have been used to study small molecules [36–42], and assess their human [43–53] and environmental [54–57] safety in silico.

A major gap in modeling materials for consumer products, e.g. plastic materials, is at the molecular description of their composition. It is our opinion that both measures and modeling of soft materials in context of specific compositions deserves more attention, and holds much value for productivity and innovation. This chapter discusses modeling aspects.

From molecular scale properties of soft materials, we recognize formation of higher scale nano- to micro-structures, and at these intermediate scales our macroscopic scale performance properties are determined. Despite impressive progress in molecular scale modeling of materials, it remains arguably a more practical approach to obtain samples, measure properties, and engineer the required performance… in the short term. Such approaches do not adequately guide design or specification of such materials, nor do they address the effects of additives. The latter have significant impact on the aging properties of materials, a central area of concern in our business.

Occasionally, years of R&D development effort have been spent trying to solve problems at the wrong scale, i.e. seeking mixing and forming methods when materials properties are inappropriate, or failing to recognize process solutions to complex fluid behaviors. Best practices in modeling start with measurement to serve as a reference point and signature of the underlying complexity. Emerging explicit modeling tactics add new insight, separating composition factors from process history.

This chapter will provide an introduction to some of the current challenges in material design and modeling associated with packaged consumer goods. A brief overview of the methodology we feel relevant to addressing these problems from first principles modeling approach will be presented. We will discuss the current literature on modeling efforts related to the challenges. We address general application challenges in context of critical gaps.

10.2 Today's Challenges: 1st Principles Determination of Materials Properties

Material modeling at P&G today is largely driven by phenomenological constructs captured in structural mechanics finite element methods, or multi-physics packages such as COMSOL for surface properties and transport phenomena. In these cases modeling is led by measurement and appropriate experimental determination of governing parameters. Such calibration captures essential specific materials properties. These techniques allow tremendous insight into the specification and control of assembled product processes and assembled articles properties, but they do not allow anticipation of materials properties given compositional changes. What happens when materials are compounded together? What is the impact of minor

additives like colorants, plasticizers, or impurities? Will a process yield a kinetically stable mixture of materials, or will the properties evolve over time toward an equilibrium state? We are interested in this aspect of materials modeling, to drive innovation of new soft materials, and anticipate fully the challenges of materials property stability for complex mixtures.

The practical rendition of such challenges are illustrated in application challenges such as:

- The loss of adhesive integrity over time due to diffusive loss of plasticizers and tackifiers.
- Package/formula incompatibilities including bottle deformation or breakage, delamination of layered composites, corrosion, or increased permeability.
- Extruded part deformation due to elongational and lateral stresses as influenced by additives or polymer material variation.
- Swelling or shrinkage of parts due to intrusion or loss of lower molecular weight species.
- Changes in surface tactile properties or appearance due to migrating species.
- Instabilities in film or fiber making processes due to mixing and flow dynamics during forming.
- Simulation capability for application to three-dimensional interactions of deformable hyperelastic solids with non-Newtonian fluid materials that include a capillary free surface.

These examples can be generalized into the following technical challenges, many of which come into play for any given application problem:

- How does polymer molecular structure control the nano- to micro-scale development of ordered, glassy, and amorphous domains?
- How do specific non-equilibrium nano- to micro-structural features impact mechanical properties (e.g., elastic or plastic responses, strain rate responses, and failure modes)?
- How do lower molecular weight additives affect micro- to macro-scale properties?
- How and at what time scale do additives migrate through polymeric networks and impact long time scale polymer relaxation effects?
- How do specific process paths in the forming of fibers, films and articles contribute to micro- to macro-scale properties?

Continued innovations in methods at various scales of simulation will allow development of governing relationships through multiscale modeling tactics, such that we can develop materials from molecular definition to macroscopic behaviors. Such research needs to be supported by both public and commercial sponsors. We advocate open science to drive fundamental capabilities, such that we lower the barrier for commercial enterprises to use virtual design for product innovations that drive economic productivity and a higher quality of living.

10.3 Tools and Methods in Materials Modeling

10.3.1 High Performance Computing

The computing resources we are familiar with today can trace their roots to the electronic numerical integrator and computer (ENIAC) of the late 1940s. With the steady increase in computing power from megaflops in the 1960s to the current petaflops performance, there has been roughly a doubling of computing speed every 2 years as described by Moore's Law. Exaflops scale computing is expected by 2020. This relentless increase in computing power has continuously expanded the boundaries of computing in scientific applications allowing larger and longer simulations to include more details of the system. Despite these large increases in computing power, and with the foreseeable resources, there are still significant limitations in linking molecular level detail with macroscopic properties. Consider, for example, that a state of the art simulation can model 10^9 atoms for 10^{-7} s. On the other hand, experimental scales are typically on the order of 10^{23} atoms with timescales that can be on the order of seconds, days, weeks or longer. For polymer systems, the relevant timescales are illustrated by considering that relaxation times in entangled polymers are on the order of $T_R \approx T_1 N_p^3 / N_E$ where N_P is the polymer chain length, N_E is the entanglement length and T_1 is an activation (or barrier crossing) time on the order of 10^{-12} s, which is larger than the molecular dynamics (MD) time step of roughly 10^{-15} s (a discussion on MD will follow below). As a result, T_R can easily exceed the MD timestep by ten orders of magnitude even for relatively short polymers (e.g. Np = 1000 and Ne = 100) [58]. These issues are compounded by the fact that the scaling of computational expense with system size is not linear, but is in fact less efficient. These limitations are a major obstacle to connecting molecular level representations directly to macroscopic properties and highlight the need for new methodologies that permit the exploration of all scales relevant to materials design.

10.3.2 Computational Material Science

Computational material science is a very broad topic and so we must stake out a relatively small region to discuss here. Computers are used extensively in all aspects of materials research from routine tasks such as plotting and performing basic statistical analysis on experimental data to complex first principles or phenomenological models that require large computational resources. We focus here on the latter and specifically on simulations of material from the atomic level up to the continuum level. Further, there is a range of material types including metals, ceramics, glasses, composites and polymers. This manuscript will focus on polymer-based materials. While the commercial polymer industry is still relatively young, polymer based materials continue to demonstrate their utility in more and

more applications. Elastomers, plastics, fibers, composites, organic electronics and biomimetic materials are some of the applications in which polymer-based materials have shown success or demonstrate great promise. While a number of Nobel Prizes have been awarded for polymer related research, the 2000 Nobel Prize, awarded for the discovery and development of conductive polymers, is especially indicative of the potential for broad ranging future applications.

10.3.3 Scales

Since we will primarily focus on particle-based simulations in this chapter, an important question that arises is that of resolution. Will each particle represent an atom, group of atoms or a region in space? Obviously, quantum and atomic level details ultimately dictate the macroscopic behavior of a polymer material. So in theory, we could completely model a system using that level of resolution. However, such approaches are computationally intractable beyond relatively small spatial and temporal scales. In practice, there is no single technique that can provide the breadth needed. While higher resolution methods provide a high level of detail, they limit the system sizes and time scales that can be simulated. On the other hand, lower resolution approaches sacrifice system details to access larger spatial and temporal scales. It is this tradeoff that creates the need for multiple methods. Figure 10.1 presents the various timescales and length scale involved and applicable methods. It should be noted that this doesn't point out hard limits for various methods, but in general, the most applicable range of a method. In the following paragraphs, we will discuss the various scales and techniques that are needed to cover a broad range of

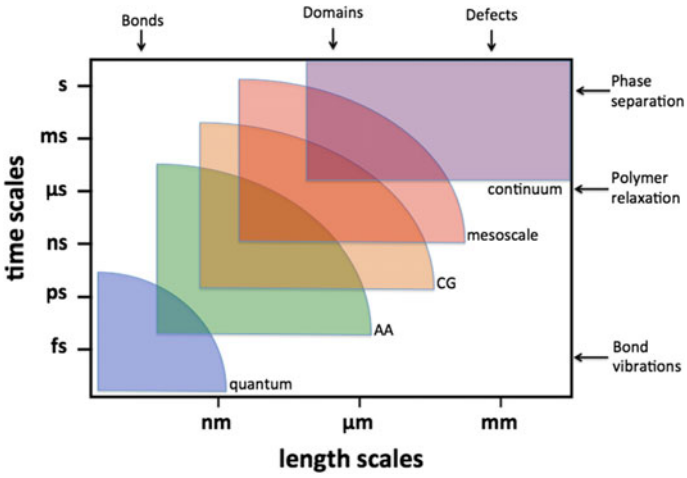

Fig. 10.1 Time and length scales associated with materials modeling and the relevant modeling approaches

time and space. While quantum mechanical (QM) approaches provide the most refined first principles representation of molecules, we will stick to classical methods in this chapter and forego a discussion on the topic.

10.3.4 Atomistic Scale

In the all-atom (AA) representation, each atom of the molecule is explicitly and independently represented. Typically, a single interaction point (particle) represents the atom center of mass with the electrons and protons effectively averaged into a single interaction potential. Atomistic descriptions provide a more direct link to "real" systems and permit the investigation of subtle molecular variations. As far as the computational burden, they are the least efficient of the simulation techniques discussed here. The dynamics are propagated in time using steps on the order of 10^{-15} s (in the case of dynamical simulations). This small time step leads to the inherent limitations in covering long timescales. In addition to the timescale limitation, the system size limitation arises due to the explicit representation of every atom. With two body interactions this implies that the computational work grows like N^2 where N is the number of atoms. In reality, more efficient algorithms reduce this computational expense to some extent but spatial limitations are still significant. Recently a 64 million-atom simulation of a HIV-1 capsid was carried out for 100 ns [59]. The simulation ran on 4000 Cray XE6 nodes using 128,000 cores and produced between 5 and 9 ns/day. While this heroic accomplishment highlights how far AA simulations have progressed, it nonetheless demonstrates the limitations associated with connecting AA simulations to macroscopic properties.

10.3.5 Coarse-Graining

To alleviate some of the computational burden associated with AA representations, methods using lower resolution descriptions of molecules have been developed. Groups of atoms are combined into single interaction sites (typically called beads) to produce what are known as coarse grain (CG) models. A number of computational benefits are produced with the CG approach including (1) a reduction in the number of degrees of freedom (many atoms become a single bead), (2) removal of high-frequency degrees of freedom allowing for a larger time step relative to AA methods and (3) higher diffusion coefficients resulting from the effectively "smoother" interaction potentials.

One of the primary drawbacks to CG simulations is the lack of a consistent parameterization strategy. Although a number parameterization approaches exist for AA representations, each are rather unambiguous as far as the methodology. This is not so for CG parameterization where the choice of resolution and methodology is a decision that is made by the CG model developer and depends on the target properties.

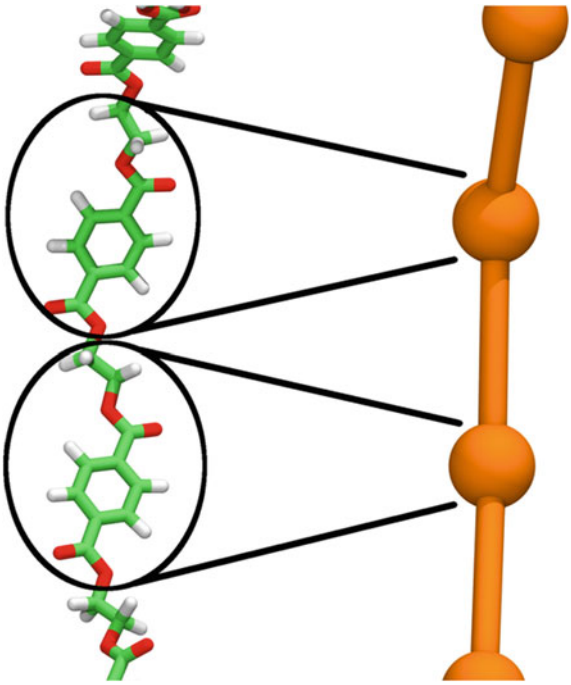

Fig. 10.2 Shown is the AA representation (*left*) and CG representation (*right*) of a fragment of a polyethylene terephthalate polymer

A common CG mapping is to group roughly three to four heavy (non-hydrogen) atoms into a single CG bead. However, other approaches may lump more atoms into a CG bead (e.g., each CG bead may represent a monomer or even several monomers). Figure 10.2 shows a section of polyethylene terephthalate polymer in the AA representation (left) and the CG representation (right). The level of mapping used in this example is one CG bead per monomer. Although a number of approaches have been published, there is no general consensus on what represents the best methodology for developing CG models for polymers or other materials [58, 60–68].

10.3.6 Molecular Dynamics and Monte Carlo

Typically simulations at the AA and CG levels are carried out using either MD or Monte Carlo (MC) approaches. MD and MC simulations are particle-based methods grounded in statistical mechanics. The interactions between particles are based on force fields, which describe the potential energy surfaces of molecules. Typically, the total interaction potential is additive and composed of intramolecular and intermolecular contributions. The intramolecular potential typically includes a bonded potential, angle potential and dihedral (improper) potential. The

intermolecular potential is composed of a van der Waals contribution and often an electrostatic contribution. Due to its long-range nature, the electrostatic contribution is typically a computational bottleneck in MC and MD simulations. MD is a deterministic method based on solving Newton's equations of motion while MC is a non-deterministic method based on stochastic sampling. As a result MD provides dynamical information while traditional MC does not. In MC, the stochastic trajectory samples only the relevant regions of phase space and from these, relevant properties are calculated. MC simulations can be lattice or continuum in nature [69]. As discussed above, the primary limitation for both AA MD and CG MD is the relatively small spatial and temporal scales that are practical. Another issue is the limitation of force fields to accurately describe the system of interest [70].

10.3.7 Mesoscale: Dissipative Particle Dynamics and Brownian Dynamics

When representations at the CG level are not sufficient to reach the time and length scales needed, mesoscale representations can be used. Technically speaking, this scale is also a CG level representation albeit typically a coarser one [71]. The real differentiation comes in the engine used to propagate the dynamics. While MD is suitable for typical CG mappings of three to four heavy atoms, it is not suitable for coarser mappings where friction and stochastic forces dominate the interactions. In this situation, stochastic dynamics is more appropriate [64]. Dissipative particle dynamics (DPD) has become the primary mesoscale simulation technique [72]. In DPD simulations, the particles, or beads, interact via "soft" potentials and are propagated in time in accordance with Newton's equations of motion. The forces involved in DPD are the conservative force, the dissipative force and a random force. The interaction parameters have been linked to the χ-parameters of the Flory-Huggins theory of polymers [73]. DPD is able to capture Navier-Stokes hydrodynamics in relatively small systems [72, 74]. One problem with DPD is the loss of connectivity in polymer chains which can permit polymers to pass through one another effectively removing entanglements [64]. Some methods have been developed to overcome this issue [75, 76].

Smoothed particle hydryodynamics (SPH) is another mesoscale particle based Lagrangian method that is useful for computational fluid dynamics [77, 78]. The mesh-free nature of SPH allows for large deformations [78]. Smoothed dissipative particle dynamics (SDPD) is a further extension based on SPH and DPD, which capture aspects of both methods [79]. This method assures that thermal fluctuations are described correctly, which is not guaranteed in SPH and also alleviates a number of problems that exist with DPD [79]. It is not yet clear what the full potential of methods based on SPH will be.

Another technique used for mesoscopic simulations is Brownian dynamics (BD). This approach addresses both the timescale and spatial scale issues associated with

simulating polymers systems. BD permits the separation of processes with significantly different time scales. For example, in polymer solutions, the polymer dynamics take place on much longer timescales than the solvent dynamics (for typical solvents). The fast solvent and polymer dynamics are averaged out thus allowing the more relevant slower polymer dynamics to set the timescales of the simulation. Of course, there is an assumption that a detailed description of the solvent dynamics is not needed. The solvent dynamics and other fast processes are replaced by stochastic noise. In fact, the solvent is completely implicit. The removal of the fast polymer dynamics is accomplished through coarse graining of the polymer molecule, which also reduces the spatial scale burden [80, 81]. The primary differences between DPD and BD is that BD does not satisfy Newton's third law and so does not conserve momentum; this leads to an inability to reproduce hydrodynamic behavior. For asymmetric block copolymers, hydrodynamic forces have been shown to play a significant role in the kinetics of microphase separation [74].

10.3.8 Field Theory

Field theories, in the context discussed here, are an approach to simplify the many body problem associated with modeling polymer systems. In technical terms, the approach involves transforming the statistical mechanical partition function from its standard many-dimensional integral representation over the particles into a functional integral representation over an auxiliary field. In essence, instead of each body interacting with every other body, each body interacts with an effective field created by every other body. The result is a significant reduction in the number of interactions that need to be calculated. Unfortunately, this partition function reformulation results in complicated integrals that are analytically intractable. So the challenge is to find methods that approximate the solution or solve it numerically. In general there are three approaches to dealing with this complexity: (1) simplify the theory such that analytical solutions are possible, (2) simplify the solution with analytical approximations then use numerical methods and (3) solve the equations associated with the exact field theory using numerical methods [82].

The mean field approximation, also called self-consistent field theory (SCFT) is a widely used analytical approximation. Approximations to SCF include the Ginzburg–Landau (GL) theory and density functional theory (DFT). Time-dependent Ginzburg–Landau (TDGL) theory is useful for studying the kinetics of polymer phase separation [83]. The combination of dynamic density functional theory (DDFT) and TDGL is the basis for the MesoDyn software package from Biovia [84]. A more recent method for the direct numerical sampling of the relevant integrals is known as field-theoretic simulations (FTS) [85]. FTS can also retain atomic level details.

10.3.9 Continuum Methods

In contrast to the methods discussed so far, continuum methods are different in that they rely on a description of the system as a continuous mass as opposed to discrete particles. As a result, assumptions are made regarding the continuity of the system and the underlying molecular composition is not considered directly. Instead, the response of the system to external stimuli are represented though constitutive relationships. These relationships can be phenomenological or derived from first principles. For example, Hooke's Law describes the relationship between applied stress and resulting strains and is in fact a constitutive equation. At large enough length scales, disregarding the molecular make up of a material is a reasonable approximation and continuum models are extremely accurate. Continuum methods provide access to far greater spatial and temporal scales than are accessible by particle based methods. A drawback to continuum methods is that the constitutive equations will fail, in general, when the underlying composition is changed. Such changes will typically require the development of new descriptions of the system.

10.3.10 Multiscale Modeling

The wide range of temporal and spatial scales is perhaps the biggest challenge associated with materials modeling (accurate models are also a concern) [86, 87]. As a result, multiple techniques are needed in order target the specific scales. As we have discussed above, there are a number of modeling techniques that cover various size and timescales. Linking methods that cover different spatial and temporal scales has received considerable attention since it provides the opportunity to effectively extend the range of applications. In general, there are two ways to achieve this goal: (1) the methods can be combined into a holistic modeling approach or (2) a parametric approach can be taken where results from one model are used as input in another.

A number of groups have attempted the first approach. Efforts to link AA MD simulations with CG MD simulations have demonstrated the possibility of mixing scales [88–91]. These methods allow for specific regions or components of the system to be represented at a high resolution (AA) while the "less interesting" part of the system is modeled more efficiently with a CG resolution. Less straightforward are attempts to mix atomic and continuum methods where critical system information calculated at the molecular scale is propagated into the continuum model. A critical step is the transformation of information from a "discrete" system (molecular level) to the continuum level [92, 93]. While a number of different schemes exist for linking the two scales together, there is no general consensus on the best method, which will likely depend on the problem at hand [94–104]. The calculation of non-Newtonian flows: finite elements and stochastic simulation

technique (CONNFFESSIT) is another example of mixed scales where finite element calculations are performed with the constitutive equation replaced by stochastic simulations of polymer dynamics [102, 103].

10.4 Applications

10.4.1 Nano- and Microstructure of Soft Materials

A cooling polymer melt can undergo phase separations (liquid/liquid, liquid/solid) and glass transitions that nucleate and progress to arrested non-equilibrium configurations due to the widely different time scales between these ordering transitions and polymer chain relaxation processes [68]. The detailed nano- to micro-structured mixture of domains is of course highly compositionally dependent as well as process dependent, i.e. influenced by cooling rates and flow. With both compositional complexity and the resulting microstructural manifestations, specific design and engineering efforts are necessarily sample dependent. The challenge to leverage molecular scale simulation tools becomes how to calibrate against reference samples and anticipate how compositional factors will influence similar samples as we envision new materials and compositions.

In our company examples, most common challenges involve low molecular weight ingredients that dictate formula—package compatibility, additives in films, coatings, or adhesives. A few notable examples in our recent R&D efforts involve polymer material advances, such as Nodax [105, 106], branched polyolefins, absorbent foam materials (Infinicel), and inorganic reinforced packaging materials. Molecular level modeling has played only minor roles in such development efforts, with qualitative principles appropriately guiding composition designs. The major resulting challenges in these efforts, and the near term opportunities for molecular level modeling is stability. We need to anticipate quantitatively how material microstructure will evolve over long time scales based on compositional control, in reference to existing samples and assuming controlled process conditions. Furthermore, we need to understand how microstructural changes impact the macroscopic properties and behavior of the material.

The desire to develop new sustainable polymeric materials based on non-petroleum resources is significant and has been pursued for several decades. Over 30 years ago a major effort was initiated to develop novel materials based on bacterial byproducts. Polyhydroxyalkanoates (PHAs) are produced by a large number of bacteria as an energy source [105]. Being an energy source presents another benefit since natural microorganisms can break down the material and use the resulting byproducts as nutrients. This biodegradability coupled with its renewable and sustainable characteristics make PHAs a very promising material. Commercialization of PHAs, in particular poly(hydroxybutyrate) (PHB), has taken

place under the trade name Biopol with a potential in medical applications especially those related to implantation in the human body.

P&G began developing PHAs in the late 1980s and over the course of two decades established a substantial amount of understanding and intellectual property. Nonetheless, this development time reflects the complexity involved with bringing a new material to market. The material developed within P&G, known by the trade name Nodax, is a copolymer of various (R)-3-hydroxyalkanoate (3HA) monomers and (R)-3-hydroxybutyrate (3HB). These materials were produced by bacterial fermentation of biomass [106].

A number of challenges are present with the development of such materials. PHBs in general are hard and brittle with a large degree of crystallinity making them less attractive candidates as materials where plastic behavior is important. We explored several copolymer blends to produce materials with desired properties. As mentioned above, Nodax is composed of 3HB and other 3HA monomers; the key to Nodax is the medium-chain-length of the side groups associated with the 3HA monomers. It was found that the 3HA monomers needed side groups with at least three carbons, which essentially produces a branched polymer [106]. Examples of such monomers are (R)-3-hydroxyhexanoate (3HHx), (R)-3-hydroxyoctanoate (3HO), (R)-3-hydroxydecanoate (3HD) and (R)-3-hydroxyoctadecanoate (3HOd). The result of such blends yields a polymer with polyolefin like thermo mechanical properties and polyester like physicochemical properties. The inclusion of the medium-chain-length monomers lowers the melt temperature (T_m) and reduces the level of crystallinity. As a consequence, it produces polymeric material with more plastic behavior. Interestingly, the inclusion of two carbons in the side group does not lead to significant changes in the properties relative to PHB.

A problem with some PHAs has been related to the aging behavior of the material [107]. They are known to undergo secondary crystallization leading to significant changes in the mechanical properties of the material over time. The properties can be modulated by the ratio and nature of the copolymers. Considering a PHB base polymer, Noda et al. demonstrated that the variation in PHA copolymer, especially the side groups as discussed above, can be used to design specific material properties [105]. The process of alloying in polymeric materials provides the opportunity to produce material highly refined for a specific application. However, the combinatorics of the problem makes it daunting.

Existing modeling techniques were insufficient during the development lifecycle to define specific impacts of copolymer blends, particularly how microcrystalline domains will nucleate and evolve over long time scales. Coarse grain techniques have been effective at illustrating qualitative trends. Given many instances of more elaborate stereochemical functional groups and hydrogen bonding contributions to semi crystalline domain evolution there remains significant opportunity to elaborate these techniques. Even small molecule crystal nucleation and growth rate is a major challenge receiving significant industrial funding and academic contributions.

10.4.2 Assessment of Mechanical Properties

The mechanical properties of polymer systems are of key importance to industrial applications. Relatively early on, Brown and Clarke carried out simulations of polyethylene like polymers to characterize elasticity, yield, plastic flow and viscoelasticity [108, 109]. That work demonstrated that simulation methods could provide qualitatively realistic elastic behavior when compared to experimental results.

Many excellent modeling efforts have succeeded in basic characterization of amorphous (or semicrystalline) polymeric materials, e.g., polyolefins, polyamides and polyesters. Methods to predict mechanical properties based on AA MD descriptions have been developed and applied to a number of systems [109–112]. Dynamic methods, based on monitoring fluctuations of molecular simulations and small deformation methods provide a range of approaches with varying strengths and weaknesses [110, 111]. While non-glassy amorphous systems are already challenging, modeling glassy amorphous polymer systems presents a more significant challenge. For example, the inability to efficiently sample phase space makes the fluctuation method less feasible [111]. Despite this difficulty, there have been advancements in methods to treat such systems.

A number of attempts have been made to use MD simulations to link chemical structure with mechanical behavior. MD simulations of glassy polymers under uniaxial strain have been carried out to investigate elastic and yield behavior [113]. The simulation predictions of the Poisson's ratio, Young's modulus and temperature dependence of the yield peak showed good agreement with experimental measures. This work was followed by a side-by-side study of the atactic polystyrene (PS) and bisphenol. A polycarbonate (PC) which possess different mechanical properties [114]. It was demonstrated that MD simulation is a powerful tool for linking molecular level details (e.g., inter and intrachain interactions) to mechanical properties. MD simulations have also been used to investigate the molecular level mechanisms that lead to the increase in mobility that accompanies plastic deformation in glassy amorphous polymers [115, 116]. Simulations show an increase in torsional transition rates; backbone rotations and chain percolation lead to yield. Simulations have shown consistently that no significant changes in bond length or bond angle distributions occur with plastic deformation. Interestingly, prior to yield, the distribution of dihedral angles remains constant although the transitions between states increase. To probe the heterogeneity, yield behavior and the origins of strain hardening in amorphous polymer glasses demonstrates the usefulness of the methods [117–120].

A number of groups have demonstrated the power of MD simulations to probe properties not easily measured experimentally. For example, probing local mechanical properties is a significant advantage of the method [121, 122]. The properties that result from the presence of interfaces in heterogeneous polymers cannot be predicted based on using available data for pure interfaces of each component in an additive way. However, simulation techniques can be used to

directly measure the mechanical properties associated with such interfaces and even spatially resolve the properties around the interface. Such information could be use to developed constitutive models. For example, Riccardii et al. used MD to probe the solid-soft interface polystyrene composites [123]. Their findings indicated that the methods overestimate the Poisson's ratio for polystyrene relative to experiment. This finding could be explained by the relatively small systems sizes explored in the simulation relative to the experiments. It could also be explained by a deficiency in the forcefield [123]. Despite these shortcomings, the method demonstrates the utility of molecular modeling to provide insight that is difficult to obtain through experiment. In fact, significant work has gone into modeling composites including nanotube-reinforced and nanoclay-reinforced polymers [124–127]. There the desire is to model the mechanical properties of the composites as a function of the nanoparticle size and the molecular details of the nanoparticle/polymer interface [127]. The challenge is covering the lengthscales involved with defining a nanoparticle, which can range from nanometers to microns, while also capturing the molecular level detail of the interface. Parameteric multiscale approaches have been used to address these challenges including mapping from AA to CG scales, carrying out CG simulations to relax polymer systems then "reverse mapping" the CG system back to an AA representation [127]. Continuum mechanics were then used to model the mechanical properties of the system.

10.4.3 Solute Impacts on Mechanical Properties

Company experience in the area of solute impacts is increasing rapidly, but still is relatively unelaborated. We expend considerable experimental efforts on package compatibility, with perfume ingredients playing a significant role in varying behaviors. Several modeling methods are effective in predicting liquid/polymer partitioning trends, but these impacts on polymer swelling, saturation, permeation rate and subsequent mechanical properties evolution appear non-obvious. The details of polymer composition, microstructure, and process history have not yet been integrated into our studies. For example, QSAR models have provided good guidance in a survey of perfume raw material permeation of film materials. While the overall molecular structure trends were quite similar, overall permeation rates were seen to vary by a few orders of magnitude. Similarly we should expect swelling and mechanical properties to reflect material process history and so we need to look to coupled transport and property evolution techniques to make good progress.

Academic studies have addressed solute effects regarding the balance of arrested mixtures of amorphous, glassy and/or semi crystalline domains. Most commonly the initial transformation is to a glassy state with the glass transition temperature (Tg) being an informative property of the system. Mechanical properties are tightly linked to the transition from a glass to a liquid. This transition is typically accompanied by a significant decrease in the elastic moduli in polymer melts [68].

The addition of lower molecular weight components to a polymer system can lead to changes in Tg and the associated mechanical properties of the glass. This phenomenon is well known and often used for achieving desired material properties. For example, plasticizers are used to lower the glass transition temperature or increase the plasticity (decreasing the elastic moduli) of the material. On the other hand, it is possible to lower Tg while also increasing the elastic modulus of the polymer. Compounds that yield this effect are known as antiplasticizers. This seemingly inconsistent behavior is telling of the complexity of polymer-additive mixtures.

Computational efforts have yielded insights into the depression of Tg. Lattice models and molecular simulations have demonstrated that the depression of Tg is essentially a linear function of the mole fraction of the additive. This appears to be a universal relationship for Tg depression. The decrease in Tg has been rationalized by packing arguments. Generalized entropy theory provided further insights into the molecular characteristics that dictate whether an additive will have a plasticizing effect or an anti plasticizing effect [128]. Small, flexible additives with strong attractive interactions with the polymer were found to have an anti plasticizing effect creating a stronger glass. Small, flexible additives with weak attractive interactions with the polymer yield a plasticizing effect. The increase in the elastic moduli (for anti plasticizers) has been rationalized by considering that the strongly interacting additive acts as an effective crosslinking agent whereas this effect is missing in the additives that interact weakly with the polymer [129]. Molecular simulations probing molecular packing and material stiffness indicated that the impact of antiplasticizers on polymer melts was dictated by changes in the local mechanical properties [130].

10.4.4 Phase Stability

The phase separation of additives in polymer blends is well known and several methods are appropriate depending on the problem context. The separation of polymer blends is well known and dominated by entropic effects for any mismatch in solubility. As molecular weight differences increase, the precise effect of solubility is increasingly important, and the accurate assessment of the polymer contribution is more challenging. These latter situations apply to the assessment of plasticizers in a wide range of materials such as films, adhesives, and articles of varying hardness.

Whether liquid/liquid phase separation of additives will occur is usually accessible by modeling, but methods do not address the rate of separation, nor provide specific information on metastable states as additives demix and one or the other continuous phase dominates overall material properties, usually the polymer. Such pathway dependent insight requires explicit simulation methods, but polymer relaxation times as well as other likely substructural confinements make these studies impractical by current methods and computational power. Most likely

additional factors are relevant when low molecular weight components also display assembled structures, statistical thermodynamic methods do not adequately address such substructure, and explicit methods should be employed.

DPD simulations have been used extensively to study polymer phase behavior. One common area of application has been in polymer blending where the fine tuning of polymer behavior can be achieved. The difficulty in blends is that care must be taken to assure they are compatible. DPD simulations have been used to study the compatabilizing effects of graft copolymers [131–133]. DPD was also used to study the microphase separations in random copolymers [134]. Other groups have used MC simulations to investigate the topic [135]. DPD and BD were used to investigate the role of hydrodynamics in phase separation [74]. Interestingly in that work, the absence of hydrodynamics in the BD method led to the system being trapped in a metastable state when the hexagonal phase was expected. On the other hand, the lamellar phase forms much faster suggesting that the hexagonal and lamellar phases form via different mechanisms.

Self-assembled microstructure has also been investigated with SCFT [136, 137]. Muller et al. used a single chain in mean field (SCMF) method to study spinodal decomposition in a binary system and evaporation of a solvent from a low molecular weight thin polymer film [138]. While this particular scheme overcomes computational barriers, it is restricted to early stages of phase behavior due to the neglect of hydrodynamic flow. To overcome such issues, attempts have been made to develop hybrid models that include hydrodynamics in self-consistent field (SCF) methods [139–141]. This work was consistent with other finding on the role of hydrodynamics. Sandhu et al. compared DPD and SCF for studying microphase separation [142].

Additives are known to have an impact on polymer properties. Gases, for example, are known to cause swelling or plasticization in some materials and are even used intentionally as plasticizers [143, 144]. Early on, methods were developed to investigate such systems using MD simulations [145]. Further methodology has appeared to calculate sorption isotherms up to high penetrant fugacity in glassy polymers with application to glassy polystyrene [146]. AA MD and MC simulations have been used to the absorption of solutes into polymer systems [147, 148]. Some of this work has been extended to predicting miscibility of plasticizers in polymer blends [149]. In that work, the techniques were shown to be useful for modeling blends and predicting enthalpies of vaporization.

10.5 Conclusions

Through high performance computing and the many demonstrated examples of multiscale modeling tactics, we have significant opportunity to address the performance and stability of soft materials and the effects of additives. Continued innovation of methods is key to practical application. To succeed we advocate method development in molecular level methods that can properly inform and assist

application of higher scale fluid dynamics, finite element, or diffusive transport models.

Solubility modeling provides the basis to understand the partitioning of additives in polymeric materials and their surroundings, be it air or product formulations. It also forms the basis for further modeling efforts to probe the impact of additives on properties such as phase transitions, changes microstructure and subsequent mechanical properties. While these methods are gaining maturity, several important aspects deserve attention:

1. Selection of optimal force fields for molecular dynamics is still critical for accurate property prediction, but broad consensus of best methods is lacking. We still can succeed by tactics of relative comparison; experiment and modeling in complement is essential.
2. Consistent and transferrable potentials for coarse grain depictions are key.
3. A gap is the inclusion of stereochemical orientation of hydrogen bonding. Emerging methods show promise either by localization of points of interaction on coarse grain beads, or dual scale simulation tactics.
4. Liquid-solid transitions are a challenge at atomistic scales, and at coarse grain scales even relative composition comparisons are uncertain. Such details are critical since they impact the degree to which additives partition in and interact with the soft material. Getting the nanoscale to microscale growth and constraints of solid domains right is essential and largely undemonstrated today.

Methods that couple molecular scale to higher scales deserves proper summary elsewhere, in the context of specific applications. We need to use the specificity of molecular scale simulations to inform elaborated fluid dynamics methods, for example to gain insight into flow history effects. In semi-solid states we need continued elaboration of finite element methods to consider details of entanglement, weak reversible bonds, and temporal evolution schemes. Coupled multiscale evaluations are at proof of principle stage and are yielding insights not accessible by analytical measurement.

Theory and computer code development deserves some comment. Collaborative commercial development has been successful for widely used platforms but is sometimes insufficient to drive fundamentally new capabilities. Publically funded collaborations such as those that led to platforms like LAMMPS, GROMACS, NAMD, GAMESS, NWCHEM and others have been critical to allow exploration, commercial and academic. These are collaborations that should be encouraged, co-funded, and focused.

New entrants into this field (and those training them in academic institutions) must focus on the fundamental computational skills and methods described above, but computational expertise alone is insufficient for breakthroughs in this field. Such breakthroughs will come most quickly at the intersection of modeling and computational sciences with material science and engineering and the chemical, physical, and biological sciences. Measurement science and the ability to prototype new materials are also critical to validate computational models as they are developed. New and experienced practitioners in this field must be able to integrate

computational approaches with experimental design and results to drive the development of truly predictive materials models.

While computational applications to soft materials have provided significant benefits and insights, there is much more that could be contributed. Currently the field has matured to a state where industrial applications could provide much more productivity as well as creativity. We are recognizing these opportunities where longer-term investments in modeling will pay off.

References

1. J.C. Shelley, M.Y. Shelley, R.C. Reeder, S. Bandyopadhyay, M.L. Klein, A coarse grain model for phospholipid simulations. J. Phys. Chem. B **105**(19), 4464–4470 (2001)
2. J.C. Shelley, M.Y. Shelley, Computer simulation of surfactant solutions. Curr. Opin. Colloid Interface Sci. **5**, 101–110 (2000)
3. X. He, W. Shinoda, R. DeVane, K.L. Anderson, M.L. Klein, Paramaterization of a coarse-grained model for linear alkylbenzene sulfonate surfactants and molecular dynamics studies of their self-assembly in aqueous solution. Chem. Phys. Lett. **487**, 71–76 (2010)
4. Y. Wang, J.A. Wallace, P.H. Koenig, J.K. Shen, Molecular dynamics simulations of ionic and nonionic surfactant micelles with a generalized born implicit-solvent model. J. Comput. Chem. **32**(11), 2348–2358 (2011)
5. B.H. Morrow, P.H. Koenig, J.K. Shen, Atomistic simulations of pH-dependent self-assembly of micelle and bilayer from fatty acids. J. Chem. Phys. **137**(19), 194902 (2012)
6. W. Shinoda, R. DeVane, M.L. Klein, Computer simulation studies of self-assembling macromolecules. Curr. Opin. Struct. Biol. **22**(2), 175–186 (2012)
7. B.H. Morrow, P.H. Koenig, J.K. Shen, Self-assembly and bilayer-micelle transition of fatty acids studied by replica-exchange constant ph molecular dynamics. Langmuir **29**(48), 14823–14830 (2013)
8. G. Fiorin, M.L. Klein, R. DeVane, W. Shinoda, Computer simulation of self-assembling macromolecules. Adv. Polym. Sci. **262**, 93–108 (2013)
9. X. Tang, P.H. Koenig, R.G. Larson, Molecular dynamics simulations of sodium dodecyl sulfate micelles in water—the effect of the force field. J. Phys. Chem. B **118**(14), 3864–3880 (2014)
10. R.C. Runnebaum, E.J. Maginn, Molecular dynamics simulations of alkanes in the zeolite silicalite: Evidence for resonant diffusion effects. J. Phys. Chem. B **101**(33), 6394–6408 (1997)
11. C. Wijmans, P. Linse, Monte Carlo simulations of the adsorption of amphiphilic oligomers at hydrophobic interfaces. J. Chem. Phys. **106**(1), 328–338 (1997)
12. D.H. Melik, Adsorption from a well-stirred solution of finite volume. I. Linear adsorption kinetics through a stagnant boundary layer. J. Colloid Interface Sci. **138**(2), 397–413 (1990)
13. H. Furuya, M. Mondello, H.J. Yang, R.J. Roe, R.W. Erwin, C.C. Han, S.D. Smith, Molecular dynamics simulation of atactic polystyrene. 2. Comparison with neutron scattering data. Macromolecules **27**(20), 5674–5680 (1994)
14. D.C. Fleming, C. Morrow, C.W. Clarke, C.E. Bird, Finite element simulation of delamination with application to crashworthy design. J. Am. Helicopter Soc. **53**(3), 267–281 (2008)
15. A. Kaushik, A. Waas, E. Arruda, A constitutive model for finite deformation response of layered polyurethane-montmorillonite nanocomposites. Mech. Mater. **43**(4), 186–193 (2011)

16. F. Karadagli, D. McAvoy, B. Rittmann, Development of a mathematical model for physical disintegration of flushable consumer products in wastewater systems. Water Environ. Res. **81**(5), 459–465 (2009)
17. H.J.G. Diersch, V. Clausnitzer, V. Myrnyy, R. Rosati, M. Schmidt, H. Beruda, B. J. Ehrnsperger, R. Virgilio, Modeling unsaturated flow in absorbent swelling porous media: Part 1. Theory. Transp. Porous Media **83**(3), 437–464 (2010)
18. H.J.G. Diersch, V. Clausnitzer, V. Myrnyy, R. Rosati, M. Schmidt, H. Beruda, B.J. Ehrnsperger, R. Virgilio, Modeling Unsaturated Flow in Absorbent Swelling Porous Media: Part 2. Numerical Simulation. Transp. Porous Media **86**(3), 753–776 (2011)
19. J.P. Hecht, C.J. King, Spray drying: Influence of developing drop morphology on drying rates and retention of volatile substances. 2. Modeling. Ind. Eng. Chem. Res. **39**(6), 1766–1774 (2000)
20. A. Braumann, M.J. Goodson, M. Kraft, P.R. Mort, Modelling and validation of granulation with heterogeneous binder dispersion and chemical reaction. Chem. Eng. Sci. **62**(17), 4717–4728 (2007)
21. D. Ronen, C.F.W. Sanders, H.S. Tan, P.R. Mort, F.J. Doyle, Predictive modeling of key process variables in granulation processes based on dynamic partial least squares. IFAC Proc. **7**, 411–416 (2009)
22. C.S. Handscomb, M. Kraft, A.E. Bayly, A new model for the drying of droplets containing suspended solids after shell formation. Chem. Eng. Sci. **64**(2), 228–246 (2009)
23. C.S. Handscomb, M. Kraft, A.E. Bayly, A new model for the drying of droplets containing suspended solids. Chem. Eng. Sci. **64**(4), 628–637 (2009)
24. A. Braumann, M. Kraft, P.R. Mort, Parameter estimation in a multidimensional granulation mode. Powder Technol. **197**(3), 196–210 (2010)
25. E. Supuk, A. Hassanpour, H. Ahmadian, M. Ghadiri, T. Matsuyama, Tribo-electrification and associated segregation of pharmaceutical bulk powders. KONA Powder Part. J. **29**, 208–223 (2011)
26. D. Ronen, C.F.W. Sanders, H.S. Tan, P.R. Mort, F.J. Doyle, Predictive dynamic modeling of key process variables in granulation processes using partial least squares approach. Ind. Eng. Chem. Res. **50**(3), 1419–1426 (2011)
27. A. Clark, P. Mort, R. Behringer, Coarse graining for an impeller-driven mixer system. Granular Matter **14**(2), 283–288 (2012)
28. V. Vidyapati, S. Subramaniam, Granular flow in silo discharge: discrete element method simulations and model assessment. Ind. Eng. Chem. Res. **52**(36), 13171–13182 (2013)
29. S.C. Thakur, H. Ahmadian, J. Sun, J.Y. Ooi, An experimental and numerical study of packing, compression, and caking behaviour of detergent powders. Particuology **12**(1), 2–12 (2014)
30. R.B. Pandey, K.L. Anderson, B.L. Farmer, Multiscale dynamics of an interacting sheet by a bond-fluctuating Monte Carlo simulation. J. Polym. Sci., Part B: Polym. Phys. **44**(18), 2512–2523 (2006)
31. R.B. Pandey, K.L. Anderson, B.L. Farmer, Exfoliation of stacked sheets: Effects of temperature, platelet size, and quality of solvent by a Monte Carlo simulation. J. Polym. Sci., Part B: Polym. Phys. **44**(24), 3580–3589 (2006)
32. C.Y. Yang, Y. Ding, D. York, W. Broeckx, Numerical simulation of sedimentation of microparticles using the discrete particle method. Particuology **6**(1), 38–49 (2008)
33. C.C. Chiu, R.H. DeVane, M.L. Klein, W. Shinoda, P.B. Moore, S.O. Nielsen, Effect of carboxylation on carbon nanotube aqueous dispersibility: A predictive coarse-grained molecular dynamics approach. J. Phys. Chem. C **116**(43), 23102–23106 (2012)
34. Y. Yang, A. Corona, M.A. Henson, Experimental investigation and population balance equation modeling of solid lipid nanoparticle aggregation dynamics. J. Colloid Interface Sci. **374**(1), 297–307 (2012)
35. R. Mercade-Prieto, B. Nguyen, R. Allen, D. York, J.A. Preece, T.E. Goodwin, Z. Zhang, Determination of the elastic properties of single microcapsules using micromanipulation and finite element modeling. Chem. Eng. Sci. **66**(10), 2042–2049 (2011)

36. D.T. Stanton, Development of a quantitative structure-property relationship model for estimating normal boiling points of small multifunctional organic molecules. J. Chem. Inf. Comput. Sci. **40**(1), 81–90 (2000)
37. D.T. Stanton, S. Dimitrov, V. Grancharov, O.G. Mekenyan, Charged partial surface area (CPSA) descriptors QSAR applications. SAR QSAR Environ. Res. **13**(2), 341–351 (2002)
38. D.T. Stanton, On the Physical Interpretation of QSAR Models. J. Chem. Inf. Comput. Sci. **43** (5), 1423–1433 (2003)
39. R. Guha, D. Stanton, P. Jurs, Interpreting computational neural network quantitative structure-activity relationship models: a detailed interpretation of the weights and biases. J. Chem. Inf. Model. **45**(4), 1109–1121 (2005)
40. J. Jaworska, N. Nikolova-Jeliazkova, T. Aldenberg, QSAR applicability domain estimation by projection of the training set in descriptor space: A review. ATLA Altern. Lab. Anim. **33** (5), 445–459 (2005)
41. D.T. Stanton, On the importance of topological descriptors in understanding structure-property relationships. J. Comput. Aided Mol. Des. **22**, 441–460 (2008)
42. D.T. Stanton, QSAR and QSPR model interpretation using partial least squares (PLS) analysis. Curr. Comput. Aided Drug Des. **8**(2), 107–127 (2012)
43. J.C. Phillips, W.B. Gibson, J. Yam, C.L. Alden, G.C. Hard, Survey of the QSAR and in vitro approaches for developing non-animal methods to supersede the in vivo LD50 test. Food Chem. Toxicol. **28**(5), 375–394 (1990)
44. J.D. McKinney, A. Richard, C. Waller, M.C. Newman, F. Gerberick, The practice of structure activity relationships (SAR) in toxicology. Toxicol. Sci. **56**(1), 8–17 (2000)
45. A. Kulkarni, A.J. Hopfinger, R. Osborne, L.H. Bruner, E.D. Thompson, Prediction of eye irritation from organic chemicals using membrane-interaction QSAR analysis. Toxicol. Sci. **59**(2), 335–345 (2001)
46. K. Kodithala, A.J. Hopfinger, E.D. Thompson, M.K. Robinson, Prediction of skin irritation from organic chemicals using membrane-interaction QSAR analysis. Toxicol. Sci. **66**(2), 336–346 (2002)
47. J.S. Jaworska, M. Comber, C. Auer, C.J. Van Leeuwen, Summary of a workshop on regulatory acceptance of (Q)SARs for human health and environmental endpoints. Environ. Health Perspect. **111**(10), 1358–1360 (2003)
48. N. Nikolova-Jeliazkova, J. Jaworska, An approach to determining applicability domains for QSAR group contribution models: An analysis of SRC KOWWIN. ATLA Altern. Lab. Anim. **33**(5), 461–470 (2005)
49. G. Patlewicz, A.O. Aptula, E. Uriarte, D.W. Roberts, P.S. Kern, G.F. Gerberick, I. Kimber, R.J. Dearman, C.A. Ryan, D.A. Basketter, An evaluation of selected global (Q)SARs/expert systems for the prediction of skin sensitisation potential. SAR QSAR Environ. Res. **18**, 515–541 (2007)
50. Y. Li, D. Pan, J. Liu, P.S. Kern, G.F. Gerberick, A.J. Hopfinger, Y.J. Tseng, Categorical QSAR models for skin sensitization based upon local lymph node assay classification measures Part 2: 4D-fingerprint three-state and two-2-state logistic regression models. Toxicol. Sci. **99**(2), 532–544 (2007)
51. Y. Li, Y.J. Tseng, D. Pan, J. Liu, P.S. Kern, G.F. Gerberick, A.J. Hopfinger, 4D-fingerprint categorical QSAR models for skin sensitization based on the classification of local lymph node assay measures. Chem. Res. Toxicol. **20**(1), 114–128 (2007)
52. G. Patlewicz, S.D. Dimitrov, L.K. Low, P.S. Kern, G.D. Dimitrova, M.I.H. Comber, A.O. Aptula, R.D. Phillips, J. Niemelä, C. Madsen, E.B. Wedebye, D.W. Roberts, P.T. Bailey, O. G. Mekenyan, TIMES-SS-A promising tool for the assessment of skin sensitization hazard. A characterization with respect to the OECD validation principles for (Q)SARs and an external evaluation for predictivity. Regul. Toxicol. Pharmacol. **48**(2), 225–239 (2007)
53. J. Liu, P.S. Kern, G.F. Gerberick, O.A. Santos-Filho, E.X. Esposito, A.J. Hopfinger, Y. J. Tseng, Categorical QSAR models for skin sensitization based on local lymph node assay measures and both ground and excited state 4D-fingerprint descriptors. J. Comput. Aided Mol. Des. **22**, 345–366 (2008)

54. C.E. Cowan, T.W. Federle, R.J. Larson, T.C. Feijtel, Impact of biodegradation test methods on the development and applicability of biodegradation QSARS. SAR QSAR Environ. Res. **5**(1), 37–49 (1996)
55. D.J. Versteeg, D.T. Stanton, M.A. Pence, C. Cowan, Effects of surfactants on the rotifer, Brachionus calyciflorus, in a chronic toxicity test and in the development of QSARs. Environ. Toxicol. Chem. **16**(5), 1051–1058 (1997)
56. L. Eriksson, J. Jaworska, A.P. Worth, M.T.D. Cronin, R.M. McDowell, P. Gramatica, Methods for reliability and uncertainty assessment and for applicability evaluations of classification- and regression-based QSARs. Environ. Health Perspect. **111**(10), 1361–1375 (2003)
57. S.H. Jackson, C.E. Cowan-Ellsberry, G. Thomas, Use of quantitative structural analysis to predict fish bioconcentration factors for pesticides. J. Agric. Food Chem. **57**(3), 958–967 (2009)
58. K. Binder, A. Milchev, Off-lattice Monte Carlo methods for coarse-grained models of polymeric materials and selected applications. J. Comput. Mater. Des. **9**, 33–74 (2002)
59. G. Zhao, J.R. Perilla, E.L. Yufenyuy, X. Ming, B. Chen, J. Ning, J. Ahn, A.M. Gronenborn, K. Schulten, C. Aiken, P. Zhang, Mature HIV-1 capsid structure by cryo-eletron microscopy and all-atom molecular dynamcs. Nature **497**(7451), 643–646 (2013)
60. K. Kremer, G.S. Grest, Dynamics of entangled linear polymer melts: A molecular-dynamics simulation. J. Chem. Phys. **92**(8), 5057 (1990)
61. R. Faller, Automatic coarse graining of polymers. Polymer (Guildf) **45**(11), 3869–3876 (2004)
62. P.T. Underhill, P.S. Doyle, On the coarse-graining of polymers into bead-spring chains. J. Nonnewton. Fluid Mech. **122**(1–3), 3–31 (2004)
63. F. Müller-Plathe, Coarse-graining in polymer simulation: from the atomistic to the mesoscopic scale and back. ChemPhysChem **3**(9), 755–769 (2002)
64. J.T. Padding, W.J. Briels, Systematic coarse-graining of the dynamics of entangled polymer melts: the road from chemistry to rheology. J. Phys.: Condens. Matter **23**(23), 233101 (2011)
65. P. Carbone, C. Avendaño, Coarse-grained methods for polymeric materials: enthalpy- and entropy-driven models. Wiley Interdiscip. Rev. Comput. Mol. Sci. **4**(1), 62–70 (2014)
66. A.J. Clark, J. McCarty, I.Y. Lyubimov, M.G. Guenza, thermodynamic consistency in variable-level coarse graining of polymeric liquids. Phys. Rev. Lett. **109**(16), 168301 (2012)
67. A.J. Clark, J. McCarty, M.G. Guenza, Effective potentials for representing polymers in melts as chains of interacting soft particles. J. Chem. Phys. **139**(12), 124906 (2013)
68. J.-L. Barrat, J. Baschnagel, A.V. Lyulin, Molecular dynamics simulations of glassy polymers. Soft Matter **6**(15), 3430 (2010)
69. K. Binder, W. Paul, Monte Carlo simulations of polymer dynamics : recent advances basics of the monte carlo method in statistical. J. Polym. Sci., Part B: Polym. Phys. **35**, 1–31 (1997)
70. G.M. Odegard, Prediction of Mechanical Properties of Polymers with Various Force Fields," no. April, pp. 1–12, 2005
71. S.C. Glotzer, W. Paul, Molecular and mesoscale simulation methods for polymer materials. Annu. Rev. Mater. Res. **32**(1), 401–436 (2002)
72. P.J. Hoogerbrugge, J.M.V.A. Koelman, Simulating Microscopic Hydrodynamic Phenomena with Dissipative Particle Dynamics. Europhys. Lett. **19**(3), 155 (1992)
73. R.D. Groot, P.B. Warren, Dissipative particle dynamics: Bridging the gap between atomistic and mesoscopic simulation. J. Chem. Phys. **107**(11), 4423–4435 (1997)
74. R.D. Groot, T.J. Madden, D.J. Tildesley, On the role of hydrodynamic interactions in block copolymer microphase separation. J. Chem. Phys. **110**(19), 9739 (1999)
75. S. Kumar, R.G. Larson, Brownian dynamics simulations of flexible polymers with spring–spring repulsions. J. Chem. Phys. **114**(15), 6937 (2001)
76. F. Goujon, P. Malfreyt, D.J. Tildesley, Mesoscopic simulation of entanglements using dissipative particle dynamics: application to polymer brushes. J. Chem. Phys. **129**(3), 034902 (2008)

77. S. Li, W.K. Liu, Meshfree and particle methods and their applications. Appl. Mech. Rev. **55** (1), 1 (2002)
78. M.B. Liu, G.R. Liu, Smoothed particle hydrodynamics (sph): An overview and recent developments. Arch. Comput. Methods Eng. **17**(1), 25–76 (2010)
79. P. Español, M. Revenga, Smoothed dissipative particle dynamics. Phys. Rev. E **67**(2), 026705 (2003)
80. P.S. Doyle, P.T. Underhill, *Brownian Dynamics Simulations of Polymers and Soft Matter*, pp. 2619–2630, 2005
81. C. Cruz, F. Chinesta, G. Régnier, Review on the Brownian Dynamics Simulation of Bead-Rod-Spring Models Encountered in Computational Rheology. Arch. Comput. Methods Eng. **19**(2), 227–259 (2012)
82. G.H. Fredrickson, *The equilibrium theory of inhomogeneous polymers* (Oxford University Press, Oxford, 2006)
83. J.G.E.M. Fraaije, B.A.C. Van Vlimmeren, N.M. Maurits, M. Postma, O.A. Evers, C. Hoffmann, P. Altevogt, I Introduction, A General, "The dynamic mean-field density functional method and its application to the mesoscopic dynamics of quenched block copolymer melts. J. Chem. Phys. **106**(10), 4260–4269 (2001)
84. P. Altevogt, O.A. Evers, J.G.E.M. Fraaije, N.M. Maurits, B.A.C. Van Vlimmeren, J. Mol. Struct. (Theochem) **463**, 139–143 (1999)
85. V. Ganesan, G.H. Fredrickson, Field-theoretic polymer simulations. Europhys. Lett. **55**(6), 814 (2001)
86. A.M. Stoneham, J.H. Harding, Not too big, not too small: the appropriate scale. Nat. Mater. **2** (2), 77–83 (2003)
87. T. Gates, G.M. Odegard, S. Frankland, T. Clancy, Computational materials: Multi-scale modeling and simulation of nanostructured materials. Compos. Sci. Technol. **65**(15–16), 2416–2434 (2005)
88. B. Ensing, S.O. Nielsen, P.B. Moore, M.L. Klein, M. Parrinello, Energy conservation in adaptive hybrid atomistic/coarse-grain molecular dynamics. J. Chem. Theory Comput. **3**(3), 1100–1105 (2007)
89. S.O. Nielsen, P.B. Moore, B. Ensing, Adaptive Multiscale Molecular Dynamics of Macromolecular Fluids. Phys. Rev. Lett. **105**(23), 237802 (2010)
90. M. Praprotnik, L.D. Site, K. Kremer, Multiscale simulation of soft matter: from scale bridging to adaptive resolution. Annu. Rev. Phys. Chem. **59**, 545–571 (2008)
91. A.J. Rzepiela, M. Louhivuori, C. Peter, S.J. Marrink, Hybrid simulations: combining atomistic and coarse-grained force fields using virtual sites. Phys. Chem. Chem. Phys. **13** (22), 10437–10448 (2011)
92. F.F. Abraham, J.Q. Broughton, N. Bernstein, Spanning the length scales in dynamic simulation. Am. Inst. Phys. **12**(6), 538 (1998)
93. W.A. Curtin, R.E. Miller, Atomistic / continuum coupling in computational. Model. Simul. Mater. Sci. Eng. **11**, R33 (2003)
94. S.P. Xiao, T. Belytschko, A bridging domain method for coupling continua with molecular dynamics. Comput. Methods Appl. Mech. Eng. **193**(17–20), 1645–1669 (2004)
95. W.K. Liu, H.S. Park, D. Qian, E.G. Karpov, H. Kadowaki, G.J. Wagner, Bridging scale methods for nanomechanics and materials. Comput. Methods Appl. Mech. Eng. **195**(13–16), 1407–1421 (2006)
96. B. Eidel, A. Stukowski, A variational formulation of the quasicontinuum method based on energy sampling in clusters. J. Mech. Phys. Solids **57**(1), 87–108 (2009)
97. B. Liu, Y. Huang, H. Jiang, S. Qu, K.C. Hwang, The atomic-scale finite element method. Comput. Methods Appl. Mech. Eng. **193**(17–20), 1849–1864 (2004)
98. S. Kohlhoff, P. Gumbsch, H.F. Fischmeister, Crack propagation in b.c.c. crystals studied with a combined finite-element and atomistic model. Philos. Mag. A **64**(4), 851–878 (1991)
99. L.E. Shilkrot, R.E. Miller, W.A. Curtin, Multiscale plasticity modeling: coupled atomistics and discrete dislocation mechanics. J. Mech. Phys. Solids **52**(4), 755–787 (2004)

100. S. Badia, M. Parks, P. Bochev, M. Gunzburger, R. Lehoucq, On atomistic-to-continuum coupling by blending. Multiscale Model. Simul. **7**(1), 381–406 (2008)
101. Q. Yang, E. Biyikli, A.C. To, Multiresolution molecular mechanics: Statics. Comput. Methods Appl. Mech. Eng. **258**, 26–38 (2013)
102. M. Laso, H.C. Öttinger, Calculation of viscoelastic flow using molecular models: the connffessit approach. J. Nonnewton. Fluid Mech. **47**, 1–20 (1993)
103. K. Feigl, M. Laso, H.C. Ottinger, CONNFFESSIT approach for solving a two-dimensional viscoelastic fluid problem. Macromolecules **28**(9), 3261–3274 (1995)
104. M.C. Araújo, J.P. Martins, S.M. Mirkhalaf, S. Lanceros-Mendez, F.M.A. Pires, R. Simoes, Predicting the mechanical behavior of amorphous polymeric materials under strain through multi-scale simulation. Appl. Surf. Sci. **306**, 37–46 (2014)
105. I. Noda, M.M. Satkowski, A.E. Dowrey, C. Marcott, Polymer alloys of nodax copolymers and poly (lactic acid). Macromol. Biosci. **4**, 269–275 (2004)
106. I. Noda, S.B. Lindsey, D. Caraway, *Nodax ™ Class PHA Copolymers : Their Properties and Applications*, vol. 14, (2010)
107. H. Alata, T. Aoyama, Y. Inoue, Effect of aging on the mechanical properties of poly (3-hydroxybutyrate- co -3-hydroxyhexanoate). Macromolecules **40**(13), 4546–4551 (2007)
108. D. Brown, J.H.R. Clarke, Molecular dynamics computer simulation of polymer fiber microstructure. J. Chem. Phys. **84**(5), 2858 (1985)
109. D. Brown, J.H.R. Clarke, Molecular dynamics simulation of an amorphous polymer under tension. 1. phenomenology. Macromolecules **24**, 2075–2082 (1991)
110. M. Parrinello, A. Rahman, Strain fluctuations and elastic constants. J. Chem. Phys. **76**(5), 2662–2666 (1982)
111. D.N. Theodorou, U.W. Suter, Atomistic modeling of mechanical properties of polymeric glasses. Macromolecules **19**, 139–154 (1986)
112. J.R. Ray, *Elastic constants and statistical ensembles in molecular dynamics* (North-Holland, Amsterdam, 1988)
113. A.V. Lyulin, N.K. Balabaev, M.A. Mazo, M.A.J. Michels, Molecular dynamics simulation of uniaxial deformation of glassy amorphous atactic polystyrene. Macromolecules **37**(23), 8785–8793 (2004)
114. A.V. Lyulin, B. Vorselaars, M.A. Mazo, N.K. Balabaev, M.A.J. Michels, Strain softening and hardening of amorphous polymers: Atomistic simulation of bulk mechanics and local dynamics. Europhys. Lett. **71**(4), 618–624 (2005)
115. F.M. Capaldi, M. Boyce, G. Rutledge, Enhanced mobility accompanies the active deformation of a glassy amorphous polymer. Phys. Rev. Lett. **89**(17), 175505 (2002)
116. F.M. Capaldi, M.C. Boyce, G.C. Rutledge, Molecular response of a glassy polymer to active deformation. Polymer (Guildf) **45**(4), 1391–1399 (2004)
117. J. Rottler, M. Robbins, Yield conditions for deformation of amorphous polymer glasses. Phys. Rev. E **64**(5), 051801 (2001)
118. R.S. Hoy, M.O. Robbins, *Strain Hardening of Polymer Glasses: Entanglements, Energetics, and Plasticity*, vol. 21218, (2008)
119. V. Sudarkodi, S. Basu, Investigations into the origins of plastic flow and strain hardening in amorphous glassy polymers. Int. J. Plast **56**, 139–155 (2014)
120. K. Yoshimoto, T. Jain, K. Van Workum, P. Nealey, J. de Pablo, Mechanical heterogeneities in model polymer glasses at small length scales. Phys. Rev. Lett. **93**(17), 175501 (2004)
121. K. Van Workum, J.J. De Pablo, Local elastic constants in thin films of an FCC crystal. Phys. Rev. E **67**(3), 31601 (2002)
122. K. Van Workum, J.J. De Pablo, U.V Wisconsin-madison, Computer simulation of the mechanical nanostructures, pp. 3–8 (2003)
123. E. Riccardi, M.C. Böhm, F. Müller-Plathe, Molecular dynamics method to locally resolve poisson's ratio: mechanical description of the solid–soft-matter interphase. Phys. Rev. E **86** (3), 036704 (2012)
124. G. Odegard, Constitutive modeling of nanotube–reinforced polymer composites. Compos. Sci. Technol. **63**(11), 1671–1687 (2003)

125. S. Frankland, The stress–strain behavior of polymer–nanotube composites from molecular dynamics simulation. Compos. Sci. Technol. **63**(11), 1655–1661 (2003)
126. M. Griebel, J. Hamaekers, Molecular dynamics simulations of the elastic moduli of polymer-carbon nanotube composites. Comput. Methods Appl. Mech. Eng. **193**, 1773–1788 (2004)
127. G.M. Odegard, T.C. Clancy, T.S. Gates, Modeling of the mechanical properties of nanoparticle/polymer composites. Polymer (Guildf) **46**(2), 553–562 (2005)
128. E.B. Stukalin, J.F. Douglas, K.F. Freed, Plasticization and antiplasticization of polymer melts diluted by low molar mass species. J. Chem. Phys. **132**, 84504 (2010)
129. R.A. Riggleman, K. Yoshimoto, J. Douglas, J. de Pablo, Influence of confinement on the fragility of antiplasticized and pure polymer films. Phys. Rev. Lett. **97**(4), 045502 (2006)
130. S.P. Delcambre, R.A. Riggleman, J.J. de Pablo, P.F. Nealey, Mechanical properties of antiplasticized polymer nanostructures. Soft Matter **6**(11), 2475 (2010)
131. Y. Xu, J. Feng, H. Liu, Y. Hu, Microphase separation of graft-diblock copolymer by dissipative particle dynamics simulation. Mol. Simul. **34**(5), 559–565 (2008)
132. X. Li, J. Guo, Y. Liu, H. Liang, Microphase separation of diblock copolymer poly (styrene-b-isoprene): A dissipative particle dynamics simulation study. J. Chem. Phys. **130** (7), 074908 (2009)
133. J.-J. Wang, Z.-Z. Li, X.-P. Gu, L.-F. Feng, C.-L. Zhang, G.-H. Hu, A dissipative particle dynamics study on the compatibilizing process of immiscible polymer blends with graft copolymers. Polymer (Guildf) **53**(20), 4448–4454 (2012)
134. A.A. Gavrilov, Y.V. Kudryavtsev, P.G. Khalatur, A.V. Chertovich, Microphase separation in regular and random copolymer melts by DPD simulations. Chem. Phys. Lett. **503**(4–6), 277–282 (2011)
135. Y. Zhu, Z. Ma, Y. Li, J. Cui, W. Jiang, Monte Carlo simulation of the compatibility of graft copolymer compatibilized two incompatible homopolymer blends: Effect of graft structure. J. Appl. Polym. Sci. **105**(3), 1591–1596 (2007)
136. L. Zhou, J. Zhang, J. Fang, B. Sun, Ordered microstructures self-assembled from A 2 m + 1 B m C m comblike copolymers. J. Polym. Res. **18**(5), 1053–1058 (2010)
137. K.C. Daoulas, M. Müller, Single chain in mean field simulations: quasi-instantaneous field approximation and quantitative comparison with Monte Carlo simulations. J. Chem. Phys. **125**(18), 184904 (2006)
138. M. Muller, G.D. Smith, Phase separation in binary mixtures containing polymers: a quantitative comparison of single-chain-in-mean-field simulations and computer simulations of the corresponding multichain systems. J. Polym. Sci., Part B: Polym. Phys. **43**(8), 934–958 (2005)
139. N.M. Maurits, A.V. Zvelindovsky, G.J.A. Sevink, B.A.C. van Vlimmeren, J.G.E.M. Fraaije, Hydrodynamic effects in three-dimensional microphase separation of block copolymers: Dynamic mean-field density functional approach. J. Chem. Phys. **108**(21), 9150 (1998)
140. T. Honda, T. Kawakatsu, Hydrodynamic effects on the disorder-to-order transitions of diblock copolymer melts. J. Chem. Phys. **129**(11), 114904 (2008)
141. L. Zhang, A. Sevink, F. Schmid, Hybrid lattice boltzmann/dynamic self-consistent field simulations of microphase separation and vesicle formation in block copolymer systems. Macromolecules **44**(23), 9434–9447 (2011)
142. P. Sandhu, J. Zong, D. Yang, Q. Wang, On the comparisons between dissipative particle dynamics simulations and self-consistent field calculations of diblock copolymer microphase separation. J. Chem. Phys. **138**(19), 194904 (2013)
143. T. Visser, M. Wessling, When do sorption-induced relaxations in glassy polymers set in? Macromolecules **40**(14), 4992–5000 (2007)
144. S.P. Nalawade, F. Picchioni, L.P.B.M. Janssen, Supercritical carbon dioxide as a green solvent for processing polymer melts: processing aspects and applications. Prog. Polym. Sci. **31**(1), 19–43 (2006)
145. A.A. Gusev, U.W. Suter, Dynamics of small molecules in dense polymers subject to thermal motion. J. Chem. Phys. **99**(3), 2228 (1993)

146. T. Spyriouni, G.C. Boulougouris, D.N. Theodorou, Prediction of sorption of CO_2 in glassy atactic polystyrene at elevated pressures through a new computational scheme. Macromolecules **42**(5), 1759–1769 (2009)
147. I. Cozmuta, M. Blanco, W.A.G. Iii, Gas sorption and barrier properties of polymeric membranes from molecular dynamics and Monte Carlo simulations. J. Phys. Chem. B **111** (12), 3151–3166 (2007)
148. O. Hölck, M. Böhning, M. Heuchel, M.R. Siegert, D. Hofmann, Gas sorption isotherms in swelling glassy polymers—detailed atomistic simulations. J. Memb. Sci. **428**, 523–532 (2013)
149. H. Abou-Rachid, L.-S. Lussier, S. Ringuette, X. Lafleur-Lambert, M. Jaidann, J. Brisson, On the correlation between miscibility and solubility properties of energetic plasticizers/polymer blends: modeling and simulation studies. Propellants, Explos. Pyrotech. **33**(4), 301–310 (2008)

Afterword

Do we need yet another book about materials and manufacturing such as this one? My answer is yes. First of all, we are currently living in times with rapid societal changes and challenges, and also with increasing complexity in terms of products and services. Out of these challenges, the necessity of a delivering a sustainable, more resource-efficient future is one of the most urgent ones—materials and the production of new sustainable products from them will play an increasingly important role. Secondly, from an industry perspective the coupling of materials development and manufacturing is key, if we are going to deliver the innovations needed to create growth and thus jobs. Thirdly, there is an urgent need to ensure that we motivate students, of both genders, to undertake studies in these fields, and also that we have exciting university curricula that really focuses on the interplay between materials science and advanced manufacturing. The largest impact universities have on societal development is through their graduates. Furthermore, the book is also interesting, highly informative and very timely for anyone already working in either the materials or manufacturing fields. With ten companies ranging from small businesses through to conglomerates contributing to the content, it provides a broad perspective.

Already today there are several universities that combine materials research with manufacturing. For example, at Chalmers University of Technology in Sweden, an institution that I know well, there is a department of Materials and Manufacturing Technology. This department carries out research activities that span from basic research of nanostructured materials to manufacturing processes for new products. Similar departments can be found, e.g., at The University of Nottingham in the United Kingdom and the Worcester Polytechnic Institute in the United States, but this is far from the norm. More often, Materials Science and Engineering (MSE) departments exist separately from manufacturing or industrial engineering. Additionally, MSE, as a discipline, is often overlooked by students entering university. For example, in the United States, only a small proportion ($\sim 1.5\%$) of students obtaining a bachelor's degree in engineering has materials declared as their major (according to the Science and Engineering Indicators for 2011). The percentage goes up for doctorate degrees, to $\sim 7.7\%$, but still is quite small.

L.D. Madsen and E.B. Svedberg (eds.), *Materials Research for Manufacturing*, Springer Series in Materials Science 224,
DOI 10.1007/978-3-319-23419-9

For me, it is obvious that in order to create real breakthroughs, and thus innovations resulting from new materials, one needs research and development that is carried out in cooperation by scientists and engineers with a wide range of disciplinary knowledge. This aspect clearly shines through in the book:

> *"The ASMC team was built around key people with backgrounds in chemistry, physics, material science, mathematics, ceramics, geology, computer modeling, mechanical and electrical engineering."—American Superconductor*

> *"Such breakthroughs will come most quickly at the intersection of modeling and computational sciences with material science and engineering and the chemical, physical, and biological sciences."—Proctor and Gamble*

> *"Development… requires candidates with multidisciplinary focus and skills across materials science, nanotechnology, and polymer processing and chemistry."—American Process*

It follows, also, that students must be able to understand the importance and the interplay between different fields and also be able to work in multidisciplinary teams. This sentiment is found in several places in the book, e.g.:

> *"At large companies most of the high-impact projects are not done by individuals, but rather by teams of engineers and scientists having diverse backgrounds. Knowing how to comfortably work with such a team, both by being an active contributor and also by being confident and comfortable in trusting others, is very important."—General Electric*

Based on my experience of having been active both in academia and in the corporate world, I firmly believe that it is of utmost important that students obtain a solid grounding in the fundamentals. As well, they should find avenues to explore non-traditional pathways in obtaining their degrees to better understand the importance at the intersections of traditional fields. It is also imperative that scientists and engineers realize that the *soft skills*—communication, interpersonal skills, business sense, and leadership are enormously important to their success. Integration of these aspects into university curriculum is vital. Entrepreneurship is another area which is often left far too vague for new graduates. I believe that this book illustrates several of these aspects and that it takes a big step towards introducing and explaining the research field of materials and providing essential insights, in its truest form, within industry.

I commend the editors for having taking their time to gather so many skilled authors in several important fields to create a very valuable book that pinpoints the necessity of combining materials science and manufacturing development. Drs. Lynnette Madsen and Erik Svedberg, both have industrial backgrounds. Lynnette worked at a telecommunications company in Canada (Nortel Networks) for about a decade. Now, at the National Science Foundation, she deals primary with US-based academics, but through programs such as GOALI (mentioned in the KEMET Electronics chapter), has connections to industry. Erik also has a strong background in industry, having worked at Seagate Research for many years and also at a small start-up. In his job today at the National Academies, he has interactions through studies and workshops with all sectors of the workforce: industry, academia and government.

Before closing, I will mention three other aspects of the book that for me stand out as being important: manufacturing is also for women, there are green aspects to manufacturing, and we can no longer ignore the supply chain of raw materials.

Women that traditionally have been underrepresented in both the materials science and manufacturing fields are slowly gaining a stronger presence in the manufacturing aspects of industry. I am pleased to see two chapters (American Process and Catalytic Materials) with lead authors who are women, and women co-authors on several of the other chapters (e.g., Corning, GE Global, and IRradiance Glass). And, of course, I should mention that the Foreword was also written by a woman. I hope these examples encourage more young women into the field; their full participation is needed.

Several chapters also have a strong environmental—sustainability connection such as the chapters from the companies American Process and Dow Chemical. American Process works with nanocellulose—a material derived from wood pulp—which is naturally renewable and biodegradable with a sustainable life-cycle carbon footprint. They discuss incorporation of nanocellulose into plastics; applications with a large potential for growth. Dow Chemical deals with the topic of water purification. It is a complex issue, but they allow us to see more clearly how desalination and re-use are tackled. Access to clean fresh water is one of the large global sustainability challenges.

Two companies contributing to the chapters in the book are highly affected by the availability and cost of critical raw materials. In the Trans Tech chapter, the manufacture of both ceramic dielectric and magnetic components are discussed. As well, the design and adaptation to material price fluctuations and the inherent importance of having parallel activities to counter-balance changes is described. Undoubtedly, American Superconductor Corporation is affected by the supply chain. The most useful superconductors identified today have rare-earth elements in them; there is no way around this aspect at present. Their focus instead is on driving down cost in others ways, e.g., by increasing capacity and developing more cost-effective deposition methods, and in improving performance.

Although each chapter is in itself a treat, the interplay between them is also a delight. I hope you enjoy the book!

Jan-Eric Sundgren, Ph.D.
Senior Advisor, Volvo Group, Gothenburg, Sweden
Former President of Chalmers University of Technology and
Professor in Thin Film Material Science

Index

L.D. Madsen and E.B. Svedberg (eds.), *Materials Research for Manufacturing*, Springer Series in Materials Science 224,
DOI 10.1007/978-3-319-23419-9